

CONCEPTUAL DESIGN OF A LARGE, PASSIVE,
PRESSURE-TUBE LIGHT WATER REACTOR

by
Pavel Hejzlar

Master of Engineering (Nuclear), Czech Technical University, Czech Republic,
(June, 1981)

Submitted to the Department of Nuclear Engineering in
Partial Fulfillment of the Requirements for the
Degree of

DOCTOR OF SCIENCE IN NUCLEAR ENGINEERING

at the

MASSACHUSETTS INSTITUTE OF TECHNOLOGY

May 1994

© Massachusetts Institute of Technology 1994
All rights reserved

Signature of Author _____
Department of Nuclear Engineering
May 1994

Certified by _____
Neil E Todreas (Thesis Supervisor)
Professor, Nuclear Engineering

Michael J. Driscoll (Thesis Supervisor)
Professor Emeritus, Nuclear Engineering

Accepted by _____
Allan F. Henry
Chairman, Department Committee on Graduate Students

Science

MASSACHUSETTS INSTITUTE
OF TECHNOLOGY

JUN 30 1994

LIBRARIES

CONCEPTUAL DESIGN OF A LARGE, PASSIVE, PRESSURE-TUBE LIGHT WATER REACTOR

by

Pavel Hejzlar

Submitted to the Department of Nuclear Engineering on May 2, 1994 in
partial fulfillment of the requirements for the Degree of
Doctor of Science in Nuclear Engineering

ABSTRACT

A design for a large, passive, light water reactor has been developed. The proposed concept is a pressure tube reactor of similar design to CANDU reactors, but differing in three key aspects. First, a solid SiC-coated graphite fuel matrix is used in place of pin-rod bundles to enable the dissipation of decay heat from the fuel in the absence of primary coolant. Second, the heavy water coolant in the pressure tubes is replaced by light water, which serves also as the moderator. Finally, the calandria tank, surrounded by a graphite reflector, contains a low pressure gas instead of heavy water moderator, and the normally-voided calandria is connected to a light water heat sink. The cover gas keeps the light water out of the calandria during normal operation, while during loss of coolant or loss of heat sink accidents it allows passive calandria flooding. Calandria flooding also provides redundant and diverse reactor shutdown. The entire primary system is enclosed in a robust, free standing cylindrical steel containment cooled solely by buoyancy-induced air flow, and surrounded by a concrete shield building.

It is shown that the proposed reactor can survive loss of coolant accidents without scram and without replenishing primary coolant inventory, while the safe temperature limits on the fuel and pressure tube are not exceeded. It can cope with station blackout and anticipated transients without scram – the major traditional contributors to core damage frequency – without sustaining core damage. The fuel elements can operate under post-CHF conditions even at full power, without exceeding fuel design limits. The heterogeneous arrangement of the fuel and moderator ensures a negative void coefficient under all circumstances. Although light water is used as both coolant and moderator, the reactor exhibits high neutron thermalization and a large prompt neutron lifetime, similar to D₂O moderated cores. Moreover, the extremely large neutron migration length results in a strongly coupled core with a flat thermal flux profile, and inherent stability against xenon spatial oscillations.

Thesis Supervisor: Neil E. Todreas

Title: KEPCO Professor of Nuclear Engineering

Thesis Supervisor: Michael J. Driscoll

Title: Professor Emeritus of Nuclear Engineering

ACKNOWLEDGEMENTS

I would like to express my deepest gratitude to my thesis supervisors Professor Neil E. Todreas and Professor Michael J. Driscoll for their superb guidance and supervision. This research has largely benefitted from many of their ideas and expertise. Working under Prof. Todreas and Driscoll has been not only an honor and privilege, but also a very enriching experience for me both personally and professionally.

Special thanks are extended to Professor David D. Lanning and Professor Allan F. Henry for their insightful comments and suggestions in the area of reactor physics. I would also like to thank Professor John E. Meyer and Professor Peter Griffith for their time in answering my questions on critical heat flux, and Professor Scott A. Simonson for his help in the area of materials research. I would also like to extend my appreciation to the following people who supplied comments and information over the course of this thesis: Ralph S. Hart (AECL), Norm J. Spinks (AECL), A. White (Ontario Hydro), Roger Hilley (formerly of the Savannah River Laboratory), Massoud T. Simnad (University of California), O. M. Stansfield (ORNL), D. A. Petti (EG&G), R. Bennett (EG&G), H. Feinroth (Gamma Eng. Corp.), T. George (Numerical Applications, Inc.), K. Washington (SNL), D. Ambrosek (CEGA), M. Hrovat (NUKEM GmbH), A. Baxter (CEGA), C. P. Tzanos (ANL), J. Delene (ORNL), L. S. Tong (formerly of Westinghouse), D. C. Groeneveld (AECL), R. Pernica (UJV Rez), and R. E. Seamon (LANL).

The sponsorship of this study by the U.S. Department of Energy is acknowledged, and greatly appreciated. I am also grateful for the superb educational environment and support provided by MIT Nuclear Engineering Department.

I want to thank my precious wife Eliska for her patience, devotion, love and support and my children Michaela, Jonatan and Marcela for bearing with me when spending time in front of the computer screen instead of on the playground. My appreciation also goes to all my family in the Czech Republic for their constant care.

I would like to give special thanks to the Park Street Church Choir and their friends who provided additional financial support for my family during my study. I will always remember the great time and fellowship I had singing with them.

Finally, I give thanks to God, the Almighty, for giving us a world to study and enjoy and a mind to comprehend at least a tiny fraction of His marvelous creation.

TABLE OF CONTENTS

Abstract	2
Acknowledgements	3
Table of Contents	4
List of Figures	16
List of Tables	31
Nomenclature	35
Dedication	41
Chapter 1 Introduction and Background	42
1.1 Motivation.....	43
1.2 Background.....	45
1.2.1 Active and Passive Safety Approaches.....	46
1.2.2 Review of Advanced LWR Concepts	47
1.2.3 The Contribution of the Present Work	50
1.4 Objectives.....	52
1.4.1 Historical Design Objectives for Nuclear Power Reactors	52
1.4.2 Proposed New Design Objectives.....	53
1.4 Thesis Organization	56
Chapter 2 General Design Approach and Brief Description of a Concept	60
2.1 Introduction.....	60
2.2 Rationale Leading to a Passive Pressure Tube LWR.....	61
2.3 Brief Description of a PTLWR Concept.....	67
2.4 Reference Design Parameters	74
2.4.1 Core and Primary System Parameters.....	76
2.4.2 Fuel Channel Parameters	76
2.4.3 Flooding System Parameters	78
2.4.4 Containment Parameters.....	79

2.5	Imposed Design Limits.....	80
2.6	Summary.....	80
Chapter 3 Materials Considerations.....82		
3.1	Introduction.....	82
3.2	Design Requirements for Matrix and Reflector Materials	83
3.2.1	Matrix material	83
3.2.2	Reflector material.....	83
3.3	Matrix Materials	85
3.4	Reflector Materials.....	92
3.5	Fuel Materials.....	93
3.5.1	Particle Fuel.....	93
3.5.2	Clad Fuel.....	94
3.6	Structural Materials	97
3.7	Summary.....	98
Chapter 4 Reactor Physics.....100		
4.1	Introduction.....	100
4.2	Basic Neutron Transport Equation.....	103
4.3	Analysis Tools	107
4.3.1	The MCNP Computer Code.....	108
4.3.2	The ORIGEN2 Computer Code.....	110
4.4	Physics Aspects of Pressure Tube Reactors with Voided Lattice	111
4.4.1	Various Moderator Configurations in Voided Calandria	112
4.4.1.1	Classification of Calandria Designs.....	112
4.4.1.2	Effects of Moderator Arrangement on Multiplication Factor in a High-Streaming Lattice	115
4.4.2	MCNP Models.....	119
4.4.2.1	MCNP Model of a Dry Calandria Cell with One Fuel Channel (Model #1)	119
4.4.2.2	Full Core Mockup (Model #2)	122

4.4.2.3 Full Core Mockup with Movable Control Rods and Variable Water Level in the Calandria (Model #3).....	124
4.4.2.4 A Two Channel MCNP Model With Variable Fuel Composition for Bi-directional Refueling Scheme (Model #4).....	128
4.4.3 Double Heterogeneity Effects	131
4.4.4 Physics Characteristics of the Dry Calandria Design.....	135
4.4.4.1 Introduction	135
4.4.4.2 Long Prompt Neutron Lifetime	135
4.4.4.3 Flat Thermal Flux Profile.....	140
4.4.4.4 Tight Neutronic Core Coupling	149
4.4.4.5 Well Thermalized Neutron Spectrum	154
4.4.4.6 High Thermal Flux Level and Fast Fluence.....	154
4.4.4.7 Strong Negative Doppler Coefficient.....	163
4.4.4.8 Negative Void Coefficient.....	166
4.4.4.9 Less Efficient Neutron Economy.....	168
4.4.4.10 Slightly Positive Reflector Temperature Coefficient.....	169
4.4.4.11 Comparison with PWR and CANDU.....	172
4.4.4.12 Summary of PTLWR Physics Characteristics	172
4.4.5 Reactor Control Considerations.....	175
4.4.6 Secondary Criticality Study During Reflood and Inadvertent Flooding.....	180
4.4.6.1 Introduction	180
4.4.6.2 In-Channel and Out-of-Channel Water Worth	182
4.4.6.3 Maximum density of steam/water mixture in the calandria space.....	185
4.4.6.4 Reflooding Process.....	187
4.4.6.5 Inadvertent Flooding Process.....	189
4.4.6.6 Hypothetical Spraying of Calandria Space without Flooding.....	195
4.4.6.7 Summary of Reactivity Behavior During Calandria Flooding.....	196
4.4.7 Burnup Study.....	197
4.4.7.1 Introduction	197

4.4.7.2	MCNP + ORIGEN2 Model	198
4.4.7.3	Burnup Results.....	201
4.4.7.4	Summary of Burnup Study	203
4.4.8	On-line Refueling Schemes.....	204
4.4.8.1	Introduction	204
4.4.8.2	Fresh Core with Uniform Enrichment and Model Consistency.....	206
4.4.8.3	Estimate of Burnup Penalty using Burnable Poison	207
4.4.8.4	Refueling Schemes Considered.....	210
4.4.8.5	Reactivity Deficit During Fuel Channel Refueling.....	224
4.4.8.6	Summary of On-Line Refueling Schemes	224
4.4.9	Disposal of Weapons-grade Plutonium.....	225
4.4.9.1	Review of Options for Pu burning	226
4.4.9.2	Challenges Posed by 100% MOX Fuel in a LWR.....	227
4.4.9.3	Consideration of Plutonium Burning in the PTLWR.....	228
4.4.10	Summary.....	234
Chapter 5	Fuel Matrix Concepts	236
5.1	Introduction.....	236
5.2	Basic Factors Influencing the Suitability of Matrix Design.....	237
5.2.1	Reactor Physics Factors of Merit	237
5.2.2	Thermohydraulics during Normal Operation.....	243
5.2.3	Thermohydraulics during LOCA	244
5.2.4	Materials Compatibility during Normal Operation and during Accidents.....	245
5.3	Proposed Dry Calandria Fuel Matrix Designs	246
5.3.1	DC-1 – A Two-ring Design with TRISO Particle Fuel in an SiC Tube.....	246
5.3.2	DC-2 – A Two-ring Design with SiC-Cladded UO ₂ Fuel Pins	254
5.3.3	DC-3 – A Fuel Matrix Design with Separate Fuel Compacts and Coolant Channels.....	258

5.3.4 DC-4 – A Fuel Matrix Design with Particle Fuel Dispersed in a Matrix.....	261
5.3.5 DC-5 – A Fuel Matrix Design with TRISO Particles Contained in an SiC Structure.....	263
5.4 Summary and Conclusion	266

Chapter 6 Fuel Matrix Performance under Normal Operating

Conditions.....	270
6.1 Introduction.....	270
6.2 Primary System Configuration and Coolant Conditions.....	271
6.3 Analysis Tools	273
6.3.1 The ALGOR Code.....	276
6.4 Analysis of Fuel Channel Thermohydraulics.....	277
6.4.1 Fundamental Equations and Simplifying Assumptions.....	277
6.4.2 Flow Distribution in Parallel Non-communicating Channels.....	279
6.4.3 Power Density Distribution and Heat Flux to Coolant.....	285
6.4.4 Energy Balance and Channel Wall Temperature Profile	289
6.4.5 Heat Transfer Coefficient and Friction Factor for Rough Surface.....	296
6.4.6 Critical Heat Flux.....	299
6.4.7 Post-CHF Heat Transfer.....	304
6.5 Discussion of the Results	305
6.5.1 Fresh Core.....	305
6.5.1.1 Thermohydraulics during Normal Operation.....	305
6.5.1.2 Fuel Matrix Analysis.....	311
6.5.1.3 Matrix Performance in Post-CHF Regime.....	315
6.5.1.4 Flow Instability Considerations.....	316
6.5.2 Equilibrium Core.....	321
6.5.2.1 Thermohydraulics during Normal Operation.....	322
6.5.2.2 Fuel Matrix Analysis.....	325
6.6 Summary.....	328

Chapter 7 Fuel Matrix Performance in a Loss of Coolant Accident.....330

7.1	Introduction.....	330
7.2	Decay Heat Generation in the Fuel Matrix	332
7.3	Considerations of Increased Contact Surface Between Matrix and Pressure Tube	335
7.4	Analysis of Transient Heat Transfer Performance.....	339
7.4.1	Introduction	339
7.4.2	A Simplified 1-D Model for Analysis of Transient Heat Transfer in a Fuel Matrix-Pressure Tube Configuration.....	340
7.4.2.1	Fundamental Equations and Simplifying Assumptions.....	340
7.4.2.2	Transition from a 2-D problem to a 1-D model	346
7.4.2.3	Natural Convection Heat Transfer in the Gap Between the Matrix and Pressure Tube	352
7.4.2.4	Numerical solution of Heat Conduction Equation	354
7.4.2.5	Power Generation in the Fuel Matrix.....	359
7.4.2.6	Contact Resistance between Fuel Compacts and Graphite Matrix	364
7.4.3	Analysis of the Fresh Core.....	365
7.4.3.1	Adiabatic Matrix Heatup.....	368
7.4.3.3	LOCA without Scram.....	370
7.4.4	Analysis of Equilibrium Core in Bi-directional Refueling Scheme.....	376
7.4.5	Finite Element 2-D Model for Quasi-steady Analysis of Fuel Matrix.....	378
7.4.5.1	Benchmark of 1-D Simplified Model against 2-D Model	378
7.4.5.2	Detailed Maximum Temperature Profile of Voided Fuel Matrix.....	379
7.4.6	Summary	381
Chapter 8 Calandria Passive Flooding.....		382
8.1	Introduction.....	382
8.2	Flooding Initiation Schemes.....	383
8.2.1	Passive Fluid-Operated Valve	384

8.2.2 DC-Powered Blower	387
8.3 Description of Passive Calandria Flooding System	389
8.4 Flooding Analysis	392
8.4.1 The Simplified Flooding Model.....	392
8.4.2 Estimate of the Steam Amount Escaping from the Flooded Space to the Upper Gas Space	399
8.4.3 Discussion of the Results.....	400
8.5 Summary.....	407
Chapter 9 Fuel Channel Considerations under Performance- Limiting Conditions	408
9.1 Introduction.....	408
9.2 Fuel Channel Description.....	409
9.3 Fuel Channel Challenges and CANDU Experience.....	410
9.3.1 Comparison of Key Conditions Affecting Pressure Tube Lifetime	411
9.3.2 Effects of Elevated Fast Neutron Flux.....	413
9.3.2.1 Dimensional Changes.....	413
9.3.2.2 Property Changes.....	416
9.3.3 Effects of Elevated Coolant Pressure and Temperature.....	418
9.3.4 Effects of the PTLWR Fuel Channel Design on Hydrogen and Delayed Hydride Cracking	419
9.4 Stress Analysis of the Pressure Tube.....	420
9.5 Quenching of Hot Calandria Tubes	425
9.6 Summary.....	431
Chapter 10 Reflector and Control Rod Cooling Considerations.....	433
10.1 Introduction	433
10.2 Reflector Heating.....	433
10.3 Reflector Cooling Concepts	437
10.3.1 Cooling of the Axial Reflector	437
10.3.2 Cooling of the Radial Reflector.....	439
10.4 Control Rod Cooling.....	445
10.5 Summary	446
Chapter 11 Passive Containment Design and Analysis.....	447
11.1 Introduction	447

11.2	Principal Considerations.....	448
11.3	Containment Configuration.....	450
11.4	Passive Cooling Considerations.....	455
11.5	Containment Analysis.....	459
11.5.1	Containment Design Basis and Beyond Design Basis Considerations.....	460
11.5.2	Analysis Tools.....	464
11.5.2.1	CONTAIN Computer Code.....	465
11.5.2.2	GOTHIC Computer Code.....	467
11.5.3	A 1-Cell CONTAIN model.....	468
11.5.3.1	Case 1 Double-Ended Rupture of a Hot Header at the Surge Line Connection with Isolation Valve Functioning.....	472
11.5.3.2	Case 2 Double-ended Rupture of a Hot Header at the Surge Line Connection, with Isolation Valve Failure.....	492
11.5.3.3	Case 3 Main Steam Line Break with Main Steam Isolation Valve Failure.	494
11.5.3.4	Case 4 Combined Double-ended Rupture of a Hot Header at the Surge Line Connection, with Isolation Valve Failure and Steam Line Break with Main Steam Isolation Valve Failure.....	494
11.5.4	A 9-Cell CONTAIN Model.....	499
11.5.4.1	Model Description.....	499
11.5.4.2	Analysis of Case 2 with the 9-Cell Model	503
11.5.5	Investigation of Effects of Thermal Stratification Inside Containment on Passive Containment Cooling Using GOTHIC	505
11.5.5.1	Introduction	505
11.5.5.2	Lumped Parameter GOTHIC Model.....	506
11.5.5.3	Key Factors Affecting Thermal Stratification.....	513
11.5.5.4	Conclusions.....	527
11.6	Summary.....	530
Chapter 12 Assessment of PTLWR System Response to Accidents.....		532

12.1	Introduction	532
12.2	Incidents of Moderate frequency.....	535
12.2.1	Loss of Regulation.....	535
12.2.2	Inadvertent Opening of SG Relief or Safety Valve.....	536
12.2.3	Excessive Increase in Secondary Steam Flow	537
12.2.4	Turbine Trip, Loss of External Electrical Load, and Inadvertent Closure of Main Steam Isolation Valve.....	538
12.2.5	Partial or Loss of Forced Reactor Coolant Flow	539
12.2.6	Loss of Normal Feedwater Flow.....	540
12.2.7	Chemical and Volume Control System Malfunction.....	540
12.2.8	Loss of Auxiliary AC Power	541
12.2.9	Increase in Feedwater Flow or Decrease in Feedwater Temperature.....	542
12.2.10	Inadvertent Opening of Pressurizer Safety or Relief Valve or Instrument Line Break	542
12.3	Infrequent Events.....	543
12.3.1	Complete Loss of Forced Reactor Coolant Flow	543
12.3.2	Refueling Incidents.....	544
12.3.3	Flow Blockage of a Coolant Channel.....	545
12.3.4	Small Loss of Coolant Accidents	547
12.4	Limiting Faults.....	550
12.4.1	Steam Line Break.....	550
12.4.2	Reactor Coolant Pump Shaft Seizure.....	551
12.4.3	Feedwater System Pipe Break.....	552
12.4.4	Large Break Loss of Coolant Accidents	553
12.5	Special events.....	554
12.5.1	Station Blackout.....	554
12.5.2	Anticipated Transients without Scram.....	555
12.6	Summary	557
Chapter 13 Economic Considerations		562
13.1	Introduction	562
13.2	Fuel Cycle Cost Estimate	562
13.3	Capital Cost: Qualitative Estimate	571
13.4	Operating and Maintenance Costs: Qualitative Estimate.....	572
13.5	Summary	573

Chapter 14 Overall Summary Description of the Integrated PTLWR	
Design	575
14.1 Introduction	575
14.2 Key Objectives and Rationale.....	576
14.3 Design description and main design parameters	577
14.4 Reactor Physics Characteristics.....	585
14.4.1 Method of Analysis.....	588
14.4.2 Long Prompt Neutron Lifetime.....	589
14.4.3 Flat Thermal Flux Profile	589
14.4.4 Tight Neutronic Coupling	591
14.4.5 Well-Thermalized Neutron Spectrum.....	591
14.4.6 High Thermal Flux and Fast Fluence	593
14.4.7 Large Negative Doppler Coefficient	594
14.4.8 Negative Coolant Void Coefficient	595
14.4.9 Less Efficient Neutron Economy	596
14.4.10 Slightly Positive Reflector Temperature Coefficient.....	596
14.4.11 Diverse and Redundant Shutdown.....	597
14.4.12 High Discharge Burnup.....	600
14.5 Fuel Channel Thermal Hydraulic Characteristics During Normal Operation	601
14.5.1 Method of Analysis.....	601
14.5.2 Performance for the Fresh Core.....	602
14.5.3 Matrix Performance in Post-CHF Regime.....	604
14.5.4 Performance for the Equilibrium Core.....	605
14.6 Fuel Channel Characteristics During LOCA.....	607
14.6.1 Method of Analysis	608
14.6.2 Fuel Channel Performance in LOCA without Scram	609
14.7 Passive Flooding Characteristics.....	613
14.8 Containment Design Characteristics.....	615
14.8.1 Containment Design Features.....	615
14.8.2 Analysis Results.....	617
14.8 PTLWR Performance in Various Accidents.....	624
14.9 Comparison with Other Reactor Designs.....	625
14.10 Conclusions and Future Work Recommendations	629
Chapter 15 Conclusions and Future Work Directions.....	631

15.1	Conclusions.....	631
15.2	Future Work Directions	633
15.2.1	Comprehensive Detailed Analysis of the Proposed Concept	633
15.2.2	Improvements and Modifications of the Proposed Concept	636
15.2.3	New Promising Alternatives for a Passive Pressure Tube Reactor.....	638
15.2.2.1	PTLWR for the Disposal of Weapons-Grade Plutonium.....	639
15.2.2.2	PTLWR Thermal Breeder.....	639
15.2.2.3	Passive Pressure Tube Reactors with Alternative Coolants.....	641
	References	649
	Appendix A Reactor Physics	672
A.1	Benchmark of MCNP on PWR and CANDU Lattices.....	672
A.2	Benchmark of MCNP+ORIGEN2 Tandem Against PWR Burnup Curve.....	672
	Appendix B Critical Heat Flux Correlations	675
B.1	Review of Considered CHF Correlations.....	675
B.1.1	W-3 Correlation.	675
B.1.2	Pernica and Cizek Correlation (PI-1).....	677
B.1.3	Bowring Correlation.....	678
B.1.4	Shah Correlation.	678
B.1.5	AECL Lookup Table.....	680
B.1.5	Katto Correlation	682
B.2	Two Methods for Calculating the CHF Margins in Subcooled or Low-Quality Regions	684
B.3	Comparison of the Selected Correlations	692
	Appendix C Passive Containment Cooling and Analysis	695
C.1	Controlling Heat Transfer Resistance Between Containment Atmosphere and Ambient Air.....	695

C.2 RISRAD - A Computer Program for Evaluation of Heat Transfer from a Cylindrical Body Cooled by Coupled Convection to Buoyancy-induced Air Flow and Radiation	697
C.2.1 Problem Formulation and the Assumptions Employed	697
C.2.2 Brief Description of the Model	700
C.2.2.1 Heat balance	700
C.2.2.2 Determination of Mass Flow Rate.....	701
C.2.2.3 Solution Procedure	704
C.2.2.4 Correlation for the Heat Transfer Coefficient to Air Flow in an Annular Gap.....	707
C.2.2.5 Comparison of Smooth Wall Correlations.....	712
C.2.3 Verification of the RISRAD Code.....	715
C.2.4 Heat Rate Removable from the Containment Wall.....	717
C.2.4.1 Bare Containment Wall without Chimney.....	718
C.2.4.2 Bare Containment Wall with Chimney	720
C.2.4.3 Ribbed Containment Wall without Chimney	721
C.3 FINAIR – A Computer Program for Evaluation of Heat Transfer from a Finned Containment Wall Surrounded by a Supporting shell.....	722
C.3.1 Description of the Model.....	722
C.3.1.1 Derivation of Effective Heat Transfer Coefficient.....	722
C.3.1.2 Determination of Mass Flow Rate.....	728
C.3.2 Achievable Heat Rates Removable from the Finned Containment Wall	730

LIST OF FIGURES

2-1	Principles to maximize reactor power rating set by decay heat removal limits, in the total absence of coolant, and their application in the passive pressure tube LWR.....	62
2-2	Various fuel matrix configurations in a LWR core and road to fuel modularity.....	64
2-3	Importance of the heat storage capability of the fuel matrix	66
2-4	Schematic of the passive pressure tube LWR – overall concept	68
2-5	Passive pressure tube LWR – operation during LOCA.....	70
2-6	Fuel matrix in a fuel channel during normal and accident operation.....	73
2-7	Schematic of the PTLWR primary heat transport system and shutdown cooling circuit.....	75
3-1	Summary of material compatibility with fuel matrix conditions	91
3-2	Layers of TRISO fuel particle.....	93
4-1	Configurations of Light Water Moderator in a PTLWR.....	113
4-2	Effects of out-of-channel moderator geometrical arrangement on multiplication factor	116
4-3	Case A dry calandria concept with moderator tubes in rectangular array.....	117
4-4	Dependence of multiplication factor on the volume of out-of-channel moderator for Case A.....	119
4-5	Reference dry calandria design–fuel channel MCNP model	121
4-6	Reference calandria design–MCNP model of a full core with reflector.....	123
4-7	Reference calandria design–MCNP model of a full core for flooding (core region).....	125
4-8	Reference calandria design–MCNP model of a full core for flooding (side-reflector region with control rods).....	126
4-9	Arrangement of channel ends with shield plug.....	127

4-10	MCNP model for checkerboard bi-directional refueling	129
4-11	Expanded cross-sectional view of a cell with two neighboring channels.....	130
4-12	Model arrangement of 2346 TRISO particles.....	132
4-13	Comparison of neutron spectrum for a full cell model and 2346-particle homogenized model.....	134
4-14	Comparison of prompt criticality excursions for PWR and PTLWR for excess reactivity of 0.25β above prompt critical	139
4-15	3-D thermal flux profile in a PTLWR fuel channel	141
4-16	3-D thermal flux profile in a PTLWR fuel channel with tight pitch.....	142
4-17	3-D fast flux profile in a PTLWR fuel channel.....	143
4-18	Power density profile in fuel compacts for the fresh PTLWR core	144
4-19	Comparison of fresh core axial power density profiles for the PTLWR concept and a typical PWR	145
4-20	3-D thermal flux profile in a PTLWR core	146
4-21	Schematic of CRDs a PTLWR core.....	147
4-22	3-D fast flux profile in a PTLWR core with inserted control rods.....	148
4-23	Comparison of energy spectra for the PTLWR with PWR and CANDU	155
4-24	Comparison of ^{135}Xe transients following reactor shutdown	161
4-25	Reactivity insertion needed to overcome ^{135}Xe poisoning following step power level decrease to 50% (fresh core).....	162
4-26	Reactivity as a function of fuel temperature for the PTLWR design.....	165
4-27	Doppler coefficient for the PTLWR as a function of fuel temperature and coolant density.....	165
4-28	Doppler coefficient constant, k_D , as a function of coolant density	166

4-29	Effect of coolant voiding on reactivity	167
4-30	Neutron balance in the reference PTLWR design.....	168
4-31	Comparison of neutron absorption in ^{238}U and parasitic losses	169
4-32	Effect of reflector temperature on the multiplication factor.....	171
4-33	Schematic arrangement of control rods in the side reflectors of the PTLWR design	176
4-34	Proposed PTLWR control and safety systems and comparison with CANDU.....	177
4-35	Reactivity worth apportionment of control rods located in the reflector	178
4-36	Water worth inside and outside fuel channel for a fixed total mass of H_2O	184
4-37	Reactivity behavior for calandria reflooding with saturated steam in the upper space	188
4-38	Reactivity behavior for calandria reflooding with hypothetical water entrainment into the upper space	190
4-39	Reactivity behavior for calandria reflooding -expanded scale.....	190
4-40	Reactivity behavior for calandria inadvertent flooding with saturated steam in unflooded region for cold core with all CRDs inserted	192
4-41	Reactivity behavior for calandria inadvertent flooding with hypothetical water entrainment for cold core with all CRDs inserted	194
4-42	Reactivity behavior for calandria inadvertent flooding with hypothetical water entrainment for hot core.....	194
4-43	Calandria spraying from cracked pressure tube without flooding.....	196
4-44	Effective multiplication factor as a function of burnup for various initial enrichments.....	202
4-45	Axial power density distribution in fuel compacts for uniform enrichment.....	207
4-46	Linear model of burnup with burnable poison	208
4-47	Bundle arrangement #1.....	211

4-48	Axial power density profile for Case #1.....	211
4-49	Axial power density profile for Case #2.....	213
4-50	Thermal flux profile for Case #2.....	213
4-51	Bundle arrangement #2.....	215
4-52	Axial power density profile for Case #3.....	215
4-53	Thermal flux profile for Case #3.....	216
4-54	Axial power density profile for Case #4.....	217
4-55	Bundle arrangement #3 with Be slug.....	219
4-56	Axial power density profile for Case #5 with beryllium slug.....	219
4-57	Thermal flux profile for Case #5 with beryllium slug.....	220
4-58	Axial power density profile for Case #5 without beryllium slug.....	222
4-59	Thermal flux profile for Case #5 without beryllium slug.....	222
4-60	Effect of coolant voiding for the case with beryllium slug.....	223
4-61	Comparison of energy spectra for the ^{239}Pu -fueled and ^{235}U -fueled PTLWR cores.....	230
4-62	Comparison of reactivity for the ^{235}U and ^{239}Pu fueled PTLWR.....	231
5-1	Flow chart for various combinations of fuel arrangement in a fuel channel of the PTLWR.....	247
5-2	DC-1 – A two-ring design with TRISO particle fuel in a silicon carbide tube.....	248
5-3	Effect of coolant voiding for the two-ring design with TRISO particle fuel.....	251
5-4	Axial power density profile for the two-ring design with TRISO particle fuel.....	251
5-5	Cladding and pressure tube temperature histories following LOCA for the two-ring design with TRISO particle fuel.....	253
5-6	Temperature profile in a fuel channel following LOCA for the two-ring design with TRISO particle fuel.....	253
5-7	DC-2 – A two-ring design with SiC-clad UO_2 fuel pins.....	255

5-8	Effect of coolant voiding for the two-ring design with SiC-cladded UO ₂ fuel pins	257
5-9	Axial power density profile for the two-ring design with SiC-cladded UO ₂ fuel pins	257
5-10	DC-3 – A Fuel matrix design with separate fuel compacts and coolant channels.....	259
5-11	DC-4 – A fuel matrix design with particle fuel dispersed in a matrix.....	262
5-12	DC-5 – A fuel matrix design with TRISO particle fuel contained in an SiC structure.....	264
5-13	Effect of coolant voiding for matrix design with TRISO particle fuel in an SiC structure	265
5-14	Comparison of neutron spectra for the DC-3 and DC-5 matrix designs.....	266
5-15	Comparison of parasitic captures and captures in ²³⁸ U for individual matrix designs, CANDU and PWR.....	267
6-1	Schematic of the PTLWR primary heat transport system.....	272
6-2	Communication between the thermohydraulic codes PARCHANL and ALGOR.....	275
6-3	Coolant channels of the reference matrix design with their dimensions	281
6-4	Alignment of two neighboring fuel elements.....	282
6-5	Subcooled boiling regions with temperature profiles.....	290
6-6	Approximation of single-phase component of heat flux in partial subcooled boiling region, after Bowring.....	293
6-7	Schematic of partial subcooled boiling region in the nodalization scheme.....	294
6-8	Comparison of Dipprey-Sabersky correlation with Dittus-Boelter and Gnielinski correlation	298
6-9	Comparison of Fanning friction factor for smooth and roughened channels.....	300
6-10	Bulk coolant temperature profile in the PTLWR coolant channels.....	306

6-11	Wall temperature profile in the PTLWR coolant channels.....	307
6-12	Equilibrium quality development in the PTLWR coolant channels.....	307
6-13	Pressure along the PTLWR coolant channels.....	308
6-14	Heat transfer coefficient along the PTLWR coolant channels.....	308
6-15	CHF and operating heat flux along the PTLWR coolant channels.....	310
6-16	DNB power ratio along the PTLWR coolant channels	310
6-17	Boundary conditions for a 2-D finite element model.....	312
6-18	Maximum fuel matrix temperature profile for the fresh core	313
6-19	Azimuthal temperature and heat flux profiles in the central coolant channel	314
6-20	Azimuthal temperature and heat flux profiles in the intermediate coolant channel	314
6-21	Azimuthal temperature and heat flux profiles in the outer coolant channel	315
6-22	Transition of heat transfer coefficient to the post-CHF regime	317
6-23	Fuel matrix performance during normal operation and in the post-CHF regime.....	317
6-24	Operating characteristics of coolant channels at nominal power input.....	318
6-25	Simplified stability criterion for thermally induced flow oscillations in intermediate coolant channel	321
6-26	Bulk coolant temperature profile in the PTLWR channels for equilibrium core	322
6-27	Wall temperature profile in the PTLWR channels for equilibrium core	323
6-28	CHF and operating heat flux along the PTLWR coolant channels for equilibrium core.....	323
6-29	DNB power ratio along the PTLWR coolant channels for equilibrium core	324
6-30	DNBR along the PTLWR coolant channels for equilibrium core.....	324

6-31	Maximum fuel matrix temperature profile for the equilibrium core	326
6-32	Maximum fuel matrix temperature profile for the equilibrium core using HOBEG technology	327
7-1	PTLWR fuel channel in LOCA scenario and its temperature limits.....	331
7-2	Fuel matrix with 3 full-length runners.....	337
7-3	Regions on a boiling curve.....	343
7-4	Transition to simplified 1-D fuel matrix model for steady state and transient analysis.....	347
7-5	Schematic of a simplified 1-D model with nomenclature.....	348
7-6	Lumping of graphite matrix material into the first ring.....	349
7-7	Nodalization scheme for 1-D PTLWR fuel channel model.....	355
7-8	Contact conductance between fuel compacts and graphite matrix.....	365
7-9	Effective thermal conductivity of the gap between the pressure tube and calandria tube and transferred heat flux	367
7-10	Adiabatic fuel channel heatup from decay heat	369
7-11	Time development of temperature profile across the fuel channel during adiabatic heatup	369
7-12	Time development of limiting temperatures following LOCA without scram	372
7-13	Radial temperature profile in the fuel channel following LOCA without scram	372
7-14	Linear heat rates during LOCA without scram	373
7-15	Reactivity changes during LOCA without scram.....	374
7-16	Time development of limiting temperatures for sustained film boiling at calandria tube surface.....	375
7-17	Linear heat rates for sustained film boiling at calandria tube surface	376
7-18	Time development of limiting temperatures for the equilibrium core	377

7-19	Temperature profiles across the fuel channel for equilibrium core	377
7-20	Comparison of 1-D model with ALGOR 2-D model for the fresh core at steady state	379
7-21	ALGOR temperature profile of a voided fuel matrix for equilibrium core at 200 seconds.....	380
8-1	Schematic of a passive fluid-operated valve – operating mode.....	385
8-2	Schematic of a passive fluid-operated valve – loss of heat sink accident mode.....	386
8-3	Schematic of calandria with dc-powered air-lock blower – operating mode.....	388
8-4	Cross section of calandria with passages for flood water intake and gas relief.....	390
8-5	Main dimensions of flood water and gas release passages	391
8-6	Computational schematic of calandria flooding with nomenclature.....	394
8-7	Water level for calandria flooding Case #1	401
8-8	Water level oscillations for calandria flooding Case #1	402
8-9	Inlet and in-calandria pressure losses for calandria flooding Case #1.....	403
8-10	Calandria pressure and water flow rate for calandria flooding Case #1.....	403
8-11	Water level for calandria flooding Case #2	405
8-12	Calandria pressure and water flow rate for calandria flooding Case #2.....	405
8-13	Liquid bulk temperature in calandria for flooding Case #2.....	406
8-14	Calandria flooding curves for 4-out-of-4 and 2-out-of-4 valves opened	406
9-1	Axial profile of the fast flux on the high-power pressure tube	412
9-2	Effect of fluence on the tensile strength of Zr-2.5%Nb pressure tubes at 300°C	417

9-3	Effect of fluence on fracture toughness of Zr-2.5%Nb pressure tubes.....	417
9-4	Growth of oxide layer in Zr-2.5%Nb pressure tubes	418
9-5	Stress on protected pressure tube during flooding at operating pressure	424
9-6	Temperature profiles in protected pressure tubes at various times.....	424
9-7	Stress on unprotected pressure tube during flooding at operating pressure.....	425
9-8	Temperature traces in the calandria tube wall for hypothetical quenching with nucleate boiling	428
9-9	Time development of thermal stress in calandria tube wall for hypothetical quenching with nucleate boiling.....	428
9-10	Calandria tube cooldown for inadvertent flooding process.....	429
9-11	Time development of thermal stress in the calandria tube wall for inadvertent flooding process.....	429
9-12	Calandria tube cooldown for LOCA without scram scenario	430
9-13	Time development of thermal stress in the calandria tube wall for LOCA without scram scenario.....	431
10-1	Power density distribution in the radial reflector	436
10-2	Fuel channels penetrating the reflector and a 2-D computational cell.....	438
10-3	Possible arrangement of graphite reflector and fuel channel.....	439
10-4	2-D Temperature profile in an axial reflector around a fuel channel	440
10-5	Concept of radial reflector cooling and a 2-D computational cell	442
10-6	Temperature profile in the radial reflector adjacent to a cooling channel	444
11-1	Schematic of containment arrangement for passive pressure tube LWR.....	451
11-2	Considered alternatives for containment passive cooling	457

11-3	Schematic flow diagram of primary system with break location.....	462
11-4	Effective heat transfer coefficient and power as a function of containment wall temperature.....	469
11-5	Arrangement and dimensions of air inlet and outlet passages.....	471
11-6	Case 1 - mass release from unaffected loop following the break of an outlet header.....	475
11-7	Case 1 - energy release from unaffected loop following the break of an outlet header.....	476
11-8	Case 1 - mass release from affected loop following the break of an outlet header.....	476
11-9	Case 1 - energy release from affected loop following the break of an outlet header.....	477
11-10	Simplified representation of reflector wall for calculation of energy release	480
11-11	Decay heat and heat rates from stored energy in the reflector and fuel matrix released into calandria water.....	486
11-12	Steam mass flow rate and integrated steam mass released from calandria as a result of decay heat and core stored energy	487
11-13	Case 1-summary of mass sources released to containment.....	487
11-14	Case 1 - containment pressurization history.....	490
11-15	Case 1 - containment gas, saturation and wall outer surface temperature histories	490
11-16	Case 1 - Decay power and heat rates to structures	491
11-17	Case 2 - mass release from unaffected loop following the break of outlet header.....	493
11-18	Case 2 - energy release from unaffected loop following the break of outlet header	493
11-19	Case 2 - containment pressurization history	495
11-20	Case 2 - containment gas, saturation and wall outer surface temperature histories.....	495

11-21	Case 2 - Comparison of pressure for the base case and a containment with reduced mass of internal concrete structures.....	496
11-22	Case 3 - mass release in steam line break accident.....	496
11-23	Case 3 - energy release in steam line break accident.....	497
11-24	Case 3 - containment pressurization history	497
11-25	Case 3 - containment gas, saturation and wall outer surface temperature histories	498
11-26	Case 4 - containment pressurization history.....	498
11-27	Case 4 - containment gas, saturation and wall outer surface temperature histories	499
11-28	A 9-cell CONTAIN model of the containment for the passive pressure tube LWR.....	501
11-29	Comparison of pressure history for Case 2 using 1-cell and 9-cell models.....	504
11-30	Histories of selected temperatures from the 9-cell model.....	504
11-31	Velocities through selected junctions from the 9-cell model.....	505
11-32	Schematic of lumped parameter GOTHIC model of PTLWR containment.....	507
11-33	Comparison of pressure histories for Case 2 by CONTAIN and GOTHIC models.....	509
11-34	Histories of liquid temperature in the pool and calandria for Case 2 from GOTHIC	511
11-35	Histories of water levels in the pool and calandria.....	512
11-36	Steam evaporation, condensate return and flow through the gas lock.....	512
11-37	Potential improvements for the performance of calandria flooding using a vapor suppression system	514
11-38	Schematic of a GOTHIC multidimensional model for the PTLWR containment.....	515
11-39	Top view of the multidimensional GOTHIC model for the PTLWR containment with location of junctions between	

	calandria space and upper containment, and the designation of cut planes.....	517
11-40	GOTHIC runs and factors affecting thermal stratification.....	519
11-41	Histories of selected containment atmosphere temperatures for Run#1	520
11-42	Temperature profile at inner surface of containment shell at 1.95×10^5 seconds for Run#1	521
11-43	Velocity vectors at 1.95×10^5 seconds for Run#1.....	522
11-44	Velocity vectors at 1805 seconds for Run#2	523
11-45	The development of inner-wall temperature profile for Run#2.....	525
11-46	Velocity vectors at 12,000 seconds for Run#3.....	526
11-47	Comparison of inner-wall temperature profile at 12,000 seconds for arrangement with and without the crane wall.....	527
11-48	Velocity vectors at 1805 seconds for Run #5.....	528
12-1	Temperature profile in the PTLWR fuel matrix with one-out-of-eighteen coolant channels plugged.....	546
12-2	Schematic of GOTHIC model for calandria flooding following in-core pressure tube rupture.....	549
12-3	Water level in calandria and calandria pressure following pressure tube rupture.....	550
13-1	Material balance for once-through fuel cycle.....	563
13-2	Parameters for SWU balance.....	567
13-3	Sensitivity of the total fuel cycle cost on the fabrication cost of the PTLWR fuel elements.....	570
13-4	Fuel cycle cost and U_3O_8 requirements for the PTLWR concept.....	570
14-1	Schematic of the passive pressure tube LWR – overall concept	578
14-2	Passive pressure tube LWR – operation during LOCA.....	581
14-3	Cross section of calandria with passages for flood water intake and gas relief.....	582
14-4	Schematic of a passive fluid-operated valve	583

14-5	Fuel matrix in a fuel channel during normal and accident operation.....	585
14-6	Power density profile in outer fuel ring.....	590
14-7	Schematic arrangement of control rods in the side reflectors of the PTLWR design	592
14-8	Comparison of energy spectra for the PTLWR with PWR and CANDU reactors.....	593
14-9	Doppler coefficient for the PTLWR as a function of fuel temperature and coolant density.....	594
14-10	Effect of coolant voiding on reactivity	595
14-11	Reactivity behavior for calandria inadvertent flooding with saturated steam in unflooded region for cold core with all CRDs inserted	599
14-12	Reactivity behavior for calandria inadvertent flooding with hypothetical water entrainment for hot core.....	599
14-13	Effective multiplication factor as a function of burnup for various initial enrichments.....	600
14-14	Bulk coolant temperature profile in PTLWR coolant channels.....	603
14-15	Pressure along PTLWR coolant channels	603
14-16	DNB power ratio along PTLWR coolant channels.....	604
14-17	Fuel matrix performance during normal operation and in the post-CHF regime.....	605
14-18	Maximum fuel matrix temperature profile for the equilibrium core	606
14-19	DNB power ratio along PTLWR coolant channels for equilibrium core	607
14-20	Time development of limiting temperatures following LOCA without scram	610
14-21	Radial temperature profile in the fuel channel following LOCA without scram	610
14-22	Reactivity changes during LOCA without scram	611
14-23	Time development of limiting temperatures for sustained film boiling at calandria tube surface.....	612

14-24	Water level in calandria flooding process.....	614
14-25	Schematic of containment arrangement for passive pressure tube LWR.....	616
14-26	PTLWR containment pressurization history for double-ended rupture of a hot header with isolation valve failure	619
14-27	Containment gas, saturation and wall outer surface temperature histories for double-ended rupture of a hot header with isolation valve failure	619
14-28	Decay power and heat rates to structures for double-ended rupture of a hot header with isolation valve failure	620
14-29	Containment pressurization history for simultaneous double-ended rupture of a hot header, with isolation valve failure and steam line break with main steam isolation valve failure.....	621
14-30	Top view of multidimensional GOTHIC model for the PTLWR containment with designation of cut planes	622
14-31	Velocity vectors at the time of maximum pressure peak	623
A-1	Comparison of infinite multiplication factor calculated by MCNP+ORIGEN2 with LEOPARD results.....	674
B-1	Heat balance and CHF curves.....	686
B-2	Comparison of CHF from AECL lookup table evaluated from local and heat balance conditions.....	689
B-3	Comparison of CHF from the PI-1 correlation evaluated from local and heat balance conditions.....	689
B-4	Comparison of CHF from the W-3 correlation evaluated from local and heat balance conditions.....	690
B-5	Comparison of CHF correlations evaluated by heat balance method	691
B-6	Comparison of CHF correlations evaluated by local method	691
B-7	Comparison of CHF correlations for the conditions of the central coolant channel	693
B-8	Comparison of CHF correlations for the conditions of an intermediate coolant channel.....	694

C-1	Achievable enhancement of heat transfer through a containment wall by varying the heat transfer coefficient on the steam or air sides	696
C-2	Comparison of heat transfer resistances for the steam side, air side and steel wall.....	697
C-3	Schematic of air cooling of a cylindrical body.....	698
C-4	Geometry and nomenclature for ribs on vertical wall	703
C-5	A simplified flow diagram for the RISRAD code	706
C-6	Comparison of various correlations for heat transfer coefficient to air.....	713
C-7	MIT experiment - sensitivity to the emissivity of the hot wall.....	716
C-8	Performance of the bare containment wall without chimney.....	719
C-9	Radiation, convection and total heat transfer rates from bare containment wall.....	719
C-10	Performance of the bare containment wall with chimney	720
C-11	Performance of the ribbed containment wall without chimney	721
C-12	Schematic of finned containment wall with supporting shell	723
C-13	Schematic of heat flow through the fin to the duct wall.....	724
C-14	Schematic of two section fin geometry.....	725
C-15	Optimization of the number of fins	731

LIST OF TABLES

2-1	Reference core and primary system design parameters.....	77
2-2	Reference fuel channel parameters.....	78
2-3	Reference flooding system parameters	79
2-4	Reference containment parameters	79
2-5	Imposed design limits	80
3-1	Requirements on matrix material.....	84
3-2	Requirements on a reflector material	85
3-3	Parameters of TRISO particle fuel	95
3-4	Thermal properties of fuel materials.....	95
4-1	Comparison for homogenized and detailed 2346-particle model	134
4-2	Comparison of prompt neutron lifetime with CANDU and PWR.....	136
4-3	Comparison of maximum fuel temperature rise and power input to the fuel in hypothetical reactivity increase, ρ_s , of \$0.25 above prompt critical	138
4-4	Lellouche's stability criteria of the first harmonic for 3% enriched ^{235}U fuel in bare and zero leakage reactors and comparison with the PTLWR design parameters.....	153
4-5	Comparison of cell volume fractions and moderator-to-fuel volume ratios for PTLWR and PWR.....	155
4-6	Comparison of fast and thermal neutron flux for PTLWR, PWR and CANDU.....	156
4-7	Comparison of steady state ^{135}Xe poisoning ratio for the PTLWR and a typical PWR.....	159
4-8	Effective multiplication coefficient for various reflectors	171
4-9	Comparison of PTLWR physics characteristics with LWR and CANDU	173
4-10	Reactivity comparison for the same amount of water inside and outside the fuel channel.....	183

4-11	Practical H ₂ O density limits in the upper calandria space	187
4-12	Discharge burnup and fuel utilization for various initial enrichments.....	202
4-13	Consistency check of MCNP model #4 with MCNP model #1.....	206
4-14	Fractional reduction due to burnable poison in burnup for on-line refueling.....	209
4-15	A Summary of peaking factors and multiplication factor for case #1.....	212
4-16	A Summary of peaking factors and multiplication factor for case #2.....	214
4-17	A Summary of peaking factors and multiplication factor for case #3.....	217
4-18	A Summary of peaking factors and multiplication factor for case #4.....	218
4-19	A Summary of peaking factors and multiplication factor for case #5 with beryllium slug.....	221
4-20	A Summary of peaking factors and multiplication factor for case #5 without beryllium slug	223
4-21	Reactivity deficit for the most reactive fuel channel during refueling.....	224
4-22	Comparison of reactivity change during steam line break.....	231
5-1	Key factors and parameters influencing the suitability of a matrix design.....	238
5-2	Comparison of thermohydraulic characteristics.....	269
6-1	Main parameters of the PTLWR primary heat transport system.....	273
6-2	Heat generation distribution in the PTLWR concept and CE-CANDU	286
6-3	Parameters of the PTLWR and the recommended ranges for considered CHF correlations.....	301
6-4	Comparison of PTLWR thermal-hydraulic characteristic parameters with CANDU-CE (in the hottest channel)	329

7-1	Important parameters for gamma heat deposition in the reference PTLWR cell.....	333
7-2	MCNP results for gamma heating of flooded cell	334
7-3	Decay group constants for the 11-decay group model	361
7-4	Delayed group constants	361
7-5	Material properties used in the fuel channel transient analysis	366
9-1	Operating conditions for CANDU and PTLWR pressure tubes.....	411
9-2	Fluence comparison between CANDU and dry calandria	412
11-1	Accident sequence for containment analysis-Case 1.....	472
11-2	Mass and energy inventory for the proposed pressure tube LWR	473
11-3	Comparison of mass and energy primary system inventory for PWR, CANDU, CE-CANDU and PTLWR.....	474
11-4	Events assumed to calculate mass/energy release data from calandria	479
11-5	Summary of internal heat sinks	489
11-6	Comparison of internal heat sink mass for various commercial LWR containments and PTLWR heat sinks used in the analysis	489
11-7	Cell volumes and heights for the 9-cell CONTAIN model.....	500
11-8	Junction data for a 9-cell CONTAIN model	502
11-9	List of GOTHIC runs with the key factors influencing thermal stratification.....	518
12-1	Summary of considered accidents in the PTLWR.....	534
12-2	Potential reactivity accidents in PWR, CANDU and PTLWR	558
12-3	Summary of PTLWR behavior for various class of accidents with the key advantageous aspects	560
13-1	General reactor specifications for PWR, CANDU, CE-CANDU, and PTLWR design	564

13-2	Discharge burnup versus enrichment for the dry calandria design.....	565
13-3	Economic parameters for once-through fuel cycle.....	566
13-4	Comparison of fuel cycle cost for PTLWR with PWR and CANDUs.....	569
14-1	Summary of PTLWR design parameters.....	586
14-2	Main characteristics of the PTLWR, CANDU, PWR and RBMK.....	625
14-3	Physics characteristics of the PTLWR, CANDU, PWR and RBMK.....	626
14-4	Safety-related intrinsic characteristics of the PTLWR, CANDU, PWR and RBMK.....	627
15-1	Possible combinations in passive pressure tube reactors.....	641
15-2	Alternative Coolants for Passive Pressure Tube Reactors.....	642
C-1	Comparison of RISRAD results with experimental data.....	717

NOMENCLATURE

General English notation

<u>Symbol</u>	<u>Description</u>	<u>Unit</u>
A	Flow area	(m ²)
A _{Dop}	Doppler feedback constant	(\$/K)
B	Burnup	(MWd/tonne)
	Geometric buckling	(m ⁻²)
Bo	Boiling number	(-)
\bar{c}	Normalized precursor concentration	(-)
c _p	Specific heat capacity at constant pressure	(J/kg-K)
c _v	Specific heat capacity at constant volume	(J/kg-K)
D	Diameter	(m)
	Diffusion constant	(m)
e	Enrichment	(%)
	Roughness height	(m)
	Fin efficiency	(-)
e ⁺	Roughness Reynolds number	(-)
E	Energy	(J)
	Dimensionless entrainment number	(-)
	Young's modulus	(Pa)
E _d	Relative yield for decay group model	(-)
f	Friction factor	(-)
	Fraction	
	Fission spectrum	(1/eV)
f _{red}	Reduction coefficient	(-)
f _v	Volume fraction	(-)
F	Feedback constant	(\$/MJ)
	Force	(N)
F _c	Capacity factor	(-)
F _d	Decay heat redistribution factor	(-)
F _g	Geometry factor	(-)
F _E	Entrance effect factor	(-)
F _{peak}	Peaking factor	(-)
F _x	Quality factor	(-)
g	gravitation constant	(m/s ²)

G	Mass flux	(kg/m ² -s)
G _z	Graetz number	(-)
h	Enthalpy	(J/kg-K)
	Heat transfer coefficient	(W/m ² -K)
	Height or water level	(m)
	Conductor node thickness	(m)
h ^s	Surface weight	(m)
h ^v	Volume weight	(m ²)
H	Water level	(m)
j	Superficial velocity	(m/s)
J	Net neutron current	(n/eV-s)
k	Thermal conductivity	(W/m-K)
	Neutron multiplication coefficient	(-)
K	Form loss coefficient	(-)
l	length	(m)
L	Length	(m)
	Loss fraction	(-)
L _E	Effective length	(m)
M	Mass	(kg)
	Molecular weight	(kg/kmol)
	Neutron migration length	(m)
	Polynomial coefficient	(-)
ṁ	Mass flow rate	(kg/s)
\tilde{n}	normal vector	(-)
N	Neutron density in phase space	(n/cm ³ -eV)
NP	Number of types of parallel coolant channels	(-)
N _{pch,eq}	Equilibrium phase change number	(-)
N _{sub}	Subcooling number	(-)
Nu	Nusselt number	(-)
NZ	Number of axial nodes	(-)
p	Pressure	(Pa)
p _r	Reduced pressure	(-)
P	Pitch	(m)
	Power	(MWt)
	Perimeter	(m)
Pe	Peclet number	(-)

Pr	Prandtl number	(-)
q'	Linear heat rate	(W/m)
q''	Heat flux	(W/m ²)
q''_{co}	Basic critical heat flux of Katto	(W/m ²)
q'''	Power density	(W/m ³)
\dot{Q}	Heat rate	(W)
r	Carrying charge rate	(-)
r_{Xe}^*	Steady-state xenon poisoning ratio	(-)
r_{Xe}	Transient xenon poisoning ratio	(-)
R	Radius	(m)
	Universal gas constant	(J/kg-K)
Ra	Rayleigh number	(-)
R_D	Ratio of average decay heat rate to operating power	(-)
Re	Reynolds number	(-)
Re^+	Roughness function	(-)
S	Heat transfer surface or flow area	(m ²)
St	Stanton number	(-)
u_b	Bubble rise velocity	(m/s)
t	Thickness	(m)
T	Temperature	(°C)
TC	Time constant	(s)
v	Velocity	(m/s)
	Specific volume	(m ³ /kg)
V	Volume	(m ³)
W_∞	Saturated value of Wigner energy	(J/kg)
x	Flow quality, mass fraction	(-)
x^+	Nondimensional coordinate	(-)
x_f	Feed enrichment	(%)
x_p	Product enrichment	(%)
x_w	Tails enrichment	(%)
y	Direct yield, mole fraction	(-)
Y	Shah's correlating parameter	(-)
z	Axial coordinate	(m)

General Greek Symbols

α	Angle	(°)
----------	-------	-----

	Thermal diffusivity	(m ² /s)
	Ramp rate	(\$/s)
	Void fraction	(-)
	Coefficient of thermal expansion	(1/K)
β	Delayed neutron fraction	(-)
	Thermal volume expansion coefficient	(1/K)
γ	Isentropic expansion coefficient, volume fraction	(-)
γ_H	Heat flux ratio	(-)
ϵ	Pressure ratio, emissivity	(-)
	Strain	(-)
$\dot{\epsilon}_t$	Transverse creep rate	(m/s)
ζ	Surface roughness	(m)
	Axial profile factor	(-)
η	Gravity factor	(-)
θ	Nondimensional temperature	(K)
Λ	Prompt neutron lifetime	(s)
λ	Delayed neutron group constant	(1/s)
λ_d	Decay group constant	(1/s)
μ	Dynamic viscosity	(kg/m-s)
μ_a	Gamma absorption coefficient	(m ² /kg)
ν	Average number of neutrons per fission	(-)
ρ	Specific density	(kg/m ³)
	Reactivity	(\$)
ρ_m^+	Two-phase momentum density	(kg/m ³)
Σ	Macroscopic cross-section	(1/m)
σ	Surface tension	(N/m)
	Microscopic cross section	(cm ²)
	Boltzman constant	(W/m ² -K ⁴)
	Stress	(Pa)
σ_ϕ	Hoop stress	(Pa)
τ	Time	(s)
	Shear stress component	(N/m ²)
Φ	Neutron flux	(n/cm ² -s)
ϕ_{lo}^2	Two phase friction multiplier based on all-liquid flow	(n/cm ² -s)
φ	Wetting angle	(°)

ξ	Relative coordinate	(-)
Ψ	Directional neutron flux density	(n/cm ² -s-rad)
Ω	Direction vector	(rad)
Ω	Thermal loading factor	(-)

Subscripts

0	Initial	eff	Effective
a	Absorption, air	eq	Equilibrium
ac	Acceleration	f	Fluid, saturated liquid, fission, fuel, fin, flood water
at	Atmospheric	fe	Fluid entrained
ave	Average	fg	Difference between fluid, and gas
b	Bulk, buoyancy bubble	fld	Flooding
bot	Bottom	FLW	Flood water
BP	Burnable poison	FDB	Fully developed subcooled nucleate boiling
c	Calandria, coolant, capture, convection, compact	g	Saturated vapor, gas, graphite
ch	Channel	GC	Guide tube
CHF	Critical heat flux	h	Heated
col	Collapse, coolant	in	Inlet
cond	Conduction	init	Initial
conv	Convection	ir	Inner ring
cp	Coated particle	k	Kernel
cr	Critical	I	Iodine
CRD	Control rod	l	Liquid, left
CT	Calandria tube	m	Mixture
CTi	Calandria tube inner	mat	Matrix
CTo	Calandria tube outer	max	Maximum
d	Discharge, delayed, Decay	ME	McEligot
D	Duct	ONB	Onset of nucleate boiling
Dop	Doppler	oper	Operating
e	Equivalent hydraulic, exit	o	Outer
ev	Equivalent volumetric hydraulic diameter	or	Outer ring

pch	Phase change
PT	Pressure tube
PTi	Pressure tube inner
PTo	Pressure tube outer
r	Right, radial
rad	Radiation
R	Reflector
RL	Reflector liner
s	Scattering, slab, steam
sat	Saturation
SCB	Surface heat flux by bubble nucleation
sp	Spacer
SPL	Single-phase convection
sub	Subcooled
t	Total
th	Thermal
tot	Total
TP	Two-phase
v	Vapor
vap	Vapor
w	Wall, wetted
WG	Wigner
Xe	Xenon
Zy	Zircaloy

Superscripts

m	Time step index
s	Surface
v	Volume

Special symbols

∞	Infinity
Δ	Difference
∇	Gradient
—	Average

DEDICATION

I dedicate this thesis to my family for their support in this endeavor

Eliska, Michaela, Jonatan and Marcela

Chapter 1

INTRODUCTION AND BACKGROUND

This work is focused on a conceptual design of a large, passive light water-cooled reactor. The main effort is directed towards the reactor's ability to reliably discharge decay heat to the ultimate heat sink without the need for replenishment of primary coolant in loss of coolant accidents while ensuring the integrity of the fuel and reusability of major reactor components. Additionally, it is required that the accidents leading to large temperature increases result in inherent reactor shutdown. The target power rating is at least 1000 MWe.

The proposed concept achieving these goals is a passive pressure tube light water reactor (PTLWR) of similar design to CANDU reactors. A solid fuel matrix is used in place of conventional fuel rod arrays to enhance the dissipation of decay heat from the fuel in the absence of primary coolant. There is no moderator in the calandria, the moderating function is performed by the light water coolant inside the pressure tubes. The calandria contains low pressure gas and is connected to a light water heat sink. The purpose of the gas is to keep the light water out of the calandria during normal operation, while during loss of coolant or loss of heat sink accidents it is vented to allow passive calandria flooding. The entire primary system is enclosed in a robust, free standing cylindrical steel containment, cooled solely by buoyancy-induced air flow, and surrounded by a concrete shield building. The large heat capacity of the water pool outside the calandria, absorbs a significant amount of decay energy and reduces the peak pressure during the long term containment pressurization.

1.1 MOTIVATION

Historically, the dominant design philosophy for nuclear reactors has been to improve economics by increasing unit power output. To ensure safety, the principle of defense in depth, employing active devices was adopted. The current trend in reactor development has shifted towards stronger emphasis on improved means of maintaining the defense in depth approach of protecting the public and plant investment: in particular, passive or semi-passive safety systems, which rely on natural processes and do not need complex active safety systems for their reliable operation. This approach leads to substantial simplification of the system, while enhancing safety. On the other hand, the use of passive systems for decay heat removal generally necessitates lower achievable heat transfer rates, which results in lower unit power outputs, and hence, in higher cost per installed kW. This disadvantage may, however, be offset by considerable simplification of the plant and elimination of a number of redundant and complicated safety components, yielding a cost per installed kW roughly comparable to first generation plants with higher power outputs. A plant which could combine the benefits of simplification with enhanced safety, while running at a high power output of about 1000 MWe, would decrease the cost per kWhr even further, making nuclear power more economically advantageous than fossil fuels. Also, many utilities in Europe and Japan prefer to retain the current size range of about 1000 MWe because of the difficulty in securing suitable plant sites. Therefore, this study will be focused on the development of a conceptual design of a nuclear power reactor having passive decay heat removal capability from the fuel to the ambient and simultaneously having a large power rating of at least 1000MWe.

For nearly half a century, reactor designers have conceived hundreds and built dozens of reactor concepts. This creative outpouring has derived from the fundamental physics of the fission and energy extraction processes which permits a variety of solutions to the fissioning, moderating and cooling functions. Achievement of these functions has been possible through utilization of a variety of materials and configurations. These approaches have succumbed to the superior economic performance of the

light water cooled reactor, a reactor whose dominant manifestation worldwide, the Pressurized Water Reactor (PWR) concept was developed for submarine propulsion. Light water cooled reactors, especially PWRs and Boiling Water Reactors (BWRs) dominate the world nuclear market by a large margin (84% of operating power reactors are LWRs: 62% PWRs and 22% BWRs). Since light water coolant has been successfully demonstrated in reactor operation on a large scale and has simultaneously low unit cost, it has been selected for the reactor concept studied here. The choice of light water coolant also reflects the results of the research and development program initiated by the U.S. utilities for future nuclear power electricity generation in the early 1980s. A dominant message from this program, managed by the Electric Power Research Institute (EPRI), was that light water technology is a valid base for future expansion, but that the future systems must be simpler. This choice further influenced the decision to restrict this study's search for an innovative, passive nuclear power reactor to a light water reactor concept.

The extensive introduction of passive features in light water reactors received increased attention only recently, motivated by the proposal for the Process Inherent Ultimately Safe Reactor (PIUS), developed by ABB Atom. Since the PIUS introduction, many LWR designs or concepts have been conceived and several are under active development. They incorporate passive safety features at various levels, but all have one feature in common – the need to replenish the lost primary coolant to the voided fuel bundles to assure removal of the decay heat from the fuel. In contrast, the objective of this study is to ensure sufficient decay heat removal from the voided fuel without the need for replenishing the primary coolant. This goal is partially motivated by the Modular High Temperature Gas Cooled Reactor (MHTGR), being developed by General Atomics, which has the capability to survive the absence of coolant without fuel damage. It has, however, a very low power output (140 MWe), and more importantly, the absence of a conventional containment building will require very high quality particle fuel. The present study will achieve a similar capability to survive the absence of primary coolant in a LWR while retaining the current defense in depth philosophy with multiple barriers to fission product release, including the final barrier–containment.

One disadvantage of all light water cooled reactors is the relatively high coolant pressure needed to raise primary system temperature. If the high-pressure primary system boundary breaks, the coolant inventory is rapidly discharged, resulting in fuel uncovering if no protective action is taken. The consequences of such a loss of coolant accident (LOCA) scenario have been recognized since the early days of reactor technology [Emergency core cooling, 1967], and the plants were designed to safely handle the double-ended break of the largest primary system piping. However, catastrophic failure of the pressure vessel containing the fuel, was excluded from the design basis accident. The vessel is designed such that the probability of catastrophic failure is extremely low; moreover reactor vessels are very closely monitored during the plant lifetime to detect any signs of eventual deterioration. For advanced reactor concepts, this hypothetical pressure vessel failure remains in the beyond design basis accident domain. This work will attempt to move the protection level one step further and include catastrophic pressure boundary failure as a design basis accident by designing a light water reactor which could safely survive any break of the primary system boundary, including the catastrophic failure of the core region boundary.

1.2 BACKGROUND

It has now been almost four decades since the first nuclear power plants made their way into the energy industry and became an important factor in electricity generation. Although the majority of nuclear power plants have operated safely, there were several failures that aroused doubts and resentment towards nuclear technology among the public and some experts, and halted further deployment for several years. In particular, the accidents at Three Mile Island and Chernobyl contributed to these worries. These accidents revealed certain vulnerabilities of current nuclear power plants, particularly, to human errors and chains of small failures which may result in a bigger accident. These experiences and the negative attitude of the public towards nuclear power initiated a major shift to a much stronger emphasis on more convincing protective features.

1.2.1 Active and Passive Safety Approaches

There are three main issues in reactor safety – reactor shutdown which stops the instantaneous fission reaction in case the reactor reaches preset limits, maintenance of core cooling, and long term decay heat removal from the reactor core following the shutdown. In the early days of nuclear technology, the main emphasis was put on reactivity control and safe reactor shutdown. The need for inherent feedbacks which rely on natural law was recognized and passive means were incorporated into the design to control fission power increases. The fundamental requirement was that if power increases, the intrinsic design features of the core would cause the reactivity to decrease without the need to move control rods. This requirement has been adopted in essentially all light water reactors except for the RBMK design, where the absence of this fundamental feature was an important contributor to the Chernobyl accident.

Core cooling and ultimate decay heat removal functions have traditionally employed active means to deliver emergency coolant to the core if normal cooling is impaired. Active devices are, however, often complicated, expensive, and in particular, susceptible to human error. These and other economic reasons led the manufacturers to a passive safety approach. The passive safety approach utilizes natural processes which operate without or with little human intervention, and thus considerably reduce or completely eliminate the need for active means for decay heat removal. The term “passive” has been extensively used in recent years to describe certain approaches to safety, although its precise definition is still debated. Several definitions of the word “passive” have been offered; this work will adopt the definition proposed in the ALWR utility requirements issued by EPRI. Passive systems are defined here as systems which “rely on natural forces such as gravity or natural circulation; stored energy such as batteries and compressed gases; or energy inherently available in the system itself, such as from steam or pressure. They do not rely on modulating valves or other types of valves except to initiate operation of the safety function” [Marston et. al., 1993].

1.2.2 Review of Advanced LWR Concepts

Advanced light water reactor concepts incorporate passive safety features at various levels and can be divided in this aspect into three major categories:

- evolutionary concepts,
- passive concepts, and
- innovative concepts.

The evolutionary LWR concepts include the concepts based on previous designs with safety-related improvements, which are often derived directly from the experience with the older reference designs. To indicate the advancement compared to their predecessors, these concepts are called “advanced” by their vendors. The improved LWR concepts include for PWRs: the Westinghouse-Mitsubishi Advanced Pressurized Water Reactor [Hirata et. al., 1989], ABB Atom-CE’s System 80+™ [Turk and Matzie, 1992], Framatome’s N4+ [in Frisch et. al., 1993], Siemens’ Konvoi 95+ [Meyer, 1991] and Nuclear Power International’s (NPI) concept being studied by the joint venture of Siemens and Framatome [Vignon and Schneider, 1992]; and for BWRs: the ABWR 1300 designed by GE, Hitachi and Toshiba [Wilkins et. al., 1992], and ABB Atom-CE’s BWR90 [Rastas and Sundqvist, 1990]. These designs can be generally characterized by increased safety margins, increased coolant inventories to mitigate transients, larger degree of separation between control and safety functions, more consistent separation of redundant trains, and larger and improved containments with features for the mitigation of consequences of severe accidents. Incorporation of passive features in this category of advanced plants is very limited.

Passive concepts are also based to a large extent on proven designs. However, they incorporate new features with emphasis on passive safety system functions for emergency core cooling and decay heat removal. The major representatives in this category are Westinghouse’s Advanced Plant 600 MWe (AP600) for PWR, and the Simplified Boiling Water Reactor (SBWR) being developed by GE.

In the AP600 [Tower et. al., 1988], decay heat removal is accomplished by a passive safety injection system and by passive containment cooling. The passive safety injection system provides the residual heat removal (RHR) function and maintains the coolant inventory in the reactor coolant system (RCS). In the RHR function, the coolant from the hot leg flows to the RHR heat exchanger located in the In-containment Refueling Water Storage Tank (IRWST) above the loops and returns to the cold leg driven by gravity head. Passive reactor coolant makeup is provided from two core makeup tanks, two accumulators, and, in the long term, from the IRWST. However, the RCS must be depressurized to enable the utilization of this last water source. Passive decay heat removal to the ambient is accomplished by natural convection of air, and water film evaporation from the containment shell. The water film on the containment shell is provided by draining water tanks located at the top of the containment structure. Draining of the tanks is actuated by air-operated valves.

The decay heat removal system in the SBWR is comprised of three main systems – the Gravity Driven Cooling System (GDCCS), the isolation condenser system, and the passive containment cooling system (PCCS) [McCandless and Redding, 1989], [Wilkins, et. al., 1992]. Emergency core cooling is accomplished by the GDCCS. It includes elevated large pools located inside the containment with sufficient capacity to flood the entire containment to a level at least one meter above the top of the core. The isolation condenser (IC) system can remove the decay heat from both the reactor vessel and the containment (in case of accidental steam release to the containment). The steam is channeled through pipes to the condenser located in a water pool outside the containment where it condenses and the condensate returns to the reactor vessel by gravity head. The heat from condensing steam is transferred to the boiling water in the pool and released ultimately to the atmosphere. Both the AP600 and the SBWR depend on the automatic depressurization system to initiate long term decay heat removal.

Besides the widely known AP600 and SBWR, which have reached a rather advanced design stage, other passive LWR conceptual designs have been conceived. However, their design features are much less detailed.

These include the VVER-500 [Voznessensky et. al, 1992] being developed by Atomenergoprojekt, Babcock and Wilcox's concept B600 PWR [in Frisch et. al., 1993] and simplified medium size PWR and BWR concepts being developed by Japanese vendors [Oka et.al., 1991].

Innovative concepts also employ passive features to a large extent but, in addition, they utilize new principles to achieve a higher level of safety, which often deviate significantly from traditional LWR designs. Two reactor concepts from the LWR arena – the Safe Integral Reactor (SIR™) [Matzie, et. al., 1992], developed jointly by ABB Atom-CE, Rolls-Royce and Associates Ltd., Stone & Webster Engineering Corp. and AEA Technology, and PIUS [Hannerz, 1987] developed by ABB Atom-CE, can be included under this category. A similar concept to PIUS is also being studied in Japan under the name ISER (Intrinsically Safe and Economical Reactor) [Wakabayashi, 1988].

The SIR design has all major primary system components – the core, steam generators, reactor coolant pumps and the pressurizer – contained within a large pressure vessel. In addition to the normal decay heat removal path via steam generators and the main condenser, SIR employs three independent decay heat removal systems: the Secondary Condensing System (SCS), the Emergency Coolant Injection System (ECIS) and the Safety Depressurization System (SDS). The SCS is initiated by battery-powered valves which open the path between the steam generators and the separate condensing pools, sized to absorb a minimum of 72 hours of decay heat by boiloff. The ECIS provides reactor vessel refilling by injecting water from suppression tanks into the pressure vessel downcomer using a passive steam injector. The injector takes high pressure steam from the upper head of the reactor vessel, which is used to accelerate cold water from a low pressure source. The SDS is initiated manually and allows primary system discharge into the pressure suppression tanks located above the reactor vessel. Water from the pressure suppression tanks returns by gravity back into the reactor vessel. The SIR design uses a mixture of passive and active means to accomplish long-term cooling. However, catastrophic failure of the large pressure vessel would render most of these means ineffective.

The PIUS design takes a more radical approach. It aims for the preservation of core integrity by reliance on processes based entirely on natural laws. PIUS consists of the reactor active core, a once-through steam generator, and the main recirculation pump, submerged in a large pool of cold pressurized borated water. The primary system is separated from the cold pool by low pressure ducting and is thermally insulated except for two hydraulic locks, which provide a communication path between the core and the pool. The pool of borated water is contained in a prestressed concrete reactor pressure vessel. There are no control rods in the reactor; reactivity is controlled by the boron concentration and the temperature coefficient. If the steam generators are not available, decay heat is removed through density locks into a pool. The pool is cooled by convectional forced-circulation systems and backed up by a passive natural-circulation cooling system to ambient air via natural draft cooling towers. If all cooling systems fail, the amount of water in the prestressed reactor vessel is sufficient to cool the fuel for 7 days before the level reaches the top of the core. The PIUS concept does not require system depressurization or any valves to initiate passive decay heat removal. However, it may be sensitive to perturbations that normally occur during operation and which could lead to inadvertent reactor shutdown.

1.2.3 The Contribution of the Present Work

With respect to the classification of advanced light water reactors in Section 1.2.2, the conceptual LWR design presented in this work is an innovative concept. It departs significantly from the traditional LWR designs in terms of thermohydraulics during normal operation, reactor physics, and the decay heat removal process from the fuel. Compared to the SIR concept, as well as all passive LWR concepts, it eliminates the need for primary system depressurization, which is associated with large dynamic forces on the discharge piping and suppression pools. Similarly to the PIUS reactor, the proposed Passive Pressure Tube LWR concept (PTLWR) uses a lock (although the type of the lock is different) to keep the cold water pool outside the core during normal operation, and to allow the pool to provide for redundant reactor shutdown and serve as a heat sink during accidents.

However, there are several important differences between the PIUS and PTLWR concepts:

- While PIUS removes the decay heat by directly cooling the fuel elements with its water heat sink, the PTLWR concept cools the pressure boundary enclosing the fuel elements. Hence, the fuel elements do not require the presence of primary coolant, and are cooled by radiation, conduction and convection of their ambient steam/air mixture.
- The PIUS cold water pool is maintained at high operating pressure; therefore it necessitates a large pressure vessel. Any hypothetical failure of this pressure vessel would result in the depletion of the pool and would have deleterious consequences on fuel cooling capabilities. Moreover, such a system is susceptible to interfacing LOCAs, such as failure of steam generator tubes, which could lead to depletion of the pool inventory. On the other hand, the PTLWR heat sink is maintained at atmospheric pressure and does not require any pressure vessel. Hence, there is no possibility of a large pressure vessel break in the PTLWR concept. Breaks of the primary pressure boundary anywhere are handled as a design basis accident. This is one of the key contributions of the proposed PTLWR concept.
- The power rating of PIUS is limited to relatively low power because of the constraints on the size of the large prestressed-concrete pressure vessel. The PTLWR has no such constraint, since its power rating can be easily increased by adding more pressure tubes. Hence, the economy of scale can be realized with the PTLWR while preserving passive safety features.
- No boron is needed in the water pool to shut down the reactor or in the primary coolant to compensate for excess reactivity. Hence all the systems associated with boron control are eliminated.

It can be seen from the above discussion that the PTLWR concept proposed in this study offers certain important safety enhancements in the LWR arena. It is, however, noted that the implementation of all passive

safety features needs to be quantified in terms of core damage frequency. Such a quantification is beyond the scope of this study. In addition to its safety implications, the new LWR concept, with its unique reactor physics characteristics, opens the path for additional explorations of various alternatives of fuel-channel-in-a-voided-space design.

1.4 OBJECTIVES

The primary objective of this study is to develop a conceptual design for a light water cooled nuclear power reactor of a large power rating having passive decay heat removal capability. Conventional light water cooled reactor designs rely on normal functioning of the primary coolant system or emergency cooling systems to provide primary makeup inventory and to remove the decay heat. As noted earlier, the advanced LWR concepts retain the need to provide coolant makeup, but the processes for coolant delivery rely more on passive or semi-passive features. The effort in this work will aim at designing a light water cooled reactor compatible with passive safety features that can ensure integrity of the fuel and reusability of reactor components, including the fuel, without the requirement for the delivery of primary coolant. The passive decay heat removal phenomena employed involve thermal conduction, radiation, natural convection of a steam/air mixture, and the boiling/condensation processes of the heat sink, which is not primary coolant, but put in place passively upon sensing a LOCA.

1.4.1 Historical Design Objectives for Nuclear Power Reactors

A primary objective in designing nuclear power reactors has been the achievement of required safety at acceptable cost. In addition, however, other objectives have had parallel emphasis. These include dual production of electricity and defense materials, design compactness and enhancement of uranium utilization.

The dual production objective was a feature of early gas-cooled reactor designs in the UK and France and of the current water-cooled, graphite-moderated RBMK design in the former USSR. These approaches were not successful in supplanting the light water reactor concept for civilian electricity production, and the pressurized water reactor (PWR) appeared

as the dominant power-generating reactor worldwide. Among the reasons for the success of the PWR was its superior economic performance because the objective of compactness and the consequent minimization of the primary system size and weight, which governed the design evolution of the PWR system, also led to minimum cost of the reactor plant. This PWR objective also led to embracing the approach of a reactor core within a monolithic pressure vessel. At the high pressures employed in light water systems, these pressure vessels are necessarily of limited size, leading to high power densities in large modern LWRs.

The third objective, enhancement of uranium utilization, has been pursued to minimize the impact of potential fuel cost increases and to preserve natural uranium reserves. This objective, pursued through strict attention to neutron economy, has dominated the development of the Canadian pressure tube reactor concept. In this concept, promotion of neutron economy by adoption of heavy water as the moderator, and natural uranium as the fuel resulted in a large volume, low specific power, reactor block. Further, enhancement of neutron economy has also favored retention of heavy water as the coolant, although concepts have been developed which employed alternate coolants such as light water, gas or organics.

1.4.2 Proposed New Design Objectives

The current development of new reactor concepts needs to appreciate but not be constrained by these past efforts. Importantly, the design objective should be enhanced safety at acceptable cost. The other three historic parallel objectives noted above are not applicable as individual goals. In fact, by recognizing and rejecting these parallel objectives, greater opportunity to realize the primary objective can be achieved.

Specifically, it is recognized that achievement of enhanced safety requires attention to the three primary goals of ensuring

- control of reactivity,
- maintenance of core cooling, and
- ultimate removal of decay heat.

Reactivity control has historically been a design focus, and sufficient alternative means of achieving assured shutdown are available for the range of reactor concepts. Maintenance of core cooling can be attained by means which are not dependent on successful delivery of emergency core coolant by active systems. Finally, provision for ultimate removal of decay heat is constrained by the geometric path for vapor or heat flow from the core to the heat sink afforded by the concept geometry.

Concepts which will achieve these three safety related objectives with acceptable cost are sought. Two major postulates are made:

- (1) advanced reactors will not be produced in sufficient quantity such that savings due to serial production will outweigh economies of scale. Hence, modular reactors of small size (under 200 MWe) will not produce competitive economic power blocks of the anticipated needed plant capacity (600 to 1000 MWe).
- (2) advanced reactors will minimize technological and economic risk by using a coolant already successfully demonstrated in hundreds of years of fossil and reactor plant operation, which simultaneously has low unit cost. Such a coolant is light water. Gas is a less effective coolant and has not achieved a sustained satisfactory operating history. Heavy water has a relatively high unit cost.

These postulates limit the search to thermal reactor concepts. For the intermediate term this is acceptable since practical breeder reactors do not appear to offer overriding safety or economic advantages, and are not necessary to provide fissile fuel because of the current surplus.

Based on the above discussion, the new design objectives can be summarized as the basis for design criteria applied in the conceptual design of passive water-cooled power reactors.

- (1) For the intermediate term, i.e., the next generation or two, fast breeder reactors are not necessary to provide fissile fuel, hence thermal converter reactor concepts are to be employed.

- (2) Successful reactor operation involves the smooth interaction of a large number of components, systems, coolant and materials. Consequently, the accumulated operating experience with light water reactors should be taken advantage of insofar as possible in future designs.
- (3) The successful demonstration of light water coolant use over a long period of time, its low unit cost and the design flexibility conferred by light water are highly beneficial. The cost of building the infrastructure necessary to assure heavy water supply can be a concern for countries which do not have large heavy water facilities. Hence, the study will be restricted to light water reactor concepts.
- (4) It is unlikely that the small sized reactors under 200MWe will be deployed in numbers sufficient to offset the economies of scale offered by the larger size units of over 600 MWe needed for base load. Consequently, the concept should have power rating above 600 MWe, preferably above 1000 MWe.
- (5) The reactor physics characteristics should satisfy the fundamental requirement that power increase leads to inherent reactivity reduction. Also, accidents leading to large temperature increases should lead to inherent reactor shutdown.
- (6) The safety of future reactors will be stringently judged on their inherent ability to reliably discharge decay heat to an ultimate heat sink. This can be accomplished most convincingly if the fuel bundles do not require replenishment of primary coolant.
- (7) Economic competition among energy production means will require the plant investment to be protected by designing for the reusability of major reactor components after major accidents. Therefore design limits will be imposed permitting the reusability of major components after all design basis accidents.
- (7) To minimize research and development cost associated with the new technologies, use of conventional technology will be relied on to the largest extent possible.

(8) Whatever the level of safety, any nuclear power plant contains radioactive material and involves a certain amount of risk. Since one cannot rule out what is physically possible, the objective of the design should be to reduce the risk of severe accidents and their consequences to extremely improbable values, comparable to other risks, which are commonly accepted. Hence, it is the goal of this design to retain conventional defense in depth, i.e., to put as many barriers between the fuel and the environment as possible to prevent fission product release.

1.4 THESIS ORGANIZATION

This work is only concerned on the development of a conceptual design which is focused on basic characteristics such as reactivity control, maintenance of core cooling during normal operation, decay heat removal from the core and ultimate decay heat removal from the containment. Economic considerations and various accidents are also briefly discussed. Many reactor design details such as the reactor control and instrumentation system, coolant makeup and purification system and the entire secondary system are not covered.

Chapter 2 presents the key rationale leading to the passive pressure tube LWR concept and a brief description of the concept. The key features of the proposed concept are described and the reference design and its parameters are presented. It is shown that the reactor consists of a dry calandria surrounded by a solid reflector, filled by gas during normal operation and flooded by a light water heat sink during accidents.

Chapter 3 discusses materials compatibility issues. It covers fuel matrix materials, fuel materials, structural materials for the fuel channel, and reflector materials.

Chapter 4 is devoted to reactor physics. Limitations of the application of the conventional diffusion equation to the proposed design and the need for the neutron transport equation are discussed. Several Monte Carlo code models which have been developed to analyze the reference design are described. The major body of the chapter presents the physics characteristics of the proposed design. These include prompt neutron

lifetime, Doppler coefficient, coolant void coefficient, neutron coupling of the core, neutron spectrum, fast and thermal neutron flux and their implication to pressure tube fluence and xenon poisoning, neutron economy, and reflector temperature coefficient. Reactor control is briefly discussed. One section is devoted to reactivity behavior during the flooding process of the calandria space. Fuel burnup and the effect of a bi-directional refueling scheme on the power density profile are also explored. The last section discusses the possibility of using the proposed concept for plutonium burning.

The fuel arrangement used in the reference design is only one alternative. Chapter 5 explores other possible alternatives for fuel arrangement and their advantages and disadvantages. First, basic factors influencing the suitability of various fuel arrangements with respect to reactor physics, thermal hydraulics during normal operation and during accidents are discussed. Fuel alternatives are listed and evaluated with respect to these merits.

Chapter 6 concentrates on fuel matrix performance during normal operation. The primary system configuration and its parameters are briefly described. A model for analyzing the thermohydraulics of the parallel non-communicating coolant channels in the fuel matrix is presented. The multidimensional finite element code ALGOR is used to calculate the matrix temperature profile and heat flux distribution. The results are discussed with particular respect to the limits of the critical heat flux ratio, fuel centerline temperature, and the pressure loss across the coolant channels. Both the fresh core and the equilibrium core are analyzed. Consideration is also given to fuel matrix performance in the post-critical heat flux (CHF) regime.

Chapter 7 carries out the fuel channel analysis in the loss of coolant accident. It shows that the decay heat generated in the fuel matrix is significantly decreased after the calandria is flooded. A simplified one-dimensional, transient heat transfer model of the fuel channel coupled to the point kinetics equation is described and used to analyze the loss of coolant accident scenarios. The results show superior thermal

performance of the proposed design in LOCA without scram and no primary coolant replenishment.

One of the key features of the proposed design is flooding of the calandria by passive means. Chapter 8 describes the means employed to achieve calandria flooding when primary system parameters exceed pre-defined limits. Analysis of the flooding process is carried out to confirm the feasibility of a sufficiently rapid flooding process.

Chapters 9 and 10 discuss materials, solid mechanics and thermal hydraulic considerations of the fuel channel and solid reflector design. CANDU experience with fuel channels is reviewed and the effects of higher operating conditions and higher fast fluence in the proposed design are discussed. Stress analysis of the pressure tube and calandria protective tube are performed to confirm the capability of these tubes to withstand thermal stresses during the flooding process. Cooling issues of the solid reflector and control rods penetrating the reflector are reviewed in Chapter-10.

Chapter 11 is devoted to containment analysis. A large, free standing steel shell containment, cooled solely by buoyancy-induced air flow, is proposed and analyzed. Two computer codes – CONTAIN and GOTHIC – are used to carry out the analysis. The results show that the proposed containment with a design pressure falling within the range of conventional large dry PWR containments can dissipate the decay heat load. The GOTHIC code is also used to study the effects of thermal stratification inside the containment on passive containment shell cooling.

Chapter 12 evaluates the response of the reference design to various accident scenarios. Detailed analysis of the entire spectrum of accidents is beyond the scope of this work, hence only comparative evaluations with LWRs and CANDUs are performed.

Chapter 13 touches on some economic considerations. A fuel cycle cost estimate is performed. Capital cost and operating and maintenance costs are estimated only in a qualitative manner.

Chapter 14 presents an integrated evaluation of the overall concept. A summary of major design features and their performance is presented.

Finally, Chapter 15 gives the concluding remarks and recommends future work directions. Future work is divided into three areas – improvements in the analysis of the reference design, improvements or modifications within the reference design, and new promising alternative versions of a passive pressure tube reactor with voided calandria. These range from a passive LWR plutonium burner, to a thermal breeder, to a fast liquid metal cooled pressure tube reactor.

Chapter 2

GENERAL DESIGN APPROACH AND BRIEF DESCRIPTION OF A CONCEPT

2.1 INTRODUCTION

Development of a passive LWR concept which could survive absence of primary coolant involves new core configurations which are able to dissipate the decay heat from fuel bundles by radiation, conduction and natural convection of steam/air mixtures. Initial work on such LWR concepts was done by Owens [1990] and Hejzlar et. al.[1991]. The potential feasibility of achieving this goal has been identified in these studies and further confirmed by Tang [1992]. Owens studied the geometry of LWR cores which can provide large heat storage capacity and which can effectively dissipate decay heat from the core. Hejzlar examined various approaches of passive heat transfer from the fuel to the ultimate heat sink. Choke points on the path between the core and the vessel wall, the cavity between the vessel wall and the containment wall, and between the containment wall and ambient were identified. The study by Hejzlar et. al. [1991] yielded the key idea of the modularity of the fuel. As a result, a concept with a fueled solid matrix in a pressure tube was suggested as the most promising alternative. This work builds on the conclusions drawn from this study and complements the investigations performed by Tang [1992].

In this Chapter, the rationale behind the pressure tube LWR and the overall description of the proposed reference design are presented. The main fundamental principles allowing one to maximize the heat removal rate from voided fuel bundles, to be utilized in the design of the passive LWR concept, are identified and listed in Section 2.1. The overall layout and

principle of operation of the reference passive pressure tube LWR are given in Section 2.3. Reference design parameters are listed in Section 2.4.

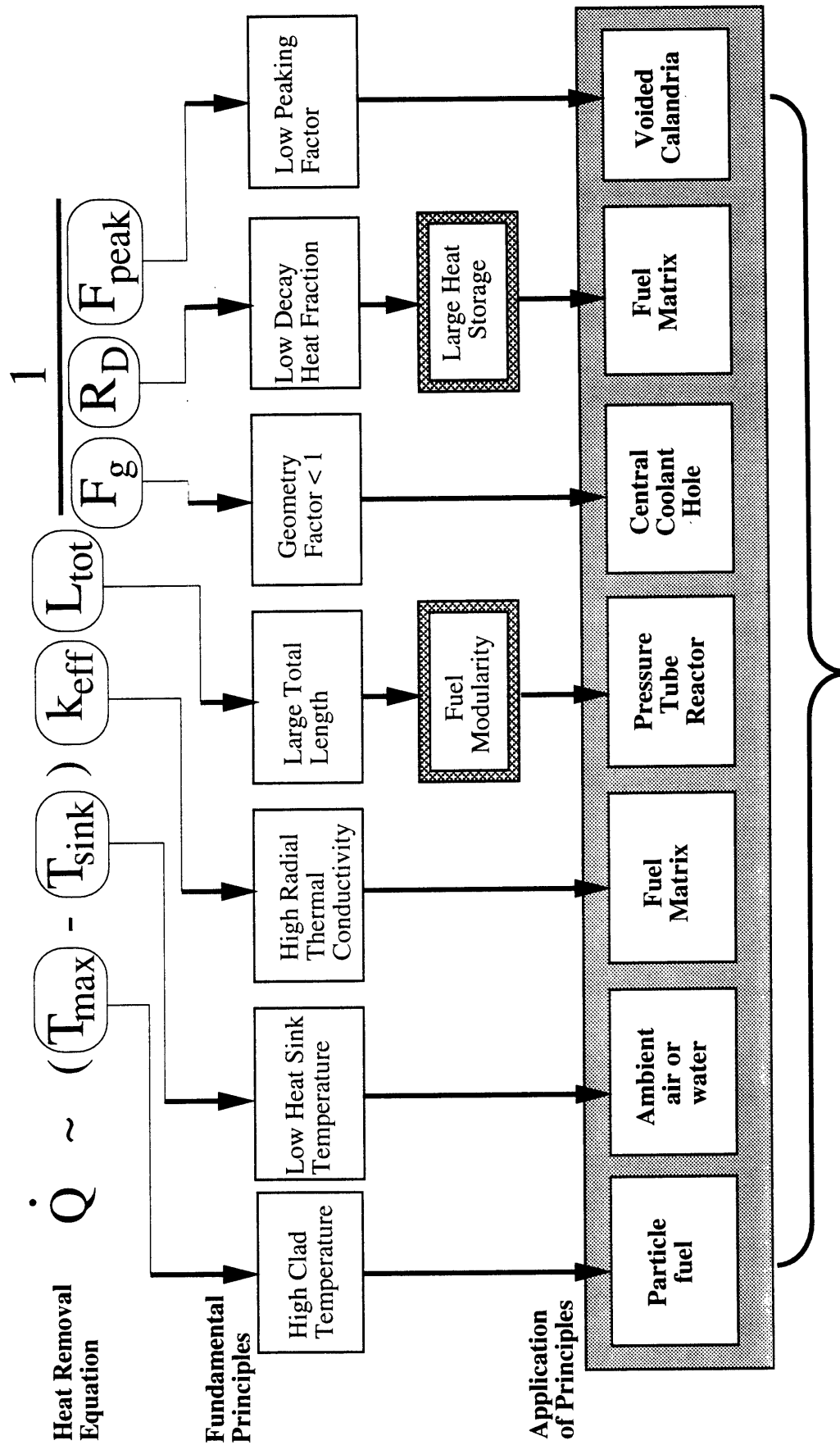
2.2 RATIONALE LEADING TO A PASSIVE PRESSURE TUBE LWR

The achievable power rating of nuclear reactors is limited by their coolant's capability to remove generated power at the location of highest power density without exceeding safe temperature limits on the cladding and the fuel. The traditional approach is to establish a nominal power such that these safe limits are not exceeded, both during steady state operation and plant transients. To stay within the safe limits in loss of coolant accident scenarios, the practice is to replenish inventory rapidly with emergency coolant (either by active or by passive means). The approach presented here is based on the postulate that the fuel elements should safely survive the total loss of coolant, hence eliminating the necessity of primary coolant replenishment. As a result, an additional constraint on the achievable reactor power output arises. This constraint stems from the requirement that voided fuel elements must be capable of dissipating the decay heat by natural phenomena such as conduction, radiation, and convection in steam/air mixtures, without exceeding safe temperature limits. The rated core power which would satisfy this requirement can be estimated from the simplified conduction equation in cylindrical geometry

$$\dot{Q} \approx (T_{\max} - T_{\text{sink}}) k_{\text{eff}} L_{\text{tot}} \frac{1}{F_g R_D F_{\text{peak}}} \quad (2-1)$$

In compliance with the objective of high power rating, it is desirable to maximize the right hand side (RHS) of Eq. (2-1). The fundamental principles used to maximize the RHS of Eq. (2-1) and application of these principles to a LWR design are shown in Figure 2-1.

T_{\max} is the maximum limiting temperature of the fuel or, more frequently, of the cladding. Considerable enhancement in this temperature can be achieved by using high temperature fuel in the form of particles with ceramic coating. The temperature of the ultimate heat sink, T_{sink} , is related to the temperature of the ambient, and is effectively a fixed value. The effective conductivity due to conduction, radiation and convection, k_{eff} ,



Passive Pressure Tube LWR

Figure 2-1 Principles to maximize reactor power rating set by decay heat removal limits, in the total absence of coolant, and their application in the passive pressure tube LWR

which is marginal for voided LWR fuel bundles, can be considerably increased by introducing a solid matrix with dispersed fuel and coolant channels.

Various arrangements of the fuel matrix in an LWR core have been investigated and are summarized in [Hejzlar et. al., 1993a]. The main results of these studies are shown in Figure 2-2. Figure 2-2 was generated for fixed maximum clad temperature, T_{\max} , heat sink temperature, T_{sink} , and peaking factor, F_{peak} . Power Q , shown in Figure 2-2, is the core nominal power allowed by the decay heat removal constraint in case the fuel elements are voided, i.e., the maximum temperature limit on cladding cannot be exceeded. Two arrangements of fuel and coolant channels in the matrix have been assessed. One arrangement uses coupled fuel/coolant channels with clad fuel pins inserted in the center of coolant channels and the coolant flows around the rods. The second configuration uses separate fuel/coolant channels, where the fuel is in a set of fuel holes and coolant flows through separate coolant channels. The latter arrangement is beneficial from the decay heat removal standpoint since it exhibits higher effective thermal conductivity, and hence higher achievable rated power. This can be observed by comparing the power increase in an annular core configuration from $3Q$ to $4.5Q$ in Figure 2-2. The lower effective thermal conductivity of the former configuration is the consequence of high heat transfer resistance between the fuel pin and the coolant-channel wall (heat transfer is primarily by radiation). Therefore, the matrix configuration with separate fuel/coolant channels has been selected for the reference design.

An additional benefit of high effective thermal conductivity, not captured by Eq. (2-1) is the low maximum fuel matrix temperature during normal operation, and hence, low initial stored energy. Low initial stored energy results in reduced temperature of the matrix/steam interface during LOCA.

The geometry factor, F_g , is equal to 1.0 for solid cylinders, but it can be decreased by using an annular geometry. The gain in achievable power is about 300%, i.e., power increase from $1Q$ to $3Q$, as can be seen in Figure 2-2 by the transition from a solid core to an annular core configuration.

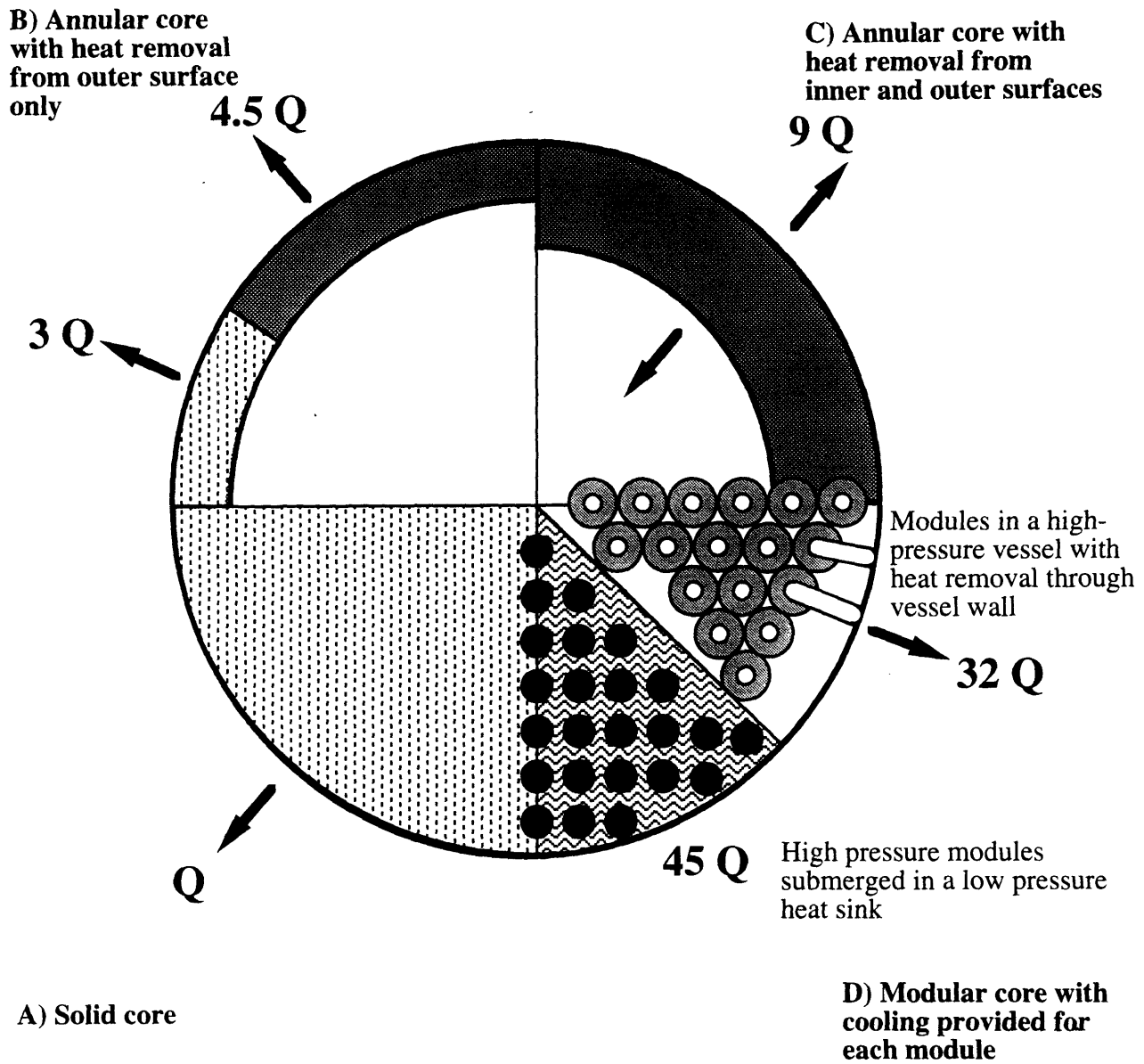
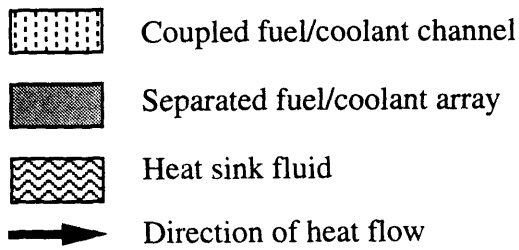


Figure 2-2 Various fuel matrix configurations in a LWR core and road to fuel modularity, from [Hejzlar, 1993a]

Lower geometry factor can be achieved by arranging the fuel matrix such that a coolant channel is located in the center, creating thus an annular geometry. By introducing heat removal on the inner surface of the annulus, the power can be doubled. The implementation of this design is, however, rather impractical.

The effective total heat transfer length can be expressed as $L_{tot} = N L_{core}$ where N is the number of modules containing voided fuel elements which are in direct communication with the heat sink (not necessarily the ultimate heat sink). For example, if the heat sink is located outside a typical LWR vessel, $N=1$ since the whole core is one module from which the heat must be dissipated, from the core center radially across the entire voided core. When N voided fuel modules are distributed in a low pressure heat sink, each module communicates independently with the heat sink and the total heat transfer length in Eq. (2-1) is the sum of all the lengths of these modules. There are two possible practical applications of this principle – fuel matrix modules in a high-pressure vessel with heat removal through the vessel wall, and high-pressure modules submerged in a low-pressure heat sink. The former approach requires provision of heat sinks (e.g. thermosyphon loops) for each module capable of transferring the heat from the module to the high-pressure vessel wall (32Q). However, thermosyphon loops or similar devices, while efficient mechanisms of heat transport, may pose design complications and are vulnerable to failure during rapid depressurization events. Moreover, previous studies showed [Hejzlar et. al., 1993a] that the heat transfer rate through a thick pressure vessel is limited. Therefore such an approach was discarded from further considerations. A more practical application of the fuel modularization principle is a pressure tube reactor where N is the number of pressure tubes immersed in the calandria. It can achieve the highest decay-heat limited power rating (45Q) and can build on conventional technology and experience provided by CANDU reactors. Consequently, the pressure tube reactor approach has been selected.

R_D represents the ratio of the average decay heat rate to rated operating power. It can be decreased by maximizing the heat storage capability of the fuel. Introducing a fuel matrix effectively delays the time at which the heat

removal rate must equal the heat generation rate by storing a substantial amount of decay energy in the matrix. This can be observed in Figure 2-3, which shows the decay power fraction and integrated decay energy as a function of time. If the storage capabilities of the matrix are zero, the decay heat to be removed is almost 7% of full power. On the other hand, if the fuel matrix can store generated decay heat for 300 seconds, the decay heat rate needed to be removed is about a factor of three lower*. Hence a matrix material with high specific heat is desirable.

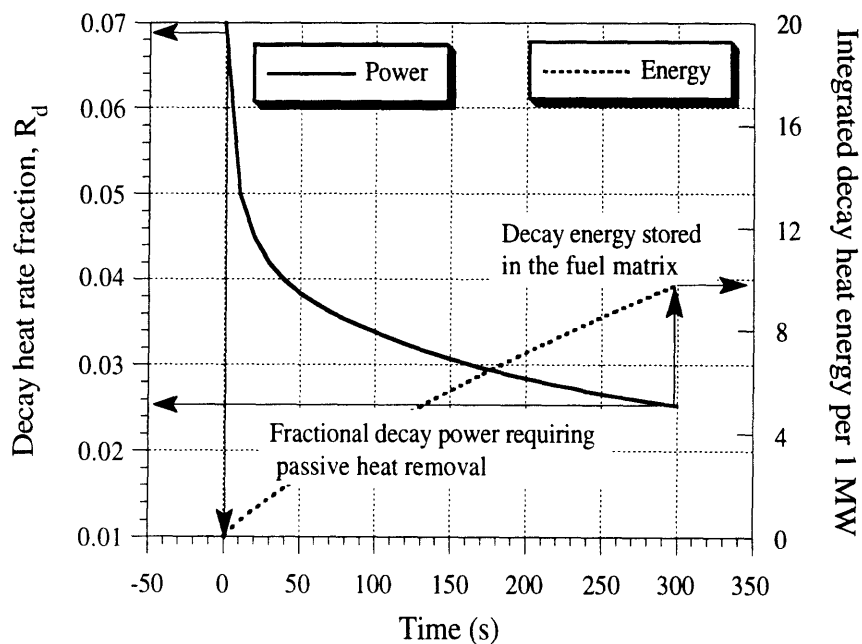


Figure 2-3 Importance of the heat storage capability of the fuel matrix

Finally, reducing the total peaking factor, F_{peak} , results in lower peak parameters at the locations where the limits are reached first, hence allowing for a further increase in power rating. A considerable decrease in peaking factor can be achieved by increasing calandria void fraction. This

* Of course, the energy stored in the matrix is subsequently removed at a rate which corresponds to the excess in heat removal rate over heat generation rate with consideration of system temperatures.

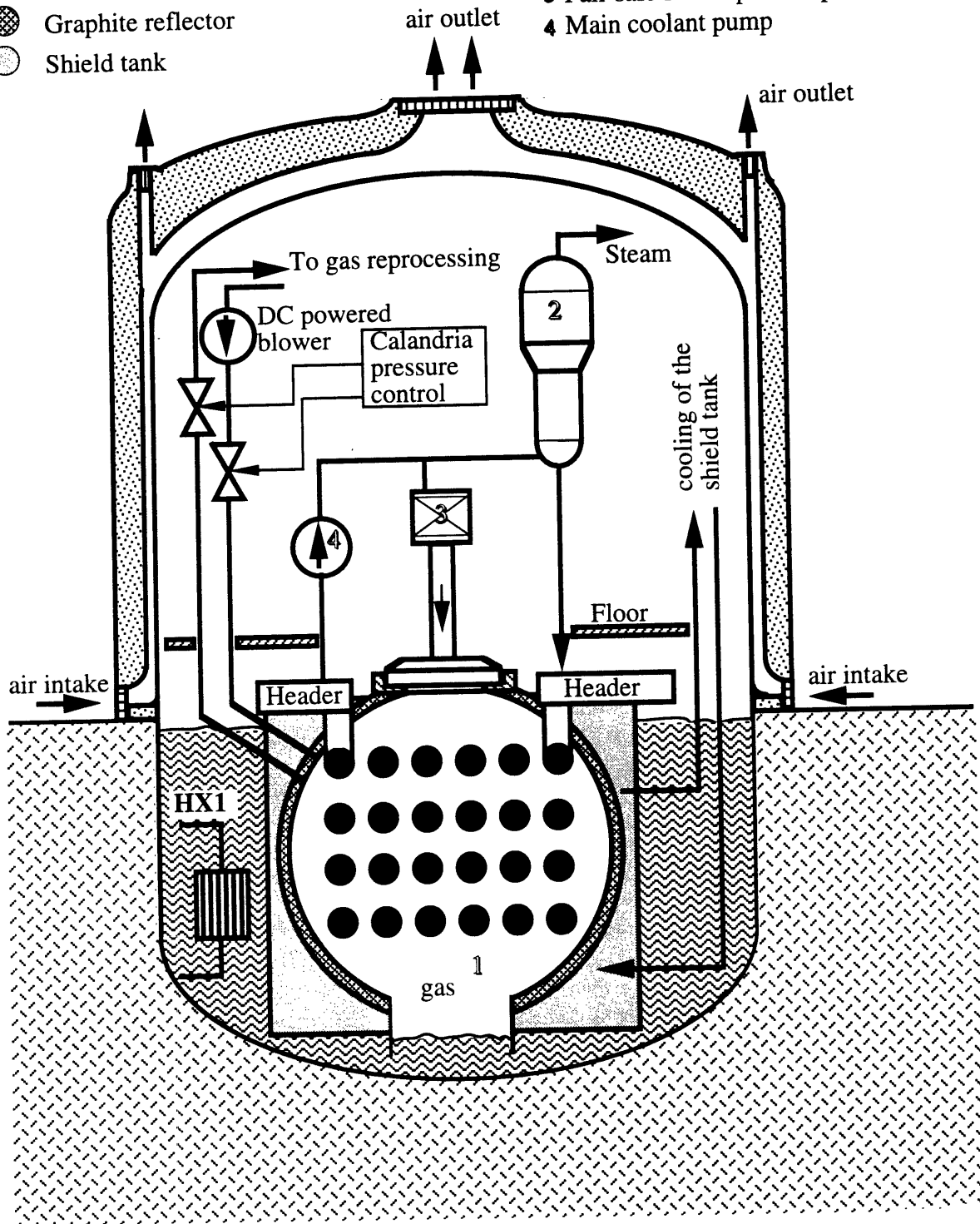
approach is consistent with reactor physics requirements in a light water moderated pressure tube reactor. The minimum channel pitch is restricted by the space requirements associated with header plumbing. The space between the pressure tubes cannot be filled with light water moderator since the high slowing down power of H₂O would result in a highly overmoderated system. Also the high absorption cross section of H₂O would require extremely high enrichment to make the system critical. However, the reduction of moderator-to-fuel volume ratio could be achieved by a mixture of H₂O and voids.

The issue of maximizing decay heat dissipation from the voided fuel elements, discussed above, has been the main thrust behind the development of the passive pressure tube LWR concept. Besides heat transfer performance without primary coolant, there are other important factors which influenced the design development process. These include inherent reactor shutdown in accidents leading to a large temperature increase. To satisfy this objective, the reactor must be designed with negative fuel and coolant temperature coefficients under all circumstances. The desire to use conventional technology and experience bases to the largest extent practical resulted in adoption of many CANDU features. Besides reducing the development and research cost, this strategy also allows one to base the issues common to both CANDU and the passive pressure tube LWR on CANDU experience. Taking into consideration all these principles and applying them to the overall design resulted in the passive pressure tube LWR, which will be described next.

2.3 BRIEF DESCRIPTION OF A PTLWR CONCEPT

A schematic of the passive pressure tube LWR, also called the dry calandria design, is shown in Figure 2-4. Note that Figure 2-4 is highly schematic to show the principle of operation rather than the actual arrangement. To build on proven technology to the largest extent possible, the proposed design is based on CANDU reactors. It consists of fuel channels, calandria vessel, shield tank and the entire primary system very

- Pressure tubes with fuel matrix
 - ☞ Containment light water pool
 - ⊗ Graphite reflector
 - Shield tank
- 1 Dry calandria
 - 2 Steam generator
 - 3 Fail-safe fluid-operated passive valve
 - 4 Main coolant pump



Not to scale

HX1 heat exchanger to maintain containment water at $\sim 40^{\circ}\text{C}$ during operation

Figure 2-4 Schematic of the passive pressure tube LWR – overall concept

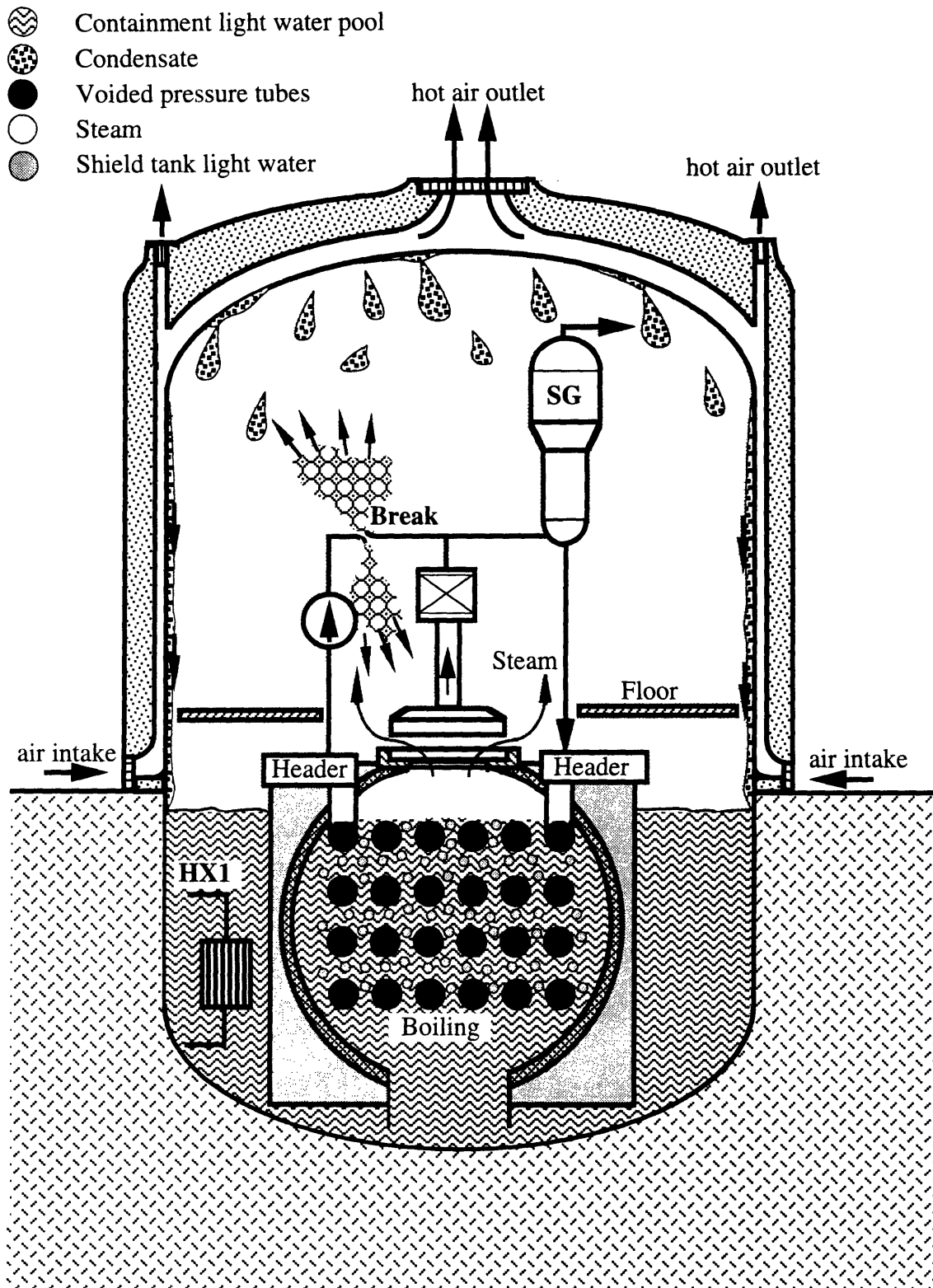
similar to those of CANDU units. There are, however, several major features which differ from current CANDU designs. These include

- dry calandria, with no moderator, surrounded by a solid reflector and connected by a gas lock to a large water pool,
- passive means to flood the calandria,
- passively air-cooled large containment, and
- fuel matrix in the pressure tube.

Under normal operation, the dry calandria space is filled with a gas under pressure slightly above atmospheric. The calandria bottom is equipped with passages with extended vertical walls submerged in a large water pool in the containment (designated the containment water pool), the temperature of which is maintained at about 40 °C by heat exchanger HX1. During normal operation, the containment water level is kept below the calandria bottom in the space within the extended vertical walls by maintaining the gas pressure in balance with the containment water column. The pressure level is maintained by a dc powered blower.

To minimize neutron losses, the calandria space is surrounded by a graphite reflector with an inner liner. The reflector is internally heated by neutrons and gamma rays during operation and must be continually cooled. The temperature of the graphite reflector is maintained sufficiently high (above 300 °C) to eliminate stored energy buildup in the graphite. The axial reflector is cooled by the coolant in the pressure tubes penetrating the reflector. Cooling of the radial reflector is accomplished by non-fueled pressure tubes. Note that the high reflector temperature enables one to recover practically all the heat generated in the reflector, and hence improve plant efficiency. Finally, the calandria is submerged in a shield tank which attenuates neutrons escaping from the graphite reflector.

Figure 2-5 shows the reactor operation during LOCA. Upon a pre-defined disturbance of the primary system conditions the gas is released from the calandria, resulting in calandria flooding.



Not to scale

Note: No emergency cooling systems in the primary system

Figure 2-5 Passive pressure tube LWR – operation during LOCA

Several means to initiate flooding of the calandria are possible. A passive fluid-operated fail-safe valve could accomplish this purpose. The valve works on primary system pressure. Its dead bands are set such that they envelope pressure disturbances and transients which do not require reactor shut down. When the predefined envelope is exceeded, the valve opens the calandria closure seal and the water from the containment water pool floods the calandria. Note that the valve must open both in case of “low pressure” accidents, e.g. loss of coolant accident, or in case of “a high pressure” accident, e.g. loss of heat sink. The valve is designed such that failures of various valve parts lead to valve opening. Hence the valve was designated as fail-safe in the sense that any failure results in the desirable action, i.e. valve opening. One possible design of a passive fluid-operated valve which can accomplish this purpose is described in Chapter 8. Other means (or the combination of various means) of calandria flooding can be also used. For example, the electrically powered blower maintaining the gas pressure while operating could be designed to lose power and hence depressurize the gas space upon predefined disturbances in the primary system parameters.

Calandria flooding has four important purposes:

- it ensures the removal of decay heat from the calandria tubes by boiling, evaporation and subsequent condensation on containment walls during an accident,
- it provides a large amount of water, which stores a considerable amount of decay energy, thus substantially reducing the heat rate transported through the containment walls early in the accident,
- it shuts down the reactor (if still operating) and renders it deeply subcritical by excessive neutron absorption (even in the boiling mode)*, and

* Note that the flooding water is non-borated, and still provides a negative reactivity of about 250β , once all pressure tubes are fully covered.

- it considerably reduces the decay heat load on the fuel matrix (by about 40%) by absorbing a large portion of gamma heating which would have been otherwise deposited in the fuel matrix.

Once the temperature of the flooding water in the calandria gets close to saturation, steam which begins to escape from the calandria will condense on containment walls, and the condensate returns to the water pool, completing the heat transport circuit. The containment steel shell is cooled by an annular air chimney created by the space between the steel shell and the protective prestressed concrete shell. The containment decay heat removal system must handle both the full blowdown of the primary system and the decay heat generated in the core.

Figure 2-6 shows the reference (one of several considered) fuel matrix arrangement in a fuel channel both in normal operation and in a LOCA situation, i.e., without a coolant. Several matrix materials have been considered. The most promising appears to be nuclear grade graphite fully coated by silicon carbide such that the graphite does not contact the coolant. Although graphite is compatible with light water coolant at operating coolant temperatures of 300 °C, the silicon carbide coating is required to prevent excessive graphite oxidation at high temperatures in the absence of coolant. Fuel compacts contain TRISO* particles and are arranged in two concentric rings. Cooling is accomplished by light water coolant flowing through 19 circular channels and one outer annular channel. The matrix elements are 50 cm long and slide in the channel on bearing pads.

The pressure tube is surrounded by a protective tube, also termed the calandria tube. This tube has the primary function of preventing excessive pressure tube stresses which would have resulted had the cold water during flooding come into contact with a hot pressure tube still under pressure. The detailed design of the gap between the calandria tube and pressure tube has not been finalized at this stage. The main requirement is

* Four layer coating consisting of a composite structural coating, made up of two relatively dense PyC layers encasing a SiC layer over a buffer coating.

that the effective thermal conductivity is about 2W/m-K. This can be achieved by filling the space with a packed bed of graphite pebbles, proposed by Tang [Tang, 1992], zirconia spheres as proposed by Dutton [Dutton, 1993], or a duplex tube, similar to those used in EBR-II sodium-water steam generators. Similarly as in current CANDU reactors, it is desirable to maintain gas in the gap to monitor for leakage from pressure tubes.

- | | |
|---|---------------------------------------|
| ⊗ Pressure tube | ⊗ Containment water pool in calandria |
| ⊗ Coolant | ○ Steam/air mixture |
| ● Fuel matrix (silicon carbide coated graphite) | ⊗ Protective calandria tube |
| ⊗ Fuel compacts with particle fuel | |

Normal Operation

Accident Operation

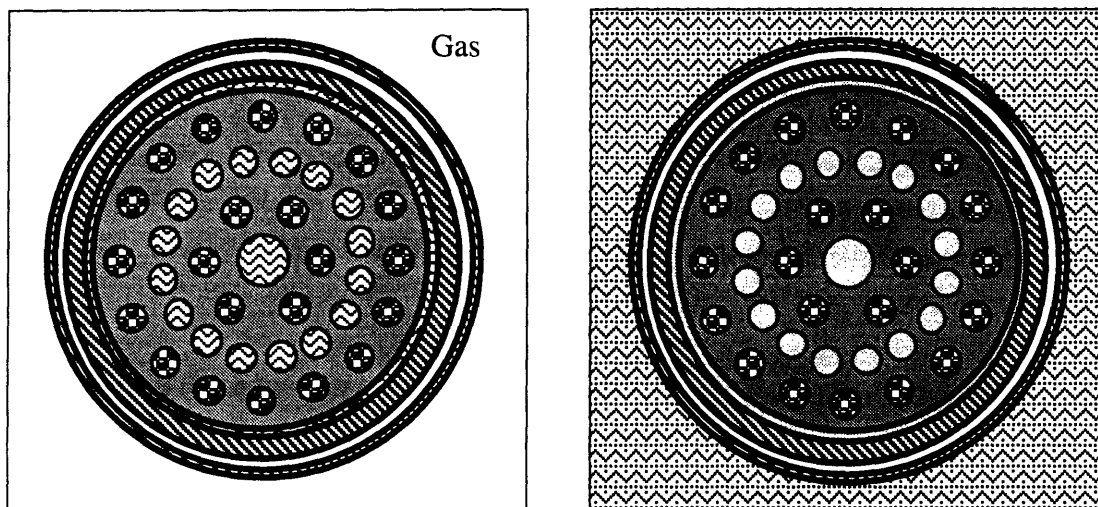


Figure 2-6 Fuel matrix in a fuel channel during normal and accident operation

The PTLWR primary system is essentially the same as that of a published CE-CANDU design except for the Emergency Core Cooling System (ECCS), which has been eliminated. Instead flood water in the calandria provides the heat sink for the decay heat. Another philosophy is to retain the ECCS and use the heat sink in the calandria as a backup. However, since the fuel elements do not require reflood and since the calandria flooding system can be designed to provide a reliable heat sink, it is argued that the ECCS is not needed. Elimination of the traditional ECCS

allows simplification, cost reduction associated with elimination of piping, valving and an ac safety grade power supply including diesel generators. Moreover, once the coolant is lost and the temperature of the fuel matrix is raised to about 900 °C, direct reflooding of the fuel matrix is not desirable because it would lead to rapid quenching of the fuel matrix coating. Although the matrix coating will be able to withstand such phenomena, it is preferred that the fuel matrix be cooled down more slowly from the outside of the fuel channel.

The PTLWR retains CE-CANDU's shutdown cooling system. This cooling system supplements the heat removal system through the steam generators and is used to reduce the temperature of the reactor coolant system (RCS) in post shutdown periods from normal operating temperature to a plant maintenance temperature and to maintain this temperature for a period of time. It also has the capability of operating under post loss of coolant accident or loss of heat sink conditions to cool the plant and bring it to a cold shutdown condition.

The schematic of the shutdown cooling system circuit and primary heat transport system is shown in Figure 2-7. During shutdown cooling, a portion of the reactor coolant flows out the shutdown cooling nozzles located on the reactor outlet headers. The coolant is recirculated through the shutdown cooling heat exchangers by the shutdown cooling pumps and returned to the reactor cooling system at the reactor inlet headers. During normal operation, the system is isolated from the RCS.

2.4 REFERENCE DESIGN PARAMETERS

The specific conceptual design of a passive pressure tube LWR discussed in this paper is based on the Combustion Engineering (CE) study of a large heavy water reactor for U.S. siting [Shapiro and Jesick, 1979]. This reactor concept, denoted CE-CANDU, has 740 fuel channels and a power rating of 1260 MWe. The main difference between the CE-CANDU concept and CANDU reactors is its larger number of pressure tubes and higher primary system pressure (by about 5 MPa).

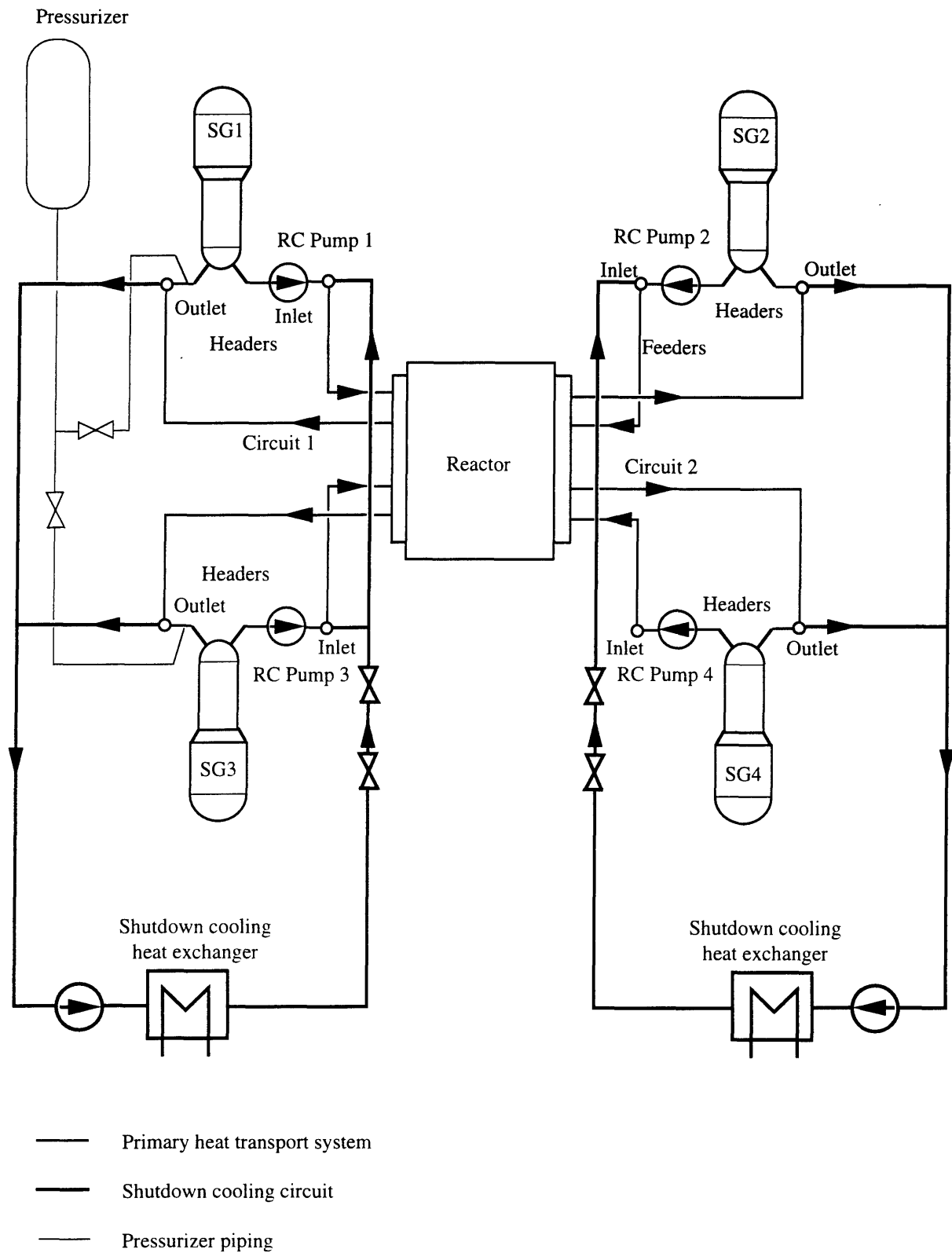


Figure 2-7 Schematic of the PTLWR primary heat transport system and shutdown cooling circuit

There are several motivations for this choice:

- the CE-CANDU reactor has a high power rating which covers the targeted range,
- it has the same power density as CANDU units and is based on CANDU experience,
- it allows one to avoid the need for detailed assessment for design parameters not central to PTLWR features.
- it was designed with US regulatory and market practices in mind, and
- detailed information on CE-CANDU design parameters was available.

The reference design parameters will be listed in four categories – core and primary system parameters, fuel channel parameters, flooding system parameters and containment parameters.

2.4.1 Core and Primary System Parameters

Core and primary system parameters for the reference PTLWR concept are listed in Table 2-1. In essence, core and primary system parameters are identical to the reference CE-CANDU design, except for core thermal power, which takes into account recovery of PTLWR heat losses in the core, and was calculated such that the net power output of the PTLWR equals that of CE-CANDU. Total power peaking depends on the refueling scheme. The maximum power peaking for the bi-directional refueling scheme is 1.35. For the fresh core, peaking is only 1.2.

2.4.2 Fuel Channel Parameters

Fuel channel parameters for the reference PTLWR concept are summarized in Table 2-2. Dimensions of the fuel channel, except for the fuel matrix geometry and the gap between the pressure tube and calandria tube are the same as for the CE-CANDU design. As discussed in Section 2.3, the gap design remains to be finalized. For the purpose of the present analysis, a 2 mm-wide gap is assumed. Lattice channel pitch was selected the same as for the CE-CANDU design. However, it is noted that the

PTLWR concept is not constrained by reactor physics characteristics resulting from changed fuel channel pitch as is the case in CANDU reactors. Hence, the pitch can be decreased as far as the header arrangement allows. If the currently used faceseal closure is used, the minimum pitch is 22.86 cm; employing a boroseal closure would allow a minimum pitch even lower, i.e., 20.4 cm [Hart, 1991]. This would allow more pressure tubes in the same space (by about 160), and hence increase net power to about 1550 MWe. Moreover, neutron leakage would be decreased due to the decrease in neutron streaming.

Table 2-1 Reference core and primary system design parameters

Core and primary system parameters	Values
Total core thermal power	3899 MWt ^a
Core radius	8.77 m
Core length	5.94 m
Reflector material/thickness	graphite/1 m
Total number of fueled pressure tubes	740
Total power peaking	≤1.35
Primary system pressure	15.34 MPa
Primary system temperature at fuel channel inlet	298.9 °C
Total mass flow rate through fuel channels	14,100 kg/s

^a Yields net power output of 1260 MWe with an overall thermal efficiency of 32.3%. Net power output is identical to that of the CE-CANDU, thermal efficiency is higher than that of CE-CANDU due to elimination of heat losses in the moderator.

Table 2-2 Reference fuel channel parameters

Fuel channel parameters	Values
Pressure tube inner diameter	128 mm
Pressure tube thickness	5.79 mm (Zr-2.5Nb)
Pressure tube-calandria tube gap thickness	2 mm
Calandria tube thickness	1.52 mm (Zr-2)
Pressure tube pitch	285.75 mm
Fueled pressure tube length	5.94 m
Fuel matrix outer diameter	120.8 mm
Fuel matrix element length	0.5 m
Number of fuel compacts per fuel matrix	26
Number of coolant channels in the matrix	19
Diameter of fuel compacts in the inner fuel ring	12.4 mm
Diameter of fuel compacts in the outer fuel ring	12.7 mm
Diameter of intermediate coolant channels	8.4 mm
Diameter of central coolant channel ^a	22.7 mm
Fuel/Initial fuel enrichment	UO ₂ /7%

^a Central coolant channel employs sand-grain type roughness.

2.4.3 Flooding System Parameters

Main flooding system parameters used in analysis of the reference PTLWR concept are summarized in Table 2-3. The volume of flooding water in the containment was selected to provide sensible and latent heat for about 60 hours, i.e., beyond the time when the containment peak pressure is reached. This reduces the containment pressurization rate as well as the maximum pressure peak.

Table 2-3 Reference flooding system parameters

Flooding system parameters	Values
Volume of flooding water	4200 m ³
Flood water temperature	40°C
Height of driving water column	14.5 m
Number of bottom intakes for flood water	3
Total flow area of bottom intakes	2.25 m ²
Number of passive valves for flooding initiation	4
Flow area for gas exhaust per valve	0.125 m ²
Operating gas pressure in the calandria space	0.24 Mpa

2.4.4 Containment Parameters

Main containment parameters used in analysis of the reference PTLWR concept are summarized in Table 2-4.

Table 2-4 Reference containment parameters

Containment parameters	Values
Containment shell inner diameter	60 m
Containment shell height	81 m
Containment free volume	1.7x10 ⁵ m ³
Thickness of steel shell	4 cm
Thickness of vented air gap	0.5 m
Total flow area of air inlet passages	100 m ²
Total flow area of air outlet passages	90 m ²

2.5 IMPOSED DESIGN LIMITS

Key design limits imposed on the PTLWR concept are summarized in Table 2-5. These limits are based on the requirements of existing designs and on the evaluation of materials of choice. More detailed discussion of these limits will be given in the pertinent chapters.

Table 2-5 Imposed design limits

Design limits	Values
Normal full power conditions	
Maximum fuel centerline temperature	≤ 1300 °C
Minimum CHF ratio (local)	≥ 1.3
Coolant pressure drop across fuel channel	~ 1 MPa
Coolant void reactivity	zero or negative
Accident conditions	
Maximum fuel centerline temperature	≤ 1600 °C
Maximum matrix temperature	≤ 1300 °C
Maximum pressure tube temperature	≤ 500 °C
Maximum calandria tube temperature	≤ 500 °C

2.6 SUMMARY

The philosophy adopted in developing the PTLWR concept, with emphasis on passive decay heat removal from voided fuel elements is presented. Using a simple assessment process, it is concluded that a pressure tube reactor with matrix-type fuel has the most promising potential to achieve high power density and still be able to safely dissipate the decay heat from voided fuel elements. Applying fundamental principles derived from a simple conduction equation, a passive pressure tube LWR

concept is proposed. The conceptual design is briefly described and the main functions are explained. Major design parameters for the reference PTLWR, based to a large extent on the CE-CANDU design, are selected.

Chapter 3

MATERIALS CONSIDERATIONS

3.1 INTRODUCTION

The design objective of passive decay heat removal from the voided fuel elements poses new challenges to the fuel element materials. This chapter summarizes the issues considered in the choice of fuel matrix materials and identifies a matrix material compatible with light water coolant under normal operating conditions and with steam/air mixtures under accident conditions. Design requirements on the fuel matrix are listed in Section 3.2. The matrix material selection is based on an extensive review of experiments, experience, and research and development results published in the open literature. Materials covered in the search, the conclusions and the final selection are given in Section 3.3.

The reflector plays a more important role in the PTLWR concept than in typical LWRs because it affects the entire core. In fact, criticality could not be reached without the reflector because of very high leakage. Hence, it is desirable that the reflector material has very low absorption cross section and good reflective power. Reflector materials are covered in Section 3.4.

Section 3.5 reviews the fuel materials. Two types of fuel have been considered – coated particle fuel and pin fuel with cladding. Coated particle fuel is used for matrix-type fuel elements, either arranged in fuel compacts or dispersed in the matrix. Cladded pin-type fuel can be also used in the PTLWR fuel channels, although it affords less effective decay heat removal. Various fuel arrangements possible with the PTLWR fuel channels are further discussed in Chapter 5. The reference PTLWR design, analyzed throughout this work, uses TRISO particle fuel arranged in compacts. UO_2 , UC or UN fuels in silicon carbide cladding are proposed for pin-type fuel.

The structural materials covered in Section 3.6 include zirconium-niobium alloy pressure tubes. To satisfy the objective of reusability of the pressure tubes after major accidents, the design limits used for the fuel channel analysis, are identified. Other structural materials used in the primary system are the same as in the CE-CANDU and/or conventional CANDU concepts and are not discussed.

3.2 DESIGN REQUIREMENTS FOR MATRIX AND REFLECTOR MATERIALS

3.2.1 Matrix material

The design requirements for the matrix material are summarized in Table 3-1. For normal operating conditions, the matrix material must be compatible with the light water coolant at temperatures around 300 °C during the time the fuel elements reside in the core. For the reference PTLWR concept, this residence time is about 1.6 years. Another important requirement is good irradiation stability.

Accident conditions are understood as the sequence of phenomena occurring during the time period following a total loss of primary coolant accident. During such an event, the system is depressurized, the primary coolant is discharged and the matrix material becomes surrounded by a mixture of air and steam. Since the heat removal capabilities are considerably decreased in the absence of coolant, the material undergoes a temperature excursion. The most limiting requirement in such scenarios is the capability of the material to withstand this time period without substantial degradation due to high temperature oxidation or corrosion in an air/water vapor environment. Design requirements on matrix material are discussed in detail in [Hejzlar et. al., 1993c].

3.2.2 Reflector material

The primary purpose of the reflector is to reflect neutrons back into the core, and hence to minimize leakage from the reactor. The important nuclear property of the reflector is minimum absorption cross section, and

Table 3-1 Requirements on matrix material,
from [Hejzlar et. al., 1993c].

Requirement description	Operating conditions	Accident conditions
Corrosion and oxidation	resistant in H ₂ O at temperature of 300 °C for a long time period	resistant in mixture of water vapor/air at temperatures up to 1300°C ^a for several hours
Irradiation stability	lifetime up to fluence 1.05x10 ²² (E>.05MeV) ^b at irradiation temperature in the range 350-600°C	N/A
Stored energy	no or negligible accumulation of stored energy in temperature range 350 -600°C	no or negligible release of stored energy in temperature excursions above 350 °C
Water-material reaction	no water-material reaction at 350 °C	no or negligible energy release from steam - material reaction up to temperature of 1300 °C ^a .
Thermal conductivity	k≥10 W/m-K ^c	N/A
Surface emissivity	N/A	ε ≥ 0.7
Thermal stress resistance	ability to withstand thermal stresses during plant operation	good thermal stress and shock resistance in large temperature excursions

^aA temperature of 1300°C was specified based on anticipated matrix temperatures needed to dissipate decay heat during LOCA. However it is to be noted that for the reference design with matrix-type fuel, a maximum matrix temperatures of only 900 °C suffices to dissipate projected decay heat levels from the matrix to the heat sink outside the calandria tube. For the concepts with cladded pin-type fuel, maximum temperatures are envisioned to be around 1300 °C.

^bThis value pertains to the reference fuel matrix design; alternative fuel arrangements may have difference fluence limits.

^cApplies for the reference design with separate fuel and coolant holes.

to a lesser extent, high moderating ratio. These properties are satisfied by graphite, beryllium, beryllium oxide and heavy water. However, D₂O must be discarded since, in the case of a hypothetical break of the inner calandria wall separating the D₂O reflector from the gas space, flooding of the core with D₂O would cause a large positive reactivity excursion. Therefore only graphite, Be, and BeO were considered in this study.

Requirements for the reflector material are summarized in Table 3-2. The most important requirements are good irradiation resistance, since the reflector should be able to withstand plant lifetime without replacement, and no or negligible accumulation of stored energy.

Table 3-2 Requirements on a reflector material,
from [Hejzlar et. al., 1993c]

Requirement description	Operating conditions	Accident conditions
Irradiation stability	lifetime up to fluences of 2×10^{22} n/cm ² at irradiation temperatures of 350 °C to 800 °C	N/A
Thermal stress resistance	ability to withstand thermal stresses during plant operation	good thermal stress and shock resistance in cooldown transients
Stored energy issue	no or negligible accumulation of stored energy at temperatures of 350 °C to 800 °C	no or negligible release of stored energy in temperature excursions above 350 °C

3.3 MATRIX MATERIALS

The following candidate materials were identified for the matrix and reviewed:

- graphite,

- silicon carbide,
- silicon nitride,
- beryllium,
- beryllium oxide,
- beryllium carbide,
- beryllium silicon nitride,
- aluminum oxide,
- zirconium oxide,
- zirconium carbide, and
- zirconium hydride.

An extensive review is given in [Hejzlar et. al., 1993c]; only the main results and final choice will be presented here. Regarding the traditional solid moderator materials, beryllium, beryllium oxide, and graphite, none was found to be entirely satisfactory as a matrix material.

Beryllium has excellent nuclear and thermophysical properties. Its thermal properties are superior to those of graphite; in particular, the heat capacity of beryllium exceeds that of graphite by a factor of two and its thermal conductivity is not affected by irradiation. However, the data accumulated so far do not conclusively support the long term use of beryllium in high temperature water. Further, the irradiation behavior at operating matrix conditions does not seem satisfactory either. Most of all, beryllium is compatible with water vapor only up to temperatures of 600°C, which is far below the envisioned temperature peak during an accident – 1000°C. Toxicity, high cost, and problems with waste management are additional factors contributing to rejection of beryllium as a matrix material

Beryllium oxide exhibits good corrosion resistance in water vapor up to a temperature of 1175°C, which is a substantial improvement over beryllium metal. Also, corrosion behavior in high temperature water seems to be good, but this is supported only by one set of data. The major obstacle to the application of beryllium oxide is poor irradiation resistance. Irradiated beryllium oxide exhibits microcracks and cannot sustain the projected doses. The disadvantages of high cost, toxicity, and waste

management problems apply as well. Thus, beryllium oxide was eliminated from any further considerations.

Graphite has very good long term corrosion behavior in high temperature water and good resistance to irradiation damage, as well as excellent thermal, mechanical and neutronic physical properties. However, the resistance to oxidizing gases at high temperatures is low. The rates of oxidation of graphite in air or air/water vapor mixtures at temperatures around 1000°C are high, so that the graphite matrix would be burned out in a relatively short time (if sufficient air supply is provided). To avoid graphite contact with air/vapor mixtures, a protective coating on the graphite matrix is necessary. The primary function of the coating is to protect graphite in an oxidizing environment at high temperatures. The coating should be capable of retaining its integrity in fast temperature excursions and during irradiation. Hence, matching coefficients of thermal expansion of graphite substrate and the coating material is desirable.

Although there are several coating materials which could be used to protect graphite, silicon carbide coating is the most promising one. Also, considerable experience has been obtained with silicon carbide coating of graphite. Silicon carbide coating of large graphite blocks with coolant holes is possible using current technology. In fact, large graphite blocks are routinely coated with silicon carbide. Two major technical difficulties with a silicon carbide coated graphite matrix in the proposed application are the possibility of hair-line cracks in the coating in heatup cycles and oxidation of graphite substrate through these cracks, and delamination due to irradiation. The first problem may be alleviated by selecting a compatible grade of graphite to accommodate thermal expansion and by coating techniques which allow for gradual transition of the silicon carbide concentration between the graphite outer surface and the silicon carbide coating layer so that the thermal stresses typical of sharp interfaces are reduced. The second problem may be solved by employing a low density buffer carbon layer between the graphite matrix and the silicon carbide coating. Earlier tests showed very good performance of irradiated and thermally cycled silicon carbide-coated graphite [Jackson, 1966]. Recent

research and development program results on silicon carbide coated graphite blocks for nuclear applications indicate that the silicon carbide coated graphite matrix is a viable option [Eto and Shindo, 1992], [Kugeler,1992], [Schulten, 1993]. Another important advantage of the selection of silicon carbide-coated graphite is the ongoing research for even more strenuous applications such as the first wall liner and divertor in fusion technology. Any progress in coating technology achieved for these applications can be directly applied to the matrix for the proposed pressure tube concept.

The molded block fuel elements developed by HOBEK (Hochtemperatur-Brennelement GmbH) [Hrovat et. al., 1975] are especially attractive for the PTLWR matrix-type fuel. These monolithic blocks consist of an isotropic highly crystalline graphite matrix with coolant channels and fuel regions with TRISO particles embedded in a graphite matrix. The important characteristics are the elimination of the gap between the fuel compact and graphite matrix typical of MHTGR blocks, excellent thermal contact between fuel particles, and highly dense graphite matrix material. This allows operation at higher power density while keeping the maximum operating fuel temperature relatively low. Another advantage is that graphite losses during manufacturing are avoided since no machining of the graphite is required. Irradiation experiments on these blocks in the Peach Bottom HTGR showed very good performance [Wallroth et. al., 1976]. Because of these attractive properties, molded monolithic blocks coated by silicon carbide are considered as a very promising option.

Regarding non-traditional materials, the following materials were reviewed: silicon nitride, beryllium carbide, zirconium oxide, beryllium silicon nitrides, silicon carbide, zirconium hydride and aluminum oxide.

Silicon nitride was eliminated from further consideration because of its progressive corrosion in high temperature water. Beryllium carbide and zirconium oxide had to be rejected because of their very low thermal conductivity. The possibility of the use of beryllium silicon nitride still remains uncertain because of the lack of available information, but it is felt that its rather high absorption cross section will prevent its use.

The most promising material appeared to be silicon carbide. It has reasonably good nuclear properties, good thermal properties and resistance to irradiation damage. Furthermore, its long term corrosion behavior in high temperature water was found to be excellent. Silicon carbide is also compatible with water vapor and air up to temperatures of about 1300°C. Therefore, silicon carbide is the best candidate of the materials reviewed for matrix conditions. There are, however, several important issues – the cost, and relatively high absorption cross section, and hence more expensive fuel cycle. Since the mass of silicon carbide matrix in the core is relatively high, parasitic absorption in the silicon carbide matrix would require about 0.5% higher enrichment compared to a graphite matrix. Additionally, the relatively low thermal conductivity of irradiated silicon carbide and associated thermal stresses may limit the power rating during normal operation. Consequently, a graphite matrix with silicon carbide coating was deemed to be preferable.

Another promising material is zirconium carbide. But the issue of high parasitic neutron losses due to a relatively high absorption cross section holds for zirconium carbide as well as for silicon carbide. An attractive option would be to use zirconium carbide for coating of both the particle fuel and the graphite matrix. The main advantage of zirconium carbide coatings is the increased peak fuel temperature permissible under operating and accident conditions, compared to silicon carbide. However, analysis of the reference PTLWR concept shows that the maximum fuel temperatures reached during normal operation and during an accident should not exceed 1300°C, hence this increase is not essential and silicon carbide coating is more than sufficient. Moreover, silicon carbide coatings have undergone extensive development to reach the present state of technology (over 10 years), while it will probably take a similar time period to develop the technology for the production of consistent high-quality zirconium carbide-coated particle fuels [Kasten, 1990]. But more importantly, zirconium carbide has poor oxidation resistance and the emissivity of zirconium carbide pales in comparison with that of silicon carbide. Such a small emissivity would lead to unacceptably high matrix temperatures in the PTLWR reference design.

Zirconium hydride is attractive for the PTLWR concept, where the space for H₂O moderator/coolant inside the fuel channel is limited, because it can provide additional moderation due to its high moderation ratio. It has relatively good thermal properties and irradiation resistance. However, more data are needed to confirm the corrosion resistance in high temperature steam/air mixtures and long term corrosion behavior in high temperature water. Also, the effects of hydrogen redistribution on reactivity changes would need to be quantified.

Finally, aluminum oxide was considered as another possible candidate. Although the corrosion rates of high density alumina are acceptable, the corrosion behavior in high temperature water is not as good as that of silicon carbide. Conclusive irradiation data over the whole range of conditions are not available, but it is judged from irradiation tests at temperatures around 400°C that the irradiation behavior could be satisfactory. Compatibility with water vapor is very good up to 1550 K. The disadvantage of aluminum oxide is its relatively low conductivity, which excludes alumina as a matrix material for the reference PTLWR fuel design employing a fuel matrix with separate fuel and coolant holes. Moreover, as for silicon carbide, higher enrichments and higher manufacturing cost would make aluminum oxide economically uncompetitive with silicon carbide-coated graphite matrix fuel.

The conclusions above are briefly summarized in Figure 3-1 .

It follows from the above that silicon carbide-coated graphite appears to be the most promising choice for the matrix material. Chemical vapor deposited (CVD) SiC can provide long term oxidation protection at temperatures below 1300°C if variability due to small flaws in the coating can be eliminated. Silicon carbide is also a very stable material in high velocity steam up to 1100°C and the presence of hydrogen or helium in the steam does not affect the corrosion of SiC. CVD SiC, however, tends to crack and peel off during severe thermal cycles. The behavior of a SiC-coated graphite matrix under thermal cycles arising in the proposed design needs to be further investigated. To confirm the compatibility of SiC-coated graphite with PTLWR conditions, a small-scale experimental program has been initiated at MIT.

Material	<div style="display: inline-block; width: 15px; height: 15px; border: 1px solid black; margin-right: 5px;"></div> -not compatible <div style="display: inline-block; width: 15px; height: 15px; border: 1px solid black; background: repeating-linear-gradient(45deg, transparent, transparent 2px, black 2px, black 4px); margin-right: 5px;"></div> - uncertain <div style="display: inline-block; width: 15px; height: 15px; border: 1px solid black; background: radial-gradient(circle, black 1px, transparent 1px); background-size: 3px 3px; margin-right: 5px;"></div> -compatible	Description
Graphite		low oxidation resistance in water vapor and air at high temperatures
Beryllium		unsatisfactory corrosion resistance in high temperature steam, unsatisfactory irradiation behavior
Beryllia		unsatisfactory irradiation behavior, inconclusive data on corrosion resistance in high temperature water
Beryllium carbide		low thermal conductivity
Beryllium silicon nitride		insufficient corrosion and irradiation data
Silicon nitride		progressive corrosion in high temperature water
Zirconia		low thermal conductivity
Zirconium carbide		poor oxidation resistance in water vapor and air
Zirconium hydride		insufficient data on oxidation in high temperature steam/air mixture
Alumina		possible candidate, but relatively low thermal conductivity
Silicon carbide		possible candidate

Current Choice : SiC coated graphite matrix

Figure 3-1 Summary of material compatibility with fuel matrix conditions from [Hejzlar et. al., 1993c]

3.4 REFLECTOR MATERIALS

Three reflector materials were considered – graphite, beryllium and beryllium oxide. Light water was discarded due to its high absorption cross section and heavy water was also dismissed because of the theoretical possibility of flooding the calandria upon breach of the wall separating the reflector and the calandria space, which would render the reactor supercritical.

The review of irradiation effects on beryllium [Hejzlar et. al., 1993c] showed that beryllium and beryllium oxide have poor irradiation properties. The lifetime of beryllium is significantly less than that of graphite, especially at higher irradiation temperatures. Moreover, neutron irradiation of the beryllium reflector during reactor operation results in the buildup of ${}^6\text{Li}$ and ${}^3\text{He}$, which are characterized by their large thermal neutron absorption cross sections. As a result, nonnegligible reactivity loss would occur. Beryllium and beryllium oxide were therefore dismissed from further considerations.

Graphite appears to be the best choice as a PTLWR reflector material. Fast neutron flux in the reference PTLWR design at the location of reflector contact with the liner is quite high, i.e., 1×10^{14} n/s-cm² ($E > 0.05\text{MeV}$), which leads to a fluence in the portion of the graphite reflector with the highest exposure accumulated after 30 years of operation to be 1×10^{23} n/cm² ($E > 0.05\text{MeV}$). However, fast flux decreases very rapidly with radial coordinate towards the outer periphery. For example, at the position representing the radial midplane of the reflector, the fast neutron flux is lower by an order of magnitude, i.e., 9×10^{12} n/s-cm² ($E > 0.05\text{MeV}$), or a fluence of only 8.5×10^{21} n/cm² ($E > 0.05\text{MeV}$) after 30 years of operation. Hence, in practice, the most exposed inner part of the reflector must be designed to be replaceable. The use of pin-type fuel substantially decreases fast fluence on the reflector, hence the replacement of the inner reflector may not be needed for this alternative.

3.5 FUEL MATERIALS

There are two important considerations when selecting the fuel materials for the PTLWR concept – use of existing fuel technologies to the largest extent and maximizing the temperature limit of the fuel and cladding to withstand the higher temperatures needed for radiative heat transfer. Two types of fuel are applicable to the PTLWR fuel channel. The first type is matrix-type fuel, where coated fuel particles are dispersed in the fuel matrix or arranged in the matrix heterogeneously in separate fuel compacts. The second type is the traditional cladded pin fuel arranged in two concentric rings in the fuel channel. The geometry is the same as in conventional CANDU 37-rod bundles but the central fuel rod and the innermost fuel ring are removed to shorten the path for heat transfer between the fuel and the pressure tube wall.

3.5.1 Particle Fuel

Particle fuel was developed for high temperature gas cooled reactors (HTGRs). It comprises a small heavy metal kernel coated with several (typically two to four) layers of ceramic material, usually pyrolytic carbide and silicon carbide. Two types of coated particles have been developed – BISO particles and TRISO particles. TRISO particles offer better fission product retention than BISO due to the additional protective layer. In the current U.S. HTGR program, the fuel kernel material comprises a two component mixture of 19.9 weight percent enriched uranium dioxide (UO_2) and uranium dicarbide (UCO). A coated fuel particle is shown in Figure 3-2.

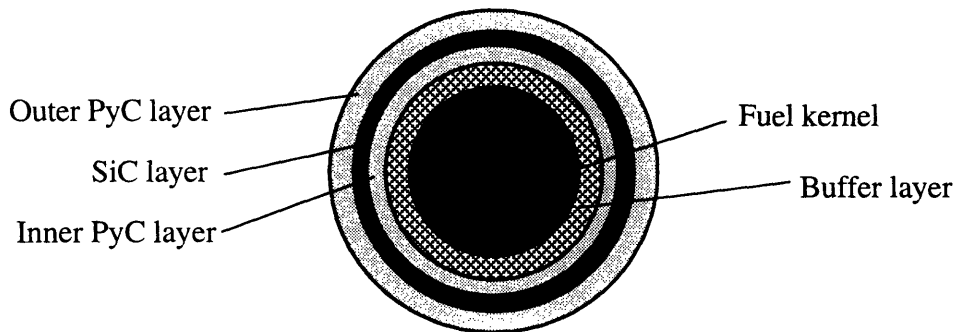


Figure 3-2 Layers of TRISO fuel particle

The heavy metal kernel is surrounded by a buffer layer of low density isotropic carbon which provides expansion volume for fission gases and protection against fission product recoil damage. The buffer layer is followed by an inner pyrolytic carbon (PyC) layer which provides a smooth substrate for successive coatings. The next coating layer is a silicon carbide primary structural coating which serves as an impermeable barrier to fission products and pressure boundary. An outer pyrolytic carbon layer provides a redundant pressure barrier to the SiC and serves as a bonding surface between the particle and the carbonaceous binder. Newer particles employ an additional outer layer of protective pyrocarbon. U.S. and German tests of millions of TRISO coated particles have shown that the particles can retain retain fission products up to temperatures of 1600°C [Sleicher and Wistrom, 1992]. During normal operation, the limiting fuel temperature is set at a lower value to reduce fission gas release by diffusion into the primary circuit. To ensure that the radiation dose resulting from accidental release of the primary system inventory to the atmosphere remains within regulations, the limit on fuel particle center temperature is 1300 °C at 100% power [Todreas and Kazimi, 1990]. Parameters of TRISO coated particles used in the analysis of the reference PTLWR concept are summarized in Table 3-3. The main disadvantage of coated fuel particles is a small core heavy metal loading, and hence high absolute levels of both thermal and fast neutron flux.

3.5.2 Clad Fuel

Although the coated particle fuel offers superb thermal performance, the relatively high core-average fast fluence associated with a small heavy metal loading is a disadvantage. To decrease the fast fluence on pressure tubes, clad fuel in a two ring arrangement is proposed in Chapter 5. This section discusses fuel material issues for this fuel arrangement alternative.

The most experience has been obtained with uranium dioxide fuel in a Zircaloy cladding. UO₂ has a high melting point, mechanical stability due to absence of metallic phase transitions, low fission gas release and less swelling and chemical compatibility than carbide fuel, and is not leached out of the clad by water in case of a leak. The drawbacks are very low

Table 3-3 Parameters of TRISO particle fuel [Lefevre, 1977],
[Dahlberg et. al., 1969]

<u>Particle layer</u>	<u>Thickness (μm)</u>	<u>Density (g/cm^3)</u>
Kernel (U235-enriched UO_2)	300 (diameter)	10.97
Buffer	50	1.1
Inner PyC	20	1.9
SiC	20	3.18
Outer PyC	40	1.8
<u>Other parameters</u>		
Binder content	36 vol%	
Maximum temperature at full power	1300 °C	
Maximum transient temperature	1600°C	

Table 3-4 Thermal properties of fuel materials [Chalder et. al., 1967],
[Smith, 1967]

Property	UO_2	UC	UN	U_3Si	U-metal
Theoretical density (g/cm^3)	10.97	13.63	14.32	15.58	19.04
Melting point (°C)	2880	2390	2650	1400	1133
Thermal stability upper limit (°C)	2880	2390	2650	1400	665
Average thermal conductivity at 200-1000°C (W/m-K)	3.6	23	21	15	32

thermal conductivity and relatively low density. Since the PTLWR with a two-ring arrangement has less fuel pins than the reference CANDU design and operates at the same core power, fuel with higher density is desirable to compensate for less fuel volume. It can be seen from Table 3-4 that other

fuels offer higher densities and much better thermal conductivity. The choice is, however, limited by the high temperature which the fuel must withstand without damage during accidents. Because of this consideration, two fuels with the highest density – metallic uranium and U_3Si were dismissed. UN appears to be an attractive fuel with its high melting point, high thermal conductivity and high density. Russian scientists recently proposed replacing UO_2 fuel in advanced light water reactors with uranium nitride (with N-15 enriched nitrogen to obtain a low neutron absorption cross section) [Subbotin, 1993]. While this fuel appears to be attractive for the PTLWR concept, it needs more research and development and it may be costly.

Most operating water-cooled reactors use Zircaloy as the cladding material. It has a low absorption cross section and good compatibility with the fuel and light water coolant. However, it undergoes an exothermic reaction with steam at relatively low temperatures. Since the maximum temperatures of the voided fuel elements in a two-ring arrangement are predicted to be higher than $1200^{\circ}C$ (the temperature at which the metal/water reaction becomes significant) another cladding material needs to be considered. The major candidate materials for this application are alumina, zirconia and silicon carbide. Alumina and zirconia have been dismissed because of their very low emissivity (about 0.4), which significantly effects the maximum cladding temperature during an accident.

The most attractive option appears to be silicon carbide. It has very high tensile strength, good fracture toughness, and creep does not occur even at temperatures of $500^{\circ}C$. High thermal conductivity and a lower thermal expansion coefficient than that of Zircaloy results in lower thermal stresses during LOCA. SiC does not react with UO_2 fuel pellets and is stable in high temperature water. Production of silicon carbide tubes is a mastered technology. Silicon carbide tubes for nuclear application were manufactured on a large scale in the U.K. for AGR advanced fuel elements. They contained a packed bed of lightly bonded coated fuel particles [Kennedy and Shennan, 1974]. Feinroth also considered silicon carbide cladding in a feasibility study on use of ceramic cladding to reduce

the severity of light water reactor accidents [Feinroth, 1990]. Feinroth's study concluded that silicon carbide is a quite acceptable candidate cladding material for LWR application during normal operating conditions, but questionable for LOCA accidents due to its reactions with steam at high temperatures (above 1500 °C). Preliminary calculation of the two-ring arrangement shows that the maximum temperature of cladding should not exceed 1350°C, which is quite below the temperature ranges considered in Feinroth's study. At these temperatures, silicon carbide oxidation in steam/air mixtures is negligible [Hejzlar et. al., 1993]. Hence silicon carbide cladding in the two-ring fuel arrangement should be capable of surviving LOCA, without primary coolant replenishment, undamaged. More research is, however, needed to confirm its compatibility with fuel pin material.

3.6 STRUCTURAL MATERIALS

Structural materials of the primary system are the same as for the reference CE-CANDU design and hence do not need to be discussed here. The critical component of pressure tube reactors is the pressure tube. Since the desired objective is the reusability of major components after a major accident, pressure tubes need to be designed to conform to this requirement. The purpose of this section is to identify the design limits for the pressure tubes which would allow their reusability.

CANDU reactors use pressure tubes made of Zr-2.5 wt% Nb material. This material has demonstrated superior performance over the previously used Zircaloy-2 material. Pressure tubes are designed for 5% diametral increase and 2% elongation due to creep and growth for 30 years of operation [Ross-Ross, 1978]. Extensive experience has been gained with this material. It has very good corrosion behavior and picks up less hydrogen than does Zircaloy-2. Some failures of pressure tubes, however, have been experienced because of the presence of delayed hydride cracks, and AECL is developing improved fuel channels to minimize these problems and to extend pressure tube lifetime [Cheadle et. al., 1993].

To prevent pressure tube damage and to permit their reusability in LOCA or loss of heat sink accidents, the maximum temperature of the

hottest pressure tube should not exceed about 500°C [Spinks, 1991]. Shewfelt's failure maps for pressure tubes under accident conditions also suggest that the maximum tolerable temperature of the hottest pressure tube under full pressure should not exceed 500°C [Shewfelt, 1986]. Hence, the temperature of 500°C will be used throughout this work as a limiting value. More details on fuel channel behavior under PTLWR conditions will be given in Chapter 9.

3.7 SUMMARY

The materials covered in the subject assessment include fuel matrix materials, reflector materials, fuel materials and pressure tube materials. Among all matrix materials under consideration, a graphite matrix with silicon carbide coating appears to be the most promising candidate. It has low neutron absorption cross section, high thermal conductivity, is compatible with light water coolant at operating conditions and it is corrosion resistant in air/steam mixtures at temperatures up to 1300°C. It also exhibits good irradiation stability. However, the stability of the SiC coating under thermal shock and long-term irradiation must be further confirmed.

Graphite has been selected as a reflector material since it provides much better irradiation stability than beryllium or beryllium oxide and is available at lower cost.

Two key fuel arrangements have been considered for the PTLWR. The first arrangement, used for the reference design, is a matrix-type fuel with fuel compacts inserted in a matrix, and consisting of TRISO fuel particles. This fuel is based on the technology developed for HTGRs, and does not require extensive development. The second arrangement comprises fuel pins with silicon carbide cladding arranged in the two outer fuel bundle rings. Fuel pins can employ UO₂ fuel or preferably higher density fuel such as UC or UN with N-15. Compatibility of all these fuels with silicon carbide cladding would need to be further confirmed.

Zr-2.5%Nb material has been selected for pressure tubes. It has shown very good performance in CANDU reactors and more development to

increase its lifetime is underway at AECL. To meet the requirement of reusability after major accidents, the design limit of the maximum pressure tube temperature was identified to be about 500°C.

Chapter 4

REACTOR PHYSICS

4.1 INTRODUCTION

The objective of this Chapter is to assess the key reactor physics characteristics of the reference PTLWR design, and to show that these characteristics fall within the limits currently accepted in nuclear industry, or that they bring certain advantages. The reference design must also satisfy the objective of achieving an inherent shutdown in accidents leading to a large temperature increase, as stated in Chapter 1. Consideration will also be given to physics aspects of alternative fuel arrangements within the fuel channels and to using alternative fuel such as plutonium for plutonium disposal.

The reactor physics chapter is divided into three major sections. The first section discusses, briefly, the fundamental equation which governs neutron behavior in the system of interest, the second section describes the tools used to solve the governing equation and the third section, which represents the main body, discusses the results describing the physics characteristics of the proposed PTLWR concept.

The proposed passive pressure tube reactor concept is a light water cooled and moderated reactor with an overall layout very similar to a Pressurized Heavy Water Reactor (PHWR) such as the CANDU. Similarity with LWRs lies in the use of light water as both the coolant and moderator. One can think of the PTLWR as an array of LWR bundles pulled apart and placed in a voided space surrounded by a reflector. The PTLWR resembles very closely a PHWR configuration, however, heavy water coolant is replaced by light water, and the typical CANDU fuel bundles are replaced by a matrix fuel. Consequently, reactor physics characteristics of the PTLWR are unique, and differ in several aspects from those of either LWRs

or PHWRs. The key design feature distinguishing the proposed concept from both LWRs and PHWRs, as well as from any other operating power reactor, is a voided calandria space. Neutron behavior in such a system significantly differs from that in conventional LWRs and PHWRs, and deserves special attention.

Section 4.5.1 investigates the effect of various geometrical arrangements of heterogeneously distributed light water moderator in a voided calandria space on reactivity. This study shows that for the reference fuel matrix with TRISO particle fuel, no light water moderator in the calandria space is needed to achieve sufficient moderation, thus simplifying the calandria design. Section 4.4.2 describes the models used for the analysis of the reference design. To make the computation feasible using available computer technology, TRISO particle fuel is treated as a homogenized region rather than modeling every fuel particle. The effect of this simplification is evaluated in Section 4.4.3.

Voiding of the calandria space results in a significant increase of neutron mean free path in the core, which becomes comparable to core physical dimensions. The proposed concept is, in this aspect, similar to reflector moderated reactors with gaseous fuel in the core conceived in the early days of nuclear technology by Bell and Cohen [Bell,1955], [Cohen,1962], or to the concept of the graphite-moderated heterogeneous gas core reactor studied at Oak Ridge National Laboratory (ORNL) [Barrett et. al., 1980]. Long neutron mean free path will significantly affect core physics characteristics, in particular core coupling, nuclear peaking, prompt neutron lifetime and stability against xenon spatial oscillations. The study of these characteristics is performed in Section 4.4.4.

Very important nuclear characteristics are the Doppler coefficient and the coolant void effect. It is desirable that both the Doppler and void coefficients are negative. This goal can be easily satisfied with the Doppler coefficient since the PTLWR is a thermal reactor with low-enriched fuel, but is more difficult to achieve for the void coefficient. Many pressure tube reactors such as the CANDU-PHW (pressurized heavy water reactor), the CANDU-BLW (boiling light water reactor) and the CIRENE (an Italian design of a heavy water moderated and light water cooled pressure tube

reactor) operate with slightly positive void reactivity. This leads to concerns over accidents resulting in coolant voiding, such as a LOCA, and imposes very strict requirements on reliable functioning of shutdown systems. The issue of positive coolant void reactivity has become an even more important factor after the reactivity accident at Chernobyl, which involved a graphite moderated and boiling light water cooled pressure tube reactor. Hence, it is considered essential that the proposed PTLWR exhibits negative coolant void reactivity at all operating conditions. That this can be accomplished in a pressure tube reactor, has been demonstrated by the UK's steam generating heavy water reactor (SGHWR) and the Japanese FUGEN HWR. Both the Doppler and void coefficients are investigated in Section 4.4.4.

Other characteristics of the reference dry calandria design, evaluated in Section 4.4.4, include fluence on the pressure tubes and the reflector temperature coefficient. Section 4.4.5 discusses the issues of reactor control.

Passive flooding of the voided calandria space with light water is unique to the PTLWR concept, and does not have any experience base in the LWR or HWR arena. Since it introduces large reactivity changes, detailed calculations need to be performed to prove that the flooding will result in a reactor shutdown, and that no reactivity excursions, which could lead to a large power increase, are possible. These issues are discussed in Section 4.4.6.

TRISO particle fuel can achieve much higher burnups than typical UO_2 fuel pellets, which are constrained by mechanical limits. Section 4.4.7 investigates fuel depletion, and the options to utilize this high burnup potential. Power distribution in the PTLWR equilibrium core depends on the refueling scheme. The PTLWR concept employs bi-directional on-line refueling, as is common practice in CANDU reactors. The power density profile in an equilibrium core using bi-directional refueling and the effects of bundle shuffling in the channel are studied in Section 4.4.8.

To reflect the recently increased interest in weapons-grade plutonium disposal, a qualitative assessment of the proposed concept using plutonium fuel is performed in Section 4.4.9.

4.2 BASIC NEUTRON TRANSPORT EQUATION

The fundamental neutron balance equation describing a reactor in a steady state critical condition is [Henry, 1986]:

$$\nabla \cdot \mathbf{J}(\mathbf{r}, E) + \Sigma_t(\mathbf{r}, E) \Phi(\mathbf{r}, E) = \int_0^\infty dE' \left[\sum_j f^j(E) \nu^j \Sigma_f^j(\mathbf{r}, E') + \Sigma_s(\mathbf{r}, E' \rightarrow E) \right] \Phi(\mathbf{r}, E') \quad (4-1)$$

Equation (4-1) states the fact that neutron leakage plus neutron removal from the system equals neutron production. \mathbf{J} is the net neutron current defined as

$$\mathbf{J} = \int_{\Omega} \Omega \, d\Omega \, \psi(\mathbf{r}, \Omega, E) = \int_{\Omega} \Omega \, d\Omega \, v(E) N(\mathbf{r}, \Omega, E) \quad (4-2)$$

where Ω is the direction vector in 3-D space, \mathbf{r} is the vector describing space coordinates, E is neutron kinetic energy relative to the laboratory system, and $\Psi(\mathbf{r}, \Omega, E)$ is the directional flux density defined as the product of neutron speed, $v(E)$ and the neutron density in the phase space, $N(\mathbf{r}, \Omega, E)$. In Eq. (4-1), $f^j(E)$ is the fission spectrum for isotope j , ν^j is the number of neutrons per fission for isotope j , Σ_f^j is the fission macroscopic cross section for isotope j , Σ_t is the total macroscopic interaction cross section, $\Sigma_s(\mathbf{r}, E' \rightarrow E)$ is the differential scattering cross section from energy E' into interval dE , and Φ is the scalar flux density defined as

$$\Phi = \int_{\Omega} \psi(\mathbf{r}, \Omega, E) \, d\Omega, \quad (4-3)$$

commonly called neutron flux. The most common approach for finding the unknown neutron flux, which is widely used in most reactor-design calculations, is to solve Eq. (4-1) directly for Φ . This approach necessitates relating neutron current to neutron flux. The approximation satisfactory for most reactors is Fick's law relating \mathbf{J} and Φ by the equation

$$\mathbf{J}(\mathbf{r}, E) = -D(\mathbf{r}, E) \nabla \Phi(\mathbf{r}, E) \quad (4-4)$$

where D is the diffusion coefficient. Substituting Eq. (4-4) for neutron current in Eq. (4-1) yields the diffusion equation

$$\begin{aligned}
 & -\nabla \cdot D(\mathbf{r}, E) \nabla \Phi(\mathbf{r}, E) + \Sigma_t(\mathbf{r}, E) \Phi(\mathbf{r}, E) = \\
 & = \int_0^\infty dE' \left[\sum_j f^j(E) v^j \Sigma_f^j(\mathbf{r}, E') + \Sigma_s(\mathbf{r}, E' \rightarrow E) \right] \Phi(\mathbf{r}, E')
 \end{aligned} \tag{4-5}$$

which is widely applied in reactor analysis.

The validity of the key approximation introduced to obtain the diffusion equation, i.e., Fick's law, must be re-examined when applied to the dry calandria design with significant void space in the core. Fick's law is based on the analogy of gas diffusing through media where the molecules, driven by concentration gradient, diffuse from regions of high concentrations to regions with low concentration. There are two important conditions for the diffusion analogy to be valid. First, if the neutrons are to behave like gas molecules diffusing through porous media, significant scattering must be ensured, i.e., $\Sigma_s \gg \Sigma_a$ and Σ_s and Σ_a should not vary rapidly as a function of position in the region under investigation. If the scattering macroscopic cross section is very small compared to macroscopic absorption cross section, neutrons will exhibit a beam-like distribution in preferred directions – a quite different situation from diffusion-like behavior. Secondly, the mean free path of the neutrons should be small compared to the physical dimensions of the system under investigation.

Unfortunately, none of these conditions is satisfied in the dry calandria design. Neutron scattering in the voided space is virtually zero, while large in the reflector and in the coolant channels. Neutron absorption is very large in fuel regions, but almost zero in the voided space. Also both the Σ_s and Σ_a vary considerably within the core as a function of position. But more importantly, neutron mean free path is large (on the order of several meters, compared to several cm in LWRs) and is comparable to the core physical dimensions. Hence the commonly used argument that Fick's law is valid several mean free paths within regions in which the Σ_s and Σ_a do not change rapidly with position and where the $\Sigma_s \gg \Sigma_a$ [Henry, 1986] is clearly not satisfied for the dry calandria concept. In fact, no such a region can be found within the entire core. One can also observe, that in some

selected directions (i.e., parallel with fuel channels), neutrons can easily travel throughout the entire core without having any collision while in some other directions the probability of collision is large. Therefore, the directional distribution needs to be taken into account, a property which cannot be described well by Fick's law.

Limitations of Fick's law for the dry calandria design can also be demonstrated from the thermal flux profile. Section 4.4.4.3 will show that the thermal flux in the core center is almost constant across a substantial portion of the core. Constant thermal flux in Eq. (4-4) implies zero current density, \mathbf{J} , and hence zero leakage of thermal neutrons from the core center. This does not correspond, however, to the real situation where thermal neutrons leak easily from the center of the core to the outer boundary.

In view of the above arguments, a second, more rigorous, approach needs to be applied in finding neutron flux. The neutron flux can be calculated directly from the definition (4-3), if the directional flux density, $\psi(\mathbf{r}, \Omega, E)$, is known. Knowledge of the directional flux density requires the solution of the static neutron transport equation [Henry, 1986]

$$\begin{aligned} & \Omega \cdot \nabla \psi(\mathbf{r}, \Omega, E) + \Sigma_t(\mathbf{r}, E) \psi(\mathbf{r}, \Omega, E) = \\ & = \int_0^\infty dE' \int_\Omega d\Omega' \left[\sum_j f^j(E) v^j \Sigma_f^j(\mathbf{r}, E') + \Sigma_s(\mathbf{r}, \Omega' \rightarrow \Omega, E' \rightarrow E) \right] \psi(\mathbf{r}, \Omega', E') \end{aligned} \quad (4-6)$$

where $\Sigma_s(\mathbf{r}, \Omega' \rightarrow \Omega, E' \rightarrow E)$ is the differential scattering cross section from energy E' and direction Ω' into interval $dE d\Omega$.

Solving Eq. (4-6) for the directional flux density poses enormous mathematical difficulties. Four methods have been developed to solve the transport equation – the spherical-harmonics method, the Fourier-transform method, the discrete-ordinates technique, and the Monte Carlo method. The spherical-harmonics and Fourier transform methods are practically intractable for more complex geometries, such as the core of the dry calandria design, while the discrete-ordinates method suffers from ray effects [Henry, 1986]. To avoid ray effects in the proposed design, a very

large number of ordinates would have to be employed, thus increasing the computation time. The Monte Carlo method, which is the best suited method for the complex geometry of the dry calandria core, was chosen to solve the neutron transport equation. It is also the best developed and benchmarked method available.

Note that Monte Carlo is a statistical method, while the other three methods are deterministic methods. The Monte Carlo method simulates the random histories of a large number of neutrons in a system, and statistically samples probability distributions governing these events to describe a total phenomenon. The deterministic methods solve the integro-differential equation (4-6) directly, while the Monte Carlo method solves the same transport equation, but in the integral form. Since the Monte Carlo method solves the transport problem by simulating particle histories rather than solving an equation, the integral transport equation does not even need to be written to solve the transport problem by Monte Carlo. The disadvantage of the Monte Carlo method is that a very large number of particles need to be run to achieve accurate results, especially if the quantities desired are a function of position in the core.

The voided calandria core is neutronicly similar to the nuclear vapor thermal rocket (NVTR) engine, which employs a gaseous uranium tetrafluoride (UF_4) fuel contained in bottled channels reflected at the top and bottom as well as at the outer radial edge of the core. A large mean free path in the fuel zone in the NVTR, comparable to the channel length, necessitated transport code analysis for nuclear criticality assessment [Watanabe and Dugan, 1993]. Attempts have been made to apply buckling corrections by modifying the core height or by generating fictitious materials whose cross sections closely simulate axial loss from streaming through additional absorption. The approach of effective core height, however, encountered difficulties (in terms of achieving sufficient accuracy) for heterogeneous problems with significant axial streaming [Watanabe and Dugan, 1993].

Finally, it is noted that the application of the neutron diffusion equation would be possible if the diffusion constants are corrected for neutron streaming effects. Several methods for obtaining effective diffusion

coefficients in lattices with neutron streaming have been developed [Gelbard, 1983], although mostly for a lattice where voided space is small compared to space taken up by solid or liquid material. This differs from the dry calandria design, where most of the space is occupied by voids (80%). Hence the validity of the methods developed for lattices where solid material is dominant would need to be confirmed for void-dominant lattices. Note that the methods reviewed by Gelbard still need the solution of the neutron transport equation in some form to obtain the effective diffusion constants. The advantage of using these methods lies in the fact that the set of effective diffusion coefficients, spanning the conditions of interest, can be precomputed once and then used as input data in the standard computer codes based on the neutron diffusion equation. This would speed up reactor analysis, since the diffusion equation-based codes are much faster than the Monte Carlo method. This approach was not chosen in this work, however, because it requires an extensive development effort.

4.3 ANALYSIS TOOLS

As has been discussed in the previous section, the Monte Carlo method has been selected to solve the static neutron transport equation. There are several Monte Carlo codes available; some widely known being MCNP [Briesmeister, 1986], RCP01 [Candelore et. al., 1978], SAM-CE [Lichtenstein et. al., 1979], and KENO [Petrie and Landers, 1984]. From these, the Monte Carlo Neutron Photon Transport (MCNP) code, developed at Los Alamos National Laboratory, was selected as the main analysis tool, due to its availability, versatility and extensive verification for a variety of applications including heterogeneous lattices for thermal reactors. The MCNP code will be briefly described in Section 4.3.1.

One of the MCNP limitations is its inability to calculate core depletion. To perform the scoping burnup calculations in the dry calandria design, the ORIGEN2 code [Croff, 1980], [Croff,1983], developed at Oak Ridge National Laboratory (ORNL), has been chosen. Since the effective one-group cross section library required by the ORIGEN2 code is not available for the

PTLWR core, the ORIGEN2 code was combined with MCNP, as will be described in Section 4.3.2.

4.3.1 The MCNP Computer Code

The MCNP code [Briesmeister, 1986] is a general-purpose coupled neutron/photon Monte Carlo transport code. The strength of MCNP is its easy application to complex geometric configurations. It treats an arbitrary three-dimensional configuration of materials in geometric cells which are bounded by first- and second-degree surfaces. Special cases, e.g., elliptical tori with four-degree surfaces are also available.

The code can be used for neutron, photon, or coupled neutron/photon transport as well as for calculation of eigenvalues of critical systems. The code's versatility offers the capability to use the code in three modes; neutron transport only, photon transport only, or combined neutron/photon transport, where the photons are produced by neutron interactions.

The MCNP code uses continuous energy cross section data libraries. The neutron energy regime is from 10^{-11} MeV to 20MeV, and the photon energy regime spans the range between 1keV and 100MeV. The major sources of nuclear data are the Evaluated Nuclear Data File (ENDF/B) [Kinsey, 1979] system, the evaluated nuclear data library (ENDL) [Howerton et. al., 1975] and the Activation Library (ACTL) [Gardner and Howerton, 1978] from Livermore, and evaluations from the Applied Nuclear Science Group at Los Alamos. Cross section data are available for neutron interactions, photon interactions (allowing one to account for coherent and incoherent scattering, photoelectric absorption with the possibility of fluorescent emission, and pair production), neutron dosimetry or activation, and thermal particle scattering $S(\alpha,\beta)$. Thermal data tables with a $S(\alpha,\beta)$ scattering treatment include chemical binding and crystalline effects that become important for low energies. This treatment is available for moderator materials.

The MCNP code has been extensively verified for a variety of applications [Whalen et. al., 1991], [Forster et. al., 1990]. The adequacy of

ENDF/B nuclear data for use in thermal reactors has been assessed by numerous researchers, such as [Mendelson, 1968], [ENDF-313, 1981] to name a few, although mostly for homogeneous cores at room temperature. Heterogeneous designs at room temperature have also been validated [Haga et. al., 1979], [Manaranche et. al., 1979]. Recently, extensive validation of ENDF/B data using MCNP has been done for multibundle systems in full three-dimensional configurations for LWR temperatures representative of both cold and operating conditions [Sitaraman and Rahnema, 1993]. The eigenvalue predictions of the MCNP code coupled with ENDF/B-V data showed excellent agreement with critical measurements, and MCNP was recommended as a benchmarking tool to validate faster, more approximate codes used in LWR core design and analysis [Sitaraman and Rahnema, 1993]. In addition to predicting eigenvalue with very good accuracy, MCNP can also predict well local parameters such as fission densities.

The MCNP code can also track photon generation and energy deposition associated with these iterations. Application of the MCNP energy deposition tracking method to the Advanced Neutron Source (ANS) reactor design showed that MCNP is capable of generating very accurate results (within 1%) for the total energy deposition within a reactor, including the photon heating in the reflector and the heating associated with delayed secondary decay mechanisms in activation daughter products [Wemple and Jashan, 1991]. Monte Carlo methods have been also validated against critical experiments for fuel assemblies with low hydrogen densities which can arise if moderating media from fire sprinkle heads or fire hoses enter dry fuel storage racks [Elmaghrabi and Klotz, 1991]. A good level of accuracy was achieved.

Very good results obtained in the MCNP validation effort show that the MCNP code is capable of calculating correct eigenvalues, fission density profiles and energy deposition for the proposed passive pressure tube light water reactor concept. There are, however, limitations in using MCNP. The most serious drawback with respect to this conceptual study is the inability of MCNP to calculate fuel depletion. While complete MCNP burnup calculations are not available, MCNP full core calculations at various stages of burnup can be done. To obtain the change of fuel

composition with burnup, the ORIGEN2 computer code was used, while the change of reactivity with burnup is calculated by MCNP using fuel composition from ORIGEN2. More details about this approach will be given in Section 4.4.7. Very recently, a new MCNP-ORIGEN2 Coupled Utility Programs (MOCUP) package has been developed at Idaho National Engineering Laboratory (INEL) that provides the means to use MCNP for the neutronics solution and ORIGEN2 to perform depletion [Babcock et. al., 1993]. Unfortunately, this package was not available at the time of the present burnup study.

4.3.2 The ORIGEN2 Computer Code

ORIGEN2 [Croff, 1983] is a versatile point-depletion and radioactive-decay computer code. It is used to simulate nuclear fuel cycles and calculate the nuclide compositions and characteristics of materials during the fuel cycle. The ORIGEN2 code is a revised and updated version of the ORIGEN [Bell, 1973] computer code developed at ORNL.

The ORIGEN2 code maintains a data base of 1700 nuclides, divided into three segments: 130 actinides, 850 fission products, and 720 activation products. Nuclide properties computed by ORIGEN2 include mass, thermal power in watts of recoverable energy, fractional isotopic composition, radioactivity, radioactive and chemical ingestion, radioactive inhalation, neutron absorption rate, fission rate, neutron emissions and photon emissions. In addition, the code calculates the infinite multiplication factor as a function of burnup and instantaneous neutron flux.

Effective cross sections for all nuclides, particularly the actinides, are generally a strong function of the type of reactor and the concentration of the nuclides. ORIGEN2 uses one-group effective cross sections (n, γ) to ground and excited state, $(n, 2n)$ to ground and excited states, $(n, 3n)$ and $(n, fission)$ for the actinides, and (n, p) and (n, α) for the activation products and fission products. Since these cross sections depend highly on reactor and fuel type, several data bases of one-group effective cross sections are available. These include data bases for PWRs and BWRs for the U-Pu cycle, PWRs with alternative fuel cycles (e.g., for thorium based fuels and

extended burnups), CANDU reactors with natural or slightly enriched U-Pu cycle, LMFBRs with U-Pu cycle, LMFBRs with thorium cycle, and also specifically for the fast flux test facility and Clinch River Breeder Reactor. Clearly, a one-group effective cross section library for the proposed PTLWR is not available in ORIGEN2. Calculation of this library is a complex process, beyond the scope of this work, that is specific to the reactor type, and must be performed using sophisticated codes other than ORIGEN2. At this stage of the study, a simplified approach has been chosen. The PTLWR fuel was burned by ORIGEN2 using one-group cross section data for a PWR on the U-Pu cycle, with the cross sections of the major actinides modified to match reaction rates obtained by MCNP. More details about this approach are given in Section 4.4.7.

A number of verification activities has been performed. These included a comparison of ORIGEN2 decay heat results with both calculated and experimental values [Schmittroth et. al., 1980], and comparison of predicted spent fuel compositions with measured values [Croff, 1981]. The agreement between the ORIGEN2 results and data is generally very good.

4.4 PHYSICS ASPECTS OF PRESSURE TUBE REACTORS WITH VOIDED LATTICE

The dry calandria design employs light water as both the coolant and moderator*. Light water is placed inside the pressure tubes which are arrayed in a void space surrounded by a graphite reflector. Light water coolant and the fuel compacts inside the pressure tubes are located in separate holes in the graphite matrix. Finally, the fuel kernels of TRISO fuel particles, surrounded by buffer, inner pyrolytic carbide (PyC), silicon carbide, and outer PyC layers, and distributed in a graphite binder, give rise to fuel microheterogeneity in a fuel compact. This triply-heterogeneous system exhibits certain unique features, which differ in several aspects

* Most moderation necessary to thermalize neutrons from fission is accomplished by the light water coolant inside the fuel channels; some moderation also takes place in the graphite reflector and in the graphite fuel matrix.

from those of either LWRs or PHWRs. The most important factor is a significant fraction of voids present in the core. This section will examine the key reactor physics aspects of reactor core having heterogeneously distributed fuel channels in a voided cavity, called a calandria, surrounded by a reflector. First, various possible configurations of a moderator in the calandria space are briefly explored, and the two main design options – the dry calandria design and the wet calandria design are identified. The rest of this section is devoted to the reference dry calandria design.

4.4.1 Various Moderator Configurations in Voided Calandria

4.4.1.1 Classification of Calandria Designs

In compliance with the premises listed in Chapter 1, light water coolant is to be used as both the moderator and coolant. Use of light water in a pressure tube reactor, however, necessitates changes to a PHWR of the CANDU type due to differences in the nuclear properties of heavy water and light water. The much smaller slowing down power of D_2O than that of H_2O requires a large moderator-to-fuel volume ratio, and hence large pitch between fuel channels to accommodate a sufficient amount of D_2O moderator. Replacing D_2O moderator with H_2O while maintaining the same slowing down power would require such a small channel pitch that the calandria tubes would have to touch each other. Even for such a small pitch, the design would still be overmoderated and would have a positive reactivity coefficient. One also needs to consider that the minimum channel pitch is restricted by the space requirements associated with header plumbing and on-line refueling. To stay within the current CANDU on-line refueling practice, channel pitch is kept the same as in CANDUs, and the reduction of moderator-to-fuel volume ratio is achieved by a mixture of H_2O and voids in the calandria space, i.e., outside the calandria tubes.

Figure 4-1 shows the two basic types of arrangements of the light water moderator in the calandria. In the first arrangement type, designated as the wet calandria design, low-pressure H_2O moderator is in permanent contact with the fuel channel, wetting the outer surface of the calandria

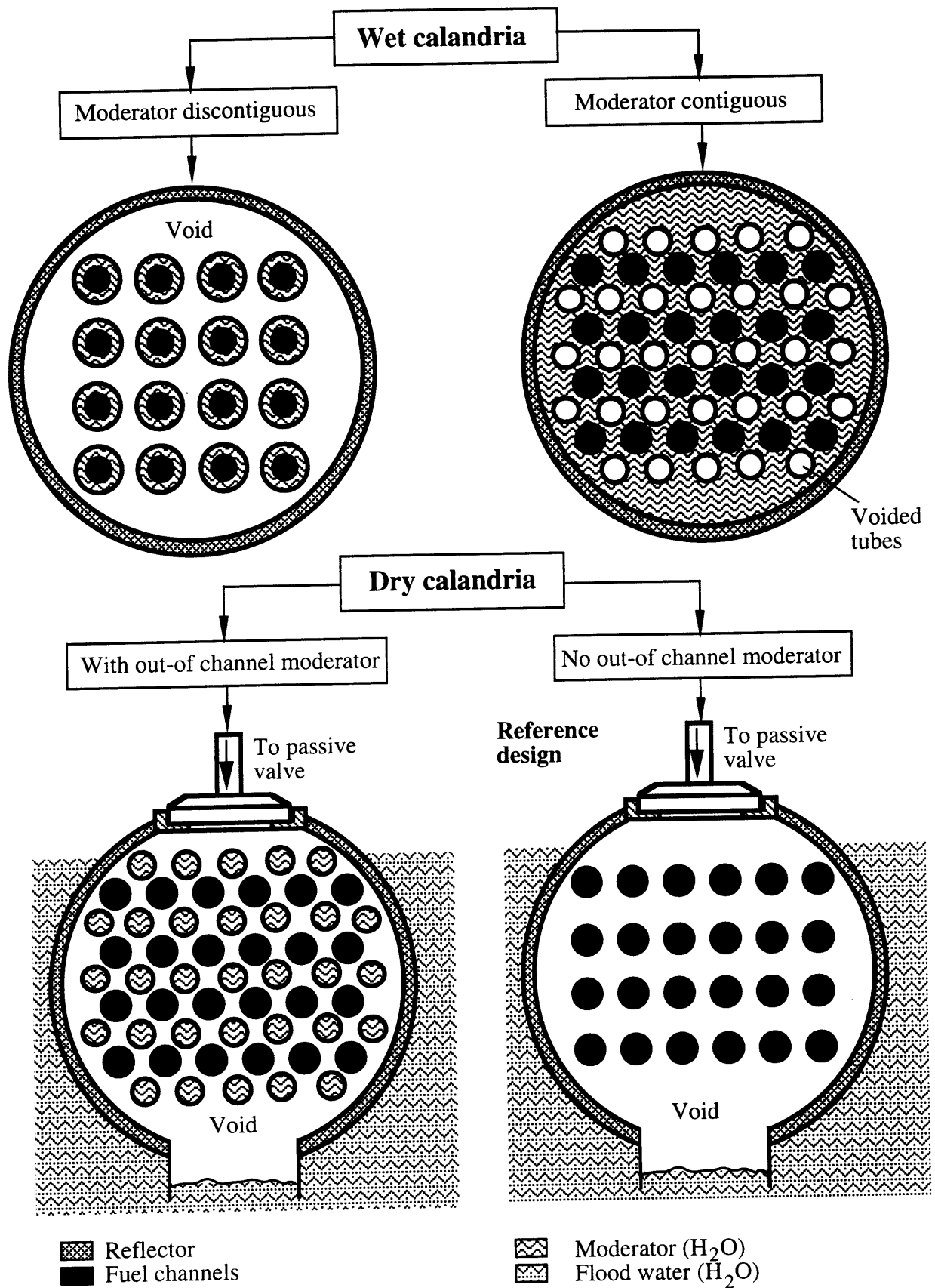


Figure 4-1 Configurations of light water moderator in a PTLWR

tube. There are two possible versions of the wet calandria design. In the first version, moderator is discontinuous, separated by voids. One such possible arrangement, shown in Figure 4-1 employs a moderator annulus contained in a Zircaloy tube (designated henceforth as the moderator tube) surrounding the calandria tube. In the second version, moderator fills the calandria as a contiguous medium. To provide the optimum moderator-to-fuel ratio, voided Zircaloy tubes are introduced. The advantage of the wet calandria design is that the low-pressure moderator, which also serves as a backup passive heat sink in a loss of coolant or loss of heat sink accidents, is available at all time, and does not require any initiation for its function. The disadvantage is the need to provide a “thermal switch” between the pressure tube and the calandria tube to minimize heat loss during normal operation and to enhance heat transfer into moderator during an accident. Such a switch is difficult to design and adds mechanical complexity. Another disadvantage, especially of the discontinuous-moderator version, is the susceptibility to moderator tube failure and subsequent loss of low pressure heat sink, in case of pressure tube rupture. The wet calandria approach has been investigated by Tang [Tang, 1992], [Tang et. al., 1992].

In the second arrangement type, no H₂O moderator is in permanent contact with the fuel channels. The calandria tubes are dry during normal operation, hence the designation as the dry calandria design. A large, light-water pool, which is kept outside the calandria space by a gas lock has the designated function of a heat sink, but does not serve as a moderator, as was the case in the wet calandria design. The dry calandria design does not require any thermal switch, but it needs a reliable, passive mechanism to initiate calandria flooding following loss of coolant or loss of heat sink accidents. The dry calandria design has two versions. The first version employs Zircaloy tubes containing low-pressure light water moderator, while the second version does not have any out-of-channel moderator. The out-of-channel moderator (in addition to the inside-the-channel moderator) allows good optimization of moderator-to-fuel ratios for fuel arrangements with high heavy metal loadings. The second version is applicable to a fuel matrix with TRISO particle fuel, since the heavy metal loadings achievable with particle fuel are low, and no additional out-of-channel moderator is

needed. The latter version has been selected as the reference dry calandria design for the evaluation in the present work.

4.4.1.2 Effects of moderator arrangement on multiplication factor in a high-streaming lattice

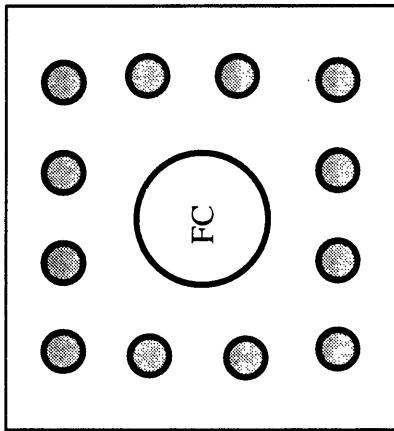
It has been illustrated above, that the out-of channel moderator can be arranged in the calandria in a variety of ways. The purpose of this section is to investigate how the geometrical arrangement of the out-of-channel moderator affects the multiplication factor, and to determine if there is any preferred arrangement which gives the highest eigenvalue. All the investigated arrangements represent lattices with large neutron streaming, since the voided volume fraction is high.

The selected arrangements for one fuel channel are shown in Figure 4-2. Note that the drawings are highly schematic because the limited space does not allow showing all the moderator tubes and other details. There are three configurations with moderator tubes (Cases A through C) for the dry calandria concept and two configurations (Cases D and E) for the wet calandria concept. Case A employs 32 moderator tubes in a rectangular array, Case B has 32 moderator tubes in a circular array placed far from the channel centerline, and Case C has the same number of moderator tubes, also in a circular array but in the close proximity to the fuel channel. All the moderator tubes have the same inner and outer diameter to keep both the volume of the moderator and Zircaloy fixed for all cases. Also the dimensions of the moderator annulus for Cases D and E are calculated such that the volume of moderator and Zircaloy exactly match the dry calandria cases. The fuel channel consisting of the pressure tube, calandria tube and graphite fuel matrix with 24 fuel regions filled with TRISO particle fuel and 13 coolant channels is kept the same for all cases as well.

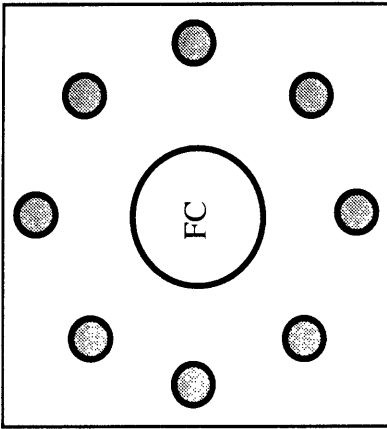
Multiplication factors for an infinite lattice, calculated by MCNP are given in Figure 4-2 (see reflective cell boundaries and the dimensions of a fuel channel in Figure 4-3, which shows Case A arrangement to scale). It can be observed that the differences in multiplication factors are very small, hence the effect of geometrical arrangement of light water moderator in a

Dry calandria concepts

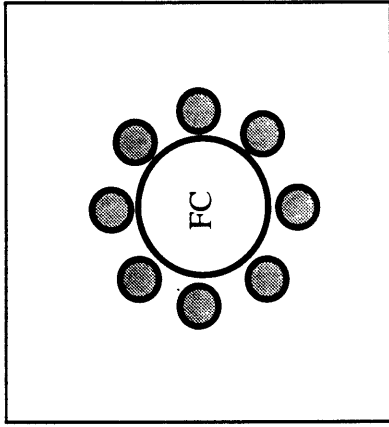
Case A $k = 0.989 \pm 0.003$



Case B $k = 0.985 \pm 0.003$

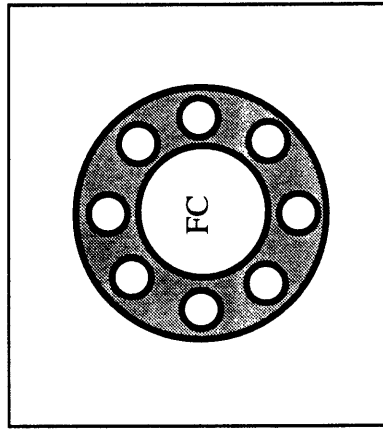


Case C $k = 0.990 \pm 0.003$

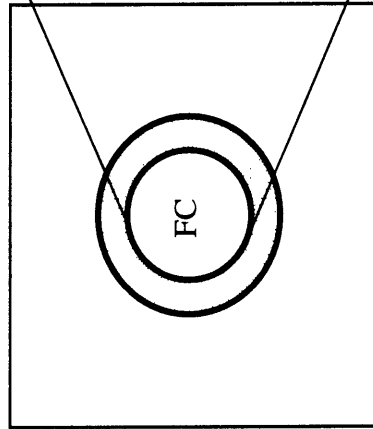


Wet calandria concepts

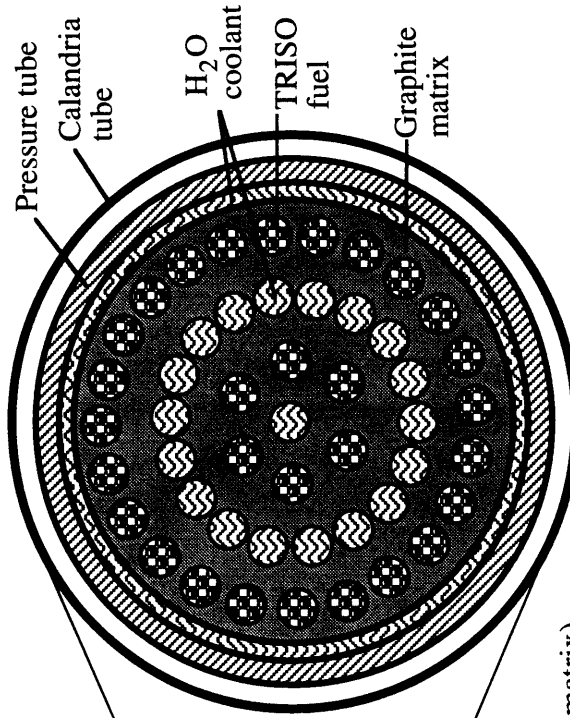
Case D $k = 0.985 \pm 0.005$



Case E $k = 0.987 \pm 0.002$



Configuration of fuel channel (FC)



- Constants:**
- configuration of fuel channel (FC) kept the same -24 fuel holes with TRISO particles, 13 coolant holes with H₂O, graphite fuel matrix)
 - volume of moderator (H₂O) and Zircaloy kept constant ; moderator density = 0.972 g/cc
 - enrichment =2.5%

Figure 4-2 Effects of out-of-channel moderator geometrical arrangement on multiplication factor

- fuel
- ⊗ coolant or moderator
- ⊘ matrix
- ⊙ pressure tube (PT)
- calandria tube (CT)
- ⊘ moderator tube (MT)
- insulating gap or void

fuel hole OD=12.7 mm	gap thickness=10 mm
coolant hole OD=11.33 mm	CT thickness=1.52 mm
graphite matrix OD=120.8 mm	MT thickness=1.52 mm
pressure tube ID=128 mm	pitch=285.75 mm
PT thickness=5.79 mm	

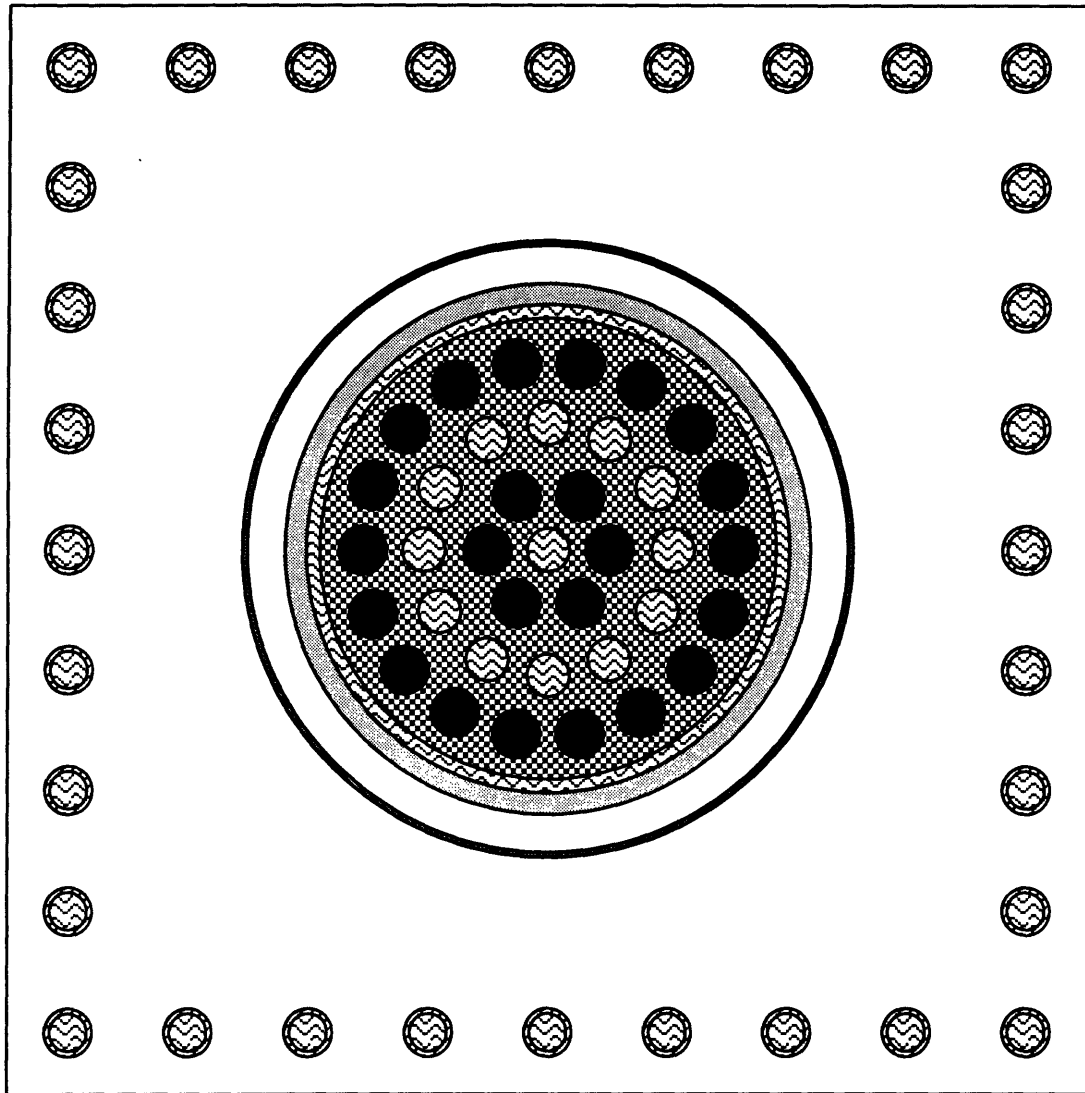


Figure 4-3 Case A dry calandria concept with moderator tubes in rectangular array

Scale = 1/2 real scale

voided space on reactivity is negligible. These results also indicate a fairly flat thermal flux profile in this region since the change of moderator location does not seem to alter reaction rates in the cell.

Figure 4-4 shows the dependence of the multiplication factor on the out-of-channel moderator volume for Case A with moderator tubes arranged in a rectangular array. Change of volume fraction was simulated by changing the diameter of all moderator tubes while keeping the number of moderator tubes constant. Figure 4-4 shows that the optimum moderator-to-fuel volume ratio is achieved for a moderator tube diameter of about 0.2cm. For larger tube diameters, the system is overmoderated and results in a positive void coefficient. Therefore this region must be avoided. It can be also observed that this configuration (recall that Case A employs a fuel matrix with particle fuel) does not need any moderator outside the fuel channel since the point on the k-curve for zero fraction of out-of-channel moderator ensures negative void coefficient and is close to optimum. Moreover, the curve is relatively flat in this region, which would result in small reactivity insertion in accidents with cold water ingress. Note that the point at zero moderator fraction was calculated by keeping the diameter of the Zircaloy tube equal to 0.25 cm and setting moderator density inside the tubes to zero. The diamond point, designated “Zy tubes out”, shows the reactivity increase if all moderator-tube structures are removed.

The results from Figures 4-2 and 4-4 suggest that the geometrical arrangement of out-of-channel moderator does not have any significant effect on reactivity, and that the amount of moderator is what matters. The fuel matrix with particle fuel design does not need any additional moderator outside the fuel channel. This reduces complexity and the amount of structural material inside the calandria, and hence decreases neutron parasitic losses. These factors contributed to the choice of particle fuel for the reference design.

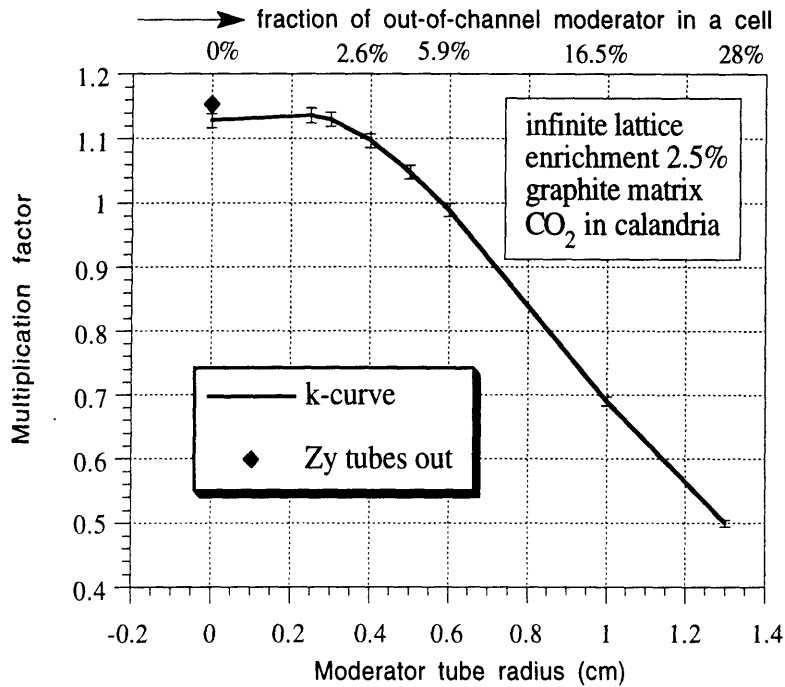


Figure 4-4 Dependence of multiplication factor on the volume of out-of-channel moderator for Case A

4.4.2 MCNP Models

Several MCNP models have been constructed to explore physics aspects of the reference PTLWR design. Key models include the fuel channel cell, full core mockup, full core mockup with movable control rods and variable water level in the calandria to simulate flooding, and the two-channel cell with axially-variable fuel composition for a bi-directional refueling scheme. This section will briefly describe these models. MCNP input data and the codes which facilitate generation of input data are too bulky to be included here: they are given in a separate report [Hejzlar,1994].

4.4.2.1 MCNP Model of a Dry Calandria Cell with One Fuel Channel (Model #1)

Figure 4-5 illustrates the cross sectional view of the dry calandria cell with one fuel channel. A fuel channel comprises 13 coolant holes, 26 fuel

regions containing TRISO particle fuel, the graphite matrix, an annular coolant channel, a pressure tube and a calandria tube. The dimensions are summarized in Figure 4-5. The square, with side length equal to channel pitch and enclosing the fuel channel, represents reflecting boundaries with zero current boundary conditions. In the axial direction, only half of the channel length is modeled, with a reflecting surface at the core midplane. Two versions of the model with respect to channel end were used. The first version uses a reflective surface at the end of the active core length, representing thus an infinite lattice. The second version incorporates a Zircaloy liner followed by a 1m-thick reflector to account for the axial leakage. Coolant density and fuel composition are assumed axially uniform.

The fuel channel is represented accurately except for the silicon carbide coating of the matrix, and graphite bearing pads, which have been neglected. However the coolant displaced by bearing pads was accounted for. These simplifications have a negligible effect on the results. Another simplification of more importance is the homogenization of the TRISO particles in fuel regions, since it decreases the resonance escape probability in fertile isotopes, and consequently leads to a reactivity decrease. More detailed study of this effect, however, showed that the reactivity decrease is relatively small (see Section 4.4.3). Model #1 is intended for scoping calculations of void reactivity coefficient, neutron energy spectra, fluence on pressure tubes, and detailed mapping of the flux profile inside the channel.

The input deck for the MCNP model #1 is generated by a PASCAL code developed to facilitate the data building process. The code allows convenient changes of variable parameters such as coolant density, fuel enrichment etc. It also gives the options to choose various reflector and matrix materials, types of coolant, types of fuel and to introduce various moderators in the space outside the calandria tube. In addition, the code can correctly generate scaled plots of the cell, such as in Figure 4-5. A listing of the code, sample input data and sample code output (MCNP input data deck) is given in [Hejzlar et. al., 1994].

- fuel
- ⊗ coolant
- ⊗ graphite matrix
- ⊗ pressure tube (PT)
- calandria tube (CT)
- insulating gap or void

fuel hole OD=12.7, 12.4mm	PT thickness=5.79 mm
coolant hole OD=8.40 mm	gap thickness=10 mm
matrix OD=120.8 mm	CT thickness=1.52 mm
pressure tube ID=128 mm	pitch=285.75 mm

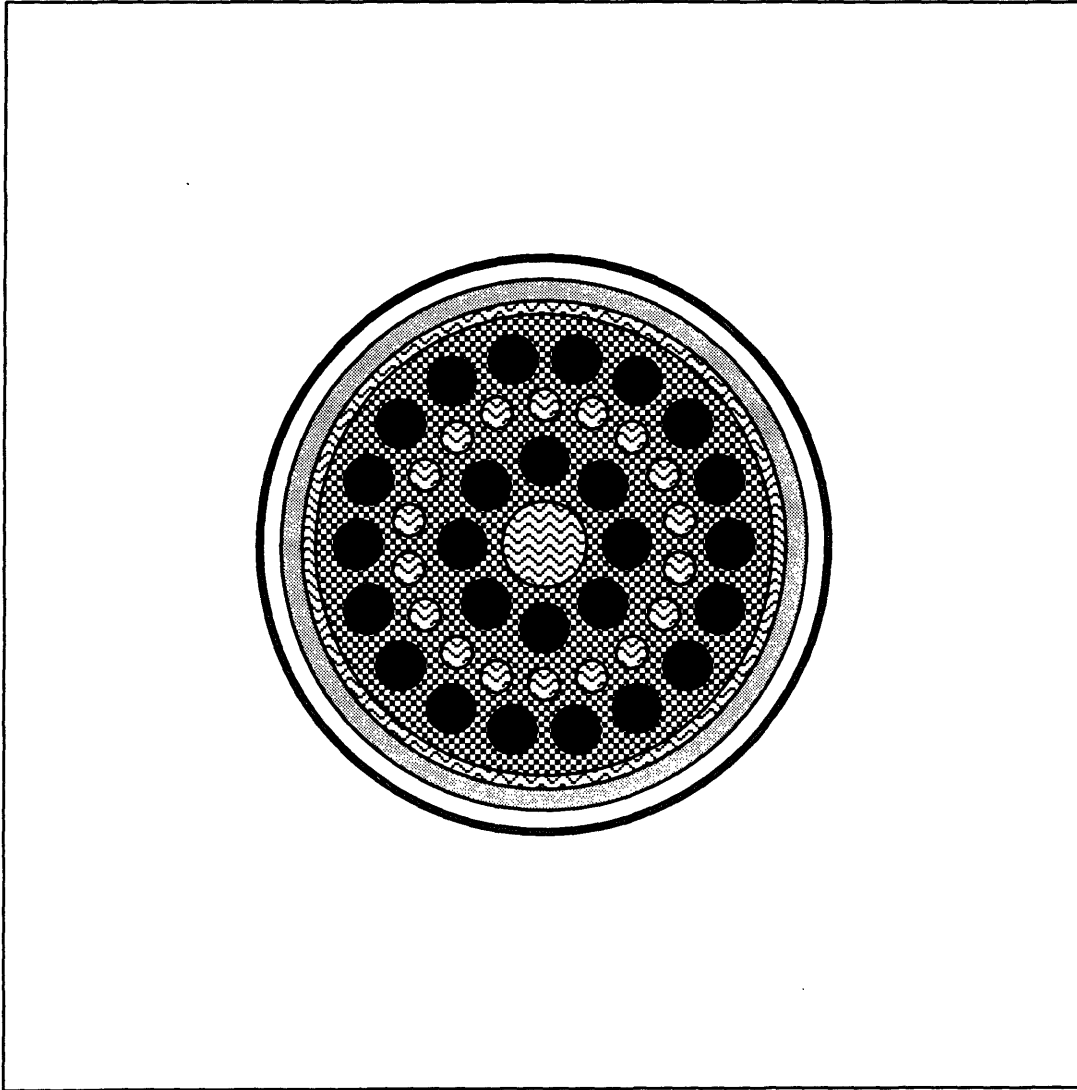


Figure 4-5 Reference dry calandria design - fuel channel MCNP model
scale = 1/2 real scale

4.4.2.2 Full Core Mockup (Model #2)

Although the model of one fuel channel can give insight into many physics aspects of the design, it cannot describe adequately the behavior of the whole core, because leakage (which is significant in the voided core) is not represented correctly. Moreover, thermal neutrons from the reflector will affect a substantial portion of the core due to the large neutron mean free path. Hence, a full core mockup is necessary for more accurate calculations.

A full core mockup representation with dimensions is shown in Figure 4-6. The model takes advantage of symmetry by representing one quarter of the core in the radial direction and one half in the axial direction. Cut planes are modeled as fully reflective with zero current boundary conditions. The full core consists of 740 fuel channels. The geometry of every individual channel is the same as shown in Figure 4-5. Coolant properties and fuel composition is assumed uniform. Fuel channels are surrounded by a graphite reflector with a Zircaloy liner. Finally, the core is submerged in a light-water shield tank. The end reflector employs a similar arrangement to that shown for the radial reflector. In addition, control rods inserted in the end reflector between the fuel channels can be modeled. However, only fully inserted control rods can be represented in this one-quarter core model to preserve the symmetry. Simplifications in the model of the fuel channel are the same as explained in Section 4.4.2.1. The end reflector is simplified by neglecting the detailed arrangement of the channels penetrating the end reflector. The model is intended primarily for flux profile mapping in the core.

The input deck for the MCNP model of the full core mockup is generated by a PASCAL code. Similarly as for MCNP Model #1, the code allows convenient changes of variable parameters and the choice of various options. A listing of the code, sample input data and sample code output (MCNP input data deck) is given in [Hejzlar et. al., 1994].

Dimensions:

fuel hole -outer ring	OD = 12.7mm
fuel hole -inner ring	OD = 12.4mm
coolant holes	OD = 8.4mm
central coolant hole	OD = 22mm
matrix	OD = 120.8mm
pressure tube (PT)	ID = 128mm
pressure tube thickness	= 5.79mm
gap thickness	= 4mm
calandria tube thickness	=1.52mm
fuel channel pitch	=285.75mm
number of fuel channels	= 740
reflector	ID=9000mm
reflector thickness	=1000mm

Note: In axial direction, one half of the core is modeled with an end reflector

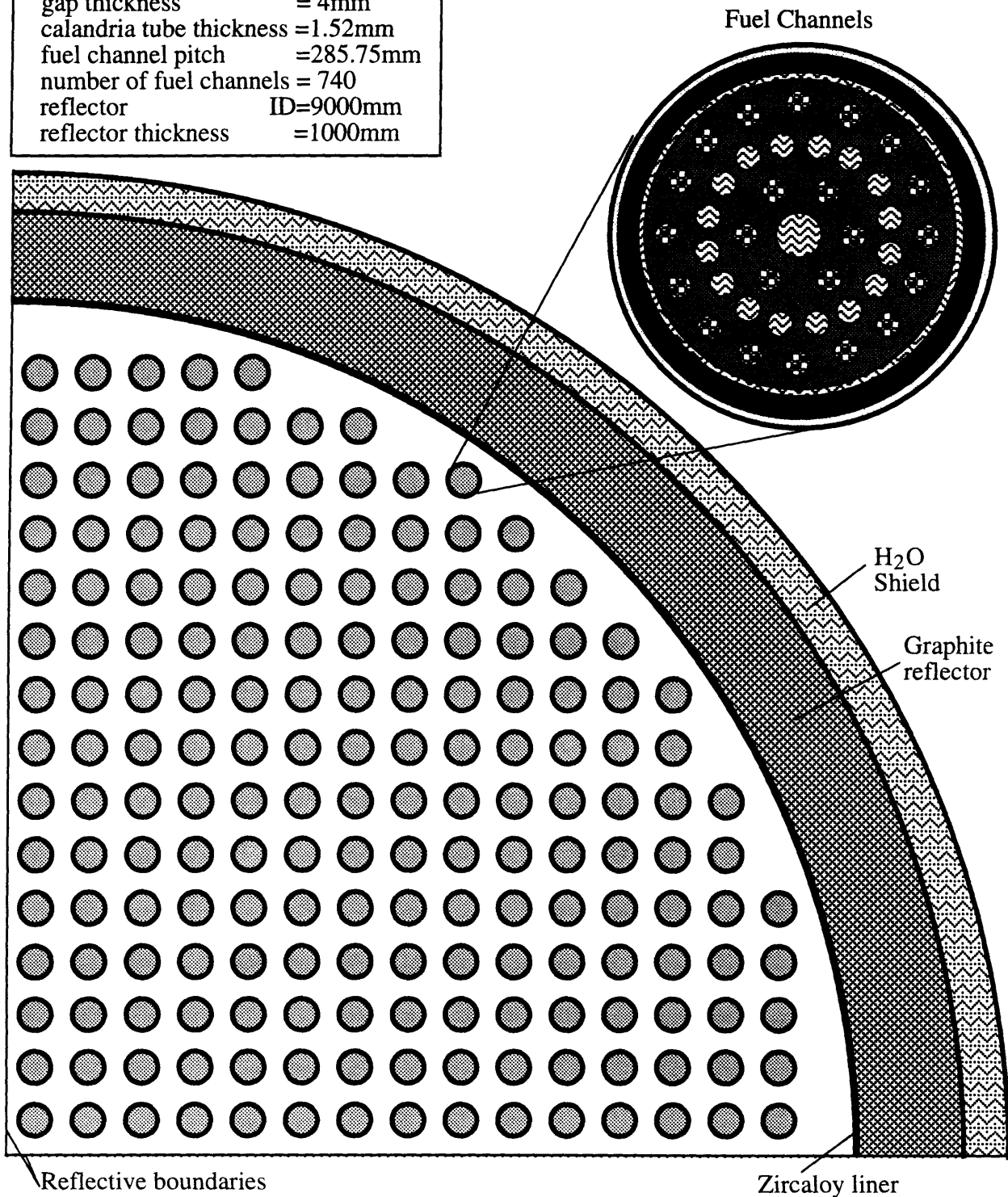


Figure 4-6 Reference calandria design - MCNP model of a full core with reflector

4.4.2.3 Full Core Mockup with Movable Control Rods and Variable Water Level in the Calandria (Model #3)

The disadvantage of MCNP Model #2 is that it cannot be used for reactivity calculations in processes with calandria flooding. To calculate such a process, the model must be able to represent the calandria space between fuel channels in two regions – a lower portion with flood water having arbitrary density (to account for the possibility of a subcooled state as well as boiling) and the upper portion filled with either gas, saturated steam or a steam/water mixture. Therefore, it is necessary to model half of the core, as shown in Figure 4-7. The end reflector is modeled with all control rods and the fuel channels penetrating the reflector. A cross section of the end reflector is shown in Figure 4-8. Control rods are arbitrarily positionable in the modeled half of the core; the control rods in the other half are a mirror reflection of the right half by virtue of symmetry. Details of the fuel channel portion penetrating the reflector, similar to CANDU practice, are shown in Figure 4-9. The MCNP model #3 considers the shield plug with coolant outlet channel, the annular coolant channel between the shield plug and the pressure tube, the pressure tube, the gap between pressure tube and calandria tube, and the calandria tube, as shown on the expanded channel view in Figure 4-8. Conical coolant passages in the shield plug are simplified by modeling cylindrical passages of such diameter that they have the same coolant volume as the original passages, to represent correctly moderation and absorption of light water coolant in the shield plug. Model #3 is the most detailed model of the reference design, and is used for analysis of the flooding process, reactor control, and best-estimate criticality and void reactivity calculations.

To facilitate construction of MCNP input data, a PASCAL program has been developed. The code enables the user to easily change parameters of the fuel, coolant, conditions in both the flooded and unflooded portions of the calandria, and to position the control rods. A listing of the code, sample input data and sample code output (MCNP input data deck) is given in [Hejzlar et. al., 1994].

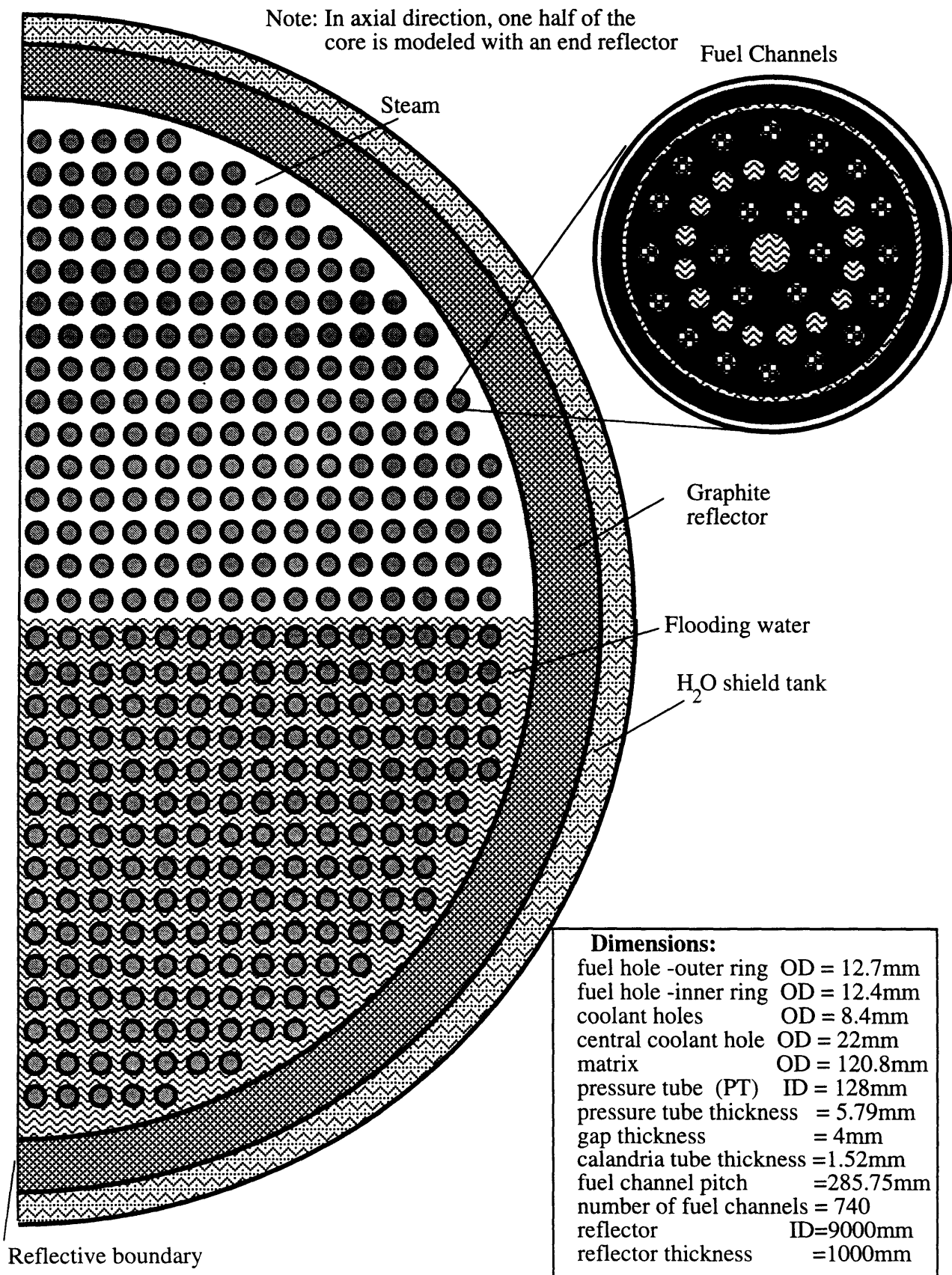


Figure 4-7 Reference calandria design - MCNP model of a full core for flooding (core region)

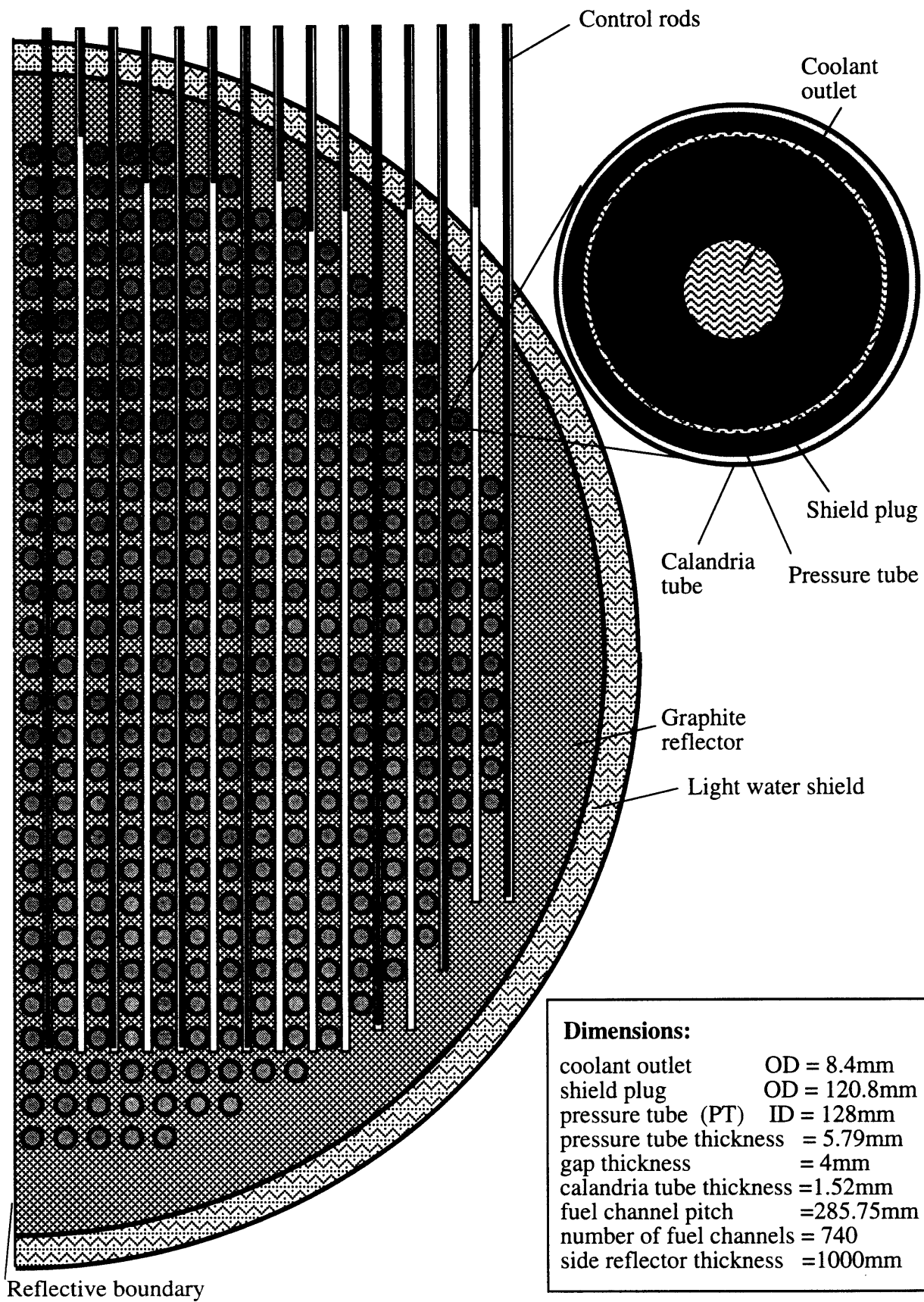


Figure 4-8 Reference calandria design - MCNP model of a full core for flooding (side-reflector region with control rods)

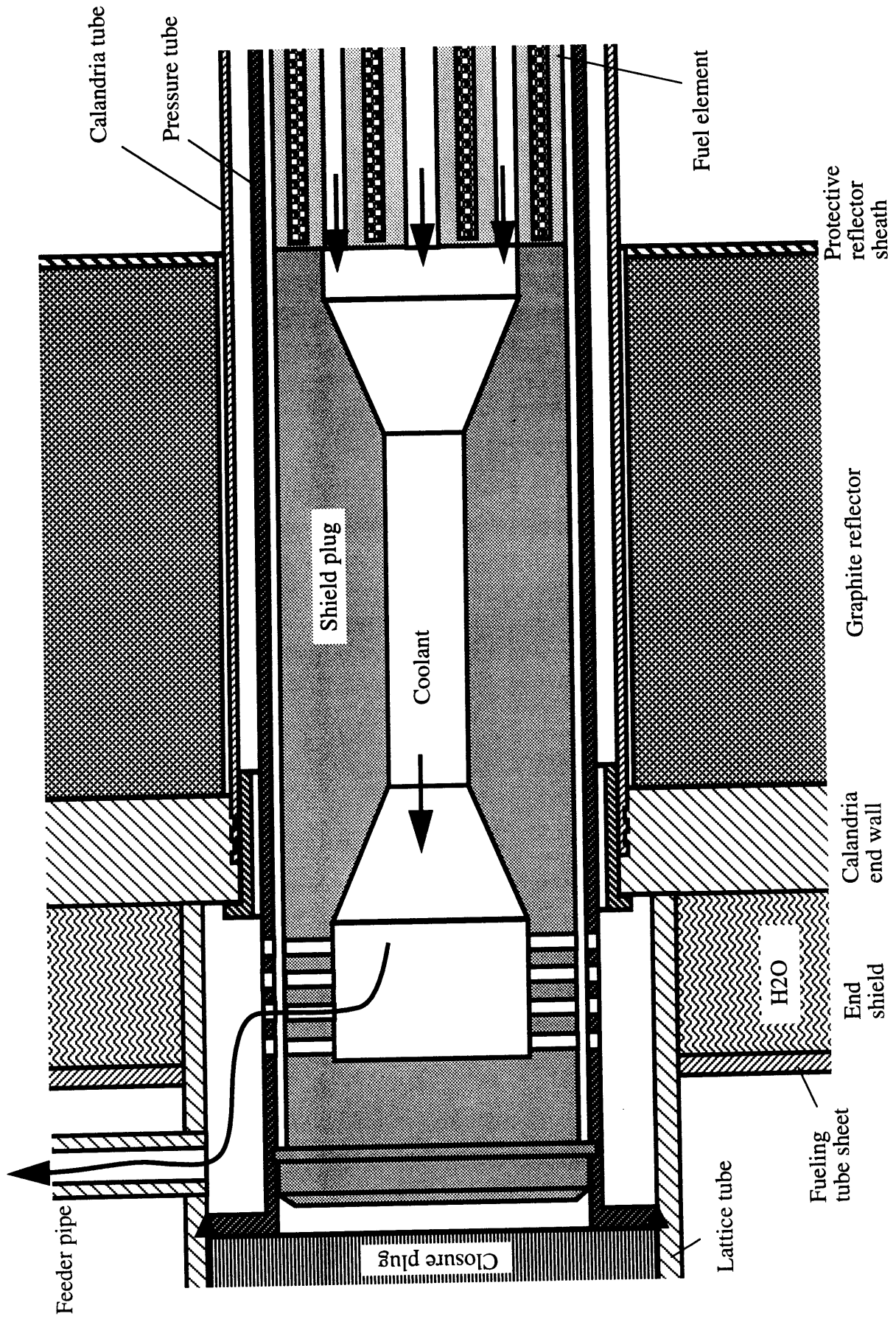


Figure 4-9 Arrangement of channel ends with shield plug

4.4.2.4 A Two Channel MCNP Model With Variable Fuel Composition for Bi-directional Refueling Scheme (Model #4)

All previously described models assumed an axially-uniform fuel composition in the channel. This assumption, however, is applicable only to the fresh core, or for on-line refueling strategies which refuel the entire channel at one time. More common practice is, however, to refuel only several bundles at a time. Also, the bi-directional on-line refueling, adopted for the proposed PTLWR concept, refuels several bundles at a time. Therefore, individual fuel elements in the channel have different fuel composition, depending on fuel element burnup. To take into account this important fact, a full-length MCNP model of the two neighboring channels, which models separately every fuel bundle, has been developed.

Figure 4-10 shows schematically two neighboring fuel channels with individual fuel elements; one channel (with pattern-filled fuel elements) is refueled from the left end, the other channel from the opposite end. Fuel channels are arranged in the core in a checkerboard scheme. Using the symmetry, the model can be simplified into two one-quarter channels facing each other as shown in Figure 4-10. The expanded cross sectional view of the two-channel cell is shown in Figure 4-11. Both channels are enclosed by a square reflective boundary. In the axial direction, the entire channel length is modeled with 1m-thick graphite reflectors on both ends. Every fuel element can have different fuel composition and coolant density. Fuel compositions are obtained using the ORIGEN2 code and coolant densities are obtained from a separate thermohydraulic model described in Chapter 6.

The input deck for the MCNP model of the two neighboring channels in checkerboard arrangement is generated by a PASCAL code.. The code allows reshuffling of fuel elements with arbitrary fuel compositions to arbitrary positions. Other parameters, such as coolant density, matrix and

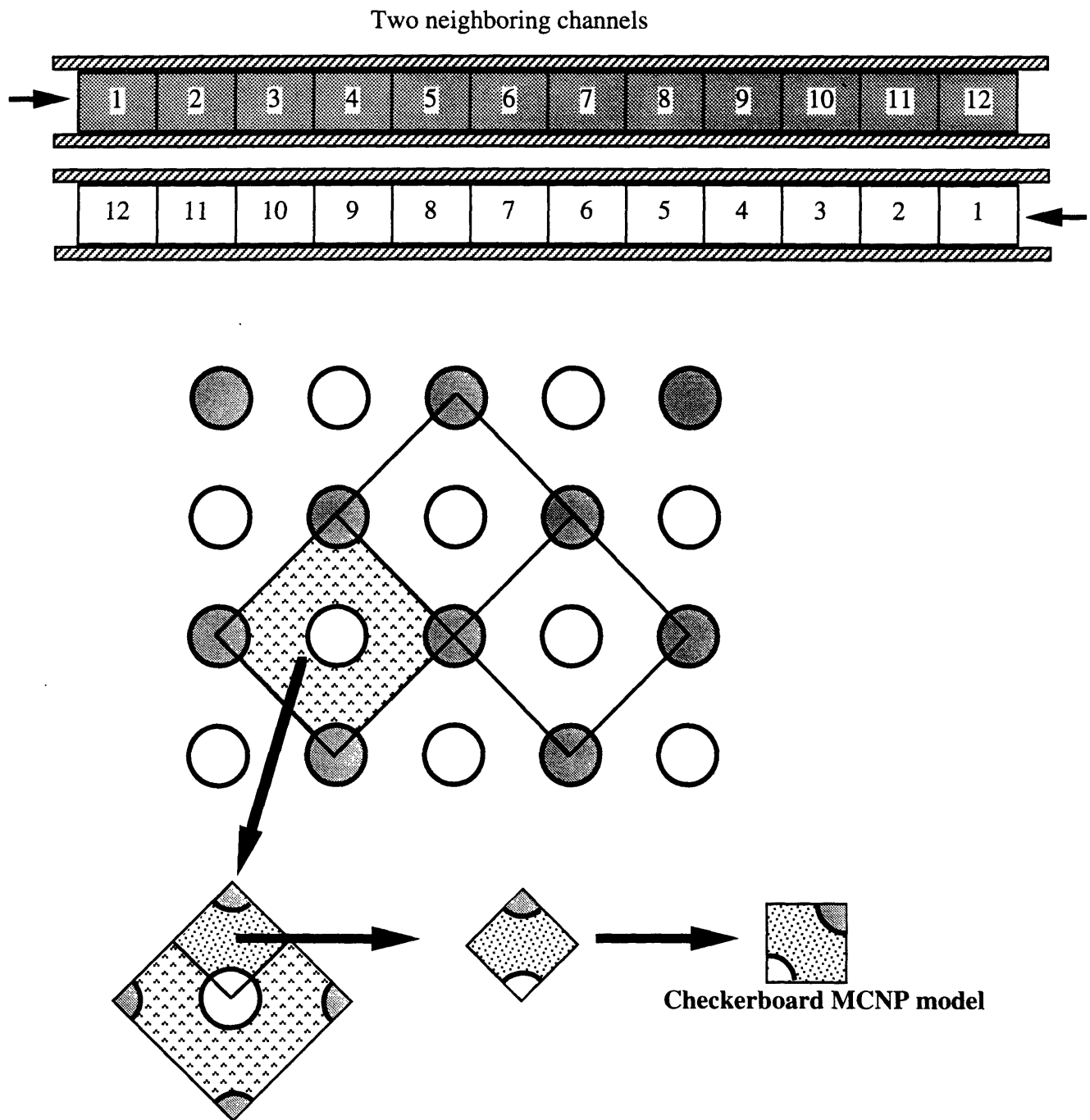
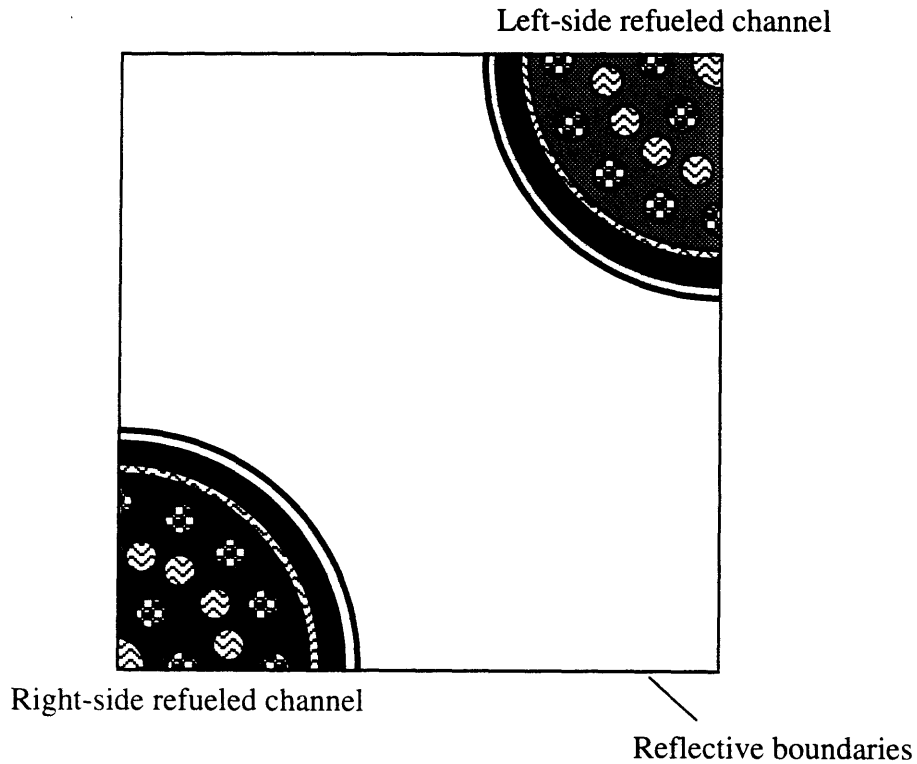


Figure 4-10 MCNP model for checkerboard bi-directional refueling

Dimensions:

fuel hole -outer ring	OD = 12.7mm
fuel hole -inner ring	OD = 12.4mm
coolant holes	OD = 8.4mm
central coolant hole	OD = 22mm
matrix	OD = 120.8mm
pressure tube (PT)	ID = 128mm
pressure tube thickness	= 5.79mm
gap thickness	= 4mm
calandria tube thickness	=1.52mm
fuel channel pitch	=285.75mm



Note: In the axial direction, all twelve fuel elements are modeled for both channels, and each bundle in each channel can have arbitrary fuel composition. The ends of both channels are reflected by a 1m-thick graphite reflector.

Figure 4-11 Expanded cross-sectional view of a cell with two neighboring channels

reflector material and various moderator options in the calandria space are also possible. A listing of the code, sample input data and sample code output (MCNP input data deck) are given in [Hejzlar et. al., 1994].

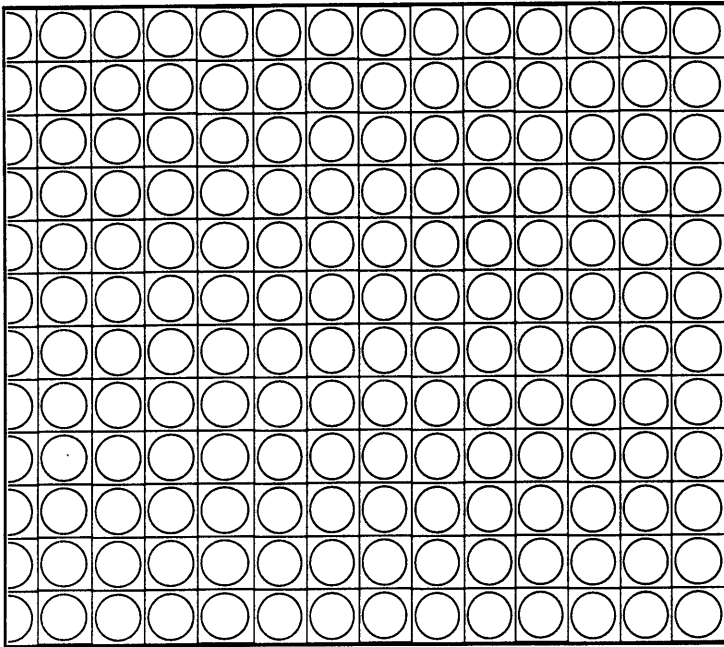
4.4.3 Double Heterogeneity Effects

The MCNP models of the reference dry calandria design, described in Section 4.4.2, modeled fuel compacts containing TRISO particle fuel as homogenized regions. The real arrangement of the fuel compacts is composed of TRISO particles comprising the fuel kernel, surrounded by a low-density buffer layer, an inner pyrolytic carbon layer, a silicon carbide layer and an outer pyrolytic carbon layer binded in a graphite matrix. Thus, in addition to heterogeneous placement of fuel regions within the fuel channel, fuel kernels within the fuel compact itself are heterogeneously distributed. This introduces secondary heterogeneity, or microheterogeneity, into the system. Homogenization of fuel compacts with particle fuel results in an increase of resonance absorption in resonance-absorber materials, and hence in a decrease in reactivity and an increase in the Doppler coefficient. This section will make an assessment of the bias in multiplication factor introduced by the homogenization of the fuel region as compared to the real case, i.e., when the cross-section spatial-shielding in resonance-absorber isotopes is fully accounted for.

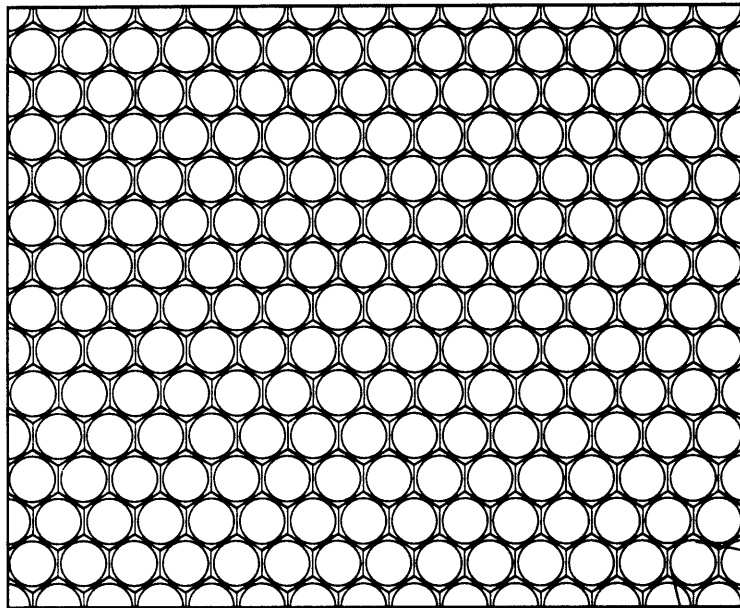
Several methods for self-shielding cross sections in such doubly heterogeneous systems have been developed and tested [Walti, 1971], [Walti and Koch, 1972], [Stamatelatos, 1976], [Stamatelatos and LaBauve, 1978] for HTGR applications. Since these models were not readily available, MCNP was used to estimate these effects.

An MCNP model of 2346 particles arranged in a hexagonal lattice, as shown in Figure 4-12, was prepared. The size of the hexahedron is chosen to be about the same as the size of the fuel compact in the radial direction. The spacing between individual particles is selected to keep the same packing density as for the reference dry calandria design. Note that the actual geometrical arrangement of the particles will be irregular and cannot be exactly determined since it has a rather statistical character. Monte Carlo calculations by others have shown that the geometrical

Front view



Top view



TRISO particle

Outer PyC layer

SiC layer

Inner PyC layer

Buffer

Fuel kernel

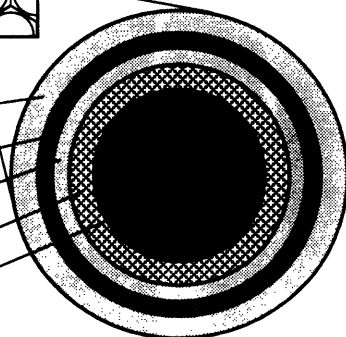


Figure 4-12 Model arrangement of 2346 TRISO particles

arrangement of the particles is rather independent of their packing [Askew et. al., 1971], hence the results obtained for the regular lattice should be fairly representative.

Ideally, one would run the MCNP model of the hexahedron with boundary flux conditions obtained from the full cell model. However, since MCNP does not allow flux boundary conditions, a different approach is used. To achieve the same neutron spectrum as in the dry calandria design, the hexahedron is surrounded by a light-water moderator annulus (not shown in Figure 4-12), having an inner radius of 1.5cm. The thickness of the moderator annulus is chosen such that the moderator-to-fuel volume ratio is the same as for the reference dry calandria design. A zero-current boundary condition is assumed on the outer surface of the moderator layer and on both ends. The voided space between the hexahedron and the annulus increases the neutron mean free path, similarly as in the dry calandria design. Particles in the hexahedron were homogenized, in the same manner as for the full cell model, and the energy spectrum obtained from the hexahedron homogenized model was compared with the energy spectrum obtained from the full cell model. If good agreement between the two spectra can be achieved, neutrons in the hexahedron model will have conditions close to those coming from the core. As shown in Figure 4-13, the agreement is quite good except for the fast spectrum. However, neutrons with energies higher than 0.1 MeV (region of energies with disagreement) do not participate in resonance absorption which is responsible for spatial self shielding, hence the results obtained from the model will be fairly representative.

The effect of spatial self shielding is then computed in two steps. In the first step, all particles with the kernel and all coating layers, and the graphite binder were homogenized in the same way as for the full cell MCNP model. Using this homogenized hexahedron surrounded by a moderator annulus, the multiplication factor was calculated. In the second step, a hexahedron with particles in all detail, keeping the same moderator annulus and boundary conditions as for the homogenized-system, was modeled, and the multiplication factor of this model was

calculated. The results for the equilibrium and for the fresh core are given in Table 4-1.

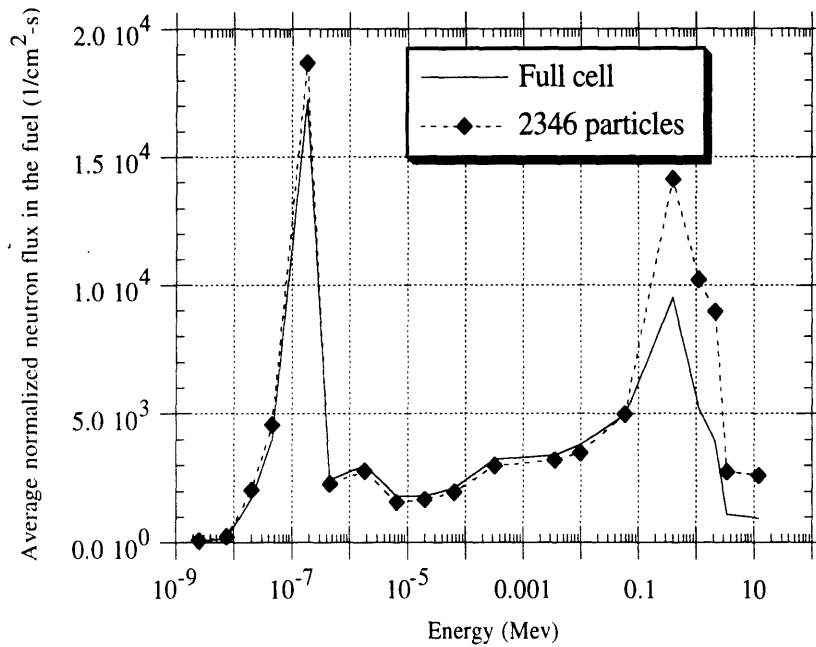


Figure 4-13 Comparison of neutron spectrum for a full cell model and 2346-particle homogenized model

Table 4-1 Comparison for homogenized and detailed 2346-particle model

	Multiplication factor	Reactivity	$\Sigma_c^{28}/\Sigma_a^{25}$
Homogenized- fresh core	1.1846±0.0031	0.15583	0.528
- equilibrium core	1.2061±0.002	0.17088	0.538
Non-homogenized - fresh core	1.1969±0.0012	0.16451	0.517
- equilibrium core	1.2106±0.0031	0.17396	0.527
Difference - fresh core	-	+0.0151	-2%
- equilibrium core	-	+0.0094	-2%

The results in Table 4-1 suggest that the effect of spatial self shielding is not significant in the reference dry calandria design. The criticality results which are calculated by MCNP models based on homogenized fuel regions, presented throughout this study, will be slightly biased by yielding underestimated reactivity. For the fresh core, the gain in reactivity is higher than the decrease in the conversion ratio, hence the achievable burnups will be slightly higher than those calculated from the homogenized particle models. In this sense, the results cited in this work are conservative underestimates of performance.

4.4.4 Physics Characteristics of the Dry Calandria Design

4.4.4.1 Introduction

The purpose of this section is to evaluate basic physics characteristics of the reference dry calandria design. Using MCNP models described in Section 4.4.3, it is demonstrated that the proposed PTLWR concept has several unique physics aspects which differ from those in currently operating LWRs. These include long prompt neutron lifetime, flat thermal flux profile, well thermalized neutron spectrum, and tight core-wide neutron coupling. Attention is paid to ensuring negative void coefficient. Characteristics different from current LWRs and CANDUs are pointed out and comparisons with these reactors are made.

4.4.4.2 Long Prompt Neutron Lifetime

Table 4-2 shows the comparison of prompt neutron lifetime for the PTLWR with CANDU and PWR lattices. Although light water is used in the dry calandria design, the prompt neutron lifetime is longer by an order of magnitude than for a typical LWR, and slightly longer than for a typical CANDU heavy water lattice (about 1.5 times). Most neutrons in the system are absorbed in the fuel. However, due to the large voids in the calandria, the neutrons have to travel a long distance, and hence it takes a long time, before they hit fuel nuclei. The reflector also contributes to an increase of

the prompt lifetime since the neutrons undergo a large number of collisions in the reflector before they are returned back to the core. Prompt lifetime calculated for the infinite lattice, i.e., without reflector is about 8×10^{-4} seconds, which is about one half of the core value (which considers the reflector) given in Table 4-2.

The magnitude of the prompt neutron lifetime is unimportant from the standpoint of controllability during normal reactor operations, since the reactor time constant is determined by the effective delayed neutron precursor constants, which are several orders of magnitude longer than the prompt neutron lifetime. However, from the standpoint of power excursions with reactivity insertions beyond prompt critical, prompt neutron lifetime is important.

Table 4-2 Comparison of prompt neutron lifetime with CANDU and PWR

Reactor	PWR ^a	CANDU ^b	PTLWR ^c
Prompt neutron lifetime ^d , Λ , (seconds)	2.0×10^{-5}	8.55×10^{-4}	1.5×10^{-3}

^a Typical PWR value

^b Obtained from [Banerjee and Hancox, 1981]

^c Calculated using MCNP model #3

^d For the fresh fuel

To appreciate the benefits of such a large prompt lifetime, consider a hypothetical accident which leads to a prompt supercritical scenario. It will be assumed that the reactivity is increased stepwise to $\beta + 0.25$ above prompt critical*. Maximum fuel temperature rise and power generation in the fuel may be estimated from a simple quasi-static model [Nyer, 1964], [Haefele,

* Such a reactivity insertion is possible in case of BWR control rod ejection, although the reactivity increase would be in the form of a ramp rather than a step increase. Note, however, that such a fast increase is highly unlikely in the PTLWR concept since rapid ejection of control rods, which are all inserted in the reflector and are under atmospheric pressure, is not possible. Moreover no control rod has a worth higher than β .

1963], [Kohler,1969]. The governing equation for an imposed reactivity increase, with linear temperature feedback can be written [Haefele, 1963] as

$$\frac{dP}{dt} = \left[\frac{\beta}{\Lambda} \alpha t - F \int_0^t P(\tau) d\tau \right] P \quad (4-7)$$

where P is reactor power in MW, β is delayed neutron fraction, Λ is the prompt neutron lifetime in seconds, α is ramp rate in \$/sec, and F is feedback constant in \$/MJ. Solution of the above equation gives periodic reactivity oscillations and power bursts. Assuming that the only reactivity feedback in this fast scenario is the Doppler effect, and neglecting delayed neutrons, Eq. (4-7) has been solved for a step reactivity increase of ρ_s dollars to yield maximum power [Kohler, 1969]

$$P_{\max} = \frac{\beta \rho_s^2}{2 \Lambda F} \quad (4-8)$$

and total energy release in one pulse and corresponding temperature rise above initial temperature

$$E_T = \frac{2 \rho_s}{F}; \quad \Delta T_{\max} = \frac{E_T}{C_f} \quad (4-9,10)$$

with the feedback constant

$$F = \frac{A_{\text{Dop}}}{\beta C_f T_0} \text{ $/MJ} \quad (4-11)$$

where A_{Dop} is the Doppler feedback constant. Since the Doppler feedback varies with temperature like $\sqrt{T} (dk/\Delta T) = -A_{\text{Dop}}$, using a constant value of A_{Dop} is only an approximation, but sufficient for this comparative study. C_f is the core fuel heat capacity in MJ/°C and T_0 is the initial fuel average temperature. Maximum power generated in the fuel and maximum temperature rise using Eqs. (4-8) through (4-11) are compared in Table 4-3.

Table 4-3 shows that although the increase in the average fuel temperature is not significantly affected by a long prompt neutron lifetime, the maximum rate of power generation in the fuel differs by several orders of

Table 4-3 Comparison of maximum fuel temperature rise and power input to the fuel in hypothetical reactivity increase, ρ_s , of \$0.25 above prompt critical

	T_0 (°C)	$\Delta k/\Delta T$ (1/°C)	Λ (s)	C_f (MJ)/°C	β	P_{\max} (MW)	ΔT_{\max} (°C)
PWR	1100	2.1×10^{-5}	2.0×10^{-5}	36	0.0065	141,256	193
PTLWR	970	2.4×10^{-5}	1.5×10^{-3}	10.5	0.0065	493	173

magnitude. Although the PWR power generation peak is large, it lasts for a very short period of time. Therefore, the integrated energy deposited in the fuel, which drives the temperature rise is comparable for both cases. A significantly smaller and long-duration PTLWR power peak in prompt critical excursions can also be shown by solving simultaneously the energy balance equation in the fuel

$$\rho c_{p,f}(T) \frac{dT}{dt} = q'''(\tau) \quad (4-12)$$

with the equation for power density in the fuel, which is proportional to fission rate, driven by the point neutron kinetics equations

$$\frac{1}{q_0'''} \frac{dq'''}{d\tau} = \frac{\rho(\tau) - \beta}{\Lambda} \frac{q'''}{q_0'''} + \sum_{j=1}^6 \lambda_j \tilde{c}_j(\tau), \quad (4-13)$$

$$\frac{d\tilde{c}_i(\tau)}{d\tau} = \frac{\beta_i}{\Lambda} \frac{q'''}{q_0'''} - \lambda_i \tilde{c}_i(\tau) \quad i=1, \dots, 6 \quad (4-14)$$

where

$$\rho(\tau) = \rho_s + \beta - \frac{k_D}{\sqrt{T}} (T - T_{\text{ref}}) \quad (4-15)$$

The initial conditions are steady state average fuel temperature $T_0 = T(\tau=0)$ and the average fuel power density $q_0''' = q'''(\tau=0)$. Note that Eq. (4-12) assumes that all heat generated during the excursion remains in the fuel

and the point kinetics equations include the effect of delayed neutrons. The coefficient for the Doppler effect, k_D , is calculated in Section 4.4.4.6. The results obtained by integrating the above system using a 4th order Runge-Kutta method with variable time step, for both the PWR and the PTLWR are shown in Figure 4-14.

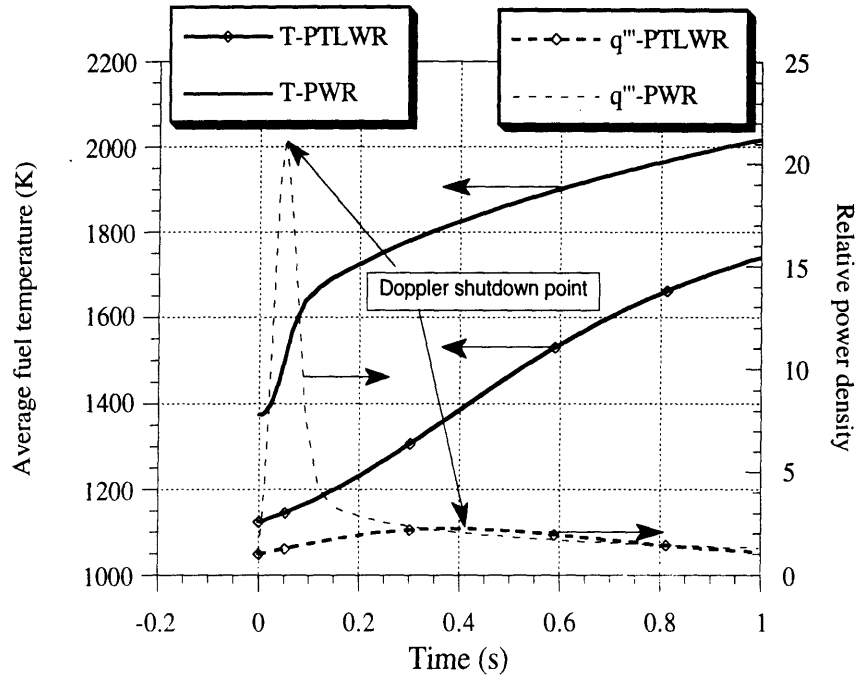


Figure 4-14 Comparison of prompt criticality excursions for PWR and PTLWR for excess reactivity of 0.25β above prompt critical

The axis on the left shows the average fuel temperature, and the right axis shows the relative power density, q'''/q_0''' . It is evident from Figure 4-14 that the power generation peak is significantly smaller for the dry calandria design than for a typical PWR. Moreover, the relatively long time constant for the prompt excursion of the PTLWR, will allow some energy to dissipate into the particle coating and graphite binder (time constant of heat transfer from the center of the kernel to the buffer zone is of the order of 0.05 seconds; much shorter than the time constant for a PWR UO₂ pellet: ~ 5 seconds), hence slowing further the rate of temperature growth and allowing more time for the control systems to shut down the reactor.

4.4.4.3 Flat Thermal Flux Profile

The large void fraction in the calandria significantly increases the migration area, allowing for homogeneous dispersion of thermal neutrons over a large area of the core. Moreover, at the core periphery, where the population of thermal neutrons might otherwise tend to decrease, neutrons which have undergone moderation in the reflector are supplied. This provides for the exceedingly flat profile of the thermal neutron flux in both the axial and radial directions.

The detailed 3-D profile of thermal flux in a PTLWR fuel channel with fresh fuel of axially uniform enrichment is shown in Figure 4-15. Flux tallies were obtained from MCNP model #1, using the channel model with graphite reflector at the end of the channel. The error on flux tallies is between 0.5% to 2%. Zero coordinates on Figure 4-15 correspond to the intersection of the channel centerline and core midplane, hence the reflector is at the end of the axial coordinate and the view is from the channel center towards the reflector. The two valleys represent the fuel compacts, where thermal flux decreases towards the center of the fuel compact due to absorption of thermal neutrons in the fuel. It can be observed that the thermal flux is very flat, with slight peaking near the graphite reflector because a large number of thermal neutrons coming from the reflector return to the core. As has been mentioned, this flatness is primarily a consequence of the large void fraction in the calandria. If this void fraction is decreased, the flatness disappears. This is shown in Figure 4-16, which was obtained with MCNP model #1 for the same channel, but with very tight channel pitch (the pitch was chosen such that the outer surfaces of the calandria tubes were just touching). The 3-D fast neutron flux profile for the reference PTLWR fuel channel, shown in Figure 4-17, exhibits the typical chopped cosine shape. Note that to give a better view of the shape, the axial coordinate was reversed, i.e., the observer is looking from the end reflector towards the core center. Power peaking near the reflector can be decreased by extending the shield plug (see Figure 4-9 for the shield plug) about 15cm into the core region, so that the fuel is not located in this thermal flux peak. The MCNP calculations for this

Thermal flux profile in the fuel channel

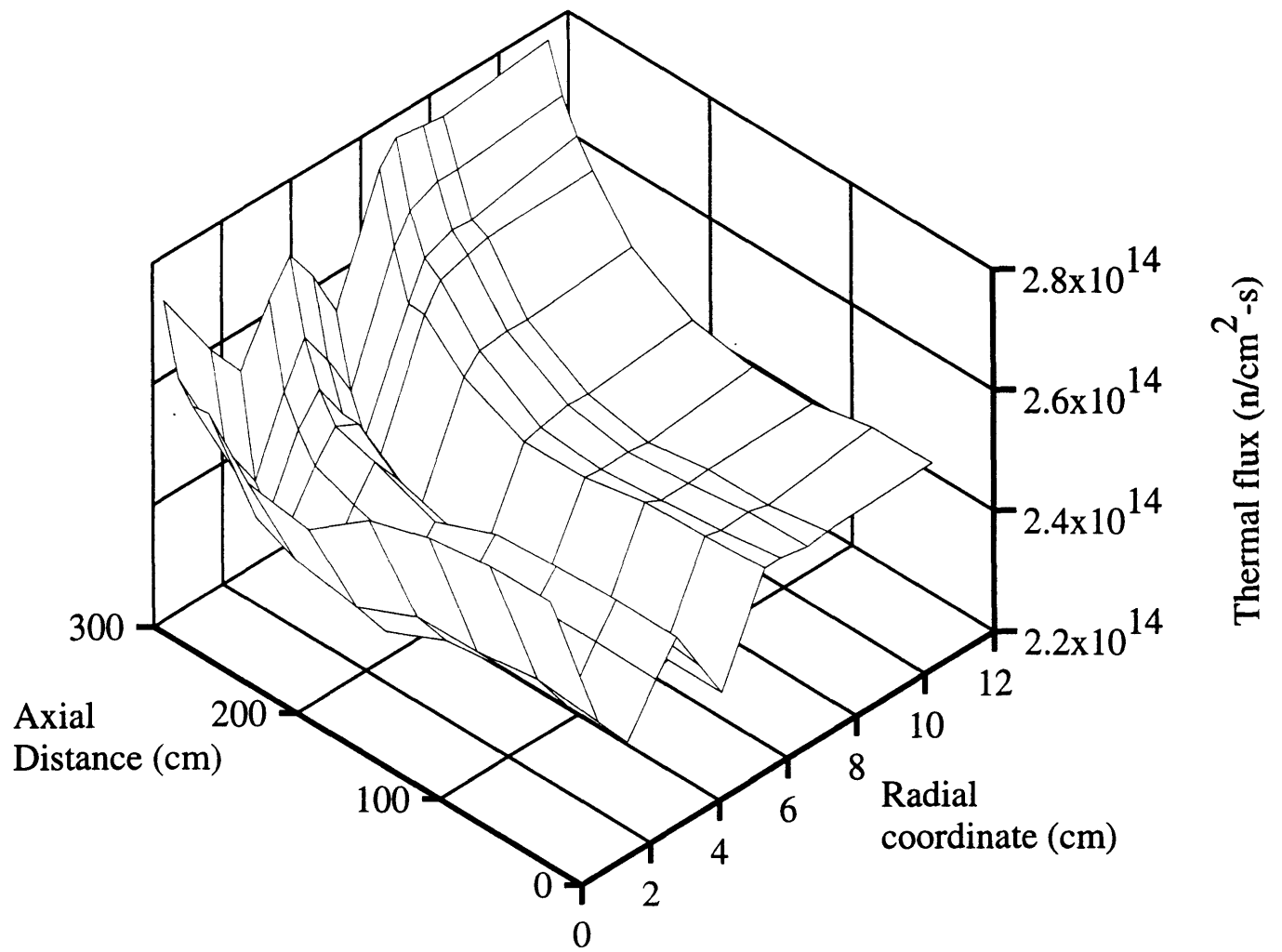


Figure 4-15 3-D thermal flux profile in a PTLWR fuel channel

Thermal flux profile - tight pitch cell

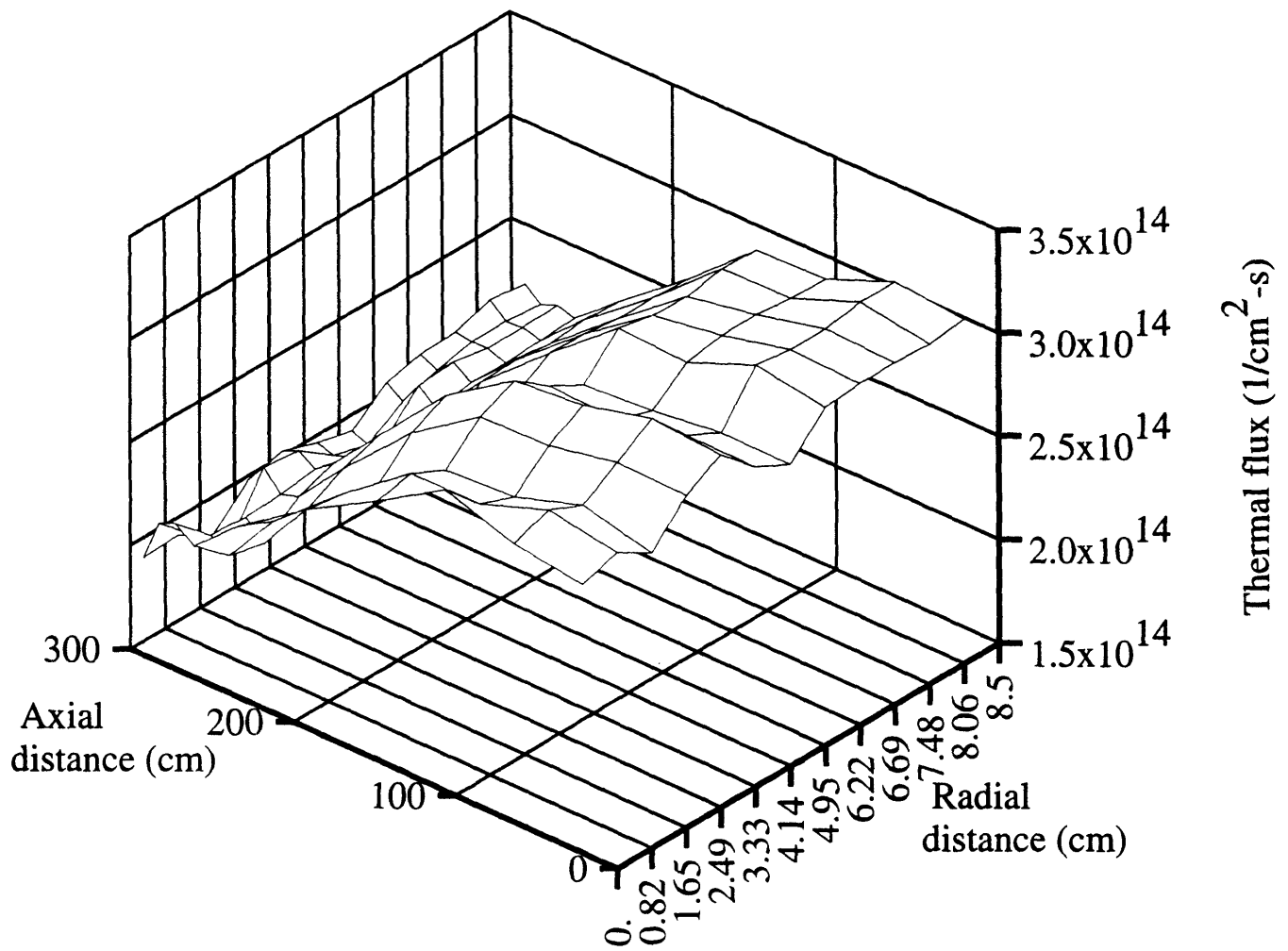


Figure 4-16 3-D thermal flux profile in a PTLWR fuel channel with tight pitch

Fast flux profile in the fuel channel

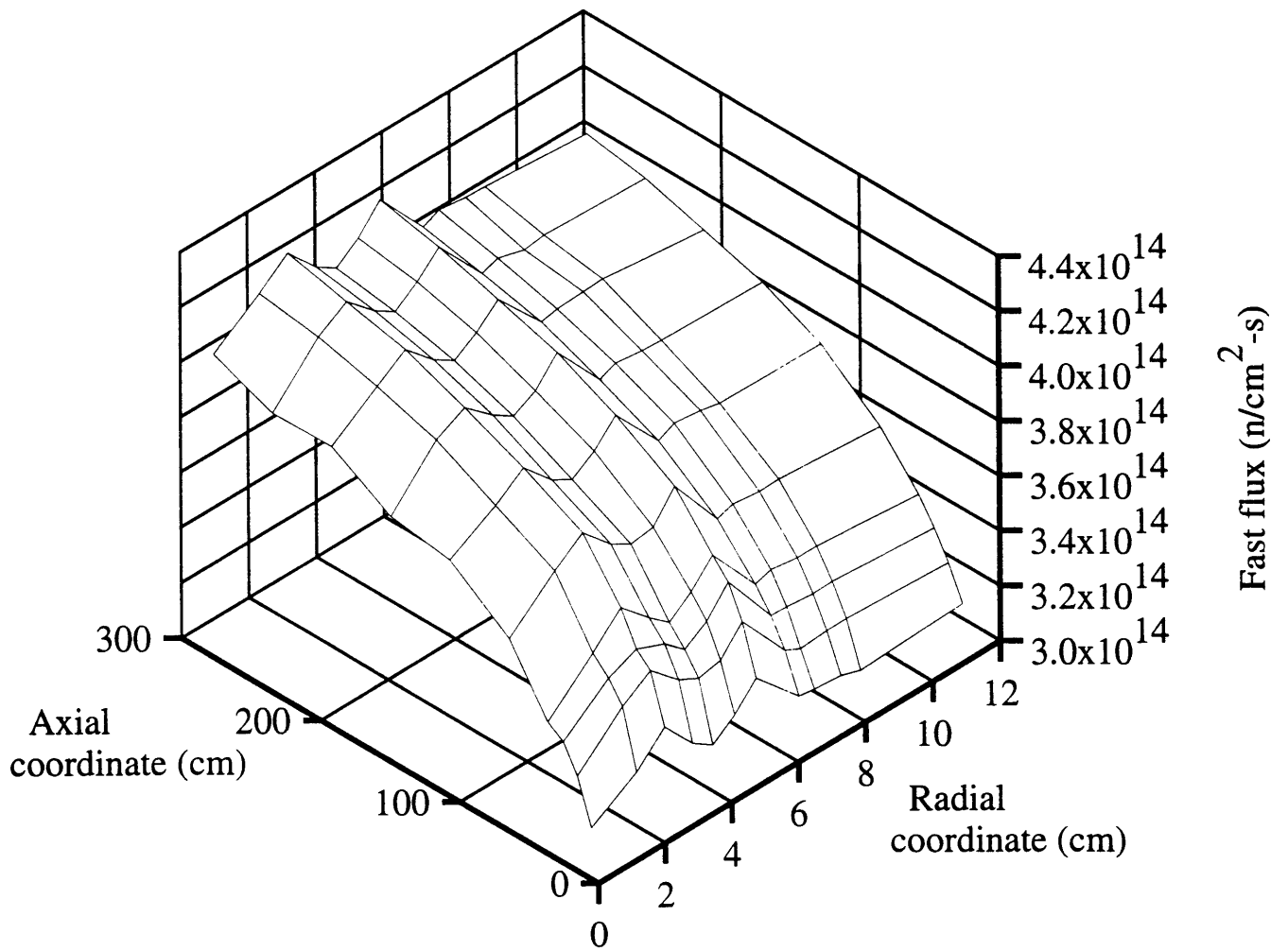


Figure 4-17 3-D fast flux profile in a PTLWR fuel channel

configuration showed a decrease in peaking factor to 1.1. This option is, however, not warranted because it leads to slightly lower core heavy metal loading and because the small reduction in peaking is offset by the arrangement of the fuel elements during the bi-directional refueling (i.e., placement of a fuel element with high burnup into the thermal flux peak near the reflector will reduce this peak to a larger extent than an extended shield plug).

The power density profile (which includes contributions from both thermal and fast fissions) in fuel compacts with fresh fuel of uniform enrichment, is shown in Figure 4-18. Except for the short region near the reflector, power density is almost constant, and slightly less than the average power density for PWR pins. The axial peaking factor is only 1.13 and 1.14 for the inner and outer fuel rings, respectively. This is a significantly lower axial peaking factor than for other thermal reactors. This can be also observed in Figure 4-19, which shows a comparison of relative axial power density distributions for a typical (beginning-of-life) PWR and the dry calandria design.

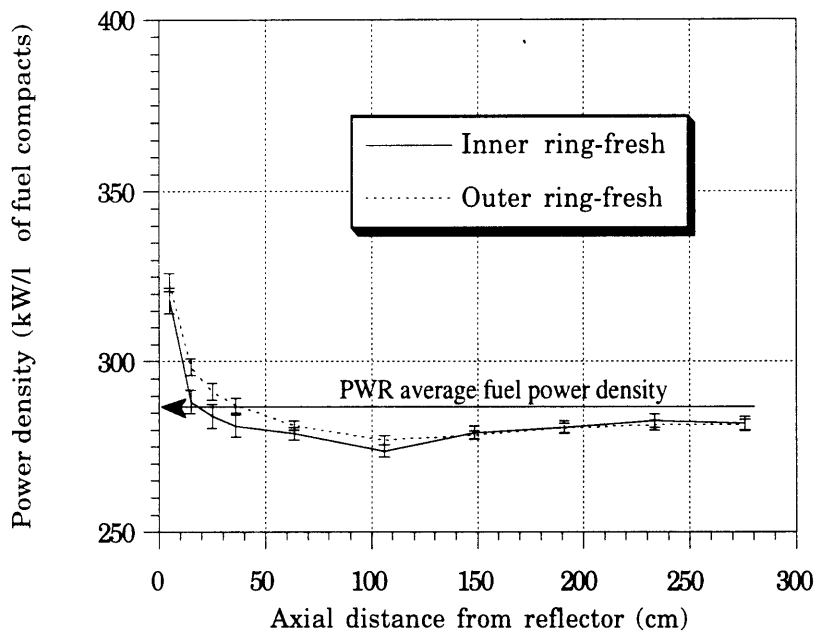


Figure 4-18 Power density profile in fuel compacts for the fresh PTLWR core

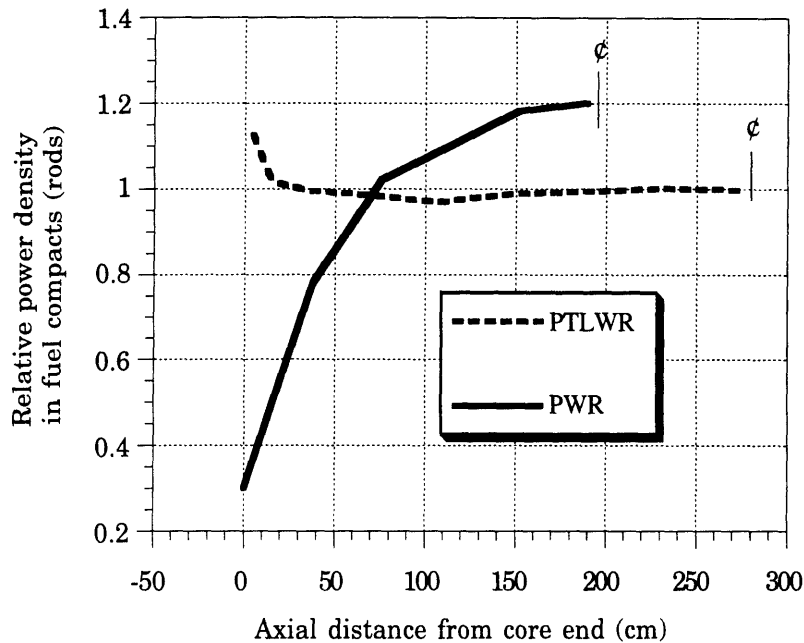


Figure 4-19 Comparison of fresh core axial power density profiles for the PTLWR concept and a typical PWR

One, however, needs to consider also the equilibrium core, where the fuel composition is not uniform but varies along the channel, depending on the refueling scheme. Such a situation will be investigated in Section 4.4.8.

Figure 4-20 shows the 3-D thermal flux profile through the entire core, obtained from MCNP model #2. Zero coordinates represent the intersection of the core centerline and core midplane. The entire thermal flux surface is very flat, with slight peaking near the end reflector and near the core centerline. The overall peaking is 1.18 and the maximum-minimum flux ratio is 1.26. Peaking near the radial reflector is less pronounced due to the distance between the fuel channels and the radial reflector. The shape of the thermal flux is also affected by control rod positions. Twenty two boron carbide control rods fully inserted into the end reflector, as shown in Figure 4-21; were considered (note that Figure 4-21 shows only 1/8th of the core). The thermal flux profile for this configuration of control rods is given in Figure 4-22. The change in the flux shape, compared to Figure 4-20 without control rods, is noticeable. Inserted control rods invert the flux profile changing it from a concave to a convex surface, although the peaking still

Core thermal flux distribution

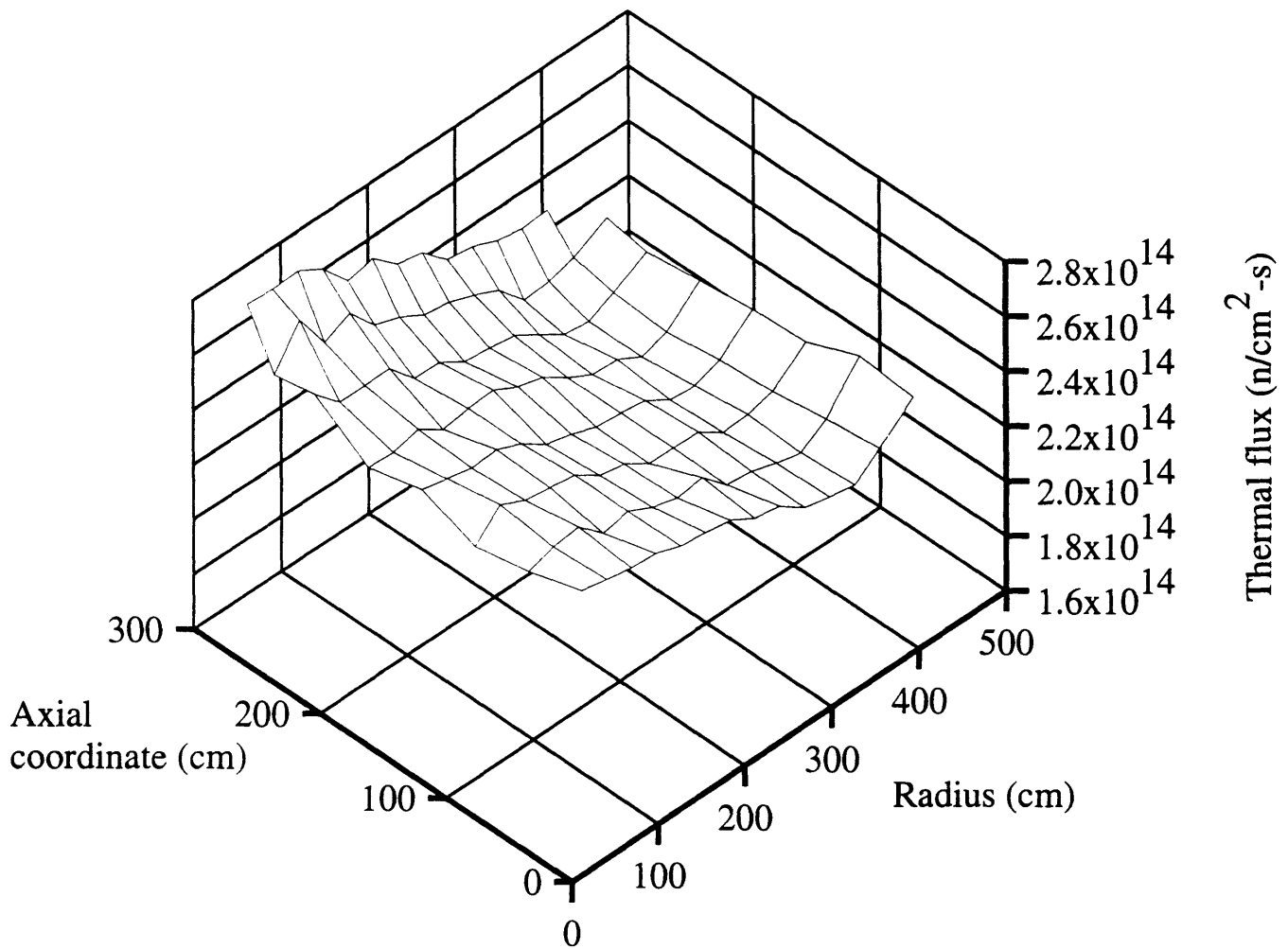
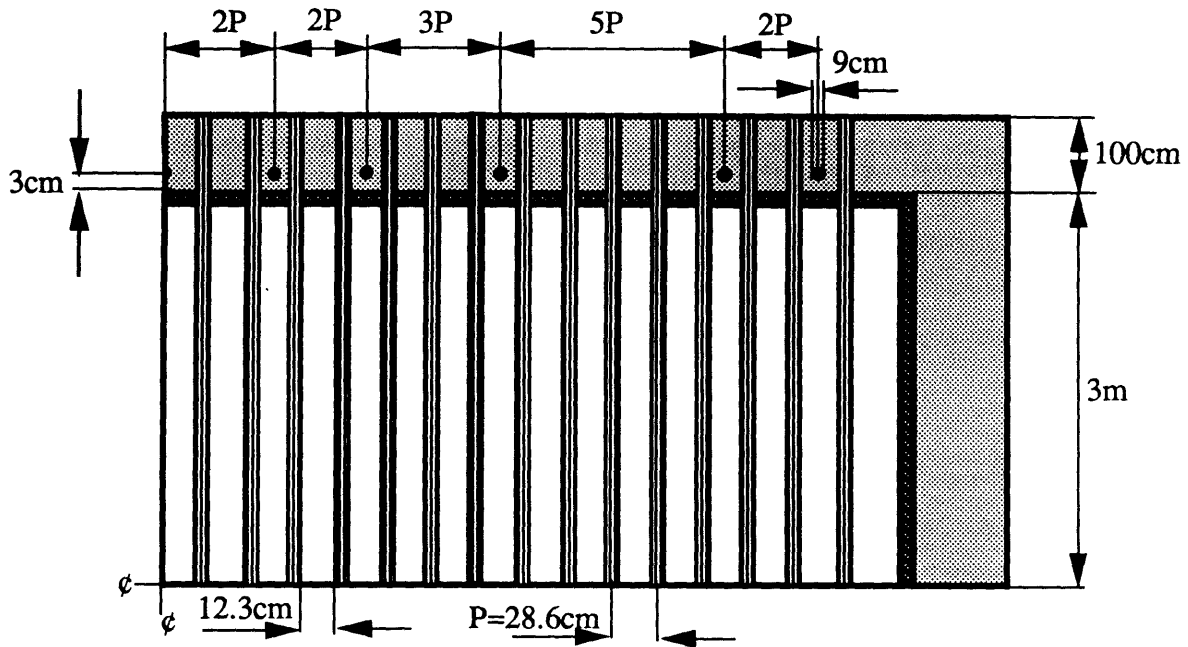


Figure 4-20 3-D thermal flux profile in a PTLWR core

Top view of 1/8th of the core with reflector



- Graphite reflector
- B₄C control rods
- ▨ Pressure tubes with fuel matrix and coolant channels

Worth of these 22 (per whole core) fully inserted control rods is 3.4β

Figure 4-21 Arrangement of control rods in the PTLWR for study of their effect on thermal flux shape

Core thermal flux distribution for CRDs fully in

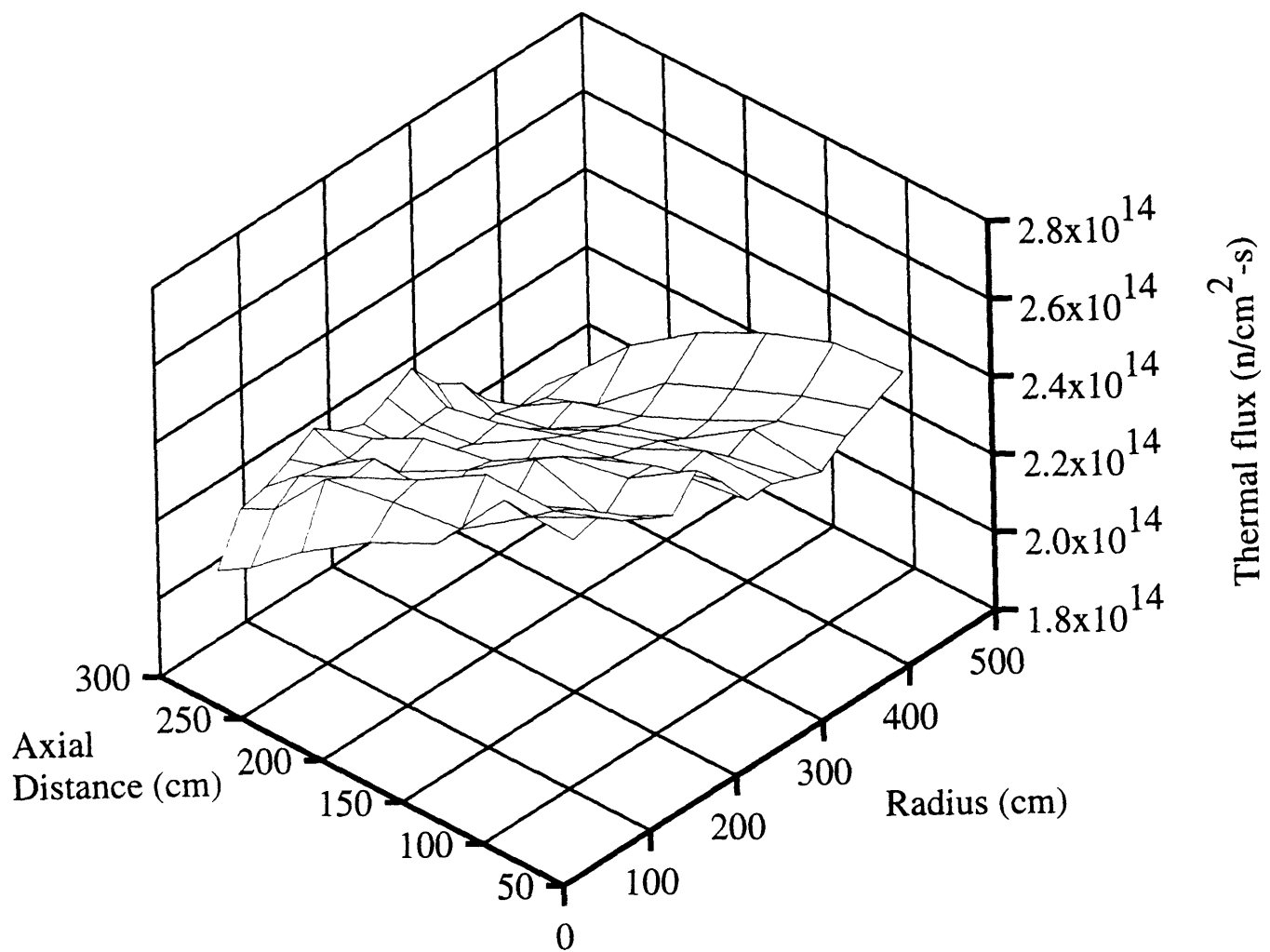


Figure 4-22 3-D fast flux profile in a PTLWR core with inserted control rods

remains small. Figure 4-22 also shows that the control rods located in the reflector can reach a large portion of the core, since the flux bending begins about 1 m from the core midplane.

It has been demonstrated that the fresh PTLWR core with uniform enrichment exhibits extremely flat thermal flux and power density profiles. Such a flat power density profile throughout the entire core increases safety margins associated with the hot spot, and consequently allows one to operate at higher power ratings.

4.4.4.4 Tight Neutronic Core Coupling

The large void space, in combination with the relatively low density of heavy metal and the heterogeneous arrangement of the H₂O moderator results in a large neutron mean free path, and hence in very tight core coupling. To get more insight into the reactor core coupling, it is of interest to compare the neutron migration area with LWR and CANDU reactors. Neutron migration area, M^2 , can be easily estimated from the criticality equation for a bare cylindrical core:

$$\frac{k_{\text{eff}}}{k_{\infty}} = \frac{1}{1+B^2 M^2}, \quad (4-16)$$

using MCNP results. The multiplication factor for the infinite lattice, k_{∞} , was calculated from MCNP model #1. The effective multiplication factor for the entire core, k_{eff} , but without any reflector, i.e. bare core, was calculated using MCNP model #2. The results are

$$k_{\infty} = 1.13, \text{ and}$$

$$k_{\text{eff}} = 0.674.$$

Using for buckling the equation for a bare cylinder

$$B^2 = \frac{\pi^2}{L_{\text{core}}^2} + \frac{2.405^2}{R_{\text{core}}^2} = \frac{\pi^2}{594^2} + \frac{2.405^2}{450^2} = 6.6535 \times 10^{-5} \text{ cm}^{-2} \quad (4-17)$$

neutron migration area can be calculated as

$$M^2 = \left(\frac{k_{\infty}}{k_{\text{eff}}} - 1 \right) \frac{1}{B^2} = \left(\frac{1.13}{0.674} - 1 \right) \frac{1}{6.6535 \times 10^{-5}} = 11967 \text{ cm}^2, \text{ or } M=110 \text{ cm} \quad (4-18)$$

Another possibility is to compute M^2 directly from the definition. Since M^2B^2 is the number of neutrons that leak from the core over the number of neutrons that die inside the core, one can calculate using results from MCNP model#2 for a bare core

$$M^2B^2 = 0.38/0.62 = 0.613, \text{ which gives } M=104, \text{ for } B^2 \text{ given by Eq. (4-17).}$$

The neutron migration area of about 10,000 cm² is very large. This compares to about 50 cm² for LWRs and 380 cm² for CANDUs. As a result neutrons can see practically the entire core, hence no local criticality is possible. Such a tight core coupling has three important consequences:

- no concerns with local criticality,
- the potential for reactor control from outside the core region, and
- absolute stability against Xenon spatial oscillations.

Physically, the entire core behaves as one nuclear unit. Either the whole core is critical or no local region of the core can go critical. This differs from typical LWRs where several adjacent fuel assemblies can go locally critical.

All reactor control can be achieved from outside the core, i.e., from the reflector since the control rods reach out to a large core area. Hence the local flux perturbations from control rods inside the core can be eliminated. Reactor control considerations will be discussed in Section 4.4.5.

Xenon Spatial Oscillations

Detailed calculations of Xe spatial oscillations would require at least a 2-D model of the core by nodal methods (which represent correctly extensive neutron streaming) and incorporate xenon equations. Although, such codes are available, obtaining the input data representative of the dry calandria design is difficult. Cross sections from MCNP as well as discontinuity factors need to be edited. Since the current version of MCNP does not offer tallies for group-to-group scattering, the scattering cross

section can be obtained only by neutron balance. This can be relatively easily done for 2-groups, and perhaps for 3-groups, with considerable effort. Moreover, it is not easy to obtain space dependent cross sections for the dry calandria design from MCNP because the entire core is affected by the reflector. Therefore to get a good representation of currents and face average nodal fluxes, at least a one-quarter-core model is necessary. But to get meaningful statistical results in individual nodes which are only very small portions of the one-quarter-core model, a huge population of neutrons would be necessary to force a sufficient number of neutrons into every small node. This procedure would require excessive computer time. In view of the above, a simplified method, which relies on the simple Randall and Lellouche criteria for reactor stability to Xe spatial oscillations, will be used.

Stability to Xe spatial oscillations is decreased by:

- increasing the core size,
- increasing the thermal neutron flux (but for sufficiently high flux levels, higher flux level is stabilizing),
- increasing the flatness of the thermal-neutron-flux distribution,
- decreasing the magnitude of negative temperature coefficients, and
- reducing the neutron migration length.

Probably, the simplest way to scope out the problem is by the argument given by Randall who states *“Xenon-induced oscillations in the power distribution can exist only in reactors that (a) operate at flux levels where Xe burnup is appreciable and (b) have “large” cores-cores having a linear dimension whose square is larger than the neutron migration area by a factor of 1000 or so. This last requirement can be easily checked by remembering that the square of the linear dimension in feet must exceed the migration area in cm² for oscillations to occur. “* [Randall and John,1958] For example, for an LWR with $M^2=50 \text{ cm}^2$, one would need to worry about oscillations if one of the dimensions of the core would be more than 225 cm, i.e.

$$225^2 / 50 = 50625/50 = 1012.$$

Current commercial PWRs have core dimensions larger than 225 cm, hence potential Xe oscillations exist and must be prevented.

For CANDUs, the migration length is substantially larger, $M^2=381$ cm², but the core length and core diameter are also larger, i.e. 600 cm and 632 cm, respectively. Hence the above ratio

$$600^2/381 = 950 \text{ and } 632^2/381 = 1048,$$

which is very close to the criterion of 1000, and suggests that CANDU reactors are subject to Xe oscillations, in particular in the azimuthal direction. And indeed this is the case [Mamourian and Akhtar, 1978]. Also, two-dimensional digital simulation of Pickering indicated that the reactor was unstable with respect to azimuthal xenon-induced spatial power oscillations, and one-dimensional digital simulations indicated that it was stable with respect to axial oscillations [Kern,1969]. Therefore, the agreement of the approximate Randall criterion with detailed calculations is good.

For the dry calandria concept, the longest linear dimension, the diameter is 900 cm and the migration length is about 100 cm. It is evident that the ratio

$$900^2/100^2 = 90$$

is an order of magnitude less than the stated factor of 1000. Therefore the dry calandria core should not be subject to Xe induced spatial oscillations. Randall further says regarding Xe oscillations:” *Physically, this means that oscillations of this kind are possible when the core gets so large, that two or more regions begin to function as independent nuclear units-i.e. hardly any of the fissions in one region are caused by neutrons born in the other region.*” [Randall and John,1958] This is clearly not the case in the proposed voided core, where neutrons from any place in the core can reach any other place.

Lellouche, who intensively investigated Xe stability in the 1960s derived a very handy criterion. His criterion gives “*critical reactor size which is absolutely stable independently of flux level against higher spatial mode*

xenon oscillations in the presence of zero or negative temperature feedback" [Lellouche,1962]. Stability conditions are given in the form of tables for various fuels. Lellouche conditions are compared with the dry calandria parameters for 3% enriched ^{235}U fuel in Table 4-4.

Again it is evident from Table 4-4 that the ratio of both the radial and axial dimension to migration length for the dry calandria design are far below the Lellouche critical ratio. Hence no Xe oscillations are possible. This is an inherent feature. On the other hand, both PWR and CANDU reactors do not satisfy the Lellouche condition. Hence they need to incorporate special measures to avoid problems with Xe spatial oscillations. In terms of physical dimension to migration length ratio, the dry calandria design can be compared to a LWR of diameter only $9 \times 7 = 63$ cm, where 9 is the diametral ratio from Table 4-4, and 7 is the PWR neutron migration length. For such a miniature LWR, nobody would think seriously about potential Xe oscillations. It is also interesting to note that the Lellouche criterion agrees quite well with the Randall criterion, i.e. for bare cores from Table 4-4, $31.5^2 = 992$, which agrees very well with the 1000 factor from the Randall criterion.

Table 4-4 Lellouche's stability criteria of the first harmonic for 3% enriched ^{235}U fuel in bare and zero leakage reactors and comparison with the PTLWR design parameters

	Axial		Diametral	
	Bare $(B_1)^2=(2\pi/h)^2$	Zero leakage $(B_1)^2=(\pi/h)^2$	Bare $(B_1)^2=(3.83/r)^2$	Zero leakage $(B_1)^2=(1.84/r)^2$
Lellouche conditions	$h/M < 31.5$	$h/M < 18.2$	$(2r)/M < 34.4$	$(2r)/M < 21.3$
PWR	$h/M=57$	$h/M=57$	$(2r)/M=71$	$(2r)/M=71$
CANDU	$h/M=31$	$h/M=31$	$(2r)/M=24$	$(2r)/M=24$
PTLWR	$h/M=5.94$	$h/M=5.94$	$(2r)/M=9$	$(2r)/M=9$

To conclude, the above arguments show that the dry calandria design, in spite of its large core physical dimensions (core length and diameter are 6m and 9m, respectively), is inherently resistant to Xe spatial oscillations. This is primarily the consequence of an extremely large neutron migration length.

4.4.4.5 Well Thermalized Neutron Spectrum

Figure 4-23 shows the comparison of energy spectra for the dry calandria design, CANDU and PWR units. The spectrum for the dry calandria design was obtained using MCNP model #1 with fully reflective boundaries; the spectra for PWR and CANDU were calculated using MCNP benchmark models of representative cells (also infinite lattice), given in Appendix A.1. With respect to the thermal to fast flux ratio, the pressure tube LWR is comparable to a CANDU heavy water lattice. Figure 4-23 also shows the PTLWR neutron spectrum for the equilibrium core. A significant decrease of the thermal flux compared to the fresh core can be observed. This is due to the relatively large fraction of ^{239}Pu present in the PTLWR equilibrium core with high-burnup fuel. Table 4-5, which compares the cell volume fractions for the fuel and moderator, and moderator-to-fuel volume ratio for the PTLWR and a typical LWR, shows that the PTLWR has a significantly higher moderator-to-fuel volume ratio. Good neutron thermalization is achieved primarily due to this large moderator-to-fuel volume ratio and the large resonance escape probability.

4.4.4.6 High Thermal Flux Level and Fast Fluence

Figure 4-23 also shows that the magnitude of the neutron flux is considerably higher than that of the CANDU or PWR. Fast (above 0.6 eV) and thermal neutron fluxes are compared in Table 4-6. The differences in neutron flux between the dry calandria concept and PWR are large. In particular, the thermal flux of the dry-calandria concept is about 6 times higher than that for the PWR. On the other hand, the fast flux is only 1.9 times higher. More important, however, is the approximately 3 times

higher fast flux compared to that of the CANDU, because it has negative implications on the lifetime of the pressure tubes.

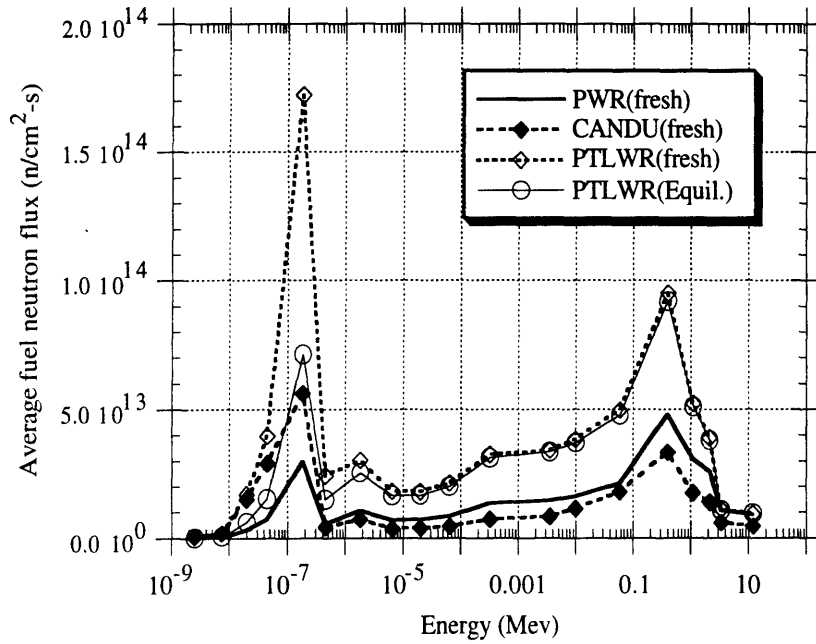


Figure 4-23 Comparison of energy spectra for the PTLWR with PWR and CANDU

Table 4-5 Comparison of cell volume fractions and moderator-to-fuel volume ratios for PTLWR and PWR

Constituent volume fractions in a cell	PWR	PTLWR
UO ₂	0.33	0.007998
H ₂ O	0.55	0.0333
Void	0	0.81
H ₂ O/UO ₂	1.67	4.2

This higher flux is a result of the low heavy metal loading, characteristic of particle fuel. A typical 1000 MWe PWR plant has a fuel loading of about 101 tonnes of UO₂. The CE-CANDU reactor (1260 MWe) has a fuel loading of about 190 tonnes [Shapiro and Jesick,1979]. The dry calandria concept fuel loading can be calculated using the geometry of the reference matrix design as follows:

Table 4-6 Comparison of fast and thermal neutron flux for PTLWR, PWR and CANDU

	PWR	CANDU	PTLWR
Thermal (n/cm ² -s) (E<0.6eV)	4.6x10 ¹³	1.1x10 ¹⁴	2.5x10 ¹⁴
Fast (n/cm ² -s) (E> 0.6 eV)	2.3x10 ¹⁴	1.4x10 ¹⁴	4.5x10 ¹⁴
Fast/thermal	4.9	1.32	1.8

$$\begin{aligned}
 V_{UO_2} &= N_f (\pi R_f^2 L_f) f_{cp} \left(\frac{R_k}{R_{cp}} \right)^3 N_{PT} = \\
 &= 24 (\pi 0.635^2 594) 0.635 \left(\frac{300}{430} \right)^3 740 = 2.88 \times 10^8 \text{ cm}^3
 \end{aligned}
 \tag{4-19}$$

where N_f is the number of fuel regions in the matrix, R_f and L_f are the radius and effective total length of fuel regions, f_{cp} is the fraction of coated particles in the fuel region, R_k/R_{cp} is the radius ratio of the fuel kernel and outer pyrolytic graphite coating, and N_{PT} is the number of pressure tubes. Fuel mass is thus

$$m_{UO_2} = \rho_{UO_2} V_{UO_2} = 10.97 \text{ g/cm}^3 (2.88 \times 10^8 \text{ cm}^3) 10^{-6} \text{ g/tonne} = 31 \text{ tonnes}
 \tag{4-20}$$

Which is three times less than for the PWR and eight times less than for the CE-CANDU. The amount of ²³⁵U in the PTLWR core for a given enrichment of 2.5% is

$$m_{U^{235}\text{-dry}} = 0.025 (31) \frac{238}{238+2 (16)} = 0.68 \text{ tonnes of } ^{235}\text{U}$$

which compares to

$$m_{U^{235}\text{-PWR}} = 0.035 (101) \frac{238}{238+2 (16)} = 3.1 \text{ tonnes of } ^{235}\text{U}$$

for a PWR and

$$m_{U^{235}\text{-CE-CANDU}} = 0.00711 (190) \frac{238}{238+2 (16)} = 1.2 \text{ tonnes of } ^{235}\text{U}$$

for the CE-CANDU. The ratios of the ^{235}U loadings roughly corresponds to the inverse of the thermal flux ratios in Table 4-6; e.g.. for CE-CANDU

$$(1.2\text{tonnes}/0.68\text{tonnes}) = 1.8 \approx (2.5\text{n/cm}^2\text{-s}/1.1\text{n/cm}^2\text{-s})$$

since the thermal flux is proportional to the atom density of fissile isotopes for fixed reactor power density.

A high flux level has two negative consequences:

- high fast fluence,
- a large xenon reactivity deficit following reactor shutdown,
- higher radiolysis dose to coolant, higher N-16 activity in coolant, and high fast fluence on the inner part of the reflector.

High fast neutron fluence is an important issue, in particular with regard to the pressure tubes. Using MCNP model #1 the average fast fluence on the pressure tubes was calculated to be about three times higher than for current CANDU reactors. This is a considerable drawback, because the axial and diametral growth of the pressure tube, which is linearly dependent on fluence, will be accelerated. Means to extend pressure tube lifetime under these high flux conditions would be required. More details about the fast fluence and its effects on the pressure tubes will be given in Chapter 9.

Xenon Poisoning during Steady State and Following Reactor Shutdown

High thermal flux results in a higher xenon poisoning ratio at steady state, but, more importantly, after reactor shutdown or after a large power decrease. Fission product ^{135}Xe has the largest absorption cross section of all the nuclides in a thermal flux and its buildup affects the neutron

balance in the reactor. The effect of ^{135}Xe on the neutron balance for the equilibrium core can be estimated by calculating the xenon poisoning ratio

$$r_{\text{Xe}}^* = \frac{\text{neutrons absorbed by poison } (^{135}\text{Xe})}{\text{neutrons absorbed in fission}} = \frac{N_{\text{Xe}} \sigma_{\text{Xe}} \bar{\Phi}}{\Sigma_f \bar{\Phi}}$$

which can be derived as [Benedict et. al., 1981]

$$r_{\text{Xe}}^* = \frac{\sigma_{\text{Xe}} \bar{\Phi}}{\lambda_{\text{Xe}} + \sigma_{\text{Xe}} \bar{\Phi}} (y_{\text{I}} + y_{\text{Xe}}), \quad (4-21)$$

where $\bar{\Phi}$ is the average thermal flux, σ_{Xe} is the effective one-group absorption cross section of ^{135}Xe , λ_{Xe} is the decay constant of ^{135}Xe , and y_{Xe} and y_{I} are direct xenon and iodine yields from ^{235}U fissions. Note that the above poisoning ratio is related to reactivity by the factor $1/v$ where v is the number of neutrons per fission. Equation (4-21) neglects the ^{135}Te buildup due to its very short half-life, hence the chain is assumed to originate with iodine, i.e., $y_{\text{Te}} = y_{\text{I}}$. Using for the one-group effective microscopic absorption cross section of ^{135}Xe for the PTLWR concept the same value as for the PWR, the results from Eq. (4-21), including the input data, are summarized in Table 4-7.

The core average flux in the fuel for the PTLWR concept, shown in Table 4-7, was obtained from thermal flux profiles from the relation

$$\bar{\Phi} = \bar{\Phi}_{\text{cell model}} k_{\text{core-cell}} k_{\text{cell-fuel}}, \quad (4-22)$$

where the peaking factors $k_{\text{core-cell}}$ and $k_{\text{cell-fuel}}$ are defined as

$$k_{\text{core-cell}} = \frac{\bar{\Phi}_{\text{core model}}}{\bar{\Phi}_{\text{cell model}}}; \quad k_{\text{cell-fuel}} = \frac{\bar{\Phi}_{\text{fuel}}}{\bar{\Phi}_{\text{cell model}}}. \quad (4-23)$$

The average core thermal flux,

$$\bar{\Phi}_{\text{core model}} = \frac{\int_{V_{\text{core}}} \Phi_{\text{core model}}^{\text{thermal}}(V) dV_{\text{core}}}{\int_{V_{\text{core}}} dV_{\text{core}}}, \quad (4-24)$$

Table 4-7 Comparison of steady state ^{135}Xe poisoning ratio for the PTLWR and a typical PWR (Eq. 4-18)

	PWR	Dry
^{135}Xe decay constant, λ_{Xe} (s)	2.09×10^{-5}	2.09×10^{-5}
Iodine decay constant, λ_{I} (s)	2.87×10^{-5}	2.87×10^{-5}
^{135}Xe direct yield from ^{235}U fission, y_{Xe} (atoms per atom fissioned)	0.0032	0.0032
Iodine yield from ^{235}U fission, y_{I} (atoms per atom fissioned) (^{135}Te buildup is neglected)	0.0609	0.0609
^{135}Xe cross section (barns)	2.64×10^6	2.64×10^6
Average thermal flux (n/cm ² -s)	3.5×10^{13}	2.16×10^{14}
^{135}Xe poisoning ratio (per 1 neutron absorbed in fission)	0.052	0.0614

was obtained using the full-core MCNP model #2, and the average cell thermal flux,

$$\bar{\Phi}_{\text{cell model}} = \frac{\int_{V_{\text{cell}}} \Phi_{\text{cell model}}^{\text{thermal}}(V) dV_{\text{cell}}}{\int_{V_{\text{cell}}} dV_{\text{cell}}}, \quad (4-25)$$

was obtained from the one-channel MCNP model #1. Note that to obtain good statistical results, the full-core model edits the thermal flux over the entire channel, but it cannot edit flux microstructure inside the channel. Finally, the average thermal flux in the fuel is defined as

$$\bar{\Phi}_{\text{fuel}} = \frac{\int_{V_{\text{fuel}}} \Phi_{\text{cell model}}^{\text{thermal}}(V) dV_{\text{fuel}}}{\int_{V_{\text{fuel}}} dV_{\text{fuel}}} \quad (4-26)$$

Table 4-7 shows that the xenon poisoning ratio is higher for the PTLWR concept than for a PWR. This difference, which is not very significant, is a consequence of the higher thermal flux in the PTLWR. Note that the xenon poisoning ratio saturates at the value of 0.0641 for very high fluxes.

The transient ^{135}Xe poisoning can be calculated by solving the buildup equations for iodine and ^{135}Xe , neglecting the buildup of ^{135}Te

$$\frac{dN_I}{d\tau} = y_I \Sigma_f \bar{\Phi} - \lambda_I N_I, \quad (4-27)$$

$$\frac{dN_{\text{Xe}}}{d\tau} = \lambda_I N_I + y_{\text{Xe}} \Sigma_f \bar{\Phi} - \lambda_{\text{Xe}} N_{\text{Xe}} - \sigma_{\text{Xe}} \bar{\Phi} N_{\text{Xe}}. \quad (4-28)$$

An analytical solution in terms of the transient poisoning ratio, i.e., the ratio of the neutron absorption in ^{135}Xe to fission absorption if the reactor is to be started up again after shutdown time t , can be derived [Benedict et. al., 1981]

$$\begin{aligned} r_{\text{Xe}} &= \frac{N_{\text{Xe}} \sigma_{\text{Xe}}}{\Sigma_f} = \\ &= y_I \bar{\Phi} \sigma_{\text{Xe}} \frac{\exp(-\lambda_I t) - \exp(-\lambda_{\text{Xe}} t)}{\lambda_{\text{Xe}} - \lambda_I} + \frac{y_I + y_{\text{Xe}}}{1 + \lambda_{\text{Xe}}/(\bar{\Phi} \sigma_{\text{Xe}})} \exp(-\lambda_{\text{Xe}} t) \end{aligned} \quad (4-29)$$

Figure 4-24 shows the reactor poisoning ratio following reactor shutdown as calculated using Eq. (4-29), for the PTLWR, a typical PWR and a typical CANDU. Figure 4-24 assumes that, prior to shutdown, the reactor had been operating long enough to achieve ^{135}Xe equilibrium. It is evident that the xenon poisoning of the dry calandria design following the reactor shutdown

is quite large (about 190 mk*). However, for the equilibrium core, the average thermal flux is significantly less (1.2×10^{14} n/cm²-s), due to the higher fission cross section of ²³⁹Pu, hence the xenon poisoning ratio of the PTLWR will be only slightly above that of a CANDU.

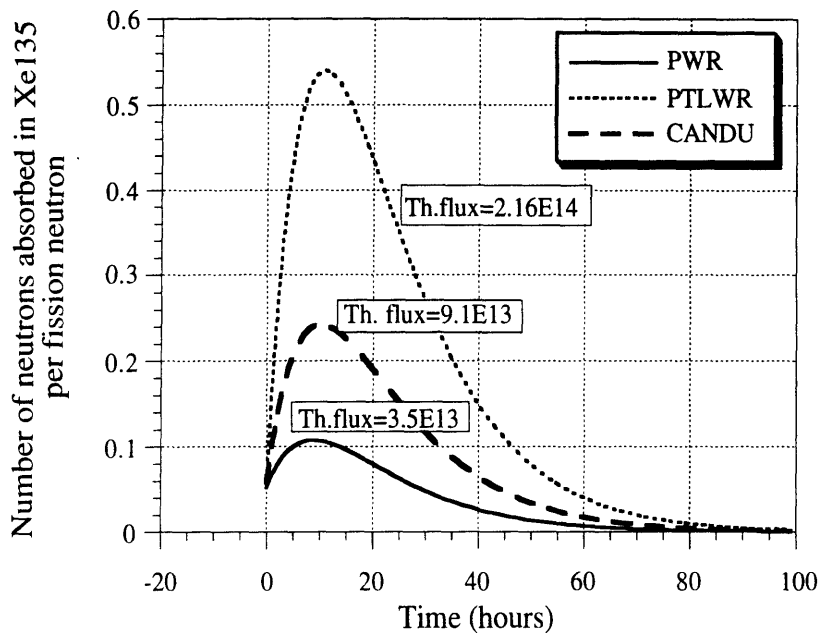


Figure 4-24 Comparison of ¹³⁵Xe transients following reactor shutdown

Provisions for full compensation of the large negative reactivity due to transient xenon buildup following reactor shutdown would be deleterious to fuel cycle economics. Hence only partial compensation is proposed. This is similar practice to CANDU reactors, which employ adjuster rods to compensate for the buildup of ¹³⁵Xe in the first 30 minutes following reactor shutdown [Pasanen, 1980]. If the reactor cannot be restarted before xenon poison reaches higher values than the compensation can provide, it is necessary to wait until xenon decays below the level allowing reactor restart (approximately 40-50 hours). Another alternative, following the Nuclear

* Poisoning ratio is related to reactivity by $\Delta k/k = r_{Xe}/\nu$ where ν is the average number of neutrons per fission; 1mk = 1000 $\Delta k/k$.

Power Demonstration (NPD) example, is to use cooled booster rods with enriched fuel, which could be inserted into the voided space to boost the reactivity.

Concern also arises that the extremely high xenon poisoning during transients involving a power decrease can affect reactor maneuverability. This issue is addressed in Figure 4-25 which shows the reactivity needed to overcome xenon poisoning following the step decrease of reactor power from the nominal power output to 50% power. Figure 4-25 has been generated for the fresh core data by integrating Eqs. (4-24) and (4-25) by a 4-th order Runge-Kutta method with variable time step. The maximum reactivity of 43 mk is much less than the peak after reactor shutdown, and can be compensated by the reactor control system.

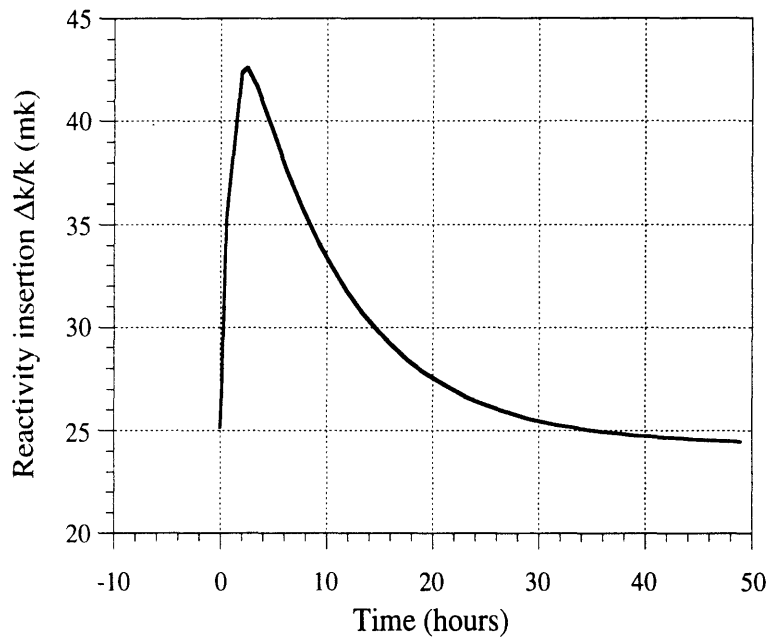


Figure 4-25 Reactivity insertion needed to overcome ^{135}Xe poisoning following step power level decrease to 50% (fresh core)

It is evident that the low fuel loading achievable with particle fuel results in undesirable high fast fluence and large xenon poisoning following reactor shutdown. Remedies to this problem have been sought by using uranium carbide (UC) fuel which has higher density and by using alternative fuel arrangements which could achieve higher fuel loadings.

Replacing the UO_2 fuel by UC fuel in particle kernels leads only to modest improvements, since the specific density of the UC fuel is only about 13% higher. Alternative fuel arrangements are explored in Chapter 5. It will be shown that high fuel loadings comparable to CANDU reactors can be achieved with a two-ring fuel bundle arrangement, which does not have any solid matrix.

4.4.4.7 Strong Negative Doppler Coefficient

The Doppler effect arises from the fact that neutron cross section resonances in fertile nuclides broaden with temperature as a consequence of increased relative speed between neutrons and nuclei. This leads to an increase in resonance captures, primarily in ^{238}U and ^{240}Pu , and hence to a decrease in reactivity. Besides the Doppler effect there are other fuel properties which are influenced by fuel temperature and affect the neutronic behavior, such as the scattering properties of the oxide fuel, fuel pellet density and gap thickness. These, however, are much less important than the Doppler effect. Hence, only the Doppler effect will be considered further as a fuel temperature feedback. The particle kernels employ slightly enriched UO_2 fuel – a mixture of fertile and fissile material. The change of the temperature occurs almost instantaneously with the change of fission power, since the fission fragments transfer their energy to the nuclei within the kernel in a very short time. As in other thermal reactors, the Doppler effect is an inherent and prompt feedback mechanism which terminates hypothetical large power surges.

Since the changes in reactivity with fuel temperature are typically small, they are difficult to predict accurately using statistical methods, such as the Monte Carlo method used in MCNP. Nevertheless, the limited capabilities of MCNP can be used to estimate the Doppler coefficient for this scoping study. This estimate can be performed by running the one-channel MCNP model #1 at several different temperatures of the fuel while all other fuel channel parameters are fixed. This approach is limited to the fresh core and to three temperatures: 300K, 600K and 900 K, since ^{235}U and ^{238}U MCNP libraries are available at only these three temperatures. The

changes of the Doppler coefficient with burnup are beyond the scope of this preliminary stage of study, and will not be calculated. The results for three coolant densities (note that the Doppler coefficient is also dependent on coolant density) are presented in Figure 4-26. Three reactivity points obtained by MCNP can then be fitted by a curve k_D/\sqrt{T} , since the Doppler coefficient in thermal reactors is typically proportional to the inverse of the square root of temperature. The fits, together with the fitting coefficients, k_D , are also shown in Figure 4-26.

The Doppler coefficient

$$\frac{\Delta k}{k \Delta T} = - \frac{k_D}{\sqrt{T}} \quad , \quad (4-30)$$

as obtained from the fit, is compared for various coolant densities with a typical BWR Doppler coefficient in Figure 4-27. In case of voiding, the Doppler coefficient goes up as in all LWRs, which is a good safety feature. The dependence of the coefficient k_D on coolant density can be expressed by the second-degree polynomial

$$k_D = M_0 + M_1\rho_c + M_2\rho_c^2 \quad (4-31)$$

where the coefficients of the polynomial were obtained from the best fit to the three points given in Figure 4-28.

As in all thermal reactors, the Doppler coefficient of the proposed concept is negative. At nominal conditions, its magnitude is larger than for a typical BWR. The Doppler effect is more strongly dependent on coolant voiding than for a BWR due to a higher coolant-to-fuel volume ratio. In accidents which would lead to fuel temperature increase, and consequently, to a decrease in coolant density, the negative magnitude of the Doppler effect can be more than doubled. Taking into account that the fuel operates at about 1100 °C, but can safely withstand temperatures up to 1600 °C, the large temperature margin on the fuel, combined with the large Doppler coefficient (which is even substantially increased upon coolant voiding) leads to reactor inherent shut down in large-temperature-increase scenarios without ATWS, by Doppler only (even if the negative reactivity change due to coolant voiding is not considered).

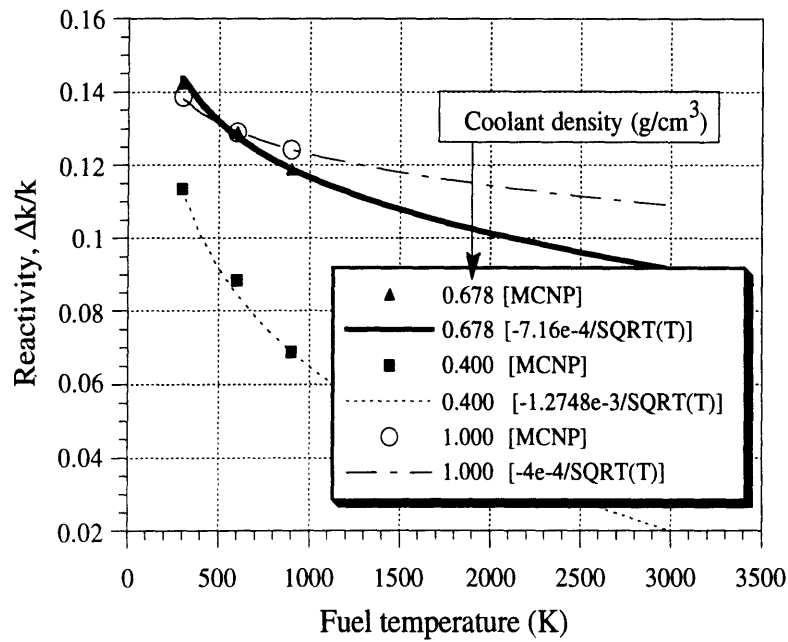


Figure 4-26 Reactivity as a function of fuel temperature for the PTLWR design

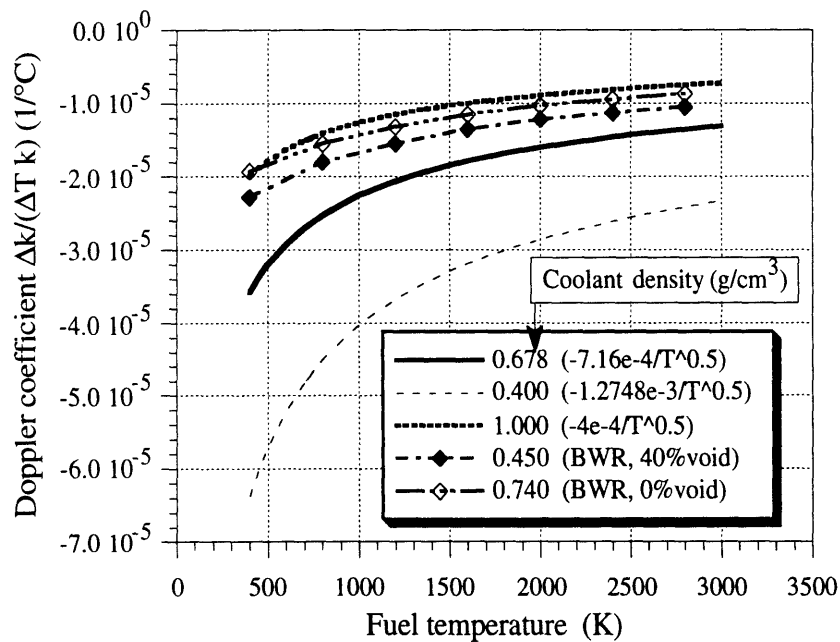


Figure 4-27 Doppler coefficient for the PTLWR as a function of fuel temperature and coolant density

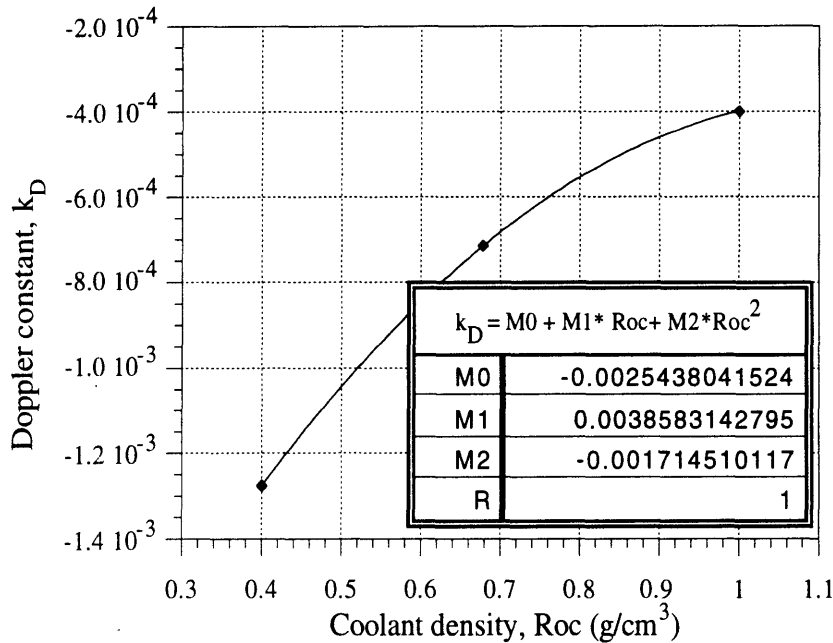


Figure 4-28 Doppler coefficient constant, k_D , as a function of coolant density

4.4.4.8 Negative Void Coefficient

The void coefficient denotes the reactivity derivative with respect to the steam volume fraction of the reactor coolant at constant power level. Most currently operating reactors have negative void coefficients. CANDU reactors have demonstrated successful operation with positive coolant void coefficient. However, a positive void coefficient is in conflict with the passive safety approach adopted for this design concept because it requires the reliable functioning of shutdown systems in loss of coolant accidents which increase voiding. Moreover, a positive void reactivity coefficient was one of the main causes of the reactivity accident at Chernobyl. Hence, it is an important goal to design the PTLWR to have a negative void coefficient under all conditions.

Figure 4-29 shows the multiplication factor for the reference PTLWR design as a function of coolant density. Both curves were obtained using full-core MCNP model #3. The curve denoted “Fresh core ($e=2.5\%$)” was

calculated for a uniform enrichment of 2.5% and 30 control rods (out of a total of 60) fully in. The curve designated “Equil.core(e=7%)” was calculated for an equilibrium core at a burnup of 40,000 MWd/tonne (initial enrichment 7%). As illustrated, the void coefficient is negative for both the fresh core and the equilibrium core. The equilibrium core exhibits a more negative void coefficient. This is a consequence of ^{239}Pu , which hardens the neutron spectrum, and hence increases resonance absorption in ^{238}U and ^{239}Pu . It is interesting to note that even though the H_2O moderator-to-fuel volume ratio is much higher in the dry calandria design than in a typical PWR (4.16 compared to 1.67 in a PWR) the system still exhibits a negative coolant void coefficient. Taking into account the moderating effect of graphite in the reflector, the total effective moderator to fuel ratio is even

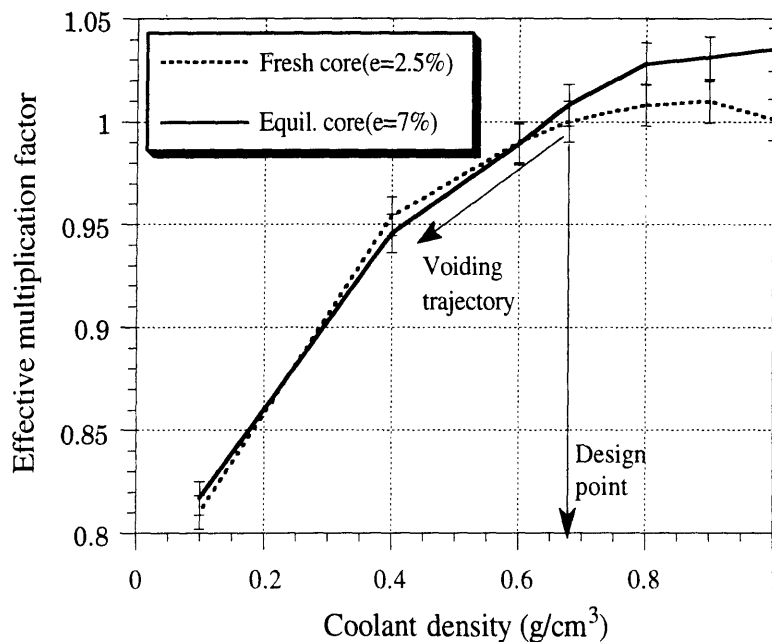


Figure 4-29 Effect of coolant voiding on reactivity

higher. The heterogeneity of the H_2O moderator plays an important role in this aspect, since the neutrons collide with the H_2O moderator less frequently than they would have done in a typical PWR geometry, where the moderator is evenly distributed around the fuel rods. In LOCA scenarios, this void coefficient inherently shuts down the fission reaction as in other typical LWRs. However, in the reflooding phase of a typical LWR, great care

has to be taken that the emergency coolant is borated, while in the proposed pressure tube reactor, non-borated flooding water in the calandria space behaves like a neutron trap, and renders the reactor subcritical.

4.4.4.9 Less Efficient Neutron Economy

The proposed PTLWR concept has a less efficient economy than a typical LWR. This is the consequence of higher parasitic losses compared to LWR cores. Thick pressure tubes to accommodate high operating pressure, higher leakage, and the low mass of fuel compared to the total mass of the core are the main factors contributing to relatively high parasitic losses. This drawback is, however, compensated by on-line refueling and the high burnup achievable with particle fuel. A neutron balance for the fresh core of the PTLWR reference design, calculated using full-core MCNP model #2, is shown in Figure 4-30. Figure 4-31 compares neutron parasitic losses and absorptions in ^{238}U with PWR and CANDU units. The data plotted in Figure 4-31 were obtained from one-channel MCNP model #1 for an infinite

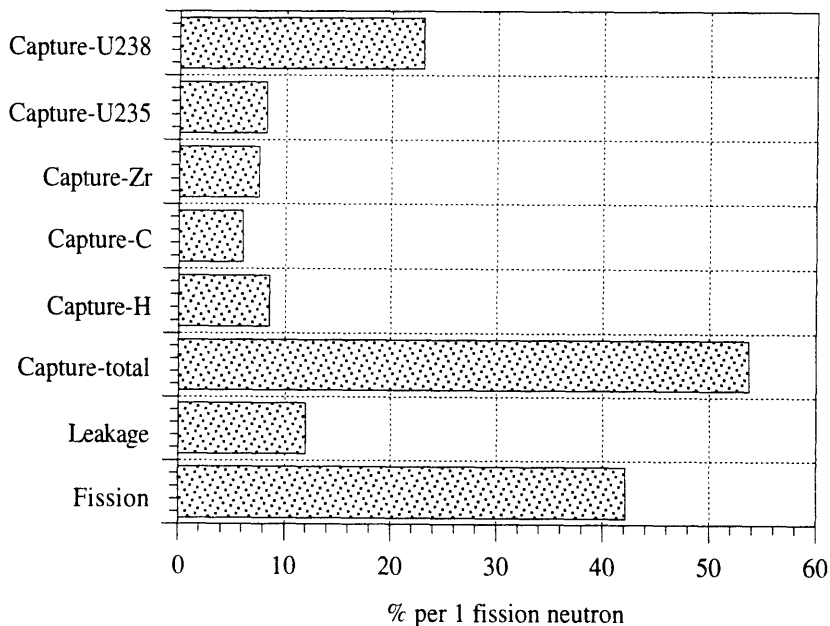
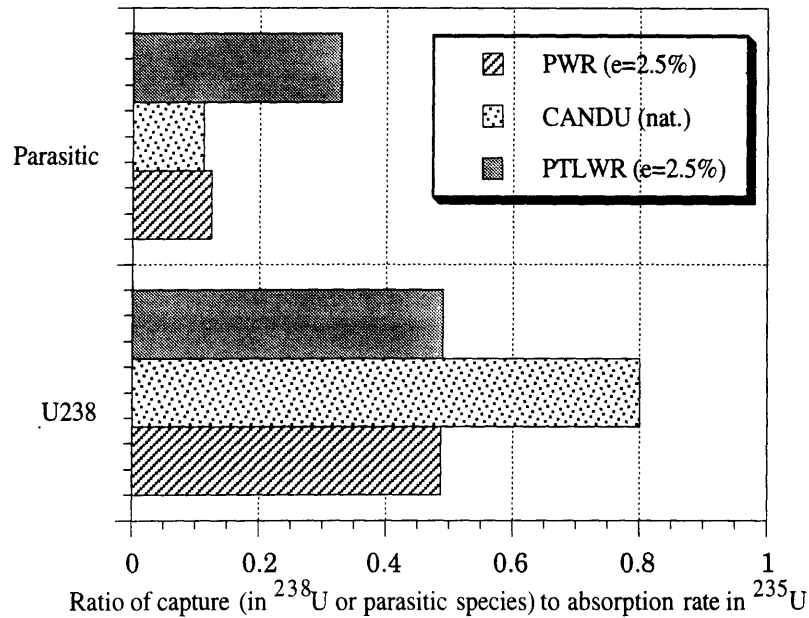


Figure 4-30 Neutron balance in the reference PTLWR design



Note: All values for infinite lattice

Figure 4-31 Comparison of neutron absorption in ²³⁸U and parasitic losses lattice, and from PWR-pin and CANDU-channel MCNP benchmark models (see Appendix A.1), also in the configuration of an infinite lattice. Significantly higher parasitic losses for the PTLWR design are evident even without including the leakage. Note, however, that the parasitic losses can be significantly improved by increasing fuel loading in the core. This will be shown in Chapter 5 using an alternative two-ring fuel arrangement.

4.4.4.10 Slightly Positive Reflector Temperature Coefficient

Several reflector materials have been considered – H₂O, D₂O, beryllium and graphite. Light water has a relatively high absorption cross section which would result in a significant reactivity reduction in a high-leakage PTLWR core and therefore it must be discarded. The remaining three materials are basically equivalent with respect to reactivity, as shown in Table 4-8. The effective multiplication coefficients in Table 4-8 were calculated using full-core MCNP model #3 with fresh fuel of uniform 2.7% enrichment, with 28 fully inserted control rods. Reflector thickness was

kept the same, equal to 1m, for all reflector materials. A heavy water reflector would be easy to design and cool, however, it must be discarded due to potential supercriticality problems. These problems would arise if the wall separating the reflector and the voided calandria space fails and heavy water floods the calandria space. Flooding of the calandria space with heavy water would substantially increase the reactivity of the system and lead to superprompt critical excursions. Beryllium has poor irradiation properties. The lifetime of beryllium is significantly less than that of graphite, especially at higher irradiation temperatures (a review of irradiation effects on beryllium is given in [Hejzlar et. al., 1993c]. Moreover, neutron irradiation of the beryllium reflector during reactor operation results in the buildup of ^6Li and ^3He , which are characterized by their large thermal neutron absorption cross sections. As a result, nonnegligible reactivity loss would occur. Beryllium was therefore dismissed from further consideration.

Graphite has been selected as a reflector material. The disadvantage of a graphite reflector is its slightly positive temperature coefficient. Higher reflector temperature changes the scattering properties of the reflector and leads to an increase in temperature of the neutrons coming from the reflector. Higher neutron temperature produces a shift in the neutron thermal spectrum, and consequently affects the microscopic cross sections of graphite and nuclides in the fuel. The absorption cross sections of graphite, ^{238}U , and ^{235}U decrease with reflector temperature, while the absorption cross section of ^{239}Pu increases with temperature. The overall effect is an increase of reactivity. Figure 4-32 shows the effective multiplication factor for the fresh core and for the equilibrium core. The magnitude of the reflector temperature coefficient is, however, small (for the fresh core, an increase of reflector average temperature from the operating point of 800K to 1600K leads to an increase of reactivity by about 8mk only) and the temperature increase proceeds very slowly due to the long thermal time constant of the large graphite mass. Note that if all the reflector cooling is lost and the reactor continues to operate at its nominal power rating, the rate of reflector temperature increase is about 0.1°C/s , i.e., it would take about 2.2 hours to increase the reactivity by these 8mk. Such small and extremely slow reactivity changes with reflector

temperature should not pose any significant safety problems. The “fresh core” curve in Figure 4-32 was calculated for the fresh core without xenon and samarium, and without control rods. Xenon and samarium effective cross sections are decreased for higher reflector temperatures, because the thermal spectrum shifts further from their absorption peaks. This increases the reflector temperature coefficient, but the presence of control rods tends to compensate the positive xenon effect. The overall effect is a slight increase of reflector temperature coefficient, as can be seen by comparing the curves for the fresh core and for the equilibrium core, which was calculated for 20 control rods fully inserted.

Table 4-8 Effective multiplication coefficient for various reflectors.

Reflector material	Graphite	D ₂ O	Beryllium
Effective multiplication factor	1.002±0.004	1.004±0.005	1.005±0.002

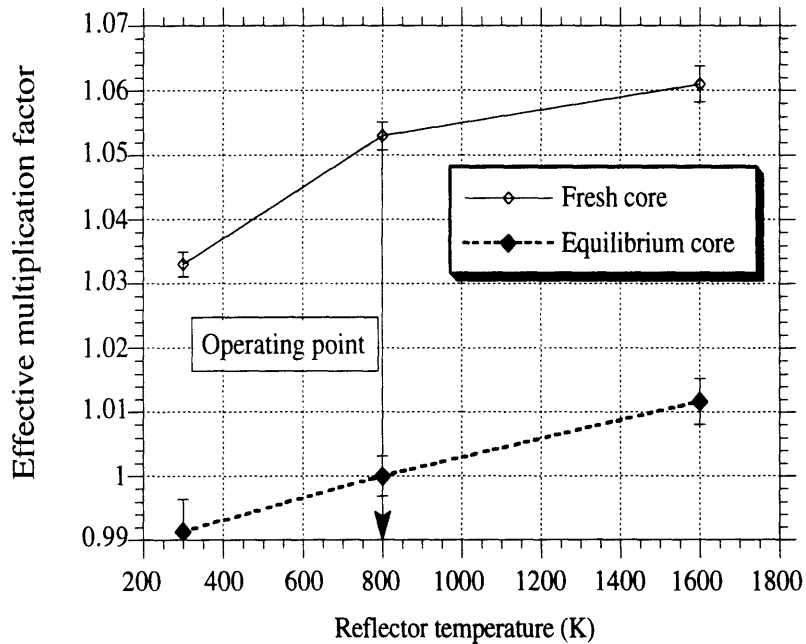


Figure 4-32 Effect of reflector temperature on the multiplication factor

4.4.4.11 Comparison with PWR and CANDU

Selected physics characteristics of the PTLWR reference design are compared to PWR and CANDU parameters in Table 4-9. The values given in Table 4-9 were obtained for fresh fuel and for an infinite lattice, except for the Doppler coefficients and power peaking for the PWR and CANDU lines, which were taken from [Diamond et. al.,1986] and [Pasanen, 1980], respectively.

4.4.4.12 Summary of PTLWR Physics Characteristics

The proposed dry calandria design exhibits large prompt neutron lifetime, comparable to heavy water moderated lattices. Similarly as for CANDU reactors, long prompt neutron lifetime, in combination with low excess reactivity due to on-line refueling, significantly reduces potential concerns with prompt excursions, and reduces the requirements on the performance of shutdown systems.

Significant void fraction in the calandria space surrounded by a reflector results in a flat thermal flux profile across the entire core with the total peaking less than 1.2. The power density profile, which is proportional to thermal flux and the atom density of fissile isotopes, is also exceedingly flat for the fresh core with uniform fuel enrichment. For the equilibrium core, the power density profile depends on the refueling scheme: it will be shown in Section 4.4.8 that low power peaking can be also achieved.

A unique characteristic of the dry calandria design is tight neutronic core coupling, primarily due to the large voided space in the calandria. It has been demonstrated that the neutron migration area is about 200 times larger than for a typical PWR. Consequently, the entire core is very well coupled, no local criticality is possible, and the reactor is inherently stable to xenon spatial oscillations, i.e. no additional means to prevent xenon spatial oscillations are necessary. An ancillary benefit of a large migration area is that the control rods can affect a substantial portion of the core. Hence, the control rods can be placed in the reflector, and the reactor can be

Table 4-9 Comparison of PTLWR physics characteristics^a with LWR and CANDU

	PWR	CANDU	PTLWR
Void coefficient	negative	positive	negative
Doppler coefficient ($10^5 \Delta k/k/^\circ\text{C}$)	-4.3 to -3.7	-1.8 ^b	-4.0 to -1.1
Average thermal flux (n/cm ² -s) (E≤0.6eV)	4.6x10 ¹³	1.1x10 ¹⁴	2.5x10 ¹⁴
Average fast flux (n/cm ² -s) (E>0.6eV)	2.3x10 ¹⁴	1.4x10 ¹⁴	4.5x10 ¹⁴
Fast/thermal flux ratio	4.9	1.32	1.8
Peak ^c fast flux (n/cm ² -s) (E>0.6eV)	5.9x10 ¹⁴	2.6x10 ¹⁴	5.8x10 ¹⁴
Heavy metal loading (kg/MWth)	29	59	8
Power peaking factor	2.6	1.8	1.2
Parasitic absorption ^d	0.0701	0.0571	0.179
²³⁵ U-capture ^d	0.109	0.077	0.090
²³⁵ U-fission ^d	0.504	0.432	0.456
²³⁸ U-capture ^d	0.272	0.407	0.268
²³⁸ U-fission ^d	0.027	0.02	0.0078
$(\Sigma_c^{28} \Phi)/(\Sigma_a^{25} \Phi)^{d,e}$	0.44	0.8	0.49
Prompt neutron lifetime, Λ (s)	2.0x10 ⁻⁵	8.55x10 ⁻⁴	8x10 ⁻⁴
Neutron migration length, M (cm)	7.7	19.5	110

^a Data for the fresh core

^b The fuel temperature coefficient for CANDU is -0.3×10^{-5} for an equilibrium core, and slightly positive at high burnups

^c Fast flux peaking factor for PWR and CANDU assumed equal to power peaking factor, 1.3 for the PTLWR

^d Calculated by MCNP for infinite lattices, normalized per one fission neutron

^e Subscript *a* stands for total absorption (including absorption leading to fission)

controlled from the reflector without the usual local flux depressions induced by control rods inside the core.

The large moderator-to-fuel-volume ratio in a heterogeneous arrangement of the fuel and light water moderator results in a well-thermalized neutron spectrum, comparable to heavy water lattices. Such well-thermalized spectra lead to efficient fissioning of fissile isotopes and requires a comparatively smaller fissile inventory to make the system critical.

The key disadvantage of the proposed PTLWR of the reference design is the high absolute level of the core-average fast and thermal flux, a consequence of the small heavy metal loading achievable with particle fuel. This results in a high fast fluence on the pressure tubes and a large xenon poisoning ratio after reactor shutdown. Since the lifetime of pressure tubes is limited by fast fluence, it is important to decrease the core-average fast flux. Alternative fuel arrangements, which could accomplish this task are proposed in Chapter 5. Note, however that the PTLWR peak values of both the fast and thermal flux are much closer to PWR and CANDU peak fluxes (peak fast flux is about the same as the PWR peak fast flux and about twice as large as that of CANDU) due to the low PTLWR peaking factors. Another drawback of the reference dry calandria design is relatively high neutron parasitic losses. The negative effect of parasitic losses on fuel cycle economy can be compensated by on-line refueling and high burnups. Neutron economy can be also improved by the use of the alternative fuels suggested in Chapter 5, since it is closely related to heavy metal loading.

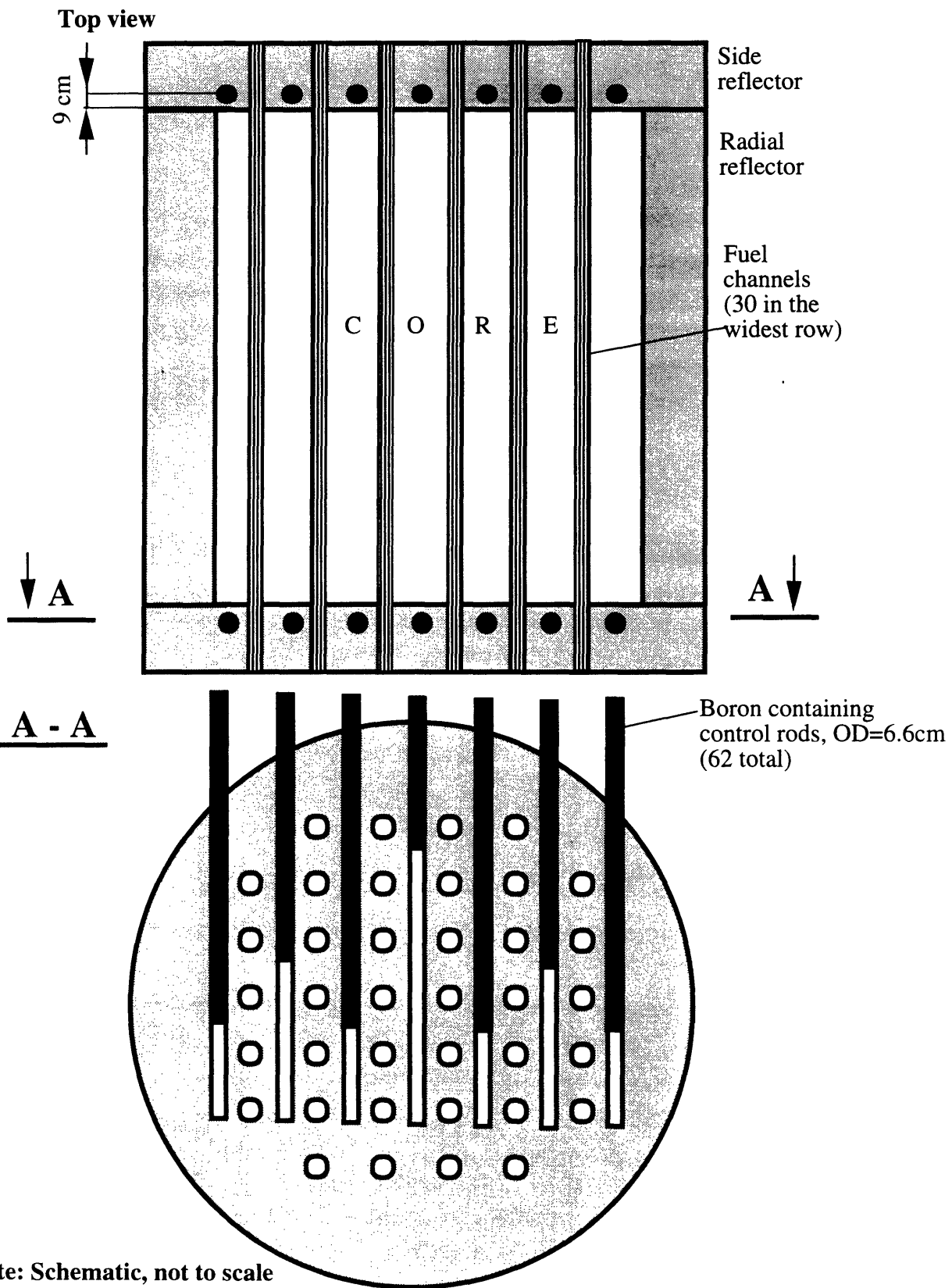
Both the Doppler coefficient and the coolant void coefficient of the reference PTLWR are negative. As in other LWRs, these mechanisms provide inherent feedbacks for reactor shutdown in accidents leading to large temperature increases. The reflector temperature coefficient is slightly positive, but its magnitude is small and the rate of insertion of positive reactivity from this phenomenon is small as well, due to the extremely large thermal time constant of the graphite reflector.

4.4.5 Reactor Control Considerations

Similarly as in CANDU reactors, the primary method used to control the reactivity is through on-line refueling. Besides the on-line refueling, other means of changing the reactivity state of the core are employed. As mentioned in the previous section, reactivity control absorbers placed in the reflector can affect the entire core, hence most of the control devices are located in the end reflector, as shown in Figure 4-33. The advantage of placing control rods outside the core is that localized flux perturbations from control rods inside the core are eliminated. Control rods move in vertical channels located in the axial reflector in the space between fueled pressure tubes. Sixty two control rods grouped into several groups, all in the end reflectors; are proposed:

- a fine control group for fine control (corresponding to CANDU liquid zone controllers),
- a power cutback group for power cutbacks (corresponding to CANDU mechanical control absorbers),
- a power insertion group for reactivity reserve if refueling machines are not available, and for transient Xe increase (corresponding to the CANDU adjuster rod absorber system), and
- a power compensation group for the hot-cold reactivity difference and Xe and Sm equilibrium (corresponding to CANDU moderator poison).

These control rod groups and their CANDU-equivalent control means are summarized in Figure 4-34. The worth apportionment for control rods in the reflector is given in Figure 4-35. The fine control group provides the continuous fine reactivity control, and hence determines reactor power level. It compensates for discontinuities in on-line refueling (on-line refueling is done in small increments by refueling several bundles at a time) and for small perturbations in temperatures and other parameters. It is not used, however, for spatial control of power distribution to prevent xenon-induced power oscillations. This differs from CANDU liquid zone controllers which are used also for this purpose.



Note: Schematic, not to scale

Figure 4-33 Schematic arrangement of control rods in the side reflectors of the PTLWR design

Control and Safety Systems

Name	Function	Location	During normal operation	CANDU equivalent (location)	Purpose	Total worth (mk)	
						Dry	CANDU
FC group	Control	Side reflector	In	Liquid zone controllers (calandria)	Provides for fine control (in CANDU also spatial Xe control)	10	7
	Control	Side reflector	Out	Mechanical control absorbers (calandria)	Extends range of control in negative direction Provides for power cutbacks	10	10
	Control	Side reflector	In	Adjuster rod absorber system (calandria)	Adjusts reactivity in positive direction -fueling machines not available -transient Xe increase (located such that power is flattened)	15*	15
C group	Control	Side reflector	Out	Moderator poison (calandria)	Compensates for hot-cold reactivity difference and for Xe and Sm absorption	45	-
	Safety	Calandria	Out	Shutoff units (calandria)	Rapid shutdown	100	80
Flood system	Safety	Calandria	Out	Poison injection nozzles (calandria)	Redundant and diverse shutdown	1300	>300

1mk is a $\Delta k/k$ value of 0.001

Key: FC - Fine Control
 PC - Power Cutback
 PI - Power Insertion
 C - Compensation

*Liquid zone controllers are also possible for the PTLWR design. Low-pressure tubes filled with light water can provide a reactivity increase of about 35 mk for the equilibrium core and help to override xenon. They work in the opposite direction than in CANDU, i.e., adding light water increases reactivity while in CANDU adding light water decreases reactivity.

Figure 4-34 Proposed PTLWR control and safety systems and comparison with CANDU

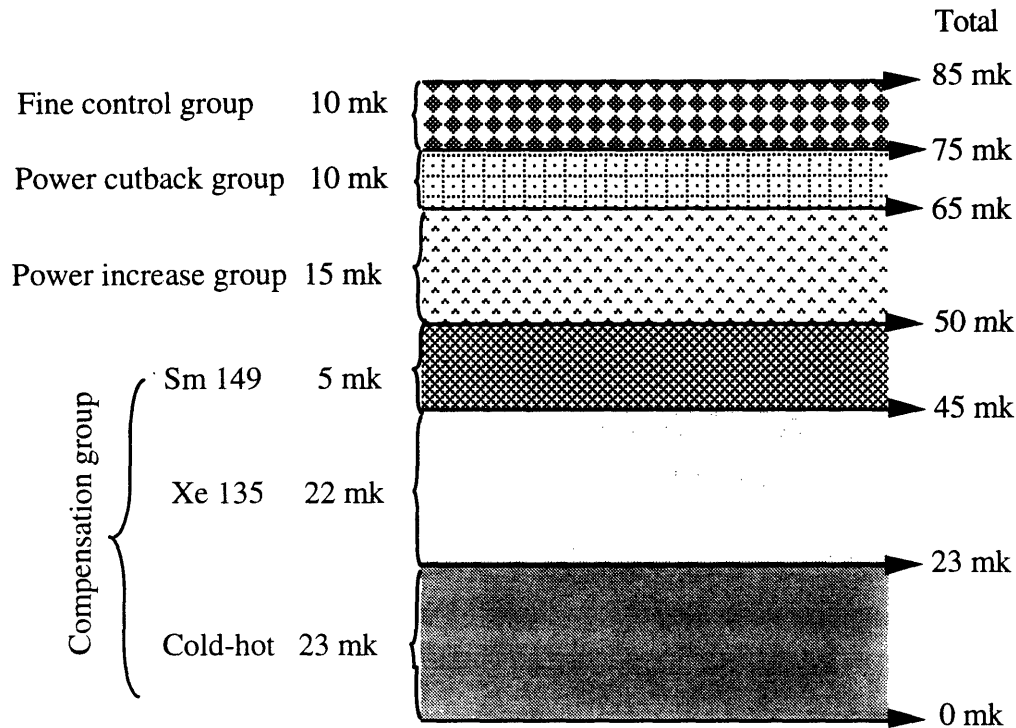


Figure 4-35 Reactivity worth apportionment of control rods located in the reflector

The power cutback group provides negative reactivity insertion if the rapid reduction of reactor power is demanded, e.g., in case of primary pump coastdown. Power cutback control rods are fully withdrawn from the reflector during normal operation and are driven by gravity into the reflector upon activating signal.

The power insertion group extends the range of the reactor control system. Power insertion control rods are fully inserted in the reflector during normal operation and are withdrawn if reactivity insertion beyond the capability of the fine control group is needed. The group is typically needed if refueling machines are not available for some time period or to compensate for xenon poisoning following a reduction of reactor power. As discussed in Section 4.4.4.6, similar to CANDU practice, which employ adjuster rods to compensate for the buildup of ^{135}Xe in the first 30 minutes following reactor shutdown [Pasanen, 1980], only partial compensation for

Xe override is provided. If better capability for xenon override is required, liquid zone controllers with spectral shift (discussed next) or cooled booster rods with enriched fuel could be used.

The compensation group compensates for reactivity difference between the cold, zero-power and hot, full-power reactor and for xenon and samarium absorption at their equilibrium levels. Control rods of this group are fully withdrawn during normal operation, and are fully inserted if the reactor is cold at zero power with very low xenon levels.

In addition to the control system, a scram system corresponding to CANDU shutoff units is available. Scram rods are the only rods which are driven into the core (into the channels located in the voided space between pressure tubes). Since these are out of the core during normal operation, they do not cause any flux depression. Redundant and diverse shut down can also be achieved by flooding the calandria. This would be comparable to moderator dumping in CANDU systems, except for the difference that the dumping of the CANDU moderator results also in the undesirable loss of heat sink, while in the dry calandria design flooding provides both the heat sink and shutdown.

Spectral shift control using liquid zone controllers

The PTLWR can also employ liquid zone controllers. These controllers would comprise vertically oriented Zircaloy thin-wall low-pressure tubes running interstitially in the voided calandria space between the fuel channels. These tubes would be empty for the fresh core and would be gradually filled with the light water moderator as the fuel burnup increases. Figure 4-29 suggests that the additional light water (about 30 tubes of diameter 8cm would be sufficient) in the equilibrium core to provide a reactivity increase of about 35mk while keeping the void reactivity coefficient negative. Note that these liquid controllers work in the opposite direction to CANDU liquid zone controllers. Increasing the amount of light water in the tubes leads to a reactivity increase, while in CANDUs more light water in the system leads to a reactivity decrease. The advantage of the liquid controllers is the improved neutron economy and the possibility to continually adjust the operating point close to the optimum point on the

moderator-to-fuel ratio reactivity curve. Also almost zero coolant void coefficient could be continually maintained by adjusting light water volume in the tubes. The liquid zone controllers could also be utilized to increase the capability of xenon override without sacrificing neutron economy. The disadvantage is the more complex design of the core and need for additional systems associated with maintaining the moderator and its cooling.

Liquid controllers in the voided calandria space are also an attractive option for the high-loading two-ring fuel element design proposed in Chapter 5. This design employs two rings of clad fuel pins, and is highly undermoderated. Lack of moderation in the core maintains an appreciable neutron population segment in the epithermal resonance region at the expense of some of the thermal neutron component. Increased neutron population in the resonance region increases significantly the capture rate in ^{238}U , and consequently the conversion ratio and plutonium breeding. Later in the cycle, light water can be gradually introduced into the liquid zone controllers, thus shifting the neutron spectrum back to highly-thermal. This spectrum shift will compensate for the reactivity loss due to fission product buildup, and moreover, it will efficiently burn plutonium so that at discharge, the ^{239}Pu content is low. Ideally, one would like to maintain on-line refueling to maximize the conversion ratio. Such a reactor would need two regions – a hard spectrum region for Pu breeding and a soft-spectrum region for Pu burning. This may be a problem because the large neutron migration area would make it difficult to create separate regions, but it might be possible with batch refueling. The potential of such a reactor could be explored and quantified in future work.

4.4.6 Secondary Criticality Study During Reflood and Inadvertent Flooding

4.4.6.1 Introduction

Flooding of the calandria with light water introduces large reactivity changes into the system. Once the calandria is flooded, a large amount of light water, which has a relatively high neutron absorption cross section, renders the reactor deeply subcritical even if the flooding water is in bulk

boiling. The concern is the reactivity behavior during the flooding process. When the flooding water enters the calandria, only a portion of the calandria is submerged, yielding therefore lower water density per unit of total calandria space, and hence the hypothetical possibility of increasing the reactivity. Moreover, one can imagine a situation such that the steam or steam/water mixture (entrained from violently boiling flooding water in the lower portion of the calandria) fills the upper calandria space and causes an increase in reactivity. All these possibilities need to be examined to ensure that no large reactivity insertions are introduced during the calandria flooding process.

There are two major scenarios of calandria flooding. The first scenario includes intentional calandria flooding after loss of coolant (designated further as reflooding). The second scenario arises if the calandria is flooded inadvertently during normal operation (designated further as inadvertent flooding). Both scenarios behave differently because of the different amount of light water coolant inside the fuel channels. Another scenario, which is not associated with calandria flooding but has similar reactivity aspects, is the rupture of both pressure tubes and calandria tubes resulting in spraying into the calandria space of light water coolant. Important factors during these processes are the density of the steam/water mixture outside the fuel channel and the presence of control rods. Section 4.4.6.2 will examine general aspects of in-channel and out-of-channel water worth for the reference PTLWR design. It will be shown that the heterogeneous arrangement of light water outside the fuel channel does not affect reactivity, while the homogeneous arrangement in the form of a steam/water mixture leads to a reactivity decrease. Section 4.4.6.3 will assess the limits on the steam/water mixture density based on thermohydraulics laws. A steam/water mixture reduces the neutron mean free path in the calandria space, and hence makes the inserted control rods less effective. All these factors need to be taken into consideration when calculating reactivity during the reflooding process. The results, obtained from full-core MCNP model #3, for various scenarios, will be presented in Sections 4.4.6.4 through 4.4.6.7.

4.4.6.2 In-Channel and Out-of-Channel Water Worth

This section will evaluate water worth inside the fuel channel and outside the fuel channel. Light water outside the fuel channel will be considered in the heterogeneous arrangement of H₂O and voided space, and in the form of steam/water mixtures homogeneously distributed over the entire voided space.

The heterogeneous arrangement of light water and void outside the fuel channel is formed by placing an annular H₂O ring around the calandria tube, the rest of the out-of-channel space being filled by void. Water worth is evaluated using MCNP model #1, with a 1m-thick graphite end reflector, by applying the following procedure:

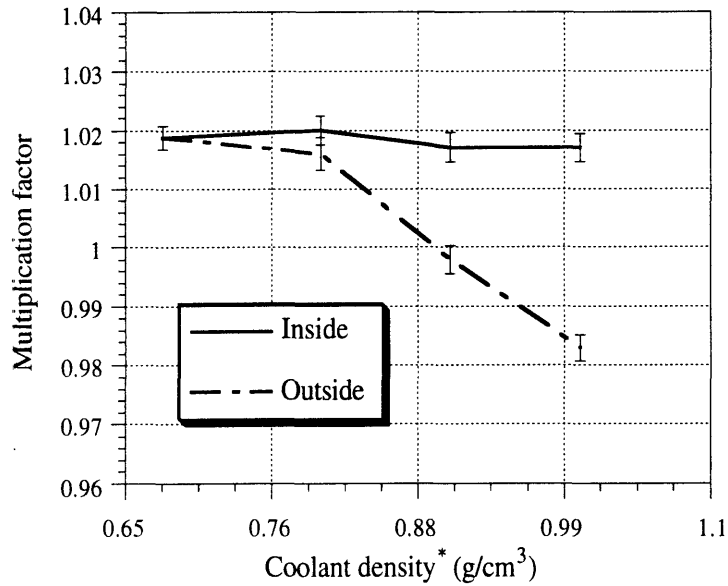
1. Reactivity was calculated for water inside the fuel channel at nominal conditions using an annulus thickness of 3 mm.
2. Reactivity was calculated for water inside the fuel channel at nominal conditions using an annulus thickness of 2 mm.
3. The difference in mass of cold moderator water between the 3mm-thick and 2mm-thick annuli was computed.
4. The mass difference from 3) was subtracted from the light water mass inside the fuel channel and the effective coolant density was computed.
5. Reactivity was calculated for coolant with effective coolant density from 4) using an annulus thickness of 3mm and compared to reactivity from 2). The comparison is shown in the Table 4-10.

Table 4-10 shows that the difference in reactivity is very small and is within the error margin. Thus, moving the light water from inside the fuel channel to outside does not make a difference in reactivity as long as the water is heterogeneously distributed in a voided space.

Table 4-10 Reactivity comparison for the same amount of water inside and outside the fuel channel

	Moderator density (g/cm ³)	Coolant density (g/cm ³)	Annulus thickness (mm)	Multiplication factor (-)	Moderator mass (g)	Coolant mass (g)
H ₂ O in-channel	0.972	0.6787	2	1.053±0.003	2985	5487
H ₂ O out-of-channel	0.972	0.4903	3	1.054±0.002	4506	3958

A different situation arises if the water outside the fuel channel is distributed homogeneously in the form of a steam/water mixture, as shown in Figure 4-36. The curve designated "Inside" was calculated by increasing the coolant density inside the fuel channel from reference coolant density to maximum coolant density (1.0g/cm³) while having no water outside the fuel channel. The curve "Outside" was computed for fixed coolant density inside the fuel channel, equal to the reference coolant density. The steam/water mixture density outside the fuel channel was increased in such a manner that the amount of the water outside the fuel channel is exactly equal to the amount of water due to the density change of the coolant obtained from the first curve (i.e., the difference between coolant density and the reference coolant density). The opposite trend of these curves shows that water outside the fuel channel in the form of a homogeneous mixture has larger worth and results in a reactivity reduction. This is due to the increased absorption rate in a slightly higher flux region. Also, the neutron mean free path outside the fuel channel is substantially decreased, which in turn leads to a decrease in the thermal flux profile at the core periphery. This is an interesting finding since one would expect that due to the negative void coefficient, adding water in the form of a homogeneous steam water mixture would increase the reactivity. Figure 4-36 shows, however, otherwise.



* For the "Outside" curve, the total water mass in a cell is such that it equals the mass of water which would correspond to this coolant density if all the water was inside the channel only

Figure 4-36 Water worth inside and outside fuel channel for a fixed total mass of H₂O

Finally, it is to be noted that this trend, which was shown to be valid for the reference design with fresh fuel cannot be generalized for other fuel matrix designs. The outcome depends on the location of the operating point on the moderator-to-fuel ratio curve. If the operating point is located further from the top of the curve where the slope of the curve is steeper, the reactivity change by adding a steam/water mixture outside the fuel channel is positive. The reactivity change will be, however, less than for the same coolant density increase inside the fuel channel. Therefore this effect will be always less than that of cold water ingress, which must be dealt with in LWRs. Also, for the equilibrium core the situation will change, since the operating point shifts with increased plutonium content further from the peak into the undermoderated region. Of more importance is the presence of control rods in the reflector, which has not been taken into account in the above calculations. Control rods will be included in subsequent sections simulating the entire core. First, the maximum steam/water density physically possible in the dry calandria will be evaluated.

4.4.6.3 Maximum density of steam/water mixture in the calandria space

An important question to be answered is “what is the maximum possible density of a steam/water mixture in the upper calandria space (still unflooded) during the flooding process?”. The most probable scenario is that the upper calandria space is filled with saturated steam with the density corresponding to the partial pressure of the vapor. The largest steam density in the saturated state will be achieved if no gas is assumed to be present in the calandria, i.e., the upper space contains only steam. Assuming atmospheric pressure in the calandria (note that calandria flooding is initiated several seconds after LOCA, before a significant pressure rise in the containment is experienced) this density is 0.0006 g/cm³.

Higher density in the upper calandria space can be reached if the boiling process in the lower flooded portion is so vigorous that droplets of liquid are entrained high above the water level, and thereby increase the water content in the upper portion. The amount of liquid entrained into the unflooded calandria region can be estimated using the theory of entrainment from a free surface. The following estimate is quite conservative (yielding maximum water densities).

The assessment is based on the entrainment from a free surface study performed by Kataoka [Kataoka, et. al., 1981], which represents some of the best information available in this area. The notion of entrainment loses its validity when the superficial gas velocity is so great that there is no distinct water level. This occurs at the dimensionless entrainment number, $E_{fg}=5.0$, defined as

$$E_{fg} = \frac{\rho_f j_{fe}}{\rho_g j_g} \quad (4-32)$$

where subscript fe refers to the entrained liquid phase. This can be also viewed as the criterion for the transition from churn-turbulent to annular or annular dispersed flow. The choice of 5 for the entrainment number is a conservative estimate for two reasons. First, it represents the upper limit for a churn-turbulent pool (the most violent pool). Secondly, a bubbly flow

pool is more likely, since no gas is blown through the pool, only vapor bubbles from boiling contribute to the superficial gas velocity, j_g . Moreover, it will be shown in Chapter 8 that most of the vapor bubbles will condense in the considerably subcooled flood water before they can reach the surface. Another conservatism is introduced by taking the pool surface gas superficial velocity equal to 2m/s. This is the upper limit for pool entrainment data for which the correlation is valid. Using these data, the superficial velocity of entrained liquid can be evaluated

$$j_{fe} = \frac{E_{fg} \rho_g j_g}{\rho_f} = \frac{5 (0.598) 2}{1000} = 0.00598 \text{ m/s} \quad (4-33)$$

where water properties were taken for an atmospheric pressure of 0.1 MPa.

Eliminating total mass flow rate from the relations for superficial velocity of entrained liquid and superficial gas velocity defined as

$$j_{fe} = \frac{\dot{m} (1-x)}{A \rho_f}, \quad j_{fg} = \frac{\dot{m} x}{A \rho_g}, \text{ respectively,} \quad (4-34,35)$$

yields the equation

$$j_{fe} = j_g \frac{\rho_g}{\rho_f} \frac{(1-x)}{x} \quad (4-36)$$

which can be used to solve for the flow quality, $x=0.1667$. This quality is, however, only in close proximity to the pool surface. The quality will increase with the height above the pool free surface. Although flow quality as a function of the height can be obtained from Kataoka's correlation, it is not done here. Instead it will be conservatively assumed that the near-surface quality remains the same throughout the whole upper calandria space. Void fraction is then evaluated assuming the slip ratio is equal to 1.0 as

$$\alpha = \left[1 + \frac{\rho_g}{\rho_f} \frac{(1-x)}{x} \right]^{-1} = 0.997 \quad (4-37)$$

and finally the maximum attainable steam/water mixture density

$$\rho_{m,max} = (1 - \alpha) \rho_f + \alpha \rho_g = 0.0035 \text{ g/cm}^3 \quad (4-38)$$

Another hypothetical scenario for creating a steam/water mixture with densities higher than steam at saturation is by spraying into the upper calandria space. This sequence would be possible if both the pressure tube and calandria tube rupture and the escaping coolant sprays into the calandria. The highest achievable densities for water sprinklers purposefully designed for that purpose are [McCaughey and Bidinger, 1988]

$$\leq 0.1 \text{ vol\% H}_2\text{O}.$$

This translates to a mixture density of $0.001 \times 1 \text{ g/cm}^3 = 0.001 \text{ g/cm}^3$. Table 4-11 summarizes H₂O practical density limits in the unflooded portion of the calandria.

Table 4-11 Practical H₂O density limits in the upper calandria space

	Saturated steam	Entrainment limit	Spray limit
H ₂ O density (g/cm ³)	0.0006	0.0035	0.001

4.4.6.4 Reflooding Process

The reflooding process involves the loss of coolant from the fuel channels and subsequent flooding of the calandria. Two scenarios will be investigated. The first scenario is the most probable event, which assumes that the upper, unflooded calandria space is filled with steam at saturation density corresponding to the pressure partial pressure of vapor in the calandria. The second scenario is a hypothetical event which assumes that the water droplets, entrained into the upper calandria space, increase the H₂O density even beyond the thermalhydraulic limits given in the previous section.

Case with Saturated Steam in the Upper Calandria Space

This most probable scenario assumes that after the coolant is lost and the calandria flooding is initiated, the yet-unflooded space becomes rapidly filled with saturated steam. The lower, flooded portion of the calandria is

assumed to contain boiling water. Reactivity behavior for this process is shown in Figure 4-37. The results were obtained using MCNP model #3 for the fresh, hot core with uniform enrichment of 2.7% and 28 control rods fully inserted. Note that the reactivity held down by control rods is about 54mk – a conservatively high hold down during normal operation. After the coolant is lost, reactivity is significantly reduced due to the negative coolant void coefficient. As the number of flooded rows increases, reactivity is further decreased until the core is rendered deeply subcritical.

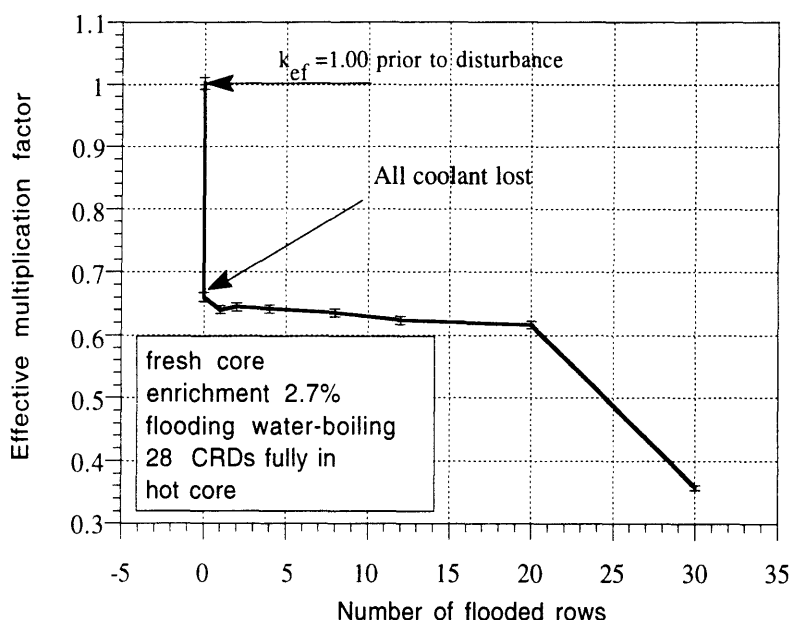


Figure 4-37 Reactivity behavior for calandria reflooding with saturated steam in the upper space

Case with Hypothetical Water Entrainment into Upper Calandria Space

The second scenario assumes that the steam/water density in the unflooded calandria space can be increased by droplet entrainment beyond the thermohydraulic limit (by 1400%). The results are shown in Figure 4-38. Two curves are shown – for the core with 28 control rods fully inserted and for the core with all control rods out. The portion of the curve with inserted control rods is expanded in Figure 4-39. After the coolant is lost significant reactivity reduction can be observed, i.e., the first point in Figure 4-39. The

second point in Figure 4-39 represents the state with flood water level just below the first row of fuel channels and CO₂ filling the upper calandria space. It shows an additional reactivity decrease, since boiling water at the calandria bottom behaves like a neutron trap, by absorbing most of the incoming neutrons. The third point exhibits an additional reactivity drop as the water level is increased to flood the first row of fuel channels. The fourth point describes the same configuration of the water level as for the third point, but the CO₂ gas in the upper calandria space is replaced by saturated steam. Introducing steam into the unflooded space increases reactivity because the system is strongly undermoderated, as there is no coolant inside the fuel channels. Increasing the steam/water mixture density further while keeping the water level just above the first row leads to a reactivity increase until the maximum point is reached at a density of about 0.05 g/cm³. For larger mixture density, neutron absorption in H₂O prevails and results in a reactivity drop. Figure 4-38 shows that for the case with control rods out, the maximum reactivity peak is lower than for the case with control rods in. This is because inserted control rods are shaded by the steam water mixture, resulting in less neutron absorption in control rods. The important thing to note is that even for the optimum mixture density, the fresh core remains below the prior critical state. For the equilibrium core, the system is more undermoderated and the reactivity peak for the optimum steam/water mixture density becomes higher. A check has been done using MCNP model #3 for the fuel with average burnup of 40,000 MWd/tonne and it was found that the peak just reached the prior critical value for hypothetical optimum density of 0.05g/cm³.

4.4.6.5 Inadvertent Flooding Process

In the inadvertent flooding process, the calandria is inadvertently flooded during normal operation. The major difference from the reflooding process is that all the fuel channels retain their light water coolant. In the most likely scenario, the unflooded calandria space will remain filled with steam at saturation density corresponding to calandria pressure. Similarly as for the reflooding process, the hypothetical event which assumes that the

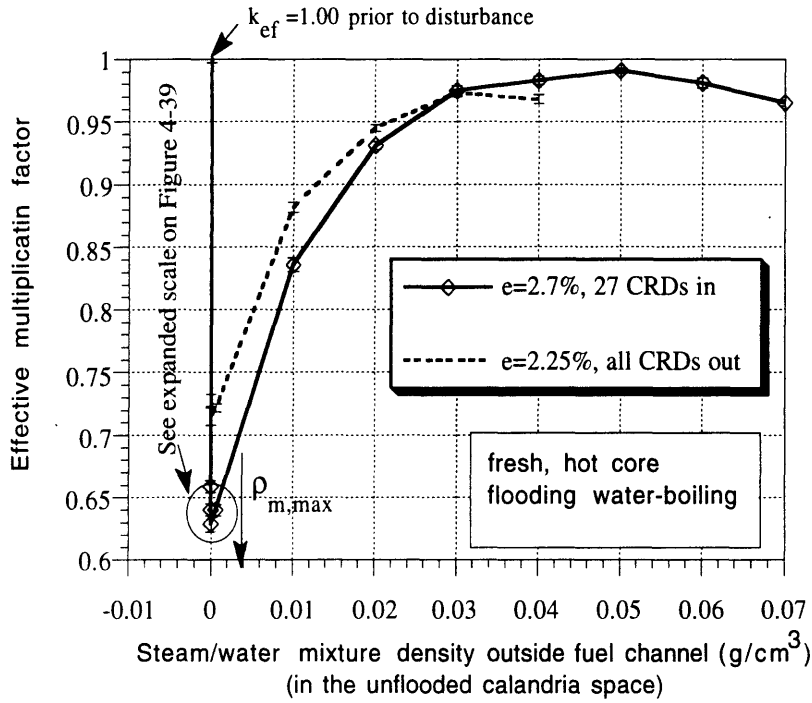


Figure 4-38 Reactivity behavior for calandria reflooding with hypothetical water entrainment into the upper space

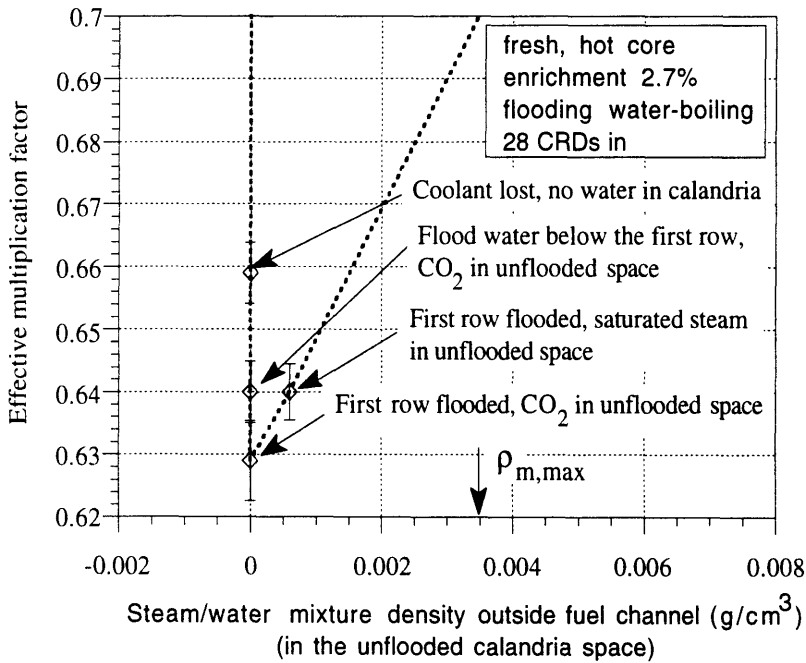


Figure 4-39 Reactivity behavior for calandria reflooding -expanded scale

water droplets, entrained into the upper calandria space, increase the H₂O density even beyond the thermalhydraulic limit will be also studied.

Case with Saturated Steam in the Unflooded Calandria Space

It is assumed that after flooding is initiated, the flooding water starts to boil and the unflooded calandria portion fills with saturated steam and remains at this condition during the entire flooding process. To maximize the positive effect from control rod shading, it is further assumed that the core is critical at cold conditions with all 60 control rods fully inserted, to compensate for the cold to hot reactivity difference, and that between zero xenon content and xenon equilibrium. The results are shown in Figure 4-40. It can be observed that the reactivity decreases monotonically, at a slower rate at first and much faster once more than one half of the core is flooded. One important design feature needs to be pointed out. It can be seen in Figure 4-8, which shows the arrangement of control rods in the end reflector, that the guiding channels for CRDs end just above the third row of fuel channels rather than at the bottom. This arrangement is on purpose to avoid positive reactivity insertion during the first stage of flooding. Once the flood water level rises above the control rod tips, control rod tips below this water level become ineffective. If these tips are located too low, they become submerged and hence ineffective before sufficient flood water has been introduced to compensate for this loss of control effectiveness. Ending the guide channels above the third row allows for substantial negative reactivity insertion from the flood water before the isolating effect on the control rod tips takes place, and hence the neutron absorption in light water becomes more important than the control rod isolation, preventing a reactivity increase. Note that once the whole calandria is flooded, control rods have virtually no effect on reactivity, since the neutron migration length decreases to about 7cm, and the number of neutrons reaching control rods is marginal. Care must be exercised when reestablishing a voided calandria space after flooding. An automatic block should be designed into the system, to prevent the operator from reestablishing a voided space without having all control rods in their fully inserted position.

This procedure would ensure that criticality is achieved by withdrawal of control rods after the voided space is re-established, rather than by depleting light water in the calandria.

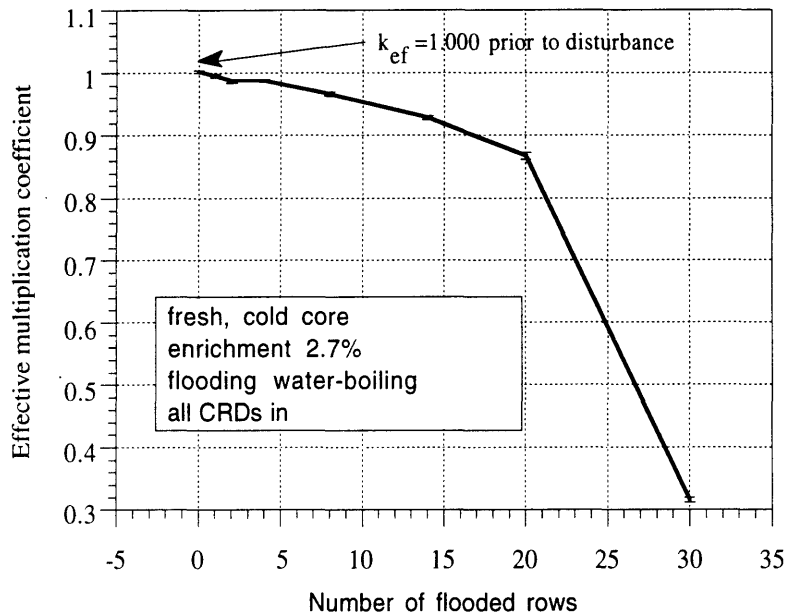


Figure 4-40 Reactivity behavior for calandria inadvertent flooding with saturated steam in unflooded region for cold core with all CRDs inserted

Case with Hypothetical Water Entrainment into the Unflooded Calandria Space

Similarly as for the reflooding process, this scenario assumes that the steam/water density in the unflooded calandria space can be increased by droplet entrainment beyond the thermohydraulic limit. Two cases will be studied. The first case will assume that the reactor is cold critical with all control rods fully inserted, the second case will study inadvertent flooding of the hot core at nominal conditions. The results for the cold core case are shown in Figure 4-41. The reactivity behavior trend for the first two points, marked by arrows is the same as for the reflooding, shown in Figure 4-39 except for the reactivity drop due to loss of coolant. For higher steam/water mixture densities the trend is quite different than that shown in Figures 4-38 and 4-39. In particular, no reverse to higher reactivity is observed. This

is because the cold core with high density of the coolant has the operating point close to the optimum on the moderator-to-fuel ratio curve, and any additional water leads to reactivity reduction.

The second case is presented in Figure 4-42. Points on the reactivity curve (from the left) can be described as follows (ρ_m denotes the density of steam/water mixture):

- $\rho_m=0 \text{ g/cm}^3$, $k_{ef}=1.00$ operating point.
- $\rho_m=0 \text{ g/cm}^3$, $k_{ef}=0.99$ one row of fuel channels is flooded with boiling water, the upper calandria space is filled with CO_2 . Reactivity drop is due to neutron absorption in water pool at the bottom of the calandria.
- $\rho_m=0.0006 \text{ g/cm}^3$, $k_{ef}=0.98$ one row of fuel channels is flooded with boiling water, the upper calandria space is filled with saturated vapor corresponding to atmospheric pressure. Additional reactivity drop is due to absorptions in H_2O vapor in the upper calandria.
- $\rho_m=0.01 \text{ g/cm}^3$, $k_{ef}=0.997$ one row of fuel channels is flooded with boiling water, the upper calandria space is filled with steam/water mixture of density 0.01g/cm^3 . Reactivity increase is caused by shading of the control rods (shading of control rods prevails over absorption in steam/water mixture).
- $\rho_m=0.02 \text{ g/cm}^3$, $k_{ef}=0.99$ one row of fuel channels is flooded with boiling water, the upper calandria space is filled with steam/water mixture of density 0.02g/cm^3 . Reactivity decrease is due to prevailing absorption in steam/water mixture over the shading effect of CRDs.

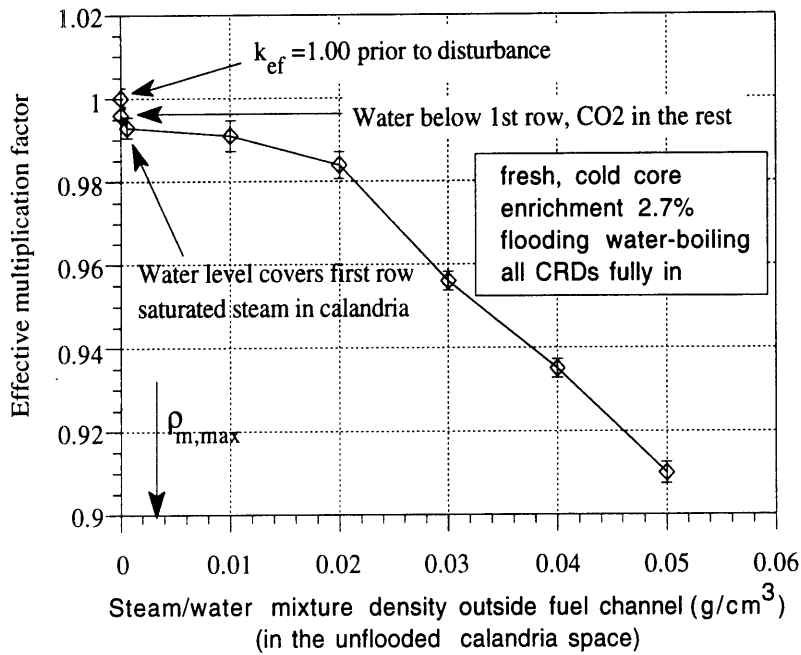


Figure 4-41 Reactivity behavior for calandria inadvertent flooding with hypothetical water entrainment for cold core with all CRDs inserted

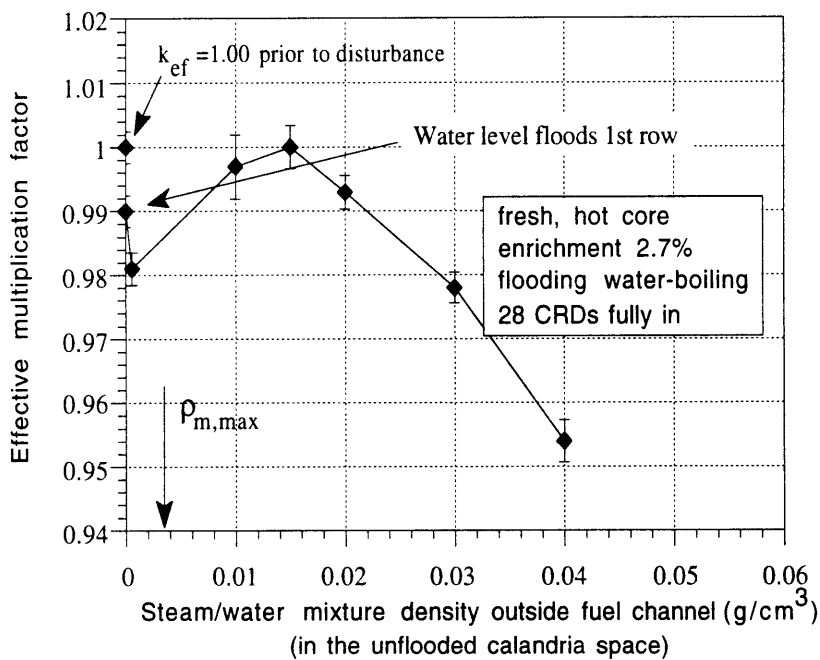


Figure 4-42 Reactivity behavior for calandria inadvertent flooding with hypothetical water entrainment for hot core

It can be observed from Figure 4-42 that secondary criticality could be achieved at the optimum mixture density of about 0.15 g/cm^3 . It is noted however, that this point is just critical, i.e., the same as prior to the disturbance with all coolant in the channels. Moreover, this is a hypothetical scenario, since the optimum density of 0.15 g/cm^3 cannot be practically reached, as it is higher by an order of magnitude than the maximum possible mixture density, $\rho_{m,\max}$, also shown in Figure 4-42.

4.4.6.6 Hypothetical Spraying of Calandria Space without Flooding

The last scenario to be studied involves rupture of both the pressure tube and calandria tube and spraying of the calandria space. It is assumed that the coolant leak from the rupture is slow enough not to initiate calandria flooding. It is further assumed that the water released from the crack will be homogeneously distributed over the entire calandria space. Figure 4-43 shows the reactivity behavior for such a scenario. For comparison, reactivity behavior in the cold water ingress (in the coolant) event is also plotted. Cold water ingress is an incident when the reactor coolant temperature drops (for example if heat removal to the secondary system is increased). This leads to increased coolant density accompanied by an increase in reactivity. Note that to be able to plot coolant density change on the same density axis, the coolant density change was smeared into the out-of-channel space. Reactivity behavior is similar to that shown in Figure 4-41, with a slight reactivity drop at first and a reactivity increase for higher mixture densities because of the prevailing effect of control rod shading. Because there is no neutron trap in the form of flooding water on the bottom of the calandria, as was the previous case, the reactivity is increased above the prior critical value. However, the increase is very modest (8mk) which can be compensated by the fine control group, and is less than for the cold water ingress event. More importantly, the steam/water mixture densities which would cause a reactivity increase above the prior critical value cannot be reached in practice due to the spray density thermohydraulic limit, $\rho_{m,\max}$.

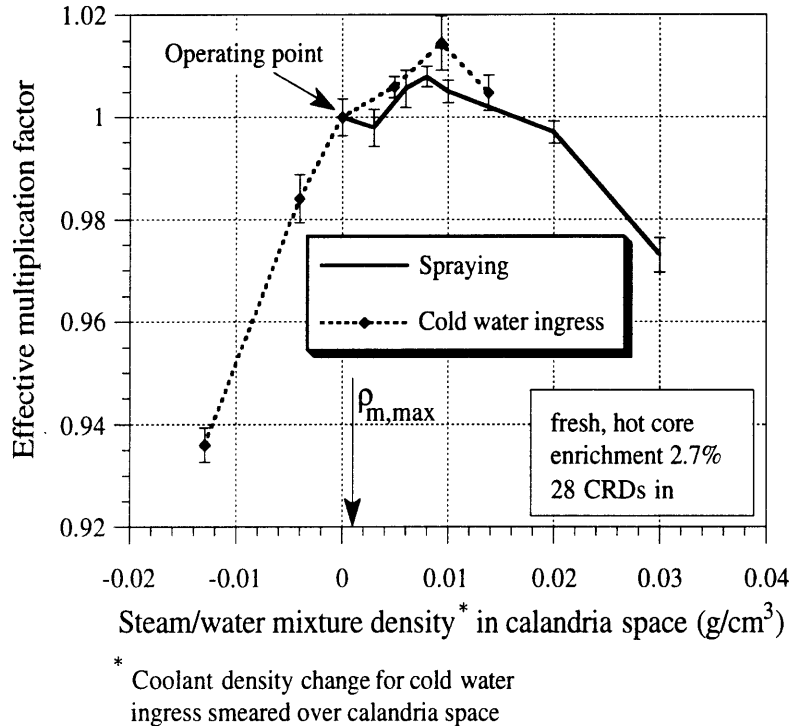


Figure 4-43 Calandria spraying from cracked pressure tube without flooding

4.4.6.7 Summary of Reactivity Behavior During Calandria Flooding

A study of the reactivity behavior of the reference PTLWR design in various calandria flooding scenarios has been performed. Reactivity is influenced, primarily, by the water level in the calandria, the density of the steam/water mixture in the unflooded calandria space and by the presence of control rods. The results reveal that

- for the most likely scenarios, with saturated vapor in the unflooded calandria space, the reactivity monotonically decreases with rising water level;
- for scenarios with entrainment of water droplets into the unflooded calandria space, reactivity first drops and later increases, but it does not exceed the prior critical value, even for the optimum mixture density;

- for scenarios of coolant spraying from a ruptured pressure and calandria tube without bottom flooding, reactivity can slightly exceed the prior critical value; but
- steam/water mixture densities yielding the maximum reactivity peak cannot be achieved either by spraying or by entrainment because they exceed thermohydraulic limits on spray density by an order of magnitude.

Overall, it can be stated that the reference PTLWR design does not exhibit reactivity excursions in scenarios involving the ingress of steam/water mixtures into the voided calandria space. This conclusion, however, cannot be generalized for other dry calandria designs with alternative fuel arrangements. In particular, the high-loading, two-ring design with a high conversion ratio will be less resistant to reactivity excursions in these scenarios.

4.4.7 Burnup Study

4.4.7.1 Introduction

This section will address change of fuel composition with burnup. There are three important characteristics which need to be evaluated. The first characteristic is the initial enrichment needed to achieve specified discharge burnup. The PTLWR reference design uses ^{235}U -enriched coated particle fuel. Coated particle fuel has good fission product retention capabilities and structural integrity even at high burnups. A very high burnup capability of more than 700,000 MWd/tonne has been demonstrated for MHTGR particle fuel [Alberstein et. al., 1993]. HTGR experience has been gained for more modest burnups of about 80,000 MWd/tonne. The goal set for the PTLWR is to achieve these burnups, i.e., in the vicinity of 80,000MWd/tonne. In addition, discharge burnup should be assessed as a function of initial enrichment, since both the initial enrichment and the discharge burnup affect fuel cycle cost. This dependence will be later used in the fuel cycle cost evaluation.

The second characteristic of interest is the fuel composition for the equilibrium core. The fresh core, for which most of the calculations have been performed so far, is representative only for a short period of time, after first fuel loading. Most of its lifetime, the PTLWR will operate with an equilibrium core. The changed fuel composition shifts the neutron energy spectrum, as compared to the fresh core, and will affect many reactor physics parameters.

Finally, the power density profile for the equilibrium core depends strongly on the on-line refueling scheme, since the fuel elements present in the core have spent different times in the core, and hence have different fuel composition. To evaluate the power density profile for any particular on-line refueling scheme, the local fuel composition needs to be known as a function of burnup.

To address these issues, the changes in concentration of fissile and fertile nuclides and fission products during neutron irradiation must be calculated. A wide variety of computer codes are available for calculating nuclide composition during irradiation. However, these neutronics-depletion codes rely almost exclusively on diffusion theory. It has been shown in Section 4.2 that diffusion theory breaks down for the PTLWR reactor concept, hence other means to estimate fuel depletion needs to be sought. The method selected for this purpose combines the MCNP code and the ORIGEN2 code [Croff, 1981,1983], and will be described next.

4.4.7.2 MCNP + ORIGEN2 Model

While the MCNP code does not include the capabilities to calculate burnup, MCNP full core calculations at various stages of burnup can be done as long as the concentration of major actinides and fission products at various burnups is available. To obtain fuel composition as a function of burnup, the ORIGEN2 code has been selected. MCNP is used to calculate the core multiplication factor, while ORIGEN2 provides input for MCNP regarding fuel composition as a function of burnup. The benchmark of this

procedure with PWR results from the LEOPARD code [Barry, 1963], enclosed in Appendix A.2, shows very good agreement.

The major problem in applying this approach to the PTLWR is that ORIGEN2 uses a one group effective cross section library for about 1700 nuclides, which is not available for the new PTLWR concept. Effective cross sections of all nuclides, in particular the actinides, depend strongly on neutron spectrum and nuclide concentration. Obtaining such a library is a complex process using other sophisticated codes, which is beyond the scope of this study. Instead, the following simplified approach was used:

- The ORIGEN2 code is run using a PWR one-group effective cross section library for the U-Pu fuel cycle.
- The concentration of major actinides and lumped fission products obtained from the ORIGEN2 run is used as input data for the MCNP run.
- Reaction rate ratios (with respect to ^{235}U absorptions) for major actinides obtained by MCNP are compared to those obtained by ORIGEN2. Then the one-group effective cross sections of these actinides in the ORIGEN2 library are modified to match the reaction rate ratios obtained by MCNP.
- The process is repeated, if needed, to obtain a match of reaction rate ratios. Once a good match has been obtained, concentrations of actinides and fission products calculated from ORIGEN2 for various burnups are used as input data for MCNP. MCNP is then run to get the reactivity as a function of burnup. A computer program was written to facilitate transfer of data between ORIGEN2 output and the MCNP-input-data generating code.

There are two factors in considering which ORIGEN2 cross section library to choose. The first is the energy spectrum, the second is the reaction rate ratios, in particular for the actinides

- captures in ^{238}U /absorptions in ^{235}U ,
- fissions in ^{238}U /absorptions in ^{235}U ,
- fissions in ^{239}Pu /absorptions in ^{235}U ,
- captures in ^{240}Pu /absorptions in ^{235}U , and

- fissions in ^{241}Pu /absorptions in ^{235}U .

The energy spectrum for the dry calandria concept is more similar to that in a CANDU reactor, while reaction rate ratios for the actinides are close to those of a PWR. Preserving reaction rate ratios is more important for two reasons:

- For high burnups, contributions from fissions of fissile actinides are considerable (about 30 %), hence the concentrations of these actinides with changing burnup should be computed as accurately as possible.
- Most codes, MCNP included, employ few-member lumped fission products. Their effective cross sections vary with the neutron spectrum of the reactor being analyzed. Hence, using fission products (from the “Livermore fuzzy average fission product library” used by MCNP) for the PTLWR involves a certain degree of approximation. This is not an appreciable shortcoming; not nearly comparable to the effect of the spectrum on actinide cross sections – which are adjusted.

Therefore, the PWR one-group effective cross section library was selected for use with ORIGEN2. Fission products are lumped together except for ^{135}Xe and ^{149}Sm , which are treated separately. Cross section data from the Livermore fuzzy average fission products library, ENDL-85, with MCNP designation 50120.35, was used for the treatment of lumped fission product in the MCNP code.

Note that the procedure described above is laborious, and yields only approximate solutions, sufficient for this scoping study, but not for detailed design calculations. Very recently, the MOCUP code [Babcock et. al., 1993] has been developed at Idaho National Engineering Laboratory (INEL), which couples the MCNP and ORIGEN2 codes. MOCUP provides an automatic bridge between MCNP and ORIGEN2 without modifying any of these codes. The code allows one to analyze a given complex-geometry system as a function of irradiation with the accuracy of a transport neutronic solution. The MOCUP code automatically creates correct one-group effective cross sections for ORIGEN2 using MCNP tallies. This MCNP-ORIGEN2 tandem could provide effective and more exact burnup

solutions for the PTLWR concept, however; the code was not available at the time of the PTLWR analyses.

4.4.7.3 Burnup Results

The burnup curves for PTLWR fuel with initial enrichments of 4%, 6% and 7% are shown in Figure 4-44. To save computer time, the MCNP code was run using the one-channel model #1 for all-reflecting boundaries to obtain the infinite multiplication factor, k_{∞} . Then the reactivity penalty due to axial and radial leakage was subtracted. This penalty can be easily found by comparing k_{eff} for the full-core MCNP model #3 and k_{∞} for the infinite lattice, both calculated for the fresh core, i.e.,

$$\Delta k_{\text{leak}} = k_{\infty} - k_{\text{eff}} = 1.135 - 1.047 = 0.088, \text{ or in terms of reactivity}$$

$$\Delta \rho_{\text{leak}} = 0.074.$$

This leakage penalty is assumed constant with burnup.

It can be observed that the multiplication factor varies almost linearly with burnup. This differs from CANDU where the ^{239}Pu buildup contributes significantly to a reactivity increase at the beginning of the cycle. The linear trend is similar to LWRs, since the initial enrichment is high and the PTLWR conversion ratio is close to that of LWRs. For the continual on-line refueling, which is equivalent to an infinite number of batches, the discharge burnup, B_d , is twice as large as the core equilibrium burnup, B_{eq} . The discharge burnup can be found directly from the curves in Figure 4-44 as two times the value of the equilibrium burnup (burnup when core reactivity = 0). The discharge burnup is summarized, together with uranium utilization as a function of initial enrichment, in Table 4-12, and compared to typical PWR and CANDU values. Uranium utilization in Table 4-12 was calculated from the definition

$$U = B_d \frac{X_F - X_W}{X_P - X_W}, \text{ MWd/tonne} \quad (4-39)$$

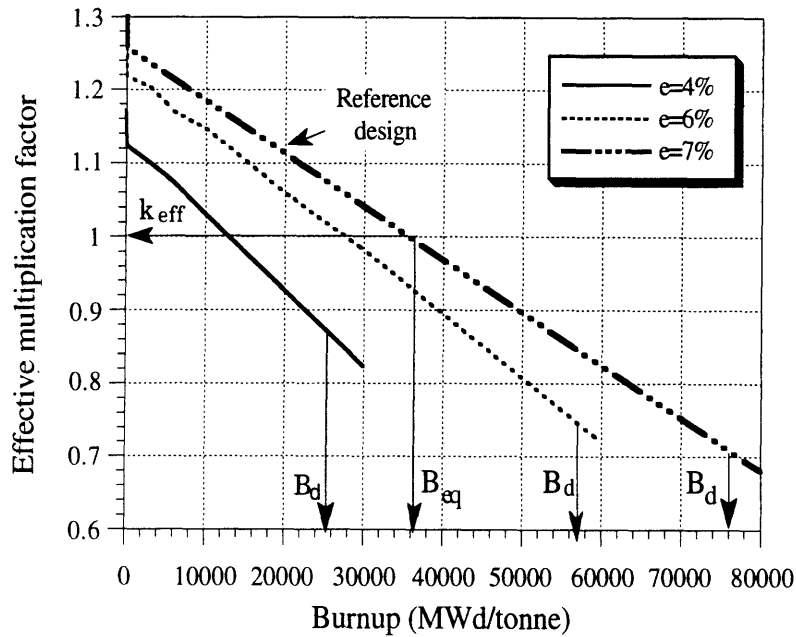


Figure 4-44 Effective multiplication factor as a function of burnup for various initial enrichments

Table 4-12 Discharge burnup and fuel utilization for various initial enrichments

Reactor/ Initial enrichment	Discharge burnup, B_d , (MWD/tonne)	Uranium utilization, U (MWD/tonne U_{NAT})
PTLWR-4%	25,000	3,460
PTLWR-6%	56,000	4,930
PTLWR-7%	77,000	5,700
Current PWR-3.6% ^a	35,100	5,280
Advanced PWR-4.4% ^a	50,000	6,080
CANDU-600-Nat. ^b	7,500	7,500
CE-CANDU-1.2% ^b	19,750	10,090

^a from [Driscoll et. al., 1990], ^b from [Shapiro and Jesick, 1979].

where x_p , x_f , and x_w are the weight percent of ^{235}U in the enrichment plant product, feed (0.711 wt%), and tails (0.2wt%), respectively. Equation (4-38) neglects the small composite loss fraction in the fabrication and chemical conversion steps.

Using the discharge burnups achievable for given enrichments from Table 4-12, the discharge burnup can be approximated by the linear equation

$$B_d = 25 + 17.33 (e\% - 4), \text{ MWd/kg} \quad (4-40)$$

where e is enrichment in %. Since the PTLWR fuel elements are compatible with CANDU fuel bundles, spent PTLWR fuel could be used directly in CANDU reactors as a partial reload. Note that the discharged PTLWR bundles with burnup of 80,000 MWD/tonne, which contain only 0.85% ^{235}U (compared to 0.92% for PWR spent fuel), 0.53% ^{239}Pu , 0.17% ^{241}Pu , and a significant amount of fission products, would not make a CANDU core critical if the entire CANDU core is loaded with these fuel elements ($k_\infty = 0.95$).

4.4.7.4 Summary of Burnup Study

It can be seen from Table 4-12 that the PTLWR can achieve high discharge burnups realizable with particle fuel, but at the expense of higher enrichment than for a PWR. This is a consequence of the less efficient neutron economy in a high-leakage, low-loading PTLWR core. Uranium utilization falls in between current and advanced PWRs. The burnup rate in the proposed PTLWR concept is faster than for current CANDUs, because of low heavy metal loading. However, fuel residence time is longer than for current CANDUs (the refueling rate is about one half that of a CANDU unit) due to the high achievable discharge burnups.

4.4.8 On-line Refueling Schemes

4.4.8.1 Introduction

A pressure tube LWR with void space between the pressure tubes exhibits a very uniform thermal flux profile over the entire calandria space and tight core coupling. Hence it would be an ideal candidate for 1-batch refueling. One-batch refueling is not, however, an economically viable option because one cannot afford to forgo the advantages of multi-batch refueling, especially in view of the higher parasitic losses and higher leakage which require higher enrichment. One-batch refueling would therefore lead to much higher fuel cycle cost compared to a typical LWR. Consequently, on-line refueling which compensates for these losses, and which is easily implemented in pressure tube reactors, was adopted. Excellent experience with on-line refueling acquired in CANDU reactors further supports this option.

However, on-line refueling in the dry calandria design poses the difficulty of avoiding large power ripples. These local power ripples, introduced by the fresh fuel elements, are more severe than in CANDU reactors for two reasons:

- relatively high initial enrichment, and
- uniformity of the thermal flux profile.

The need for relatively high enrichment to attain high burnups has been discussed in the previous section. The uniformity of the thermal flux profile is primarily a result of the large migration length. The entire core is transparent to thermal neutrons. As a result the fresh fuel element, with a high amount of fissile material, inserted into the reactor by the refueling machine, sees thermal neutrons from the entire core. Because the number of fissions is proportional to thermal flux and the number of fissile nuclides in the fuel element, the power generation in the fresh fuel bundle is high.

To minimize power ripples in CANDU reactors, fresh fuel bundles can be placed in the regions of low thermal flux or next to low power bundles.

Placing fresh bundles in a low-thermal-flux regions in the present instance is possible only to some extent, since the flux is almost uniform. Placing fresh bundles next to bundles with high burnup helps to decrease power ripple, but it is less effective than in CANDUs because of the core's transparency to thermal neutrons.

To reduce peaking due to non-uniform distribution of fissile material*, bi-directional refueling (used also in CANDU reactors) was chosen†. Two neighboring channels are fueled from the opposite ends, such that the fresh fuel bundle at the end of one channel faces the bundles with the highest burnup in the four neighboring channels as shown in Figure 4-10. Fuel bundles are axially arranged such that the bundles with high fissile content are close to the channel inlet and high-burnup bundles are placed at the channel exit. This arrangement has an important advantage from the point of view of Critical Heat Flux Ratio (CHFR), since the lowest power density bundle transfers the heat into regions with the highest coolant temperature (the coolant flow is also bi-directional in CANDUs). Note that in the PTLWR, the power density profile can be shaped by the on-line refueling scheme as desired.

The objective of this section is to evaluate the power density profile in the fuel channels using a bi-directional refueling scheme. The two-channel MCNP model #4, which allows for arbitrary fuel composition in every individual fuel bundle, will be used for this purpose. Various

* Note that the power peaking concept in the PTLWR differs from typical LWRs and PHWRs, where power peaking arises from peaking in the thermal flux, while in the PTLWR peaking arises primarily from the non-uniform distribution of the fissile material.

† Another possible refueling scheme would be to refuel an entire channel. This would eliminate axial peaking, but introduce channel-to-channel peaking. Channel-to-channel peaking may be reduced by refueling channels in low-thermal flux regions always with fresh fuel for partial burnup and moving partially burned fuel from these regions to higher-flux regions; one could also orifice the channels to match flow to power.

arrangements of fuel bundles and various alternative means to minimize power peaking will also be explored.

4.4.8.2 Fresh Core with Uniform Enrichment and Model Consistency

To check if the two-fuel channel MCNP model #4 is consistent with one-channel MCNP model #1 and to demonstrate the difference in power density profile for uniform fuel composition and axially variable fuel composition, the two-channel model will be first run for fresh fuel with 2% enrichment. The 2%-enriched fuel, as well as the same average coolant density, is used in all fuel bundles. The comparison of multiplication factors obtained for the infinite lattice using model #1 and model #4, given in Table 4-13, shows that both models are consistent.

Table 4-13 Consistency check of MCNP model #4 with MCNP model #1

	k_{∞}
One-axial cell model (MCNP model #1)	1.064±0.003
Multiple-axial cell model (MCNP model #4)	1.065±0.002

The power density profile for the fresh core with the same fuel enrichment in every fuel bundle is shown in Figure 4-45. Figure 4-45 was calculated for the infinite lattice without the end reflectors, hence there is no peaking from a thermal flux peak near the reflector. Every calculated point on the curves represents the average power density in an outer fuel ring in a given fuel bundle*. It is evident from Figure 4-45 that thermal flux in the PTLWR infinite lattice is basically constant. Hence, it can be

* See Figure 4-11 for the geometry showing the fuel channels with fuel rings. "Left" denotes the fuel channel in the lower left corner, "Right" denotes the fuel channel in the upper right corner.

expected that for fuel bundles with variable fuel composition, the power density will be roughly proportional to the content of fissile material.

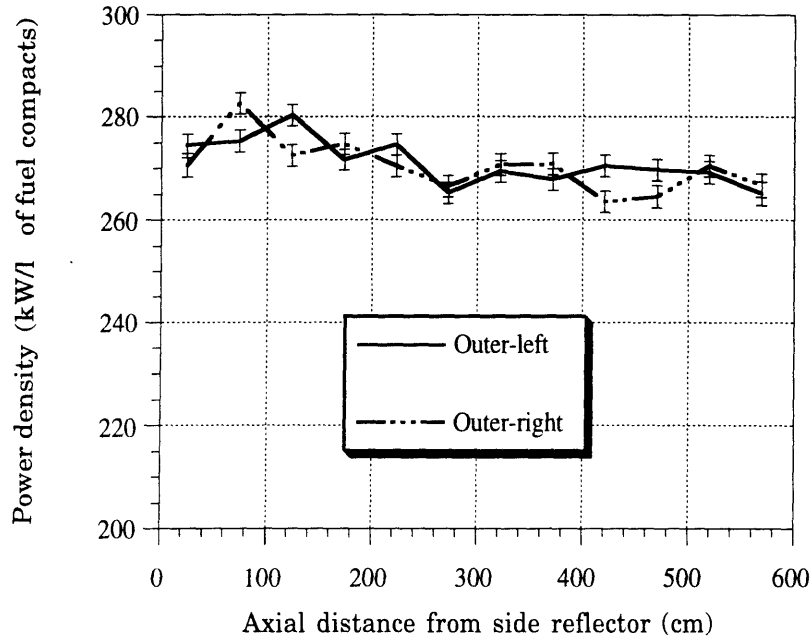


Figure 4-45 Axial power density distribution in fuel compacts for uniform enrichment

4.4.8.3 Estimate of Burnup Penalty using Burnable Poison

One of the options to decrease power ripple from high fissile content in the fresh fuel bundles is the use of burnable poison. The penalty on burnup from burnable poison can be estimated using a linear reactivity model. Neglecting the effect of burnable poison on conversion ratio, and hence on the slope of the burnup curve, and using the burnable poison scenario and nomenclature shown on Figure 4-46, the burnup penalty can be calculated as follows:

Requiring the average reactivity, ρ , to be zero, one can write

$$\frac{1}{2} \rho_0 B_1 - \frac{1}{2} \Delta\rho_{BP} B_3 = \frac{1}{2} (\rho_0 - AB_d) B_2 \quad (4-41)$$

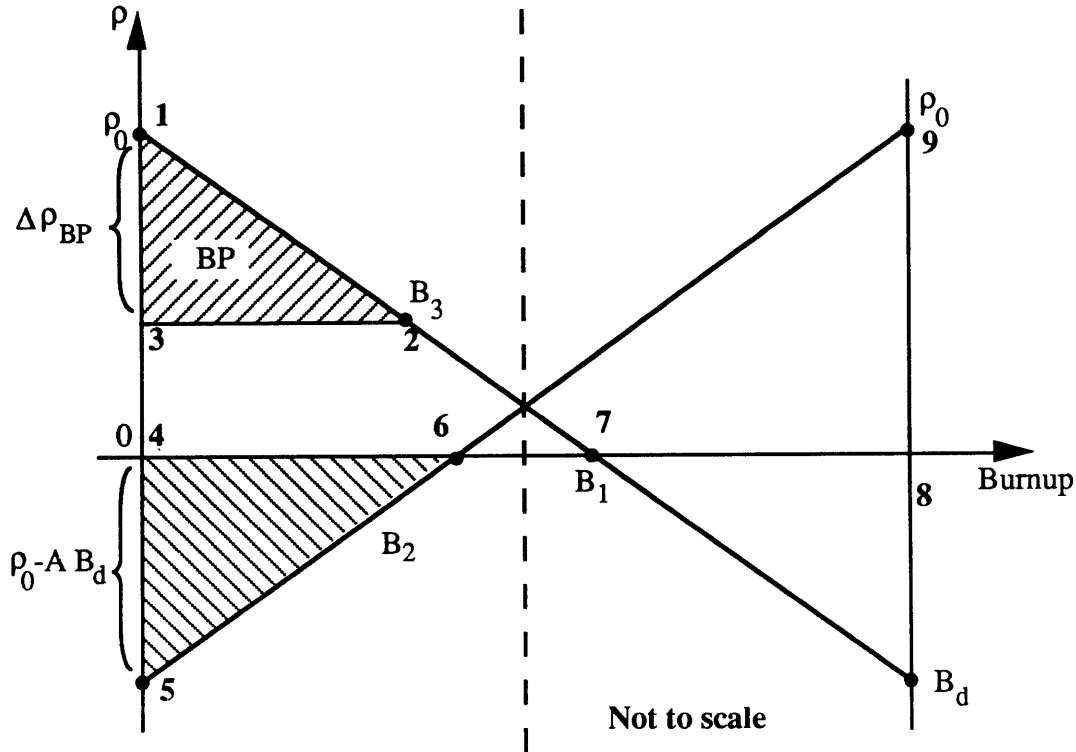


Figure 4-46 Linear model of burnup with burnable poison

where A is the slope of the burnup curve and $\Delta\rho_{BP}$ is reactivity reduction due to the presence of burnable poison. Using symmetry and the relations from similar triangles 123 and 174, and 465 and 698, yields

$$\frac{B_3}{B_1} = \frac{\Delta\rho_{BP}}{\rho_0}; \quad \frac{B_2}{B_1} = \frac{-(\rho_0 - AB_d)}{\rho_0} \quad (4-42,43)$$

Substituting ratios from Eqs. (4-42) and (4-43) into Eq. (4-41) and solving for the discharge burnup, B_d , results in

$$B_d = \left(\frac{\rho_0}{A}\right) \left[1 + \sqrt{1 - \left(\frac{\Delta\rho_{BP}}{\rho_0}\right)^2} \right] \quad (4-44)$$

Equation (4-43) gives the effect of reactivity tied up in burnable poison ($\Delta\rho_{BP}$) on the discharge burnup. In the limit where $\Delta\rho_{BP} = 0$, discharge burnup $B_d = 2 \rho_0/A$ as it should. The fractional reduction in burnup compared to the poison-free case is then

$$f = \frac{1}{2} \left[1 + \sqrt{1 - \left(\frac{\Delta\rho_{BP}}{\rho_0} \right)^2} \right] \quad (4-45)$$

Equation (4-45) is tabulated in Table 4-14.

Table 4-14 Fractional reduction due to burnable poison in burnup for on-line refueling

$\Delta\rho_{BP}/\rho_0$	f, from Eq. (4-45)
0	1
0.3	0.98
0.5	0.93
0.7	0.86
0.8	0.80
0.9	0.72 ^a
1.0	0.50 ^b

^a Roughly equivalent to 3 batch PWR scheme

^b One batch core, i.e., burnup just replaces burnable poison

Table 4-14 suggests that a substantial reduction in the peak reactivity can be achieved at a relatively low penalty on discharge burnup. For example, the reactivity of the hot bundle can be decreased by 50% while the discharge burnup is decreased only by 7%.

To model burnable poison by the MCNP+ORIGEN2 combination, the following procedure was used:

1. Put ¹⁰B into the fresh fuel and run the MCNP model #1 for poisoned fuel and for the fresh fuel to obtain the reactivity for fuel with boron, ρ_{BP} , and for the fuel without boron, ρ_0 , respectively. Adjust the amount of boron in the fresh fuel such that $\Delta\rho_{BP}/\rho_0=0.5$. Obtain the ratio of absorption rate in boron to absorption rate in ²³⁵U, $(\Sigma a\Phi)^b/(\Sigma a\Phi)^{25}$.
2. Put the amount of boron which gives 50% reactivity reduction into the ORIGEN2 code, burn up the fuel, and obtain the ratio of absorption rate in boron to absorption rate in ²³⁵U, $(\Sigma a\Phi)^b/(\Sigma a\Phi)^{25}$. Adjust the effective one-group absorption cross section of boron such that the absorption rate ratio obtained by ORIGEN2 matches the ratio

obtained from MCNP. In a similar manner adjust effective one-group effective absorption cross sections of the actinides.

3. Run the MCNP code using fuel composition obtained from ORIGEN2 to obtain the burnup curve and maximum achievable discharge burnup which still guarantees criticality.
4. Run MCNP with the bi-directional refueling scheme to obtain the power density profile

4.4.8.4 Refueling Schemes Considered

The following cases will study the effects of various options on the power density profile. Cases studied included use of burnable poison, reshuffling of fuel bundles, or changing the thermal flux profile. All the results, presented next, were obtained using the two-channel MCNP model #4 with graphite end reflector on both sides of the channel. Bundle-average coolant density in individual fuel bundles has been calculated using the steady-state thermohydraulic code described in Chapter 6.

Case #1 – Pure Bi-directional Refueling without Burnable Poison

Case #1 employs pure bi-directional refueling with no burnable poison. The arrangement of fuel bundles (designated arrangement #1) is shown in Figure 4-47. The fresh fuel bundle is always inserted at the channel inlet, in the direction of coolant flow, and the bundle with the highest burnup is at the channel outlet.

The axial power density profile in the outer fuel ring of the two neighboring channels is shown in Figure 4-48; power peaking factors and the multiplication factor are summarized in Table 4-15. The axial peaking in the power density profile is significantly higher for the equilibrium core using pure bi-directional refueling than that shown for the fresh core with uniform fuel composition, i.e., compare 1.52 to 1.13 (see Section 4.4.4.3 for peaking in the fresh core).

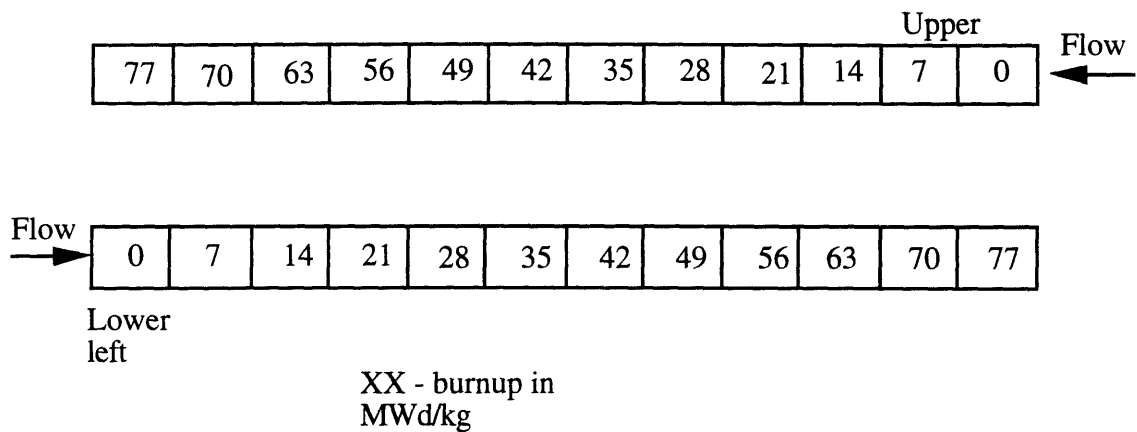


Figure 4-47 Bundle arrangement #1.

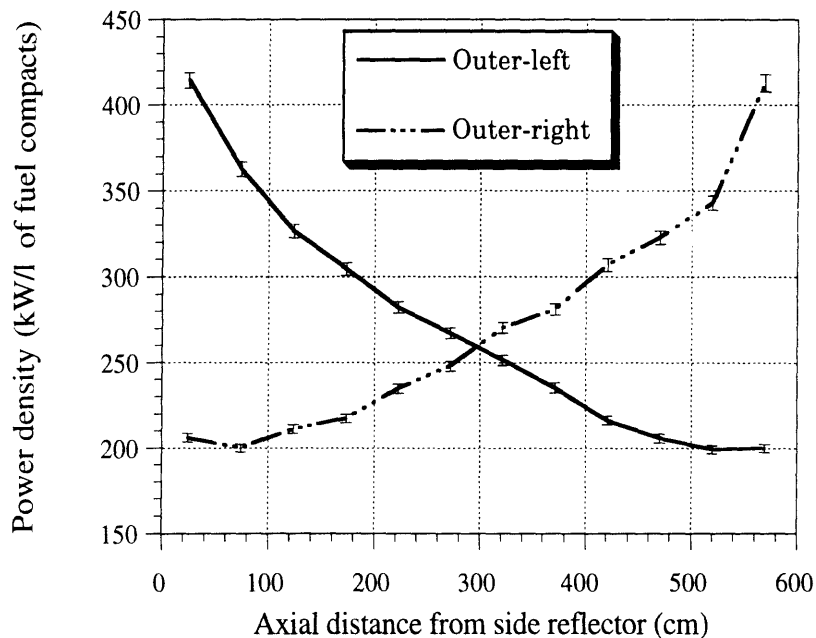


Figure 4-48 Axial power density profile for Case #1

Case #2 – Pure on-line Refueling with Burnable Poison

Case #2 uses burnable poison in the fresh fuel bundles and the same fuel bundle arrangement (arrangement #1) as for Case #1. Figure 4-49 and Figure 4-50 show the power density profile and thermal flux profile as a function of axial position, respectively. Peaking factors and multiplication factor are summarized in Table 4-16.

The effect of burnable poison can be seen by comparing Table 4-15 and Table 4-16. The decrease in peaking factor in the outer fuel ring (peaking factor in the outer fuel ring is always larger than in the inner fuel ring) achieved by introducing burnable poison is from 1.52 to about 1.39. Note that the peaking values for the lower left channel and the upper right channel must be the same due to symmetry. If they are not the same due to statistical errors, the average value between the upper right and the lower left channel is taken. Although this decrease in peaking is a good improvement, it is not very large, especially when one considers that the fresh bundle with burnable poison has only 50% of the excess reactivity compared to the fresh bundle without burnable poison.

Table 4-15 A Summary of peaking factors and multiplication factor for case #1

Multiplication factor ^a	1.078
Effective multiplication factor ^b	0.998
Peaking factor/ $q'''_{ave}(kW/l)$ -lower left channel, inner fuel ring	1.49/268.8
Peaking factor/ $q'''_{ave}(kW/l)$ -lower left channel, outer fuel ring	1.52/272.1
Peaking factor/ $q'''_{ave}(kW/l)$ -upper right channel, inner fuel ring	1.48/265.9
Peaking factor/ $q'''_{ave}(kW/l)$ -upper right channel, outer fuel ring	1.52/271.1

^a Modeled as an infinite lattice in radial direction, axial reflectors are included

^b The difference between the multiplication factor of the axially-reflected infinite lattice and the effective multiplication factor for the whole core with radial reflector assumed the same as for uniform fuel distribution ($\Delta k=0.08$).

Case #3 – Bi-directional Refueling without Burnable Poison using Bundle Reshuffling.

The disadvantage of burnable poison is the decrease in core reactivity (about 3%), and hence, decreased discharge burnup. Because neutron losses are higher in the proposed PTLWR than in a typical LWR even

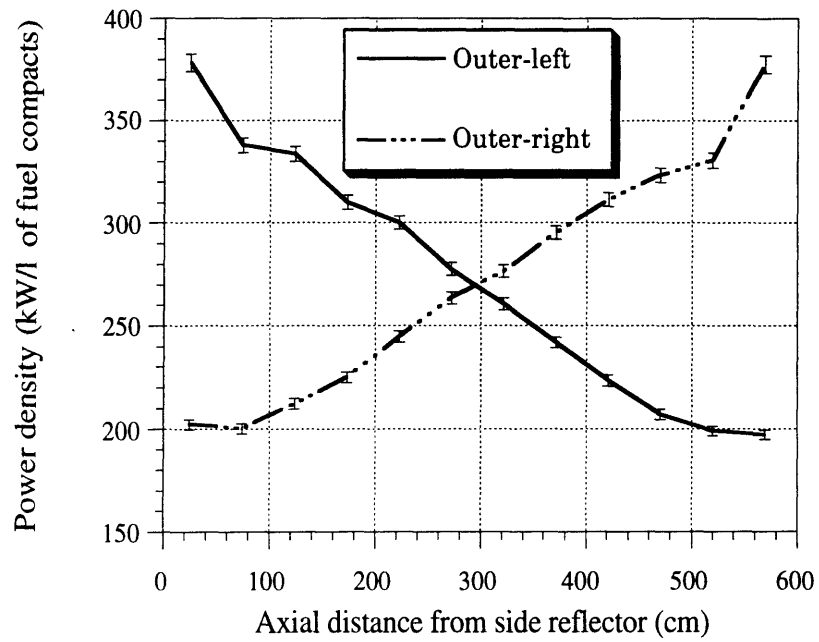


Figure 4-49 Axial power density profile for Case #2

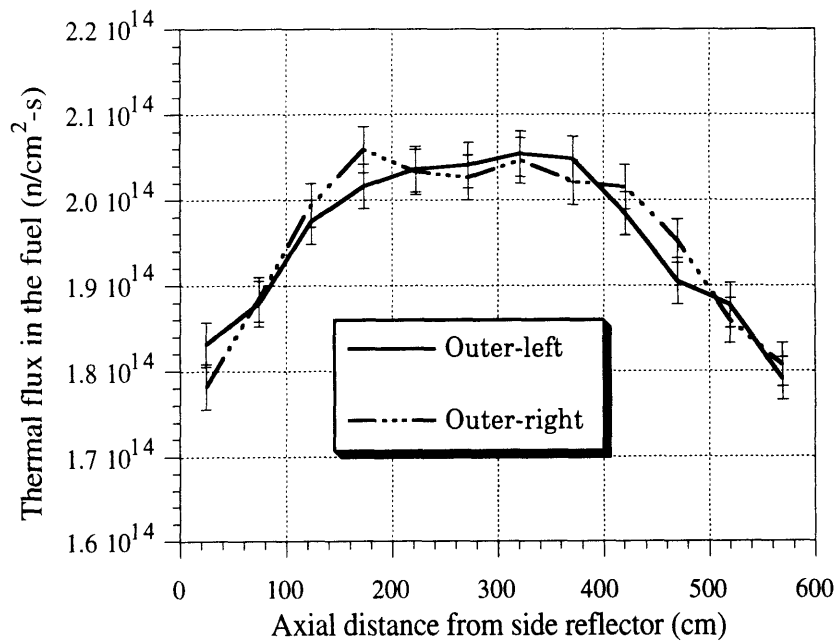


Figure 4-50 Thermal flux profile for Case #2

Table 4-16 A Summary of peaking factors and multiplication factor for case #2

Multiplication factor ^a	1.045
Effective multiplication factor ^b	0.965
Peaking factor/ q'''_{ave} (kW/l)-lower left channel, inner fuel ring	1.32/268.4
Peaking factor/ q'''_{ave} (kW/l)-lower left channel, outer fuel ring	1.39/272.2
Peaking factor/ q'''_{ave} (kW/l)-upper right channel, inner fuel ring	1.33/267.4
Peaking factor/ q'''_{ave} (kW/l)-upper right channel, outer fuel ring	1.39/271.8
Maximum peaking factor on thermal flux/ Φ_{ave} (n/cm ² -s)	1.1/1.9E14

^a Modeled as an infinite lattice in radial direction, axial reflectors are included

^b The difference between the multiplication factor of the axially-reflected infinite lattice and the effective multiplication factor for the whole core with radial reflector assumed the same as for uniform fuel distribution ($\Delta k=0.08$).

without the burnable poison, this practice is undesirable. Moreover, the advantages of on-line refueling – the possibility of eliminating most reactivity control absorbers and minimization of the excess reactivity – suffer if burnable poison is utilized. Therefore, other ways to decrease power peaking are worthy of consideration. The first option appears to be bundle rearrangement. This can be easily done with current refueling schemes; in fact in CANDUs all bundles can be pulled out of the channel into the magazines of the refueling machines, mixed with the new fuel, rearranged and inserted back into the fuel channel in any desired scheme. The first attempt is to surround the fresh bundle by high burnup bundles in a sequence better than in arrangement #1. Another important consideration is the higher thermal flux in the vicinity of the end reflectors; hence it is desirable to place fresh fuel bundles further from the reflector. Arrangement #2, shown on Figure 4-51, addresses these issues.

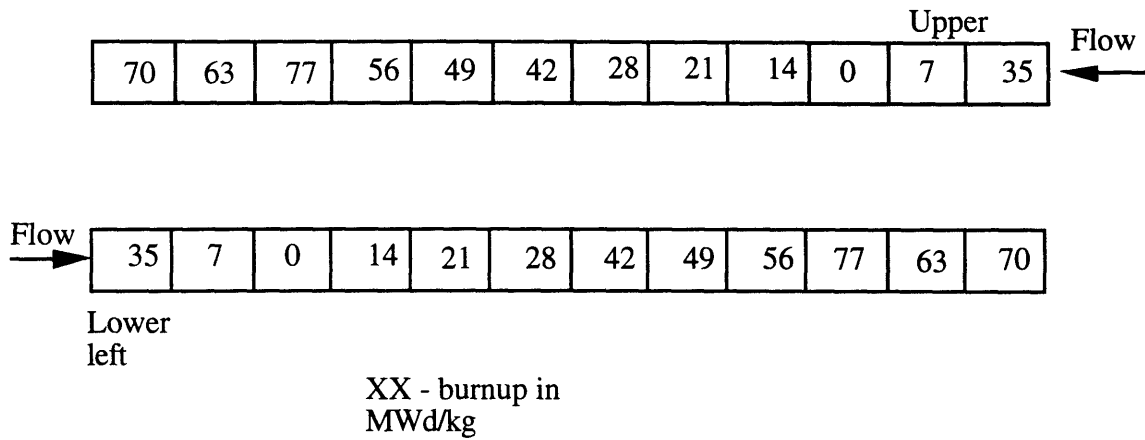


Figure 4-51 Bundle arrangement #2

Figure 4-52 shows the power density profile as a function of axial position and Figure 4-53 shows the corresponding thermal flux profile. Table 4-17 gives the effective multiplication factor and peaking factors.

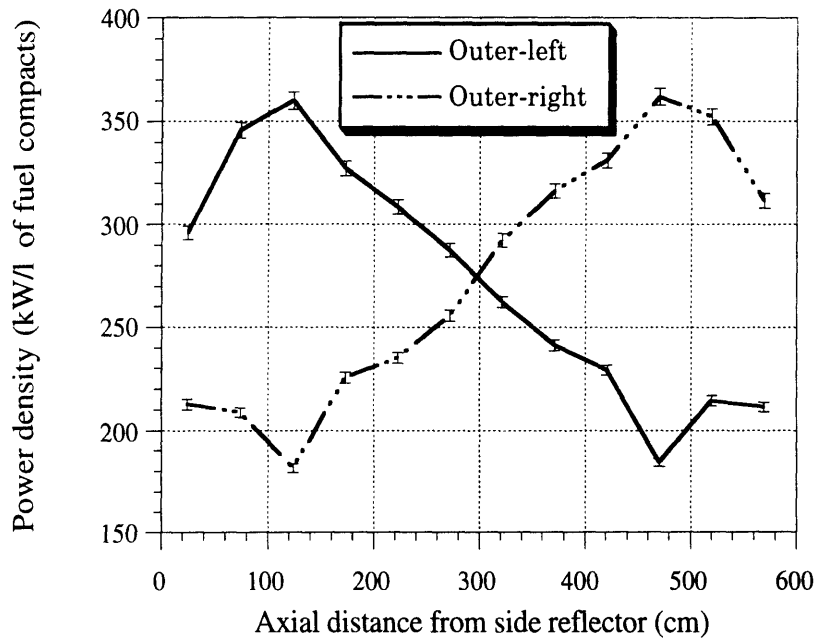


Figure 4-52 Axial power density profile for Case #3

Comparing Table 4-15 and Table 4-17, it can be seen that the improvement in power flattening by bundle rearrangement is significant. The maximum peaking factor in the outer fuel ring is 1.34, which is even

less than for the fuel with burnable poison in bundle arrangement #1. Moreover, reactivity is not decreased, but is even slightly higher due to lower leakage (instead of having fresh bundles facing the reflector, bundles with some burnup are placed close to the reflector, which results in less fissions in the region immediate to the reflector, and less high energy neutrons streaming to the reflector). Hence, the bi-directional refueling scheme in arrangement #2 gives improved peaking at no reactivity expense.

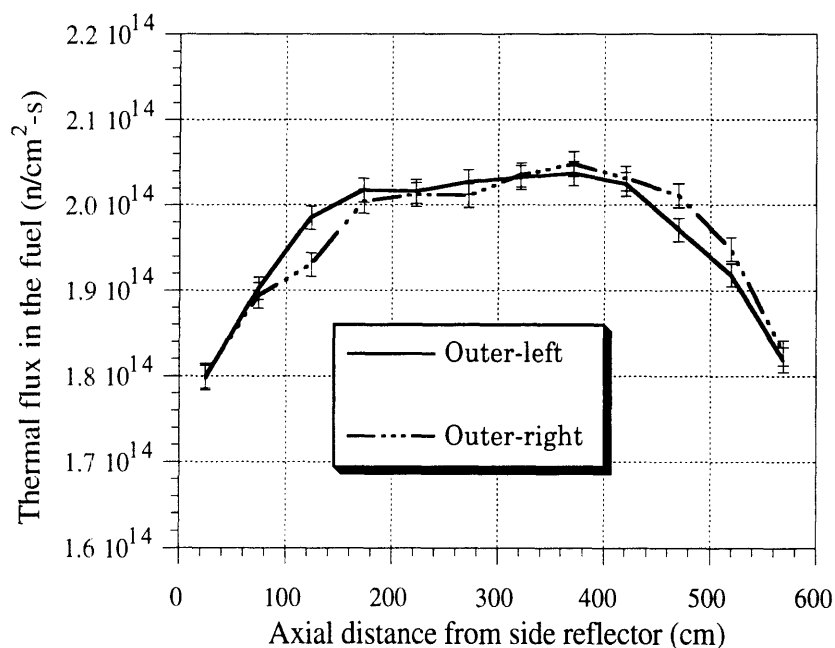


Figure 4-53 Thermal flux profile for Case #3

Case #4 – Bi-directional refueling with Burnable Poison and Bundle reshuffling.

If burnable poison is used in combination with bundle arrangement #2, a further decrease in power peaking can be achieved. This is shown in Figure 4-54 and in Table 4-18. The decrease in power peaking in the outer fuel ring is by 7.4% (compared to arrangement #2 without burnable poison) to about 1.24, at a reactivity expense of 3.2%. However, from the fuel cycle cost point of view, it is preferable to stay with the higher peaking factor of

Table 4-17 A Summary of peaking factors and multiplication factor for case #3

Multiplication factor ^a	1.083
Effective multiplication factor ^b	1.003
Peaking factor/ q'''_{ave} (kW/l)-lower left channel, inner fuel ring	1.34/268.3
Peaking factor/ q'''_{ave} (kW/l)-lower left channel, outer fuel ring	1.32/272.3
Peaking factor/ q'''_{ave} (kW/l)-upper right channel, inner fuel ring	1.33/271.4
Peaking factor/ q'''_{ave} (kW/l)-upper right channel, outer fuel ring	1.32/273.7
Maximum peaking factor on thermal flux/ Φ_{ave} (n/cm ² -s)	1.1/1.9E14

^a Modeled as an infinite lattice in radial direction, axial reflectors are included

^b The difference between the multiplication factor of the axially-reflected infinite lattice and the effective multiplication factor for the whole core with radial reflector assumed the same as for uniform fuel distribution ($\Delta k=0.08$).

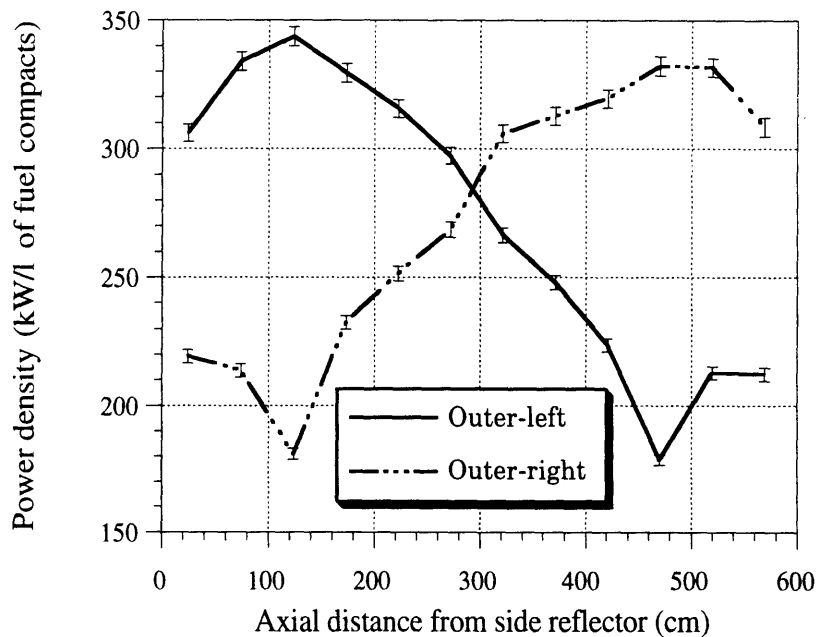


Figure 4-54 Axial power density profile for Case #4

Table 4-18 A Summary of peaking factors and multiplication factor for case #4

Multiplication factor ^a	1.0473
Effective multiplication factor ^b	0.9673
Peaking factor/ q'''_{ave} (kW/l)-lower left channel, inner fuel ring	1.26/268.2
Peaking factor/ q'''_{ave} (kW/l)-lower left channel, outer fuel ring	1.26/272.3
Peaking factor/ q'''_{ave} (kW/l)-upper right channel, inner fuel ring	1.20/268.3
Peaking factor/ q'''_{ave} (kW/l)-upper right channel, outer fuel ring	1.22/273.1
Maximum peaking factor on thermal flux/ Φ_{ave} (n/cm ² -s)	1.1/1.9E14

^a Modeled as an infinite lattice in radial direction, axial reflectors are included

^b The difference between the multiplication factor of the axially-reflected infinite lattice and the effective multiplication factor for the whole core with radial reflector assumed the same as for uniform fuel distribution ($\Delta k=0.08$).

1.34 (which is quite flat already) without using burnable poison to flatten the power profile further. The channel inlet peaking is also an advantage with respect to steady state thermal-hydraulic behavior as will be discussed in Chapter 6.

Case #5 – Bi-directional refueling with Bundle Reshuffling and Beryllium Screen.

Another means to flatten the power density profile without sacrificing reactivity is to use additional moderator for local thermal flux shaping, placed in the voided space between the fuel channels in such a way that, in combination with appropriate bundle arrangement, flatter power can be achieved. Beryllium would be an effective moderator due to its low absorption cross section, and the possibility of an increased neutron population due to its (n, xn) reaction. It would, however, have to be designed

to be removable, because of the irradiation damage in the high fast flux environment.

To explore potential benefits of such a design, a beryllium slug was introduced into the voided space between the fuel channels, as shown in Figure 4-55. Placing a beryllium slug at the channel midplane increases

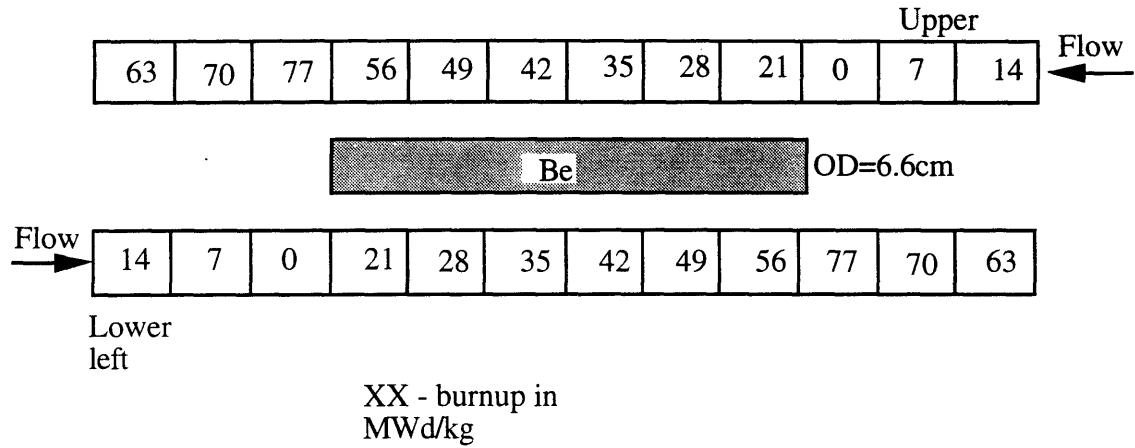


Figure 4-55 Bundle arrangement #3 with Be slug

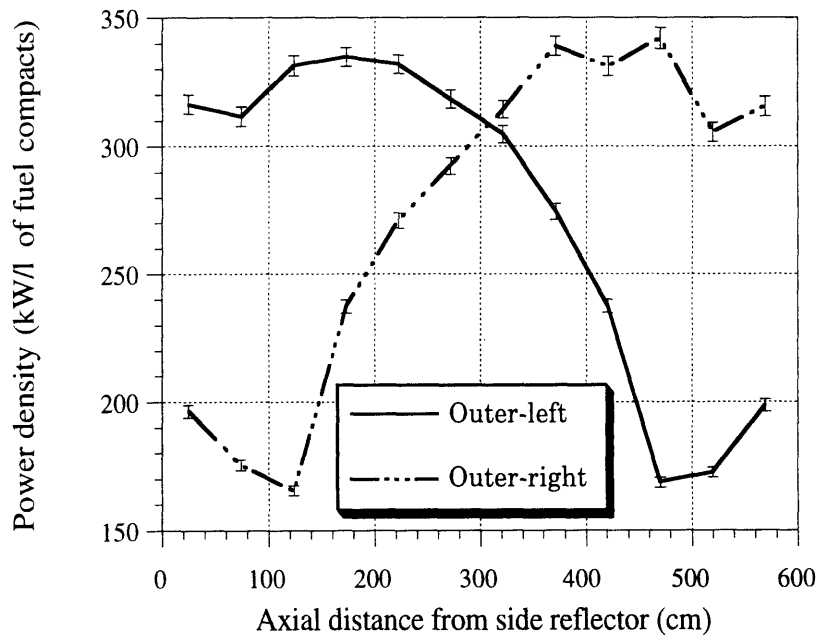


Figure 4-56 Axial power density profile for Case #5 with beryllium slug

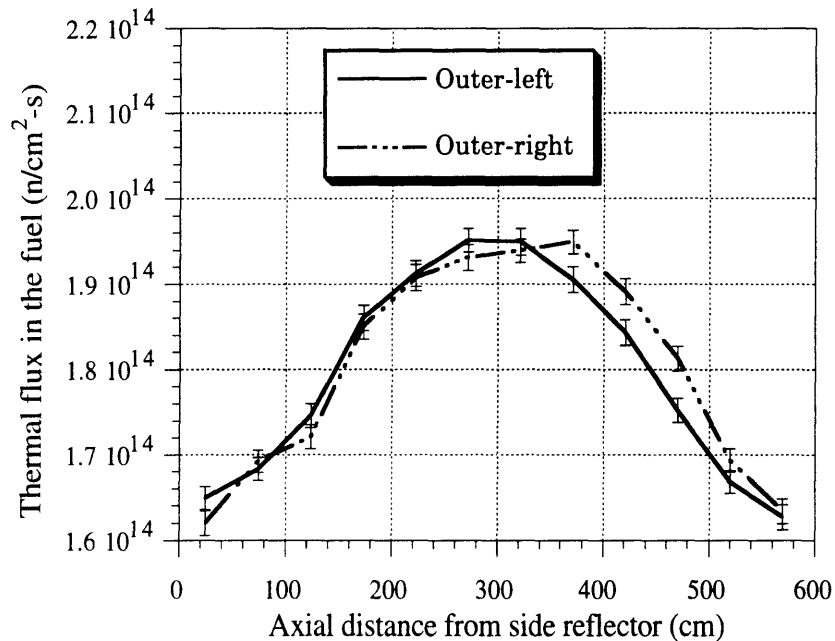


Figure 4-57 Thermal flux profile for Case #5 with beryllium slug

the thermal flux in this region. The fuel bundles were reshuffled (arrangement #3) so that the highest-power bundles are located in the lower-flux region, and such that they face fuel bundles with the largest burnup in the neighboring channels.

The results for this configuration are shown in Figure 4-56, Figure 4-57 and in Table 4-19. It can be observed that this arrangement gives the lowest peaking in the outer fuel ring of all cases considered. Moreover, the reactivity is significantly increased. Hence, this is much better option than arrangement #2 with burnable poison, although there may be some complications involved with the calandria mechanical design.

To see the effect of the beryllium slug on power flattening and reactivity more clearly, bundle arrangement #3 is recalculated without the beryllium slug. The results are presented in Figure 4-58 and Figure 4-59 and in Table 4-20. Comparing Figure 4-56 with Figure 4-58 and Figure 4-57 with Figure 4-59, it can be seen that the beryllium slug in the middle increases the thermal flux at this position, which results in an increased power of the bundles facing the beryllium slug. The power of the bundles with high

fissile content is lower in the case with the beryllium slug because the thermal flux at the ends where these bundles are located is decreased.

Table 4-19 A Summary of peaking factors and multiplication factor for case #5 with beryllium slug

Multiplication factor ^a	1.121
Effective multiplication factor ^b	1.041
Peaking factor/ q'''_{ave} (kW/l)-lower left channel, inner fuel ring	1.23/261.7
Peaking factor/ q'''_{ave} (kW/l)-lower left channel, outer fuel ring	1.22/275.0
Peaking factor/ q'''_{ave} (kW/l)-upper right channel, inner fuel ring	1.28/259.4
Peaking factor/ q'''_{ave} (kW/l)-upper right channel, outer fuel ring	1.25/273.8
Maximum peaking factor on thermal flux/ Φ_{ave} (n/cm ² -s)	1.1/1.8E14

^a Modeled as an infinite lattice in radial direction, axial reflectors are included

^b The difference between the multiplication factor of the axially-reflected infinite lattice and the effective multiplication factor for the whole core with radial reflector assumed the same as for uniform fuel distribution ($\Delta k=0.08$).

Since a beryllium slug adds additional moderation into the system, a check should be made if the void reactivity coefficient remains negative. The negative void coefficient for this configuration has been confirmed, as shown in Figure 4-60.

Finally, it is noted that a tube filled with light water can also achieve thermal flux shaping leading to a decrease in power peaking. Replacing the beryllium slug with a tube of the same dimensions, filled with light water as the slug, leads to power peaking of about 1.26 and almost zero void coefficient. However, the multiplication factor is less than for the beryllium slug configuration by about 31 mk. Water also requires installation of a cooling system while beryllium could be cooled by radiative heat transfer to the pressure tubes.

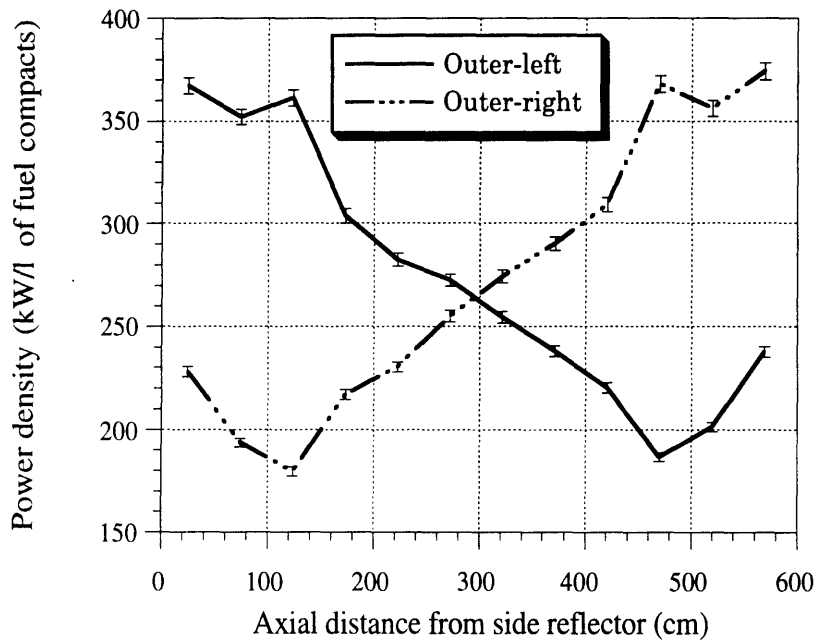


Figure 4-58 Axial power density profile for Case #5 without beryllium slug

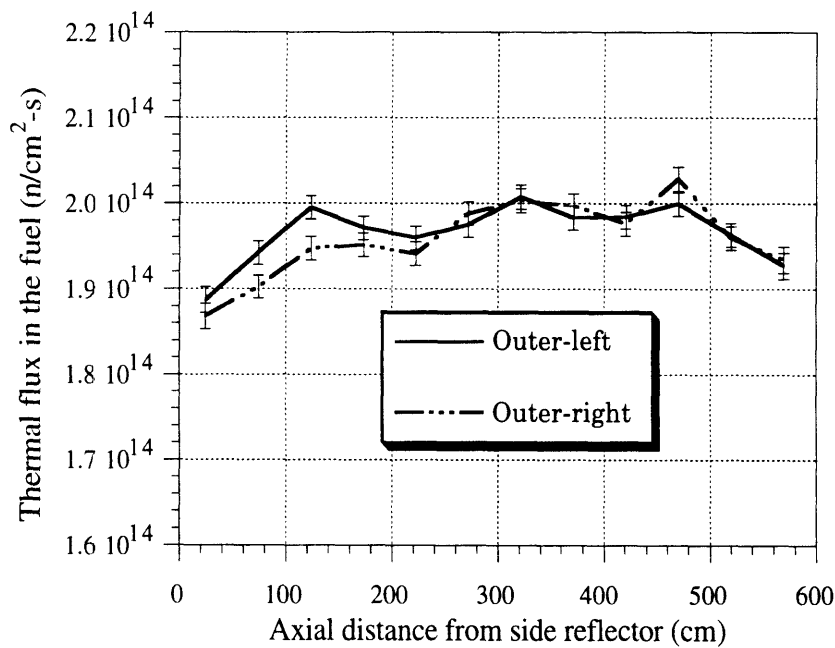


Figure 4-59 Thermal flux profile for Case #5 without beryllium slug

Table 4-20 A Summary of peaking factors and multiplication factor for case #5 without beryllium slug

Multiplication factor ^a	1.0824
Effective multiplication factor ^b	1.0024
Peaking factor/ q'''_{ave} (kW/l)-lower left channel, inner fuel ring	1.32/266.2
Peaking factor/ q'''_{ave} (kW/l)-lower left channel, outer fuel ring	1.34/273.1
Peaking factor/ q'''_{ave} (kW/l)-upper right channel, inner fuel ring	1.36/270.1
Peaking factor/ q'''_{ave} (kW/l)-upper right channel, outer fuel ring	1.37/273.0
Maximum peaking factor on thermal flux/ Φ_{ave} (n/cm ² -s)	1.0/1.9E14

^a Modeled as an infinite lattice in radial direction, axial reflectors are included

^b The difference between the multiplication factor of the axially-reflected infinite lattice and the effective multiplication factor for the whole core with radial reflector assumed the same as for uniform fuel distribution ($\Delta k=0.08$).

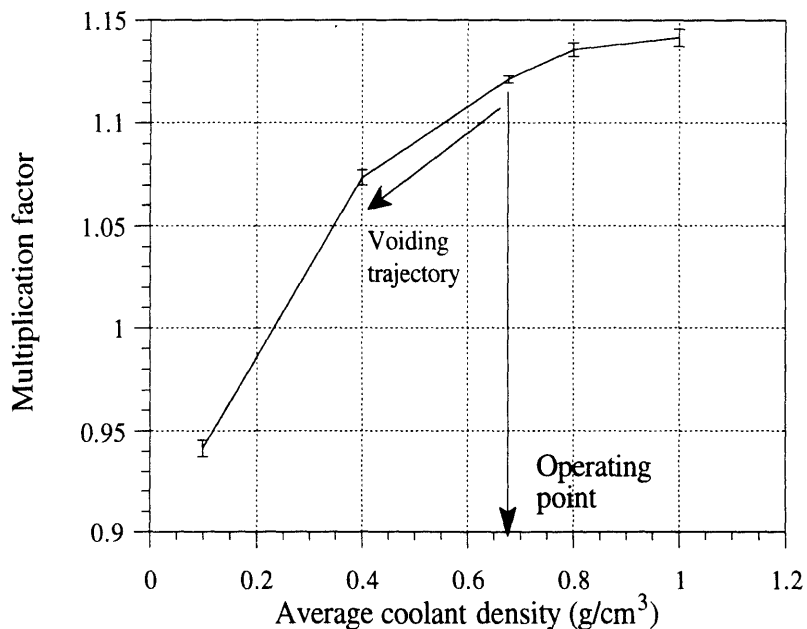


Figure 4-60 Effect of coolant voiding for the case with beryllium slug

4.4.8.5 Reactivity Deficit During Fuel Channel Refueling

Refueling with bundle reshuffling requires emptying the entire fuel channel before the fuel bundles can be reshuffled and returned into the fuel channel in a desired order. This practice is also used in advanced CANDU refueling strategies to flatten the power density profile [Dastur and Chan, 1993]. Emptying the entire fuel channel results in a reactivity decrease. This reactivity should be sufficiently small to be handled by the fine control rod group. To calculate the magnitude of this reactivity deficit, full-core MCNP model #3 was used. Since only one half of the core is modeled, it is not possible to model only one empty channel. Hence, the two most reactive fuel channels, in the core center, were depleted of all fuel elements and were assumed full of light water coolant. The reactivity deficit for one empty fuel channel was then taken as one half of that for the two empty fuel channels. The results, shown in Table 4-21, confirm that the reactivity deficit is small, i.e., only 2mk, which compares to the 10mk worth of the fine control rod group.

Table 4-21 Reactivity deficit for the most reactive fuel channel during refueling

Effective multiplication factor for the reference core	1.000±0.002
Effective multiplication factor with the two most reactive fuel channels filled with coolant	0.996±0.002
Deficit in effective multiplication factor (two empty channels)	4 mk ±2
Deficit in effective multiplication factor (one empty channel)	2 mk ±1
Fine control rod group worth	10 mk

4.4.8.6 Summary of On-Line Refueling Schemes

It has been shown that the power peaking in the proposed pressure tube LWR arises from variation in the bundle-to-bundle content of fissile

material, rather than from thermal flux peaking, as is the case in currently operating reactors. The bi-directional refueling scheme, currently also used in CANDU reactors, has been adopted. Several options to minimize power peaking have been studied. These included use of burnable poison, reshuffling of fuel bundles and use of beryllium screens for shaping the thermal flux profile. Use of burnable poison can decrease power peaking but results in reduced discharged burnup. Since even better reduction can be attained by bundle reshuffling, use of burnable poison is not warranted. The alternative of placing beryllium structures in the voided space between the fuel channels combined with bundle reshuffling was found to give the lowest power peaking and the highest reactivity. However, it introduces additional complexity into the design. Therefore, the bi-directional refueling scheme with bundle reshuffling was selected for the reference PTLWR design. It gives a relatively low peaking of about 1.35, and it provides the capability to match power density profile to the critical heat flux curve. The latter is a key consideration, since the critical heat flux margin is the limiting factor for fuel channel power.

Finally it is noted that power peaking can be further reduced using the high-loading, two-ring fuel arrangement proposed in Chapter 5. A high loading of heavy metal requires lower initial enrichment, and hence, less fissile material in the fresh fuel bundle. Other refueling schemes may also provide flatter power density profiles. One alternative would be to refuel channels in the lower-flux regions with the fresh fuel to achieve partial burnup, and then move partially burned fuel bundles to fuel channels having higher thermal flux.

4.4.9 Disposal of Weapons-grade Plutonium

Recent political changes leading to the end of the cold war and dismantling of nuclear weapons have brought the nuclear community to an unanticipated dilemma of disposing of a large surplus of weapons-grade plutonium. Currently, there are about 150 tonnes of Pu from dismantled U.S. and Russian weapons, and consequently, new efforts towards the disposition of this material have been initiated [von Hippel and Feiveson, 1993], [Bowman and Veneri, 1993], [Biswas et. al., 1993], [Alberstein, et. al., 1993], [Brownson and Hanson, 1993]. This section will discuss some aspects

of plutonium burning in the PTLWR, although the discussion will be mostly of a qualitative character.

4.4.9.1 Review of Options for Pu burning

There are many options for plutonium disposal which could be classified according to the timing of the deployment into short term, intermediate term and long term categories [Brownson and Hanson, 1993]. These include:

a) short term options

- ALWR (Advanced Light Water Reactors) with MOX fuel,

b) intermediate term options

- ALMR (Advanced Liquid Metal Reactors) with U-Pu fuel or pure Pu fuel,
- MHTGR,
- PTLWR,

c) long term options

- ABC (Accelerator-Based Conversion),
- MSR (Molten-Salt Reactor), and
- PBR (Particle Bed Reactor).

The ALWR can be deployed on the shortest time scale. The second category will require probably more than 10 years to be deployed. All intermediate term options offer extensive passive features. If built for the purpose of Pu burning only, their operation could provide a data base for testing of these passive features. The PTLWR reactor was included in this category, although it requires more development than do the MHTGR and ALMR. On a more general level, the PTLWR concept offers some advantages compared to the ALMR (such as PRISM) and the MHTGR.

- it provides containment, in addition to three other barriers to fission product release (SiC coating of particle fuel, matrix SiC coating and primary system boundary),
- it achieves a large power rating in one unit (1000-1400 MWe),
- it uses light water - a technologically proven and most common coolant.

4.4.9.2 Challenges Posed by 100% MOX Fuel in a LWR

Replacing ^{235}U fissile isotopes by ^{239}Pu affects several reactor physics characteristics. These are primarily neutron spectrum hardening, changes in moderator temperature coefficient and in power peaking, and single assembly criticality.

Neutron Spectrum Hardening.

Thermal fission and absorption cross sections of ^{239}Pu are higher by about 30% and 170%, respectively, compared to ^{235}U . This difference in thermal cross sections is the main reason for the hardened neutron spectrum, i.e., in lower thermal flux and increased fast/thermal flux ratio. This ratio is for a Pu-fueled LWR core about 23, or 4-5 times more than for a ^{235}U fueled core [Biswas et. al., 1993]. The shift of neutron spectrum to higher energies has the following consequences:

- *Substantial reduction of boron worth.* To compensate for low boron worth, a higher concentration of boron is necessary. Higher boron levels at EOL result in lower discharge burnup and higher fuel cycle cost.
- *Reduction of control rod worth.* To satisfy control and shutdown margin requirements, more control rods need to be provided, which may pose a problem due to space limitations.

Moderator Temperature Coefficient (MTC).

A hardened neutron spectrum increases resonance absorption in ^{238}U and ^{239}Pu , and causes a decrease in the fission to capture ratio in ^{239}Pu .

Also, a higher fast/thermal flux ratio increases leakage of neutrons out of the core. All these factors shift the MTC to more negative values. The more undermoderated Pu core (compared to the ^{235}U -fueled core) requires increased negative reactivity to satisfy shutdown margins, especially in accidents leading to moderator temperature decrease, such as steam line break.

On the other hand, high initial enrichments require a large amount of soluble boron to compensate for the reactivity excess at the beginning of cycle. This is even more pronounced in the Pu-fueled core, where the concentration of soluble boron is higher because of low boron worth. However, a higher concentration of soluble boron in the coolant tends to shift the MTC to positive values. As a result, initial enrichment and, hence, the achievable burnup is limited by the requirement of negative moderator temperature coefficient at BOL. The highest burnup in the Westinghouse PDR600 concept for disposition of weapons grade Pu is limited to a discharge burnup of 40,000MWd/tonne, primarily by the criterion of negative MTC at all operating conditions [Biswas et. al., 1993]. Hence, relatively low burnups are achievable with a typical LWR concept.

Power Peaking.

To maximize the transformation rate of Pu, high fuel loadings and Pu enrichments are desirable. Higher initial Pu enrichments, however, lead to higher peaking factors. If MOX assemblies are used in combination with ^{235}U assemblies, the higher thermal flux from ^{235}U assemblies neighboring MOX assemblies induces additional power peaking in the outer rods of the MOX assemblies. Hence, the MOX fuel must be zoned (typically in three zones with lowest Pu content in the outer assemblies) which adds complexity to the fuel design.

Single Assembly Criticality Limit.

It is required that a single assembly remain subcritical during all phases of the fuel fabrication process. A single assembly must satisfy $k_{ef}=0.95$ in a credible worst case condition, i.e., fully immersed in maximum-density light water, and fully reflected on all sides. MOX from

weapons grade Pu, which is more reactive than ^{235}U , can achieve this limit for relatively low enrichments, thus limiting initial enrichment values. Stainless steel can be employed instead of Zy as a cladding to help satisfy this limit for higher enrichments.

4.4.9.3 Consideration of Plutonium Burning in the PTLWR

Neutron Spectrum Hardening.

The PTLWR ^{235}U -fueled core has an exceedingly well-thermalized spectrum. The spectrum is the softest spectrum of all LWRs, and is comparable to a heavy water moderated lattice (Fast/thermal flux ratio is 2 compared to 4.9 for a typical LWR). However, as for a typical LWR, the spectrum hardens if ^{235}U fuel is replaced by ^{239}Pu fuel. Spectra for the ^{235}U -fueled and ^{239}Pu -fueled PTLWR cores are compared in Figure 4-61. Figure 4-61 shows that spectrum hardening is significant. Fast/thermal flux ratio is increased to 16.4, which is about 7.8 times higher than for the ^{235}U -fueled PTLWR core. This increase is higher than the increase in fast/thermal flux ratio of 4-5 for a typical LWR. Nevertheless, a fast/thermal flux ratio of 16.4 is still less than the typical LWR ratio of 23, hence the Pu-fueled PTLWR core spectrum is softer than a typical MOX-fueled LWR core. Compared to a ^{239}Pu -fueled ALMR, ALWR, and MHTGR, the PTLWR with ^{239}Pu fuel has the softest spectrum. Because of its soft spectrum and low conversion ratio it will burn ^{239}Pu very effectively.

As in LWRs, a hardened spectrum will decrease control rod worth, but this can be easily compensated by a larger number of control rods. Increasing the number of control rods does not pose a problem, since there is a lot of free space between the fuel channels (note that for a ^{235}U -fueled core, control rods placed only in the reflector were sufficient). Placing additional control rods in the core between the fuel channels will lead to local flux depression, which however, will be small due to the very large migration area. Further, long term reactivity control is accomplished by on-line refueling, hence the worth of control devices needed in the core to compensate for the reactivity excess is substantially reduced. This enables

use of higher Pu enrichments without employing additional burnable absorbers and the achievement of high discharge burnups. A significant decrease of the absolute level of the thermal flux in the ^{239}Pu -fueled core will result in less equilibrium ^{135}Xe poisoning, and, more importantly, reduced control rod worth requirements for xenon override. Contrary to typical LWRs, no soluble poison is used, hence, problems with higher boron concentrations for Pu-fueled LWRs do not apply in the PTLWR.

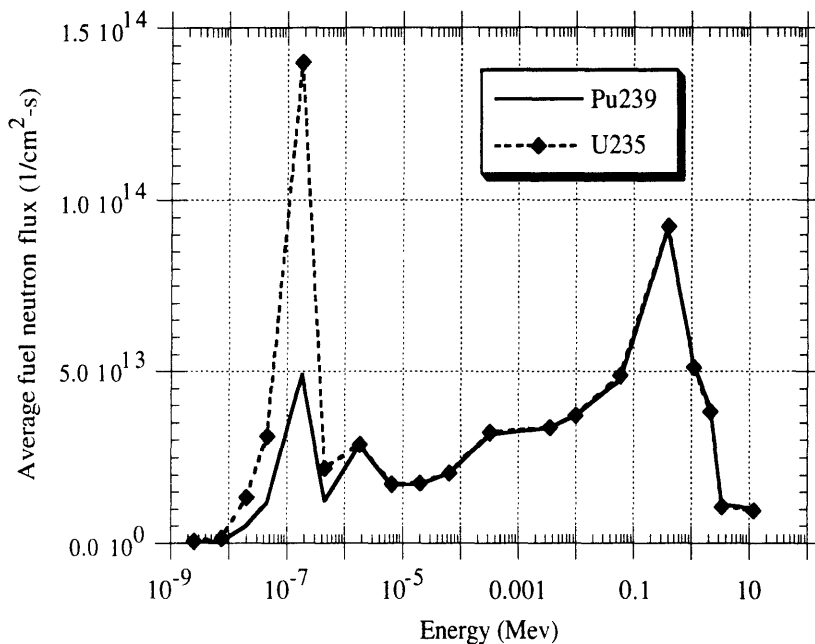


Figure 4-61 Comparison of energy spectra for the ^{239}Pu -fueled and ^{235}U -fueled PTLWR cores

Similarly as in LWRs, the Pu-fueled PTLWR exhibits a more negative moderator temperature coefficient. Reactivity as a function of coolant density is compared for ^{239}Pu - and ^{235}U -fueled PTLWR cores in Figure 4-62. The more undermoderated Pu core (compared to a ^{235}U core) requires increased negative reactivity to satisfy shutdown margins, especially in accidents leading to moderator temperature decrease such as steam line break - the same effect as for LWRs. However, as Figure 4-62 shows, the magnitude of the moderator temperature coefficient is relatively small for the PTLWR. Table 4-22 shows that during a steam line break, a typical ^{235}U -fueled LWR core experiences a reactivity increase due to the MTC of

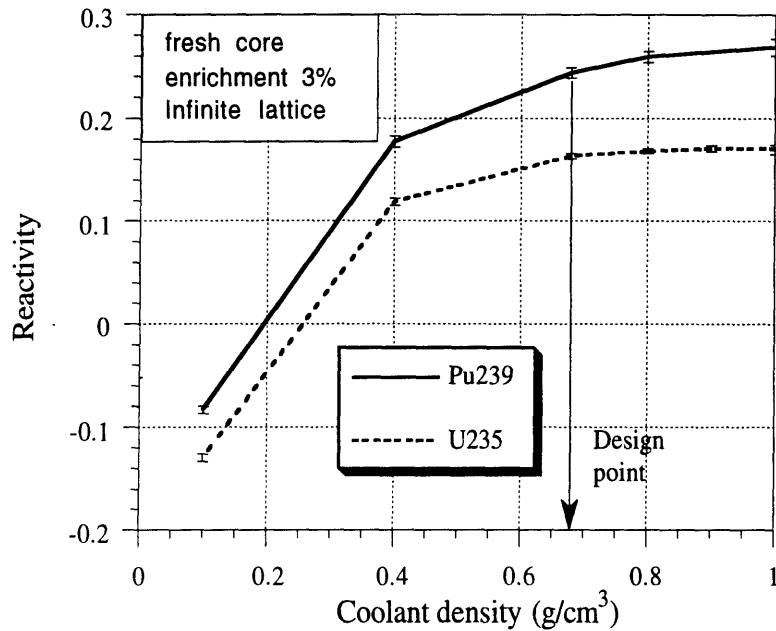


Figure 4-62 Comparison of reactivity for the ²³⁵U and ²³⁹Pu fueled PTLWR

Table 4-22 Comparison of reactivity change during steam line break

	Typical PWR (²³⁵ U-fueled)	PTLWR (²³⁵ U-fueled)	PTLWR (²³⁹ Pu-fueled)
Average core coolant temperature decrease	70°C	75°C	75°C
Coolant density change	0.114 g/cm ³	0.158 g/cm ³	0.158 g/cm ³
Reactivity change due to the MTC	+0.03	+0.005	+0.0178

about $\Delta\rho=0.03$ (note that $\Delta\rho$ for a ²³⁹Pu-fueled LWR will be even more than that) while a ²³⁹Pu fueled PTLWR core exhibits a reactivity increase of only +0.0178, which amounts to about one half of the PWR value. The table suggests that the undermoderation in the PTLWR ²³⁹Pu-fueled lattice is significantly smaller than in a typical PWR, even less than for a ²³⁵U-fueled

PWR. Therefore, using ^{239}Pu instead of ^{235}U as the PTLWR fuel should not pose problems with shutdown margins. Finally, it is to be noted, that the results in Table 4-22 were obtained for the fresh fuel and for the infinite lattice. If the comparison is done for an equilibrium ^{235}U core, and equilibrium ^{239}Pu PTLWR cores, rather than for fresh cores the difference between these two would be even less, since an equilibrium ^{235}U core contains a significant amount of ^{239}Pu .

Power Peaking.

Higher local peaking in a ^{239}Pu core with higher initial Pu enrichments, due to the thermal flux distribution, is not a problem in the PTLWR because thermal neutron flux is flat throughout the core. However, power density peaks will appear in freshly loaded fuel elements because of the higher content of fissile material. The higher initial Pu enrichment needed to maximize the transformation rate of Pu and burnup will result in larger power ripples in the fresh fuel inserted into the channel during on-line refueling. Bi-directional or other suitable refueling strategies decrease these power ripples significantly. Nevertheless, the initial enrichment, and hence the discharge burnup, will be limited by these power ripples. Burnable poison may help to decrease these ripples, while allowing for higher enrichment.

Single Assembly Criticality Limit.

A single assembly must satisfy $k_{\text{ef}} \leq 0.95$ in the credible worst case condition, i.e., fully immersed in maximum-density light water, fully reflected on all sides. PTLWR fuel elements have much less fuel than a typical LWR, and if immersed in water, they are deeply subcritical. Calculations performed for ^{235}U fuel fully submerged in a square tank (with sides of 28.57cm) and fully reflected yielded $k_{\text{ef}}=0.6$ even for 90% enrichment .

High-burnup Particle Fuel

Particle fuel used in the PTLWR concept can achieve very high burnup. Burnups of more than 700,000 MWd/tonne have been demonstrated for both

^{235}U and Pu particles [Alberstein et. al., 1993]; large scale practical experience has been accumulated for burnups of 80,000 MWd/tonne. Hence, provided that the core physics characteristics allow one to attain such high burnups, a large absolute destruction level of the charged ^{239}Pu can be achieved in a single pass through the core. The less efficient neutron economy, however, results in a relatively high fissile content at discharge. Since on-line refueling is used, fissile content at discharge can be decreased by increasing initial enrichment (note that the content of the charged ^{239}Pu increases linearly with burnup while the production rate of ^{239}Pu from ^{238}U is small due to the small conversion ratio, and saturates at high burnups). Increasing the initial enrichment from 4% to 7% reduced the fissile content at discharge by about 20%. Therefore it is desirable to maximize initial enrichment, and hence the discharge burnup, to reduce the plutonium content at discharge. An ancillary benefit of high burnups is that plutonium at discharge gets more degraded. Unfortunately, initial enrichment is limited by power ripples when inserting fresh fuel bundles. Improved on-line refueling schemes to minimize these power ripples would need to be sought for. Another alternative of reducing the power ripples would be to use stable fluorite-like compounds from oxides of plutonium, thorium, and aluminum mixed with zirconium/gadolinium oxide burnable poison, developed recently by the Japan Atomic Energy Research Institute's Nuclear Fuel Chemistry Laboratory as a high burnup fuel [Nuclear News, 1993].

Small Conversion Ratio.

It is desirable that the Pu burner exhibit a small conversion ratio to minimize the amount of Pu in the discharged fuel. A ^{235}U -fueled PTLWR exhibits about 10% lower conversion ratio than the typical ^{235}U -fueled LWR. This conversion ratio is significantly decreased if ^{235}U is replaced by ^{239}Pu , due to the higher fission and absorption cross section of ^{239}Pu . MCNP calculations using a one-channel model for the infinite lattice of the reference PTLWR design showed that the ratio of the neutron capture rate in ^{238}U to the neutron absorption rate in ^{239}Pu , $(\Sigma_c^{28}\Phi)/(\Sigma_a^{29}\Phi)$, which is a good measure of conversion ratio, is about 40% less than the ratio

$(\Sigma_c^{28} \Phi) / (\Sigma_a^{25} \Phi)$ for the ^{235}U -fueled core. Comparing the former ratio with that of a Pu-fueled PWR, The PTLWR value is about 15% less, and hence it is expected that the conversion ratio of the Pu-fueled PTLWR will be less than for the Pu-fueled LWR.

Possibility of Separate Pure Pu and Uranium Dioxide Particles.

MOX fuel using separated plutonium is more expensive than for low-enriched uranium fuel (\$1300-\$1600/kgHM compared to \$1000/kgHM). Therefore there is no strong economic incentive to use MOX. Particles with Pu fuel may be manufactured solely from ^{239}Pu , and mixed with particles separately manufactured solely from natural uranium or uranium tailings, thus avoiding the manufacture of mixed oxides. This may reduce cost (assuming that the cost of producing MOX is larger than the cost of producing UO_2 and PuO_2 separately). However, separation of fissile ^{239}Pu from ^{238}U leads to an undesirable increase of the time constant for the Doppler effect. This problem may be alleviated by mixing ^{239}Pu with erbium or other resonance absorbers.

4.4.10 Summary

The proposed new type of pressure tube reactor with light water coolant and a significant volume fraction of void in the calandria exhibits certain unique reactor physics characteristics. It has been shown that the key factor distinguishing this reactor from the other reactor types is an extremely large neutron migration area which significantly increases the neutronic core coupling, the stability against xenon spatial oscillations, and the flatness of the thermal flux profile.

The feasibility of the proposed reference PTLWR design from the reactor physics perspective has been confirmed. The reference design satisfies the objective of achieving an inherent shutdown in accidents leading to a large core temperature increase by virtue of its strong negative Doppler coefficient and the negative coolant void coefficient. The advantages of the reference PTLWR design include the tight neutronic core coupling, inherent stability against xenon spatial oscillations, no possibility of local criticality, very long prompt neutron lifetime, inherently flat thermal flux

profile, and high attainable discharge burnups. The main disadvantages are high absolute levels of both the fast and thermal fluxes, which result in high fast fluence on the pressure tubes, and difficulties with xenon override. The reactor's less efficient neutron economy requires relatively high initial enrichment, which increases power ripples in the fresh fuel bundles inserted into the core during on-line refueling. It has been confirmed that a suitable on-line refueling scheme can reduce these power ripples to relatively low levels.

A unique feature of the dry calandria design is the flooding of the calandria space with light water following the loss of coolant or loss of heat sink accidents. Extensive study of reactivity behavior during these processes, as well as in case of inadvertent flooding, showed that the reactivity introduced into the system will always lead to reactor shutdown, and the PTLWR design will not exhibit reactivity excursions.

Using the proposed PTLWR design for weapons-grade plutonium burning has also been considered. The brief assessment of physics aspects of a Pu-fueled PTLWR suggests that this reactor concept may be a good candidate for burning weapons-grade plutonium.

The reference PTLWR design with coated particle fuel is by no means the only alternative for a dry calandria design. In future work, it is desirable to decrease fast fluence on the pressure tubes, and to decrease neutron parasitic losses, and power ripples when inserting fresh fuel bundles. All these parameters can be significantly improved by increasing heavy metal loading in the fuel channel. Other fuel alternatives to accomplish this purpose are explored in the next chapter. The fuel arrangement with two rings of fuel pins with silicon carbide cladding will be identified as an attractive design in this respect.

Chapter 5

FUEL MATRIX CONCEPTS

5.1 INTRODUCTION

The achievement of the key objective, i.e., surviving the loss of coolant accident without replenishment of primary coolant by a large power reactor, requires significant changes in the core geometry and in the fuel compared to a typical LWR core. The rationale behind this goal, presented in Chapter 2, identified the main core characteristics which lead to a large passive pressure tube LWR. The major changes introduced in Chapter 2 include modularity of the fuel, replacement of traditional LWR pins by a matrix fuel with high thermal conductivity, increase of maximum temperature limit of the cladding, and improvements in the heat storage capability of the fuel zone. Except for the fuel modularity, which is achieved by using pressure tubes dispersed in a heat sink, all other changes apply to the fuel itself. Hence, the fuel matrix* is a critical component of the proposed design which deserves special attention. This Chapter will focus on the evolution and evaluation of the various fuel configurations considered, which have the potential to satisfy this objective.

To judge the suitability of a fuel matrix design, many factors need to be taken into account. Key factors in the areas of reactor physics, materials compatibility, thermal hydraulics, and performance under accident

* There are two basic types of fuel arrangement within a pressure tube. The first type consists of cladded fuel pins which are surrounded by coolant but do not employ any solid matrix, i.e., CANDU-like bundle-type fuel. The second type uses a solid matrix which contains the fuel and coolant channels. The fuel can be either in the form of fuel pins, fuel compacts or dispersed fuel in the form of small particles. The terminology "fuel matrix" or "fuel arrangement" will refer to both types of fuel and will be used interchangeably throughout this Chapter.

conditions will be summarized in Section 5.2. Several potential candidates for fuel configurations which can satisfy the given objective are proposed and evaluated in Section 5.3. At this stage the evaluation is more of a qualitative character rather than a detailed quantitative evaluation. The advantages and drawbacks of individual fuel arrangements are pointed out and the reference fuel matrix design is selected.

5.2 BASIC FACTORS INFLUENCING THE SUITABILITY OF MATRIX DESIGN

The fuel arrangement within a pressure tube affects a broad spectrum of core characteristics relating to performance during normal operation as well as during accidents. It is essential that the fuel matrix parameters are chosen such that the reactor remains within the prescribed safety limits under all conditions. It is also desirable that the fuel matrix is designed to be economically competitive with current LWR fuel and to allow good uranium utilization. Basic factors having an impact on safety limits and economic aspects of the fuel matrix design can be divided into four categories:

- reactor physics,
- thermohydraulics during normal operation,
- thermohydraulics during LOCA (without coolant), and
- materials compatibility during normal operation and during accidents.

Major factors and the design parameters influencing these factors for each category are summarized in Table 5-1.

5.2.1 Reactor Physics Factors of Merit

It is essential from the safety point of view that the Doppler coefficient is negative and prompt. All thermal reactors with low-enriched UO_2 fuel have a negative Doppler coefficient. The magnitude of the Doppler coefficient depends on nuclear characteristics of the fuel, primarily the initial enrichment and fuel burnup. Lower initial enrichment and higher burnup make the Doppler coefficient more negative due to the higher concentration

Table 5-1 Key factors and parameters influencing the suitability of a matrix design

Reactor physics	
Desired factor	Fuel matrix design parameters
Negative and prompt Doppler coefficient	<ul style="list-style-type: none"> • nuclear characteristics of the fuel • moderator/fuel volume ratio • arrangement of fissile/fertile material • fuel temperature
Negative void coefficient	<ul style="list-style-type: none"> • moderator/fuel volume ratio • nuclear characteristics of the fuel (e.g. enrichment, Pu content etc.) • leakage
High reactivity for a given enrichment	<ul style="list-style-type: none"> • moderator/fuel volume ratio • parasitic losses
Low fast fluence	<ul style="list-style-type: none"> • fuel loading • neutron spectrum
High burnup	<ul style="list-style-type: none"> • initial enrichment • conversion ratio • mechanical limits
Thermohydraulics during normal operation	
Desired factor	Fuel matrix design parameters
Satisfy MDNBR or MCPR	<ul style="list-style-type: none"> • heat transfer surface • heat flux profile (peaking) • heat transfer coefficient • coolant quality • coolant mass flux
Small fuel channel pressure drop	<ul style="list-style-type: none"> • flow area • hydraulic diameter • coolant mass flux • form losses and surface treatment • coolant quality

Table 5-1 (continued)

Desired factor	Fuel matrix design parameters
Low centerline fuel temperature	<ul style="list-style-type: none"> • path length between fuel center and coolant • heat flux profile • fuel and matrix thermal conductivity • contact resistance between fuel and matrix • heat transfer coefficient
Thermohydraulics during LOCA	
Desired factor	Fuel matrix design parameters
Low fuel centerline temperature	<ul style="list-style-type: none"> • matrix and fuel thermal conductivity • matrix emissivity • contact resistance between matrix and pressure tube • length of conduction path • large heat capacity • low linear decay heat rate
Low temperature of matrix/steam interface	<ul style="list-style-type: none"> • matrix and fuel thermal conductivity • matrix emissivity • contact resistance between matrix and pressure tube • length of conduction path • large heat capacity • low linear decay heat rate
Materials compatibility during normal operation and during accidents	
Desired factor	Fuel matrix design parameters
Long-term corrosion resistance in light water coolant	<ul style="list-style-type: none"> • temperature • coolant chemistry • coolant velocity • matrix material

Table 5-1 (continued)

Desired factor	Fuel matrix design parameters
Short-term resistance in steam/air mixture at high temperature	<ul style="list-style-type: none"> •matrix material •steam/matrix interface temperature
Irradiation stability	<ul style="list-style-type: none"> •matrix material •fast fluence
No water-material reaction	<ul style="list-style-type: none"> •matrix material •steam/matrix interface temperature
Structural integrity	<ul style="list-style-type: none"> •temperature gradient •matrix temperature •material properties •load

of fertile isotopes. Also, the neutron spectrum, which depends on the moderator/fuel volume ratio, affects the Doppler coefficient by changing absorption rates in the resonances of fertile isotopes, primarily of ^{238}U and ^{240}Pu . The arrangement of the fertile material with respect to fissile material affects the speed with which the negative component of the Doppler coefficient responds. If fissile isotopes (which have a positive Doppler coefficient) are mixed with the fertile isotopes, as in low-enriched UO_2 fuel, the response of the fertile Doppler coefficient is prompt, as the heat generated in the fissile material is transferred almost immediately into the fertile material. Separation of fissile and fertile isotopes increases the time constant for heat transfer between fissile and fertile material, and hence delays the negative Doppler response time. Such a situation may arise in a matrix using particle fuel with particles of highly enriched fissile material and separate particles containing fertile material, as had been suggested as one possibility in a Pu-burning version of a PTLWR (see Section 4.4.9). All matrices under consideration here use a low-enriched fissile/fertile mixture fuel to avoid this problem. Low fuel temperature makes the Doppler coefficient more negative since the resonance broadening is more pronounced at sharp peaks corresponding to low temperatures. Low fuel temperatures can be achieved by a matrix design

with short conduction paths between coolant and fuel, and good thermal conductivity of the fuel matrix.

CANDU reactors have successfully operated with a slightly positive void coefficient, but this requires reliable function of shutdown systems – a feature not consistent with the objective of completely passive shutdown in accidents leading to temperature excursions, as stated in Chapter 1. Hence, one of the key goals for the fuel matrix design is the achievement of a negative void reactivity coefficient. The main design parameter responsible for the magnitude and sign of the void coefficient is moderator/fuel volume ratio. Hence, the fuel loading and the amount of coolant inside the fuel channel must be adjusted such that the void coefficient remains negative for all operating conditions. Void coefficient is also affected by nuclear characteristics of the fuel. For natural uranium fuel, or fuel with very low enrichment, the void coefficient can be positive because the decrease of fission rate in ^{235}U upon spectrum hardening is small. Generally in LWRs, a higher content of ^{239}Pu hardens the neutron spectrum, which leads to an increase in resonance absorption in ^{238}U and ^{239}Pu , and a decrease in fission to capture ratio in ^{239}Pu , and hence to a more negative void coefficient. PWRs use soluble boron in the coolant to compensate for the reactivity decrease with burnup. As the concentration of the soluble boron decreases with increasing burnup, the void coefficient becomes more negative. Eliminating soluble boron in the dry calandria design avoids this additional change of void coefficient with burnup and gives the designer more freedom in optimizing the design. High leakage makes the void coefficient more negative. The proposed design has a high-leakage core. Since leakage is primarily a consequence of the voided space in the calandria, changes in fuel arrangement inside the pressure tubes will have a small effect on this aspect.

A well-optimized fuel matrix should achieve high reactivity at low enrichment while keeping void coefficient negative. In the dry calandria

design* this is achieved by adjusting the fuel loading and the amount of coolant inside the fuel channel. The disadvantage of the dry calandria design is the limited space in the fuel channel. Consequently, it is very difficult to optimize the design for high fuel loading, where more moderator is needed. A wet calandria design offers an advantage of providing separate light water moderator outside the fuel channel, thus allowing the designer to better optimize the design, especially for high fuel loadings.

Low fast fluence is an important factor in pressure tube reactors because high fluence shortens the lifetime of the pressure tubes. Two main parameters decrease the fast fluence – high fuel loading and a well thermalized neutron spectrum. It is desirable to maximize the fuel loading. However, the limited space inside the pressure tubes restricts this effort. Especially, the introduction of a solid matrix significantly reduces the space left for the fuel. Use of particle fuel exacerbates this problem even more because of the low loading densities achievable with particle fuels. The proposed light water moderated reactor has a relatively well thermalized spectrum. Better thermalization can be achieved by higher moderator/fuel ratio. It is noted, however, that the best one can do with light water moderator is to achieve thermalization comparable to a CANDU heavy water moderated lattice, hence the potential to lower fast fluence through neutron spectrum thermalization is limited. The option of maximizing fuel loading is more promising. Several matrix alternatives which strive for higher fuel loading will be listed in Section 5.3.

Higher initial enrichment increases burnup, but leads to larger power peaking, and hence reduction of thermohydraulic margins. Given the fixed initial enrichment, burnup can be also increased by improving neutron economy, i.e., by decreasing the parasitic losses. Within the fuel matrix domain, neutron economy can be improved by use of low-absorption matrix material and high fuel loading to increase the fraction of neutrons absorbed

* The dry calandria design is defined in this chapter as a reactor having fuel channels with fuel matrix and coolant/moderator inside the channel and no moderator outside the channels. Note that this is a more restricted definition than that introduced in Section 4.4.1.

in the fuel. The conversion ratio for a given fuel depends primarily on neutron spectrum and parasitic losses. A fuel arrangement with a harder neutron spectrum increases resonance absorption in fertile material, but also requires higher enrichment than for a thermal spectrum. Burnup in conventional LWR fuel pins is also restricted by mechanical limits from pellet-cladding interaction (PCI) mechanisms. This limit can be significantly increased by the use of the particle fuel typical of HTGRs.

5.2.2 Thermohydraulics during Normal Operation

The Minimum Departure from Nucleate Boiling Ratio (MDNBR) and the Minimum Critical Power Ratio (MCPR) are very important design limits for PWRs and BWRs, respectively. To increase margins to these limits, the fuel matrix arrangement should have a large heat transfer surface exposed to coolant, high heat transfer coefficient, low coolant quality and high mass flux. The heat transfer coefficient can be enhanced by decreasing hydraulic diameter, decreasing flow area, and thus increasing mass flux or by surface treatment to break up the boundary layer and to promote turbulence. Coolant quality is a function of the total mass flow rate and core power and should be about the same for all channels if they are well orificed. Within the fuel channel, the matrix design must avoid large nonuniformities in coolant quality among individual channels, especially if the coolant channels do not communicate with each other. Coolant mass flux not only affects critical heat flux ratios through the heat transfer coefficient, but also through a critical heat flux correlation, since critical heat flux is typically proportional to mass flux. Decreased power peaking increases MDNBR. The axial shape of the heat flux profile is also important. CHF margins can be significantly improved if the axial shape of the heat flux corresponds to the shape of the critical heat flux. It will be shown in Section 6.5.2 that such a correspondence can be achieved with a reference matrix design using the usual CANDU bi-directional refueling scheme.

Small pressure drop favors large flow area, large hydraulic diameter, low form losses, smooth surface, small coolant mass flux and one-phase flow. Unfortunately, all of these tactics lead to reduction of heat transfer

and of critical heat flux margins, hence a compromise between the pressure drop and heat transfer performance must be found. The approach adopted in this work is to set the maximum limit on fuel-channel pressure drop equal to that of the CE-CANDU reference design, and to maximize heat transfer capabilities by changing the design parameters of the fuel matrix.

Low fuel centerline temperature brings three advantages. It decreases the energy stored in the fuel matrix, which when released during LOCA results in lower temperatures of the matrix/steam interface (or cladding in case of a configuration with fuel pins). Secondly, a large difference between the operating fuel temperature and the maximum limiting fuel temperature provides a heat sink for energy storage during loss of coolant accidents, thus allowing more time to establish a permanent decay heat removal path. Finally, for arrangements with clad fuel pins, operation at low fuel centerline temperature releases less gaseous fission products and alleviates mechanical interaction between fuel pellets and cladding. Fuel centerline temperature can be decreased by employing a matrix arrangement with a small path length between fuel center and coolant, using matrix material and fuel with high thermal conductivity, increasing the heat transfer coefficient between the coolant and the matrix, and decreasing the contact resistance between the fuel and the matrix (or between fuel pellets and cladding, for fuel pins). Lowering the peaking factor can significantly decrease the maximum fuel temperature. In the dry calandria design, peaking arises primarily from the higher content of fissile isotopes in fresh fuel bundles, and is controlled by on-line refueling. The matrix design can improve peaking by maximizing fuel loading. High fuel loading increases the fraction of neutrons absorbed in the fuel, which results in a lower initial enrichment requirement, and hence lower fission rates in fresh fuel elements.

5.2.3 Thermohydraulics during LOCA

There are two key constraints for the fuel matrix in loss of coolant accidents – the temperature of the fuel and the temperature of the matrix/steam interface (or cladding, for fuel pin alternatives) must remain below the prescribed limits. Several variables are involved with respect to

these temperatures. Similarly as mentioned in Section 5.2.2, it is desirable that the matrix and fuel have high thermal conductivity and a short conduction path length. However, the conduction path is different than during normal operation because the heat sink is no longer coolant, but the pressure tube wall. A large heat capacity of the matrix decreases maximum matrix and fuel temperatures since it stores excess energy at less temperature rise. Important parameters are the matrix emissivity and the contact resistance between the matrix and the pressure tube. Since the matrix needs to slide through pressure tube to allow on-line refueling, a gap between the matrix and the pressure tube is necessary. The primary heat transfer mode between the matrix and the pressure tube is radiation, which achieves relatively low rates. Therefore, the gap represents the primary heat transfer resistance to heat flow and strongly affects the matrix temperature. Improvements in heat transfer across this region can be achieved by using matrix material with high emissivity, and sliding pads with good contact conductance. The dry calandria design with calandria flooding has another unique feature which decreases matrix temperature during LOCA accidents by reducing the linear decay heat rate upon flooding. The large mass of flooding water in the calandria absorbs a significant portion of the gamma rays emitted by the fuel, thus decreasing the heat load on the fuel matrix.

5.2.4 Materials Compatibility during Normal Operation and during Accidents

Materials compatibility issues for the fuel matrix have been discussed thoroughly in [Hejzlar et. al., 1993] and summarized in Chapter 3. Key matrix design parameters to strive for are low matrix/steam interface temperature during LOCA, low fluence, and compatible matrix material. Silicon carbide or graphite coated with silicon carbide have been identified as the most promising candidates. In addition to the requirements on the matrix material reviewed in Chapter 3, the structural integrity of the fuel matrix must be ensured. Maintenance of this integrity depends on mechanical and thermal properties of the material, temperature gradient, matrix temperature and the load. For a matrix with coolant holes, a minimum web thickness needs to be preserved to maintain the structural

strength. This additional constraint poses a challenge to matrix design because of the limited space provided within the pressure tube, especially if a high fuel loading is desired.

5.3 PROPOSED DRY CALANDRIA FUEL MATRIX DESIGNS

The review presented in Section 5.2 shows that the requirements are many and the parameters affecting these factors are closely interrelated. Moreover, many requirements are contradictory so that all cannot be satisfied. Hence a compromise needs to be made. This section will describe several fuel matrix configurations proposed for the dry calandria design and point out their advantages and drawbacks. Except for the reference design, these matrix configurations have not been evaluated in detail; they represent ideas worthy of exploring in the future.

Figure 5-1 shows a flow chart for various combinations of fuel arrangement in a fuel channel of the proposed passive pressure tube LWR concept. There are two main categories – a bundle-type fuel arrangement and a matrix-type fuel arrangement. The bundle-type fuel uses the same geometry as CANDU fuel elements, with fuel pins surrounded by coolant, while the matrix-type fuel employs a matrix with separate coolant channels. Both fuel types can use either particle fuel or a traditional fuel pin configuration. Five fuel configurations, labeled DC-1 through DC-5 are interesting concepts appropriate for the dry calandria design, and will be described next. Matrix-type fuels with UO₂ fuel pins are more appropriate for the wet calandria design.

5.3.1 DC-1 – A Two-ring Design with TRISO Particle Fuel in an SiC Tube

The configuration of the two-ring design with TRISO particle fuel is shown in Figure 5-2. The fuel arrangement in a pressure tube is the same as in typical CANDU fuel channels, except for the center fuel rod and the inner ring which are replaced by an SiC-coated graphite cylinder. The two-ring arrangement shortens the heat transfer path between the centermost fuel rod and the heat sink (pressure tube wall) in case all coolant is lost, which leads to a significant decrease in maximum cladding temperature.

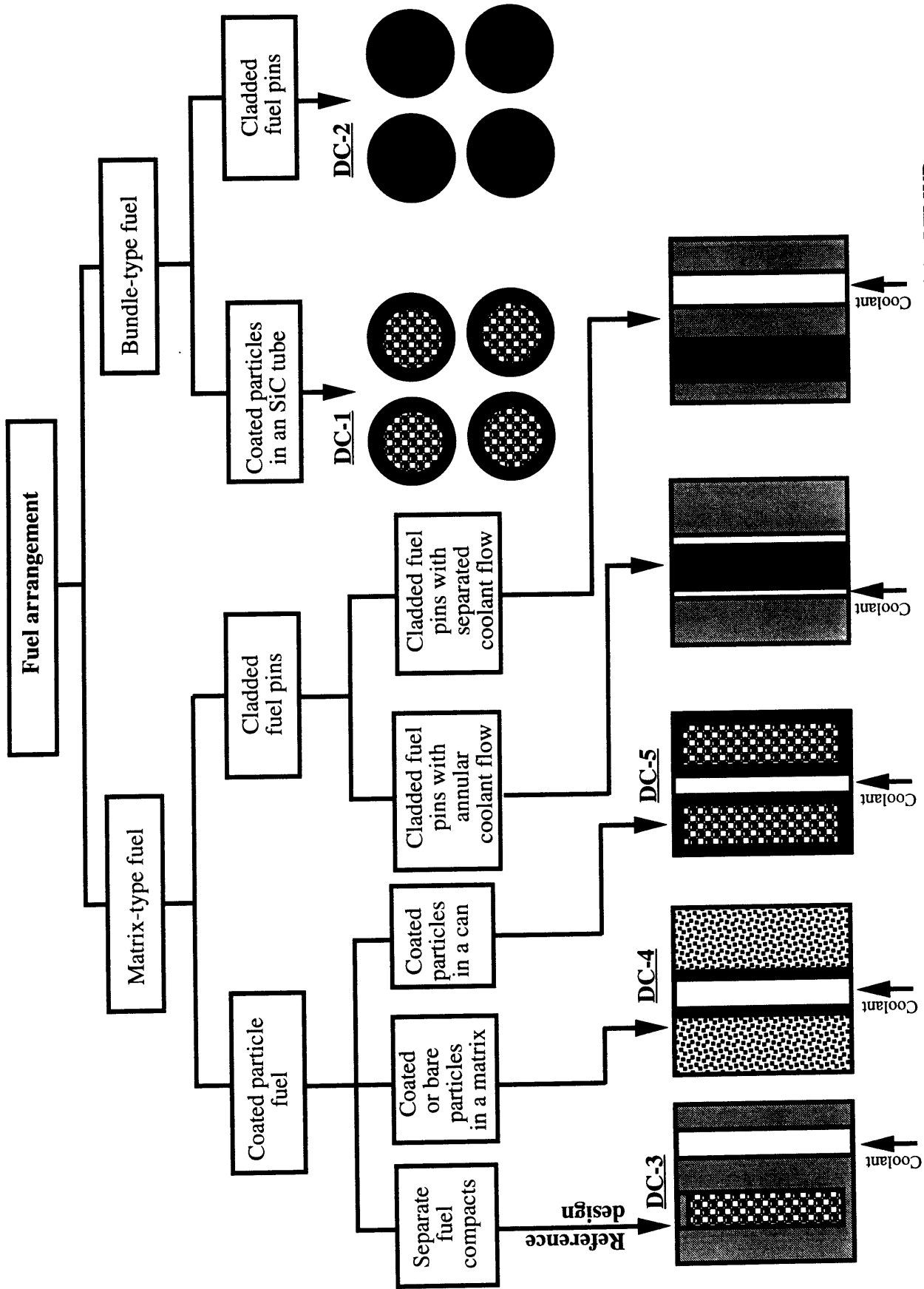
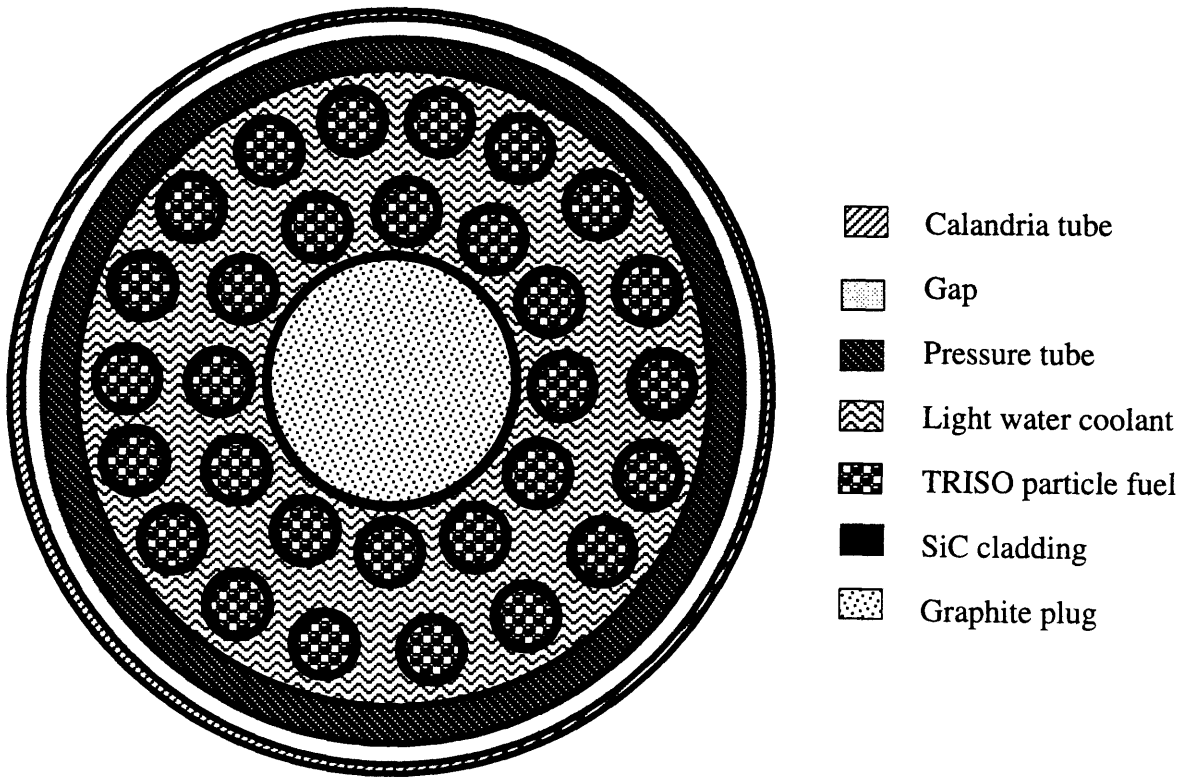


Figure 5-1 Flow chart for various combinations of fuel arrangement in a fuel channel of the PTLWR

Fuel Arrangement DC-1



Advantages	Disadvantages
<ul style="list-style-type: none"> •uses technology developed in UK for CO₂ cooled reactors and which was extensively tested and showed good performance •uses the same fuel bundle geometry as CANDU, hence the thermohydraulics is the same •flatter power density profile allows recovery of power lost by removing inner fuel rods; there is a potential to operate at even higher power rating •high fuel thermal conductivity, hence low operating fuel temperature and low stored energy 	<ul style="list-style-type: none"> •low heavy metal loading, hence high fluence on pressure tube (but less than for matrix-type fuels with particles) •low heat removal rates from voided bundles •low heat storage capability, hence the temperature of the matrix and pressure tube may get too high before the upper row is flooded

Figure 5-2 DC-1 – A two-ring design with TRISO particle fuel in a silicon carbide tube

The purpose of the graphite cylinder is to displace the coolant flow into the fuel region during normal operation. During LOCA accidents, it acts as a temporary heat sink by storing part of the energy radiated from the inner ring. This additional heat sink in close proximity to the inner ring also helps to reduce the temperature of the SiC cladding. The idea of removing the innermost fuel pins in a CANDU fuel element is not new. AECL researchers proposed to replace innermost fuel pins by a large diameter tube either voided or filled with scattering material such as graphite, beryllium or heavy water [Roshd et. al., 1977]. The purpose of such a modification was to reduce the positive coolant void coefficient, because the most important factors contributing to a positive change in reactivity – an increase in fast fission rate and a decrease in the resonance absorption rate in ^{238}U are the largest for central fuel pins. The motivation behind the two ring fuel arrangement in the present work is the reduction of maximum cladding temperature rather than the achievement of negative void coefficient, since the proposed PTLWR design with light water coolant does not have a positive void effect. The disadvantage of this approach is the slight reduction in bundle average power. This reduction can be recovered, however, due to the smaller peaking factor in the PTLWR compared to that of CANDU.

Use of a silicon carbide tube instead of Zircaloy cladding allows one to increase the temperature limit which can be withstood by cladding in LOCAs without damage. Fuel is in the form of TRISO particles bound in graphite, in the form of compacts placed in a silicon carbide tube. A similar type of fuel (the only difference was that the fuel was coated only by pyrolytic carbon) has been tested by British investigators for HTGR application with very good results [Kennedy and Shennan, 1974]. Their packed bed of coated particles, lightly bonded, and contained in a silicon carbide tube operated successfully at temperatures of 1100°C in a CO_2 -cooled reactor. Large-scale production of SiC cladding has been also successfully demonstrated [Kennedy and Shennan, 1974]. The advantage of the particle fuel is its good thermal conductivity, and hence low fuel centerline temperature and low stored energy. This further improves fuel performance in a LOCA.

Figure 5-3 shows the void coefficient calculated for the design with 30 fuel pins of the same dimensions and same geometrical layout as the two outer rings in CANDU bundles. The calculation was performed with particle data given in Section 3.5, for a fresh core with initial enrichment of 2%, an infinite lattice in the radial direction, and an axial graphite reflector. It can be observed that the proposed two ring design with TRISO particle fuel has a negative void coefficient, and that the operating point is close to the optimum.

The power density profile for the fresh core is quite flat. The axial power density distribution for the fresh core is shown on Figure 5-4. The axial peaking factor for the fresh core with uniform fuel composition is only about 1.18. Such a low peaking would allow a significant increase of the pin linear heat rate without exceeding the operating fuel centerline temperature limit of 1300 °C. Preliminary hand calculations suggest that the reactor has a potential of operating at 1800 MWe at a fuel centerline temperature of 1300 °C, keeping the same maximum pin linear heat rate as a CANDU. The problem for these high power ratings would be the necessity to significantly increase mass flow rate, and hence pressure drop. Also, for an equilibrium core with bi-directional refueling, the attendant higher power peaking would reduce the acceptable power rating. The increase of fast fluence with an increase of power rating must be also taken into account.

The disadvantage of a two-ring design with TRISO particle fuel is the high fast fluence on the pressure tube typical of the low heavy metal loading of particle fuel. However, it is noted that fast fluence for this fuel arrangement concept is less than the matrix-type design DC-3.

Regarding the thermohydraulic performance during normal operation, no problems are expected, since the main design parameters correspond to CE-CANDU. During LOCA, the heat from the fuel pins is removed by radiation, convection and conduction through bearing pads and spacers. These modes of heat transfer achieve modest heat rates compared to conductive heat transfer rates for a matrix-type fuel. Another drawback is the low heat storage capability of the fuel pins, which makes the design less resilient to late flooding than in the case of matrix-type fuel.

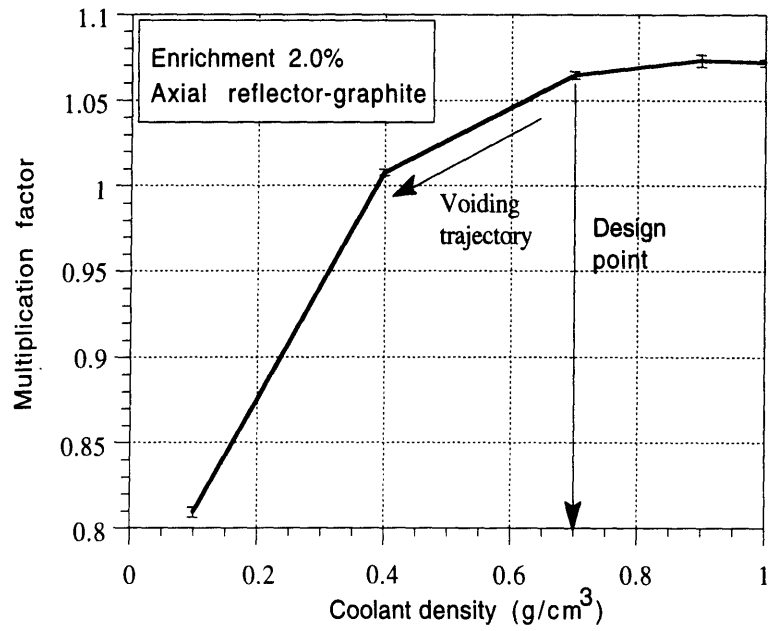


Figure 5-3 Effect of coolant voiding for the two-ring design with TRISO particle fuel

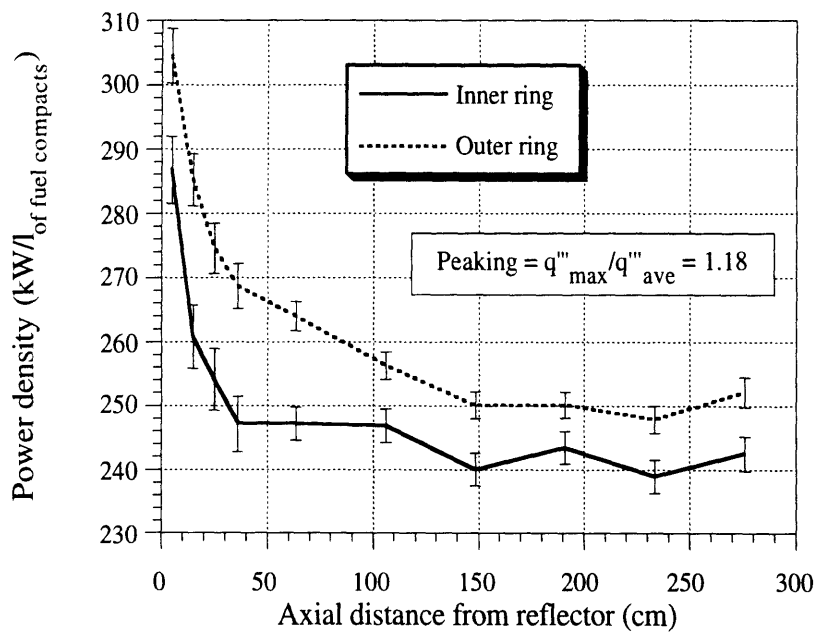


Figure 5-4 Axial power density profile for the two-ring design with TRISO particle fuel

A simplified transient model [Hejzlar et. al., 1991], based on radiative heat transfer between fuel rings and pressure tube, has been used to evaluate the maximum cladding temperature of the two-ring configuration in a loss of coolant accident without coolant replenishment. The code is conservative since it neglects convection, conduction through spacers and bearing pads and the energy carried away by coolant during blowdown. The cladding temperature traces for the inner and outer ring, as well as for the pressure tube are shown in Figure 5-5. The data used to generate Figure 5-5 assumed an average channel power which is the same as for the reference CE-CANDU design, a total peaking factor of 1.4 (higher than the previously calculated 1.18 to account for radial peaking and power ripples from bi-directional refueling), flooding time of 30 seconds, and 20% fraction of the decay heat generated directly in the flooding water. The results obtained suggest that the maximum cladding temperature does not exceed 1400°C. This temperature does not pose any problem for SiC cladding or for the fuel. The actual temperatures are expected to be lower due to the conservative assumptions outlined above. Hence, this proposed two ring design with TRISO particle fuel has very good potential to meet cooling requirements during loss of cooling accidents. Temperature profiles in the channel at various times are shown in Figure 5-6. The horizontal axis represents the radius of the fuel channel; the graphite plug is in the center (between 0 and 20mm) followed by two fuel rings and the pressure tube and the calandria tube at a coordinate of about 65mm. It can be observed that the fuel centerline temperature during operation (at time=0 seconds) is about 300°C below the operating limit of 1300°C for TRISO particle fuel and by about 800°C less than the fuel centerline temperature of the reference CE-CANDU design, even though the CANDU pins operate at an average linear heat rate 20% less than in this concept. This low temperature is due to the relatively high fuel thermal conductivity and low peaking.

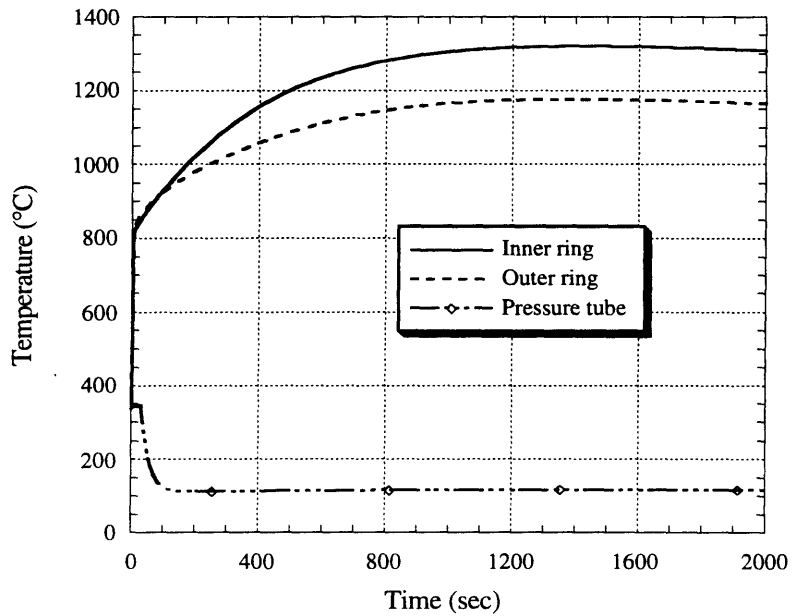


Figure 5-5 Cladding and pressure tube temperature histories following LOCA for the two-ring design with TRISO particle fuel

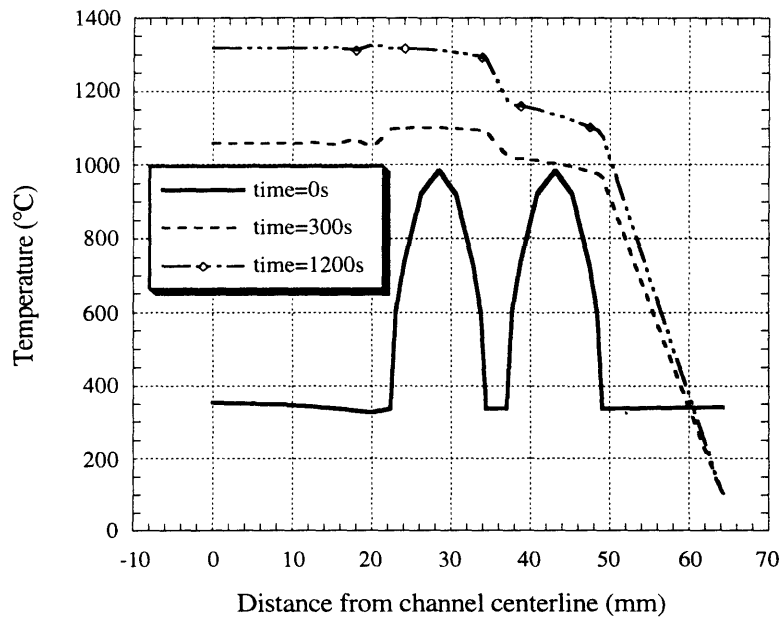


Figure 5-6 Temperature profile in a fuel channel following LOCA for the two-ring design with TRISO particle fuel

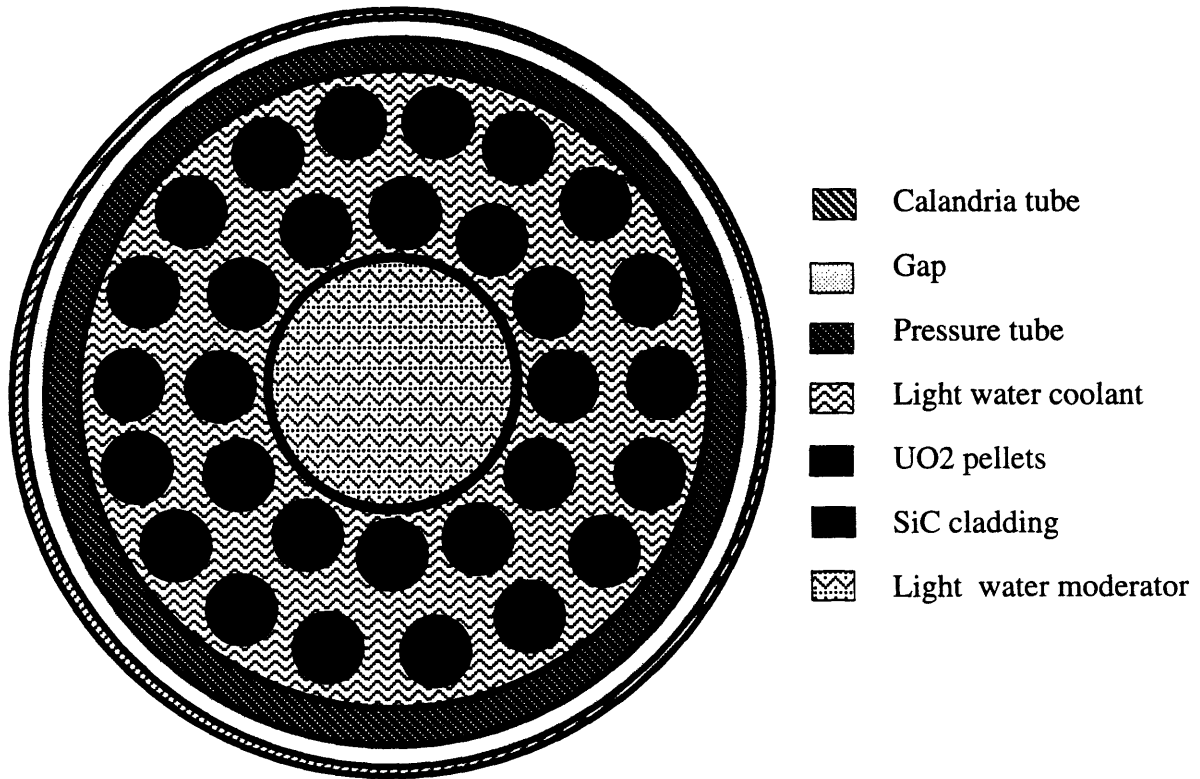
5.3.2 DC-2 – A Two-ring Design with SiC-Cladded UO₂ Fuel Pins

The configuration of the two-ring design with SiC-cladded UO₂ fuel pins is shown in Figure 5-7. The only differences from the DC-1 option are the replacement of particle fuel by traditional UO₂ pellets and use of light water instead of a solid graphite slug in the center. The main advantage of the fuel change is the significant increase (6 times) in heavy metal loading, and the consequent reduced fast fluence on the pressure tube. Increased heavy metal loading requires more moderation in the channel. This is accomplished by replacing the graphite slug in the center by a more efficient moderator – light water. To force sufficient flow into the fuel bundles, the central region of water moderator may be enclosed by a Zircaloy can (as shown on Figure 5-7) having small holes in its walls to provide sufficient flow to avoid boiling from gamma heating. In LOCA, the moderator escaping from the central region at a slow rate can provide additional cooling of the bundles.

SiC-clad UO₂ pellets were tested by British investigators, although only for modest power density [Kennedy and Shennan, 1974]. Fuel performance was found to be determined primarily by the ability of the silicon carbide tube to withstand stresses. To alleviate the stress on the SiC tube, interaction of the fuel pellets with the cladding from fission-product-induced swelling needs to be avoided. This may limit burnup to low values or require more research into how to design a conducting gap which would provide some free volume for fuel expansion without strong mechanical interaction with the cladding.

The effect of coolant voiding is shown on Figure 5-8. The calculation was performed with fuel pellet data given in Section 3.5, for a fresh core with initial enrichment of 1.5%, an infinite lattice in the radial direction, and an axial graphite reflector. The design exhibits a negative void coefficient, but the operating point is too far from the optimum peak. Shifting the operating point closer to the optimum cannot be achieved for the dry calandria design (unless the fuel is diluted) because there is no more space for the moderator inside the channel. Better optimization is, however, possible with a wet calandria design, which has additional

Fuel Arrangement DC-2



Advantages	Disadvantages
<ul style="list-style-type: none"> •uses technology tested in UK for CO₂ cooled reactors •uses the same fuel bundle geometry in the two outer fuel rings as CANDU, hence the thermohydraulics is the same •flatter power density profile allows recovery of power lost by removing inner fuel rods • high heavy metal loading, hence lower fast fluence than for matrix fuel •high conversion ratio 	<ul style="list-style-type: none"> •low thermal conductivity of fuel, hence high stored energy •PCI exerts stress on SiC clad and limits power rating and burnup •low heat removal rates from voided bundles •low heat storage capability, hence the temperature of the matrix and pressure tube may get too high before upper row is flooded

Figure 5-7 DC-2 – A two-ring design with SiC-clad UO₂ fuel pins

moderator outside the fuel channel. Operating the dry calandria design with a significantly undermoderated lattice requires more enrichment than would be needed for a better-optimized design. However, comparison of Figure 5-8 with Figure 5-3 shows that less enrichment in the undermoderated DC-2 design is needed than for the well-optimized design DC-1 to achieve about the same reactivity. This is due to the higher fraction of neutrons absorbed in the fuel in a high-loading DC-2 design. The DC-2 design will also exhibit a higher reactivity increase upon cold water ingress than the DC-1 design. On the other hand, the undermoderated DC-2 design will have a significantly higher conversion ratio. The ratio of captures in ^{238}U to absorption in ^{235}U , which is a measure of conversion ratio, is increased by 44% , as compared to the DC-1 design. This feature can be utilized in a high-converting version of the PTLWR by replacing the central H_2O moderator region with a solid graphite cylinder as in the DC-1 design. This modification hardens the neutron spectrum and increases the conversion ratio even further. Using this alternative and an enrichment of 2%, a conversion ratio of 0.93* was achieved. If UO_2 fuel pellets are replaced by UC fuel pellets with higher density, the conversion ratio is increased to 0.97. These are quite high conversion ratios at such low enrichments. Hence, this fuel arrangement has a good potential to achieve breeding by tightening the pitch of the fuel pins to squeeze out more water, and by increasing the enrichment to compensate for the reactivity decrease. The hardened spectrum, however, increases the fast fluence on the pressure tubes.

The axial power density profile for the fresh core with uniform enrichment is shown on Figure 5-9. Axial and radial peaking factors of the DC-2 design with UO_2 fuel pins are higher than for DC-1 (the axial peaking factor is higher by about 10%). Moreover, there is a difference in power generation in the inner and outer fuel rings because of the higher thermal

* Conversion ratios cited here were calculated for semi-infinite lattices (i.e., infinite in the radial direction, reflected in the axial direction) for the fresh fuel without xenon and no control rods.

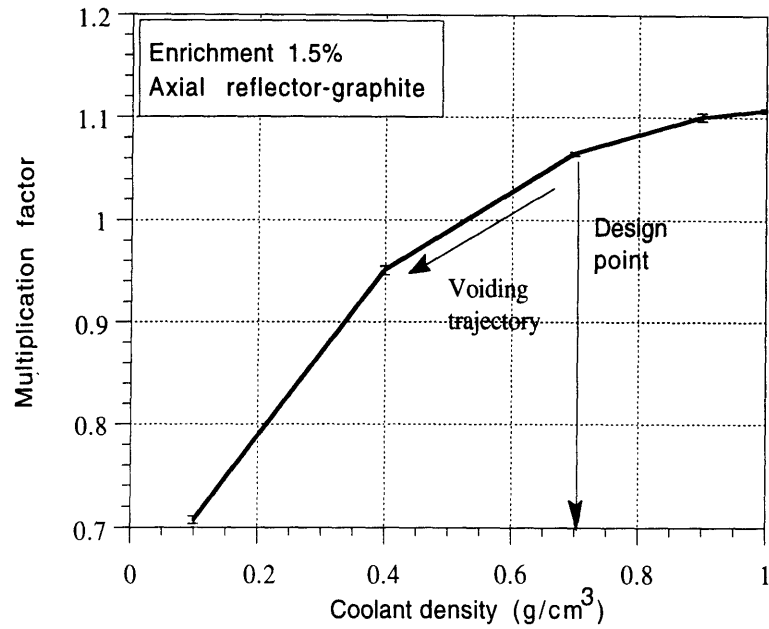


Figure 5-8 Effect of coolant voiding for the two-ring design with SiC-cladded UO_2 fuel pins

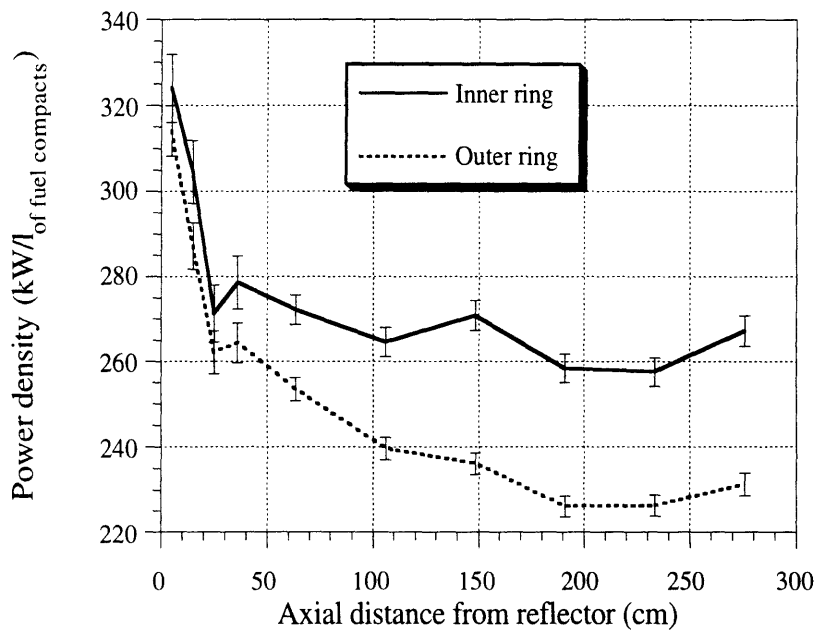


Figure 5-9 Axial power density profile for the two-ring design with SiC-cladded UO_2 fuel pins

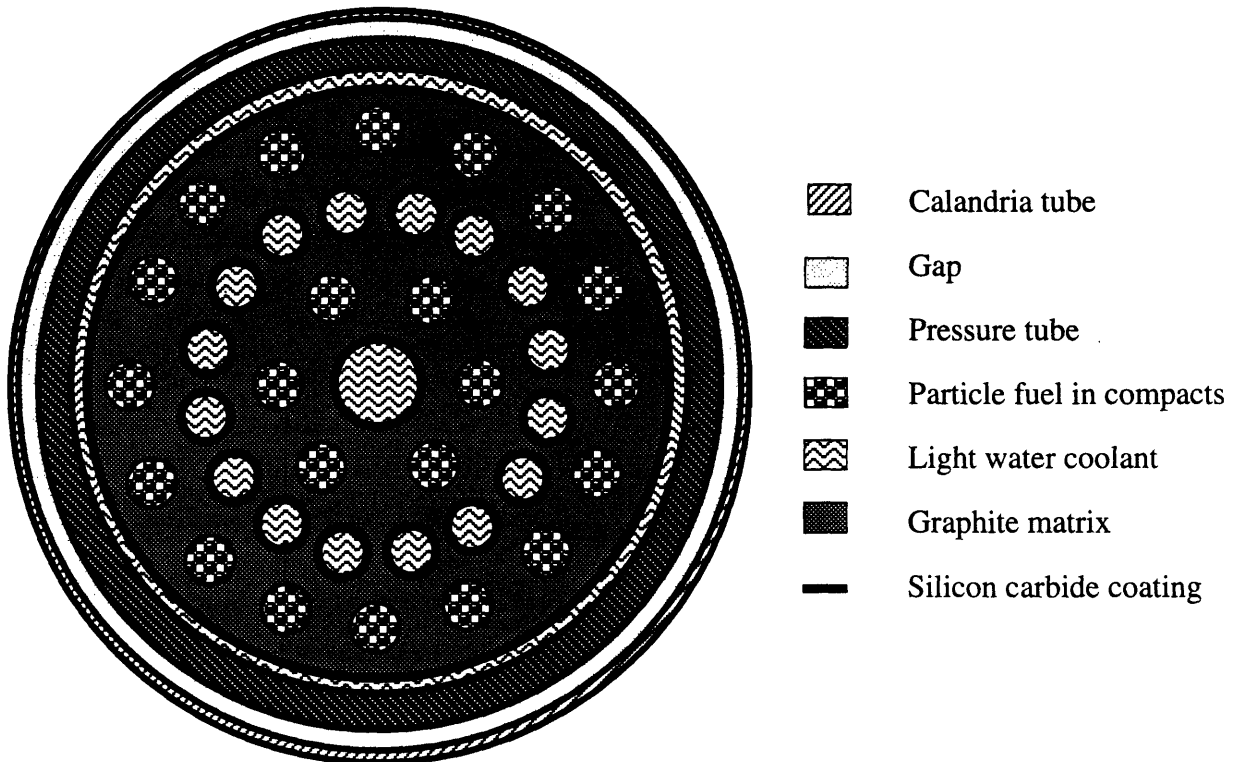
flux diffusing from the central moderator region into the inner ring. Peaking is still much less than in the CE-CANDU reference design, hence some uprating of fuel channel power, similarly as for the DC-1 design, would be possible. The disadvantage is the low thermal conductivity of UO_2 pins, which will result in a higher fuel centerline temperature and a larger stored energy than for the TRISO fuel. Problems with low heat storage capability and small heat removal rates from voided bundles discussed for the DC-1 version remain, but based on a preliminary calculation of the DC-1 design, it is expected that the DC-2 design can handle a LOCA without coolant replenishment as well.

5.3.3 DC-3 – A Fuel Matrix Design with Separate Fuel Compacts and Coolant Channels

The DC-3 fuel matrix design with separate fuel compacts and coolant channels is shown in Figure 5-10. The design makes use of the proven manufacturing technology developed for HTGR fuel elements [Melese and Katz, 1984]. Considerable experience has been accumulated with this type of fuel, albeit at different operating conditions and for a different environment than that experienced in the PTLWR. The fuel region consists of TRISO particle fuel in a graphite binder and pressed into prefabricated holes in a graphite matrix. An alternative technology uses a molded graphite block fuel element instead of a machined block. This allows one to press the fuel region together with the matrix, creating a monolithic fuel element with increased heavy metal loading. This technology, developed by HOBEG/NUKEM [Hrovat, 1978], also eliminates contact resistance between the fuel region and the matrix.

SiC-coated graphite has been selected as a matrix material. This selection was based on an extensive literature survey [Hejzlar et. al., 1993c] regarding the compatibility of matrix material with light water coolant during normal operation and with steam/air mixtures at the high temperatures reached during LOCA, as well as on good nuclear and thermal properties. The primary function of the silicon carbide coating is to provide protection against graphite oxidation at high temperatures in steam/air mixtures.

Matrix DC-3 – Reference Design



Advantages	Disadvantages
<ul style="list-style-type: none"> • uses proven manufacturing technology of MHTGR fuel or HOBEG molded blocks • has high thermal conductivity and storage capacity, hence very good performance during a LOCA accident • heterogeneous arrangement of fuel and coolant combined with voided space outside pressure tubes results in the longest prompt neutron lifetime, and flattest flux profile versus all other matrices 	<ul style="list-style-type: none"> • small number of fuel compacts results in relatively high linear heat rate • small heated perimeter, hence difficult to provide sufficient cooling during normal operation • small heavy metal loading results in high fast fluence on pressure tubes

Figure 5-10 DC-3 – A Fuel matrix design with separate fuel compacts and coolant channels

Since the DC-3 design has been chosen as a reference design, its physics and thermohydraulic performance is detailed throughout this volume. Reactor physics calculations showed that the DC-3 matrix design in a voided calandria exhibits a very well thermalized spectrum comparable to heavy water moderated lattices, long prompt neutron lifetime, negative void coefficient and flat thermal flux profile. The disadvantages include low heavy metal loading and hence large fast fluence on the pressure tubes, as well as relatively high parasitic losses and hence high initial enrichment to attain the high burnups achievable with particle fuel. The heavy metal loading in this design is even less than for the DC-1 design because the space available for fuel is decreased by the space taken up by the matrix.

Matrix thermohydraulic performance during normal operation poses a challenge to the designer for the following reasons:

- The total heated perimeter is small as a result of limited space inside the fuel channel. This leads to higher heat flux and lower CHF margins.
- The conduction path between the fuel centerline and coolant is relatively long. Compared to CANDU fuel pins, which are in direct contact with the coolant, in the DC-3 design the heat must also be transferred through the matrix, thus increasing the temperature difference between the coolant and the fuel.
- The small number of fuel compacts results in a high pin linear heat rate (at fixed total reactor power).

These drawbacks are compensated by smaller peaking factors in the PTLWR concept and by the high thermal conductivity of fuel compacts. Heat transfer to coolant is improved by increasing the mass flux. Such an increase can be afforded without compromising the pressure drop because the matrix does not need spacers, which are responsible for a significant portion of the pressure drop in bundle-type fuels.

Thermohydraulic performance of the DC-3 matrix design during LOCA is excellent because of the good thermal conductivity and high energy storage capabilities. The low mass of heavy metal compared to the mass of

flooding water in the calandria significantly decreases decay heat deposition by delayed gamma rays in the matrix (a portion of gamma heating is deposited directly in the flooding water) which also contributes to low matrix temperatures.

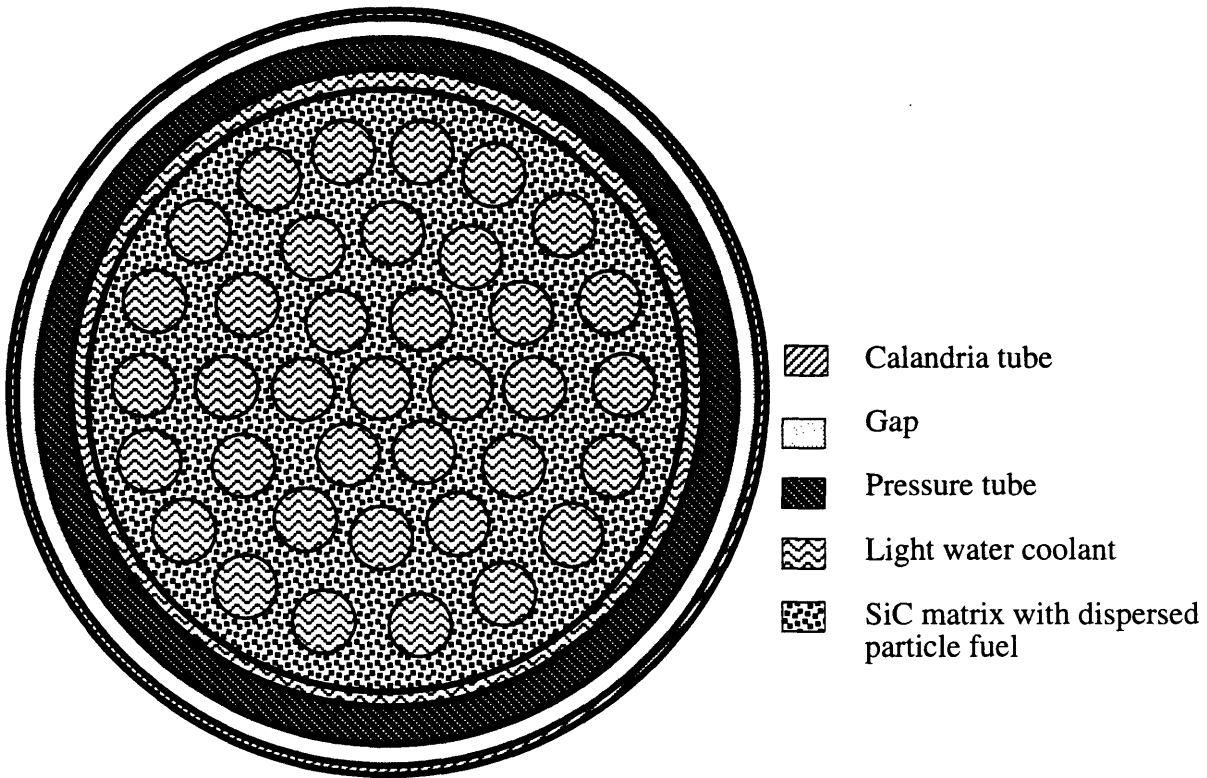
5.3.4 DC-4 – A Fuel Matrix Design with Particle Fuel Dispersed in a Matrix

A fuel matrix design with particle fuel dispersed in a matrix is shown in Figure 5-11. The design is based on the favorable experience with all-ceramic fuel developed by British investigators for use in the AGR [Kennedy and Shennan, 1974]. The fuel consisted of uranium carbide microspheres coated with pyrolytic carbon and dispersed in a self-bonded silicon carbide matrix. This fuel has been irradiated successfully at high surface temperatures (1250°C) up to burnups of 50,000 MWd/tonne without any release of fission products. However, the technology was developed for a pin-geometry matrix, i.e., the matrix did not contain coolant holes, therefore additional development for a more complex matrix geometry of larger diameter with coolant channels would be required.

Although no calculations for this type of fuel matrix have been performed, it is expected that there will be no problem to achieve a negative void coefficient and a good optimization for the operating point on the moderator/fuel volume ratio curve. Compared to the DC-3 design, heavy metal loading will be increased because of the larger fuel region volume and because of the smaller volume of the coating layers (only one PyC coating layer compared to four layers in TRISO particle fuel). Also, the density of uranium carbide is higher than that of uranium dioxide. Nevertheless, the high heavy metal loading typical of the reference CE-CANDU design cannot be achieved with the DC-4 design. The significant mass of silicon carbide in the fuel channel will require higher enrichment, since the absorption cross section for SiC is higher than that of graphite.

Thermohydraulic performance during normal operation exhibits improvement over the DC-3 design. The heated perimeter is increased, lowering the heat flux to the coolant, and improving the CHF margins. The enlarged flow area will result in a smaller pressure drop. Maximum fuel temperature is expected to be relatively low due to the small distance

Matrix DC-4



Advantages	Disadvantages
<ul style="list-style-type: none"> •uses technology developed in UK for CO₂ cooled reactors and which showed good fuel performance •high thermal conductivity and storage capacity, hence good performance during LOCA accident •large heated perimeter, hence easy to cool during normal operation - large DNBR •small distance between fuel and coolant, hence low operating fuel temperature 	<ul style="list-style-type: none"> •low heavy metal loading hence high fluence on pressure tube, •requires higher enrichment to overcome parasitic absorption in SiC •structural integrity of irradiated SiC matrix may be a problem due to decreased thermal conductivity and high thermal gradient during normal operation

Figure 5-11 DC-4 – A fuel matrix design with particle fuel dispersed in a matrix

between the fuel centerline and coolant, and due to the lower power density afforded by the large volume of the fuel region. Power peaking will be more pronounced in the fresh cores of the DC-4 design than in the DC-3 design, but it may be comparable for equilibrium cores if a proper refueling scheme is selected.

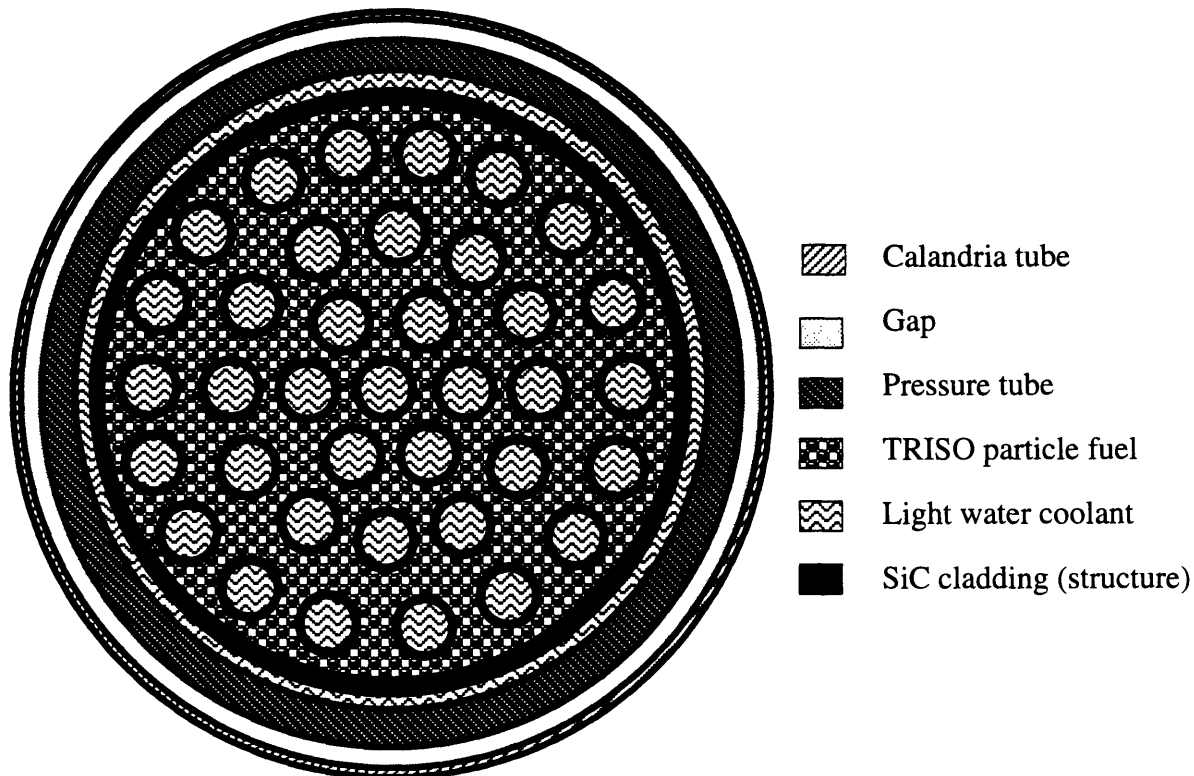
Significant degradation of the thermal conductivity of silicon carbide with irradiation may be a concern for this design because low conductivity increases thermal stresses in the matrix. An assessment of physical and mechanical property data in the British pin-matrix design indicated that thermal stresses would impose a limit on the nominal maximum power rating.

Matrix performance during a loss of coolant accident should not pose any difficulty due to its good storage capabilities and relatively good thermal conductivity. Note that the decreased thermal conductivity of irradiated SiC is still more than sufficient to dissipate the decay heat (several % of rated power) in a low temperature gradient, while a large temperature gradient is needed during normal operation to conduct full power to the coolant.

5.3.5 DC-5 – A Fuel Matrix Design with TRISO Particles Contained in an SiC Structure

The concept of a fuel matrix design with TRISO particle fuel in a silicon carbide structure is shown in Figure 5-12. The idea behind this concept is to alleviate the constraints on power rating imposed by thermal stresses in the silicon carbide matrix in the DC-4 design and to reduce parasitic neutron absorption in silicon carbide. The main principle is the same as for the particle fuel-in-a-SiC-tube design (DC-1), but the shape of the silicon carbide structure is much more complicated than for a simple tube. The structure has a cylindrical shape with bottom and extruded cylindrical walls which form coolant channels. The space between the channels is filled with packed bed of TRISO particles bonded by a graphite binder. The main disadvantage of the DC-5 concept is that it represents unproven technology, and it may be difficult to manufacture. It will be also difficult to ensure alignment of coolant channels between two neighboring fuel elements.

Matrix DC-5



Advantages	Disadvantages
<ul style="list-style-type: none"> •high thermal conductivity and storage capacity, hence very good performance during LOCA accident •large heated perimeter, hence easy to cool during normal operation - large DNBR •small distance between fuel and coolant and high thermal conductivity, hence low operating fuel temperature •higher heavy metal loading than for DC-4, hence lower fluence, also requires slightly less enrichment 	<ul style="list-style-type: none"> •non-proven fuel, may be difficult to manufacture •it will be difficult to ensure that SiC closure plugs remain tight during operation •difficult to provide good key&dowel coupling between two neighboring elements

Figure 5-12 DC-5 – A fuel matrix design with TRISO particle fuel contained in an SiC structure

Figure 5-13 shows the effect of coolant voiding on reactivity. The results obtained for the fresh core with uniform enrichment of 2.5%, particle data given in Section 3.5, infinite lattice in radial direction, and axial graphite reflector, and 37 coolant holes with diameter of 1.1cm, show that the void coefficient is negative. The operating point is close to the optimum. The thermal flux profile is relatively flat with slight peaking close to the reflector; the peaking factor is higher than in the DC-3 design. Heavy metal loading is increased as compared to the DC-3 design, but it still remains well below the CE-CANDU reference design. The neutron spectrum slightly hardens as can be observed from Figure 5-14, but the fast fluence on pressure tubes is decreased in the DC-5 design, primarily due to higher heavy metal loading. The harder spectrum results in a higher conversion ratio, hence less initial enrichment is required to achieve the same burnup as in the DC-3 design.

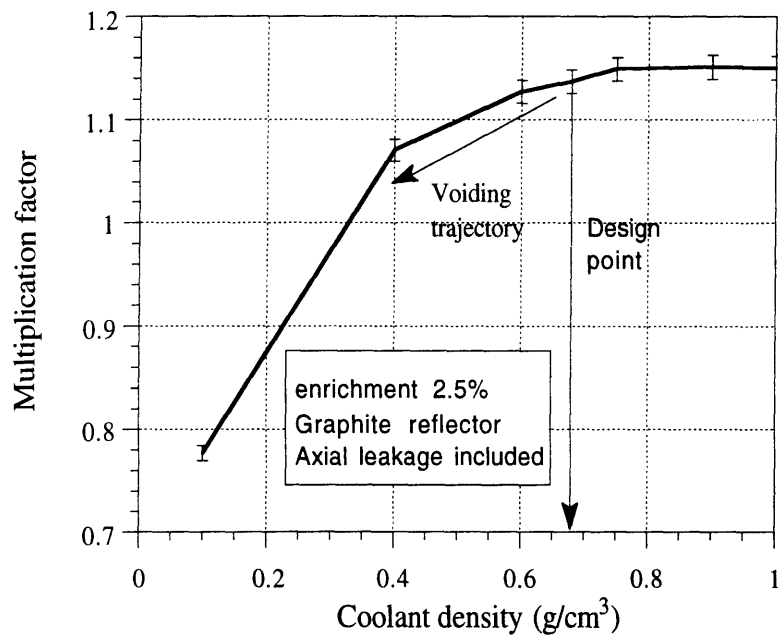


Figure 5-13 Effect of coolant voiding for matrix design with TRISO particle fuel in an SiC structure

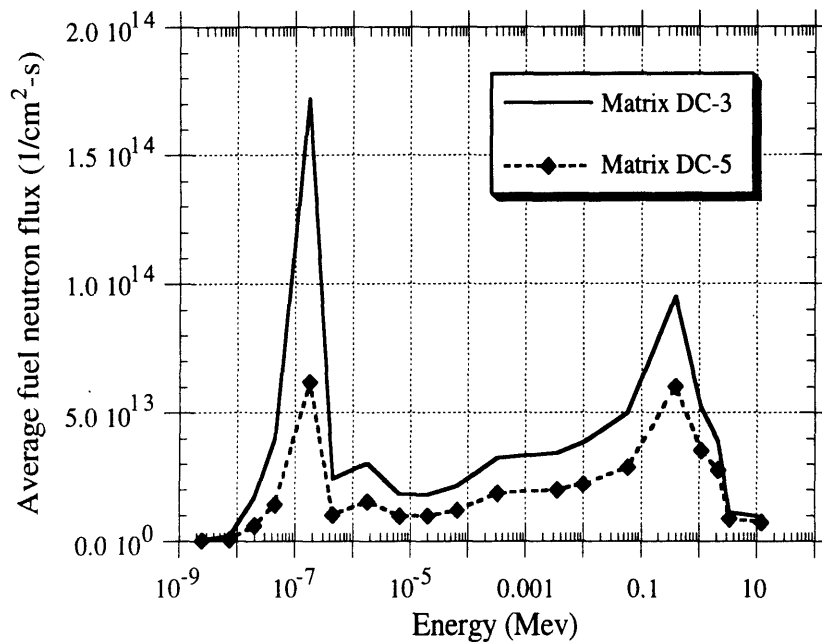


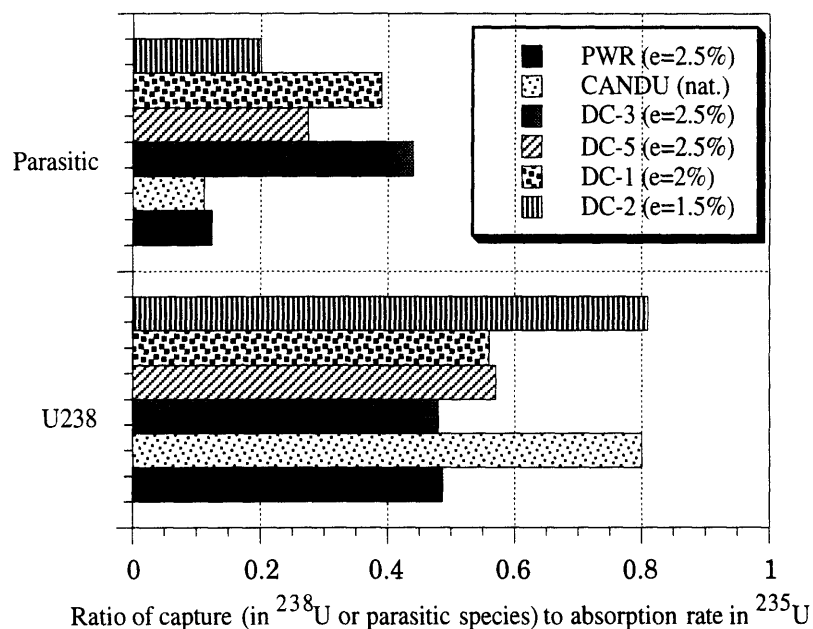
Figure 5-14 Comparison of neutron spectra for the DC-3 and DC-5 matrix designs

The thermohydraulic performance issues are similar to those discussed for the DC-4 design, since the arrangement of the fuel channels is the same. Because the thickness of the wall of the SiC structures is small and since the contribution of the fuel region/SiC structure interaction to stress is small due to the relatively low modulus and strength of the bonded particle bed (also fission gases are retained in the particles), the fuel can be run at higher power density than the DC-4 design.

5.4 SUMMARY AND CONCLUSION

Five alternative fuel configurations inside the channels of the passive pressure tube reactor have been proposed and qualitatively evaluated. The options include two bundle-type arrangements in a two-ring geometry and three matrix-type fuels. Key factors in the areas of reactor physics, thermohydraulics during normal operation and during loss of coolant accidents, and materials compatibility affecting fuel design were identified, and the matrix performance was evaluated against these factors.

All reviewed alternatives can be designed with negative void coefficient and exhibit a prompt negative Doppler coefficient. One of the main challenges in the reactor physics arena is the achievement of low fast fluence on the pressure tube, especially if particle fuel is employed. The most promising option in this aspect is the DC-2 design with full-density UO_2 fuel pellets. This design also exhibits a high conversion ratio, comparable to CANDU reactors, and has a good potential for breeding by introducing further modifications inside the channel. The DC-2 design is also a very promising route for the wet calandria version of the PTLWR, with a well-thermalized spectrum. The drawback common to all fuel designs for the PTLWR are higher parasitic losses than in a typical CANDU and LWR, because of relatively high leakage from a voided core, and low fuel mass to total core mass ratio. Figure 5-15 shows a comparison of neutron balances for the proposed designs with typical PWR and CANDU cores. The ratio of capture rate in ^{238}U to absorption rate in ^{235}U , also shown in Figure 5-15, is a good measure of conversion ratio.



Note: Values for DC-1 and DC-2 designs are for semi-infinite lattice, others are for infinite lattice

Figure 5-15 Comparison of parasitic captures and captures in ^{238}U for individual matrix designs, CANDU and PWR

Regarding the thermohydraulic performance during normal operation, matrix-type fuel options are more difficult to cool because of the limited surface area wetted by coolant. The most challenging matrix in this aspect is the DC-3 design, with separated coolant channels and fuel regions. The detailed analysis of this reference design shows that the cooling requirements, fuel centerline temperature limits and the CHF margins can be satisfied, due to relatively low power peaking and the good conductivity of particle fuel. Table 5-2 shows how the main parameters of individual fuel arrangements compare to the CE-CANDU reference design.

For loss of coolant accidents, the bundle-type fuel configuration provides a less efficient heat transfer dissipation mechanism compared to a matrix-type fuel. Preliminary calculation shows that the two-ring design can meet this challenge. All the proposed designs use silicon carbide instead of the traditional Zircaloy to withstand the high temperatures reached during these scenarios.

Design DC-3 with separate coolant channels and fuel regions was selected as the reference design. The primary motivation for this choice is the extensive experience with manufacturing of this type of fuel element for HTGRs and ongoing research for MHTGR applications. The matrix is based on currently available technology, except for the silicon carbide coating. More research and development in this area is needed to confirm the issues of economical production, and coating behavior in a reactor environment during both normal operation and transients. The molded fuel element technology developed by HOBEG/NUKEM is especially attractive due to the excellent thermal properties of the fuel/matrix interface.

Table 5-2 Comparison of thermohydraulic characteristics

Characteristic	CE-CANDU	DC-1	DC-2	DC-3	DC-5
Average power per fuel channel (MWt)	5.44	5.44	5.44	5.44	5.44
Peak power per fuel channel (MWt)	10.26	6.8	6.8	6.5	7.1
Total Peaking Factor*	1.9	1.25	1.3	1.2	1.3
Average power density in fuel region (W/cm ³)	213	263	263	277	115
Peak power density in fuel region (W/cm ³)	446	328	342	303	125
Peak heat flux to coolant (W/cm ²)	114	92.5	96.2	118	71.2
Average heat flux to coolant (W/cm ²)	59.7	74	74	98.2	54.8
Heat transfer surface with coolant per channel (cm ²)	90,310	73,230	73,230	54,990	98,490
Total fuel channel flow area (cm ²)	34.2	23.7	23.7	28.1	49.23
Fuel channel hydraulic diameter (cm)	0.74	0.74	0.74	0.85	0.96
Mass flow rate per fuel channel (kg/s)	22.1	22.1	22.1	22.1	22.1
Velocity (m/s)	9.93	13.2	13.2	12.1	6.9

* For the fresh core with uniform enrichment; the peaking factor for the equilibrium core depends on the refueling scheme, and will be different from these values.

Chapter 6

FUEL MATRIX PERFORMANCE UNDER NORMAL OPERATING CONDITIONS

6.1 INTRODUCTION

The objective of this Chapter is to confirm that the reference fuel channel design of the PTLWR reactor satisfies the key thermal-hydraulic limits during normal operation. These include the maximum fuel centerline temperature and the critical heat flux ratio. The PTLWR uses TRISO particle fuel which can withstand peak transient temperature up to 1600°C. During normal operation, the limiting fuel temperature is lower, to reduce fission gas release by diffusion into the primary circuit. To ensure that the radiation dose resulting from accidental release of primary system inventory to the atmosphere remains within regulations, the limit on fuel particle center temperature is 1300 °C at 100% power [Todreas and Kazimi, 1990]. PWR reactor designers use for the critical heat flux limit the Minimum Departure from Nucleate Boiling Ratio (MDNBR), $MDNBR \geq 1.3$, in BWR reactors the comparable limit is the Minimum Critical Power Ratio (MCPR), $MCPR \geq 1.2$. For CANDU units a CHF correlation formulated in terms of critical quality is used to determine the onset of intermittent fuel dryout – an approach similar to that used in BWRs. In this work, both approaches – the local departure from nucleate boiling conditions and the dryout conditions, which depend on channel history, will be investigated. In addition to the above limits, it is desirable that the pressure loss across the core is small to minimize the pumping power. The objective set for the reference design is to keep the pressure loss in the fuel channel the same as, or less than, that for the CE-CANDU.

Section 6.2 will give a brief description of the primary system and the fuel channel data, Section 6.3 will describe analysis tools. Putting

additional material in the form of a solid matrix into the pressure tube inevitably leads to a lower number of fuel pins (or fuel compacts in the case of particle fuel) which can be placed in the fuel channel, to a smaller heated perimeter (in contact with coolant), and to less available flow area than for typical CANDU reactors, thus posing a challenge for adequate heat transfer performance during normal operation. To address these issues, a multi-channel two-phase flow model was developed, which will be described in detail in Section 6.4. The results will be discussed in Section 6.5.

6.2 PRIMARY SYSTEM CONFIGURATION AND COOLANT CONDITIONS

To utilize existing and proven experience to the maximum extent, and to avoid the need for detailed calculation of design parameters not central to key PTLWR features, the PTLWR design was based on the CE-CANDU as the reference design. The primary heat transport system, shown schematically in Figure 6-1, is basically identical to that of CE-CANDU. The primary heat transport system consists of two independent circuits. The coolant passes through the core to a steam generator and is then pumped back through the core into another steam generator; thus the coolant makes two passes through the core. This arrangement allows refueling from both sides in the direction of the coolant flow, and compact arrangement, but makes LOCA thermal-hydraulic analysis more difficult. Also, note that in case of pump failure, the coolant flow in the circuit can be maintained high by the other pump in the loop.

The major components are four steam generators, the calandria with fuel channels, the pressurizer, and the main coolant pumps. CANDU steam generators cannot be operated with leaks because of the high cost of heavy water. Since the PTLWR uses light water as a primary coolant, extreme precautions to avoid all leaks can be relaxed. The pressurizer is connected to both circuits. The only difference between the reference CE-CANDU and the PTLWR primary heat transport system designs are some additional unfueled pressure tubes running through the radial reflector in

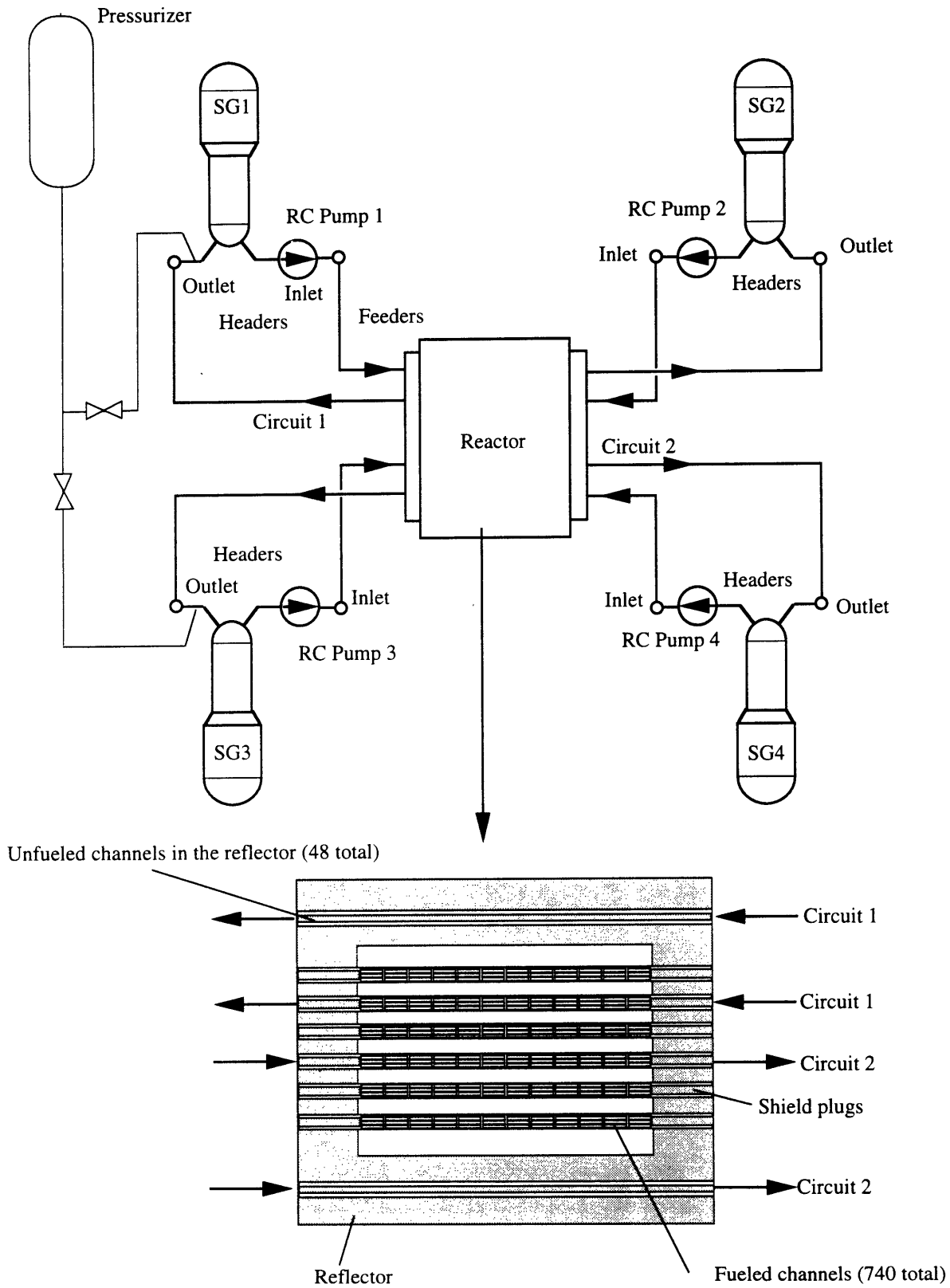


Figure 6-1 Schematic of the PTLWR primary heat transport system

the latter. Flow through these pressure tubes is orificed to provide sufficient cooling for the radial reflector. Note that the gamma and neutron heat generated in the reflector is recovered, hence the thermal efficiency of the PTLWR is higher than that of CANDUs, where about 5% of the fission energy is lost in the low-temperature D₂O moderator. Key parameters of the primary heat transport system are summarized in Table 6-1.

Table 6-1 Main parameters of the PTLWR primary heat transport system

Core parameters	CE-CANDU	PTLWR
Thermal power (MWt)	4029	3899
Primary system pressure (MPa)	15.34	15.34
Temperature at fuel channel inlet (°C)	298.9	298.9
Total number of fueled channels	740	740
Mass flow rate through fueled channels (kg/s)	14,100	14,100
Number of unfueled channels	0	32
Core bypass mass flow rate (through unfueled channels) (kg/s)	0	224

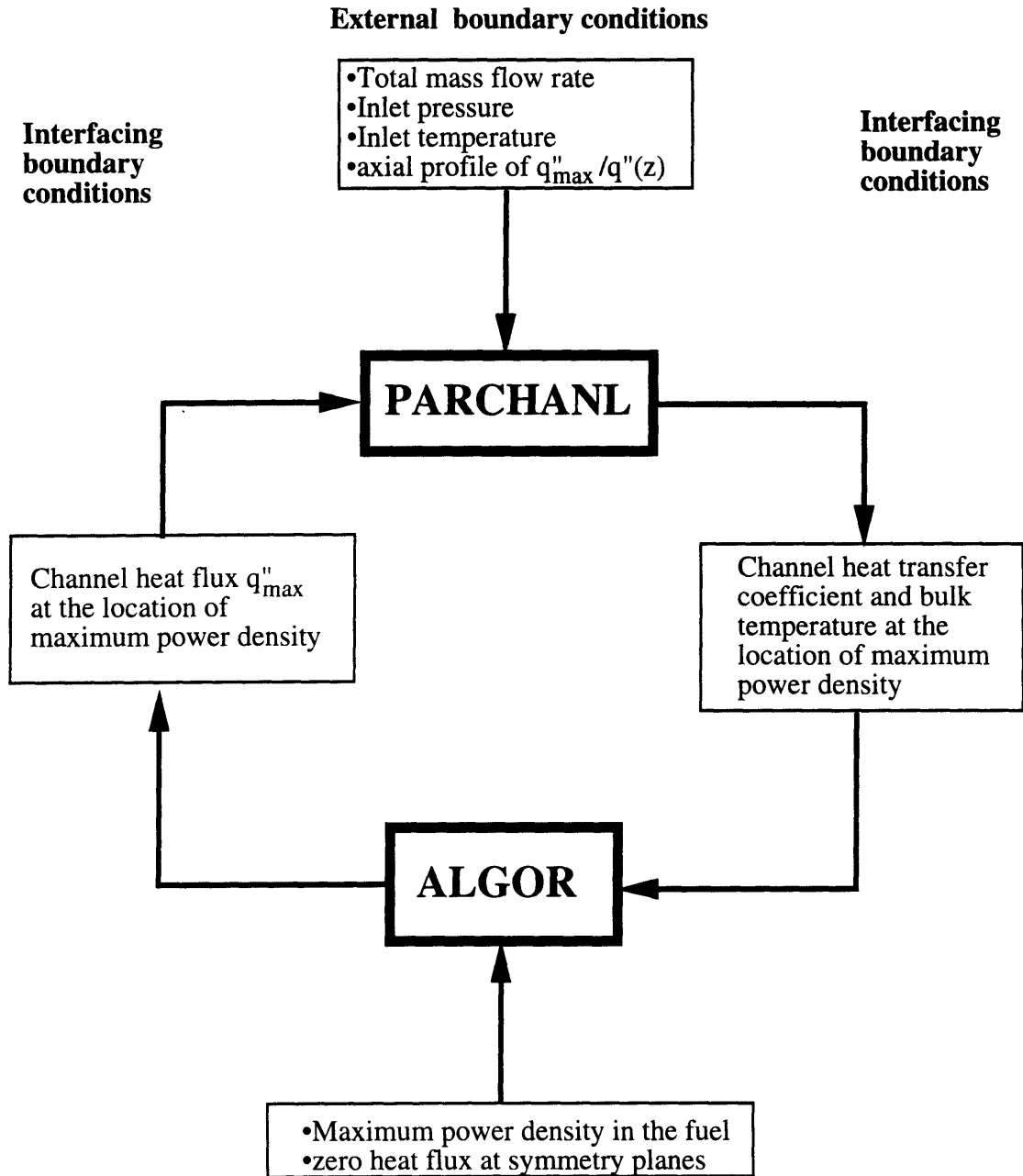
6.3 ANALYSIS TOOLS

Exact solution of heat transfer from fuel compacts to coolant is more complex than for traditional LWR fuel pins because it involves 3-dimensional heat conduction from the fuel compacts through the matrix, coupled to fluid flow in the channels. The optimum solution would be to apply a 3-D conduction code for the full-length fuel channel with conjugate heat transfer capabilities so that the conduction from the matrix could be coupled to energy and momentum equations for the coolant. The problem is further complicated by turbulent flow, and two-phase flow and heat transfer, since boiling occurs at the end of the channels. There are not many codes with all these capabilities available; moreover, application to a

6m-long channel would require a very large number of mesh nodes, which would result in large CPU requirements, even on a massively parallel computer. Hence a simplified approach will be used.

Since the heat flux in the radial direction is very large and conduction in the axial direction is negligible, the 3-D heat transfer problem can be simplified into a 2-D problem by solving the 2-D conduction equation at selected planes (perpendicular to the fuel channel centerline) of the fuel matrix, typically at the location of maximum power density. This task can be accomplished using a 2-dimensional finite element method (FEM) code, such as ALGOR [ALGOR,1990], provided that the boundary conditions – heat generation in fuel compacts and coolant parameters are known. The power density in the fuel compacts, as a function of position, is obtained from the MCNP models, described in Chapter 4.

The boundary conditions at the coolant interface involve the heat transfer coefficient to the coolant, and the fluid bulk temperature. These parameters must be obtained by solving mass and energy balance equations for the coolant along the coolant channels. A separate code, PARCHANL (parallel channels), has been developed for this purpose. The PARCHANL code calculates the flow split in parallel noncommunicating channels and the bulk fluid properties, as well as the wall temperature and the heat transfer coefficient as a function of axial position. Besides the total mass flow rate, inlet pressure and inlet coolant temperature, PARCHANL needs the heat flux to individual coolant channels as a boundary condition. This heat flux is obtained, using the ALGOR code, at the plane of maximum power density, and by combining this result with the axial power density profile to get the heat flux profile as a function of axial position for every coolant channel. Since the heat transfer coefficient and coolant bulk temperature depend on the incident heat flux to coolant, and this heat flux in turn depends on both these variables, iterations on the heat transfer coefficient and coolant bulk temperature between ALGOR and PARCHANL are necessary. Because the heat transfer coefficient to coolant is large, the convergence rate is very fast, requiring one to two iterations. Figure 6-2 shows the coupling between the codes and the external boundary conditions.



Note the simplification from the true 3-D model achieved by assuming the separation of the axial heat flux profile in the axial (z) direction from that in the r- θ plane

Figure 6-2 Communication between the thermohydraulic codes PARCHANL and ALGOR

The ALGOR code is discussed next; the equations used in PARCHANL are described in Section 6.4, and a listing of the code is given in [Hejzlar, 1994].

6.3.1 The ALGOR Code

ALGOR [ALGOR, 1990] is a finite element design and analysis system package developed by Algor, Inc. It is a robust system comprising a large number of codes for analysis of various engineering problems such as stress analysis, analysis of piping systems, kinematic/dynamic analysis, fluid flow and heat transfer analysis, and many others. With respect to this section, only the heat transfer package will be discussed. The heat transfer analysis package enables one to generate complex geometrical objects and to calculate heat flow patterns and temperature distribution in these structures. It can be used to solve both the steady state and transient problems. Material properties may be temperature dependent, either isotropic or orthotropic. However, it is noted that problems with temperature-dependent properties require an iterative process between the ALGOR heat transfer processor and another auxiliary ALGOR processor. Since these iterations are done by the user in the current version, transient problems are very laborious and time consuming.

A variety of boundary conditions can be specified including temperature, heat flux, convection and radiation. The drawback of the ALGOR heat transfer package is its inability to calculate radiative heat transfer between arbitrary surfaces. ALGOR also does not include separate provisions to handle thermal contact resistance across an interface. This drawback can be, however, circumvented by modeling the interface as a separate region having properties which yield a given contact resistance.

ALGOR has undergone an extensive verification and validation program. It is also operated under a Quality Assurance (QA) program designed to comply with the QA requirements of the United States nuclear power industry.

6.4 ANALYSIS OF FUEL CHANNEL THERMOHYDRAULICS

The objective of the fuel channel thermal hydraulics analysis is to evaluate critical heat flux and pressure drop performance along all coolant channels. Additionally, the development of bulk coolant temperature and the heat transfer coefficient as a function of axial position needs to be obtained to provide boundary conditions for the analysis of fuel matrix thermal performance using ALGOR. This section describes the procedure for calculating these thermal-hydraulic characteristics, which are transferred into the PARCHANL computer code. A listing of the PARCHANL code is enclosed in [Hejzlar, 1994].

6.4.1 Fundamental Equations and Simplifying Assumptions

Thermohydraulic analysis of the flow through the coolant channels involves the solution of the transport equations of mass, momentum and energy. The fundamental conservation equations can be simplified by eliminating the time derivatives, since only steady state solutions are of interest in this section. The flow in coolant channels is highly predominant in one direction, hence the conservation equations can be written in a one dimensional form, in an average sense. Considering the one-dimensional, two-phase flow through a channel of constant flow area A at the axial position z along the channel, the channel average, steady state equations can be derived from the fundamental conservation equations [Todreas and Kazimi, 1990] for:

mass conservation

$$\frac{\partial}{\partial z} (G_m) A = 0 \quad (6-1)$$

momentum conservation

$$\frac{d}{dz} \left(\frac{G_m^2}{\rho_m^+} \right) = - \frac{dp}{dz} - \frac{P_w}{A} \tau_w - \rho_m g \cos(\theta) \quad (6-2)$$

and energy conservation

$$\frac{d}{dz} (G_m h_m^+) = \frac{q'' P_h}{A} + q''' \quad (6-3)$$

The mass conservation equation (6-1) can be directly integrated to yield

$$\dot{m} = G_m A = \text{const.} \quad (6-4)$$

Since the coolant pressure (~15MPa) and the mass flux (~9,000kg/m²-s) through the channels are high, the homogeneous equilibrium model (HEM) is the most appropriate choice of flow model in the two phase region. Hence the dynamic (mixing cup) density defined as

$$\frac{1}{\rho_m^+} = \frac{1}{G_m^2} \{ \rho_v \alpha v_v^2 + \rho_l (1-\alpha) v_l^2 \} \quad (6-5)$$

corresponds to the mixture density

$$\rho_m^+ = \rho_m = (1 - \alpha) \rho_f + \alpha \rho_g = \left(\frac{1-x}{\rho_f} + \frac{x}{\rho_g} \right)^{-1} \quad (6-6)$$

The friction pressure gradient for the two-phase flow, $\tau_w P_w/A$, can be also simplified using the HEM mixture density as

$$\frac{\tau_w P_w}{A} = \frac{f_{TP}}{D_e} \frac{G_m^2}{2 \rho_f} = \frac{f_{fo}}{D_e} \phi_{fo}^2 \frac{G_m^2}{2 \rho_f} = \frac{f_{fo}}{D_e} \frac{G_m^2}{2 \rho_m} \quad (6-7)$$

where the two-phase flow multiplier for HEM, ϕ_{fo}^2 , was incorporated into mixture density, i.e.,

$$\begin{aligned} \frac{\tau_w P_w}{A} &= f_{fo} \frac{G_m^2}{2 \rho_f D_e} \phi_{fo}^2 = f_{fo} \frac{G_m^2}{2 \rho_f D_e} \left[1 + x \frac{v_{fg}}{v_f} \right] = \\ &= f_{fo} \frac{G_m^2}{2 \rho_f D_e} \frac{v_f + x v_{fg}}{v_f} = f_{fo} \frac{G_m^2}{2 \rho_m D_e} \end{aligned} \quad (6-8)$$

The friction factor, f_{fo} , is assumed to have the same value for liquid single-phase flow at the same mass flux as the total two-phase mass flux (Owen's approximation), i.e., $f_{fo}=f_{TP}=f$.

Since all coolant channels in the PTLWR are horizontal, the last term on the RHS of Eq. (6-2) can be dropped, and the momentum conservation equation can be rewritten as

$$\frac{dp}{dz} = - \frac{d}{dz} \left(\frac{G_m^2}{\rho_m} \right) - \frac{f_{fo}}{D_e} \frac{G_m^2}{2 \rho_m} \quad (6-9)$$

The energy conservation equation (6-3) neglects kinetic energy, and the work done on the fluid by pressure, viscous forces and body forces. The internal heat generation in the coolant, q''' , by gamma rays and neutrons is small and can be also neglected. Similarly as for the mixing cup density, the mixing cup enthalpy in the energy conservation equation

$$h_m^* = \frac{1}{G_m} \{ \rho_v \alpha h_v v_v + \rho_l (1-\alpha) h_l v_l \} \quad (6-10)$$

corresponds to mixture enthalpy, which can be written for the HEM model as a function of equilibrium quality

$$h_m = h_g x + h_f (1-x) \quad (6-11)$$

Employing these simplifications and using Eq. (6-4), the energy equation (6-3) can be written as

$$\frac{d}{dz} (h_m) = \frac{q'' P_h}{G_m A} = \frac{q'' P_h}{\dot{m}} \quad (6-12)$$

6.4.2 Flow Distribution in Parallel Non-communicating Channels

The reference matrix design is shown in Figure 6-3. It employs three types of cooling channels. The inner channel #1 has a larger diameter and is roughened. The purpose of the roughening is twofold. First, it enhances the heat transfer coefficient in the central channel, where the heat flux to coolant is the highest. Second, it increases the pressure drop of this open channel and forces more flow to the neighboring channels. The characteristic dimensions of the coolant channels are also given in Figure 6-3.

The fuel channel contains a total of 12 fuel elements, each of length 0.5m. To secure the exact alignment of all coolant channels between the two neighboring fuel elements, keys are provided on one face of every fuel element, which are inserted into the dowels of the neighboring element, as

shown on Figure 6-4*. Although this arrangement does not exclude some transverse flow of the coolant along axial faces of the elements, this flow will be marginal, hence the channels can be treated as noncommunicating.

The fuel matrix design employs coolant channels of three types – the central channel, 18 tubular channels in the intermediate ring, and the annular channel between the matrix and the pressure tube. To be able to study various fuel matrix designs, the analysis method is written for an arbitrary number of channel types, each consisting of an arbitrary number of coolant channels.

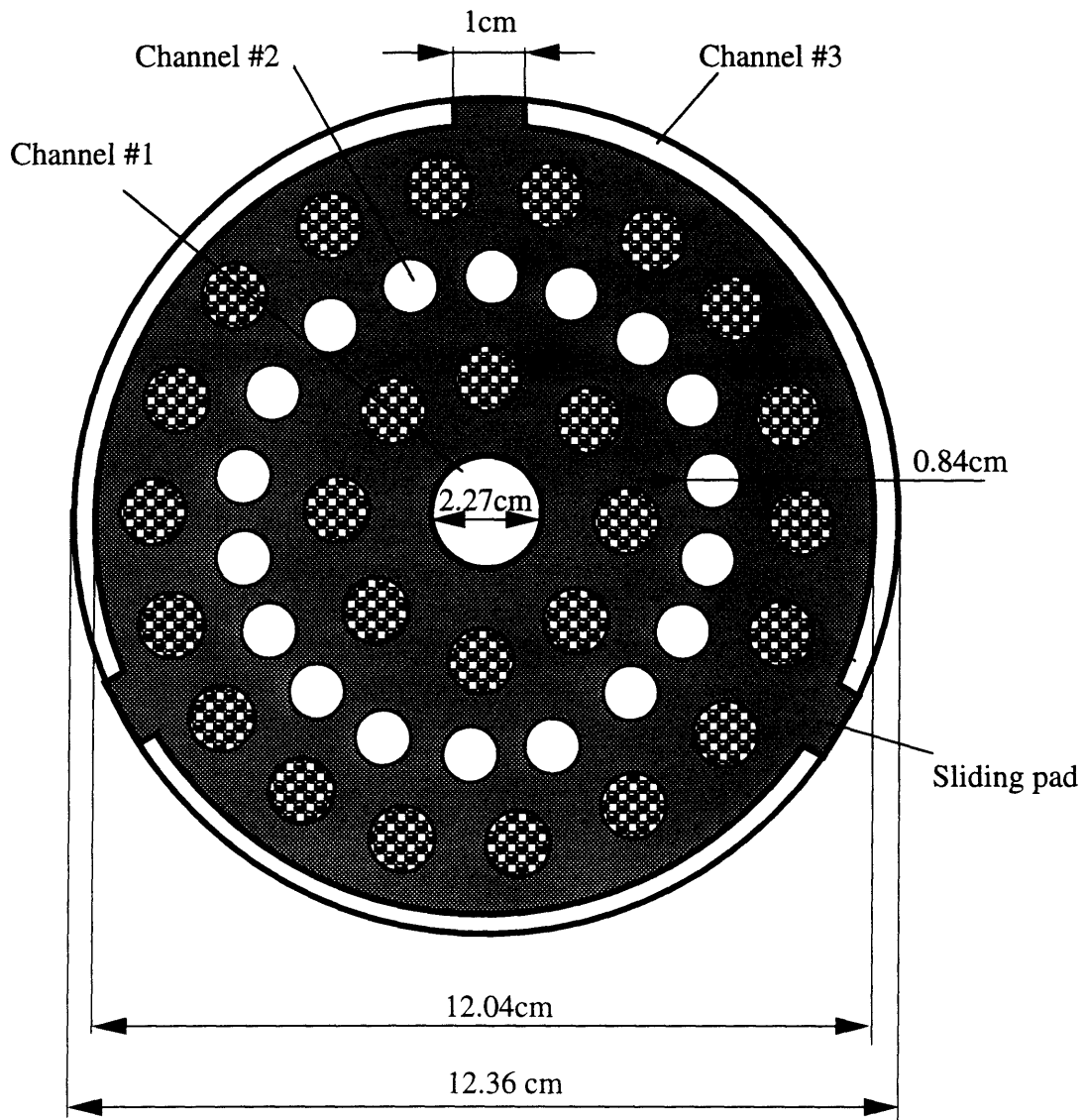
The pressure drop is calculated by applying coupled mass and momentum conservation equations to every channel, and the equality condition for total pressure drop of every parallel channel. Mass conservation gives the condition

$$\dot{m} = \sum_{i=1}^N \dot{m}_i \quad (6-13)$$

where \dot{m} is the total mass flow rate per the whole fuel channel** and N is the number of coolant channel types. Note that \dot{m}_i is the total flow rate through all coolant channels of the same type, i . Since the fluid in the channels changes in condition from the subcooled state to two-phase flow, all channels must be axially nodalized to trace correctly the fluid conditions along the channel. The steady state momentum equation for channel type i can then be obtained by integrating Eq. (6-9) along the channel and by

* Another design approach would be to provide a plenum space between neighboring fuel elements, which would allow some coolant mixing and could eliminate the necessity of exact alignment of fuel elements. However, the disadvantage of such an approach is an increased pressure loss, and erosion of the edges exposed to high coolant velocities.

** A Fuel channel consists of the matrix with coolant channels, the pressure tube and the calandria tube. The coolant channels are of various types; every channel type can consist of a number of individual coolant channels.



Channel	Flow area (cm ²)	Hydraulic diameter (cm)	Heated perimeter (cm)
#1	4.0471	2.27	8.5451
#2	0.55418	0.84	2.6389
#3	5.75	0.6	36.81

Note: channel #1 has a roughened surface

Figure 6-3 Coolant channels of the reference matrix design, with their dimensions

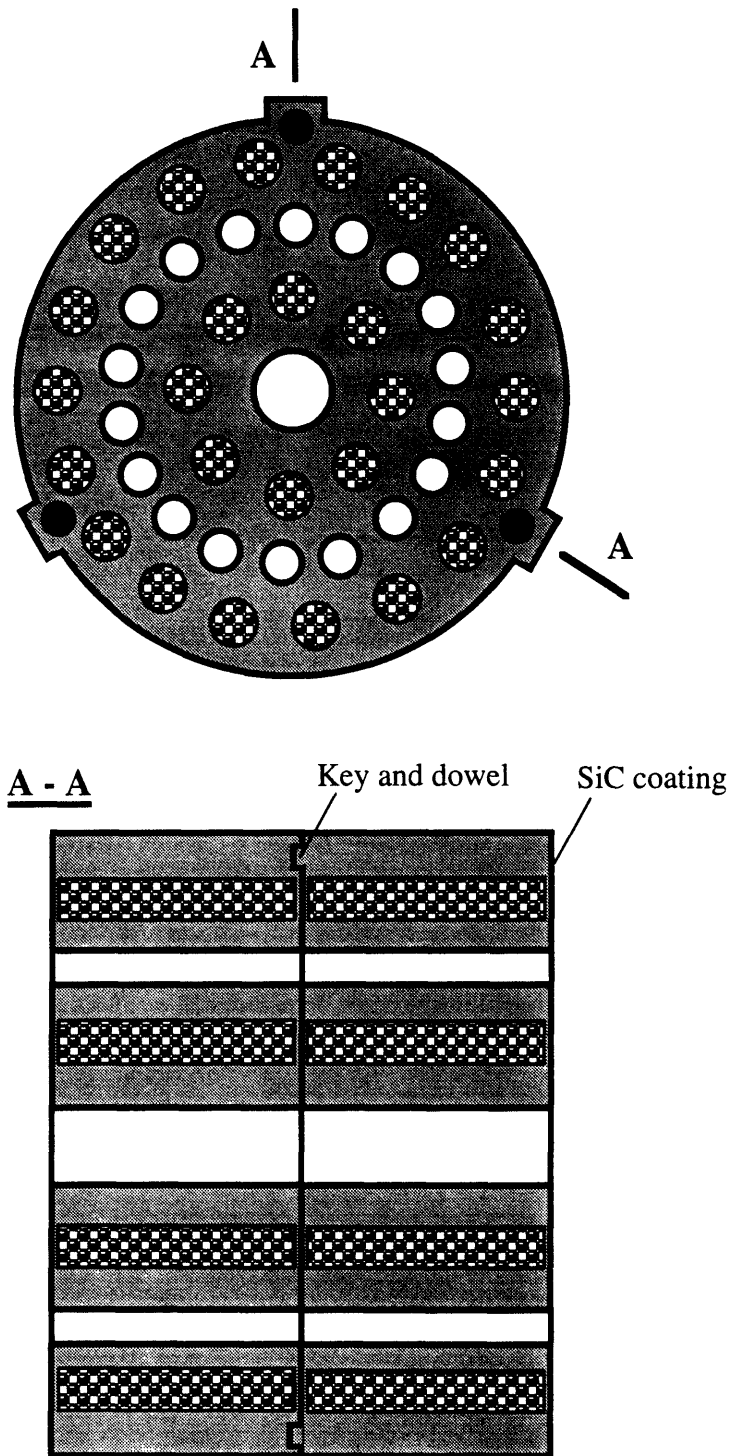


Figure 6-4 Alignment of two neighboring fuel elements

replacing the integral by the sum of piecewise constant terms over all nodes. Separating the friction and form pressure losses, the total pressure drop for the i -th type channel can be written as

$$\Delta p_i = \Delta p_{f,i} + \Delta p_{\text{form},i} + \Delta p_{\text{ac},i}, \quad (6-14)$$

with the friction pressure losses

$$\Delta p_{f,i} = \dot{m}_i^2 \sum_{j=1}^{NZ} f_j(\dot{m}_i) \frac{\Delta z_j}{D_{e,i}} \frac{1}{2 \rho_{i,j} NP_i^2 A_i^2} \quad (6-15)$$

the form losses

$$\Delta p_{\text{form},i} = \dot{m}_i^2 \sum_{j=1}^{NZ} K_j \frac{1}{2 \rho_{i,j} NP_i^2 A_i^2} \quad (6-16)$$

and the acceleration losses

$$\Delta p_{\text{ac},i} = \dot{m}_i^2 \sum_{j=1}^{NZ} \frac{1}{2 NP_i^2 A_i^2} \left(\frac{1}{\rho_{i,j}} - \frac{1}{\rho_{i,j-1}} \right) \quad (6-17)$$

NP_i is the number of channels of the same type, i , NZ is the total number of axial nodes, A_i and $D_{e,i}$ are the flow area and hydraulic diameter of one channel of type i , respectively. Form loss coefficients, $K_{i,j}$, were taken from [Idelchik,1986]. If the j -th axial node does not contain any form loss, coefficient $K_{i,j}$ is set to zero. It is assumed that the alignment of coolant channels between neighboring fuel elements is not perfect, giving rise to non-zero form losses at these locations.

Coolant density, $\rho_{i,j}$, at each node is calculated from the node bulk temperature, $T_{i,j}$, and pressure, $p_{i,j}$; in the one-phase flow regime

$$\rho_{i,j} = f(T_{i,j}, p_{i,j}) \quad (6-18)$$

using polynomials for subcooled water; and as a function of quality, $x_{i,j}$, in the two-phase flow regime, i.e.,

$$\frac{1}{\rho_{i,j}} = \frac{1}{v_{f,i,j}(p_{i,j}) + x_{i,j} [v_{g,i,j}(p_{i,j}) - v_{f,i,j}(p_{i,j})]} \quad (6-19)$$

where the thermodynamic equilibrium quality is calculated as

$$x_{i,j} = \frac{h_{i,j} - h_{f,i,j}(p_{i,j})}{h_{g,i,j}(p_{i,j}) - h_{f,i,j}(p_{i,j})}, \quad (6-20)$$

and the node-average enthalpy is obtained from an energy balance. Note that the decrease of saturation properties with pressure is taken into account. Pressure at axial position z represented by the J -th node is calculated for the i -th type channel

$$p_{i,J} = p_{in} - \dot{m}_i^2 \sum_{j=1}^J f_{i,j}(\dot{m}_i) \frac{\Delta z_j}{D_{e,i}} \frac{1}{2 \rho_{i,j} N P_i^2 A_i^2} + K_{i,j} \frac{1}{2 \rho_{i,j} N P_i^2 A_i^2} + \frac{1}{2 N P_i^2 A_i^2} \left(\frac{1}{\rho_{i,j}} - \frac{1}{\rho_{i,j-1}} \right). \quad (6-21)$$

The Moody friction factor in the axial node j of channel i , $f_{i,j}$, is calculated as a function of Reynolds number and surface roughness, ζ , after Idelchik, [Idelchik, 1986]

$$f_{i,j} = 0.11 \left[\frac{\zeta}{D_{h,i}} + \frac{68}{Re_{i,j}} \right]^{0.25}, \quad (6-22)$$

where

$$Re_{i,j} = \frac{\dot{m}_i D_{e,i}}{\mu_{i,j} N P_i A_i}, \quad (6-23)$$

$$\mu_{i,j} = f(T_{i,j}, p_{i,j}). \quad (6-24)$$

The dynamic viscosity for two-phase flow has the same value as for single-phase flow ($\mu_{TP} = \mu_f$) by virtue of Owen's approach in selecting the friction factor. The condition of equal total pressure drop for all types of channels can be written in the form

$$\Delta p_i = \Delta p_{i+1}; \quad i=1, \dots, N-1. \quad (6-25)$$

Substituting for friction, form, and acceleration terms from Eqs. (6-15) through (6-17) into Eq. (6-25) yields

$$\dot{m}_{i+1} = \dot{m}_i \sqrt{\frac{F_i(\dot{m}_i)}{F_i(\dot{m}_{i+1})}}; \quad i=1, \dots, N-1 \quad (6-26)$$

where

$$F_i(\dot{m}_i) = \sum_{j=1}^{NZ} f_{i,j}(\dot{m}_i) \frac{\Delta z_j}{D_{e,i}} \frac{1}{2 \rho_{i,j} NP_i^2 A_i^2} + K_j \frac{1}{2 \rho_{i,j} NP_i^2 A_i^2} + \frac{1}{2 NP_i^2 A_i^2} \left(\frac{1}{\rho_{i,j}} - \frac{1}{\rho_{i,j-1}} \right) \quad (6-27)$$

Mass conservation, Eq. (6-13), together with (N-1) equations (6-26), form a complete set of N equations with N unknown mass flow rates. The system of equations (6-26) cannot be solved analytically since functions F_i depend on mass flow rates through the Reynolds number, as well as through the coolant properties, which in turn depend on mass flow rates. Hence an iterative process is applied. First, a guess of mass flow rates is made, then the fluid properties are obtained from an energy balance, and the friction factor is calculated. Using Eq. (6-26), mass flow rates are updated and compared to old values. The procedure is repeated until the change in mass flow rate is less than the prescribed tolerance. Note that Eq. (6-26) ensures equality of pressure drops. To ensure mass conservation, Eq. (6-13), another iteration loop must be performed. This is accomplished by alternating the mass flow rate of the reference channel (channel #1 is the reference channel by virtue of Eq. (6-26)) using the relation

$$\dot{m}_1^{k+1} = \dot{m}_1^k \frac{\dot{m}}{\sum_{i=1}^N NP_i \dot{m}_i^k} \quad (6-28)$$

where the superscript k denotes iteration index.

6.4.3 Power Density Distribution and Heat Flux to Coolant

To solve the energy balance in the coolant, the heat flux to each axial node in each type of coolant channel must be known. The axial heat flux distribution depends on the power density profile in the fuel compacts. This profile was obtained from fission rates edited from the MCNP model. In calculating the axial power density profile from MCNP tallies, a scaling factor with respect to average fission power generated in the fuel is needed.

The reference CE-CANDU design and the PTLWR concept differ in power generation apportionment, and hence in fission power, as shown in Table 6-2.

Table 6-2 Heat generation distribution in the PTLWR concept and CE-CANDU

Heat generation in:	CE-CANDU (MWth) ^a	PTLWR (MWth)
Fuel elements	3810	3630
Out-of-fuel-channel moderator	182^b	0
Reflector	16.9	43-axial 61-radial^c
Calandria tubes	6.3	35
Pressure tubes	14	116
Other losses	14	14
Total out-of-fuel generation counted as loss	219.2	75
Total fission power	4029	3899

^a From [Shapiro and Jesick, 1979].

^b Boldface type denotes lost energy, i.e., energy that does not contribute to power generation.

^c Most of the heat generated in the radial reflector can be easily recovered using additional nonfueled pressure tubes for cooling the radial reflector. Assuming that all this heat is nonrecoverable makes the fuel channel analysis conservative because of the higher fission power needed to keep the same power rating.

Heat generation in the reflector, pressure tubes and calandria tubes of the PTLWR were calculated from an MCNP model; other heat losses were assumed the same as for the reference CE-CANDU design. To obtain the

total fission power for the dry calandria design, it is assumed that the dry calandria design generates the same amount of electricity in MWe as the reference CE-CANDU. To produce the same power rating of 1260 MWe and assuming that the other primary and secondary system parameters of the PTLWR are identical with those of CE-CANDU, the PTLWR must generate the same recoverable power as the reference CE-CANDU unit, i.e., 3810MWt recovered from fuel and 14MWt recovered from pressure tubes gives a total of 3824MWt. The total fission power for the dry calandria design is obtained by adding unrecoverable losses of 75 MWt to 3824 MWt, which yields 3899 MWt. The heat generation in the fuel channels is then calculated by subtracting all heat generated elsewhere from the total fission power, i.e., $3899 - 43 - 35 - 116 - 75 = 3630$ MWt. This approach neglects CE-CANDU heat losses across the gap between the pressure tube and the calandria tube which are non-recoverable but are small (about 0.1%, i.e., 5 MWt). Note that the PTLWR has significantly less nonrecoverable energy losses, primarily due to elimination of neutron and gamma heating of D₂O moderator, and by recovering energy generated in the end reflector. Note that although a substantial portion of energy generated in the radial reflector can be easily recovered, the analysis assumes all this energy as nonrecoverable. This assumption yields higher heat generation rates in the fuel elements, thus making the fuel channel analysis conservative. The total fission power of 3899 MWt gives the basis for establishing the correct scaling factor to acquire the power density profile from MCNP fission rate tallies.

Introducing the axial profile factor for the i-th channel

$$\zeta_i(z) = q''_i(z)/q''_{i,\max} \quad (6-29)$$

the heat flux to coolant at location z , $q''_i(z)$, can be obtained provided that the maximum heat flux to coolant, $q''_{i,\max}$ (heat flux into the i-th coolant channel type at the z -location where the maximum is attained*) and the

* Note that channel #2 exhibits significant azimuthal nonuniformities in the wall heat flux. These nonuniformities are not considered in the channel thermohydraulics analysis. Perfect coolant mixing is assumed within every coolant channel, and the heat

axial profile factor, $\zeta_i(z)$, are known. The detailed analysis of heat conduction in the fuel matrix element requires sophisticated codes. As discussed in Section 6.3, a full 3-D model of the fuel matrix coupled to fluid flow in the coolant channels is not practical. Instead, a simplified approach has been adopted.

First the guess of heat flux to coolant for each channel at the axial location of the maximum power density can be made as follows:

Using the maximum power density per fuel compact in the inner ring, $q'''_{\max,ir1}$, and the maximum power density per fuel compact in the outer ring, $q'''_{\max,or1}$, maximum linear heat rate per inner and outer ring is calculated as

$$q'_{\max,ir} = \frac{q'''_{\max,ir1} N_{ir}}{\pi R_{ir}^2}; \quad q'_{\max,or} = \frac{q'''_{\max,or1} N_{or}}{\pi R_{or}^2} \quad (6-30,31)$$

where N_{ir} and N_{or} are the numbers of fuel compacts in the inner and outer fuel rings, respectively.

The portion of the heat generated in the inner ring proceeds to the central coolant channel #1 while the remaining portion flows to the ring of coolant channels #2. How the heat flow splits depends on the thermal resistance between the fuel compact and bulk coolant as well as on the magnitude of the bulk coolant temperatures in these channels. The first guess assumes that half of the heat generated in the inner fuel ring goes to channel #1 and the other half proceeds to channel #2. A similar assumption is adopted for the outer fuel ring. Hence, the maximum heat flux to the coolant for individual channels can be written as

$$q''_{1,\max} = \frac{q'_{\max,ir}}{2 P_{h,1}}; \quad q''_{2,\max} = \frac{q'_{\max,or} + q'_{\max,ir}}{2 NP_2 P_{h,2}}; \quad q''_{3,\max} = \frac{q'_{\max,or}}{2 P_{h,3}} \quad (6-32,33,34)$$

flux and heat transfer coefficient at location z are taken as an average over the channel circumference. However, the azimuthal wall temperature profile is calculated using the 2-D finite element code ALGOR.

where P_h stands for heated perimeter. The axial heat flux distribution in the i -th channel type can then be obtained by nodalizing Eq. (6-29) as

$$q''_{i,j} = \zeta_{i,j} q''_{i,\max} \quad i=1,2,N; j=1, \dots, NZ. \quad (6-35)$$

The heat flux distribution parameter, $\zeta_{i,j}$, in the axial direction, represented by index j , is known from the axial power density profile obtained from MCNP. Index i denotes heat flow split into individual channels, which may differ from the split at the location of maximum heat flux given as the first guess by Eqs. (6-32) through (6-34). Exact determination of this split in every axial node would require running a detailed conduction analysis using ALGOR for every axial node. To save computer time, the exact 2-D heat conduction calculations will be performed only at the axial location of maximum power density, and the heat flow split into individual coolant channels obtained at this location will be assumed to be the same along the entire channel length. Since the difference of the axial bulk temperature profile between individual coolant channel types is small and since heat transfer coefficients are large (i.e., the main resistance to heat flow occurs in the fuel matrix) the error introduced by this simplification is small.

6.4.4 Energy Balance and Channel Wall Temperature Profile




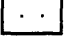
Having determined the heat flux to individual channels at each axial node, the fluid enthalpy at the exit of node j can be calculated by integrating the energy balance over the node,

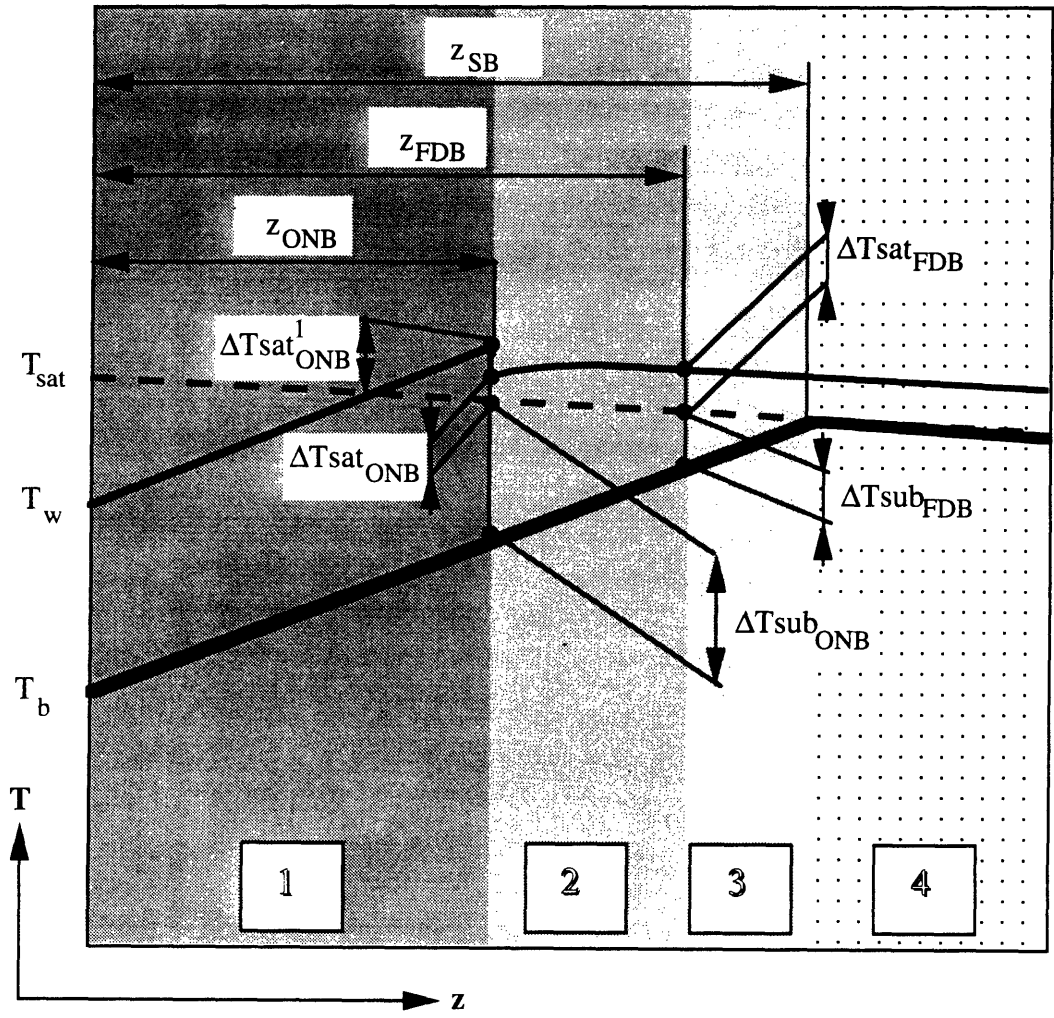
$$h_{i,j} = h_{i,j-1} + \frac{q''_{i,j} (NP_i P_{h,i}) \Delta z_j}{\dot{m}_i}. \quad (6-36)$$

Fluid bulk temperature is computed as a function of node enthalpy and pressure or as a function of pressure only, if saturated conditions are reached, i.e.,

$$T_{b,i,j} = f(h_{i,j}, p_{i,j}); \quad T_{b,i,j} = T_{\text{sat},i,j} = f(p_{i,j}). \quad (6-37)$$

As schematically shown on Figure 6-5, channel length can be subdivided into four regions - a single-phase convection region (1), a partial

-  Convection to one-phase liquid region (1)
-  Partial subcooled boiling region (2)
-  Fully developed subcooled boiling region (3)
-  Saturated boiling region (4)



- T_{sat} - saturation temperature
- T_w - wall temperature
- T_b - fluid bulk temperature
- ONB - onset of nucleate boiling
- FDB - fully developed subcooled boiling

Figure 6-5 Subcooled boiling regions with temperature profiles

subcooled boiling region (2), a region of fully developed subcooled boiling (3), and a saturated boiling region (4). Individual regions can be identified by the fluid subcooling parameter (to simplify the notation, channel and node subscripts are omitted in the following discussion)

$$\Delta T_{\text{sub}}(z) = T_{\text{sat}}(z) - T_b(z) \quad (6-38)$$

as follows:

- single-phase convection region $\Delta T_{\text{sub}}(z) > \Delta T_{\text{sub}_{\text{ONB}}}$,
- partial subcooled boiling region $\Delta T_{\text{sub}_{\text{FDB}}} < \Delta T_{\text{sub}}(z) < \Delta T_{\text{sub}_{\text{ONB}}}$,
- fully developed subcooled boiling region $0 < \Delta T_{\text{sub}}(z) < \Delta T_{\text{sub}_{\text{FDB}}}$, and
- saturated boiling region $\Delta T_{\text{sub}}(z) \leq 0$.

The heat transfer coefficient in the one-phase regime is calculated by the Dittus-Boelter correlation modified for entrance effects

$$h_c = 0.023 \text{Re}^{0.8} \text{Pr}^{0.333} [1 + (z/D_h)^{-0.35}] \frac{k}{D_h} \quad (6-39)$$

Heat transfer in the subcooled boiling region is evaluated by Bowring's approach [Bowring,1962]. In region 1, heat transfer is assumed to be by pure single-phase convection, even though wall temperature may be above the saturation temperature. The onset of nucleate boiling can be determined from fluid subcooling

$$\Delta T_{\text{sub}_{\text{ONB}}} = \frac{q''}{h_c} - \psi q''^n, \quad (6-40)$$

as suggested by Bowring [Collier,1981], where h_c is the heat transfer coefficient for single-phase convection and ψ is a pressure function. Relation (6-40) stems from the assumption that the condition for first nucleation is achieved if the wall temperature obtained from a single-phase convection correlation equals the wall temperature due to pure subcooled boiling heat transfer. Applying the Jens-Lottes correlation [Jens and Lottes, 1951]

$$\Delta T_{\text{sat}}^{\text{Jens}} = 25 \exp(p/62) q''^{0.25} \quad (6-41)$$

to the subcooled boiling portion of Eq. (6-40), Eq. (6-40) can be rewritten as

$$\Delta T_{\text{sub,ONB}} = \frac{q''}{h_c} - 25 \exp(p/62) q''^{0.25} \quad (6-42)$$

where pressure, p is in bars and the heat flux, q'' , is in MW/m^2 . Alternatively, if Thom's [Thom, 1966] correlation,

$$\Delta T_{\text{sat}}^{\text{Thoms}} = 22.65 \exp(p/87) q''^{0.5} \quad , \quad (6-41a)$$

is used, Eq. (6-40) has the form

$$\Delta T_{\text{sub,ONB}} = \frac{q''}{h_c} - 22.65 \exp(p/87) q''^{0.5} \quad (6-42a)$$

where again pressure is in bars and the heat flux is in MW/m^2 .

In the partial boiling region, Bowring assumes that the total average heat flux consists of two components: the average surface heat flux transferred by single-phase convection, q''_{SPL} , and the average surface heat flux transferred by bubble nucleation, q''_{SCB} , i.e.,

$$q'' = q''_{\text{SPL}} + q''_{\text{SCB}} \quad (6-43)$$

The single-phase component is assumed after Bowring to obey the relationship

$$q''_{\text{SPL}} = h_c (T_{\text{sat}} - T_b) \quad (6-44)$$

in region 1 and to be zero in regions 3 and 4. Using Figure 6-6, the single-phase component at the location of the onset of nucleate boiling can be approximated as

$$q''_{\text{SPL,ONB}} = \frac{\Delta T_{\text{sub,ONB}}}{(\Delta T_{\text{sub}})_{T_w=T_{\text{sat}}}} q'' \quad , \quad (6-45)$$

while the subcooled boiling component is calculated as

$$q''_{\text{SCB,ONB}} = \left[1 - \frac{\Delta T_{\text{sub,ONB}}}{(\Delta T_{\text{sub}})_{T_w=T_{\text{sat}}}} \right] q'' \quad (6-46)$$

by virtue of Eq. (6-43).

Similarly, at the location of transition between the partial subcooled boiling and fully developed subcooled boiling regions (boundary between regions 2 and 3) one can approximate

$$q''_{\text{SPL,FDB}} = \frac{\Delta T_{\text{sub,FDB}}}{(\Delta T_{\text{sub}})_{T_w=T_{\text{sat}}}} q'' ; q''_{\text{SCB,FDB}} = \left[1 - \frac{\Delta T_{\text{sub,FDB}}}{(\Delta T_{\text{sub}})_{T_w=T_{\text{sat}}}} \right] q'' \quad (6-47)$$

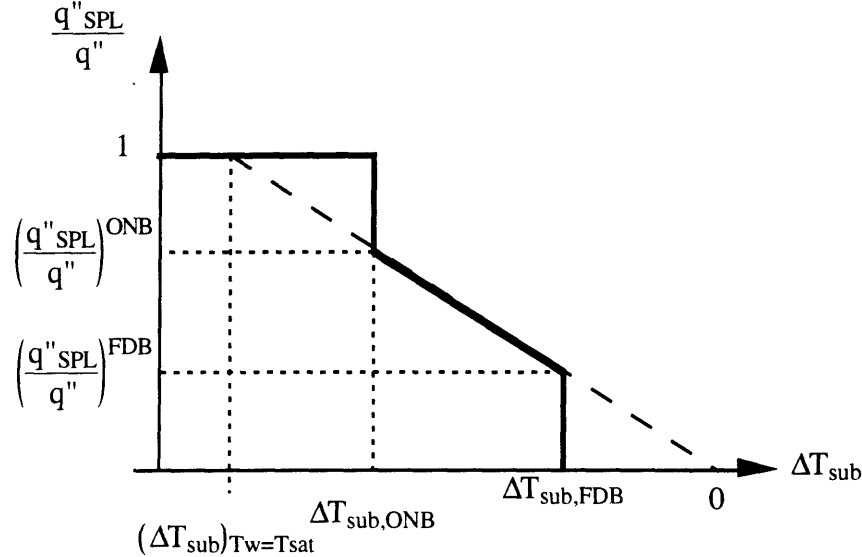


Figure 6-6 Approximation of single-phase component of heat flux in partial subcooled boiling region, after Bowring

The subcooled boiling component of the heat flux determines wall temperature at the location of ONB and FDB through Eqs. (6-41) or (6-41a), i.e.,

$$T_{w,ONB} = T_{\text{sat},ONB} + \Delta T_{\text{sat},ONB} = T_{\text{sat},ONB} + \psi (q''_{\text{SCB},ONB})^n, \quad (6-48)$$

$$T_{w,FDB} = T_{\text{sat},FDB} + \Delta T_{\text{sat},FDB} = T_{\text{sat},FDB} + \psi (q''_{\text{SCB},FDB})^n \quad (6-49)$$

where the numerical value of the coefficients ψ and n depend on whether Jens-Lottes' or Thom's correlations are used. The magnitude of subcooling at which the subcooled boiling becomes fully developed, $\Delta T_{\text{sub,FDB}}$, is calculated after Bowring [Bowring,1981]

$$\Delta T_{\text{sub,FDB}} = \frac{q''}{1.4 h_c} - \psi \left(\frac{q''}{1.4} \right)^n \quad (6-50)$$

In the nodalization scheme, interpolation must be performed to obtain node wall temperatures and correct locations of ONB and FDB. The coordinate of ONB is obtained as an intersection of the T_{sat} curve and the $(T_b + \Delta T_{\text{sub,ONB}})$ curve. This is achieved through linear interpolation; using the nomenclature in Figure 6-7 and restoring indexing:

$$z_{\text{ONB},i} = z_{j-1} + \frac{T_{\text{sat},i,j-1} - (T_{w,i,j-1} + \Delta T_{\text{sub,ONB},i})}{(T_{b,i,j} - T_{i,j-1})/\Delta z_j - (T_{\text{sat},i,j} - T_{\text{sat},i,j-1})/\Delta z_j} \quad (6-51)$$

Similarly, the location of the inception of fully developed subcooled boiling is calculated

$$z_{\text{FDB},i} = z_{j-1} + \frac{T_{\text{sat},i,j-1} - (T_{w,i,j-1} + \Delta T_{\text{sub,FDB},i})}{(T_{b,i,j} - T_{i,j-1})/\Delta z_j - (T_{\text{sat},i,j} - T_{\text{sat},i,j-1})/\Delta z_j} \quad (6-52)$$

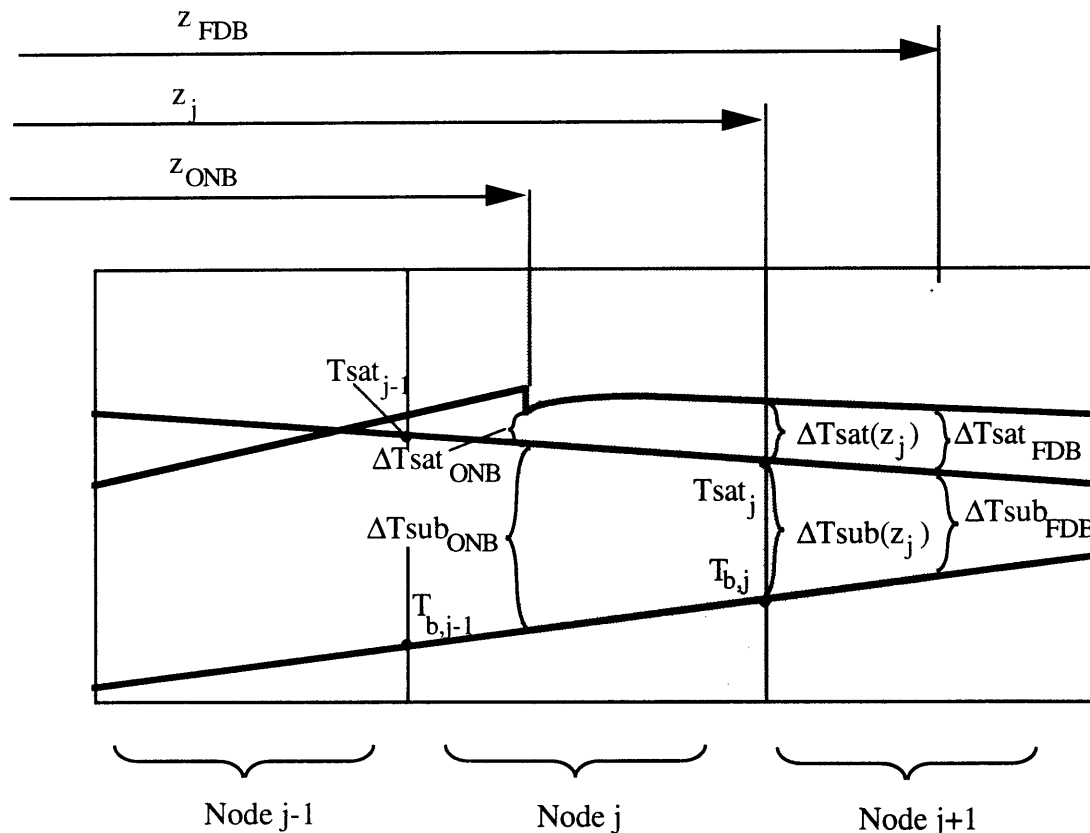


Figure 6-7 Schematic of partial subcooled boiling region in the nodalization scheme

Finally, the wall temperature of channel type i at node j is obtained by linear interpolation

$$T_{w,i,j} = T_{sat,i,j} + \Delta T_{sat,ONB,i} + \frac{\Delta T_{sat,FDB,i} - \Delta T_{sat,ONB,i}}{Z_{FDB,i} - Z_{ONB,i}} (Z_j - Z_{ONB,i}) \quad (6-53)$$

In the fully developed subcooled boiling region 3, Jens-Lottes or Thom's correlations given by equations (6-41) or (6-41a) are used with full heat flux applied to subcooled boiling, i.e., the single-phase convection portion is taken as zero. The program offers the choice between these two correlations. Jens-Lottes correlation gives, however a ΔT_{sat} lower by a factor of two than Thom's correlation. Since there has been some concern that Jens-Lottes yields lower ΔT_{sat} at high pressures [Tong and Weisman, 1979], Thom's correlation was used in the evaluation of the PTLWR fuel channel design. The wall temperature in this region is calculated as

$$T_{w,i,j} = T_{sat,i,j} + 22.65 \exp(p_{i,j}/87) \bar{q}''_{i,j}{}^{0.5} \quad (6-54)$$

where

$$\bar{q}''_{i,j} = \frac{q''_{i,j} + q''_{i,j-1}}{2} \quad (6-55)$$

Region 4 represents the saturated boiling regime; the heat transfer coefficient is calculated by Chen's correlation [Chen, 1963]. Chen's correlation is also described in [Todreas and Kazimi, 1990] and will not be repeated here.

An alternative simplified approach using Jens-Lottes or Thom's correlation for the entire subcooled boiling region can be also applied. The onset of subcooled boiling can be assumed to appear when the Jens-Lottes correlation predicts a lower wall temperature than the forced flow correlation. The wall temperature can be first calculated using the Dittus-Boelter heat transfer coefficient from Eq. (6-39)

$$T_{w,i,j} = T_{b,i,j} + \frac{\bar{q}''_{i,j}}{h_{c,i,j}} \quad (6-56)$$

Then, if the wall temperature is greater than the fluid bulk temperature, the wall temperature is calculated by Jens-Lottes or Thom's correlations. If the wall temperature calculated from Jens-Lottes or Thom's correlations is less than that obtained from Eq. (6-56), the fluid is assumed to be in the subcooled boiling regime.

6.4.5 Heat Transfer Coefficient and Friction Factor for Rough Surface

Central channel #1 experiences the highest heat flux to coolant because it partially cools 8 fuel compacts with its small available heat transfer surface. To reduce the heat flux to this channel, the heat transfer surface is increased by increasing the diameter of the channel. The strategy of roughening the channel surface is also employed. Roughening increases the pressure drop in the channel and hence forces more flow into the neighboring coolant channels. It also breaks down the laminar sublayer of turbulent flow, induces more turbulence near the wall, and hence enhances the heat transfer coefficient. Note that, contrary to the typical target of the highest heat transfer coefficient and the lowest pressure drop, this arrangement requires both a high pressure drop and a high heat transfer coefficient in the central coolant channel.

Sand-grain type roughness was chosen for channel #1 because it provides the large needed pressure drop, it is easy to manufacture, and data for both the friction factor and heat transfer coefficient are available. The approaches used for analyses of rough surfaces are based on similarity considerations developed by Nikuradse [1952]. Two surfaces are geometrically similar if the geometry of their roughness is the same in all aspects except for a scale factor. For tubes with hydraulic diameter D_e , a family of roughened tubes will differ in their e/D_e values where e is the roughness height. The model derived by Nikuradse, based on the "law of the wall" velocity distribution for flow over a rough surface, gives the friction similarity law

$$Re^+(e^+) = \sqrt{2/f} + 2.5 \ln(2e/D_e) + 3.75 \quad (6-57)$$

where Re^+ is the roughness function and e^+ is the roughness Reynolds number defined as

$$e^+ = \frac{e u^*}{\nu} = \frac{e}{D_e} \text{Re} \sqrt{\frac{2}{f}}, \text{ where } u^* = \sqrt{\frac{\tau_w}{\rho}}. \quad (6-58)$$

The friction factor in Eqs (6-57) and (6-58) is the Fanning friction factor, and the hydraulic diameter, D_e , is defined as the diameter of the base of the rough surface. The roughness function, Re^+ , is different for different families of geometrically similar surfaces. For sand-grain type roughness and for fully developed turbulent flow, this function was established by Nikuradse to be

$$\text{Re}^+(e^+) = 8.48 = \text{const. for } e^+ > 78 \quad (6-59)$$

Since the Re number in channel #1 is about 2.5×10^6 , the flow is far into the turbulent regime and Eq. (6-59) is valid. Substituting Eq. (6-59) into Eq. (6-57) yields the Fanning friction factor for sand-grain type roughness,

$$f = \frac{2}{[8.48 - 3.75 - 2.5 \ln(2e/D_h)]^2}. \quad (6-60)$$

This value, multiplied by a factor of 4 (to obtain the Moody friction factor), is used for channel #1 in the momentum equation.

A heat transfer correlation applicable to any type of geometrically similar roughness was developed by Dipprey and Sabersky [Dipprey and Sabersky, 1963]. By applying the heat-momentum-transfer analogy to flow over rough surfaces they arrived at the relation

$$g(e^+) \text{Pr}^n = \frac{f/(2 \text{St}) - 1}{\sqrt{f/2}} + \text{Re}^+(e^+) \quad (6-61)$$

where the Stanton number is given as

$$\text{St} = \frac{h}{c_p G} \quad (6-62)$$

The above relation is generally valid for geometrically similar surfaces, however, for different roughness families, there are different $g(e^+)$ functions. For sand-grain roughness, Dipprey correlated his experimental results as [Dipprey and Sabersky, 1963]

$$g(e^+) \text{Pr}^{-0.44} = 5.19 (e^+)^{0.2}. \quad (6-63)$$

Substituting for the g -function in Eq. (6-61), the Dipprey correlation (6-63) yields the Stanton number

$$St = \frac{f/2}{1 + \sqrt{f/2} [5.19 (e^+)^{0.2} Pr^{0.44} - Re^+(e^+)]} \quad (6-64)$$

where the roughness function, Re^+ , is given by Eq. (6-56).

The correctness of Eq. (6-64) can be verified in the limit of $e/D_e=0$, i.e., for a smooth wall, since it should correspond to forced turbulent convection correlations. Such a comparison is given in Figure 6-8. The Dipprey-Sabersky correlation is compared with the widely known Dittus-Boelter heat transfer correlation for smooth tubes and with the Gnielinski correlation

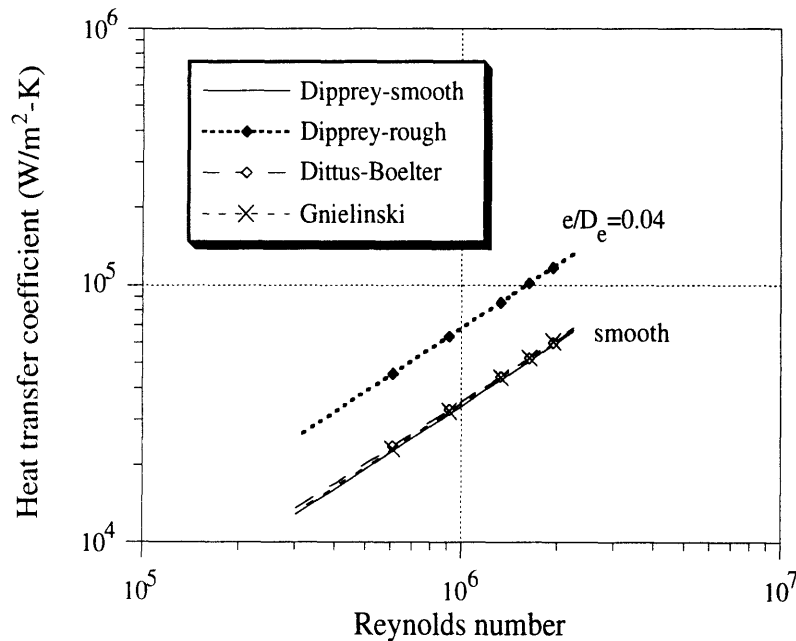


Figure 6-8 Comparison of Dipprey-Sabersky correlation with Dittus-Boelter and Gnielinski correlations

$$Nu = \frac{f/2 (Re - 1000) Pr}{1 + 12.7 \sqrt{f/2} (Pr^{2/3} - 1)}, \quad (6-65)$$

which is one of the best correlations available for forced convection regimes [Kakac et. al., 1987]. The friction factor, f , in Eq. (6-65) is a smooth tube

friction factor, which was calculated using the explicit Techo correlation [Kakac et. al., 1987]

$$f = \frac{1}{\{1.7372 \ln [\text{Re}/(1.964 \ln(\text{Re}) - 3.8215)]\}^2}, \quad (6-66)$$

considered to be one of the best forced flow convection correlations in smooth tubes. The comparison is shown for a Re number range in the vicinity of the operating conditions for channel #1. The agreement between the Dipprey-Sabersky and Gnielinski correlations is excellent. The Dittus-Boelter correlation slightly overpredicts the heat transfer coefficient, especially for lower Re numbers.

Figure 6-8 also shows the enhancement of heat transfer coefficient using sand-grain type roughness compared to a smooth tube. The heat transfer coefficient for the rough tube was calculated using the Dipprey-Sabersky correlation for an e/D_e of 0.04. It can be observed that the enhancement is significant.

The Fanning friction factor for sand-grain type roughness, calculated from Eq. (6-60), is compared with the Fanning friction factor for a smooth pipe, Eq. (6-66), in Figure 6-9.

Figures 6-8 and 6-9 suggest that by introducing sand-grain roughness with $e/D_e = 0.04$, the increase in friction factor is about 3 times, while the heat transfer enhancement is about two-fold.

6.4.6 Critical Heat Flux

The PTLWR coolant channels operate at high pressure and a high coolant mass flux. As in the CE-CANDU reference design, saturated boiling is experienced at the end of the channels, with a low exit quality. The central channel and the coolant channels in the intermediate ring are round, channel #3 is of annular shape.

Several CHF correlations have been considered to calculate the critical heat flux and CHF ratio in the PTLWR coolant channels. These include the W-3 correlation [Tong,1972], the PI-1 correlation [Pernica and Cizek, 1991], the Bowring correlation [Bowring,1972], the Shah correlation

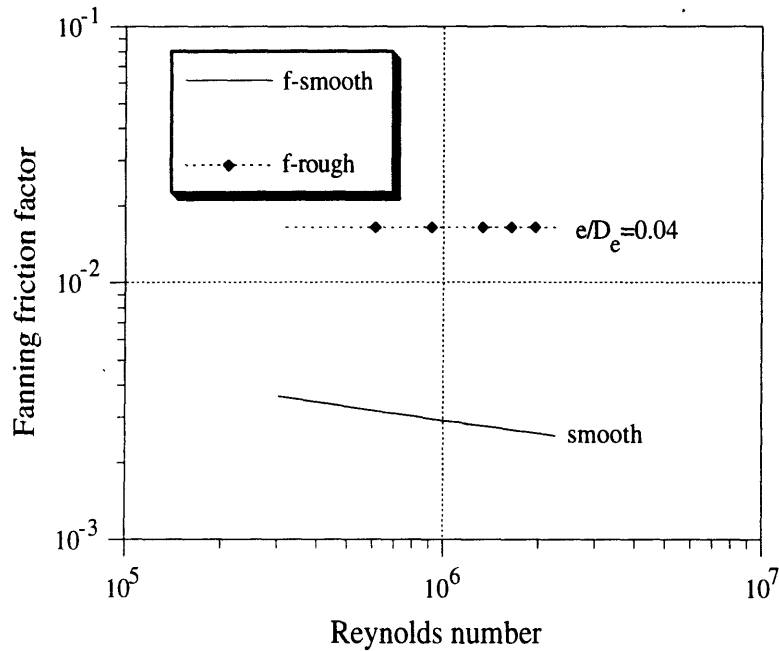


Figure 6-9 Comparison of Fanning friction factor for smooth and roughened channels

[Shah,1987], the Katto correlation [Katto, 1985], and the AECL look up tables [Groeneveld et. al.,1986]. The ranges for which the above correlations are recommended are summarized in Table 6-3. Table 6-3 also shows the conditions experienced in the coolant channels of the reference PTLWR design.

Most of the PTLWR channel parameters fall within the specified W-3 range, except for the channel length, mass flux and hydraulic diameter. The mass flux and hydraulic diameter of channel #1 are slightly above the given range. Channel length is almost twice as large as the upper limit, however, the CHF depends primarily on local conditions, represented by local quality. Since local quality falls within the range of the W-3 correlation, the fact that the channel length is much longer than the W-3 limit should not effect the correlation predictions significantly.

The Pernica and Cizek correlation (PI-1) extends the validity range compared to the W-3 correlation. However, the increased upper length limit of 4.44m still does not cover the full PTLWR channel length. Also, channel

Table 6-3 Parameters of the PTLWR and the recommended ranges for considered CHF correlations.

	PTLWR	W-3	PI-1	Bowring	Shah	AECL	Katto
Pressure (MPa)	15	7-17	2 - 18	2-19	0.031-21.2	0.1-20	0.031-21.2
Mass flux (kg/m ² -s)	7,000-9,000	1,350-6,470	50 - 7,500	136-18,600	4-29,051	0-7,500	4-29,051
Local quality	-0.29 to +0.06	-0.15 to +0.15	> -0.2	-	-2.6 to +1.0	-0.5 to +1.0	-2.6 to +1.0
Inlet quality	-0.29	-	-1.2 to +0.3	-	-4 to +0.85	-	-4 to +0.81
Length (m)	5.94	0.254 - 3.66	0.4 - 4.44	0.15-3.7	(1.3-940)D	-	(1.3-940)D
Hydraulic diameter (mm)	6 - 22	5.08 - 17.8	1.59 - 129	2-45	0.315-37.5	^a	0.320-37.8
Geometry	tube, annulus	rod bundles	rod bundles	tube	tube	tube ^a	tube

^aThe AECL look up table is compiled from data for heated vertical tubes with inner diameter of 8 mm. Correction factors allowing application of the method to rod bundle geometries, to geometries with different dimensions, as well as for other effects are provided.

mass flux slightly exceeds the upper range limit. Further, it is noted that the PI-1 correlation was tested for bundle geometries, but not for circular or annular channels. Pernica also compared several correlations, including the W-3 correlation with experimental data. The W-3 correlation was found to give a mean CHF value of 0.81, with standard deviation of 0.418,

compared to the PI-1 correlation with a mean value of 1.02 with standard deviation of 0.117 [Pernica and Cizek,1991]. Hence, the W-3 relation should be expected to yield conservatively lower CHF values.

Bowring's [Bowring, 1972] correlation encompasses high mass flux values within the verified range. Bowring's correlation was obtained for water flow in heated vertical tubes with uniform heat flux. It covers very high mass fluxes, however, the tested lengths are quite below the needed PTLWR channel length.

The Shah correlation [Shah,1987] and Katto's generalized correlation [Katto, 1985] cover a very wide range of parameters. They were also tested on many fluids other than water, including refrigerants, chemicals, cryogenes and liquid metals. The recommended range of both the Shah and Katto CHF correlations covers all parameters encountered in PTLWR coolant channels.

The AECL lookup table is based on the Chalk River Nuclear Laboratories' CHF data bank, which contains more than 15000 CHF data points. The table covers a very large range. The mass flux experienced in PTLWR coolant channels is higher than the maximum mass flux in the AECL table. Groeneveld suggests that for $G > 7500 \text{ kg/m}^2\text{-s}$, CHF values at $G = 7500 \text{ kg/m}^2\text{-s}$ can be used. Hence, the CHF predicted at these values of mass flux will be conservative. Moreover, CHF becomes less important as the post-CHF heat transfer is usually excellent at such high flows [Groeneveld et. al. 1986].

All correlations considered are listed and compared in Appendix B. The PARCHANL code offers the choice of all these correlations. The Shah correlation, the Katto correlation and the AECL lookup tables appear to be the most appropriate correlations for the PTLWR coolant channels, since all the parameters of the coolant channels fall within the range of validity of all these correlations. The AECL lookup table was selected for the CHF calculations in the PTLWR coolant channels since it was derived from an extensive experimental data bank and every data point was checked for consistency using a heat balance. It is considered a significant improvement over existing correlations because of its much wider data base

and more consistent trends at all conditions [Groeneveld,1986]. It was also incorporated into the RELAP5/MOD3 computer code [Shumway, 1989]. Also, very recent comparison of CHF correlations, used in major reactor analysis computer codes, with a large data bank showed that the AECL lookup table has the best prediction accuracy and the smallest uncertainty [Lee and Liao, 1994].

There are two fundamental approaches in calculating the CHF margins in the low-quality region. The first, traditional, approach, used in PWRs, calculates critical heat flux at local conditions and then evaluates the departure from nucleate boiling ratio (DNBR) as the CHF over the heat flux at this location. The alternative method varies power input into the fuel channel (keeping the same flux shape) until critical conditions are reached at a given location. Then the CHF margin is calculated as the ratio of the heat flux at this location (which gave rise to critical conditions) over the operating heat flux at the same location. This method could be termed as the departure from nucleate boiling power ratio (DNBPR). It is very closely related to the critical power ratio (CPR) used in BWRs and CANDUs, but it does not take into account changes in the shape of the axial heat flux profile with changes in power input. PARCHANL gives a choice between these two methods. The detailed discussion of both methods, given in Appendix B, concludes that the DNBPR method seems to be more appropriate for calculating PTLWR CHF margins. Therefore this method will be applied in the analysis of PTLWR fuel channels, presented in Section 6.5. The traditional DNBR will be also shown for comparison.

There are two other issues which have to be addressed with respect to critical heat flux in the PTLWR fuel channels. They involve critical heat flux on the roughened surface of the central channel, and the effect of azimuthal nonuniformities of the heat flux profile in the intermediate ring of circular coolant channels.

Regarding the CHF on rough surface, Tong[1965] suggests that roughness improves the CHF values in the low-quality region. However, the effect of surface roughening on critical heat flux in both pool boiling and subcooled boiling is small [Griffith,1993]. Hence, the CHF for smooth walls,

calculated from the AECL lookup table, will be used also for the central roughened channel.

To account for azimuthal nonuniformities in heat flux, critical heat flux obtained from the correlations is reduced per recommendations of Collier [Collier, 1981] as

$$q''_{CHF} = q''_{CHF} - f_{red} q''_{CHF} \quad (6-67)$$

where the reduction coefficient, f_{red} depends on the magnitude of nonuniformities,

$$\begin{aligned} f_{red} &= 0.1 & \text{for } 1 \leq q''_{max,\theta}/\bar{q}'' \leq 1.5 \\ f_{red} &= 0.2 & \text{for } 1.5 \leq q''_{max,\theta}/\bar{q}'' \leq 2.0 \end{aligned}$$

$q''_{max,\theta}$ is the peak heat flux around the channel circumference and \bar{q}'' is the azimuthal average heat flux calculated as

$$\bar{q}'' = \frac{1}{2\pi r} \int_0^{2\pi} q''(\theta) r d\theta \quad (6-68)$$

6.4.7 Post-CHF Heat Transfer

To explore the potential of a SiC-coated fuel matrix to operate in stable film boiling in case the CHF limit is exceeded, an option for heat transfer analysis of the post-CHF regime was added to the PARCHANL code. The heat transfer coefficient in the post-CHF region is calculated from the Groeneveld correlation [Groeneveld,1969], based on an extensive set of experimental data. For the round channels (channels #1 and #2), the correlation based on data from vertical and horizontal flow in round tubes is applied,

$$h = 0.00327 \left\{ \frac{G D_h}{\mu_g} \left[x + \frac{\rho_g}{\rho_f} (1-x) \right] \right\}^{0.901} \left(\frac{Cp_g \mu_g}{k_g} \right)_{wall}^{1.32} Y^{-1.5} \frac{D_h}{k_g}, \quad (6-69)$$

where

$$Y = \max \left\{ 0.1; 1.0 - 0.1 (1-x)^{0.4} \left(\frac{\rho_f}{\rho_g} - 1 \right)^{0.4} \right\} \quad (6-70)$$

For the annular channel #3, a similar equation to Eq. (6-69), based on annuli data,

$$h = 0.052 \left(\frac{G D_h}{\mu_g} \left[x + \frac{\rho_g}{\rho_f} (1-x) \right] \right)^{0.688} \left(\frac{C_p \mu_g}{k_g} \right)_{\text{wall}}^{1.26} Y^{-1.06} \frac{D_h}{k_g}, \quad (6-71)$$

is used.

In Eqs. (6-70) through (6-71), thermal conductivity in the Nusselt number and properties in the two-phase Reynolds number are evaluated at saturation temperature, while the Prandtl number is evaluated at the wall temperature.

6.5 DISCUSSION OF THE RESULTS

The results of the thermal-hydraulic analysis will be presented in two major sections. The first section will analyze the fresh core with almost flat power density profile. The second section considers the equilibrium core with bi-directional refueling scheme.

6.5.1 Fresh Core

As has been demonstrated in Chapter 4, the fresh core exhibits an almost flat power density profile, with slight peaking at the ends of the fuel channels. The analysis of the PTLWR fresh fuel channels was performed by the PARCHANL code combined with the 2-D finite element code ALGOR. The input data used for the reference PTLWR design are given in Table 6-1 and in Figure 6-3. The power density profile in fuel compacts, obtained from an MCNP model, is given in Chapter 4.

6.5.1.1 Thermohydraulics during Normal Operation

Figures 6-10 and 6-11 show the profile of bulk coolant temperature “T-fluid”, and wall temperature “T-wall” along each coolant channel. Numbers in parentheses denote channel number according to Figure 6-3. It can be observed that the central channel (#1) remains slightly subcooled at the exit, while the intermediate coolant channels (#2) and the outer

annular channel (#3) reached the saturation state close to the channel outlet. Saturation temperature, “ T_{sat} ”, is slightly decreasing because of the decrease in local pressure. The development of the wall temperature profile indicates clearly the location of the onset of subcooled boiling.

Subcooled boiling is experienced in all channels. Note that the wall temperature in Figure 6-11 is the azimuthal-average temperature. The azimuthal temperature profile for each channel will be shown in Section 6.5.1.2.

Figure 6-12 shows local equilibrium quality as a function of axial position. The exit quality is 0.5%, which is less than the average exit quality for CANDU of 2%. The highest exit quality for CANDU is 4.73%. Figure 6-13 shows the pressure decrease along each channel. The total channel pressure drop is about 0.7 MPa, which is less than the pressure drop of the reference CE-CANDU design by about 0.3 MPa. The smaller pressure drop is primarily due to significantly lower form losses in the PTLWR fuel channel. Development of the heat transfer coefficient is shown in Figure

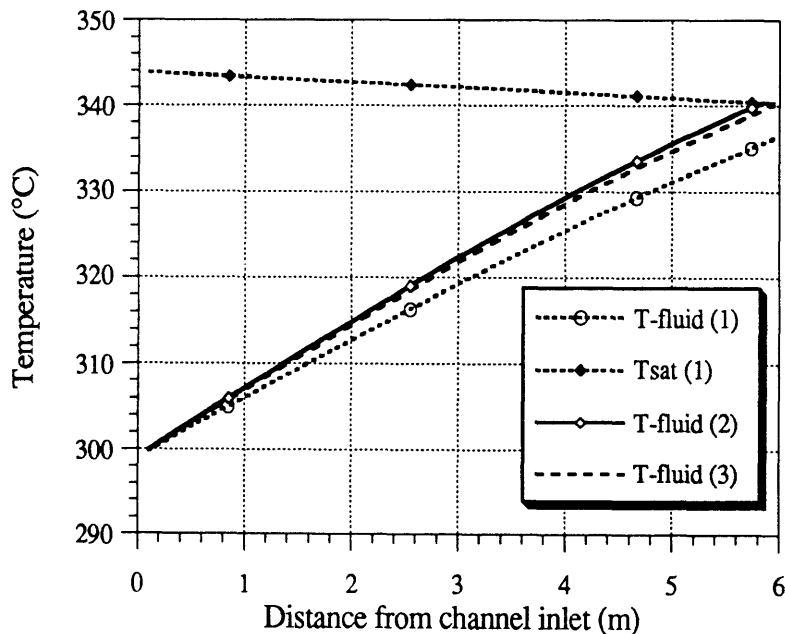


Figure 6-10 Bulk coolant temperature profile in the PTLWR coolant channels

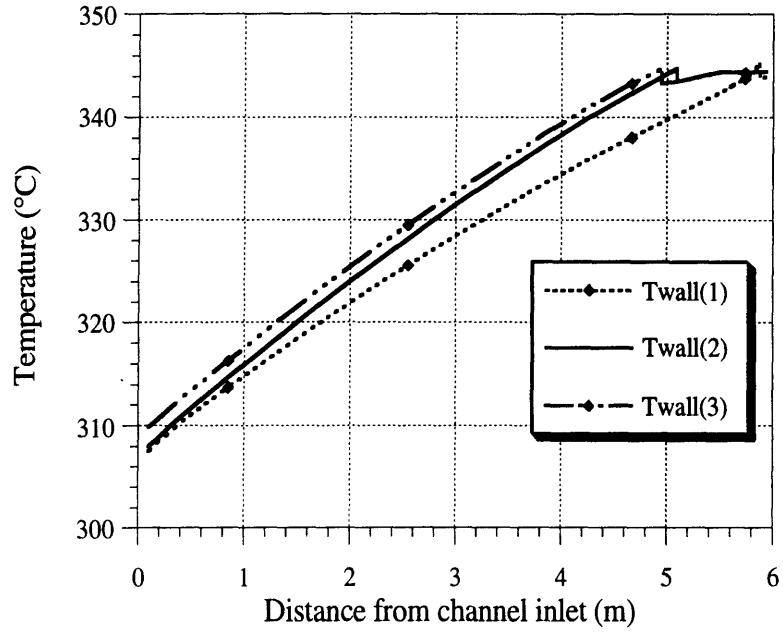


Figure 6-11 Wall temperature profile in the PTLWR coolant channels

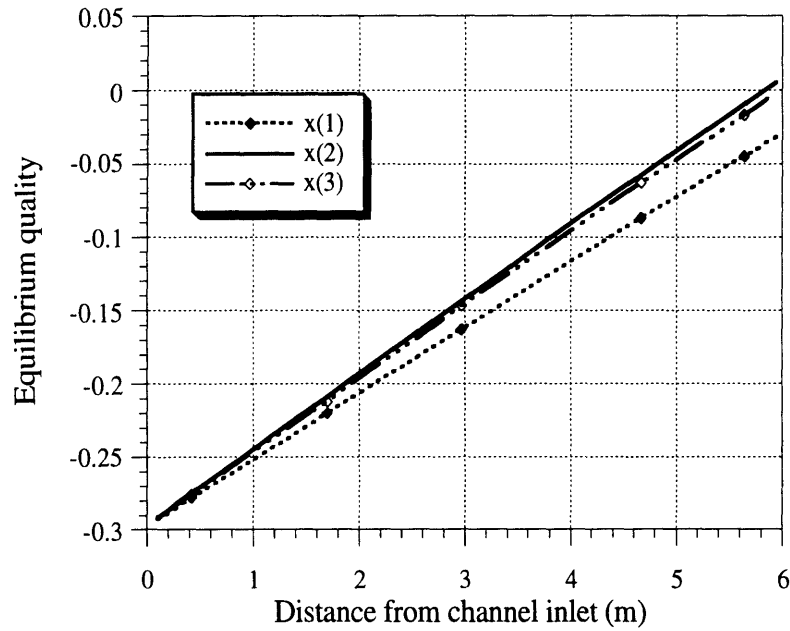


Figure 6-12 Equilibrium quality development in the PTLWR coolant channels

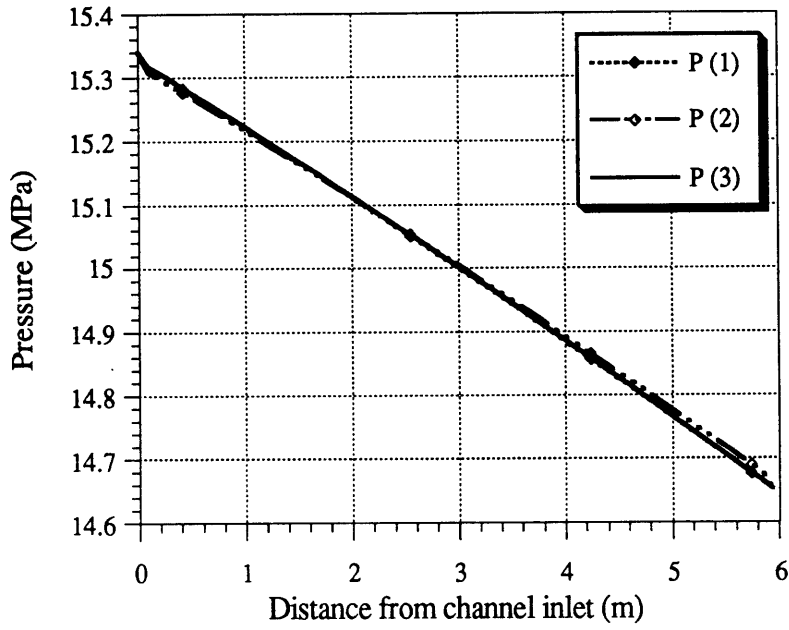


Figure 6-13 Pressure along the PTLWR coolant channels

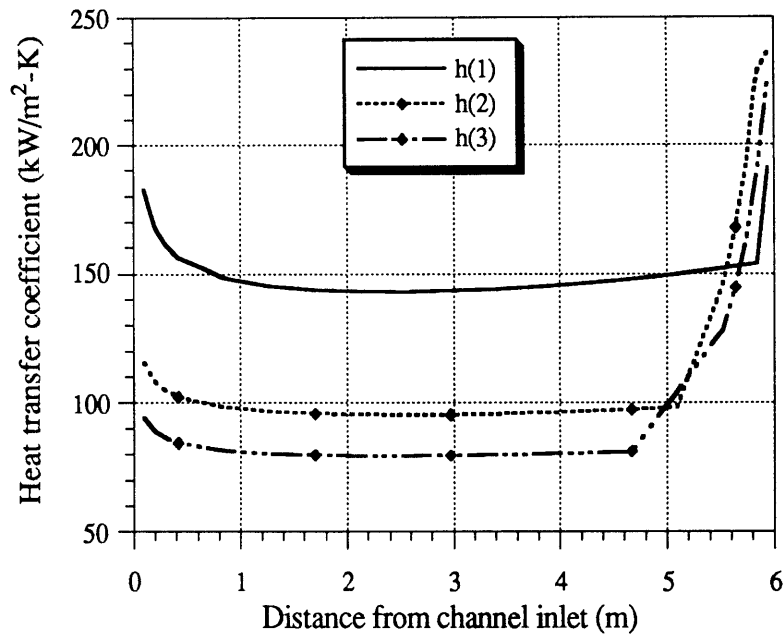


Figure 6-14 Heat transfer coefficient along the PTLWR coolant channels

6-14. The heat transfer coefficient of the central coolant channel is significantly higher than that of the other channels due to its sand-grain type roughness. Roughness height was chosen to be 1 mm. At the end of the channels, the heat transfer coefficient is significantly increased as the heat transfer regime changes from single-phase convection to fully developed subcooled boiling.

Figure 6-15 shows the critical heat flux profile, calculated by the heat balance method using the AECL lookup table and the heat flux profile along each channel. The difference between the CANDU and PTLWR axial heat flux profiles results in quite different shapes of the departure from nucleate boiling power ratio (DNBPR) curve, shown in Figure 6-16. Since the heat flux in the PTLWR fresh core is essentially flat, except for a slightly higher heat flux at channel ends, burnout will always occur at the channel exit. From the point of view of CHF, the PTLWR design with a fresh core has a disadvantage, since it exhibits the highest coolant temperature at the location of the highest heat flux, while in CANDU, the highest coolant temperature is at the point of the lowest heat flux. This problem is compensated by a small peaking factor, resulting in a much smaller maximum heat flux (for the same core power) and by the higher mass flux of the coolant. Figure 6-16 also shows the operating point for CANDU reactors, which maintains the MDNBPR at about 1.5 during normal operation. It can be seen that the lowest DNBPR point at the end of the channel corresponds to the CANDU operating point. Moreover, post CHF calculations show that the matrix can operate at full power in the post CHF regime while fuel and matrix temperature stay quite below the prescribed limits. Also, it will be shown in Section 6.5.2 that for the equilibrium core, the problem of having the highest heat flux at the location having the highest coolant temperature can be eliminated by the bi-directional refueling scheme.

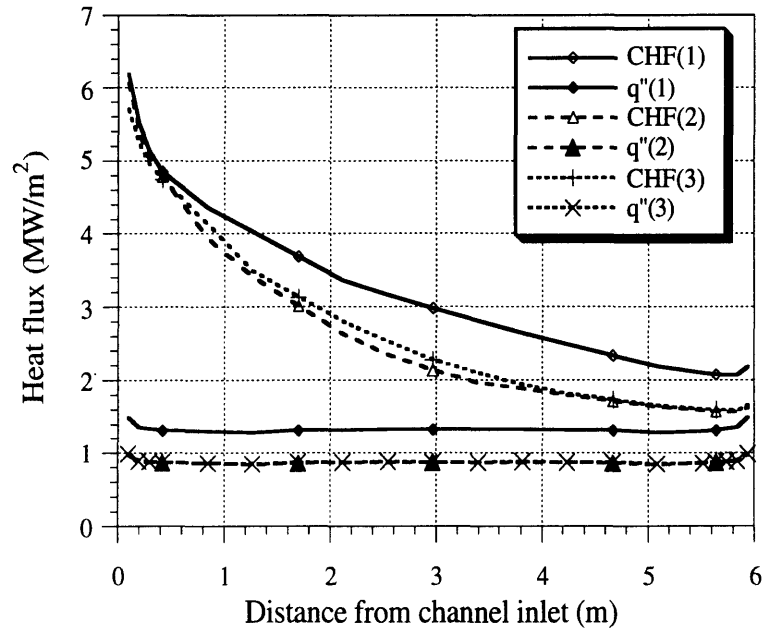


Figure 6-15 CHF and operating heat flux along the PTLWR coolant channels

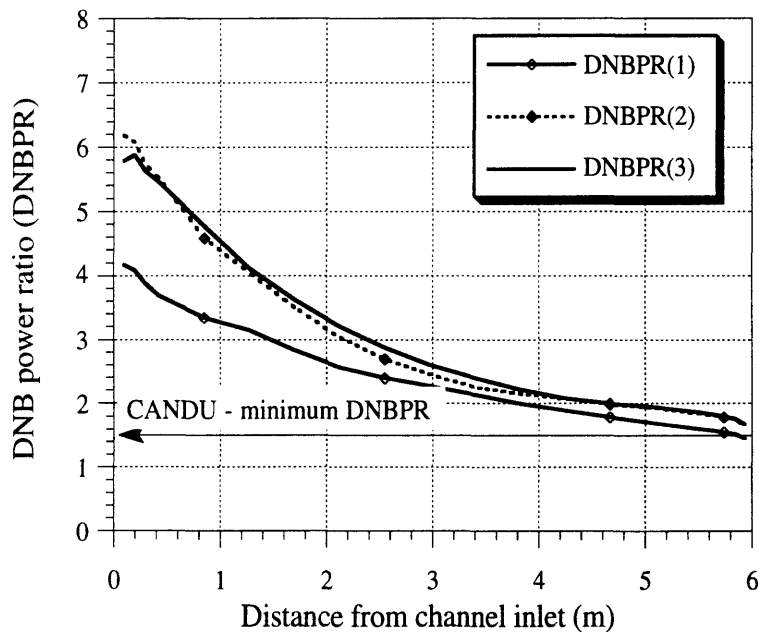


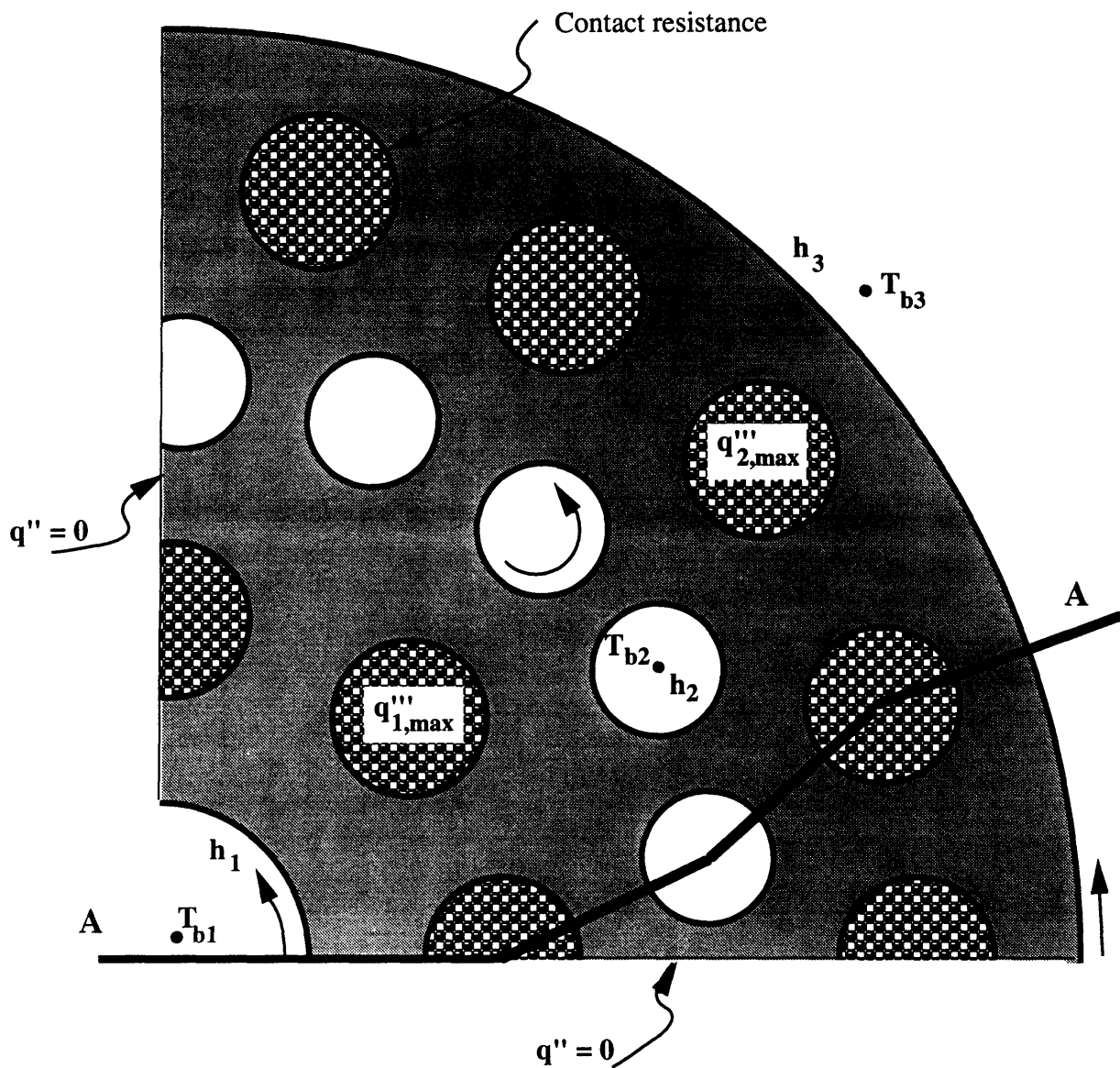
Figure 6-16 DNB power ratio along the PTLWR coolant channels

6.5.1.2 Fuel Matrix Analysis

The objective of this section is to evaluate fuel centerline temperature, radial temperature profile across the fuel matrix, and the heat flux distribution into individual coolant channels. Heat flux to coolant channels is an important input parameter for the thermal hydraulic analysis performed by the PARCHANL code.

Heat conduction across the fuel matrix was modeled in 2-D geometry at the plane of the largest power density (at the channel outlet for the fresh core), using the finite element code ALGOR. Only one quarter of the matrix was modeled (due to symmetry) with boundary conditions of zero heat flux at symmetry planes. A cross section of the ALGOR 2-D model with boundary conditions is shown in Figure 6-17. Coolant boundary conditions were obtained from PARCHANL. Peak power densities were obtained from MCNP in Chapter 4. Since ALGOR does not provide any special capabilities to model contact resistance, contact resistance between the fuel region and the graphite matrix was modeled as an additional gap, with effective properties, to yield the prescribed contact resistance value. The thermal properties of the graphite matrix were modeled as temperature dependent at high fluences to account for the decrease of thermal conductivity with irradiation.

The matrix temperature profile is shown in Figure 6-18. Figure 6-18 shows that the maximum fuel centerline temperature is about 1081 °C, which is less than the limit of 1300°C. Azimuthal profiles of heat fluxes and wall temperatures for each channel are shown in Figures 6-19 through 6-21. The direction and location of the azimuthal profiles are marked in Figure 6-17. It can be observed that the central and outer channels exhibit only small nonuniformities in both temperature and heat flux profile while the intermediate coolant channel exhibits large nonuniformities. This is not very surprising since the heat transfer coefficient in the coolant channels is large, hence most of the heat flow proceeds from fuel compacts directly to the coolant along the shortest path. Heat flux profiles from Figures 6-19 through 6-21 are used in Eq. (6-68) to obtain the average heat



Boundary conditions:

h - heat transfer coefficient

T_b - bulk coolant temperature

q'' - heat flux

q''' - power density

$q'' = 0$

Direction of azimuthal profiles

A - A Cut for presenting temperature profile

Figure 6-17 Boundary conditions for a 2-D finite element model

Fuel matrix temperature profile

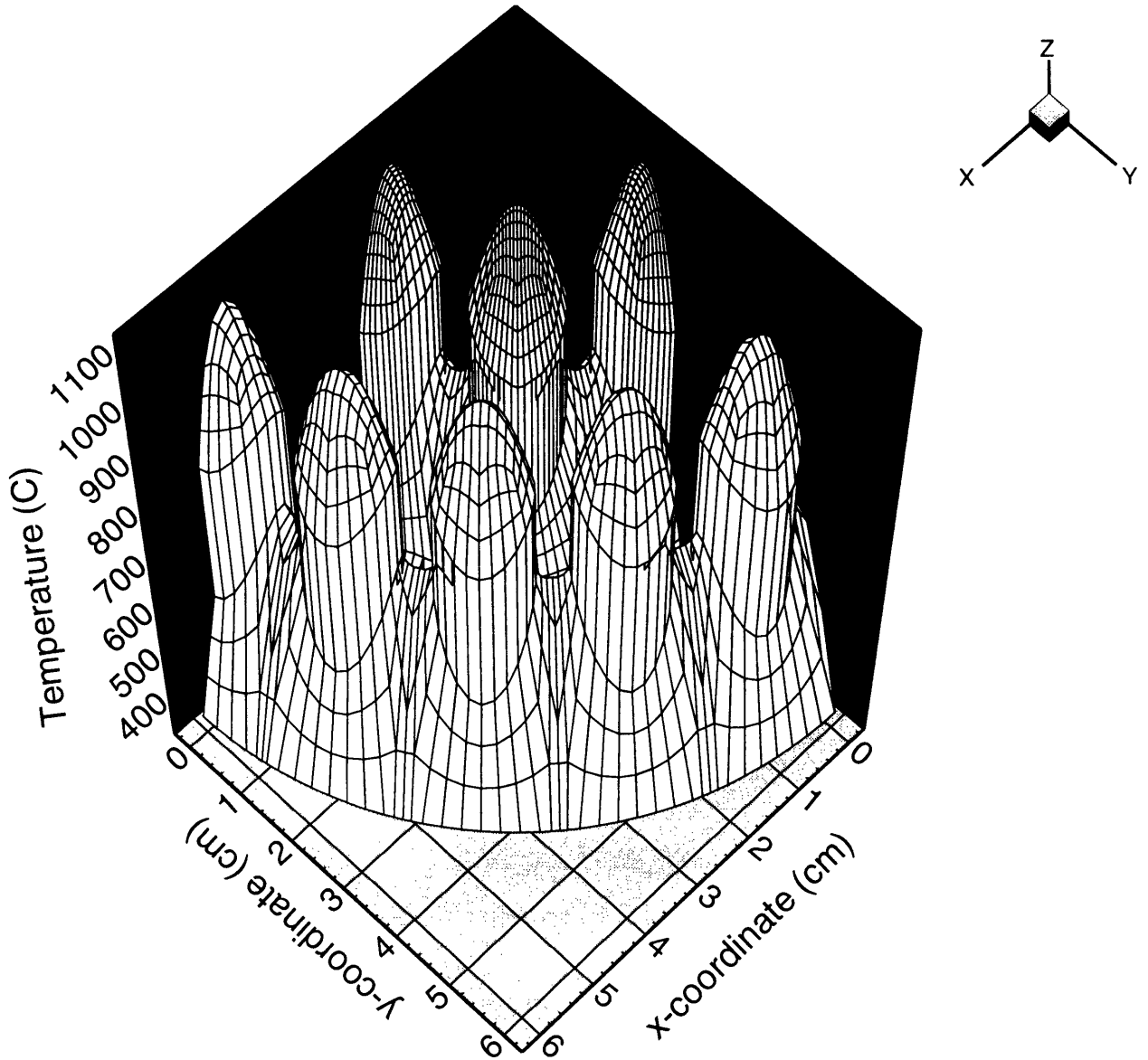


Figure 6-18 Maximum fuel matrix temperature profile for the fresh core

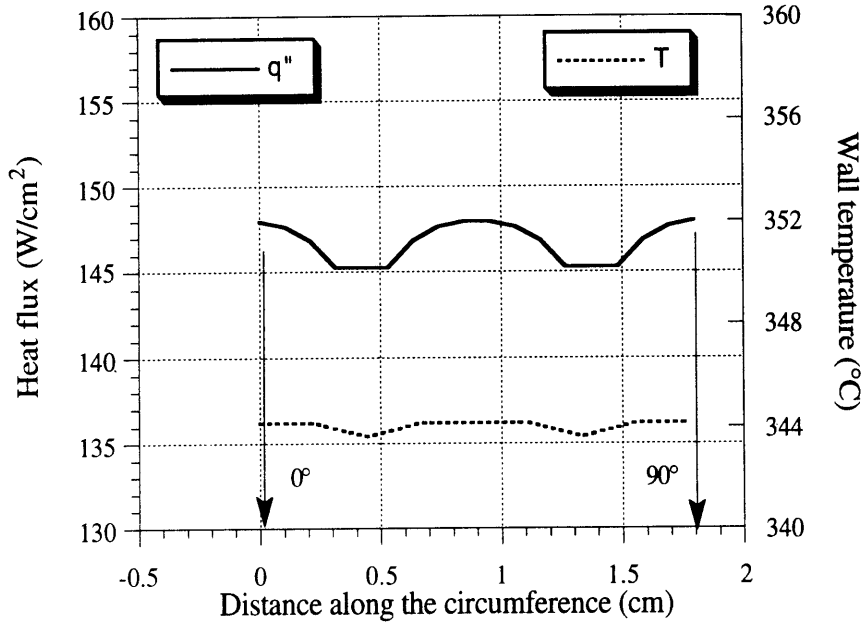


Figure 6-19 Azimuthal temperature and heat flux profiles in the central coolant channel

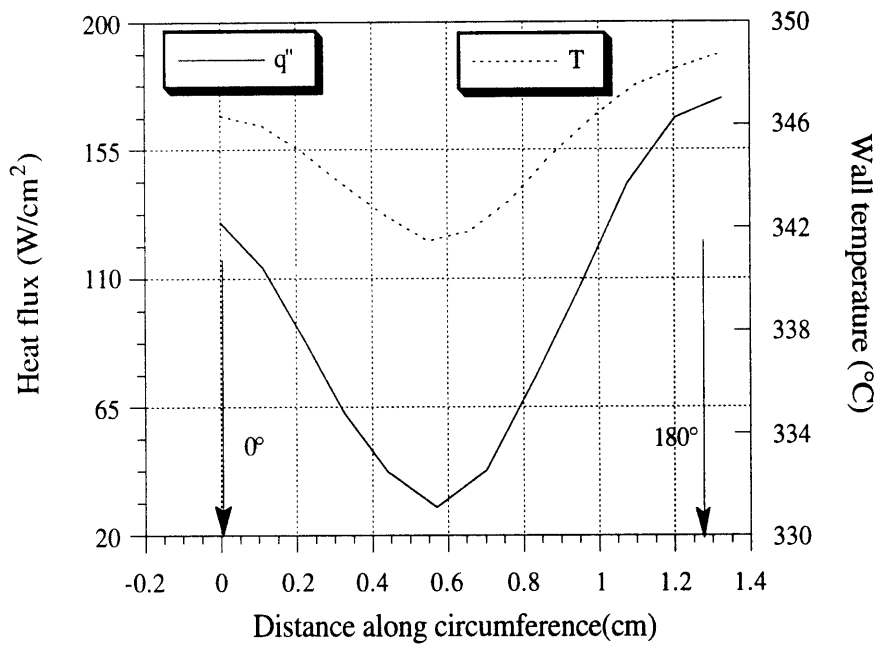


Figure 6-20 Azimuthal temperature and heat flux profiles in the intermediate coolant channel

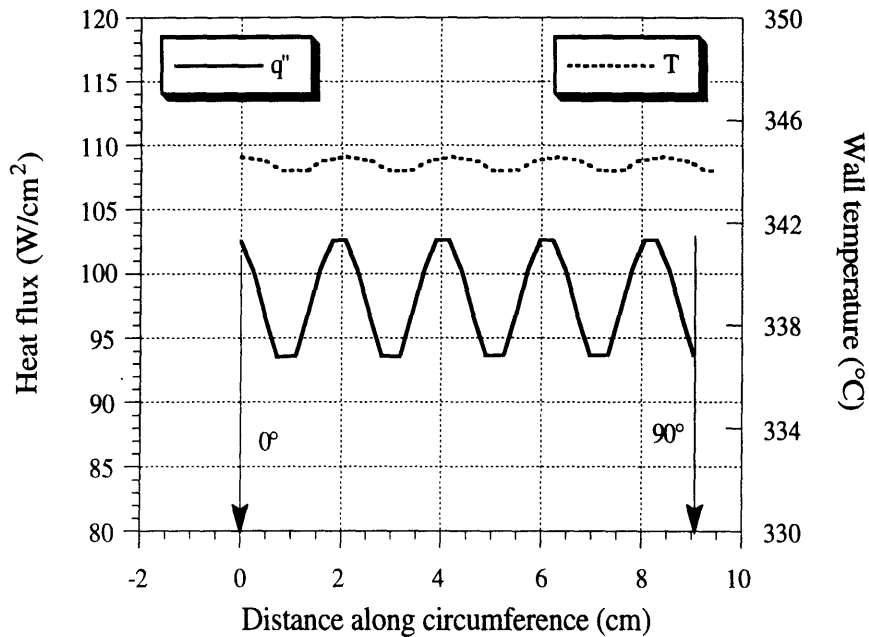


Figure 6-21 Azimuthal temperature and heat flux profiles in the outer coolant channel

flux to individual coolant channels needed in thermohydraulic analysis. The ratio of maximum azimuthal heat flux over the azimuthal-average heat flux is used to obtain the correction factor for the CHF ratio calculations.

6.5.1.3 Matrix Performance in Post-CHF Regime

This section will explore the potential of the fuel matrix to operate in stable film boiling in case the CHF limit is exceeded. Typically, concern over low DNBR arises in a main coolant pump trip, in particular, pump seizure is of primary concern since dryout occurs. Analysis of a pump seizure event in CANDUs showed that transient dryout occurs [Shapiro,1979]. Since the pump is presumed to seize in only 2 seconds, even if shutdown systems are available, they cannot alter short term flow response, resulting in dryout. Shutdown system function will, however, prevent centerline melting. In the case of the proposed matrix fuel, the low

initial stored energy in the fuel and the additional storage capabilities of the matrix, together with matrix-coating resistance to high temperature should eliminate concerns of fuel damage should the matrix operate in the post-CHF regime.

To confirm good performance of the fuel matrix in the post-CHF regime, the mass flow rate was decreased to one half of nominal value, while the power was fixed at its nominal value. These conditions lead to the establishment of post-CHF regimes at the end of all three channels. The location of the sudden transition to the post-CHF regime can be observed in Figure 6-22, which shows the development of the heat transfer coefficient along each channel. Heat transfer coefficients and bulk temperatures at the end of the channels (location of highest power density) calculated by the thermohydraulic code PARCHANL were used in a 2-D heat conduction model to obtain the temperature distribution in the fuel matrix. The resulting temperature profile along the cut plane A-A, shown in Figure 6-17, is presented in Figure 6-23.

The results show that the reactor could operate at full power with a large portion of the channels in the post CHF regime without exceeding either the fuel centerline temperature or the matrix coating temperature limits. In fact there are still large margins to reach the transient fuel centerline temperature limit of 1600°C and the SiC-coated wall temperature limit of 1300°C. Hence, the traditional MDNBR limit is not of crucial concern in the PTLWR.

6.5.1.4 Flow Instability Considerations

Parallel channels with two-phase flow may be susceptible to various instability phenomena. Two kinds of parallel channel instabilities are possible – between individual fuel channels and instabilities within the fuel channel. Potential instabilities between the fuel channels can be handled by proper orificing and should not pose a problem. CANDU reactors have operated successfully in a stable regime. The PTLWR fuel channels,

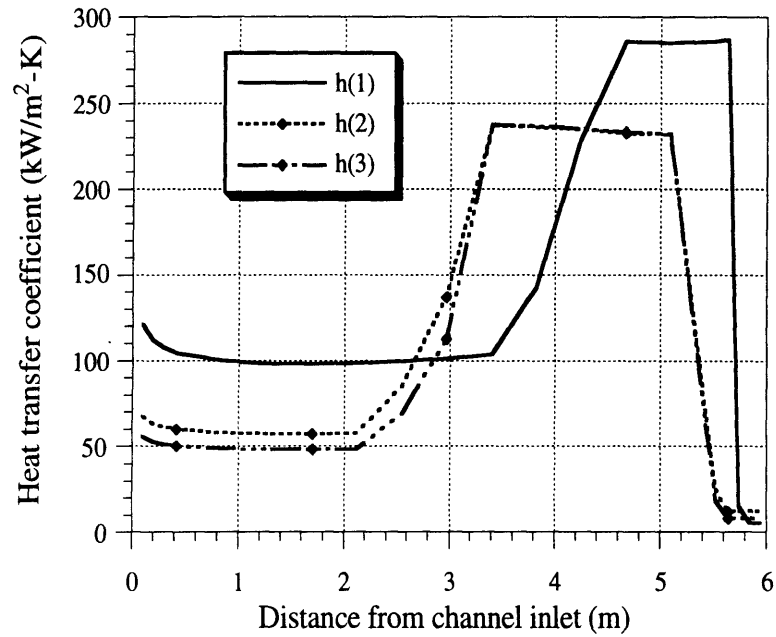


Figure 6-22 Transition of heat transfer coefficient to the post-CHF regime

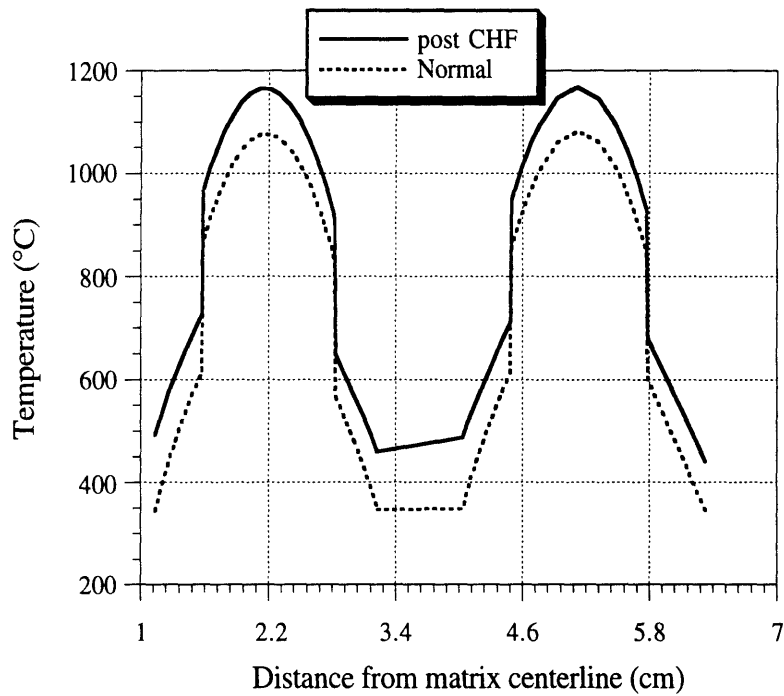


Figure 6-23 Fuel matrix performance during normal operation and in the post-CHF regime

however, differ from those of CANDU by having parallel non-communicating coolant channels, which may give rise to flow instabilities within the fuel channel.

There are two major instability types – excursive (Ledinegg) instability, and density wave oscillations. Ledinegg instability is important in low-pressure systems; high-pressure systems such as the PTLWR concept are less susceptible to this phenomenon. To check the susceptibility to Ledinegg instabilities, channel operating characteristics of all channels have been calculated for the range of flow rates between 30% and 150% at nominal power, as shown in Figure 6-24. It can be observed that even at low mass flow rates (exit equilibrium quality approaches 1.0 for the lowest mass flow rates), no reverse trend in pressure drop (bottom of the S-shaped curve) occurs.

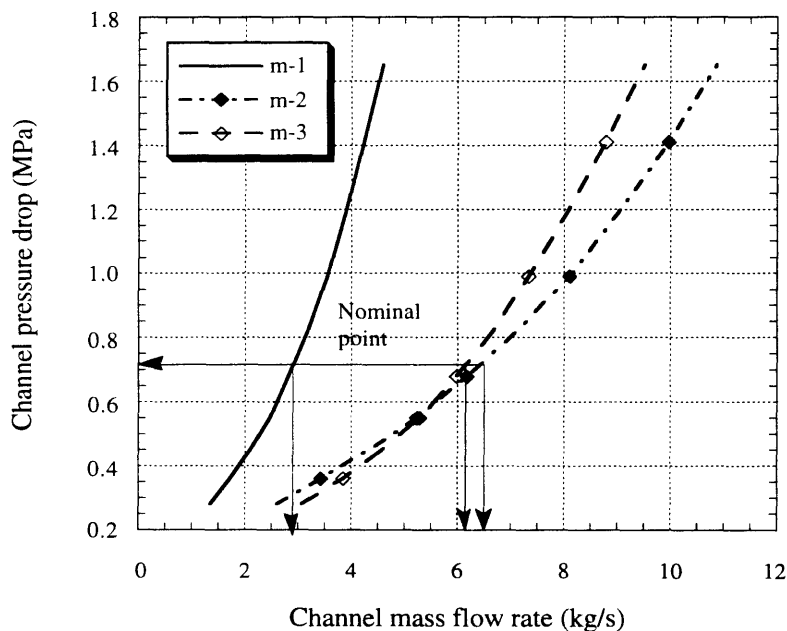


Figure 6-24 Operating characteristics of coolant channels at nominal power input

Of greater importance are density wave oscillations, which may appear in systems consisting of combined sections of single-phase and two-phase flow, such as the PTLWR fuel channels. Density wave oscillations depend

on many factors. High inlet velocities, high system pressure, large inlet pressure losses and large inlet subcooling increase channel stability to density wave oscillations. Conversely, large channel length, high heat flux and large bypass flow in parallel channels tend to destabilize the channel [Borkowski et. al., 1993]. Density wave oscillations are much more complicated phenomena than the Ledinegg instability and their comprehensive analysis is beyond the scope of this study. The PTLWR coolant channels are relatively long and operate at high heat flux, which favor instability. On the other hand, they possess stabilizing factors since they operate at high inlet velocity, large inlet subcooling and high pressure. Also, the two-phase flow section is very small (about 15cm compared to a 580 cm-long single-phase section). Hence it is not expected that the PTLWR parallel channels will be susceptible to density wave oscillations. This can be confirmed using the simplified stability criterion of Saha [Saha et. al., 1976]. Saha recommends construction of a stability map in an equilibrium phase change number-subcooling number space where the equilibrium phase change number is defined as

$$N_{pch,eq} = \frac{\rho_f - \rho_g}{\rho_g} \frac{q'' P_h L}{\dot{m} h_{fg}} \quad (6-72)$$

and the subcooling number is defined by the relation

$$N_{sub} = \frac{\rho_f - \rho_g}{\rho_g} \frac{h_f - h_{in}}{h_{fg}} \quad (6-73)$$

The map consists of two lines. The first line is a line of constant phase change number obtained at zero subcooling, $N_{pch,eq,0}$. This number has been obtained using the simplified stability criterion of Ishii [Ishii, 1971]

$$\frac{\rho_f - \rho_g}{\rho_g} x_{e,eq} = \frac{2 \left(K_{in} + \frac{f_{TP} L}{2 D_h} + K_e \right)}{1 + \frac{1}{2} \left(\frac{f_{TP} L}{2 D_e} + 2K_e \right)} \quad (6-74)$$

as

$$N_{pch,eq,0} = \frac{\rho_f - \rho_g}{\rho_g} x_{e,eq} \quad (6-75)$$

where K_{in} and K_e are form losses at channel inlet and exit, respectively, $x_{e,eq}$ is equilibrium channel exit quality and f_{TP} is a two-phase friction factor. The two phase friction factor was calculated using the HEM model. To obtain exit equilibrium quality at the onset of density wave oscillations, coolant conditions at the channel inlet were set to saturation and the power into the channel (keeping the axial heat flux profile fixed) was increased until the equality in Eq. (6-74) is reached. Note that iterations are necessary since both the RHS and LHS of Eq. (6-74) vary with changes in channel power. Moreover, redistribution of mass flux in the parallel channels due to power changes must be also considered. Intermediate cooling channels were found to be the first to reach the density wave instability for zero subcooling at 190% power with exit quality $x_{e,eq}=0.57$, which yields $N_{pch,eq,0}=2.84$ by virtue of equation (6-75). This number establishes point A on the stability map, as shown in Figure 6-25.

The second line is a constant subcooling number line, established by intersection of equilibrium phase change number and subcooling critical number calculated from nonequilibrium theory [Saha et. al., 1976], i.e.,

$$N_{sub,cr} = 0.0022 Pe \frac{A}{P_h L} N_{pch,eq,0} \quad \text{for } Pe \leq 7 \times 10^4, \text{ and} \quad (6-76)$$

$$N_{sub,cr} = 154 Pe \frac{A}{P_h L} N_{pch,eq,0} \quad \text{for } Pe > 7 \times 10^4 \quad (6-77)$$

where Pe is the Peclet number. This intersection is shown as point B in Figure 6-25. The last point, C, is calculated as an intersection of the critical subcooling number line and Ishii's stability criterion line, i.e.,

$$N_{pch,eq,c} = N_{sub,cr} + \frac{\rho_f - \rho_g}{\rho_g} \left(\frac{\bar{q}_{cr} P_h L}{\dot{m} h_{fg}} - \frac{h_f - h_g}{h_g} \right) \quad (6-78)$$

where \bar{q}_{cr} is the average channel heat flux at 190% power, i.e., the power which initiates density wave instabilities at zero subcooling. The complete stability map, including the operating point, is shown in Figure 6-25. As expected, the operating point, obtained from Eqs. (6-72) and (6-73), is deeply in the stable region. Calculations showed that at nominal subcooling, onset of density wave instabilities within the fuel channel would not be reached even at 200% power. Note that CANDU channels begin to oscillate at about

180% power [Banerjee and Hancox, 1981]. Therefore, density wave oscillations within a fuel channel are not a limiting factor to channel power.

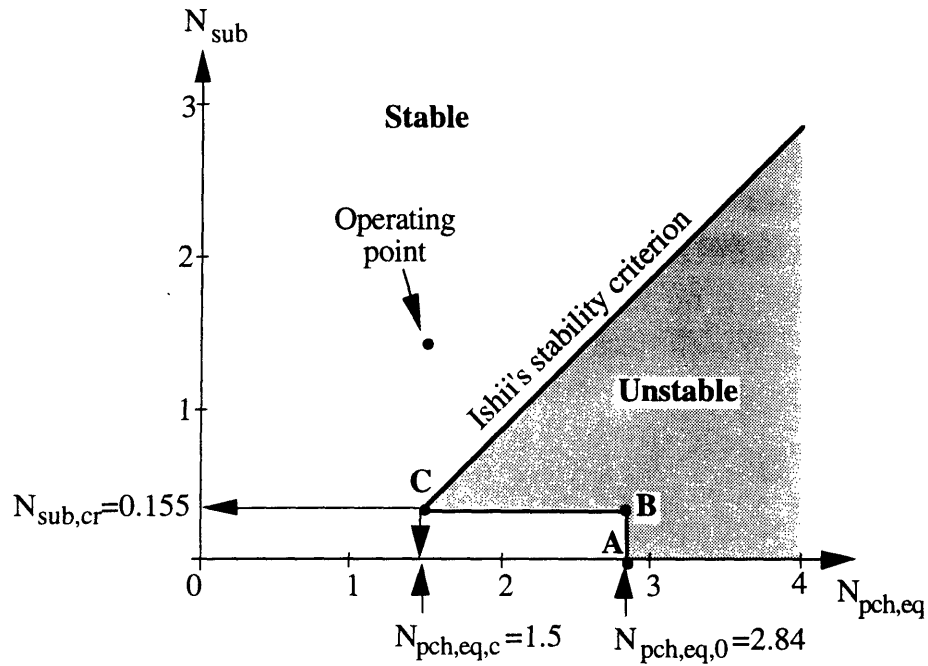


Figure 6-25 Simplified stability criterion for thermally induced flow oscillations in intermediate coolant channel

6.5.2 Equilibrium Core

The thermohydraulics of the equilibrium core differs from that of the fresh core due to its different power density profile, which depends, primarily, on the refueling scheme. Various on-line refueling schemes and their effect on the power density profile were studied in Chapter 4. A bi-directional, online refueling scheme with partial reshuffling has been selected as a reference refueling scheme. The arrangement of the bundles for this scheme is shown in Figure 4-51, and the corresponding power density profile in Figure 4-52. Thermohydraulic analysis of the fuel channel was performed in the same manner as for the fresh core. The power density profile was taken from Figure 4-52, and a 2-D heat conduction analysis using ALGOR was done in the plane at the location of maximum power density (140cm from the channel inlet).

6.5.2.1 Thermohydraulics during Normal Operation

The bulk coolant temperature profile and wall temperature profile along each coolant channel are shown in Figures 6-26 and 6-27. Both the bulk and wall temperature profiles differ from the almost linear profiles for the fresh core, shown in Figures 6-10 and 6-11, reflecting the different power density profile. The major difference in thermohydraulic performance between the fresh core and equilibrium core is in the CHF margins. Figure 6-28 shows the heat flux and CHF profiles calculated by the heat balance method for each coolant channel. Since the shape of the operating heat flux profile corresponds to the shape of the CHF profile, CHF margins are increased. Figure 6-29 plots the DNB power ratio along each channel. It can be observed that the DNBPR is almost constant along the last two thirds of the channel. The DNBPR margin is also increased by about 10% (compare Figure 6-16 and 6-29). Almost constant CHF margins are even more evident using the traditional DNBR (i.e., when CHF is evaluated by the local method).

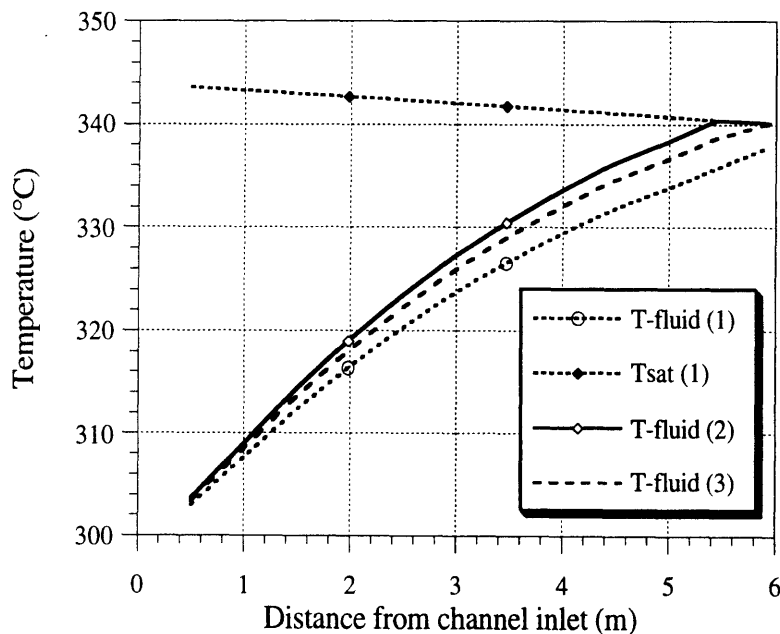


Figure 6-26 Bulk coolant temperature profile in the PTLWR channels for equilibrium core

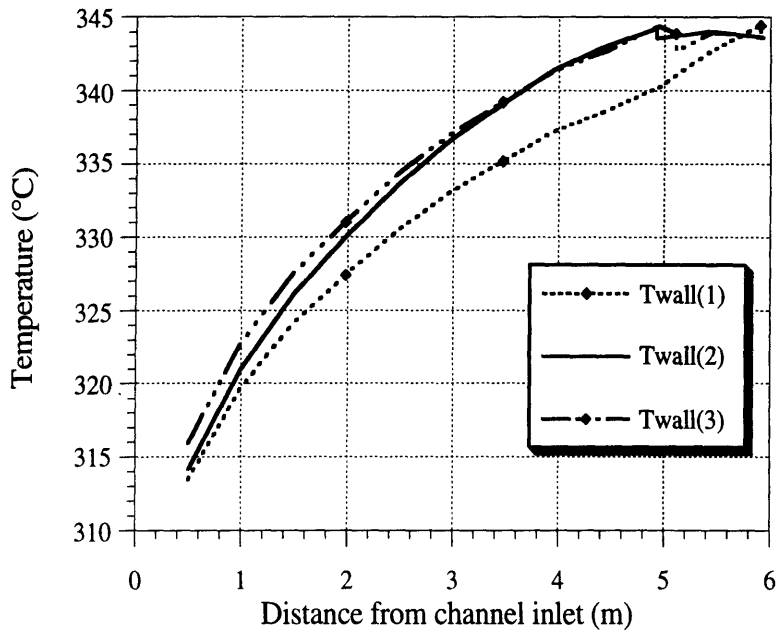


Figure 6-27 Wall temperature profile in the PTLWR channels for equilibrium core

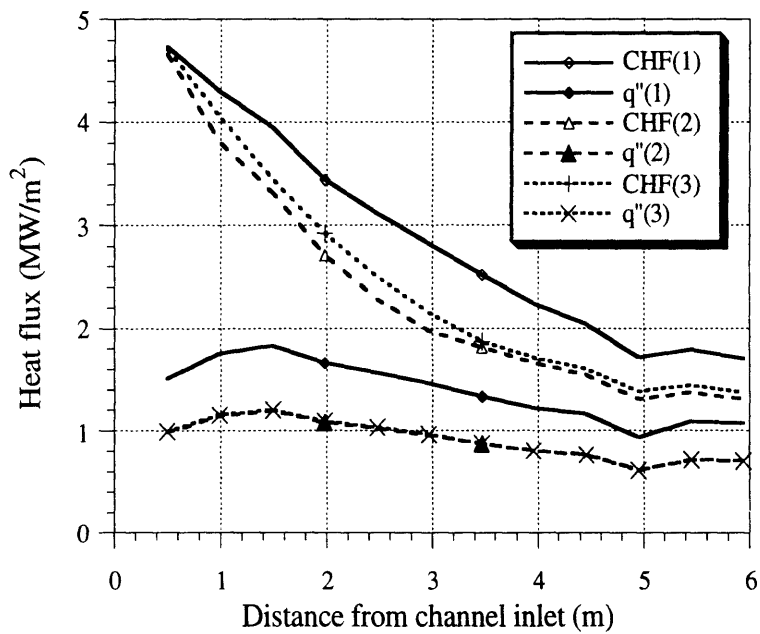


Figure 6-28 CHF and operating heat flux along the PTLWR coolant channels for equilibrium core

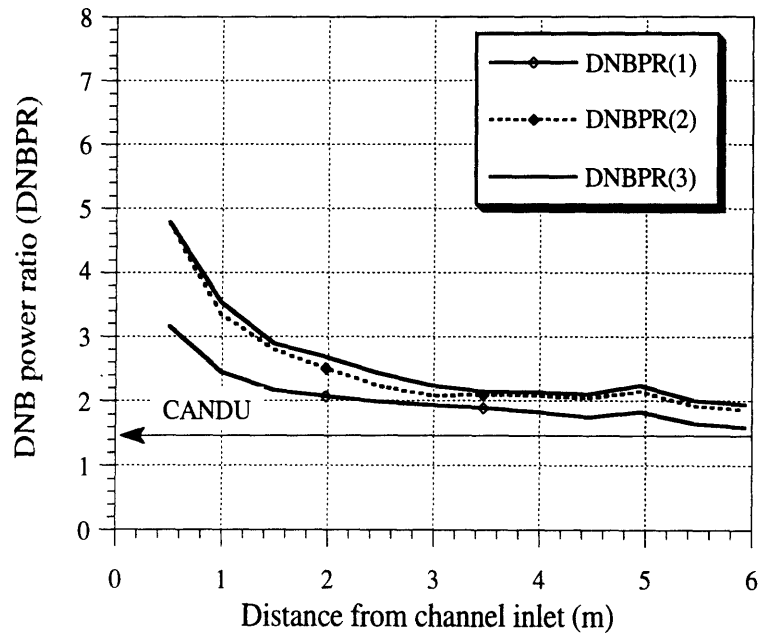


Figure 6-29 DNB power ratio along the PTLWR coolant channels for equilibrium core

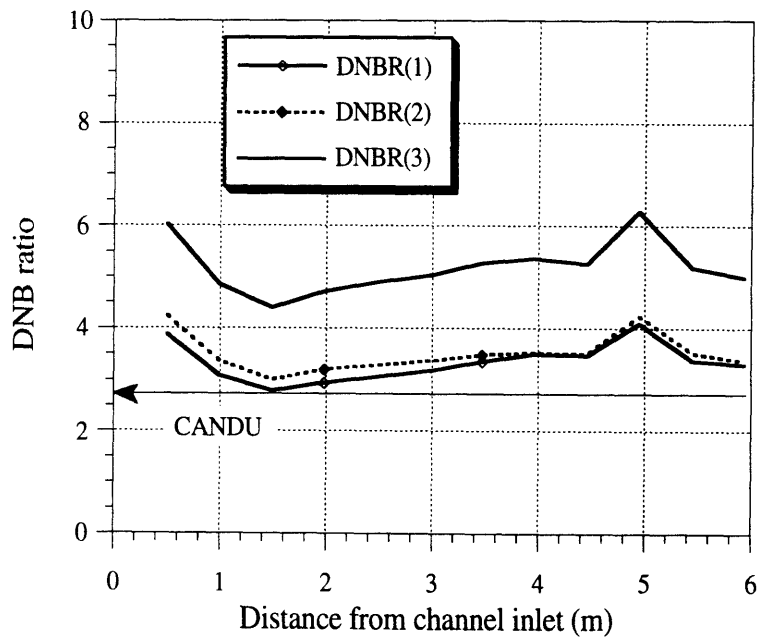


Figure 6-30 DNBR along the PTLWR coolant channels for equilibrium core

This can be seen from Figure 6-30, which shows the DNBR along each coolant channel. The MDNBR is at the location of the highest heat flux, while the minimum DNBR is at the end of the channel. Also note the much higher CHF margins using the local method compared to the heat balance method (around 3 compared to 1.6).

6.5.2.2 Fuel Matrix Analysis

The matrix temperature profile in the plane at the axial position of the highest power density is shown in Figure 6-31. Compared with the results for the fresh core, presented in Figure 6-18, the peak fuel centerline temperature is increased by about 100 °C due to higher peaking. However, it still remains well below the limit of 1300 °C. Figure 6-31 shows that there is a large temperature jump across the fuel compact-matrix interface. This jump can be eliminated by using an alternative technology for manufacturing the fuel elements, developed by HOBEG [Hrovat, 1975], [Hrovat, 1978].

HOBEG (Hochtemperatur-Brennelement GmbH) developed molded block fuel elements which consist of an isotropic highly-crystalline graphite matrix, with coolant channels and fuel regions with TRISO particles embedded in a graphite matrix. The important characteristics are the elimination of the gap between the fuel compact and graphite matrix typical for MHTGR blocks, excellent thermal contact between fuel particles, and highly dense graphite matrix material. This allows operation at a higher power density while keeping the maximum operating fuel temperature relatively low. The thermal performance of the PTLWR fuel matrix using HOBEG monolithic blocks is shown in Figure 6-32. The decrease in the fuel centerline temperature by eliminating the contact resistance between the fuel region and the matrix is significant (about 300°C).

Fuel matrix temperature profile

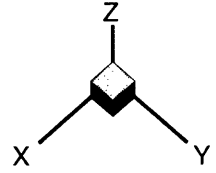
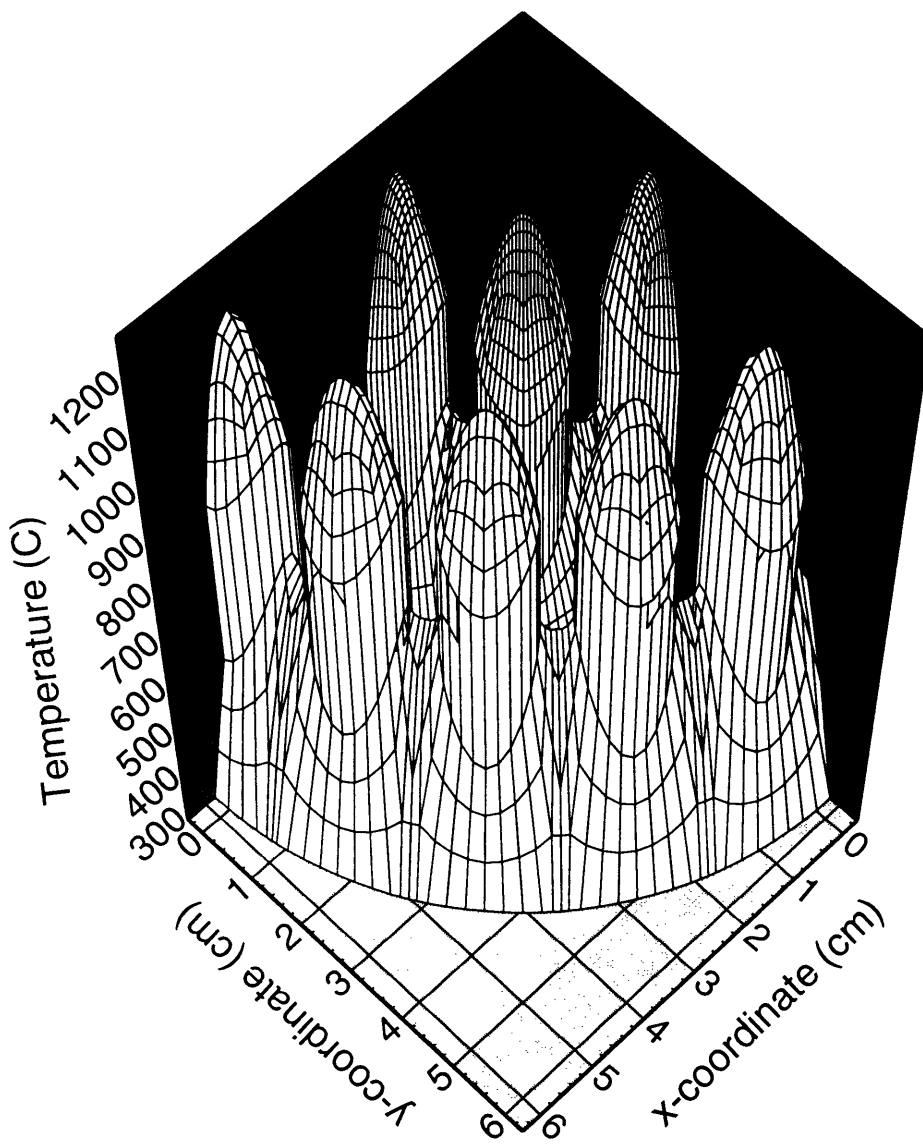


Figure 6-31 Maximum fuel matrix temperature profile for the equilibrium core

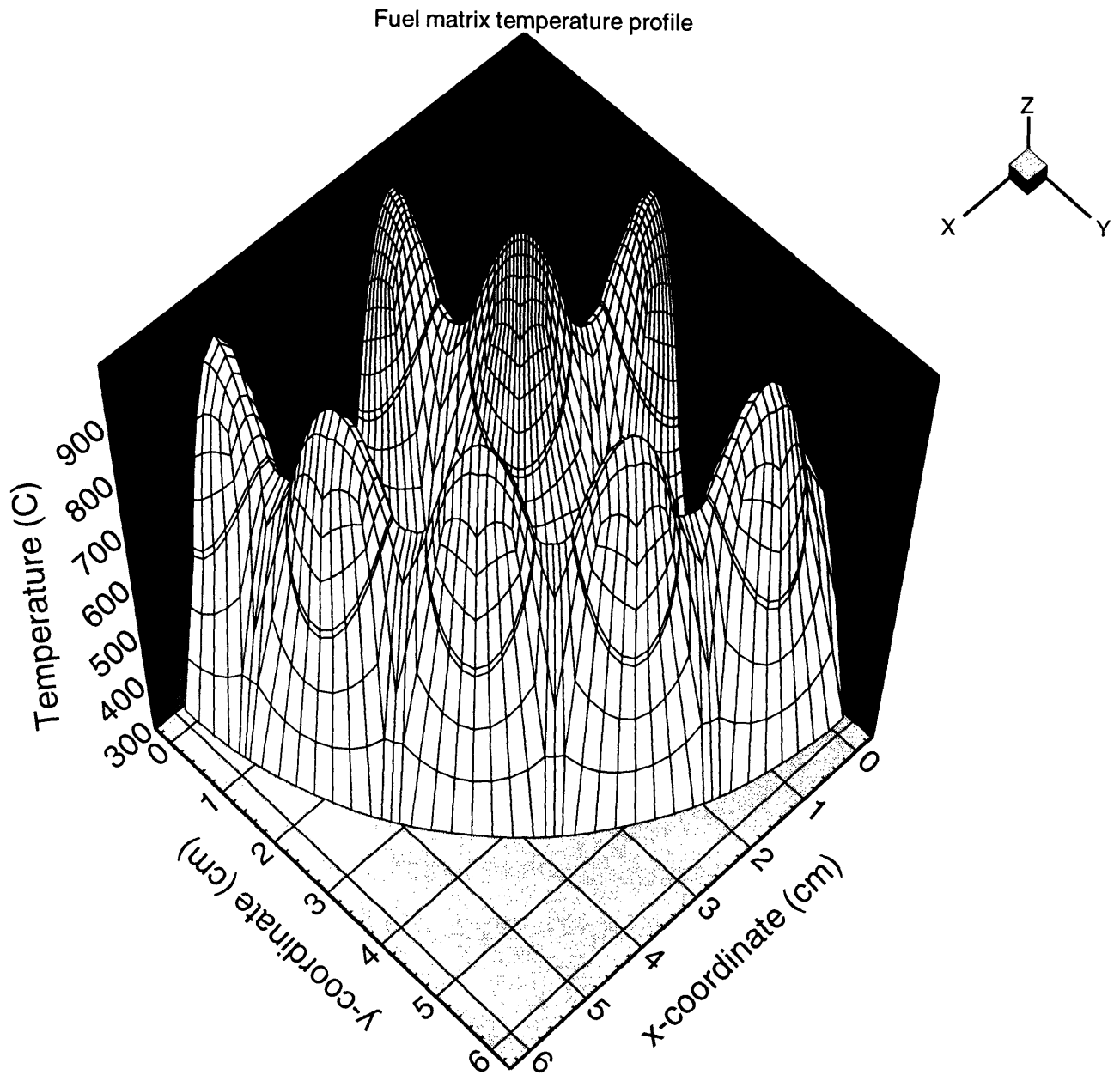


Figure 6-32 Maximum fuel matrix temperature profile for the equilibrium core using HOBEG technology

6.6 SUMMARY

Putting additional material in the form of a solid matrix into the pressure tube leads to a lower number of fuel pins in the fuel channel, to a smaller heated perimeter, and to less available flow area than for typical CANDU reactors, thus posing a challenge for adequate heat transfer performance during normal operation. Fewer fuel pins per channel results in a higher average linear heat rate in the fuel compacts. However, the peak linear heat rate, which sets limiting values for the fuel centerline temperature, is slightly lower than for CANDUs due to the flatness of the power density profile. Moreover, the thermal conductivity of fuel compacts is higher than that for UO_2 pins. Consequently, the operating temperature of the fuel compact at the location of maximum power density, is relatively low. The decrease in heated perimeter is again compensated by the flat power density profile, so that the local peak heat flux, and hence CHF margin is comparable to CANDU. A smaller flow area generally yields higher velocities, and thus higher pressure drop, for fixed mass flow rate. However, coolant channels in the matrix do not require spacers (except for the bearing pads in the annular channel between the matrix and the pressure tube). Hence, even for higher mass velocities in the coolant channels, the pressure drop is about 30% lower than in a CANDU reactor.

Thermohydraulic parameters of the reference PTLWR fuel channel design are compared to CE-CANDU parameters in Table 6-4. Overall, the thermohydraulic parameters fall within the range of the the reference CE-CANDU design. Dryout is expected to occur at power levels of 160% of nominal power for the equilibrium core and 146% for the fresh core. However, it is to be appreciated that the fuel matrix can operate in the post-CHF regime, while the temperatures of both the fuel and matrix-coolant interface remain substantially below safe limits. Hence, the traditional DNBR limit of 1.3 is of less importance in the matrix fuel, and concerns of burnout-related problems during pump coast down or pump seizure are practically eliminated.

Table 6-4 Comparison of PTLWR thermal-hydraulic characteristic parameters with CE-CANDU (in the hottest channel)

Fuel channel parameters	CE-CANDU ^a	PTLWR (fresh)	PTLWR (equilibrium)
Maximum channel power (MWth)	6.16	5.3	5.3
Maximum fuel centerline temperature (°C)	1500	1081(780) ^b	1215(912) ^b
Pressure drop (MPa)	1	0.7	0.7
Mass flow rate per fuel channel (kg/s)	23	19.05	19.05
Average channel inlet velocity (m/s)	9.34	10.54	10.54
Average channel mass flux (kg/m ² -s)	6802	7684	7684
Core average exit quality	2%	-0.2%	0.9%
Maximum local exit quality	4.73%	0.5%	2%
MDNB power ratio (AECL lookup table)	1.5	1.46	1.6

^a Data from [Shapiro and Jesick, 1979].

^b Number in parentheses applies if HOBEG molded fuel elements are used.

Chapter 7

FUEL MATRIX PERFORMANCE IN LOSS OF COOLANT ACCIDENT

7.1 INTRODUCTION

One of the key characteristics of the PTLWR fuel is its capability to survive the total absence of primary coolant without exceeding temperature limits for the fuel, the matrix and the pressure tube. The objective of this chapter is to study the performance of the fuel channel in loss of coolant scenarios and to confirm that the reference PTLWR fuel satisfies the prescribed limits. These constraints include the following temperature limits:

- 1600°C for TRISO fuel particles to avoid excessive fission product release,
- 1300°C for SiC coating to avoid excessive oxidation, and
- 500°C for pressure tube and calandria tube to minimize stress-induced deformation and assure their reusability.

A fuel channel in a loss of coolant scenario with the prescribed limiting temperatures is shown in Figure 7-1. The design basis accident for the PTLWR is postulated as the loss of all primary coolant with simultaneous failure to scram the reactor. At the same time, no emergency core cooling system delivers makeup coolant into the fuel channels. However, reliable functioning of the calandria flooding system is required. Processes during such a sequence involve inherent reactor shutdown due to negative fuel and coolant temperature feedbacks, deposition and storage of excess energy from fission and decay heat in the fuel matrix, and removal of this excess energy by conduction and radiation from the fuel channel into the flood water in the calandria.

The PTLWR with flooded calandria has a small fuel channel-to-flood water mass ratio. Hence the decay heat generated inside the fuel matrix is less than that in a typical LWR, and must be evaluated. Decay heat generation in the PTLWR fuel matrix is studied in Section 7.2. Section 7.3 discusses possibilities of enhancement of the heat transfer rate across the gap between the matrix and the pressure tube by increasing contact conductance. Section 7.4.2 describes the simplified 1-D model developed to analyze the transient performance of the fuel channel. The computer program TMATRIX, which implements this model, is listed in [Hejzlar, 1994]. Sections 7.4.3 and 7.4.4 present the discussion of the results for the fresh and equilibrium core, respectively. Section 7.4.5 verifies the temperature profile obtained from the simplified model using a more detailed 2-D finite element quasi-steady-state model.

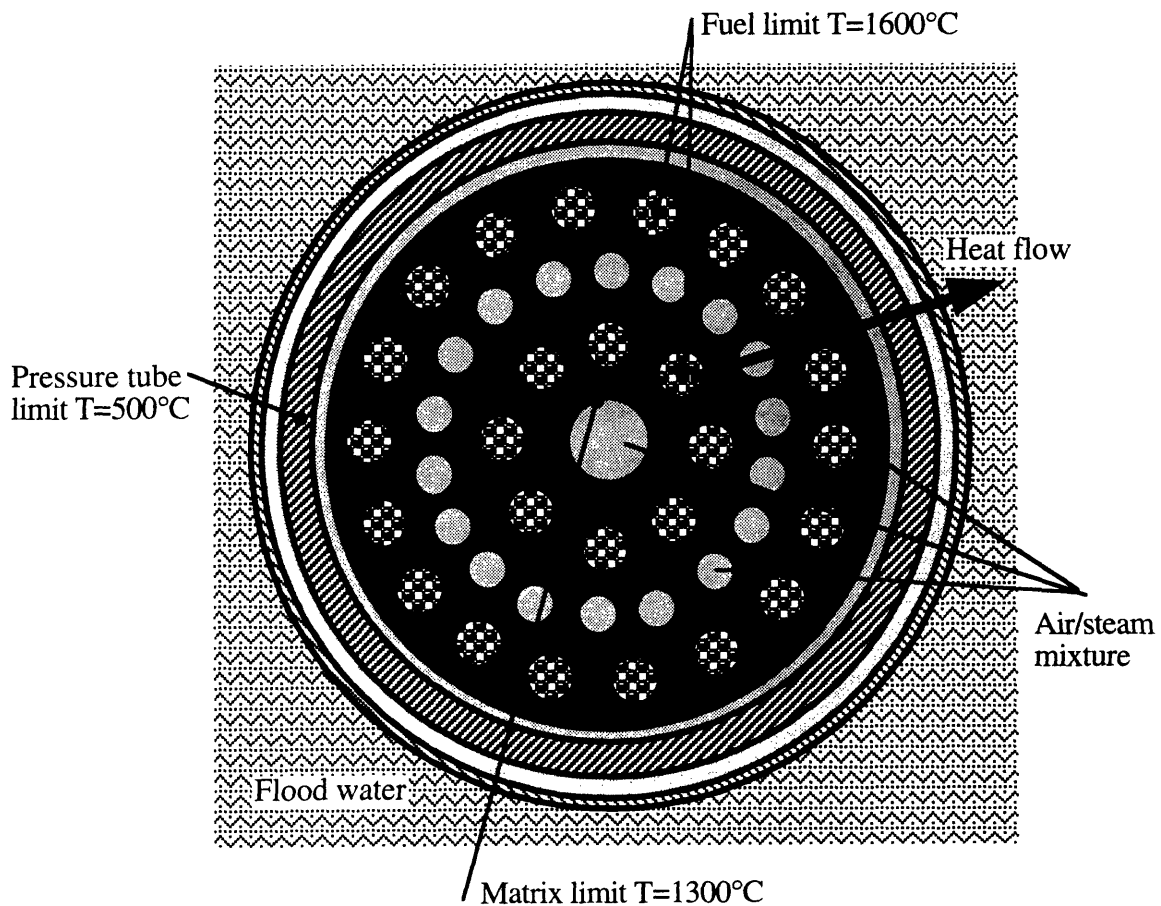


Figure 7-1 PTLWR fuel channel in LOCA scenario and its temperature limits

7.2 DECAY HEAT GENERATION IN THE FUEL MATRIX

The maximum temperature of the fuel and the matrix are strongly dependent on the decay heat generated in the fuel matrix. Once the calandria is flooded, the mass of the flooding water in the core is very large. Moreover, the mass of the fuel is relatively small due to the small heavy metal loading. These two factors affect the decay energy from gamma emission deposited in the fuel matrix. Since the energy deposited in the fuel matrix from gamma rays is proportional to the fuel matrix mass fraction, it is expected that the decay heat generation in the fuel will be decreased, as compared to a typical LWR (note that in LWRs most of the gamma heat is deposited in the fuel). The objective of this section is to estimate the fraction of decay heat deposited in the fuel matrix.

Table 7-1 shows the cell volume fractions, specific density and absorption coefficients of various materials in the PTLWR cell. Decay heat is generated by delayed gamma and beta emissions. Typical values are:

- delayed gammas $\gamma_d = 6.97 \text{ MeV} = 3.48\%$ of the total of 200MeV,
- delayed betas $\beta_d = 6 \text{ MeV} = 3\%$ of the total of 200 MeV.

The total decay heat from both gamma and beta emission is 12.97 MeV, or 6.48%. Note that the contribution from delayed neutrons is small and is neglected.

It will be assumed further that all beta particles are absorbed in the fuel. Using the data from Table 7-1, the fraction of gamma rays absorbed outside the pressure tube can be estimated as

$$f_{\text{CT+flood}} = \frac{\sum_{i=\text{flood,CT}} \rho_i f_{v,i} (\mu_a/\rho)_i}{\sum_{i=1}^6 \rho_i f_{v,i} (\mu_a/\rho)_i} = 0.605 \quad , \quad (7-1)$$

i.e., $0.605 (6.97\text{MeV}) = 4.05 \text{ MeV}$. Hence, once the calandria is flooded, the total decay heat which must be removed from the fuel matrix and the pressure tube is decreased from 12.97 MeV to 8.92 MeV, or by about 30%. From the point of view of the decay heat removal from the fuel matrix-

pressure tube configuration, this represent an advantage, since much less heat needs to be transferred across the gap between the pressure tube and the calandria tube.

Table 7-1 Important parameters for gamma heat deposition in the reference PTLWR cell

Material	ρ (g/cm ³)	f_v (cell volume fraction)	μ_a/ρ (cm ² /g)
Flood water	0.972	0.746	0.023
Calandria tube	6.55	0.0094	0.023
Fuel (UO ₂)	10.97	0.007998	0.033
Graphite	1.78	0.1136	0.021
Pressure tube	6.55	0.0978	0.023
Silicon carbide	3.18	0.00257	0.022

Note: Total lost of coolant is assumed, i.e., there is no absorption in the coolant.

Regarding the heat removal from the fuel matrix, the decay heat is decreased even further by the amount of delayed gammas deposited in the pressure tube. Applying Eq. (7-1) and adding the pressure tube to the denominator, the fraction of gamma heat deposited in the calandria tube, pressure tube and flooded water, $f_{CT+PT+flood}$, can be calculated to give $f_{CT+PT+flood} = 0.755$ yielding 5.06 MeV of delayed gammas deposited outside of the fuel matrix. The total heat rate to be removed from the fuel matrix, and across the gap between the fuel matrix and pressure tube (which is the most limiting thermal resistance) is $0.245 (6.97)+6 = 7.91$ versus 12.97, or a decrease of 40%.

The above simplified estimate was further checked by MCNP calculations. Using the detailed MCNP cell model #1 with fully flooded cell, the gamma heating of the fuel matrix, calandria tube, pressure tube, and of flood water is summarized in Table 7-2.

Table 7-2 MCNP results for gamma heating of flooded cell

	$\gamma_{\text{prompt+c}}$ (kW)	γ_{delay} (kW)	$\gamma_{\text{delay,cor}}$ (kW)
Fuel matrix including fuel	26.7	14.3	26.5
Pressure tube and calandria tube	16.1	8.6	16.2
Flood water	48.8	26.1	48.5

MCNP calculates only prompt gammas including capture gammas, i.e., $\gamma_{\text{prompt+c}}$. These results are given in the first column. Heating from the delayed gamma emissions, given in the second column, was calculated using the typical apportionment of prompt, capture and delayed gammas as

$$\begin{aligned} \gamma_{\text{delay}} &= \gamma_{\text{prompt+c}} [\gamma_{\text{delay}} / (\gamma_{\text{prompt}} + \gamma_{\text{capture}})] = \\ &= 6.97\text{MeV} / (6.72\text{MeV} + 6.33\text{MeV}) \gamma_{\text{prompt+c}} = 0.53\gamma_{\text{prompt+c}} \end{aligned} \quad (7-2)$$

The third column in Table 7-2 corrects the delayed gamma heating values, obtained from Eq. (7-2), to account for the different MCNP tallies of a non-critical system. The fully flooded cell is deeply subcritical with multiplication coefficient of 0.27. Hence the tallies obtained from MCNP do not correspond to actual values which would have resulted from a (prior to flooding) critical reactor. Hence, the total heat generation due to the delayed gamma rays is scaled to the rated power of the MCNP cell as

$$\gamma_{\text{delay,cor}} = \gamma_{\text{delay}} \frac{0.0348}{\gamma_{\text{delay,tot}} / P_{\text{cell,rated}}} \quad (7-3)$$

where 0.0348 is the known fraction of delayed gammas, $\gamma_{\text{delay,tot}}$ is the sum of all delayed gamma heat generated in the cell (from the second column) and $P_{\text{cell,rated}}$ is the fission average rated power of one half of the fuel channel (the MCNP cell models only half of the fuel channel). This approach assumes that the distribution of gamma heating among the tallied components (fuel matrix, tubes and flood water) for a subcritical cell

is the same as for the critical cell. Also note that gamma rays will also be partially absorbed in the reflector, hence the actual gamma heating of the fuel channels will be less than the above estimates.

From the third column of Table 7-2, the total delayed gamma heating of a cell can be found as

$$\gamma_{\text{delay,cor,tot}} = 26.5 + 16.2 + 48.5 = 91.2 \text{ kW} \quad (7-4)$$

from which $\gamma_{\text{delay,cor,rest}} = 64.7 \text{ kW}$ is deposited in the pressure tubes, calandria tubes and in flood water. Adding the heat generation from delayed β ,

$$\beta_{\text{delay}} = P_{\text{rated}} \frac{6\text{MeV}}{200\text{MeV}} = 0.03 P_{\text{cell,rated}} = 0.03 (2634) = 79.0 \text{ kW}, (7-5)$$

the decay heat generated in the fuel matrix can be calculated as

$$P_{\text{decay,fuel}} = \gamma_{\text{delay,cor,fuel}} + \beta_{\text{delay}} = 26.5 + 79.0 = 105.5 \text{ kW} \quad (7-6)$$

which corresponds to about 4% of rated power. The rest is generated outside the fuel matrix, i.e.,

$$P_{\text{decay,rest}} = \gamma_{\text{delay,cor,rest}} = 64.7 \text{ kW}, \quad (7-7)$$

which amounts to 2.4 % of rated power. Hence, 62% of the total decay heat is deposited in the fuel matrix while 38 % is deposited outside the fuel matrix. This result corresponds very well with the simplified estimate of 60% and 40 % presented earlier.

7.3 CONSIDERATIONS OF INCREASED CONTACT SURFACE BETWEEN MATRIX AND PRESSURE TUBE

CANDU fuel elements slide inside the pressure tube on bearing pads. Bearing pads are located at both ends and at the fuel element midplane. Another option available with the fuel matrix is to provide runners which extend along the entire length of the fuel element. Since these runners have relatively large contact surface with the pressure tube, they could significantly contribute to the heat transfer capabilities of the gap, provided that the contact resistance between the runners and the pressure tube is

small. The purpose of this section is to evaluate the potential of gap heat transfer enhancement using full-length runners.

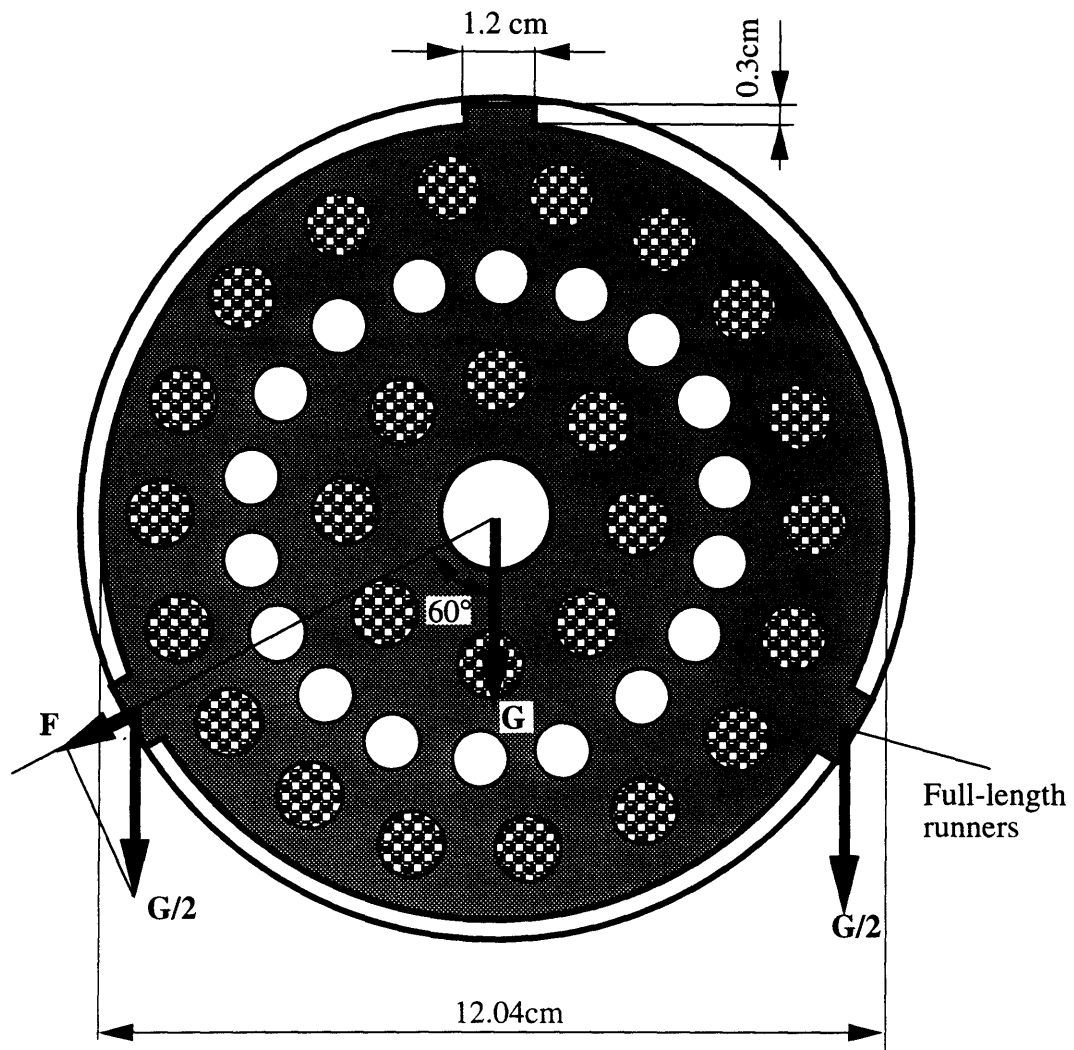
One possible arrangement of full-length runners is shown in Figure 7-2. The fuel matrix is equipped with three sliding pads (runners) which provide for the annular clearance between the matrix and the inner wall of the pressure tube. The heat rate transferred through the pads depends primarily on the contact conductance, which is typically much lower than the conductance of the runner material. Experiments [Williamson and Majumdar,1992] show that the contact conductance is directly proportional to the pressure exerted on the surfaces that are in contact. Using the total mass of the matrix, M , from Figure 7-2 and assuming that the top runner is not in contact with the pressure tube, the normal force exerted on one bottom runner is given as

$$F = (G/2) \cos 60^\circ = (M/2) g \cos 60^\circ = 360 \text{ N.} \quad (7-8)$$

Using the apparent cross-sectional area (contact area) of the runner $A = 0.075\text{m}^2$, contact pressure can be calculated to be

$$p = F/A = 360/0.075 = 4794 \text{ Pa.} \quad (7-9)$$

In addition to the pressure dependence, contact conductance also depends on the roughness of contact surfaces and the number of pressure load cycles. Typically, if pressure is applied to rough surfaces and then released, the contact conductance is increased due to plastic deformations. However, in case of matrix runners, no pressure load prior to fuel bundle insertion can be applied, hence this conductance gain cannot materialize. Regarding the surface roughness, the smoother the surface, the better the contact conductance. But even if smooth surfaces are considered, Williamson's experiments [Williamson and Majumdar,1992] show that the contact conductance corresponding to such a low contact pressure is small, i.e., $h=110 \text{ W/m}^2\text{-K}$ for a smooth aluminum surface in contact with smooth aluminum or stainless steel. The above experiments were performed in vacuum, hence there was no interstitial gas present. Since an air/steam mixture will be present in the runner-pressure tube interface, the contact



Volume and mass per fuel channel:

	Graphite matrix	Fuel compacts	Total
Volume (cm ³)	42,440	19,283	61,723
Mass (kg)	74.27	72.32	146.59

Figure 7-2 Fuel matrix with 3 full-length runners

conductance will tend to increase compared to vacuum experiments. This increase can be significant. Madhusudana's calculations [Madhusudana, 1993] suggest that the gap conductance with air as an interstitial gas can be increased by about 70 times compared to vacuum only. This value can be also confirmed by taking a typical roughness of machined surface of $\zeta=5\mu\text{m}$ (coarse) and a typical thermal conductivity of air, $k=0.035\text{W/m}^2\text{-K}$, which yields for gap conductance $h_g = 0.035/5 \times 10^{-6} = 7,000 \text{ W/m}^2\text{-K}$, i.e., about 70 times higher than the value obtain by Williamson in a vacuum.

To judge the potential of this gap conductance on heat transfer enhancement, the comparison with a pure radiation mode will be made. Heat flux from the matrix surface at the 3% decay power level is about $76,000\text{W/m}^2$. Assuming the pressure tube temperature is 300°C , the temperature needed to transfer this heat flux can be evaluated from the radiation equation

$$\begin{aligned} T_{\text{mat}} &= \sqrt[4]{T_{\text{PT}}^4 + Q_{\text{mat}}'' \frac{1}{\sigma} \left[\frac{1}{\epsilon_{\text{mat}}} + \frac{D_{\text{mat}}}{D_{\text{PT}}} (1/\epsilon_{\text{PT}} - 1) \right]} \\ &= \sqrt[4]{573^4 + \frac{7.6 \times 10^4}{5.669 \times 10^{-8}} \left[1/0.8 + \frac{6.04}{6.4} (1/0.7 - 1) \right]} = 1203\text{K} \end{aligned} \quad (7-10)$$

or about 930°C , which gives a temperature drop across the gap of about 630°C , and the effective gap conductance due to radiation

$$h_{\text{g-rad}} = \frac{Q_{\text{mat}}''}{\Delta T} = \frac{76,000}{630} = 121 \text{ W/m}^2\text{-K}. \quad (7-11)$$

While this value is comparable to gap conductance in a vacuum, it is about 55 times less than the gap conductance with air present. Since the contact surface of the runners is only 15 times less than the total matrix outer surface and since the temperature drop across the matrix is relatively small, the runners would be capable of transferring the entire heat load with the maximum matrix temperature lower than in the pure radiation mode.

Although the potential for heat transfer improvement is promising, one needs to consider practical implementation. To guarantee good heat transfer capabilities of the runners, the entire runner surface must be in

good contact with the pressure tube. This is not possible to assure because pressure tubes bend and the matrix dimensions change with irradiation. Bending of the pressure tube would cause the runners to contact the pressure tube only at the ends or middle. An increase in the gap between the pressure tube and runner in the middle region to 0.3 mm would decrease gap conductance 70 times, back to the values achieved by pure radiation. Such a decrease would eliminate any gain in the thermal performance through the use of the runners. Moreover, the full-length runners may prevent smooth axial motion of fuel elements inside a bent pressure tube during the refueling process. Therefore, full-length runners have been rejected as an option to increase heat transfer across the gap between the matrix and pressure tube. Instead, bearing pads, similar to those used for CANDUs, at both ends of the fuel elements, are proposed. The contribution of these pads to the heat transfer across the gap is very small because they provide only localized contact. This contribution will be neglected in the further analysis, yielding thus conservatively higher fuel matrix temperatures.

7.4 ANALYSIS OF TRANSIENT HEAT TRANSFER PERFORMANCE

7.4.1 Introduction

Following the loss of coolant from the fuel channels, the PTLWR reactor shuts down due to the negative coolant void coefficient. Decay heat generated in the fuel matrix is stored in the matrix at first, increasing its temperature. About 30 seconds after the initiation of LOCA, the calandria space becomes fully flooded with light water, which provides a heat sink. The decay heat is transferred from the fuel matrix through conduction, convection in the steam/air mixture present inside the fuel channels, and radiation to the pressure tube, calandria tube, and finally to the flooding water in the calandria.

The detailed analysis of this scenario would require a transient 2-D heat conduction model through the fuel matrix, coupled to radiative and convective heat transfer in the gap between the matrix and pressure tube. Although a large number of 2-D transient heat transfer codes are available, their treatment of radiative heat transfer is rather limited. Moreover, the

fission power after LOCA is determined by the magnitude of temperature coefficients, and its determination requires the coupling of the neutron kinetics equation with the heat transfer model. Therefore, a simplified 1-D heat transfer model of the fuel channel coupled to neutron kinetics, described in Section 7.4.2, has been developed. The model describes heat transfer from the matrix outer surface to the flood water very well and conductive heat transfer within the fuel matrix fairly well. To study the detailed temperature profile at selected times during the transient, a 2-D finite element model of the fuel matrix was also used. The 2-D model is based on the ALGOR package, and was used to verify the simplified 1-D model, as described in Section 7.4.5. Transient analysis of the reference PTLWR fuel channel design is presented in Sections 7.4.3. and 7.4.4.

7.4.2 A Simplified 1-D Model for Analysis of Transient Heat Transfer in a Fuel Matrix-Pressure Tube Configuration

The purpose of this section is to develop a simplified model capable of analyzing the transient response of the proposed fuel matrix-pressure tube arrangement in LOCA without scram.

7.4.2.1 Fundamental Equations and Simplifying Assumptions

Decay heat removal from the PTLWR voided fuel channel to the flood water involves four modes of heat transfer – conduction through solid material, radiation, natural convection in an air/steam mixture, and boiling on the outer flooded surface of the calandria tube.

Conduction results from a temperature gradient within a homogeneous substance (fuel matrix, pressure tube and calandria tube). A general 3-D heat conduction equation

$$\rho c_p(\mathbf{r},T) \frac{\partial T(\mathbf{r},\tau)}{\partial \tau} = \nabla \cdot \mathbf{k}(\mathbf{r},T) \nabla T(\mathbf{r},\tau) + q'''(\mathbf{r},\tau) \quad (7-12)$$

can be rewritten, neglecting the heat flow in the axial and azimuthal directions in cylindrical coordinates as

$$\rho c_p(r,T) \frac{\partial T(r,\tau)}{\partial \tau} = \frac{\partial}{\partial r} \left[k(r,T) \frac{\partial T(r,\tau)}{\partial r} \right] + q'''(r,\tau) \quad (7-13)$$

The heat flux in the radial direction is given by Fourier's Law as

$$q''(r,T) = -k(r,T) \nabla T(r,\tau) \quad (7-14)$$

The radiative heat flux is based on the Stefan-Boltzman Law

$$q'' = \sigma T^4 \quad (7-15)$$

where σ is the Stefan-Boltzman constant, $\sigma=5.6697 \times 10^{-8}$ W/m²-K. In calculating the net radiative heat flux between the two surfaces, the reflective properties of the surfaces and the view factor must be taken into account. Net radiative heat flux between gray surfaces of two infinite concentric cylinders, each of uniform temperature T_1 and T_2 , and uniform radiation characteristics can be written as

$$q'' = \frac{\dot{Q}}{\pi D_1 L} = \varepsilon' \sigma (T_1^4 - T_2^4) \quad (7-16)$$

where the effective emissivity has the form

$$\frac{1}{\varepsilon'} = \frac{1}{\varepsilon_1} + \frac{D_1}{D_2} \left(\frac{1}{\varepsilon_2} - 1 \right) \quad (7-17)$$

and subscripts 1 and 2 denote the inner and outer cylinders, respectively. For finite cylinders, Eqs. (7-16) and (7-17) will be altered due to the change in view factor. However, the length-to-gap width ratio is very large for both gaps in the PTLWR fuel channel, hence the concentric cylinders can be treated as infinite. Also the axial temperature profile along the cylinders is not uniform, but exhibits peaking. Since the peaking is small using Eqs. (7-16) and (7-17) for the analysis of the PTLWR fuel channel introduces only small errors. Moreover, the results will be conservative because the net radiative heat exchange will also proceed in the axial direction between the hot spot and colder regions, phenomena not captured by Eqs. (7-16) and (7-17).

In the convective heat transfer mode, energy is carried away by the fluid whenever a solid body is exposed to a moving fluid having a

temperature different from that of the body. The heat transfer rate is governed by Newton's Law

$$q'' = h(T_w - T_b) \quad (7-18)$$

where T_b is the bulk temperature and T_w is the wall surface temperature. The heat transfer coefficient, h , depends on many parameters and will be given for each case separately.

The boiling heat transfer mode occurs at the outer surface of the calandria tube once the calandria space is flooded with water. Heat flux in the boiling regime is governed by equation

$$q'' = h \Delta T_{\text{sat}}, \quad (7-19)$$

where the ΔT_{sat} is the temperature difference between the wall and fluid saturation temperature*.

During the flooding phase, two situations can be theoretically encountered – nucleate boiling and film boiling, depending on the heat flux and the initial temperature of the tube surface.

Typical regions on a boiling curve are shown in Figure 7-3. The most important points on the curve are the minimum film boiling point, designated as E and the critical heat flux point C. Both the point E and point C need to be quantified to identify the correct heat transfer regime.

Point E, also known as the Leidenfrost temperature, can be theoretically calculated from the minimum heat flux which will maintain film boiling, q''_{min} . If the flood water in the calandria is at saturation condition, this heat flux is given in the form [Zuber and Tribus, 1958]

* Saturated temperature of flood water is assumed although the flood water is subcooled by 60°C, immediately after it enters the calandria. This assumption has been adopted because it yields conservatively higher temperatures of fuel channels.

$$q''_{\min} = C h_{fg} \rho_g \sqrt[4]{\frac{\sigma (\rho_f - \rho_g) g}{(\rho_f + \rho_g)^2}} \quad (7-20)$$

where C is a non-dimensional constant between 0.09 and 0.18. Using the value of $C=0.13$ and properties of flooding water at atmospheric pressure, Eq. (7-20) yields the minimum film boiling heat flux of 27 kW/m².

The heat transfer coefficient for film boiling outside a horizontal cylinder is defined by the Bromley correlation [Bromley,1950]

$$h = 0.62 \sqrt[4]{\frac{\rho_g (\rho_f - \rho_g) g h_{fg} k_g^3}{\mu_g \Delta T_{\text{sat}} D}} \quad (7-21)$$

where D is the outer diameter of the cylinder, i.e. calandria tube.

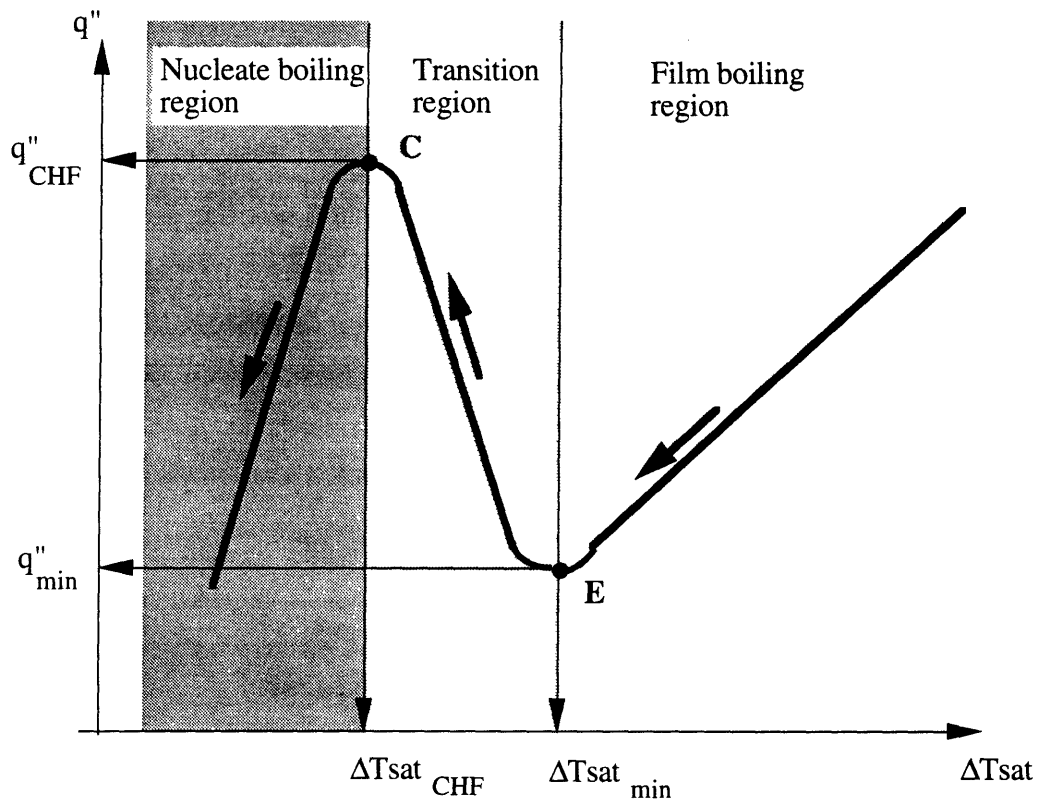


Figure 7-3 Regions on a boiling curve

If the temperature of the calandria tube at the outer surface is higher than $T_{\text{sat}} + \Delta T_{\text{sat}}_{\text{min}}$, heat transfer will be controlled by film boiling and the heat transfer coefficient is determined from Eq. (7-21). On the other hand, if

the surface tube temperature is lower than $T_{sat} + \Delta T_{sat_{CHF}}$, the heat transfer coefficient is determined from the nucleate boiling correlation [Rohsenow, 1952]

$$h = h_{fg} \mu_f \sqrt[2]{\frac{(\rho_f - \rho_g) g}{\sigma}} \left(\frac{c_{pf}}{C_s h_{fg} Pr_f} \right)^3 \Delta T_{sat}^2 \quad (7-22)$$

where C_s is a constant depending on liquid-surface combination. A typical value of $C_s = 0.013$ for a water-metal combination was used.

The CHF point is determined from the intersection of the nucleate boiling correlation, Eq. (7-22), and the CHF correlation outside a horizontal cylinder [Whalley, 1987]

$$q''_{CHF} = 0.116 h_{fg} \sqrt[3]{\rho_g} \sqrt[4]{\sigma (\rho_f - \rho_g) g} \quad (7-23)$$

$\Delta T_{sat_{CHF}}$ at point C can be determined by substituting the critical heat flux from Eq. (7-23) into Eq. (7-22) as

$$\Delta T_{sat_{CHF}} = (h_{fg} \mu_f)^{-1/3} \left(\frac{(\rho_f - \rho_g) g}{\sigma} \right)^{-2/3} \left(\frac{c_{pf}}{C_s h_{fg} Pr_f} \right)^{-1} q''_{CHF} \quad (7-24)$$

Since the process is controlled by the surface temperature, the heat flux in the transition region will be increased towards the point of CHF once ΔT_{sat} drops below $\Delta T_{sat_{min}}$, as shown by arrows on Figure 7-3. In this region, the heat flux can be obtained directly from linear interpolation,

$$q'' = q''_{CHF} - \frac{q''_{CHF} - q''_{min}}{\Delta T_{sat_{min}} - \Delta T_{sat_{CHF}}} (\Delta T_{sat} - \Delta T_{sat_{CHF}}) \quad (7-25)$$

The major uncertainty lies in the exact determination of the temperature difference between the wall and saturation temperatures at the minimum heat flux, $\Delta T_{sat_{min}}$. The theoretical value of $\Delta T_{sat_{min}}$ can be obtained by substituting Eqs. (7-21) and (7-20) into Eq. (7-19) to solve for $\Delta T_{sat_{min}} = 80^\circ\text{C}$. However, this result does not correspond to that found in experiments. In practice, the minimum film temperature is affected by the surface conditions and liquid contaminants, resulting in much higher values for both the minimum heat flux and the minimum film boiling temperature. Whalley [Whalley, 1987] states that the typical value for

minimum film boiling temperature for water at a pressure of 1 bar is 290°C. This corresponds to $\Delta T_{\text{sat}_{\text{min}}}$ of 190°C. Bergles and Thompson's [Bergles and Thompson,1970] measurements yielded substantially higher minimum film boiling heat fluxes than the values obtained by Eq. (7-20). The minimum film boiling temperature for water at atmospheric pressure obtained in Bergles and Thompson's experiments was found to be about 400°C, which is even higher than the value stated by Whalley. Accordingly, it seems that there is no well defined minimum film boiling temperature.

If the flood water is subcooled, the Leidenfrost temperature is also a function of the degree of subcooling. The most realistic estimates of the Leidenfrost temperature as a function of subcooling were obtained by Bradfield [1967] and Dhir and Purohit [1978]. Their data were obtained by quenching spheres in water at atmospheric pressure. Dhir and Purohit correlated the data by

$$\Delta T_{\text{sat}_{\text{min}}} = 101 + 8 \Delta T_{\text{sub}} \text{ (K)}. \quad (7-26)$$

Correlation (7-26) agrees very well with Bradfield's data. More recently, the effect of moderator subcooling on heat transfer conditions in CANDU fuel channels has been investigated [Gillespie, 1982]. These investigations conclude that for moderator subcoolings larger than 30°C, no film boiling should occur. Since the flooding water in the PTLWR has a temperature of 40°C, or a subcooling of 60°C, nucleate boiling is expected to occur on the outer surface of its calandria tubes.

Because of the uncertainties in the application of the correlations resulting from material and geometric differences, and because of the uncertainties in the actual value of the local subcooling, our model offers the choice among Whalley, Bergles and Thompson, and Bradfield values for $\Delta T_{\text{sat}_{\text{min}}}$. To bracket the performance, calculations are made for the best-estimate case, which preserves the nucleate boiling regime, and for the hypothetical case with Whalley data and delayed flooding, resulting in the film boiling regime.

7.4.2.2 Transition from a 2-D problem to a 1-D model

The ideas used in the transition from the 2-D heat transfer to 1-D model are laid out in Figure 7-4. Circular fuel compacts, arranged in two rings, are transformed into fueled annuli such that the fuel volume is preserved. The graphite matrix body is also reshaped into a set of annuli which interlace the fuel annuli and annular coolant region. Using the nomenclature from Figure 7-5, the outer radius of the first matrix annulus, R_2 , can be calculated from the preservation of matrix volume (volume to be preserved is shown by shaded area in Figure 7-6) as

$$R_2 = \sqrt{R_{m1}^2 - N_{f1} \frac{R_{f1}^2 \arcsin(y_1/R_{f1})}{\pi}} \quad (7-27)$$

where the y-coordinate of the intersection between the coolant hole and radius R_{m1} can be derived from the geometry shown in Figure 7-6,

$$y_1 = R_{f1} \sqrt{1 - \frac{R_{f1}^2}{4 R_{m1}^2}} \quad (7-28)$$

It follows from Figure 7-6 that the graphite material from between the fuel holes, which is within the circle connecting the centers of the fuel holes, is assumed to be lumped in the first graphite annulus, i.e., the annulus between radii R_1 and R_2 . The outer radius of the first fuel annulus, R_3 , is calculated to preserve the fuel volume,

$$R_3 = \sqrt{R_2^2 + N_{f1} R_{f1}^2} \quad (7-29)$$

Radius R_4 is calculated by a similar procedure as for radius R_2 . Lumping the material outside the circle R_{m1} and inside the circle R_{m2} into the second graphite annulus between radii R_3 and R_4 yields

$$R_4 = \sqrt{R_3^2 - R_{m1}^2 - N_{f1} \frac{R_{f1}^2 - R_{f1}^2 \arcsin(y_1/R_{f1})}{\pi} + R_{m3}^2 - N_{f2} \frac{R_{f2}^2 - R_{f2}^2 \arcsin(y_2/R_{f2})}{\pi}} \quad (7-30)$$

where

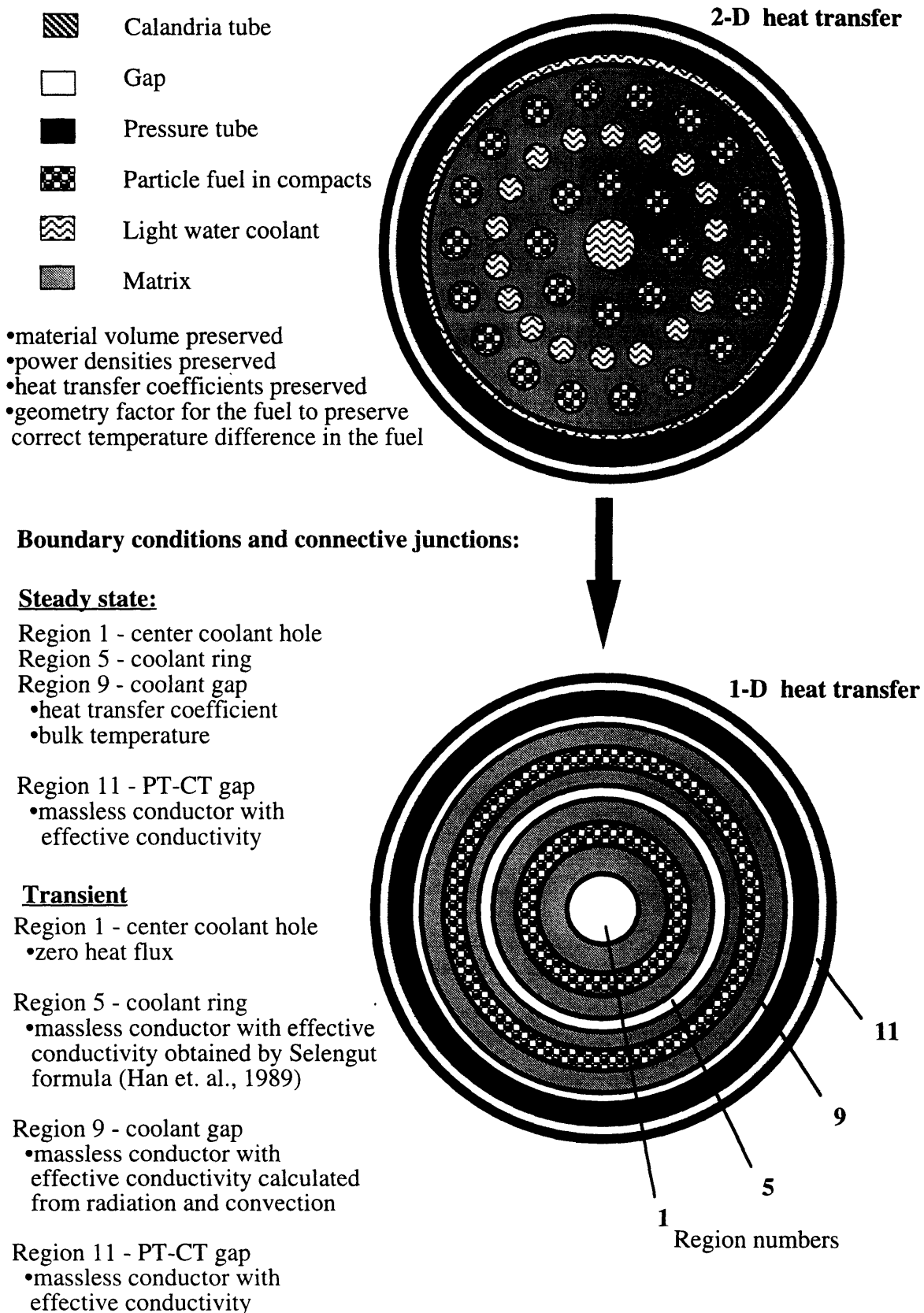


Figure 7-4 Transition to simplified 1-D fuel matrix model for steady state and transient analysis

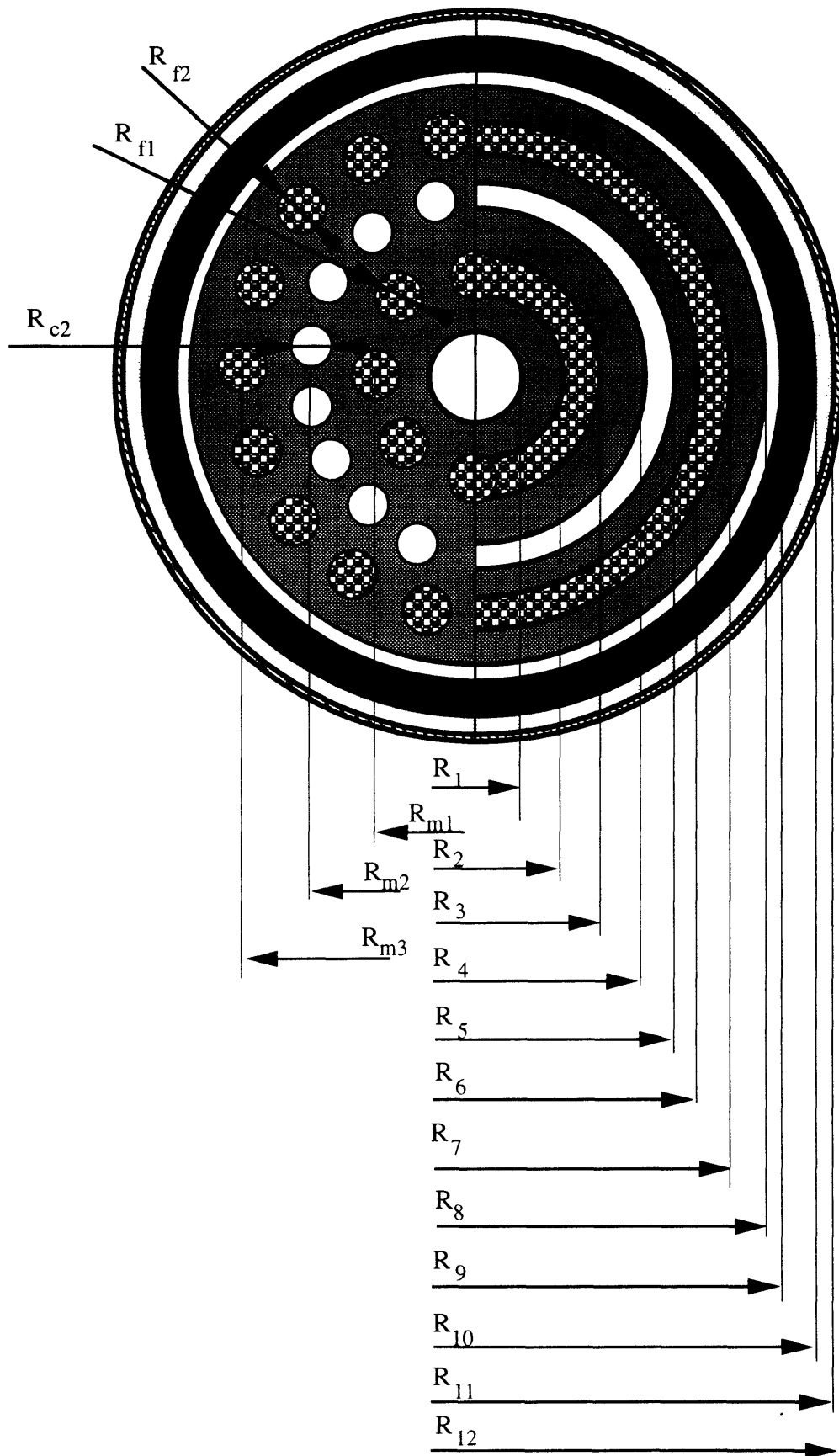


Figure 7-5 Schematic of a simplified 1-D model with nomenclature

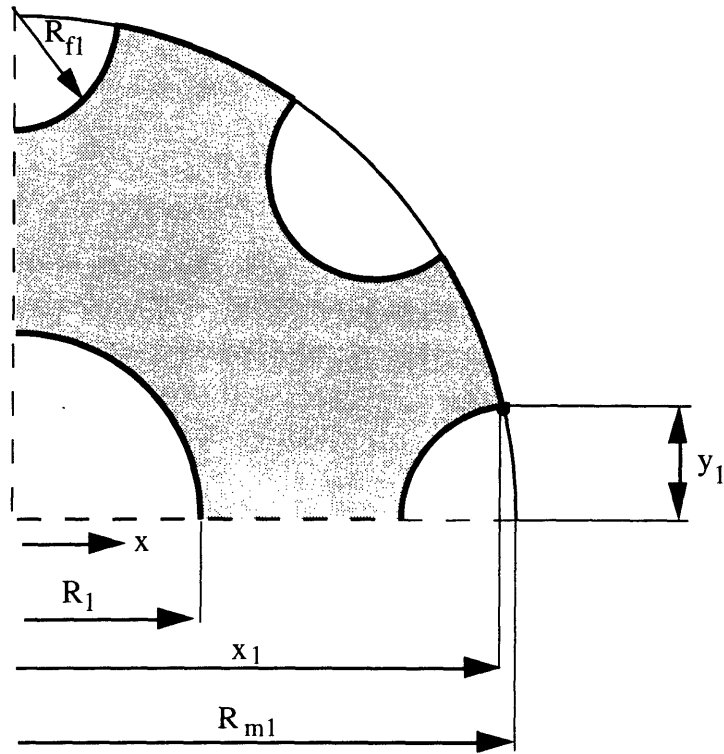


Figure 7-6 Lumping of graphite matrix material into the first ring

$$y_2 = R_{f2} \sqrt{1 - \frac{R_{f2}^2}{4 R_{m3}^2}} \quad (7-31)$$

The above procedure preserves volumes, and hence the energy storage. However, the temperature distribution in the fuel is not preserved since the thin fueled annulus exhibits a smaller temperature difference than the cylindrical fuel compact, given the same power density. To correct for this deficiency, a geometry factor is introduced. From the conduction equation the temperature difference in the cylindrical fuel compact can be expressed as

$$\Delta T_c = \frac{q''' R_f^2}{4 k} \quad (7-32)$$

The fuel annulus can be treated as a slab of thickness Δ_{slab} , with the temperature difference of

$$\Delta T_s = \frac{q''' \Delta_{slab}^2}{8 k} \quad (7-33)$$

To preserve the temperature difference in the fuel, the slab temperature difference needs to be corrected by factor F_g , derived as follows:

$$\Delta T_c = \Delta T_s \frac{q''' R_f^2}{4 k} \frac{8 k}{q''' \Delta_{slab}^2} = \Delta T_s \frac{2 R_f^2}{\Delta_{slab}^2} = \Delta T_s F_g \quad (7-44)$$

where the geometry factor F_g can be written in terms of annulus radii and the number of fuel compacts in a ring

$$F_g = \frac{2 (R_3 + R_2)}{N_{f1} (R_3 - R_2)} ; F_g = \frac{2 (R_7 + R_6)}{N_{f2} (R_7 - R_6)} \quad (7-44,45)$$

for the inner and outer fueled annuli, respectively.

The central coolant hole, coolant ring and coolant gap (regions 1, 5 and 9 on Figure 7-4) are treated for steady state analysis as convective or boiling boundary nodes with boundary conditions of the heat transfer coefficient and the bulk coolant temperature (or saturation temperature in case of boiling). The intermediate ring of coolant holes, modeled as region 5, has a graphite web between individual holes. During normal operation, there is practically no heat transfer radially across this web because all the heat is transferred to the coolant. However, following a loss of coolant accident, when no or negligible cooling is available via these cooling passages, the web becomes the primary contributor to heat dissipation out of the fuel matrix. To properly account for this phenomenon in such situations, region 5 is treated as a massless conductor (since all mass is already lumped into neighboring graphite annuli) with effective thermal conductivity calculated from Selengut's formula [Han et. al., 1989]

$$k_{eff.5} = \frac{(1+\gamma_c) k_c + (1-\gamma_c) k_g}{(1-\gamma_c) k_c + (1+\gamma_c) k_g} k_g \quad (7-46)$$

where k_c is the conductivity of the air/steam mixture in the coolant holes and k_g is the conductivity of solid graphite, and the volume fraction of cooling holes over the total ring volume is calculated as

$$\gamma_c = \frac{N_c \pi R_{c2}^2}{\pi [(R_4 + 2 R_{c2})^2 - R_4^2]} \quad (7-47)$$

A similar situation occurs in the coolant gap between the matrix and the pressure tube except that the heat transfer is primarily due to radiation, convection and gas conduction. Since this gap represents the key resistance to heat transfer, it is desirable to estimate the effective conductivity of the gap as accurately as possible. To be conservative, any contribution from the heat transferred by conduction through the bearing pads to the pressure tube is neglected. The effective conductivity of the gap due to radiation, natural convection and gas conduction is calculated as follows:

1. Using radiation Eqs. (7-16) and (7-17), calculate radiative heat flux across the gap

$$q''_{\text{rad}} = 2 \pi R_8 \sigma (T_8^4 - T_9^4) \left[1/\epsilon_8 + \frac{R_8}{R_9} (1/\epsilon_9 - 1) \right]^{-1} \quad (7-48)$$

2. Calculate the heat flux due to convection and gas conduction using the Kuehn and Goldstein [1976] correlation, $q''_{\text{conv+cond}}$, described in the next section.
3. Calculate the effective thermal conductivity of the gap which is further treated as a massless conductor

$$k_{\text{eff},9} = (q''_{\text{rad}} + q''_{\text{conv+cond}}) R_8 \ln \left(\frac{R_9}{R_8} \right) \frac{1}{(T_8 - T_9)} \quad (7-49)$$

The gap between the pressure tube and the calandria tube is also treated as a massless conductor with an effective conductivity which is given in the input data.

Boundary conditions at the outer surface of the calandria tube comprise the boiling heat transfer coefficient and saturation temperature. These were thoroughly discussed in Section 7.4.2.1.

7.4.2.3 Natural Convection Heat Transfer in the Gap between the Matrix and Pressure Tube

The heat flux due to convection and conduction through the air/steam mixture between the two horizontal annuli, $q''_{\text{conv+cond}}$, is calculated from the Kuehn and Goldstein correlation, which is one of the best correlations proposed for this geometry. Their correlation is based on extensive experimental and numerical heat transfer results and includes laminar and turbulent layer flow as well as the conduction regime. Using the nomenclature from Figure 7-5 (subscripts 8 and 9 for matrix and inner diameter of pressure tube) the correlation for the convection part is given as

$$\text{Nu}_{D8,\text{conv}} = \frac{h D_8}{k} = 2 \left[\ln \left(\frac{1 + 2/\text{Nu}_{D8}}{1 - 2/\text{Nu}_{D9}} \right) \right]^{-1} \quad (7-50)$$

where

$$\text{Nu}_{D8} = \left\{ [0.518 \text{Ra}_{D8}^{0.25} f_2(\text{Pr})]^{15} + (0.1 \text{Ra}_{D8}^{1/3})^{15} \right\}^{1/15} \quad (7-51)$$

$$\text{Nu}_{D9} = \left\{ \left[\left(\frac{2}{1-e^{-0.25}} \right)^{5/3} + [0.587 \text{Ra}_{D9}^{0.25} f_3(\text{Pr})]^{5/3} \right]^{3/5} \right\}^{15} + (0.1 \text{Ra}_{D9}^{1/3})^{15} \quad (7-52)$$

with

$$f_2(\text{Pr}) = [1 + (0.559/\text{Pr})^{3/5}]^{-5/12}, \quad (7-53)$$

$$f_3(\text{Pr}) = [(1 + 0.6/\text{Pr}^{0.7})^{-5} + (0.4 + 2.6\text{Pr}^{0.7})^{-5}]^{-1/5}, \quad (7-54)$$

$$\text{Ra}_{D8} = \frac{g \beta \rho (T_8 - T_9) D_8^3}{\mu \alpha}, \quad (7-55)$$

$$\text{Ra}_{D9} = \frac{g \beta \rho (T_8 - T_9) D_9^3}{\mu \alpha} \quad (7-56)$$

and e is the eccentricity, which was taken to be zero in this analysis.

The conduction part is given by

$$\text{Nu}_{D8,\text{cond}} = \frac{2}{\cosh^{-1} \left\{ [D_8^2 + D_9^2 - (D_9^2 - D_8^2)e^2] / (2D_8D_9) \right\}} \quad (7-57)$$

The combined Nusselt number, which includes both convection and conduction, is given as

$$\text{Nu}_{D8,\text{tot}} = \left\{ \left[\text{Nu}_{D8,\text{conv}} \right]^{1.5} + (\text{Nu}_{D8,\text{cond}})^{1.5} \right\}^{1/1.5} \quad (7-58)$$

Finally, the heat transfer coefficient due to convection and conduction, based on the inner cylinder diameter, sets the heat flux transferred across the gap,

$$q''_{\text{conv+cond}} = h (T_8 - T_9) = \text{Nu}_{D8,\text{tot}} k/D_8 (T_8 - T_9) \quad (7-60)$$

Since the pressure of the steam/air mixture is low and the temperature is high, Dalton's Law can be assumed to be valid. Given the mass fraction of air, x_{air} , the mole fractions of air and steam can be calculated

$$y_{\text{air}} = \frac{x_{\text{air}}/M_{\text{air}}}{x_{\text{air}}/M_{\text{air}} + (1-x_{\text{air}})/M_{\text{H}_2\text{O}}} ; y_{\text{H}_2\text{O}} = \frac{(1-x_{\text{air}})/M_{\text{H}_2\text{O}}}{x_{\text{air}}/M_{\text{air}} + (1-x_{\text{air}})/M_{\text{H}_2\text{O}}} \quad (7-61)$$

to obtain the partial pressures

$$P_{\text{air}} = p y_{\text{air}} ; P_{\text{H}_2\text{O}} = p y_{\text{H}_2\text{O}} \quad (7-62)$$

Properties of air and steam are calculated as a function of the average temperature in the gap and the partial pressures. The specific volume of the mixture can be calculated from Dalton's Law [Gyftopoulos and Beretta,1991]

$$v = y_{\text{air}} \frac{P_{\text{air}}}{p} v_{\text{air}} + y_{\text{H}_2\text{O}} \frac{P_{\text{H}_2\text{O}}}{p} v_{\text{H}_2\text{O}} \quad (7-63)$$

To obtain the effective transport properties of the steam/air mixture, simplified mixing laws [Rosner, 1986] are applied

$$k = \frac{y_{\text{air}} k_{\text{air}} M_{\text{air}}^{1/3} + y_{\text{H}_2\text{O}} k_{\text{H}_2\text{O}} M_{\text{H}_2\text{O}}^{1/3}}{y_{\text{air}} M_{\text{air}}^{1/3} + y_{\text{H}_2\text{O}} M_{\text{H}_2\text{O}}^{1/3}} \quad , \text{ and} \quad (7-64)$$

$$\mu = \frac{y_{\text{air}} \mu_{\text{air}} M_{\text{air}}^{1/2} + y_{\text{H}_2\text{O}} \mu_{\text{H}_2\text{O}} M_{\text{H}_2\text{O}}^{1/2}}{y_{\text{air}} M_{\text{air}}^{1/2} + y_{\text{H}_2\text{O}} M_{\text{H}_2\text{O}}^{1/2}} \quad (7-65)$$

7.4.2.4 Numerical solution of Heat Conduction Equation

To solve the conduction equation in cylindrical coordinates, (7-13), the approach used in the RETRAN computer code is utilized [McFaden et. al., 1984]. Every radial region j is divided into $N(j)$ subnodes, as shown in Figure 7-7. Integrating Eq. (7-13) over the volume about the i -th mesh point yields

$$\int_{v_i} \rho c_p \frac{\partial T(r,\tau)}{\partial \tau} dV = \int_{v_i} \frac{\partial}{\partial r} \left[k(r,T) \frac{\partial T(r,\tau)}{\partial r} \right] dV + \int_{v_i} q'''(r,\tau) dV \quad (7-66)$$

Using the divergence theorem to convert the volume integral of the temperature gradient to a surface integral yields

$$\int_{v_i} \rho c_p \frac{\partial T(r,\tau)}{\partial \tau} dV = \int_{s_i} k(r,T) \frac{\partial T(r,\tau)}{\partial r} \tilde{n} dS_i + \int_{v_i} q'''(r,\tau) dV \quad (7-67)$$

Assuming that the material properties and temperatures are constant over the half mesh intervals $h_{li}/2$ and $h_{ri}/2$ (see Figure 7-7 for nomenclature), Eq. (7-67) can be written after performing the integration as

$$\begin{aligned} & [(\rho c_p)_{li} h_{li}^v + (\rho c_p)_{ri} h_{ri}^v] \frac{dT_i}{d\tau} = \\ & = k_{li} \frac{h_{li}^s}{h_{li}} (T_{i-1} - T_i) + k_{ri} \frac{h_{ri}^s}{h_{ri}} (T_{i+1} - T_i) + q'''_{li} h_{li}^v + q'''_{ri} h_{ri}^v \end{aligned} \quad (7-68)$$

where for inner nodes

$$h_{li}^v = 2\pi \frac{h_{li}}{2} \left(R_i - \frac{h_{li}}{4} \right) ; \quad h_{ri}^v = 2\pi \frac{h_{ri}}{2} \left(R_i + \frac{h_{ri}}{4} \right), \quad (7-69,70)$$

$$h_{li}^s = 2\pi \left(R_i - \frac{h_{li}}{2} \right) ; \quad h_{ri}^s = 2\pi \left(R_i + \frac{h_{ri}}{2} \right), \quad (7-71,72)$$

and for boundary nodes

$$h_{li}^v = 0 ; h_{li}^s = 2\pi R_i ; h_{ri}^v = 0 ; h_{ri}^s = 2\pi R_i. \quad (7-73,74,75,76)$$

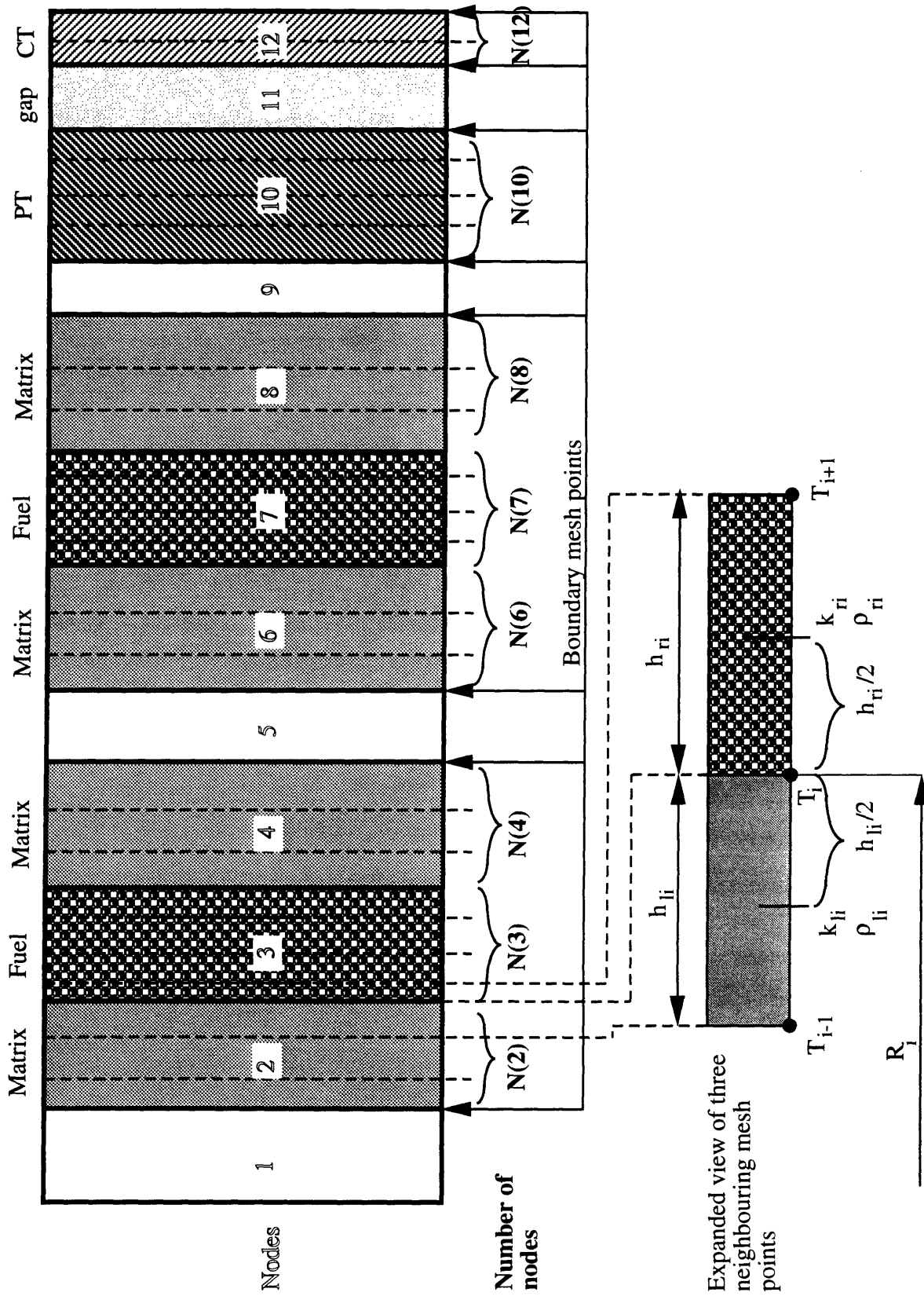


Figure 7-7 Nodalization scheme for 1-D PTLWR fuel channel model

Substituting for the time derivative

$$\frac{dT_i}{d\tau} = \frac{T_i^{m+1} - T_i^m}{\Delta\tau} \quad (7-77)$$

and adopting a fully implicit scheme, Eq. (7-68) can be written for an inner mesh point

$$\begin{aligned} T_{i-1}^{m+1} \left(\Delta\tau k_{li} \frac{h_{li}^s}{h_{li}} \right) + T_i^{m+1} \left[\Delta\tau \left(-k_{li} \frac{h_{li}^s}{h_{li}} - k_{ri} \frac{h_{ri}^s}{h_{ri}} \right) - (\rho c_p)_{li} h_{li}^v - (\rho c_p)_{ri} h_{ri}^v \right] + \\ + T_i^{m+1} \left(\Delta\tau k_{ri} \frac{h_{ri}^s}{h_{ri}} \right) = T_i^m \left[-(\rho c_p)_{li} h_{li}^v - (\rho c_p)_{ri} h_{ri}^v \right] - \Delta\tau \left(q_{li}^{m+1} h_{li}^v + q_{ri}^{m+1} h_{ri}^v \right). \end{aligned} \quad (7-78)$$

For the total number of mesh points

$$N_{\text{mesh}} = \sum_{j=1}^{12} N(j) \quad (7-79)$$

there are N_{mesh} equations which can be written in matrix form

$$\mathbf{A} \mathbf{T} = \mathbf{R} \quad (7-80)$$

where \mathbf{T} is an $N_{\text{mesh}} \times 1$ vector of unknown temperatures, \mathbf{A} is an $N_{\text{mesh}} \times N_{\text{mesh}}$ matrix of coefficients, and \mathbf{R} is an $N_{\text{mesh}} \times 1$ vector of right hand sides. The elements of matrix \mathbf{A} and RHS vector \mathbf{R} are given as follows:

for inner mesh points:

$$A_{i,i-1} = \Delta\tau k_{li} \frac{h_{li}^s}{h_{li}}, \quad (7-81)$$

$$A_{i,i} = \Delta\tau \left(-k_{li} \frac{h_{li}^s}{h_{li}} - k_{ri} \frac{h_{ri}^s}{h_{ri}} \right) - (\rho c_p)_{li} h_{li}^v - (\rho c_p)_{ri} h_{ri}^v, \quad (7-82)$$

$$A_{i,i+1} = \Delta\tau k_{ri} \frac{h_{ri}^s}{h_{ri}}, \quad (7-83)$$

$$R_i = T_i^m \left[-(\rho c_p)_{li} h_{li}^v - (\rho c_p)_{ri} h_{ri}^v \right] - \Delta\tau \left(q_{li}^{m+1} h_{li}^v + q_{ri}^{m+1} h_{ri}^v \right); \quad (7-84)$$

for left boundary mesh points with convective heat transfer boundary conditions:

$$A_{i,i} = \Delta\tau \left(h_c h_{li}^s - k_{ri} \frac{h_{ri}^s}{h_{ri}} \right) - (\rho c_p)_{ri} h_{ri}^v, \quad (7-85)$$

$$A_{i,i+1} = \Delta\tau k_{ri} \frac{h_{ri}^s}{h_{ri}}, \quad (7-86)$$

$$R_i = T_i^m \left[-(\rho c_p)_{ri} h_{ri}^v \right] - \Delta\tau \left(h_c T_b h_{li}^s + q_{ri}^{m+1} h_{ri}^v \right), \quad (7-87)$$

for right boundary mesh points with convective heat transfer boundary conditions:

$$A_{i,i-1} = \Delta\tau k_{li} \frac{h_{li}^s}{h_{li}}, \quad (7-88)$$

$$A_{i,i} = \Delta\tau \left(-k_{li} \frac{h_{li}^s}{h_{li}} - h_c h_{ri}^s \right) - (\rho c_p)_{li} h_{li}^v, \quad (7-89)$$

$$R_i = T_i^m \left[-(\rho c_p)_{li} h_{li}^v \right] - \Delta\tau \left(q_{li}^{m+1} h_{li}^v + h_c T_b h_{ri}^s \right), \quad (7-90)$$

for mesh points with massless conductor on the left side:

$$A_{i,i-1} = \Delta\tau k_{\text{eff},li} \frac{2\pi(R_j + R_{j-1})/2}{(R_j - R_{j-1})}, \quad (7-91)$$

$$A_{i,i} = \Delta\tau \left(-k_{\text{eff},li} \frac{2\pi(R_j + R_{j-1})/2}{(R_j - R_{j-1})} - k_{ri} \frac{h_{ri}^s}{h_{ri}} \right) - (\rho c_p)_{ri} h_{ri}^v, \quad (7-92)$$

$$A_{i,i+1} = \Delta\tau k_{ri} \frac{h_{ri}^s}{h_{ri}}, \quad (7-93)$$

$$R_i = T_i^m \left[-(\rho c_p)_{ri} h_{ri}^v \right] - \Delta\tau \left(+q_{ri}^{m+1} h_{ri}^v \right), \quad (7-94)$$

and for mesh points with massless conductor on the right side:

$$A_{i,i-1} = \Delta\tau k_{li} \frac{h_{li}^s}{h_{li}}, \quad (7-95)$$

$$A_{i,i} = \Delta\tau \left(-k_{li} \frac{h_{li}^s}{h_{li}} - k_{\text{eff},ri} \frac{2\pi(R_j + R_{j+1})/2}{(R_{j+1} - R_j)} \right) - (\rho c_p)_{li} h_{li}^v, \quad (7-96)$$

$$A_{i,i+1} = \Delta\tau k_{\text{eff},ri} \frac{2\pi(R_j + R_{j+1})/2}{(R_{j+1} - R_j)}, \quad (7-97)$$

$$R_i = T_i^m [-(\rho c_p)_{li} h_{li}^v] - \Delta\tau (q_{li}^{m+1} h_{li}^v). \quad (7-98)$$

In Eqs. (7-81) through (7-98), h_c is the heat transfer coefficient due to convection or boiling, T_b is the bulk temperature of the fluid or saturation temperature depending on the heat transfer mode, and index j designates the node number (see Figure 7-7) which neighbors the i -th mesh point. Material properties c_{pli} , ρ_{li} , k_{li} , c_{pri} , ρ_{ri} , k_{ri} are evaluated at the i -th mesh point temperature T_i . The calculation of effective thermal conductivities for massless conductors, k_{eff} , and of boundary conditions was given in the previous section. The initial conditions can be calculated from the same set of equations by setting all terms (ρc_p) to zero and time step $\Delta\tau$ to 1.0. The solution of the system of equations (7-80) is performed by the Gauss elimination method. Depending on the state of the nodes 5 and 9, equation system (7-80) varies. In the steady state, nodes 5 and 9 are generally boundary nodes with heat transfer coefficient and bulk coolant temperature as boundary conditions. Hence the conduction temperature field in the group of nodes 2, 3 and 4 is independent of the group of nodes 6,7,8, which in turn do not depend on the nodes 10,11 and 12. In such case, Eq. (7-80) is solved in three independent blocks

$$\mathbf{A}_k \mathbf{T}_k = \mathbf{R}_k \quad k=1,3 \quad (7-99)$$

with various matrix sizes

$$N_{\text{mesh},1} = \sum_{j=2}^4 N(j); N_{\text{mesh},2} = \sum_{j=6}^8 N(j); N_{\text{mesh},3} = \sum_{j=10}^{12} N(j) \quad (7-100,101,102)$$

Once the conduction across the gap becomes prevalent, e.g. if all coolant is lost, the entire matrix-pressure tube-calandria tube arrangement becomes coupled, and the entire system of equations (7-80) is solved in one block.

Control of the computer program is provided to rearrange matrices into various blocks depending on the state of the coolant nodes.

7.4.2.5 Power Generation in the Fuel Matrix

To close the system of equations (7-80), power densities need to be provided as a function of time. Power densities in nodes 3 (inner fuel ring), 7 (outer fuel ring) 10 (pressure tube) and 12 (calandria tube) are calculated from the expression

$$q'''_j(\tau) = q'''_j(\tau=0) F_{\text{peak},r} F_{d,j}(\tau) P(\tau) \quad j=3,7,10,12. \quad (7-103)$$

The steady state power densities in the fuel rings, $q'''_j(\tau=0)$, $j=3,7$ were obtained using MCNP model #1 at the axial location of maximum power density, i.e., axial peaking is already included. Steady state maximum power densities in the pressure tube and the calandria tube (nodes 10 and 12) from neutron and gamma heating were also obtained from MCNP. $F_{\text{peak},r}$ is the radial peaking factor. The radial peaking factor for both the fresh core with uniform enrichment or the equilibrium core is small. The value of $F_{\text{peak},r}=1.1$, obtained for the fresh core using a full-core MCNP model was used in the analysis.

The factor $F_{d,j}(\tau)$ takes into account the redistribution of gamma decay heat during flooding. This redistribution is significant for flooded calandria, and results in a substantial decrease in the heat load on the fuel matrix. It was shown in Section 7.2 that the fraction of decay heat deposited in the fuel matrix for a fully flooded calandria is only about 60% of the total decay heat prior to flooding. Adopting the assumption that all the decay heat which is deposited in the fuel matrix is generated in the fuel compacts*, the decay heat factor for the fuel rings takes the value $F_{d-fl,j} =$

* Note that this assumption will yield slightly conservative results since some of the decay heat will be deposited in the graphite matrix and it consequently needs to overcome less resistance when removed to the matrix periphery.

0.6, $j=3,7$, where subscript fl stands for a fully flooded calandria. Assuming that the amount of gamma decay heat absorbed in the flooding water is proportional to the flooded volume, the factor $F_{d,j}(\tau)$ can be calculated as

$$F_{d,j}(\tau) = 1 - (1 - F_{d-fl,j}) V(N_{rows})/V(30) \quad j=3,7,10,12 \quad (7-104)$$

where $V(N_{rows})$ is the flooded volume corresponding to the number of flooded rows N_{rows} , and $V(30)$ is the volume of the fully flooded calandria, i.e., for 30 flooded rows. The number of flooded rows as a function of time was obtained from the dynamic model of flooding described in Chapter 8.

Normalized core power, $P(\tau)$, can be written as the sum of normalized fission power, P_f , and normalized decay power, P_d

$$P(\tau) = P_f(\tau) [1 - P_d(\tau)] + P_d(\tau) \quad (7-105)$$

Normalized decay power is calculated from the 11-decay group model used in the RETRAN02 code [McFaden et. al., 1984]

$$P_d(\tau) = \sum_{j=1}^{11} E_{d,j} \exp(\lambda_{d,j} \tau) \quad (7-106)$$

with decay constants and energy yields given in Table 7-3.

Normalized fission power is calculated from the point kinetics equations

$$\frac{dP_f(\tau)}{d\tau} = \frac{\rho(\tau) - \beta}{\Lambda} P_f(\tau) + \sum_{j=1}^6 \lambda_j \tilde{c}_j(\tau) \quad (7-107)$$

$$\frac{d\tilde{c}_i(\tau)}{d\tau} = \frac{\beta_i}{\Lambda} P_f(\tau) - \lambda_i \tilde{c}_i(\tau) \quad i=1,\dots,6, \quad (7-108)$$

with initial conditions

$$P_f(\tau=0) = 1 ; \quad \tilde{c}_i(\tau=0) = \frac{\beta_i P_f(\tau=0)}{\Lambda \lambda_i}, \quad i=1,\dots,6. \quad (7-109,110)$$

where \tilde{c}_i are normalized precursor concentrations. Typical LWR delayed group parameters, listed in Table 7-4 were used. The prompt neutron

lifetime for the PTLWR was calculated from MCNP to be 1.5×10^{-3} seconds, which differs considerably from a typical LWR value.

Table 7-3 Decay group constants for the 11-decay group model
(from McFaden, 1984)

Group	Decay constant, λ_d (1/s)	Relative yield, E_d
1	1.172	0.00299
2	0.5774	0.00825
3	6.743×10^{-2}	0.01550
4	6.214×10^{-3}	0.01935
5	4.739×10^{-4}	0.01165
6	4.810×10^{-5}	0.00645
7	5.344×10^{-6}	0.00231
8	5.726×10^{-7}	0.00164
9	1.036×10^{-7}	0.00085
10	2.959×10^{-8}	0.00043
11	7.585×10^{-10}	0.00057

Table 7-4 Delayed group constants

Group	Decay constant, λ_i (1/s)	Fraction, β_i
1	0.0124	0.00022
2	0.0305	0.00142
3	0.111	0.00127
4	0.301	0.00257
5	1.14	0.00075
6	3.01	0.00027
Total β	-	0.0065

Reactivity, ρ , is computed from the expression

$$\rho(\tau) = \rho_{Dop}(\tau) + \rho_{col}(\tau) + \rho_{fld}(\tau). \quad (7-111)$$

The reactivity change due to the Doppler effect is given by

$$\rho_{\text{Dop}}(\tau) = \frac{M0 + M1 \bar{\rho}_{\text{col}} + M2 \bar{\rho}_{\text{col}}^2}{\sqrt{\bar{T}_f}} (\bar{T}_f - \bar{T}_{f0}) \quad (7-112)$$

where $\bar{\rho}_{\text{col}}$ is the average coolant density, \bar{T}_f is the core integral average fuel temperature and \bar{T}_{f0} is the core integral average fuel temperature prior to disturbance. Coefficients M0, M1 and M2 express the dependence of the Doppler coefficient on coolant density, and are given in Chapter 4. Core integral average temperature is approximated as

$$\bar{T}_f(\tau) = \sum_{i \in \text{fuel nodes}} \frac{\pi (R_{i+1}^2 - R_i^2) (T_{i+1}(\tau) + T_i(\tau))/2}{F_{\text{peak},r} F_{\text{peak},a} A_{\text{fuel}}} \quad (7-113)$$

where $F_{\text{peak},a}$ is the axial peaking factor and A_{fuel} is the total cross section area of the fuel.

Reactivity feedback from the coolant density change is calculated from the reactivity vs. coolant density curve obtained from the full-core MCNP model, presented in Chapter 4. Density variation with time is calculated as

$$\bar{\rho}_{\text{col}}(\tau) = \bar{\rho}_{\text{col},0} f_{\rho_{\text{col}}}(\tau) \quad (7-114)$$

where $\bar{\rho}_{\text{col},0}$ is the nominal core-average density and $f_{\rho_{\text{col}}}(\tau)$ is the fraction of nominal density following an accident initiation. Obtaining the change of coolant density in a LOCA scenario is a major undertaking, beyond the scope of this work. Therefore, the fraction $f_{\rho_{\text{col}}}(\tau)$ was assumed to be the same as for CANDU reactors, for which a LOCA analysis is available [Pasanen,1980]. A hypothetical 100% break of the inlet header is assumed as a reference LOCA scenario.

Finally, the reactivity change due to flooding, $\rho_{\text{fld}}(\tau)$, is given from the flooding reactivity curve as a function of the number of flooded rows. Flooding reactivity curves were calculated in Chapter 4.

The solution of Eqs. (7-107) and (7-108) is performed in a similar manner as for the system of conduction equations. Substituting for the time derivatives of normalized fission power and normalized precursor concentrations and adopting a fully implicit scheme, Eqs. (7-107) and (7-108) can be written in matrix form

$$\mathbf{N P} = \mathbf{C} \quad (7-115)$$

where \mathbf{P} is the 7x1 vector of unknowns

$$\mathbf{P} = [P_f^{m+1}, \tilde{c}_1^{m+1}, \tilde{c}_2^{m+1}, \dots, \tilde{c}_6^{m+1}]^{-1}, \quad (7-116)$$

\mathbf{C} is the 7x1 vector of right hand sides

$$\mathbf{C} = [P_f^m, \tilde{c}_1^m, \tilde{c}_2^m, \dots, \tilde{c}_6^m]^{-1} \quad (7-117)$$

and \mathbf{A} is the 7x7 coefficient matrix

$$\mathbf{A} = \begin{bmatrix} 1-(\rho-\beta)/\Lambda & -\lambda_1 \Delta\tau & -\lambda_2 \Delta\tau & -\lambda_3 \Delta\tau & -\lambda_4 \Delta\tau & -\lambda_5 \Delta\tau & -\lambda_6 \Delta\tau \\ \Delta\tau \beta_1/\Lambda & 1+\lambda_1 \Delta\tau & 0 & 0 & 0 & 0 & 0 \\ \Delta\tau \beta_2/\Lambda & 0 & 1+\lambda_2 \Delta\tau & 0 & 0 & 0 & 0 \\ \Delta\tau \beta_3/\Lambda & 0 & 0 & 1+\lambda_3 \Delta\tau & 0 & 0 & 0 \\ \Delta\tau \beta_4/\Lambda & 0 & 0 & 0 & 1+\lambda_4 \Delta\tau & 0 & 0 \\ \Delta\tau \beta_5/\Lambda & 0 & 0 & 0 & 0 & 1+\lambda_5 \Delta\tau & 0 \\ \Delta\tau \beta_6/\Lambda & 0 & 0 & 0 & 0 & 0 & 1+\lambda_6 \Delta\tau \end{bmatrix}. \quad (7-118)$$

The Gauss elimination method is used to solve the system of equations (7-115).

In addition to decay heat generation, the graphite matrix will release, during the heat up process, its Wigner energy. Although this energy will be small, since the matrix operates at high irradiation temperature, it must be included in the heat transfer performance analysis. Wigner energy stored in the matrix will be assumed conservatively high, equal to its saturated value after a long irradiation period at an irradiation temperature of 300°C, $W_\infty = 50 \text{ cal/g}$. A more detailed discussion on this topic is given in [Hejzlar et. al., 1993c]. Further, it is assumed that all Wigner energy is released linearly during heat up between the initial matrix temperature and the temperature of 1000°C, i.e.,

$$q_i'''(\tau) = \frac{W_\infty}{1000 - T_{oi}} \frac{dT_i}{d\tau} \left[\frac{W}{\text{m}^3} \right], \quad i \in \text{matrix nodes}, \quad (7-119)$$

where T_{oi} is the initial operating temperature of the i-th matrix node.

7.4.2.6 Contact Resistance between Fuel Compacts and Graphite Matrix

Contact resistance between the fuel compacts and the solid graphite matrix depends on the manufacturing technology of the fuel elements. A typical procedure used to manufacture HTGR fuel elements is to machine the graphite matrix complete with fuel holes and to separately prepare fuel compacts which are then pressed into the pre-machined holes. This technology leads inevitably to imperfect contact between the fuel compacts and the matrix, and consequently to a temperature jump across the compact-matrix interface. Contact resistance between the fuel compact and the matrix can be estimated as the ratio of the effective thermal conductivity of the gap and the gap thickness. The effective conductivity of the gap is primarily a function of the conductivity of the interstitial gas and the average interface temperature. It can be approximated by the equation

$$k_{\text{eff}} = k_{\text{cond}}(\bar{T}) + k_{\text{rad}}(\bar{T}) \approx k_{\text{gas}}(\bar{T}) + 4 \sigma \Delta x \epsilon_{\text{eff}} \bar{T}^3 \quad (7-120)$$

where

$$\epsilon_{\text{eff}} = \left(\frac{1}{\epsilon_{\text{fc}}} + \frac{1}{\epsilon_{\text{mat}}} - 1 \right)^{-1} \quad (7-121)$$

Equation (7-120) is plotted in Figure 7-8, using for the effective emissivity of the fuel compact-graphite matrix gap a typical value of $\epsilon_{\text{eff}}=0.88$ [Ambrosek, 1993], air properties, and the gap thickness of 25 μm .

An alternative fabrication technique of fuel elements with separate fuel and matrix regions was developed by HOBEG (Hochtemperatur-Brennelement GmbH) [Hrovat, 1978]. The HOBEG technology loads fuel particles into a prepressed graphite matrix with subsequent heating, final pressing and heat treatment of the entire block. Contact resistance is practically eliminated in these molded block fuel elements. Calculations of thermal performance during normal operation, presented in Section 6.5, showed a significant improvement if the molded fuel elements are used instead of machined fuel elements. The analysis performed in this chapter employs the contact resistance from Figure 7-8, since large scale experience has been gained in the production and operation of the

traditional HTGR fuel blocks. However, it is to be noted that molded block fuel elements would improve the thermal performance of the PTLWR matrix considerably. Therefore, HOBEF fuel elements are recommended for use in the PTLWR fuel channels, if at all practicable.

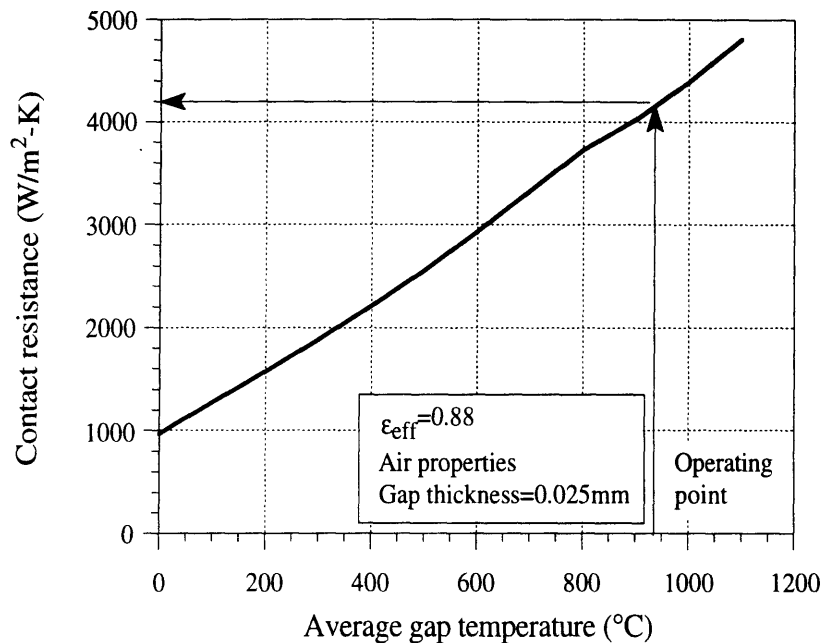


Figure 7-8 Contact conductance between fuel compacts and graphite matrix

7.4.3 Analysis of the Fresh Core

Input parameters for the transient fuel channel analysis involve geometrical variables, power densities, reactor physics characteristics, and material properties. The PTLWR reference fuel channel geometry, with dimensions, is given in Chapter 2, reactor physics characteristics are calculated in Chapter 4, and power generation parameters are discussed in the previous section. Material properties are summarized in Table 7-5.

The purpose of the gap between the pressure tube and calandria tube is to provide protection of the pressure tube from thermal shock during flooding. Therefore the gap should provide some insulation to protect the pressure tube from sudden cooldown. On the other hand the gap must retain sufficiently high thermal conductivity to allow decay heat removal

from the fuel channel at pressure tube temperatures below 500°C. Maximum heat flux needed to be transferred across the gap is about 6×10^4 W/m², which constitutes about 1.5% of rated channel power (note that this relatively low heat flux is due to the high heat storage capabilities of the matrix and the significant portion of decay heat from gammas deposited directly in the flood water).

Table 7-5 Material properties used in the fuel channel transient analysis

Property	Reference
Thermal conductivity of fuel compacts	15 ^a W/m-K [Ambrosek, 1993]
Thermal conductivity of irradiated graphite	[Stacey et. al., 1982]
Thermal conductivity of Zircaloy	[Hohorst et. al., 1990]
Air properties	[Irvin, 1984]
Contact conductance between fuel compact and graphite matrix	Figure 7-8
Emissivity of SiC coating	0.85 [Breitbach and Barthels, 1980]
Emissivity of pressure tube	[Hohorst et. al., 1990]
Effective thermal conductivity of the gap between the pressure tube and calandria tube	2 W/m-K

^a Typical average value for fully loaded compacts. For the fresh load, the conductivity can be up to 20 W/m-K. Thermal conductivity changes with fluence, but for high fuel operating temperatures, the change is very small. The exact correlation is proprietary information.

Figure 7-9 plots the effective thermal conductivity of the gap between the pressure tube and the calandria tube for various gases and gap widths. The effective conductivity includes the heat transfer contribution from

radiation, gas conduction and natural convection, and was evaluated by the same procedure as described in Section 7.4.2.2. The convection part was calculated from the correlation introduced in Section 7.4.2.3, except for the air properties, which were replaced by the properties of the appropriate gas. The heat flux from the outer surface of the pressure tube is also plotted. It can be seen that the heat flux is enhanced by increasing the gas conductivity and by decreasing the gap width. However, even if the gap is small (2mm wide) and is filled with a high-conductivity gas such as helium, the required level of heat flux cannot be achieved. Therefore, alternative gap design options are needed to increase gap effective conductivity. Possible solutions are a packed bed of graphite pebbles, proposed by Tang [Tang, 1992], zirconia spheres as proposed by Dutton [Dutton, 1993], or a duplex tube, similar to those used in EBR-II sodium-water steam generators. The detailed gap design will be postponed for future work, and the analysis will assume that the gap is designed to have a thermal conductivity of 2W/m-K, as listed in Table 7-5.

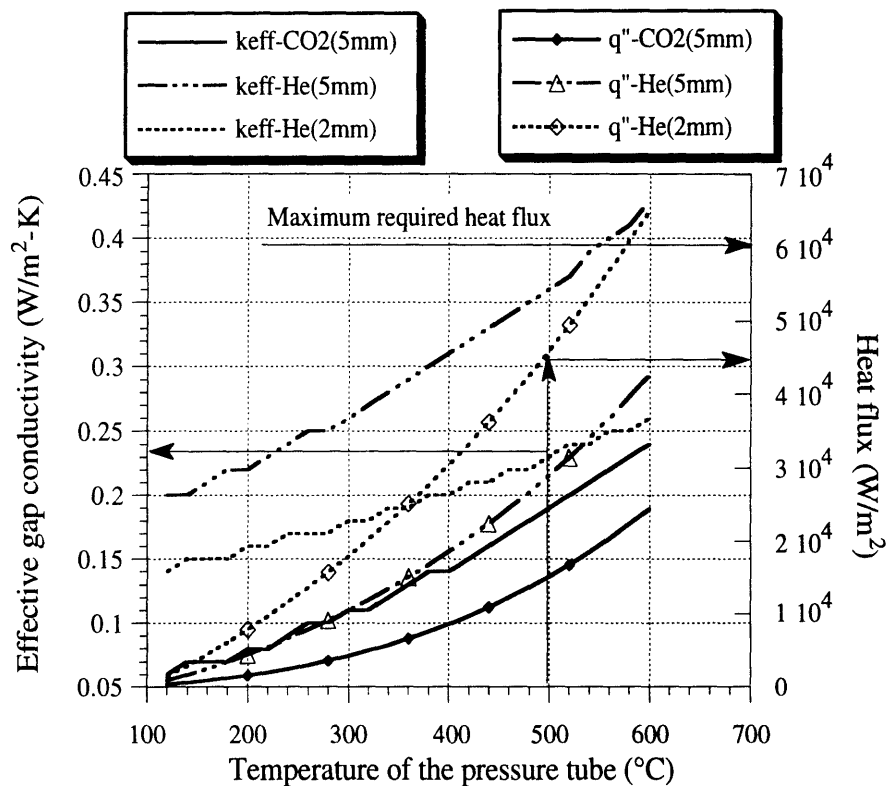


Figure 7-9 Effective thermal conductivity of the gap between the pressure tube and calandria tube and transferred heat flux

7.4.3.1. Adiabatic Matrix Heatup

To evaluate the heat storage capabilities of the fuel matrix, adiabatic heatup of the fuel channel due to decay heat was calculated. For the reactor operating at nominal power, the following actions were taken at time $\tau=0$, to initiate adiabatic heatup:

- the fission power was set to zero (heat up is assumed solely from decay heat),
- the heat transfer coefficients in all coolant channels were set to zero so that no heat is carried away by the coolant, and
- the heat transfer coefficient at the outer surface of the calandria tube was kept at zero during the entire heatup period.

The results are plotted in Figure 7-10 and Figure 7-11. Figure 7-10 shows the temperature traces for the inner fuel ring (T-fuel1), the outer fuel ring (T-fuel2), the matrix coating of the surface of the central coolant channel and the pressure tube. Fuel temperature decreases during the first 15 seconds due to the drop in power generation while the matrix surface temperature rapidly increases until about 800°C because there is no heat transfer to coolant. Subsequently, the whole fuel matrix slowly heats up due to the decay heat generation. Even after 200 seconds fuel temperature does not achieve its original values and there is still a very large margin to 1600°C, which is the transient limit on TRISO fuel particles. Also, the matrix surface temperature still has a large margin to the limiting value of 1300°C for the SiC coating in a steam/air mixture environment. Figure 7-11 shows the matrix temperature profiles at several selected times. It can be observed that after 30 seconds elapse, the temperature profile in the matrix is almost flat due to the good effective thermal conductivity of the matrix. Figure 7-10 shows that pressure tube temperature is more limiting than the fuel matrix temperature since the pressure tube temperature limit of 500°C is reached in about 70 seconds.

Two conclusions can be drawn from these results. First, the large thermal constant of the PTLWR fuel matrix allows a relatively long time before action needs to be taken. Compared to a typical LWR, where cladding

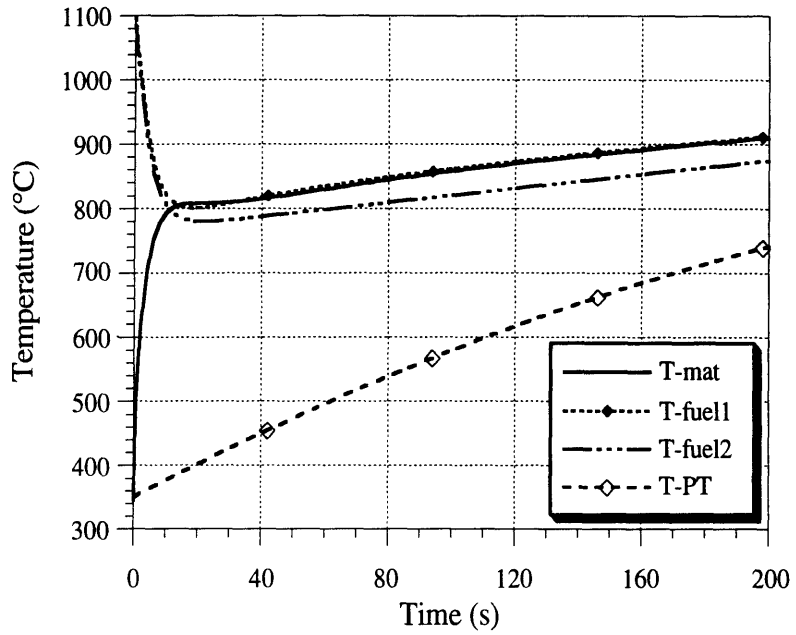


Figure 7-10 Adiabatic fuel channel heatup from decay heat

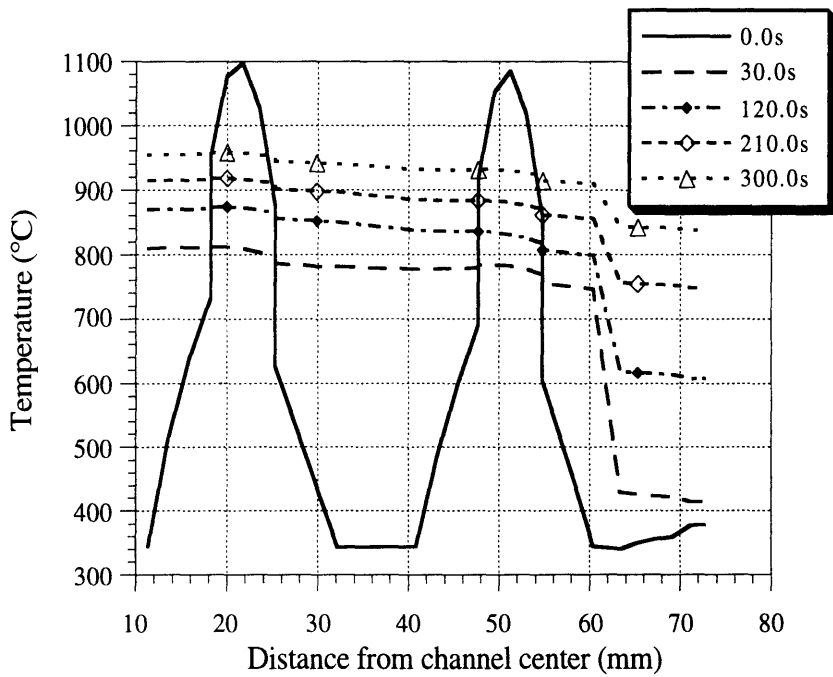


Figure 7-11 Time development of temperature profile across the fuel channel during adiabatic heatup

failure would occur in a matter of several seconds in such a severe hypothetical scenario, the PTLWR fuel matrix does not exceed safe limits for several hundred seconds. It will be shown in Chapter 8, that full calandria flooding is accomplished in about 30 seconds, hence there is still ample time left for potential flooding delay. Secondly, the largest temperature drop is across the gap between the matrix and the pressure tube, where the heat transfer is due to radiation and gas convection only. Therefore the gap between the matrix and the pressure tube is the dominant heat transfer resistance, the decrease of which could significantly reduce fuel matrix temperature. Such a decrease is, however, not necessary because the fuel matrix retains large margins to its temperature limits. Moreover, the trace of the pressure tube temperature clearly shows that this temperature would be the limiting factor, if flooding was not initiated, since at about 70 seconds, it exceeds the prescribed limit of 500°C. Any reduction of heat resistance between the fuel matrix and the pressure tube would lead to accelerated heatup of the pressure tube, hence improvements in the matrix-pressure tube heat transfer are not desirable.

7.4.3.3. LOCA without Scram

The following accident sequence was simulated for a reactor operating initially at nominal power:

- at $\tau=0$ s
 - 100 % break of the inlet header in both loops,
 - no scram and no control rod movements, and
 - heat transfer coefficients in all coolant nodes were set to zero so that no energy is carried away by the coolant;
- at $\tau=5$ s
 - flooding process is initiated;
- at $\tau=35$ s
 - flooding water reaches the last (upper) row of fuel channels.

Note that zero heat transfer coefficient is a quite conservative assumption since significant energy will be carried away by the coolant during blowdown. Although the temperature of flood water is quite below saturation, it was assumed to be saturated to investigate the potential for establishment of film boiling. The Leidenfrost temperature from Bergles' measurements was chosen, i.e., $\Delta T_{\text{sat}_{\text{min}}} = 300^{\circ}\text{C}$. Figure 7-12 shows the temperature traces of the inner fuel ring, matrix surface at the central coolant channel, the pressure tube, and the calandria tube. Figure 7-13 plots the steady state temperature profile at 0 seconds and at 160 seconds, i.e., the time when maximum fuel matrix temperature is reached. Locations of limiting temperatures are also marked.

At the time flooding water reaches the last row of fuel channels, Figure 7-12 illustrates that the calandria tube surface temperature is 435°C which is slightly higher than the Leidenfrost point determined from Bergles' experiments. Initial cooldown through the film boiling regime (after about 5 seconds) reduces the calandria wall temperature below the Leidenfrost point. Consequently, the calandria tube is rapidly quenched and its temperature drops close to the saturation temperature of flood water and is then maintained at this level until the end of the transient. The temperature of the pressure tube quickly follows that of the calandria tube, and the channel slowly cools down. Matrix and fuel centerline temperatures reach their peak at 160 seconds.

Figure 7-14 plots the linear heat transfer rates in the gap between the matrix and the pressure tube, Q'_{gap} , from calandria tube to flood water, Q'_{out} , and the linear heat generation rate in the fuel matrix, Q'_{gen} (decay heat, fission power and released Wigner energy). The heat rate across the gap increases at first due to the matrix-surface temperature rise, then it slightly decreases because the growth rate of the pressure tube temperature exceeds the growth rate of the matrix temperature. Upon flooding, the pressure tube temperature drops, which leads to an increase of the heat transfer rate across the gap. The linear heat rate into flood water jumps to high levels after flooding, because both the temperature difference between the calandria tube and the saturation temperature, and the nucleate boiling heat transfer coefficient are high. As the calandria tube temperature is

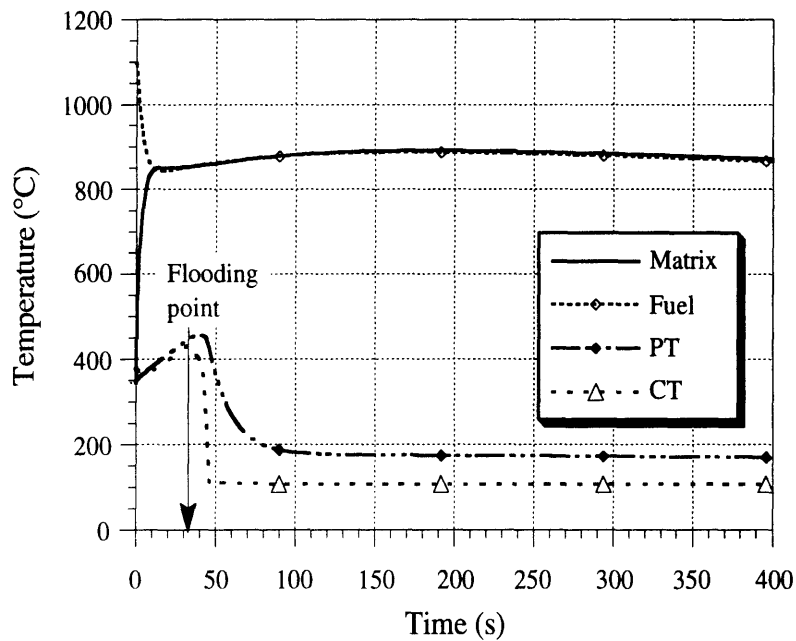


Figure 7-12 Time development of limiting temperatures following LOCA without scram

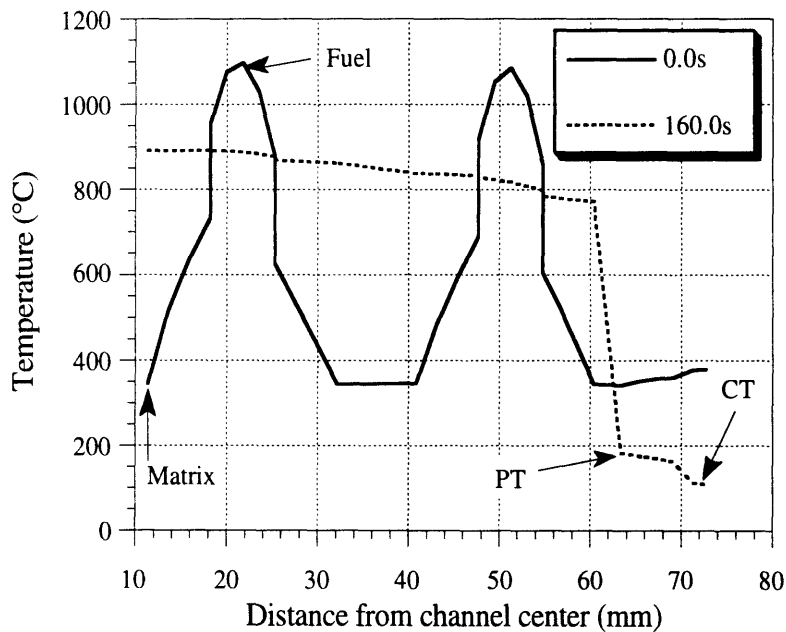


Figure 7-13 Radial temperature profile in the fuel channel following LOCA without scram

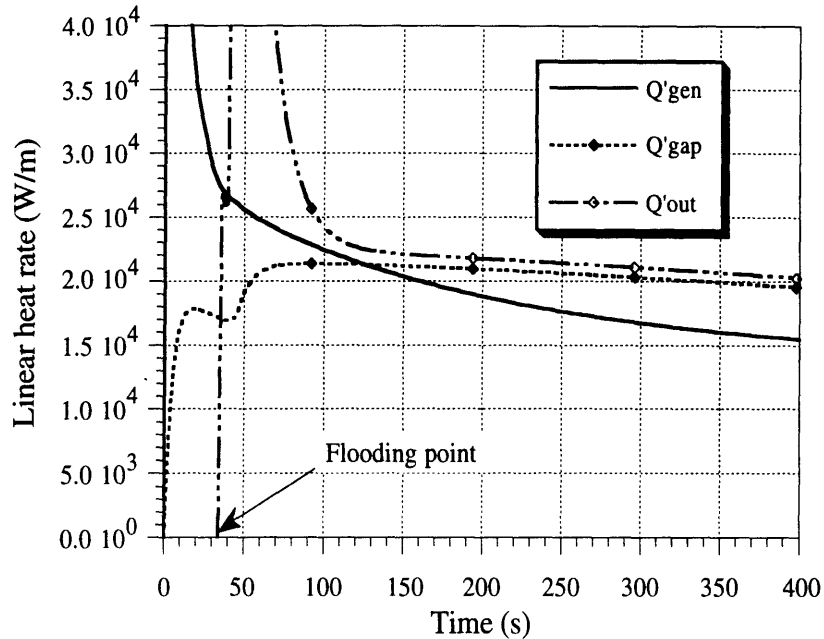


Figure 7-14 Linear heat rates during LOCA without scram

reduced, the heat rate to flood water is reduced as well. It can be observed that the rate of cooldown is controlled by the high heat transfer resistance of the gap between the fuel matrix and the pressure tube.

Reactivity changes and relative power are plotted in Figure 7-15. As the primary coolant is lost, the rapid decrease in coolant density results in a large negative reactivity insertion and reactor shutdown. The contribution from the Doppler coefficient is positive because the fuel temperature drops, but is very small compared to void reactivity. Hence, the total reactivity is driven almost exclusively by coolant conditions in this scenario. Inherent reactor shutdown during LOCA without scram is a favorable characteristic different than for CANDU reactors, which exhibit a positive void coefficient, and must rely on reliable shutdown systems. Flooding brings additional negative reactivity into the system, which renders the reactor deeply subcritical (by about -200β).

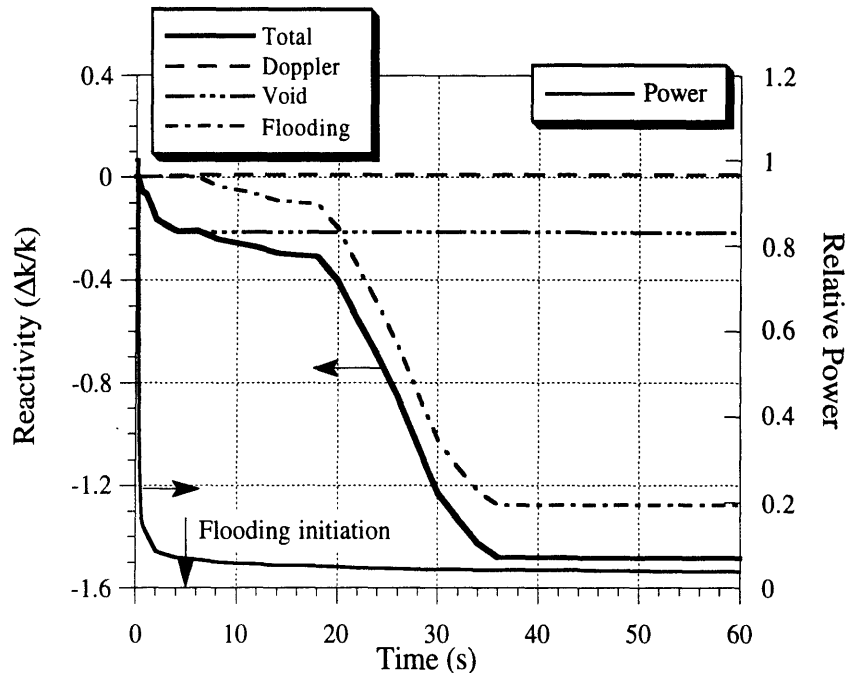


Figure 7-15 Reactivity changes during LOCA without scram

Operation in Film Boiling Regime

Because of the uncertainties with the minimum film boiling heat flux, the worst possible scenario – one having sustained film boiling at the outer surface of the calandria tube, was studied. To achieve film boiling, the Leidenfrost temperature was decreased below Bergles' values to 290°C (as cited by Whalley), and the flooding initiation was set at a later time so that the upper row is flooded at the 50th second.

Figures 7-16 and 7-17 show the time history of critical temperatures and linear heat rates. Both the fuel and maximum matrix surface temperatures reach higher maximum values than for the nucleate boiling case, but the difference is small (only about 20°C). The peak is reached at a later time (280 seconds compared to 1680 seconds in the nucleate boiling case). Pressure tube temperature rises to about 500°C, until 50 s, when the flooding water reaches the last row. Since the calandria tube outer surface temperature is quite above the Leidenfrost point, heat transfer to flooding water is by film boiling, and the pressure tube temperature remains at

about 500°C. However, the heat flow from the matrix is controlled by the large heat transfer resistance of the gap between the matrix and the pressure tube (note that the gap linear heat rate has the lowest values). At the time of about 270 seconds, decay heat generation is smaller than the heat rate transferred from the system, causing a reverse in the matrix temperature trend.

An important conclusion from this hypothetical scenario is that even if the calandria tube does not quench below the Leidenfrost point, there is no problem in removing the heat load. In fact this scenario is preferable from the thermal stress point of view. Also note that there is no traditional CHF concern since the system can remove the heat under film boiling conditions. The only difference is higher pressure tube temperature, but one which does not exceed the 500°C limit. The effect of film boiling on fuel matrix temperature is negligible, even though the pressure tube temperature is almost 400°C higher. The reason for this is the prevailing

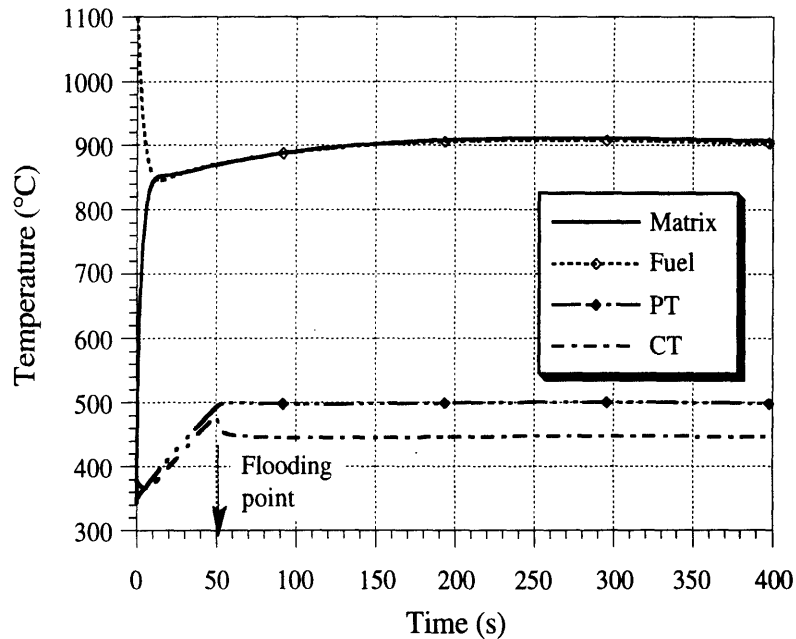


Figure 7-16 Time development of limiting temperatures for sustained film boiling at calandria tube surface

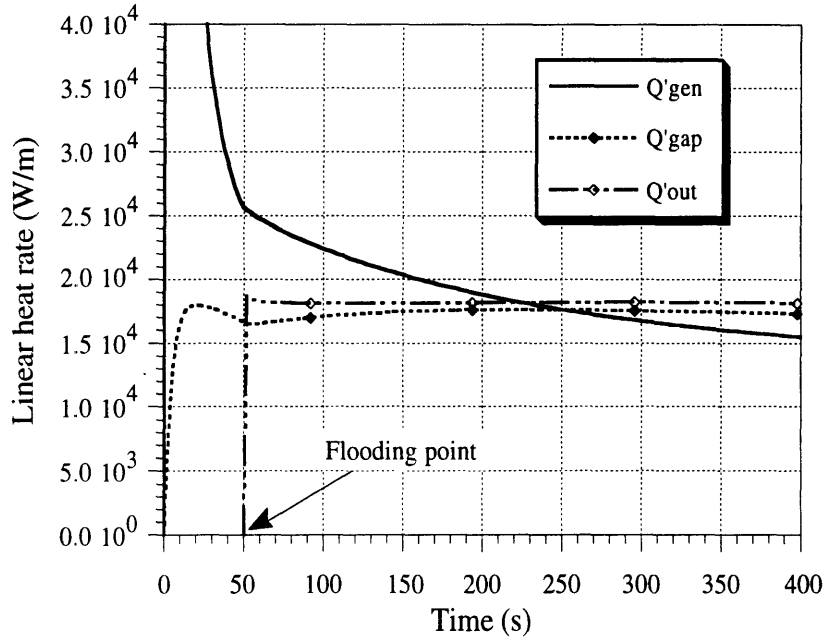


Figure 7-17 Linear heat rates for sustained film boiling at calandria tube surface

radiative heat transfer mode (about 80%) across the matrix-pressure tube gap. The radiative heat transfer is proportional to the difference of upper temperature to the fourth power and lower temperature to the fourth power. Since the lower temperature to the fourth power is a much smaller number than the upper temperature to the fourth power, the increase in lower temperature, even if this decrease is relatively large, does not influence the heat rate significantly, compared to the effect of changes in the upper temperature. Consequently, the matrix is not affected by even a large temperature change of the pressure tube.

7.4.4 Analysis of Equilibrium Core in Bi-directional Refueling Scheme

The equilibrium core exhibits a different power density profile and higher peaking than for the fresh core. Hence the only difference in a transient fuel matrix analysis lies in its higher power density. Using the data for the online refueling scheme with partial reshuffling (see arrangement of bundles in Figure 4-51 and power density profile in Figure 4-52), the results are presented in Figures 7-18 and 7-19. The scenario is

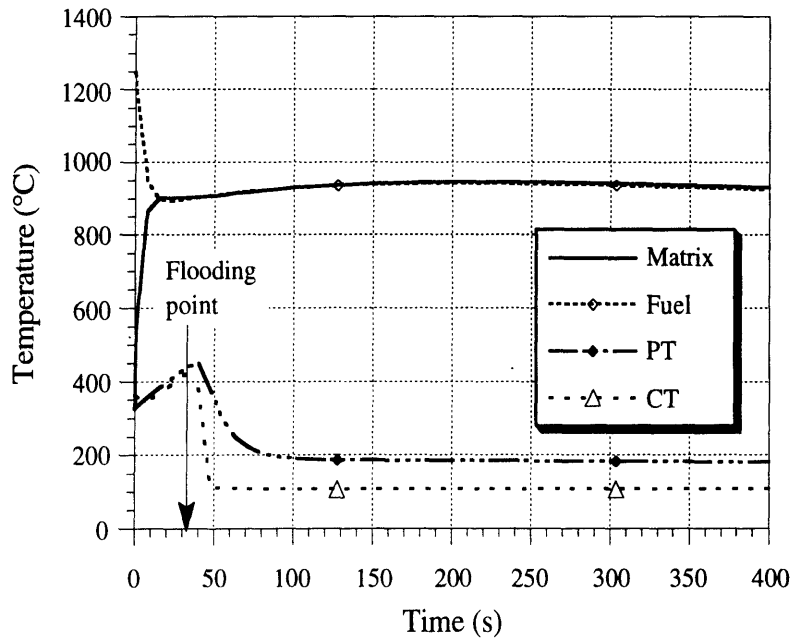


Figure 7-18 Time development of limiting temperatures for the equilibrium core

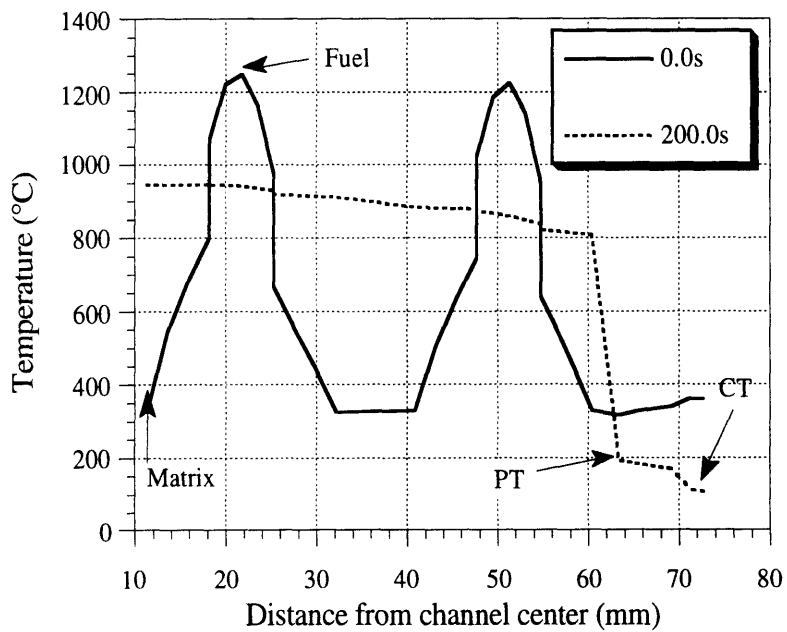


Figure 7-19 Temperature profiles across the fuel channel for equilibrium core

assumed to be the same as for the fresh core, i.e., LOCA without scram. Bergles' value of Leidenfrost temperature is taken for the outer surface of the calandria tube. All limiting temperatures reach higher peak values than those for the fresh core (by about 30°C) due to the higher local peak power density, but they all remain well below the limits.

7.4.5 Finite Element 2-D Model for Quasi-steady Analysis of Fuel Matrix

The simplified 1-D model, described in Section 7.4.2, models well the heat transfer from the matrix outer surface to flood water, since the heat transfer is basically one dimensional in this region. However, heat transfer within the fuel matrix is a 2-D phenomenon, and the transformation to a 1-D model introduces significant simplifications. Therefore it is desirable to validate the 1-D model on a more exact solution of the heat conduction equation within the matrix. Such a validation is given in this section. A detailed 2-D temperature profile of the voided fuel matrix at the time when the peak is reached is also presented.

7.4.5.1 Benchmark of 1-D Simplified Model against 2-D Model

The finite element system package ALGOR, introduced in Chapter 6, is used to validate the simplified model. A full time-dependent validation of the 1-D model with ALGOR is not feasible because the available version of ALGOR requires a manual iterative process between two processors to handle temperature dependent properties. Therefore, only quasi-steady state temperature profiles obtained from ALGOR and the 1-D model will be compared. This approach is deemed to be sufficient since most of the approximations introduced into the simplified model come from geometry transformations, which do not change with time. It is to be noted that the most challenging case is the steady state at full power because it exhibits the largest temperature gradients. Hence, the benchmark will be performed for the conditions during normal operation, i.e., prior to LOCA initiation.

Using the same boundary conditions for both models, the temperature profile has been calculated using both the 1-D and ALGOR 2-D model with fresh core data. The results are plotted in Figure 7-20. It can be observed that the agreement between both models, with respect to temperature magnitude, is excellent. The shift of the 1-D curve is caused by geometrical transformations, which are necessary to preserve material volume, and hence the heat storage capacity. The 1-D model gives conservative results since it yields a slightly higher fuel centerline temperature.

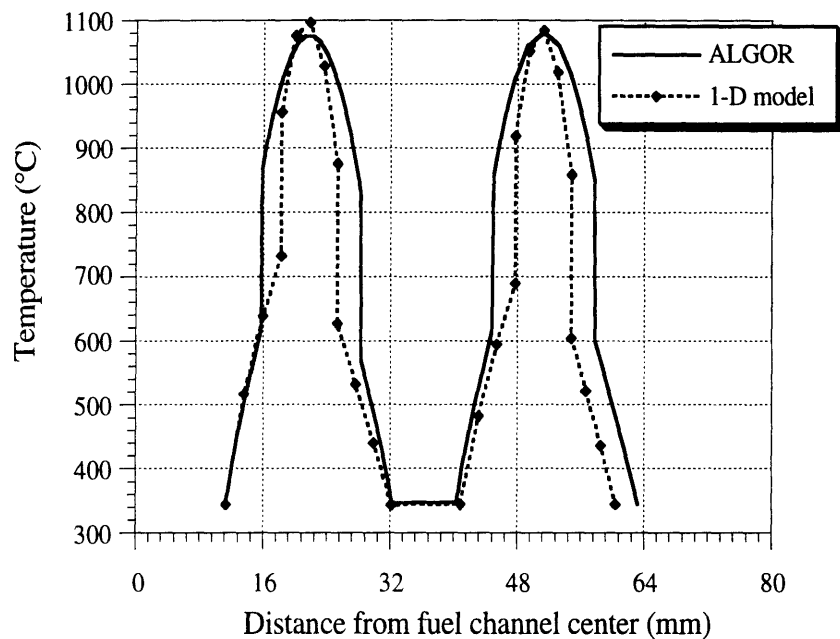


Figure 7-20 Comparison of 1-D model with ALGOR 2-D model for the fresh core at steady state

7.4.5.2 Detailed Maximum Temperature Profile of Voided Fuel Matrix

A detailed temperature profile of the voided fuel matrix is shown in Figure 7-21. The snapshot was calculated for an equilibrium core at 200 seconds (the time when peak fuel matrix temperature is reached), using the boundary conditions obtained by the 1-D model. Boundary conditions include power density in the fuel and the matrix surface temperature

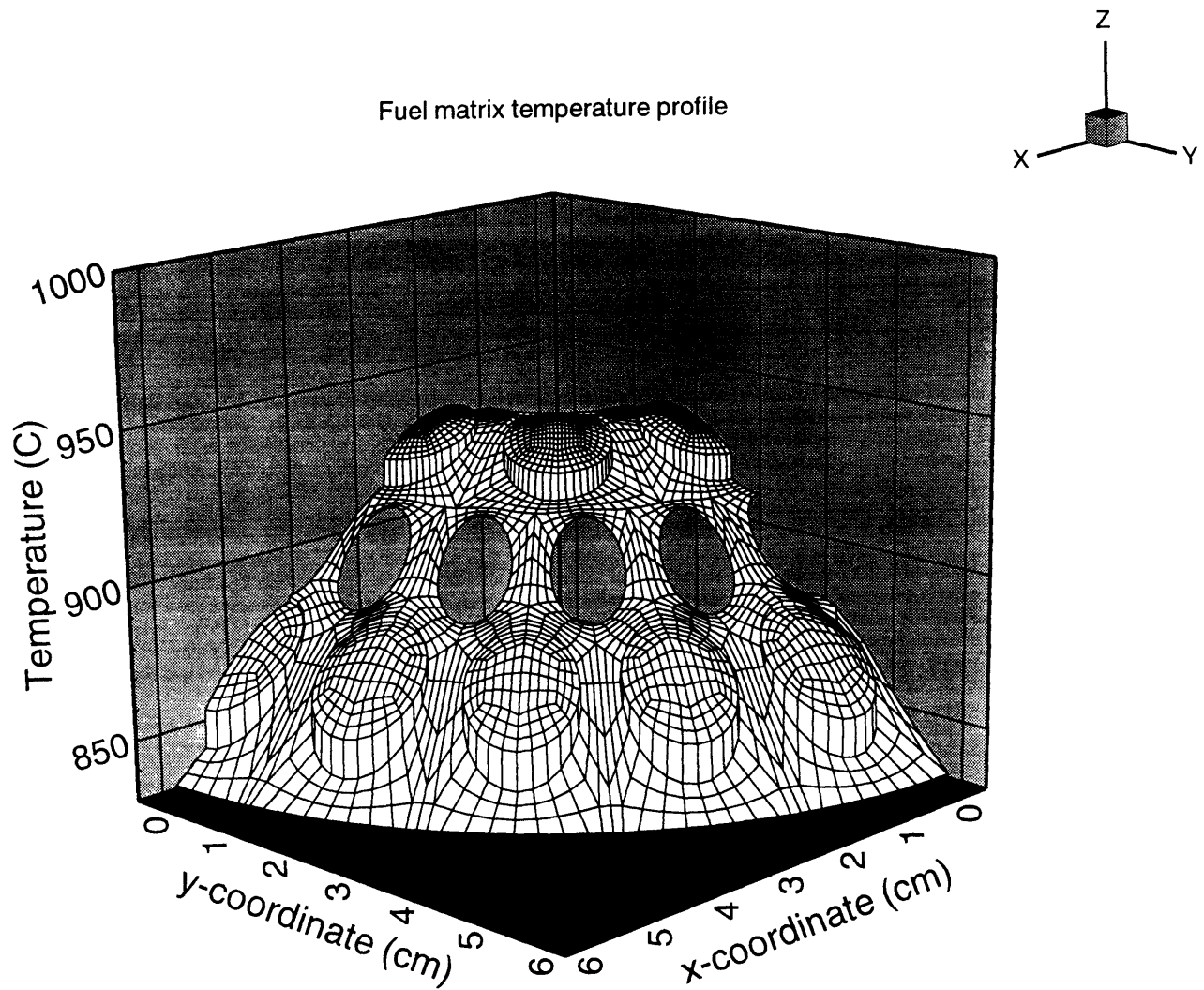


Figure 7-21 ALGOR temperature profile of a voided fuel matrix for equilibrium core at 200 seconds

at the outer periphery. Similarly as in Figure 7-19, a fairly flat matrix temperature profile can be observed, with a maximum-minimum temperature difference of about 140°C. The webs between the voided coolant channels transfer all the heat, since the contribution of radiation and convection through the tubular coolant channels was neglected.

7.4.6 Summary

The transient analyses presented in Sections 7.4.3 through 7.4.5 show that the decay heat in a LOCA without scram scenario can be removed without exceeding safe limits on the fuel, matrix and pressure tube, and without an emergency core cooling system. This capability of the proposed fuel-matrix-in-a-pressure tube design to passively dissipate the excessive power generated in the fuel to the heat sink without exceeding safe temperature limits, even if the fuel channel is voided, is the key advantage of the PTLWR. Furthermore, even one of the worst accidents which could hypothetically occur – LOCA without scram – does not result in temperatures which would lead to fuel channel damage. These characteristics are primarily due to:

- the arrangement of the fuel in small modules distributed in a heat sink, having a very short conduction path between the fuel and the heat sink,
- the introduction of the fuel matrix which
 - retains high effective thermal conductivity in the absence of coolant,
 - reduces initial energy stored in the fuel, and
 - provides for high additional energy storage,
- a relatively flat power profile throughout the entire core, which decreases thermal limits imposed by the hot spot,
- a large flooding water-to-fuel matrix mass ratio, responsible for the deposition of a substantial portion of the gamma decay heat directly in the heat sink, hence reducing the decay heat load on the fuel matrix, and
- a large negative void coefficient, responsible for inherent reactor shutdown following LOCAs.

Chapter 8

CALANDRIA PASSIVE FLOODING

8.1 INTRODUCTION

Flooding the calandria space with light water is a unique and very important feature of the PTLWR concept. It provides a heat sink independent of reactor primary coolant, and redundant reactor shutdown. Once the calandria flooding process is initiated, it is a fully passive process since it is driven solely by the gravity head between two pools with different water levels. A crucial issue is the initiation of the flooding process. The initiation should be:

- reliable,
- passive (i.e., conform to the definition of passive systems-see Chapter 1),
- resistant to spurious initiations,
- able to be initiated in both the loss of coolant and loss of heat sink accidents, allowing for sufficient prescribed deadbands,
- and as simple as possible.

Two possible flooding initiation systems are proposed. The first system is a passive, fluid-operated valve which works from primary system pressure. The valve is fully passive since it relies only on the stored energy in the fluid. To enhance the reliability, four redundant valves are employed. The second alternative is a dc-powered blower which maintains the gas pressure in the calandria during normal operation and releases the pressure upon switching off the blower power supply. This scheme cannot be classified as fully passive since it employs rotating machinery, but it is fail-safe in the sense that when the blower stops, water can enter. Both flooding initiation concepts and their advantages and disadvantages are

described in Section 8.2. The flooding system concept using the passive valve for flooding initiation will be shown in Section 8.3.

The most important parameter needed for the analysis of the PTLWR fuel channel performance in LOCA scenarios is the time at which the last (upper) row of fuel channels becomes fully flooded, i.e., immersed in a heat sink. To evaluate this parameter, a simplified flooding model has been developed. It tracks the water level in the calandria as a function of time and provides the possibility to study various flooding scenarios. The description of the model and the results of the analysis results are given in Section 8.4.

8.2 FLOODING INITIATION SCHEMES

During normal operation, the calandria is filled with gas at elevated pressure to keep the water pool outside the calandria, while during an accident the gas pressure is released allowing for passive calandria flooding. The task of maintenance of the pressure at a prescribed level and its release at prescribed conditions may be accomplished in various ways. Two possible schemes are proposed in this work – a passive fluid-operated valve, and a dc-operated blower. In the passive-operated valve scheme, the calandria is sealed by a seal closure and the pressure is maintained at a preset level by a separate calandria pressure control system using a supply of available pressurized gas. The valve senses the accident conditions from the primary system and if these conditions exceed the prescribed limits, the valve opens the seal closure, thus releasing the gas pressure. This alternative has been selected for the reference PTLWR design. The second proposed alternative employs a dc-powered blower which provides both the maintenance of the gas pressure at a prescribed level during normal operation and gas release during an accident. The signal leading to the gas release is provided electronically from sensors indicating primary system conditions. Both schemes will be described next.

8.2.1 Passive Fluid-Operated Valve

One possible solution using a passive fluid operated valve for flooding initiation is shown in Figures 8-1 and 8-2. Figure 8-1 is a schematic of the valve during normal operation and Figure 8-2 shows the valve in an open position during a loss of normal heat sink accident. The valve consists of a pilot valve and an air-operated main valve which create one body. The pilot valve part includes the main piston, the balancing piston, nuts and springs for dead band positioning, and a nitrogen pressurized balancing tank. The air-operated part comprises an air-pressurized tank of pressure p_2 (much lower than p_1), the loading piston and the release piston, both on the same shaft as the pistons of the pilot valve, and the acting piston connected with the calandria closure seal.

The valve works on primary system pressure, p_1 . The dead bands are set such that they envelope all conceivable pressure disturbances and transients which do not require reactor shutdown. In case of a "low pressure" accident, e.g. loss of coolant accident, the primary system pressure decrease leads to the movement of pistons to the left due to the difference between the force exerted by pressure in the balancing tank and the force from primary system pressure. This movement is opposed by spring 2, and continues without any action until the lower pressure limit, proportional to force $k\Delta x_2$ exerted by spring 2 (where k is the spring constant) is reached. At this point, the loading piston of the air-operated valve switches the air passages in such a way that the air pressure is released from the space above the acting piston and introduced below the acting piston, hence the acting piston moves upward and opens the calandria closure seal. In case of a "high pressure" accident, e.g. loss of heat sink, the primary system pressure acting on the main piston area, S_1 , moves the pistons to the right until the upper limit proportional to force $k\Delta x_1$, exerted by spring 1 is reached. At this point, the passage around the main piston is opened allowing primary system pressure to act additionally on area S_2 . The resulting force to the right is increased since it becomes proportional to area S_2 , and moves the pistons to the right. This leads to reswitching of air passages and opening of the closure seal, as shown in

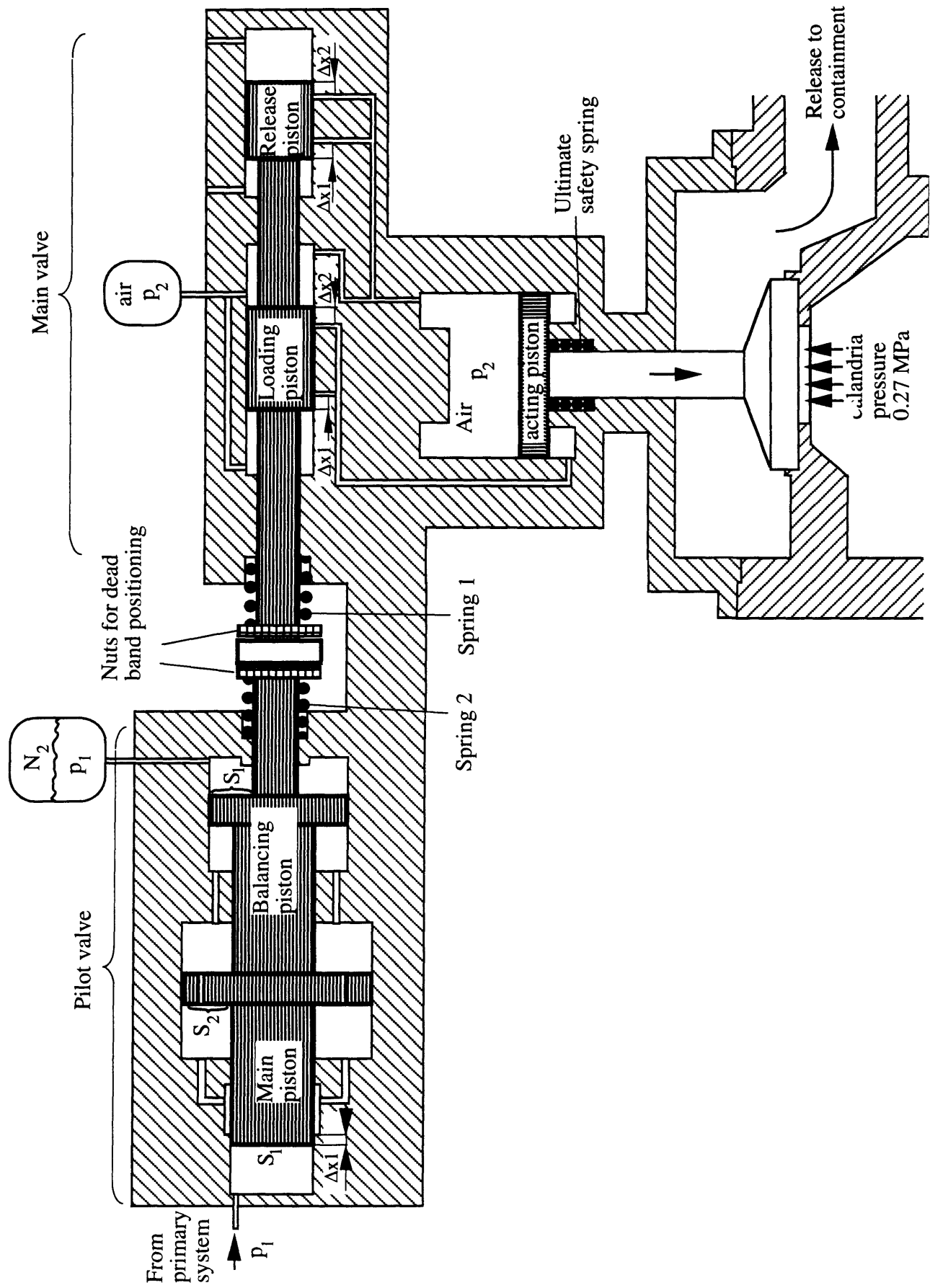


Figure 8-1 Schematic of a passive fluid-operated valve – operating mode

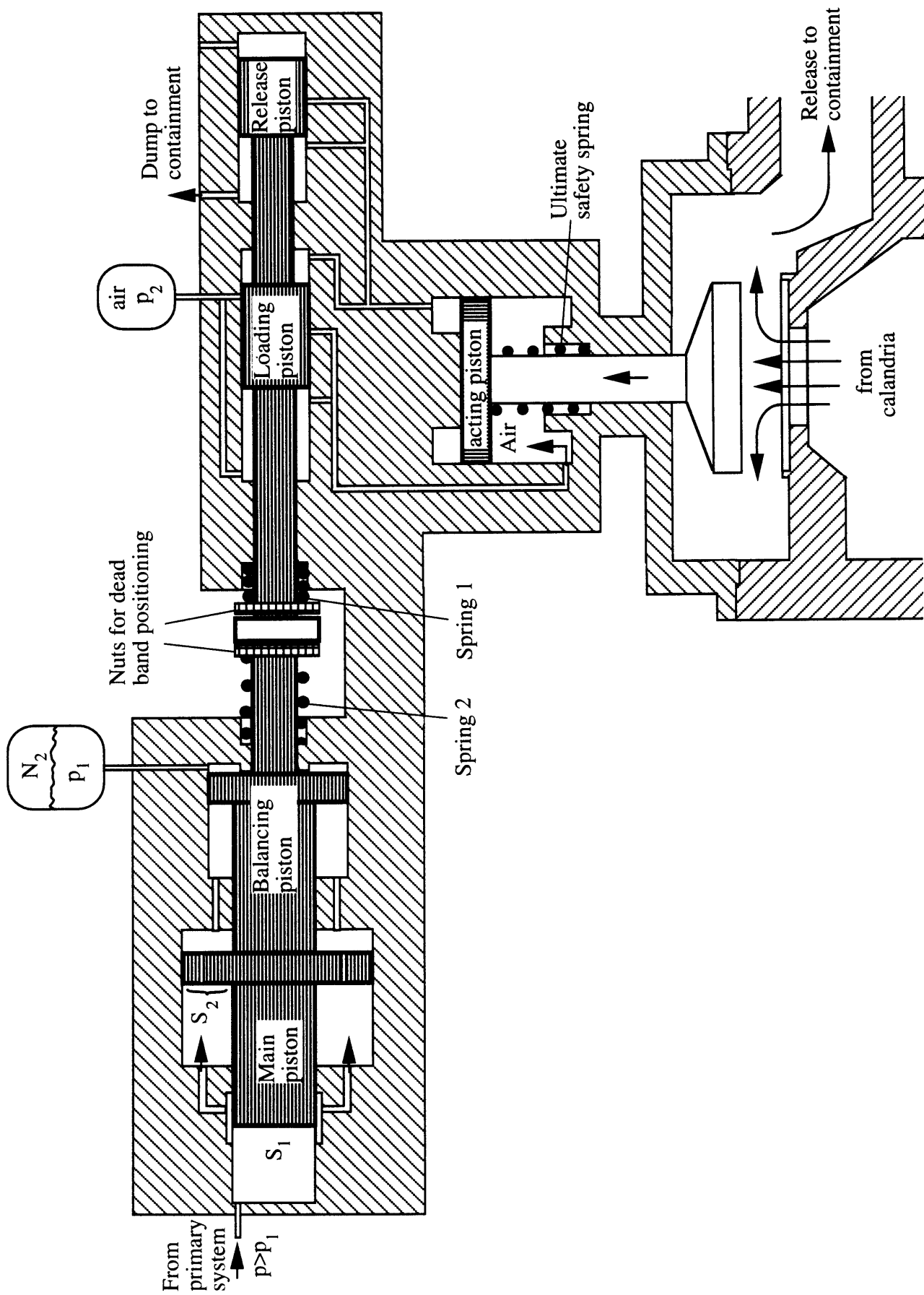


Figure 8-2 Schematic of a passive fluid-operated valve – loss of heat sink accident mode

Figure 8-2. The ultimate safety spring lifts the closure seal in case of the failure of the air tank, although it is noted that calandria pressure can lift the seal in such a scenario.

The valve is designed such that all identified failures of various valve parts lead to valve opening. These include

- break of pressure junction from primary system,
- break of pressure junction from nitrogen pressurized tank or break of the tank itself,
- break of spring 1 or spring 2,
- break of air tank or low pressure junction to air tank, and
- failure of the ultimate safety spring.

Jamming of the piston is very improbable, however, it cannot be excluded. If the pistons can be designed such that the possibility of jamming is eliminated, the valve could be designated as fail-safe in the sense that any failure results in the desirable action, i.e., valve opening. Four redundant passive valves, each of 50% capacity, are proposed. Additionally, another 100% capacity valve which can be opened from the control room is proposed to provide the operator with the capability to flood the calandria and shut down the reactor if all means fail.

8.2.2 DC-Powered Blower

A schematic of the gas-filled calandria during normal operation with a dc-powered blower is shown in Figure 8-3. The blower operates at nominal speed at all times to provide the gas pressure needed to keep the flooding water outside the calandria. It is sized such that at nominal speed it provides exactly the head needed to keep the flooding water outside the calandria at the desired level, h . The power rating of the blower can be determined from the relation

$$P = Q \rho_{\text{air}} g h \quad (8-1)$$

If the water level difference $h=14.5\text{m}$ and volumetric flow rate $Q=0.1 \text{ m}^3/\text{s}$ (selected such that it takes about 1 hour to push all water out of the fully-

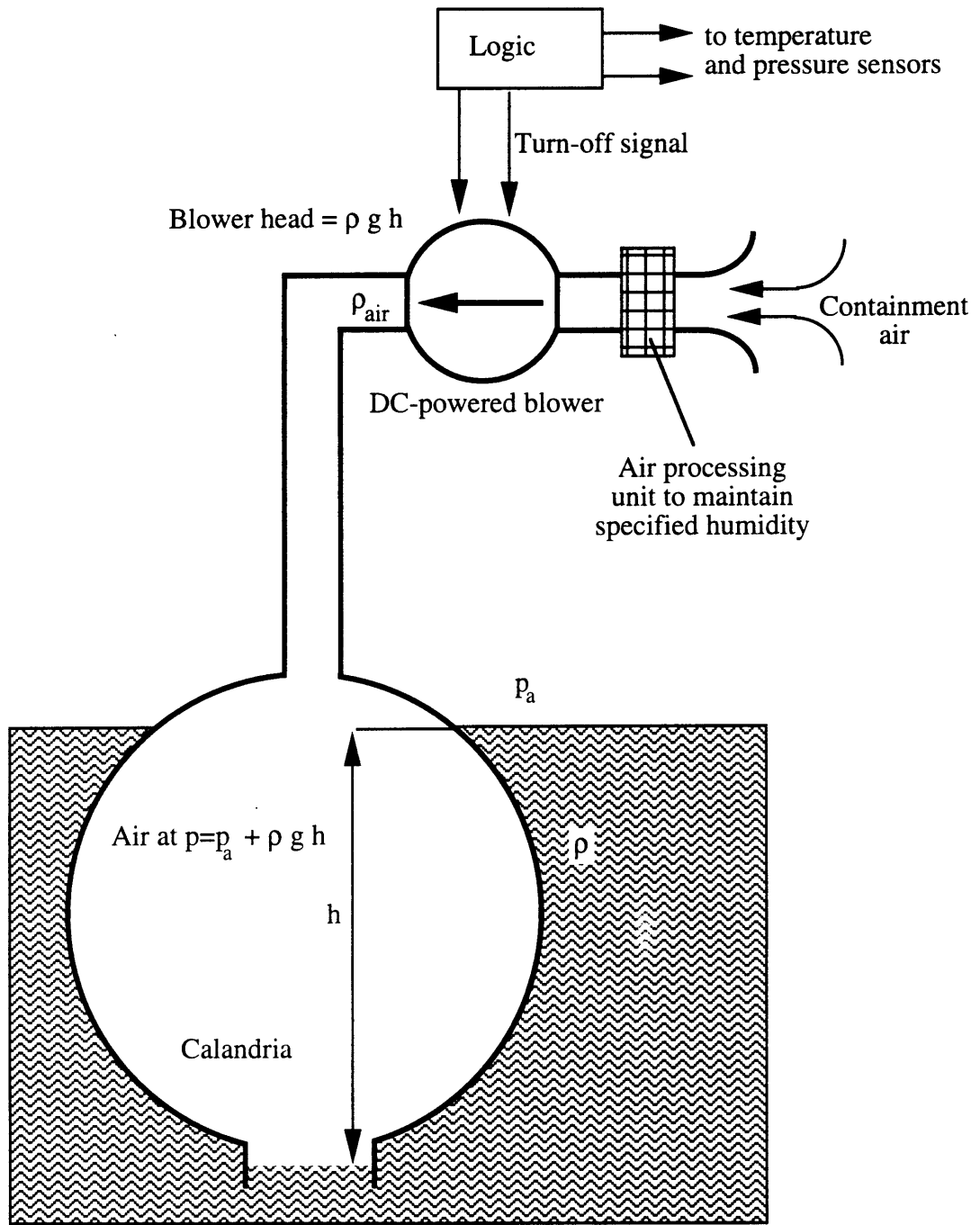


Figure 8-3 Schematic of calandria with dc-powered air-lock blower – operating mode

flooded calandria), the blower needs to be rated at about 36W – a quite modest power rating.

Calandria flooding is initiated by turning off the blower. The turn-off signals are provided electronically using a logic unit and sensors of primary system parameters, i.e., temperature and pressure. If primary system parameters exceed the limits which envelope all allowed pressure and temperature disturbances and transients, the logic unit sends the turn-off signal. The advantage of this approach is the possibility to use more parameters than in the passive valve alternative, which relies only on pressure. On the other hand, the blower scheme requires dc power and reliable sensors. Initiation is also not fully passive since it requires rotating machinery (albeit in its non-operating mode). Similarly as for the passive valve alternative, four blowers, each of 50% capacity are proposed. To enhance diversity, it is also possible to combine 2x50% capacity passive valves and 2x50% capacity dc-powered blowers. If air is used to pressurize the calandria, then argon-41 activity will be vented into the containment during the flooding process.

8.3 DESCRIPTION OF PASSIVE CALANDRIA FLOODING SYSTEM

Figure 2-4 in Chapter 2 shows the overall arrangement of the dry calandria submerged in the pool of flooding water. The schematic is a quite simplified sketch intended to show the principle. The real arrangement, although the same in principle, differs from that shown in Figure 2-4. It must provide for sufficient neutron shielding of upper decks, and space for refueling machines, as well as other equipment rooms. Furthermore, the water level below the calandria bottom should not be openly exposed to neutron flux in the calandria space to minimize parasitic losses. One possible alternative arrangement of flooding water in the containment is shown in Chapter 11, in Figure 11-1. Calandria shielding can be achieved in the same manner as in existing CANDU reactors, by a light water shield in the concrete vault which supports the calandria. In the dry calandria design, the vault needs to be larger due to its additional graphite reflector. Figure 8-4 shows a cross section of the calandria, concrete vault and

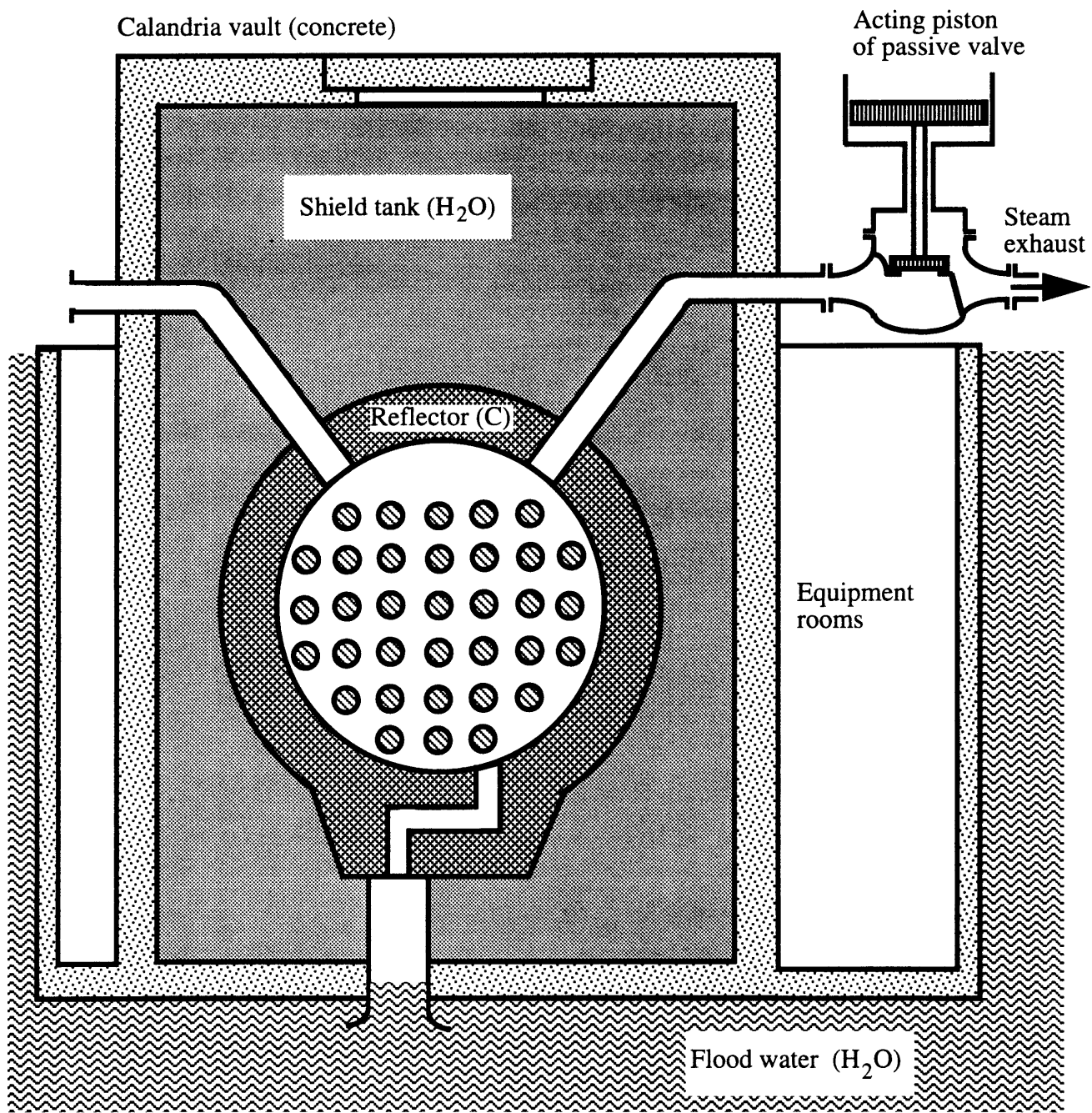
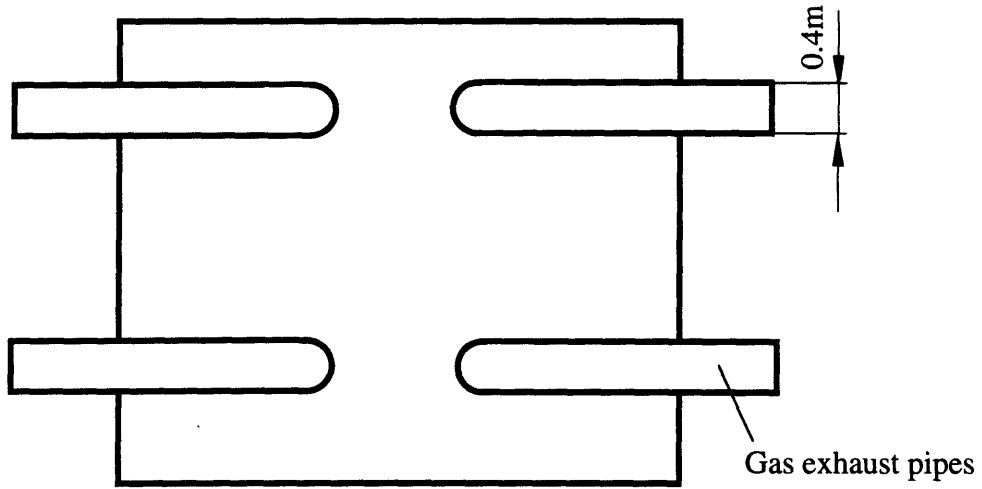
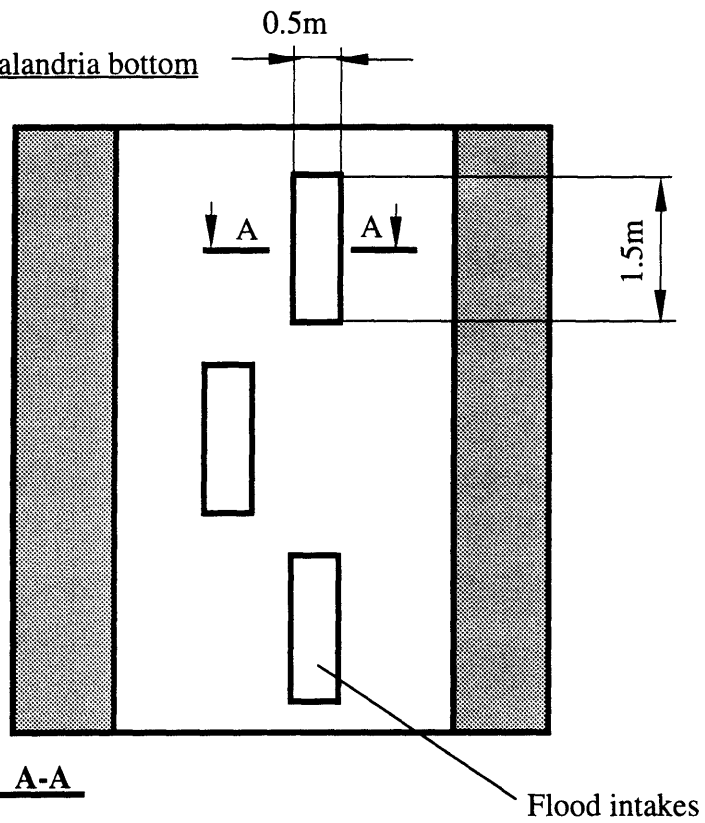


Figure 8-4 Cross section of calandria with passages for flood water intake and gas relief

Top view of the calandria



Top view of calandria bottom



A-A

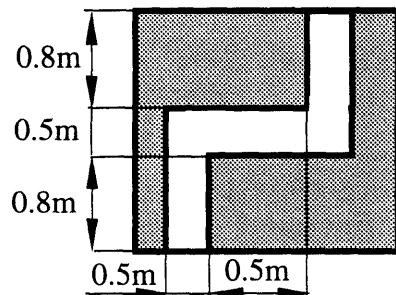


Figure 8-5 Main dimensions of flood water and gas release passages

graphite reflector with the proposed arrangement of the passages for the intakes of flooding water and gas exhausts.

The layout of the passages for flooding water and gas exhaust, with main dimensions, is shown in Figure 8-5. There are three openings at the bottom of the reflector through which the flooding water is brought into the calandria. The thickness of the reflector at the bottom is extended downward to compensate for the decrease of reflector thickness due to the space needed for the passage. During normal operation, flooding water is kept below the reflector bottom as shown in Figure 8-4. Four pressure relief pipes which penetrate through the shield tank and concrete vault are equipped with valves located outside the calandria vault. Figure 8-4 shows only the acting piston and sealing disc of the valve; the rest of the passive valve was fully described in the previous section. Flooding is initiated by opening of these valves. In addition, safety valves (not shown) are installed to prevent calandria overpressurization in case of a pressure tube rupture accident.

8.4 FLOODING ANALYSIS

The adiabatic heat up analysis of the PTLWR fuel channel in Chapter 7 has suggested that the pressure tube temperature is the first component to reach its reusability design limit of 500°C. To prevent pressure tubes from exceeding this limit in LOCA accidents, the calandria flooding system needs to be designed to provide sufficiently fast flooding. The key parameter of interest in the calandria flooding process is the time at which the top row of fuel channels can be flooded. To evaluate this flooding time, a simplified flooding model has been developed. This model and the discussion of the results obtained from the model are the subject of this section.

8.4.1 The Simplified Flooding Model

The following assumptions have been introduced:

- *Constant temperature of gas in the calandria during the entire transient.* The exact solution of pressure in the calandria as a function of time would require application of the energy equation to

the gas space. Since the gas space contains a mixture of gas and vapor which escapes from the pool, the energy equation would have to be written for a two-component mixture. This leads to rather complicated formulations which are not desirable to implement at this preliminary stage of investigation. Instead a simplified approach is used which omits treatment of the energy equation in the gas space and includes only the mass conservation equation for the gas-vapor mixture. This simplification is satisfactory, since the pressure has a marginal effect on the process of calandria flooding, i.e., only during the first second following the valve opening.

- *No density change due to voids in the water in the calandria is introduced into the buoyancy term of the momentum equation.* Although an exact treatment would require calculation of void distribution along the vertical coordinate, this is a conservative assumption since the reduced pool density in the calandria (due to voids) will increase the driving force for water flow and speed up the flooding process.
- *Pressure drop across the tube bundle is treated as for one-phase flow.* Although the presence of bubbles in the water increases the pressure drop, which would conversely decrease the water flow rate, the results will show that the pressure drop across all pressure tubes, is by several orders of magnitude, less than the inlet pressure losses. Hence including a two-phase multiplier in the pressure loss term has no visible effect on the final results.
- *A prescribed fraction, $(1-f_{steam})$, of decay heat is assumed to contribute to the pool heatup while the rest of the decay heat, f_{steam} , is assumed to generate vapor which is assumed to be released instantly into the upper space.* Because the pool remains strongly subcooled during the reflooding process, most of the vapor will condense inside the pool. Two cases are investigated: the case where all decay heat contributes to steam generation ($f_{steam}=1$) and the case where 70% of decay heat is transferred into the pool ($f_{steam}=0.3$).

A schematic of the flooding model is shown in Figure 8-6. There are four sections with different constant flow areas – section #1 of height H, section #2 representing the horizontal passage, section #3 between the

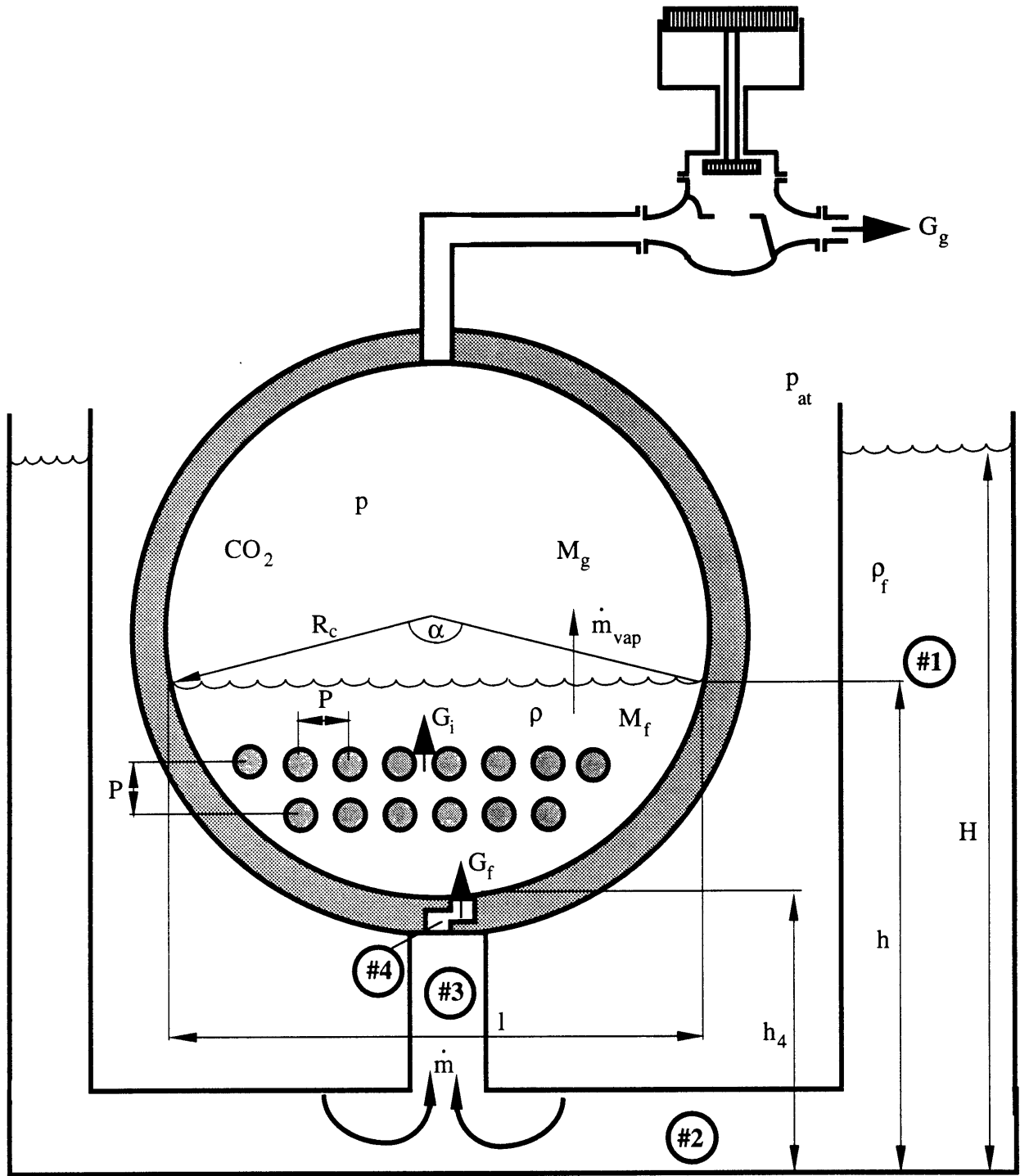


Figure 8-6 Computational schematic of calandria flooding with nomenclature

horizontal passage and the reflector, and section #4 which represents the passage through the reflector. The calandria space has a variable flow area and is treated separately. Using the postulated assumptions the behavior of the medium in the calandria space can be described by a set of conservation equations as follows:

mass conservation for the lower, flooded space

$$\frac{dM_f}{d\tau} = \dot{m} - \dot{m}_{\text{vap}} \quad (8-2)$$

with initial condition $M_f(\tau=0)=0$, mass conservation for the upper, gas space

$$\frac{dM_g}{d\tau} = -G_g A_g + \dot{m}_{\text{vap}} \quad (8-3)$$

with initial condition $M_g(\tau=0)=(V p_0 M_{\text{CO}_2})/(R T_{g0})$, and the simplified energy conservation equation for the flooded space

$$\frac{d(M_f h)}{d\tau} = \dot{Q}_{\text{flood}} + G_f A_f h_{\text{in}} \quad (8-4)$$

which can be rewritten for subcooled liquid in terms of temperatures

$$\frac{dT}{d\tau} = \frac{1}{M_f c} (\dot{Q}_{\text{flood}} + G_f A_f (T_{\text{in}} - T)) \quad (8-5)$$

with initial condition $T(\tau=0)=T_0$. Heat transferred from the fuel channels into liquid, \dot{Q}_{flood} , is computed as

$$\dot{Q}_{\text{flood}} = \frac{\dot{Q}_{\text{wall}} (1 - f_{\text{steam}})}{N_{\text{tubes}}} \sum_{i=1}^{N_{\text{rows}}} N_i \quad (8-6)$$

where N_{rows} is the number of submerged rows and N_i is the number of tubes in the i -th submerged row. The fraction $1 - f_{\text{steam}}$ is the prescribed fraction of decay heat which contributes to pool heat up. \dot{Q}_{wall} is the heat rate transferred from the hot walls. It includes both the decay heat and the stored energy released from the fuel channels. The mass flow rate of the steam generated by this heat rate is thus

$$\dot{m}_{\text{vap}} = \frac{\dot{Q}_{\text{wall}} f_{\text{steam}}}{h_{\text{fg}} N_{\text{tubes}}} \sum_{i=1}^{N_{\text{rows}}} N_i \quad (8-7)$$

The mass flow rate of flooding water is calculated from the momentum equation

$$\frac{1}{A} \frac{\partial \dot{m}}{\partial \tau} + \frac{1}{A} \frac{\partial \dot{m}v}{\partial s} = - \frac{\partial p}{\partial s} - \left(K + \frac{f}{D_e} \right) \frac{\rho v^2}{2} - \rho g \sin \beta \quad (8-8)$$

where v is velocity. Eq. (8-8) can be written after integration along the path coordinate, s , as

$$\frac{d\dot{m}}{d\tau} = \frac{\left[P_{\text{at}} - p - \frac{\dot{m}^2}{2} \left(\frac{1}{\rho_N A_N^2} - \frac{1}{\rho_1 A_1^2} \right) - \dot{m} \left| \dot{m} \sum_{i=1}^N \left(K_i + f_i \frac{l_i}{D_{ei}} \right) \frac{1}{2\rho_i A_i^2} + g \sum_{i=1}^N \rho_i \Delta h_i \right. \right]}{\sum_{i=1}^N \frac{l_i}{A_i}} \quad (8-9)$$

with initial condition $\dot{m}(\tau=0)=0$, where N is the number of sections (along the path counted from section #1 at the location of the water level in the containment up to the current location of the tracked water level) with different constant flow areas, A_i ; K_i is the total form loss in the i -th section and f_i is the friction factor in the i -th section.

The friction factor is calculated using Idelchik's relation [Idelchik, 1896]. Inside the calandria, pressure losses across the tube rows are calculated using the pressure drop relation for horizontal bundles with equal vertical and horizontal spacing

$$\Delta p_{\text{loss-rows}} = 0.96 \left(\frac{D_{\text{ev}}}{P} \right)^{0.4} \frac{P}{D_{\text{ev}} \rho(p,T)} \sum_{j=1}^{N_{\text{rows}}} \frac{G_j^2}{\text{Re}_j^{0.145}} \quad (8-10)$$

where

$$\text{Re}_j = \frac{G_j^2 D_{\text{ev}}}{\mu(T, \rho)}, \quad D_{\text{ev}} = \frac{P^2 - \pi R_{\text{CT}}^2}{2 \pi R_{\text{CT}}}, \quad (8-11,12)$$

and the number of submerged rows is

$$N_{\text{rows}} = (h-h_4) / P. \quad (8-13)$$

The mass flux through the j-th row of calandria tubes (CT) is given as

$$G_j = G_f \frac{S_f}{S_j}, \quad (8-14)$$

and the flow area of all gaps in the j-th row is given as

$$S_j = (P - 2 R_{CT}) L_c N_j + [l_j - (N_j - 1) P - 2 R_{CT}] L_c, \quad (8-15)$$

where N_j is the number of tubes in the j-th row and l_j is obtained from geometrical relations

$$l_j = 2 R_c \sin (\alpha_j/2) ; \alpha_j/2 = \arccos (1-h_j/R_c). \quad (8-16,17)$$

The distance of the j-th row from the bottom, h_j , is calculated as a multiple of channel pitch, P , i.e., $h_j = (j)(P)$.

The height of the water level in the containment, H , is calculated from the ordinary differential equation

$$\frac{dH}{d\tau} = - \frac{\dot{m}}{A_1 \rho_f} \quad (8-18)$$

with initial condition $H(\tau=0)=H_0$. If the flooded water level, h , is below the calandria bottom it is calculated from the equation

$$\frac{dh}{d\tau} = + \frac{\dot{m}}{A_i \rho_f} \quad (8-19)$$

with initial condition $h(\tau=0)=h_0$. A_i is the flow area at the location of the current water level. Once the flooded water level reaches the calandria bottom, it is computed from geometrical relations. First the volume occupied by water,

$$V_f = V_{bot} + \frac{(M_f - V_{bot} \rho_f)}{\rho(p,T)}, \quad (8-20)$$

is obtained, where V_{bot} is the volume below the bottom of the calandria which has been flooded since the time flooding has been initiated. Volume V_f is then corrected by the density of calandria tubes

$$\text{Dens}_{\text{CT}} = \frac{\pi R_c^2}{N_{\text{tubes}} \pi R_{\text{CT}}^2} \quad (8-21)$$

$$\text{as } V_{\text{filled}} = V_f (1 + \text{Dens}_{\text{CT}}). \quad (8-22)$$

Water volume, V_{filled} , from Eq. (8-22) can be used in a geometrical relation for angle α

$$\alpha = 2V_{\text{filled}} / (L_c R_c^2) + \sin\alpha \quad (8-23)$$

where L_c is the length of the calandria, and V_{filled}/L_c is the cross sectional area of the lower calandria space filled by water. Eq. (8-23) is solved for angle α iteratively. Finally, the water level is calculated using the relation

$$h = h_4 + R_c [1 - \cos(\alpha/2)] \quad (8-24)$$

Gas mass flux from the calandria is calculated from a quasi-steady flow equation through the valve using isentropic expansion of an ideal gas:

$$G_g = 0.9 \rho_g \sqrt{2 \frac{\gamma}{\gamma-1} \frac{P}{\rho_g} (\varepsilon^{2/\gamma} - \varepsilon^{(\gamma+1)/\gamma})} \quad (8-25)$$

where $\varepsilon = p_{\text{at}}/p$ is the pressure ratio and $\gamma = c_p/c_v$ is the isentropic expansion coefficient. The coefficient 0.9 in Eq. (8-25) represents losses. If the pressure ratio is less than the critical ratio, the critical pressure ratio

$$\varepsilon = \left(\frac{2}{\gamma+1} \right)^{\gamma/(\gamma-1)} \quad (8-26)$$

is substituted into Eq. (8-25) to obtain critical flow. Note that the properties of the gas/steam mixture are assumed to be equal to those of CO_2 since, during the flooding process, steam content in the upper space is small (see Section 8.4.2).

The remaining closure relations can be written as follows:

volume of the gas space

$$\begin{aligned} V_g &= V - M_f/\rho_f && \text{for } h < h_4 \\ V_g &= V - V_{\text{bot}} + \frac{(M_f - V_{\text{bot}} \rho_f)}{\rho(p,T)} && \text{for } h \geq h_4 \end{aligned} \quad (8-27,28)$$

specific volume of the gas

$$v_g = V_g/M_g, \quad (8-29)$$

and the pressure in the gas space

$$p = \frac{RT_g}{v_g M_{CO_2}}. \quad (8-30)$$

Integration of the system of ordinary differential equations (8-2), (8-3), (8-5), (8-9), (8-18), and (8-19) is performed using a the 4-th order Runge-Kutta method with automatic time step control.

8.4.2 Estimate of the Steam Amount Escaping from the Flooded Space to the Upper Gas Space

The fraction of steam released into the gas space during the flooding process can be assessed from a simple estimate of bubble condensation rate and bubble rise velocity. It can be derived from the Rayleigh-Plesset equation that in the thermally dominated regime, the vapor bubble radius in the subcooled pool decreases with time as

$$R = R_0 - \frac{2(T_b - T_\infty) \rho_l}{h_{fg} \rho_v} c_p \sqrt{\alpha_f \tau} \quad (8-31)$$

where T_∞ is the temperature of the liquid in the pool and α_f is the thermal diffusivity of the liquid. Pool temperature is changing with time due to heat-up of the pool but the change is very slow due to the large sensible heat of water and relatively low power density, hence the temperature can be treated as constant in this assessment. To estimate the initial bubble radius, the force balance between buoyancy and surface tension can be applied

$$R_0 = \frac{\sqrt{6}}{2} \sin \varphi \sqrt{\frac{\sigma}{\rho_l - \rho_v}}. \quad (8-32)$$

Eq. (8-32) yields for water properties at atmospheric pressure and for assumed wetting angle $\varphi \approx 45^\circ$ the radius $R_0 \approx 0.002\text{m}$. It can be assumed that the vapor inside the bubble typically overheats 10°C above saturation before

it detaches, i.e., $T_b=110^\circ\text{C}$. Using this value, a pool temperature of $T_\infty=40^\circ\text{C}$, $R_0=0.002\text{m}$, and the properties of water at atmospheric pressure, Eq. (8-31) gives the time to bubble collapse (i.e., when $R=0$) of about

$$\tau_{\text{col}}=2 \times 10^{-4} \text{ s.}$$

Since the bubble rise velocity is

$$u_b \cong 0.71 \sqrt{g \cdot 2 R_0 \frac{\rho_l - \rho_g}{\rho_l}} = 0.15 \text{ m/s}$$

it is evident that the bubble, once it is detached, will be able to travel only a very short distance (less than 1mm) before it collapses. Deep subcooling of the pool during the reflooding process is the main reason for such fast bubble collapse. Hence the vapor fraction which escapes the pool into the upper gas space will be very small during the reflooding process (only from the upper tube row which is in contact with the water free surface). The largest steam escape rate can be estimated at the time when the water level reaches the center of the calandria, i.e., the water surface is in contact with the highest number of hot fuel channels. At this time the number of bubble sites on hot tubes near the surface can be estimated (using the surface of tubes up to 4 mm below water level and the bubble detachment radius of 2mm) to be about 1.2×10^5 . Using the typical bubble detachment frequency of 30 detachments/second [Collier, 1981], the number of vapor bubbles escaping into the upper calandria space can be estimated as 3.4×10^6 bubbles/second, which yields about 0.12 m^3 of vapor per second. This compares to the gas volume of the upper calandria space of 160 m^3 (one half of the total calandria free volume). Hence the contribution of the steam in the gas space is negligible and the gas space can be treated as pure gas.

8.4.3 Discussion of the Results

Three cases were considered. Case #1 is a hypothetical case, which assumes that all the heat from the hot fuel channels generates vapor bubbles which all escape to the gas space ($f_{\text{steam}}=1$). Case #2 assumes a partial steam escape of 30% from the lower flooded space, i.e., $f_{\text{steam}}=0.3$.

Case #3 investigates the impact of the failure of the two valves to open at the flooding time.

The results for the first case are presented in Figures 8-7 through 8-10. Figure 8-7 shows the water level in the calandria, h , and in the containment, H , as a function of time. It can be seen that flooding of the top row of fuel channels is achieved in about 24 seconds. This time scale compares very favorably with the fuel heat up time scale, where the fuel matrix can withstand an adiabatic heat up from decay heat for hundreds of seconds without exceeding allowed temperature limits. It is also three times less than the time when the maximum pressure tube temperature reaches the limit of 500°C , in an adiabatic heat-up scenario. Figure 8-8 shows inertial water level oscillations on an expanded scale. The oscillations decay with time and do not result in transitional uncover of the top row. The difference between the containment water level and the calandria water level is due to the pressure difference needed to force the steam flow through the valve and associated piping.

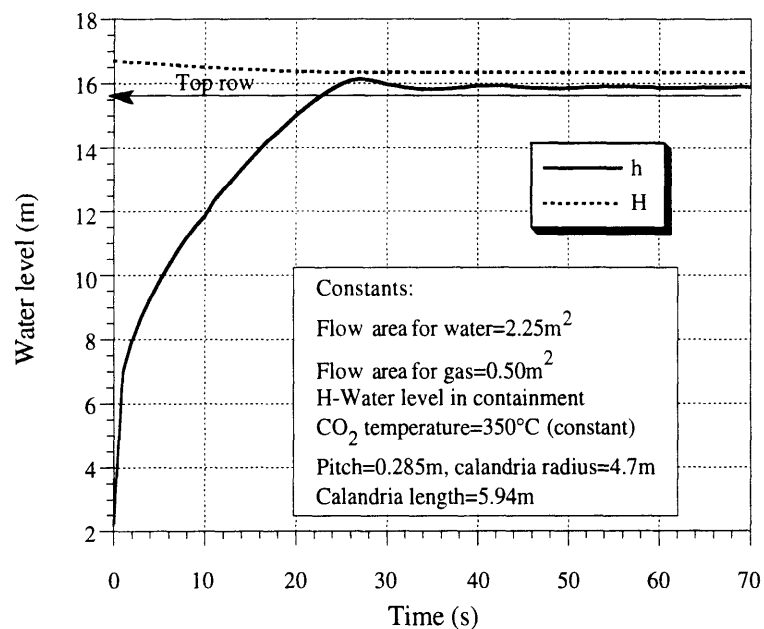


Figure 8-7 Water level for calandria flooding Case #1

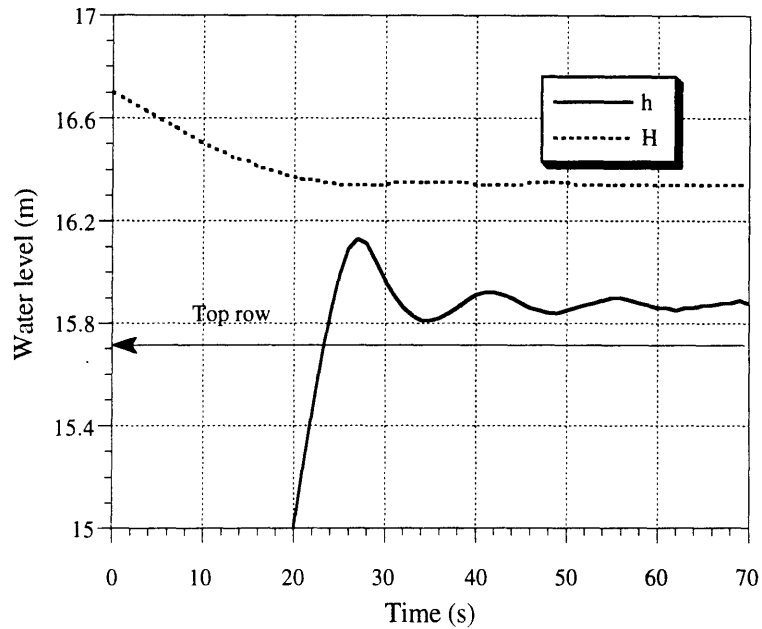


Figure 8-8 Water level oscillations for calandria flooding Case #1

Figure 8-9 plots the sum of friction, form and acceleration terms of pressure losses in the inlet sections, i.e. sections #1, #2, and #3, (Δp -inlet) and inside the calandria (Δp -cal). Most of the pressure loss occurs at inlet sections; friction and form pressure losses on the tube rows, which are not plotted separately in Figure 8-9, are negligible (lower by 4 orders of magnitude). Hence, even in case of severe vapor blanketing on the tubes, which would result in increased pressure losses on tube rows, the effect on the final result would be negligible. An interesting feature is a large pressure gain inside the calandria due to the acceleration term. The acceleration term is the dominating pressure term inside the calandria and contributes to the speedup of the flooding process. Figure 8-10 shows the mass flow rate of flooding water and calandria pressure (in the gas space) as a function of time. It is evident that the depressurization is very fast and after about one second the pressure in the calandria does not affect the flooding process. Hence the simplification in the treatment of the dynamics of the gas-vapor space by omitting the energy equation did not introduce significant errors in flooding time.

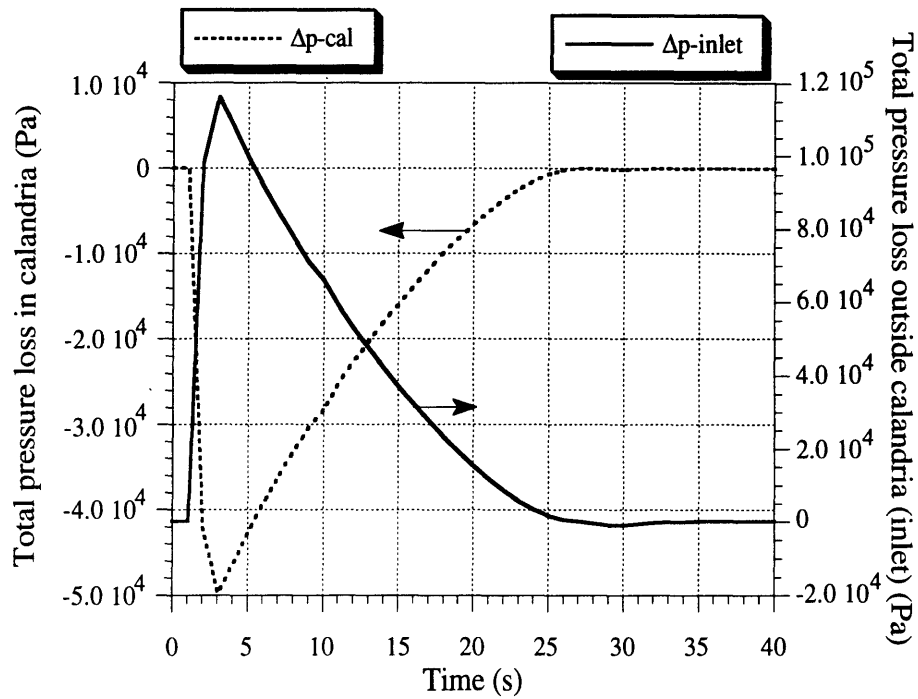


Figure 8-9 Inlet and in-calandria pressure losses for calandria flooding
Case #1

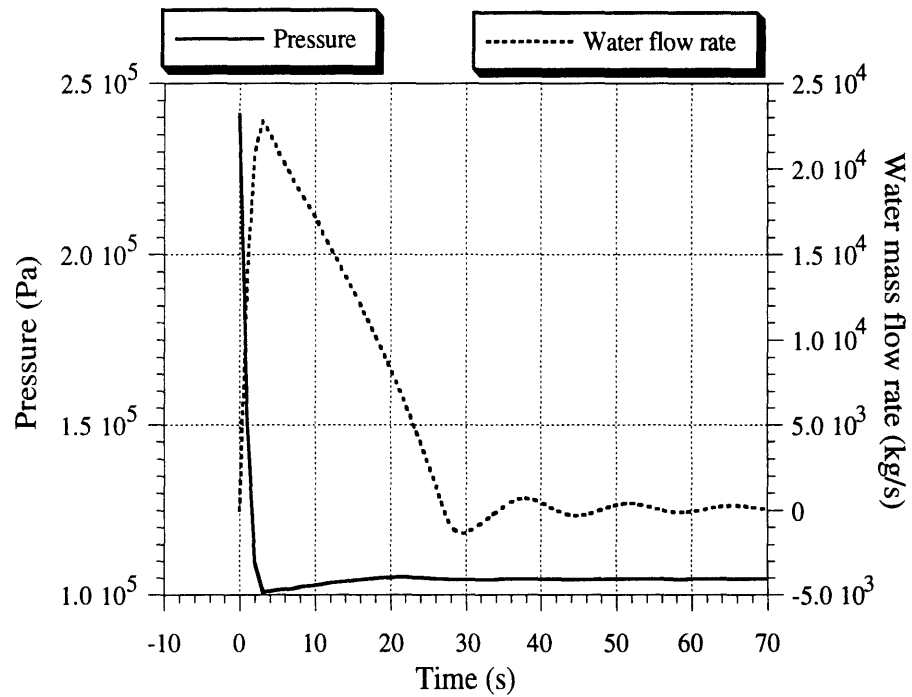


Figure 8-10 Calandria pressure and water flow rate for calandria flooding
Case #1

The results for Case #2 are summarized on Figures 8-11 through 8-13. Figure 8-11 shows that the water level covers the top tube row in 23 seconds, which is only 1 second faster than for the first case. Hence, the potential steam release into the gas space does not affect significantly the flooding time. However, since the steam flow rate from the calandria is very small, the water level reaches a higher level and can even get into the gas release pipes as the first oscillating peak suggests. In the long term, the water temperature will reach saturation level and all the steam generated inside the pool will be released through the valve as in Case #1. This will lead to a water level decrease due to the higher pressure in the upper calandria space. On the other hand, the lower density of the saturated water will tend to increase the water level. An additional factor which needs to be taken into account in the long term is sufficient condensate return rate into the containment pool to maintain the water level in the containment pool sufficiently high. These issues will be addressed in Chapter 11.

Figure 8-12 plots the water flow rate and gas pressure as a function of time and Figure 8-13 shows the time dependence of bulk liquid temperature in the flooded space. It can be seen that the liquid during the entire phase of flooding remains deeply subcooled and the temperature increase rate is very small. This is due to the large sensible heat of the flood water and relatively low power density.

Figure 8-14 compares the flooding curve for Case #3 which assumes the failure of two valves to open, with the flooding curve from Case #2. Both curves were calculated for 30% steam release into the upper gas space. It can be observed that the failure of two valves to open extends the flooding time by about 10 seconds – to completion at 33 seconds. This increase in flooding time is insignificant and there is still plenty of time left before the pressure tube would reach the limit of 500°C.

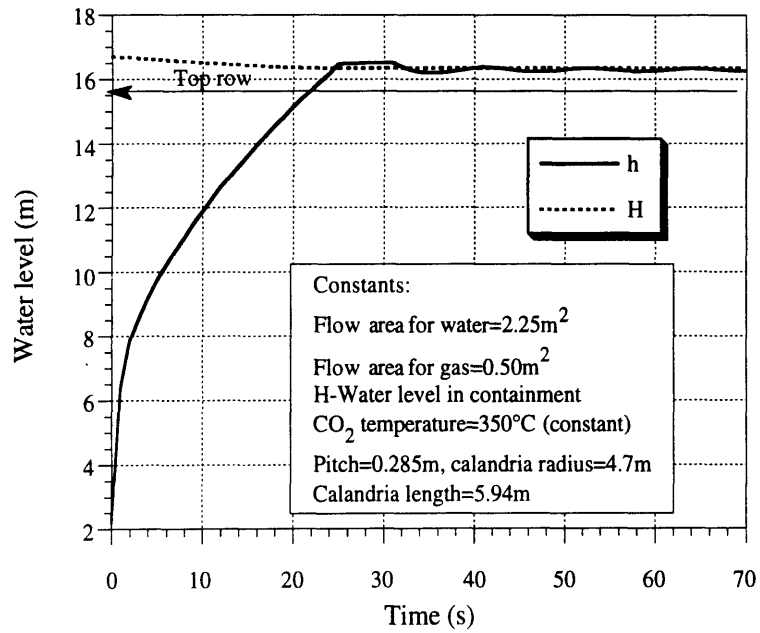


Figure 8-11 Water level for calandria flooding Case #2

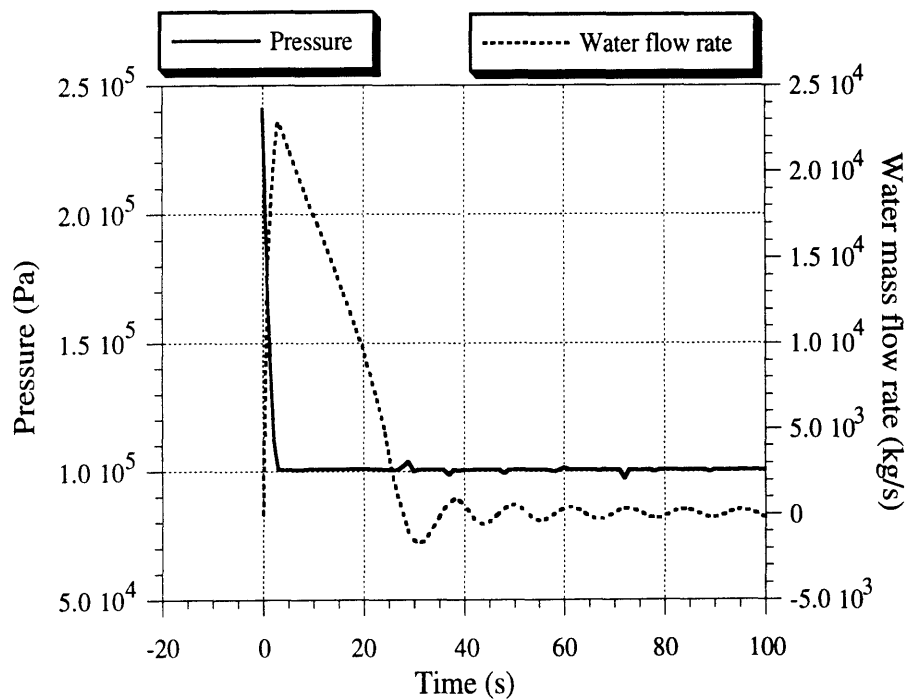


Figure 8-12 Calandria pressure and water flow rate for calandria flooding Case #2

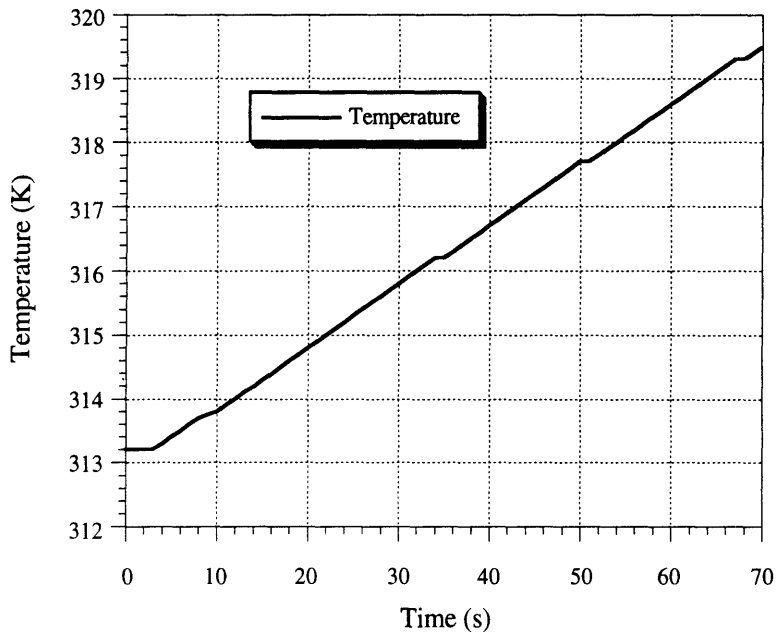


Figure 8-13 Liquid bulk temperature in calandria for flooding Case #2

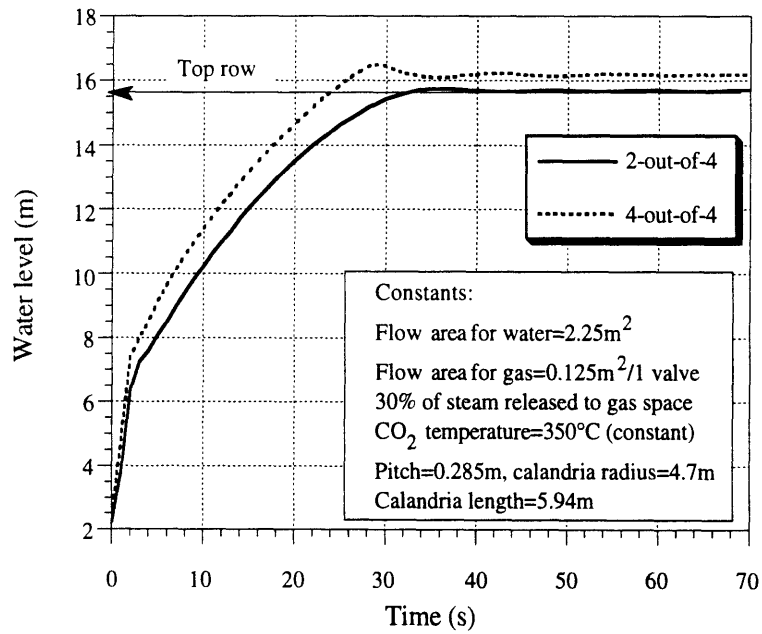


Figure 8-14 Calandria flooding curves for 4-out-of-4 and 2-out-of-4 valves opened.

8.5 SUMMARY

The PTLWR concept requires flooding of the calandria space during accidents. The flooding process is passive, driven by the gravity head. The difference with typical LWRs lies in the separation of the primary system from the low pressure heat sink. While LWRs need to depressurize the primary system to deliver a low pressure coolant inventory into the core, the passive flooding in the PTLWR is done always at low pressure, close to atmospheric, and does not require primary system depressurization. This eliminates the large dynamic forces exerted upon the piping during depressurization and allows simpler design of the flooding initiation devices.

Two schemes for flooding initiation have been proposed. The first scheme involves a dc-powered blower which maintains the gas pressure in the calandria during normal operation and releases the pressure by switching off the blower upon electronic signals from primary system sensors. The second scheme employs a fluid-operated valve, working from primary system pressure. The valve relies only on stored energy and the signal is transferred directly by the primary system fluid. The latter scheme has been adopted for the PTLWR reference design.

A simplified model for the analysis of the passive flooding process has been developed. The analysis shows that the calandria can be flooded in about 24 seconds if all four valves open and in 33 seconds if 2-out-of-4 valves fail to open. This is a sufficiently rapid process taking into account that the adiabatic heat up (from decay heat) of the fuel matrix to its limiting temperature (1300°C) takes hundreds of seconds, and heat up of pressure tubes to their limiting temperature of 500°C takes about 70 seconds.

Chapter 9

FUEL CHANNEL CONSIDERATIONS UNDER PERFORMANCE-LIMITING CONDITIONS

9.1 INTRODUCTION

It has been shown in Chapter 2 that the postulated goal of passive decay heat dissipation from the fuel in the absence of primary coolant can be most effectively achieved through fuel modularity, which is best accommodated in a practical design by using fueled pressure tubes, where the pressure tube constitutes the pressure boundary. The advantage of pressure tubes over a massive thick-walled pressure vessel is that their individual failure can be tolerated as a design basis, and they can be replaced if they are damaged. Their drawback is that they are subjected to high stress and full neutron flux, which poses a challenge to their design. The PTLWR fuel channels use the same material in a very similar configuration to those in CANDU units. Significant experience with operation of CANDU fuel channels has been accumulated over a period of about 30 years. However, the fuel channels of the PTLWR reference design operate at higher primary coolant pressure and temperature and higher fast neutron flux. The effects of these parameters on fuel channel performance will be the subject of this Chapter.

Section 9.2 gives a brief description of the fuel channel, and Section 9.3 discusses the key parameters affecting the channel lifetime and channel behavior during plant lifetime. A significant difference between the CANDU fuel channels and the PTLWR channels is the latter's high operating calandria tube temperature, and calandria tube quenching upon flooding. Thermal stresses arising during flooding are addressed in Section 9.4. Section 9.5 presents an analysis of stress in the pressure tube during flooding.

9.2 FUEL CHANNEL DESCRIPTION

The fuel channel design adopted for the PTLWR concept is in essence, the channel used in CANDU reactors. The main reason for this choice is the goal to use proven technology. Substantial operating experience with CANDU fuel channels has been accumulated since the 1960s; moreover considerable attention is being directed at AECL towards extending channel lifetime and improved performance. New advances in this area can be directly incorporated into the PTLWR fuel channels. The CANDU fuel channel consists of [Brooks and Price, 1988]

- pressure tube,
- calandria tube,
- annulus spacers, and
- end fittings.

As in CANDU reactors, the PTLWR pressure tube holds the fuel element and withstands pressure loads under high temperature and fuel weight. The material for pressure tubes used in later CANDU plants is Zr-2.5% Nb. Since the pressure tube is exposed to both high pressure and high fast neutron flux, it is the component which controls the life of the fuel channel.

The purpose of the calandria tube* in the present design is to protect the pressure tube from excessive thermal shock during calandria flooding with cold water. This purpose is quite different from that of a CANDU design, where the calandria tube isolates the pressure tube from cold moderator during normal operation. Calandria tubes are made of Zircaloy-2 and connected to calandria tube sheets by rolled joints. Rolled joints proved to be an effective leak-tight joint of zirconium alloy to ferritic stainless steel, which has about twice as large a thermal expansion coefficient as Zircaloy-2. In the dry calandria design, the calandria tube operates at high

* A more appropriate name for the thin-walled tube surrounding the pressure tube in the PTLWR application would be "protective tube", nevertheless the designation "calandria tube" is retained to preserve continuity with CANDU terminology.

temperature and is occasionally cooled down during flooding, while in CANDU units calandria tubes are kept at low temperatures at all times. Hence, some design modification of calandria tube joints may be necessary to allow for thermal contraction during flooding.

Spacers in the gap between the pressure tube and calandria tube maintain separation between tubes. In CANDUs, this separation is important to minimize heat loss to cold moderator and to prevent temperature gradients in the pressure tube, which are the cause of increased concentration of zirconium hydride and the consequent delayed hydride cracking. In the PTLWR concept, maintenance of perfect separation is not such a concern during normal operation since there are no heat losses to the moderator and both tubes operate at high temperatures, hence no significant thermal gradients in the pressure tube can develop. As mentioned in Chapter 2, the detailed design of the gap for the PTLWR fuel channel remains to be finalized. A narrow gap filled with a packed bed of zirconia spheres and CO₂ gas is envisaged.

The purpose of end fittings is the same as in CANDU reactors. They are made of martensitic stainless steel and provide a transition between Zr-2.5% Nb pressure tubes and the carbon-steel feeder piping. It also ensures the capability of on-line refueling. End fittings, including the closure seals and feeder connections are also under primary system pressure, however, they are exposed to lower neutron flux than pressure tubes, and hence they do not control fuel channel lifetime.

9.3 FUEL CHANNEL CHALLENGES AND CANDU EXPERIENCE

The life of a fuel channel is determined by the lifetime of the pressure tube since it is exposed simultaneously to high pressure and high neutron flux. Pressure tube lifetime as the controlling factor for the life of a fuel channel has been confirmed by Canadian experience [Brooks and Price, 1988]. Therefore, the discussion in this section will be focused on pressure tubes.

9.3.1 Comparison of Key Conditions Affecting Pressure Tube Lifetime

The main conditions having a negative effect on pressure tubes are operating temperature, operating pressure and fast neutron flux. Primary coolant chemistry is also important but this can be, generally, adjusted to meet the required criteria. Comparison of these conditions for a typical CANDU reactor and the PTLWR reference design is given in Table 9-1.

Table 9-1 Operating conditions for CANDU and PTLWR pressure tubes

Condition	CANDU	PTLWR
Pressure (MPa)	10	15
Outlet Coolant Temperature (°C)	300	339
Core-average fast flux, E >1MeV (n/s-cm ²)	1.97x10 ¹³	6.5x10 ¹³
Coolant/chemistry	D ₂ O/reducing	H ₂ O/reducing

Higher pressure and temperature for the dry calandria design are dictated by the higher secondary system pressure selected. The choice of secondary system pressure was driven by the desire to achieve plant efficiency comparable to current PWRs. Although the coolant of the PTLWR design is different from that of CANDU, both coolants contain hydrogen and both use reducing chemistry, i.e., an excess of hydrogen to suppress oxygen.

The average CANDU fast flux in Table 9-1 was calculated using an MCNP model of a CANDU cell. It is evident that the average fast flux on the PTLWR pressure tubes is considerably higher than the average fast flux on CANDU pressure tubes. Because of the lower fast-flux peaking, the difference between the peak values of PTLWR and CANDU fast flux on pressure tubes is less, nevertheless still significant. This fact can be observed in Figure 9-1, which compares the axial fast flux profile on the pressure tube along the high-power channel in BRUCE B station [Gendron et. al., 1992] and the fast flux profile on a pressure tube for the PTLWR

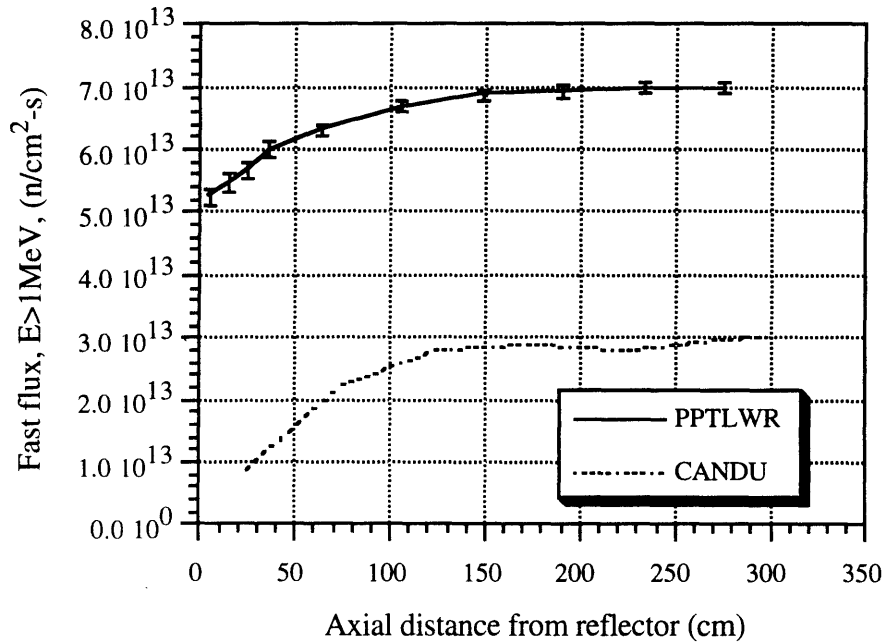


Figure 9-1 Axial profile of the fast flux on the high-power pressure tube

Table 9-2 Fluence comparison between CANDU and dry calandria

Reactor	Average fast flux, E>1MeV	Tube average fluence after 30 years (assumed capacity factor 0.8)	Fluence ratio
	(n/s-cm ²)	(n/cm ²)	$\frac{\text{PTLWR}}{\text{CANDU}}$
CANDU (reported)	-	1.5x10 ²² [Price,1984]	-
CANDU (calculated)	1.97x10 ¹³	1.5x10 ²²	-
PTLWR	6.5x10 ¹³	5.68x10 ²²	3.2

design. The fast flux on the PTLWR pressure tube was obtained from an MCNP model for an equilibrium core. Fluences resulting from the average fast fluxes in Table 9-1 are shown in Table 9-2. Note the excellent agreement between the reported fluence value and MCNP results for CANDU. The effect of higher fluence, as well as of other parameters will be discussed next.

9.3.2 Effects of Elevated Fast Neutron Flux

As shown above, the pressure tubes of the PTLWR reference design are exposed to substantially higher fast flux, i.e., 3 times higher than the CANDU pressure tubes. The reasons for high absolute fast flux levels were discussed in Chapter 4. High flux is the consequence of the low heavy metal loading achievable with particle fuel and is the major drawback of the dry calandria design. Fast flux affects the life of pressure tubes primarily through [Brooks and Price,1988]

- changes in dimensions, and
- changes in properties.

9.3.2.1 Dimensional Changes

Dimensional changes from fast irradiation are manifested by

- axial elongation,
- diametral growth, and
- tube sagging.

The rate of axial elongation is linear with fast neutron fluence and is independent of the tube pressure. Channel elongation is typically accommodated in CANDU reactors by bearing travel allowance [Brooks and Price,1988]. The higher fast neutron flux in the PTLWR concept will require a larger travel allowance. Nevertheless, it is not anticipated under these conditions that the fuel channel life could reach the desired power plant lifetime of 60 years, projected for advanced LWR plants. Therefore, one replacement of fuel channels per plant lifetime would be necessary. As of

1992, over 100 individual fuel channels have been replaced in CANDU reactors, so some experience with channel replacement is available. Large-scale retubing has also been performed to replace all fuel channels in the Pickering units. However, the retubing required a long shutdown (about 20 months to replace 390 channels) because the channels were not designed with anticipation of large-scale retubing, and because the retubing was done for the first time without extensive experience in this procedure. The CANDU 3 fuel channel program, which is in the detailed design phase, is focused on high-power channels and has the capability of quick replacement of each fuel channel. This fast and easy replaceability is achieved by employing a single-ended refueling scheme and integral design of the pressure tube and calandria tube into a single module which can be removed and installed as a unit into its lattice position [Brooks and Price,1988]. AECL fuel channel experts project the period needed to retube the entire CANDU 3 core to be about 3 months. The PTLWR concept would require employment of these integral channel designs, currently being developed at AECL, to allow for fast replacement of fuel channels and thereby reduce the cost of the associated outage.

Diametral expansion occurs primarily from irradiation-enhanced creep due to the hoop stress at high temperatures. The diametral (transverse) creep rate per hour, of pressure tubes operating in the range of conditions in CANDU reactors is given by [Evans et. al., 1971]

$$\dot{\epsilon}_t = K \sigma_t \phi (T-160). \quad (9-1)$$

where

$K=5.8 \times 10^{-25}$ for cold worked Zircaloy-2.

$K=2.1 \times 10^{-25}$ for cold worked Zr-2.5%Nb.

$K=3.2 \times 10^{-25}$ for heat treated Zr-2.5%Nb.

The above expression is valid for transverse stress $60 \text{ Mpa} \leq \sigma_t \leq 200 \text{ MPa}$, fast neutron flux $10^{13} \text{ n/cm}^2\text{-s} \leq \phi \leq 3.5 \times 10^{13} \text{ n/cm}^2\text{-s}$ ($E > 1 \text{ MeV}$) and temperatures $250 \text{ }^\circ\text{C} \leq T \leq 300 \text{ }^\circ\text{C}$.

Since the tube thickness is increased for the present conceptual design to accommodate higher pressure, the hoop stress in the tube will be about the same as for CANDU reactors. However, as can be seen from equation (9-1), the slightly higher proposed coolant temperature will lead to an increased radial creep rate. A more significant factor than the temperature is the fluence, since the increase in fast flux results in a larger contribution to creep rate than the proposed increase in operating temperature. Note that the fast flux and operating temperature of the dry calandria design exceed the verified validity range of Eq. (9-1), hence verification of an extended correlation would be necessary. Nevertheless, the trend with temperature and fluence is expected to be preserved for these higher parameters. The expansion is linearly proportional to the fast flux, hence higher diametral creep rates are expected than in CANDU reactors. The maximum diametral expansion rate of pressure tubes in BRUCE station are reported to be about 0.1mm per year and are not expected to limit fuel channel lifetime [Cheadle et. al., 1993]. However, the higher diametral expansion rate due to both higher temperature and higher fluence may be the most limiting factor for the lifetime of the PTLWR pressure tubes. Note that the limits of expansion in diameter in both the CANDU and the PTLWR designs are established by coolant flow considerations. An excessive gap between the bundle (or the matrix in the proposed design) and the pressure tube inner wall leads to flow depletion in the center of the channel. A more detailed investigation of the effects of these parameters and probably more research into the means to limit this growth will be necessary in the future evaluations of this concept.

Tube sagging results from irradiation-assisted creep due to bending stresses from fuel weight and primary coolant mass. Higher fast flux levels which tend to increase the tube sagging rate will be offset by the much smaller weight of the fuel matrix and the lower coolant mass in the PTLWR conceptual design compared to a CANDU fuel channel. On the other hand, the higher operating temperature of PTLWR calandria tubes will promote channel sagging, so that some support structure may be necessary.

9.3.2.2 Property Changes

Property changes associated with neutron damage are

- an increase in strength,
- a decrease of ductility,
- a decrease in fracture toughness, and
- an increased rate of oxidation.

The strengthening of the pressure tube is an advantage. The rate of increase is high at the beginning of life and saturates at higher fluence, as shown in Figure 9-2. Reduction in ductility for Zr-2.5%Nb is not large enough to be of concern [Price, 1984]. The rate of decrease is fast in early life and then it stays almost constant for higher fluence. Fracture toughness, which determines critical crack length, behaves similarly to ductility; it decreases rapidly in early life to about 50% of the as-manufactured value [Cheadle, 1989] and at a much smaller rate with increasing fluence, as shown in Figure 9-3. These data indicate that the critical crack length remains much larger than the tube thickness even for high fluences. Such large cracks are easily detected and should not pose a safety problem. Taking into consideration the trend and magnitude of change of the above properties with fluence, it is not expected that the higher fast flux of the proposed dry calandria design would lead to unacceptable property deterioration.

Irradiation enhances oxidation of Zirconium alloys if high oxygen concentration exists. Hence, reducing chemistry is proposed for this conceptual design to suppress radiolytic oxygen production, the same as for CANDUs or PWRs. For deoxygenated coolant, the thickness of the oxidation layer increases only marginally with fluence. Cold worked Zr-2.5%Nb material has much smaller oxidation rates than Zr-2. Specifically, in later stages when the oxide thickness reaches about 15 to 20 microns, the corrosion rate for Zircaloy-2 exhibits an increase, while for Zr-2.5%Nb, the growth rate of the oxide thickness remains low, i.e. the trend typical for thin oxide conditions is retained even if high oxide thickness is reached. Figure 9-4 shows the growth of the oxide layer for Zr-2.5%Nb with

time for 300°C. It would be expected that the corrosion rate doubles for every 10°C increase in operating temperature.

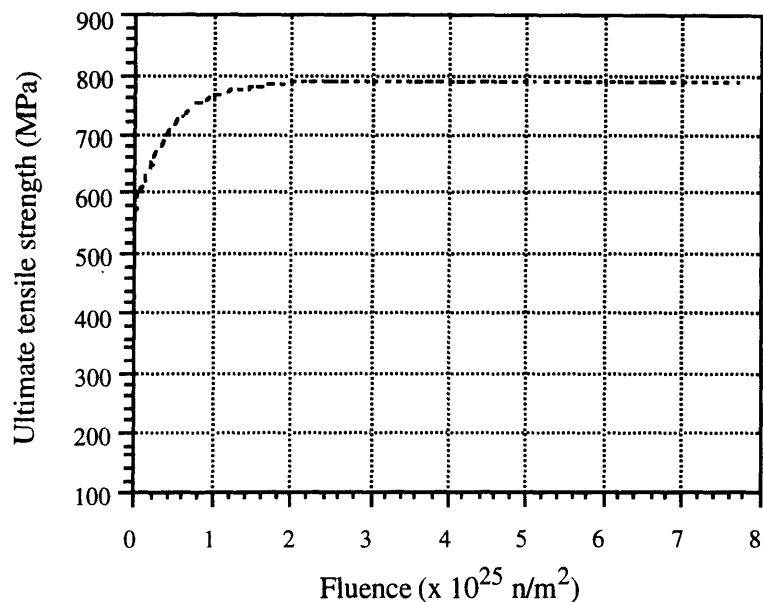


Figure 9-2 Effect of fluence on the tensile strength of Zr-2.5%Nb pressure tubes at 300°C (adapted from Cheadle, 1989)

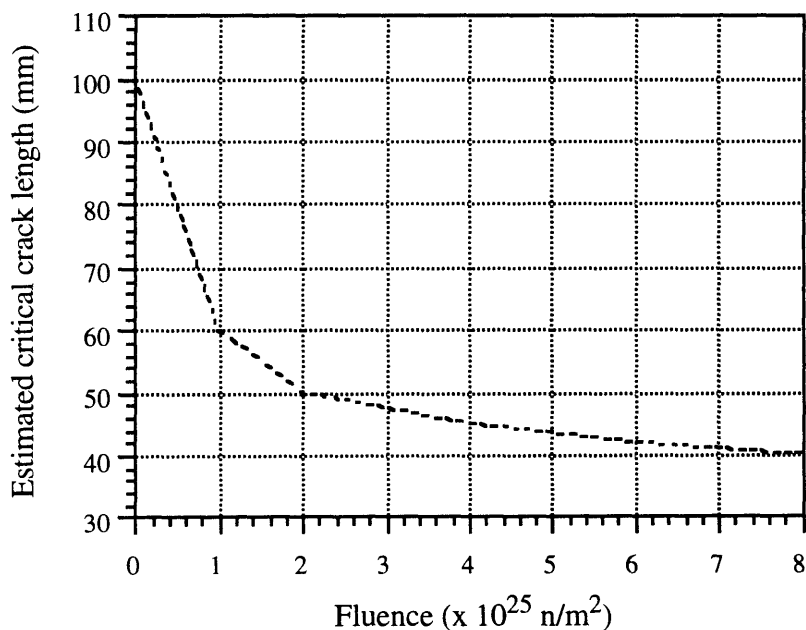


Figure 9-3 Effect of fluence on fracture toughness of Zr-2.5%Nb pressure tubes (adapted from Cheadle, 1989)

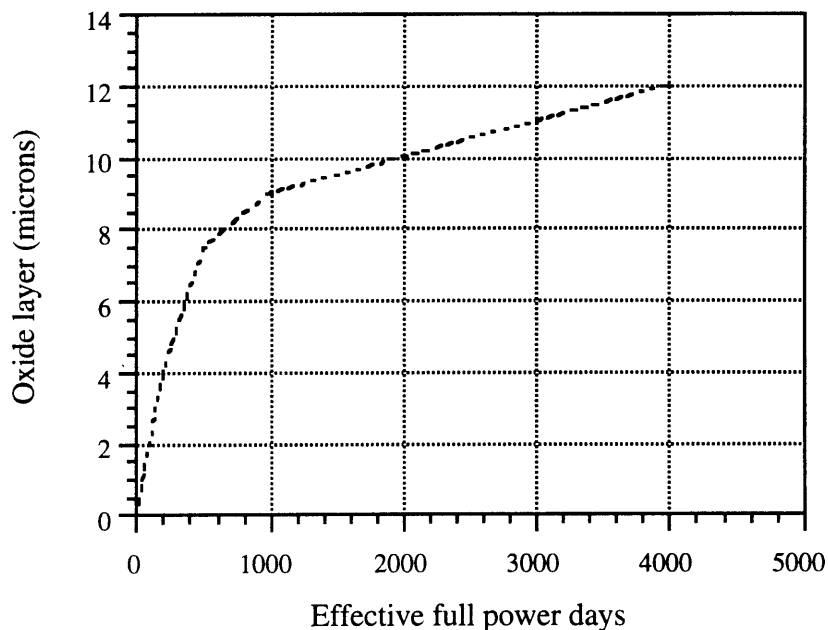


Figure 9-4 Growth of oxide layer in Zr-2.5%Nb pressure tubes
(adapted from Cheadle, 1989)

The negative consequences of high neutron flux on pressure tube lifetime are evident. Significant progress in the development of materials resistant to high neutron flux is not expected in the near future, hence the best approach to mitigate irradiation damage is to decrease the level of the neutron flux. The alternative fuel configuration in a two-ring arrangement, presented in Chapter 5, can reduce core average fast flux levels and alleviate fast fluence problems.

9.3.3 Effects of Elevated Coolant Pressure and Temperature

In addition to neutron flux, the key parameters affecting the performance of pressure tubes during normal operation are stress and temperature. To accommodate higher primary system pressure in the PTLWR, pressure tube thickness is increased. Hence the stress in the PTLWR pressure tubes is about the same as in CANDU pressure tubes, and higher coolant pressure should not have a significant effect on the pressure tubes.

Higher coolant temperature influences diametral growth. The negative consequences of higher coolant temperature on enhanced diametral growth have been discussed in Section 9.3.2, since the growth is closely related to fast neutron fluence. Elevated temperature may also increase the growth rate of the oxide layer on the pressure tube inner wall.

Another concern is the byproduct of the oxidation reaction –hydrogen – which is partially absorbed by the pressure tubes. Absorption of hydrogen in the metal of a pressure tube, also known as hydriding, depends also on the oxide thickness. In reducing water chemistry, thin oxides pick up 30 to 50% of the theoretically-evolved hydrogen for Zr-2, but only up to 5% for Zr-2.5%Nb material [Price, 1984]. For larger oxide thickness, the percentage pick-up is increased above 50% for Zr-2, while there has been no evidence of increased hydrogen pick-up for Zr-2.5%Nb tubes [Price, 1984]. Hence, it is not expected that the higher temperature of the primary coolant will produce a noticeable effect on hydrogen pick-up in the Zr-2.5%Nb tubes.

Currently, an extensive research and development effort is underway at AECL to decrease hydrogen pick-up and corrosion of CANDU pressure tubes [Cheadle, 1993]. The advances in this area could be directly applied to the PTLWR fuel channels.

9.3.4 Effects of the PTLWR Fuel Channel Design on Hydrogen and Delayed Hydride Cracking

As manufactured, pressure tubes contain typically between 5 and 15 ppm of hydrogen by weight [Price, 1984]. Solubility of hydrogen in zirconium alloys (or terminal solid solubility) is, for temperatures above 180°C, very strongly dependent on temperature. At operating temperatures, dissolved hydrogen precipitates if the hydrogen concentration builds up beyond the solubility limit. During cooling, in essence, all the hydrogen precipitates.

Hydrogen, once dissolved in zirconium, can move because of thermal, stress or hydrogen concentration gradients into certain regions and become concentrated there in the form of zirconium hydride. Among these variables, thermal gradient is the primary driving force for hydrogen

transport. If the volume of zirconium hydride exceeds the volume of parent metal in a certain location, zirconium hydride blisters, which can cause crack initiation, are formed. This gradient was the primary reason for the failure of a pressure tube in the Pickering 2 unit. Misplaced garter springs allowed the pressure tube to sag and contact the calandria tube, hence providing the thermal gradient responsible for the formation of crack-initiating zirconium hydride blisters [Hydro, 1984]. This problem is eliminated in the dry calandria design, since the calandria tube operates at high temperature – close to the temperature of the pressure tube; therefore even if these tubes are in contact, no large thermal gradients could develop. Moreover, the direction of the heat flow in the PTLWR fuel channel is from the calandria tube to the pressure tube and ultimately to the coolant. This results in a negative thermal gradient (taking the positive direction with increasing tube radius). Since hydrogen moves from hot regions to cold regions, and since most hydrogen is picked up from the coolant side, this thermal gradient, which also opposes hydrogen movement due to the concentration gradient, should prevent significant hydrogen penetration through the tube to the outer surface.

9.4 STRESS ANALYSIS OF THE PRESSURE TUBE

Flooding of the calandria by cold water results in a rapid temperature decrease of the pressure tube wall and increased thermal stresses. In a loss of coolant accident, the stress in the pressure tube from primary pressure is small since the primary pressure is lost, hence the thermal stress from flooding does not lead to excessive stresses in the pressure tube. However, if the flooding process is initiated while the pressure tubes are under operating pressure or even higher (as may be the case in a loss of normal heat sink accident), thermal stress from primary pressure is increased by the thermal stress, which could lead to unacceptable stress levels. To mitigate stress excursions in such scenarios, the pressure tube is surrounded by a protective calandria tube which absorbs the first thermal shock wave and thus protects the pressure tube. This section will evaluate the stress level in the pressure tube during such scenarios.

The following stress analysis assumes that the fuel channel undergoes LOCA while the pressure acting on the pressure tube remains at the nominal level. This hypothetical scenario was chosen because LOCA without emergency coolant delivery leads to high pressure tube temperatures, and hence, lower yield strength, and high thermal stress (a conservative approach compared to inadvertent flooding during normal operation). The analysis will be performed for the hottest pressure tube at the location of highest temperature. The analysis is one-dimensional, therefore it is assumed that the highest temperature is uniform along the entire length of the pressure tube. The thickness to radius ratio

$$t/R=5.79/64=0.09 \quad (9-2)$$

is less than 0.1, therefore the pressure tube can be treated as a thin-shell vessel. The average hoop stress, axial tensile and radial stress from primary pressure are expressed as

$$\sigma_{\phi} = \frac{R p}{t}, \sigma_z = \frac{R p}{2 t}, \text{ and } \sigma_r = -\frac{p}{2}, \quad (9-3)$$

respectively.

Introducing the auxiliary coordinate z with its origin in the middle of the wall of thickness t , and having positive direction towards the outer surface, and using for the average thermal strain the definition

$$\bar{\epsilon} = \frac{1}{t} \int_{-t/2}^{t/2} \alpha (T(z)-T_{ref}) \quad (9-4)$$

where T_{ref} is an arbitrary reference temperature and α is the thermal expansion coefficient, thermal stress can be calculated as

$$\sigma_{th} = \frac{E}{1-\nu} (\bar{\epsilon} - \epsilon(z)) = \frac{E}{1-\nu} \left[\frac{1}{t} \int_{-t/2}^{t/2} \alpha (T(z)-T_{ref}) - \epsilon(z) \right] \quad (9-5)$$

where

$$\epsilon(z) = \alpha (T(z)-T_{ref}). \quad (9-6)$$

The transient temperature profile, $T(z)$, is obtained from the numerical model of the fuel channel described in Chapter 7.

Equation (9-4) can be numerically integrated as

$$\bar{\varepsilon} = \frac{1}{t} \left[\sum_{i=1}^{N_{PT}} \alpha_i \frac{T_i + T_{i+1}}{2} h_{ri} - \alpha T_{ref} \right] \quad (9-7)$$

which yields for thermal stress

$$\sigma_{th,i} = \frac{E_i}{1-\nu} \left[\left(\sum_{i=1}^{N_{PT}} \alpha_i \frac{T_i + T_{i+1}}{2} \frac{h_{ri}}{t} \right) - \alpha_i T_i \right], \quad i=1, \dots, N_{PT} + 1 \quad (9-8)$$

where N_{PT} is the number of nodes for the pressure tube wall and h_{ri} is the thickness of the i -th node (see Figure 7-7 in Chapter 7). The temperature dependence of the coefficient of thermal expansion for Zircaloy, α , and Young's modulus, E , are calculated using the relations [Tipton, 1960]

$$\alpha(T \text{ } ^\circ\text{C}) = (6.106 + 0.01398 T) 10^{-6} [1/^\circ\text{C}], \text{ and} \quad (9-9)$$

$$E (T \text{ } ^\circ\text{C}) = 9.5 \times 10^{10} - 6.15 \times 10^7 T \text{ [Pa]}, \text{ respectively.} \quad (9-10)$$

The principal stresses due to primary pressure and thermal stress are then calculated as

$$\sigma_1 = \sigma_\phi + \sigma_{th,i}, \quad \sigma_2 = \sigma_z + \sigma_{th,i}, \quad \sigma_3 = \sigma_r \quad (9-11)$$

where $i=1$ at the inner radius and $i=N_{pt}$ at the outer radius. The Von Mises stress

$$\sigma_{eff} = \frac{1}{\sqrt{2}} \sqrt{(\sigma_2 - \sigma_1)^2 + (\sigma_3 - \sigma_1)^2 + (\sigma_3 - \sigma_2)^2} \quad (9-12)$$

is used as the effective stress which is then compared with material limits. Two criteria are typically used for design stress in pressure tubes [Ross-Ross, 1968]

- 1/3 of the ultimate tensile strength,
- 2/3 of yield strength (0.2% offset).

Sometimes the stress to produce a creep rate of 10^{-5} %/hr is also used. Design stress versus temperature curves, given in [Ross-Ross, 1968] show that the criterion of 1/3 of ultimate tensile strength gives the lowest value for heat-treated Zr-2.5%Nb. Therefore this criterion will be adopted in further evaluations. Equations (9-3) through (9-12) have been incorporated into the computer code TMATRIX discussed in Chapter 7.

Figure 9-5 shows the effective Von Mises stress as a function of time in the hypothetical "pressurized LOCA" using a calandria protective tube. It can be observed that the peak at the outer radius is relatively small. Although the peak exceeds slightly the design stress of 1/3 of ultimate tensile strength for heat-treated Zr-2.5%Nb it only exists for a short duration (about 10 seconds) Moreover, this high stress is only at the outer radius; most of the tube wall will remain below the design criteria, since further from the outer radius, thermal stress has negative values, which reduces the magnitude of the effective Von Mises stress. Temperature profiles at various times during the accident are plotted in Figure 9-6. Flooding of the top row of fuel channels comes at 35.1 seconds, hence the temperature at the time of 35 seconds, i.e., just prior to flooding is the highest because of the heat up from gammas and heat transferred from the fuel matrix across the gap. The temperature of the outer surface is about 402°C at the time when the stress peak at this location is reached. At this temperature, 1/3 of the ultimate tensile strength of heat-treated Zr-2.5%Nb is 200 MPa [Ross-Ross, 1968]. This value is shown in Figure 9-5.

Figure 9-7 plots the results for the same hypothetical scenario if the pressure tube is not protected. The peak due to thermal stress is too large in this case, almost reaching the tensile strength, thus confirming the need to protect the pressure tube from sudden quenching.

The results suggest that PTLWR pressure tubes should withstand the flooding process without impairment to their reusability. The stress peak at the outer surface of a pressure tube resulting from flooding is modest and has short duration. Hence the fact that the stress slightly exceeds the 1/3 of ultimate tensile strength criterion for several seconds should not lead to any significant consequences. Moreover, the real scenario will be less

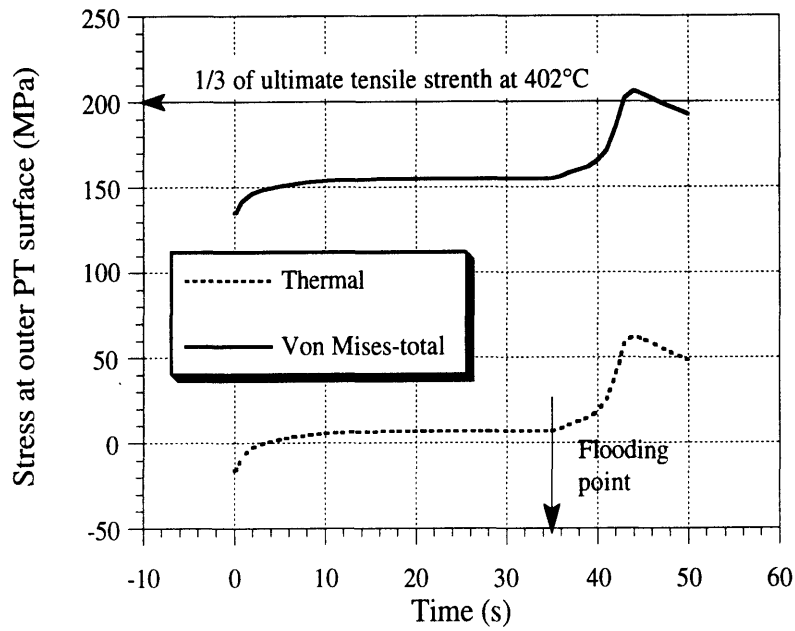


Figure 9-5 Stress on protected pressure tube during flooding at operating pressure

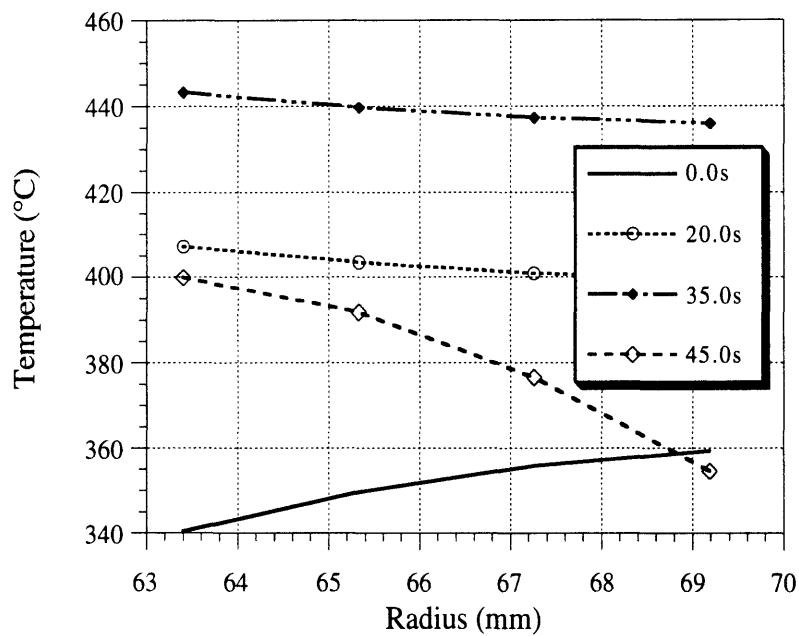


Figure 9-6 Temperature profiles in protected pressure tubes at various times

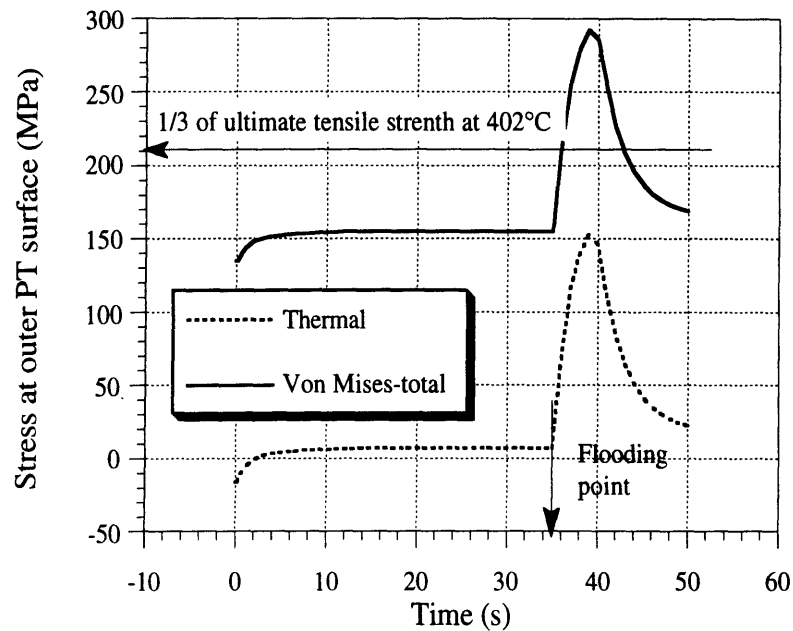


Figure 9-7 Stress on unprotected pressure tube during flooding at operating pressure

severe because flooding of fuel channels under pressure will occur at lower pressure tube temperatures due to the presence of primary coolant.

9.5 QUENCHING OF HOT CALANDRIA TUBES

The key difference between the PTLWR fuel channel and CANDU fuel channels is the high operating temperature of the calandria tube, since there is no cold moderator outside the calandria. The heat generation rate in the calandria tube from gamma and neutron heating was calculated using the MCNP model of the PTLWR channel, and is listed in Chapter 6, Table 6-2. The steady-state operating temperature of the calandria tube at the hottest spot was calculated from the fuel channel heat transfer model in Chapter 7 to be 378°C. During the flooding process, calandria tubes are suddenly submerged in cold water and quenched. Rapid temperature changes in the calandria tube will induce thermal stresses. The purpose of this section is to evaluate these thermal stresses and to confirm the capability of the calandria tube to withstand this process.

A transient analysis of the thermal stress in the calandria tube during flooding was performed in the same manner as for the pressure tube, using Eq. (9-8). Since no pressure load is exerted on the calandria tube, only thermal stress is evaluated. The procedure to obtain the time-dependent temperature distribution in the calandria tube wall was described in Chapter 7. Three scenarios have been analyzed. The first case involves inadvertent flooding of a calandria tube during normal operation, assuming a nucleate boiling regime without any limitation on critical heat flux, i.e., the critical heat flux is assumed to be infinite. The second case assumes the same process taking into account the CHF limit. The third scenario takes also into account the CHF limit, but involves a LOCA without scram sequence, in which the calandria tube heats up to temperatures above its normal operating temperature and then is flooded. The last scenario is fully described in Chapter 7.

Several comments on the critical heat flux need to be pointed out. The CHF correlation for pool boiling applicable outside a horizontal cylinder [Whalley,1987], Eq. (7-23) in Chapter 7, was used to obtain the critical heat flux at the outer surface of the calandria tube. The critical heat flux equation (7-23) is valid for saturated conditions. This equation was applied to the analysis of fuel channel temperatures in Chapter 7 since it makes the temperature analysis conservative, i.e., leads to earlier occurrence of CHF and hence higher wall temperatures, as it does not take into account the subcooling of flooding water. For the thermal stress analysis, subcooling must be accounted for because it leads to enhanced critical heat flux, and hence faster cooling rates, i.e., delayed occurrence of CHF and hence lower wall temperatures. The effect of subcooling was incorporated in the thermal stress analysis using the relation proposed by Ivey and Morris [1962]

$$q_{\text{CHF}}'' = q_{\text{CHF,sat}}'' \left[1 + 0.1 \left(\frac{\rho_f}{\rho_g} \right)^{0.75} \frac{c_{\text{pf}} \Delta T_{\text{sub}}}{h_{\text{fg}}} \right] \quad (9-13)$$

where $q_{\text{CHF,sat}}''$ is the critical heat flux obtained from Eq. (7-23) at saturated conditions and ΔT_{sub} is the subcooling. Bradfield's [1967] data, which yield the highest minimum heat flux, were utilized to obtain the minimum heat

flux on the boiling curve (see Section 7.4.2.1 for a detailed discussion of the key points on the boiling curves). The heat flux in the transition region between the minimum heat flux and the critical heat flux is obtained by linear interpolation, described in Section 7.4.2.1.

The results for the first case are presented in Figure 9-8 and 9-9. Figure 9-8 plots the temperature development in the calandria tube wall. The wall has been divided into eight annuli of equal width, hence there are nine curves, each curve representing one cylindrical surface. Since nucleate boiling is assumed during the entire process, the heat transfer coefficient at time zero is extremely high (because it is proportional to ΔT_{sat} squared) and the outer calandria surface is cooled almost instantly while the inner surface temperature still remains unchanged. This establishes a large temperature difference across the wall, and consequently leads to high thermal stress at the outer surface, as shown in Figure 9-9. It can be observed that the outer surface exceeds the 1/3 ultimate tensile strength criterion while the rest of the wall remains below this criterion (the criterion shown is for the outer surface temperature at the time when the maximum stress at this location is achieved). If Zr-2.5%Nb material is used, the outer surface would remain below the 1/3 ultimate tensile strength criterion. However, it is noted that this scenario is a hypothetical case, because the heat flux from the outer calandria surface exceeds at an early time and by far the CHF, which would alter the unrealistically rapid cooldown rates assumed.

To simulate a more realistic case, the critical heat flux limit for the heat transfer from the outer tube surface must be taken into account. This is shown in Figures 9-10 and 9-11. When the cold water hits the hot tube surface, the difference between the wall and saturation temperatures, ΔT_{sat} , is large and sets the operating point in the transition region, between the minimum and critical heat flux. The heat flux in the transition regime is sufficiently high to cause cooldown of the outer surface, albeit at a much smaller rate than in the previous case. The lower cooling rate at the outer surface allows more time for the inner surface to decrease its temperature by heat conduction to the outer surface, resulting in a less steep wall temperature profile, and hence smaller stress. Figure 9-11 shows that the

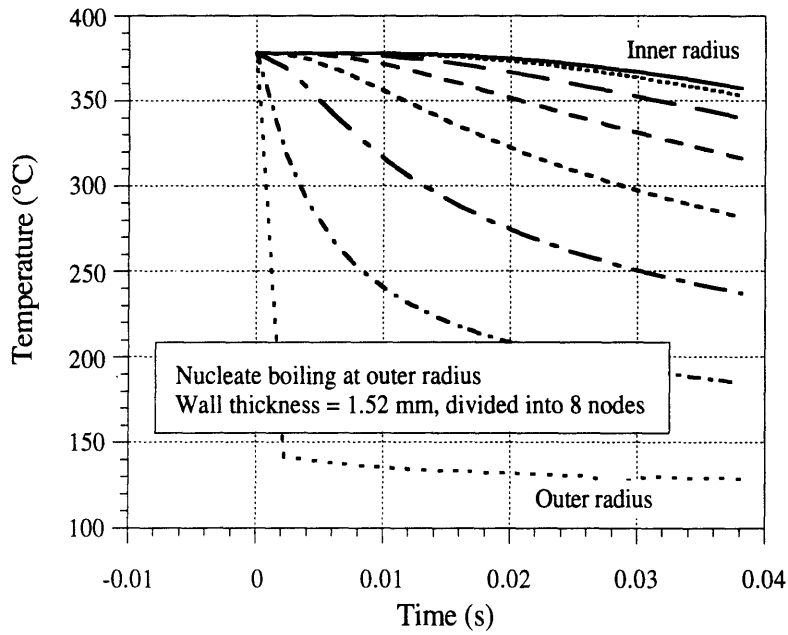


Figure 9-8 Temperature traces in the calandria tube wall for hypothetical quenching with nucleate boiling

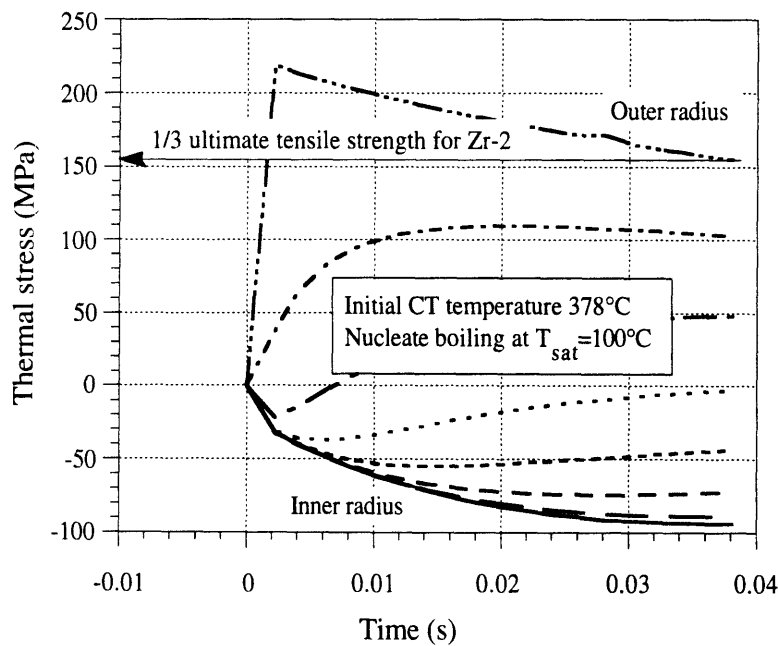


Figure 9-9 Time development of thermal stress in calandria tube wall for hypothetical quenching with nucleate boiling

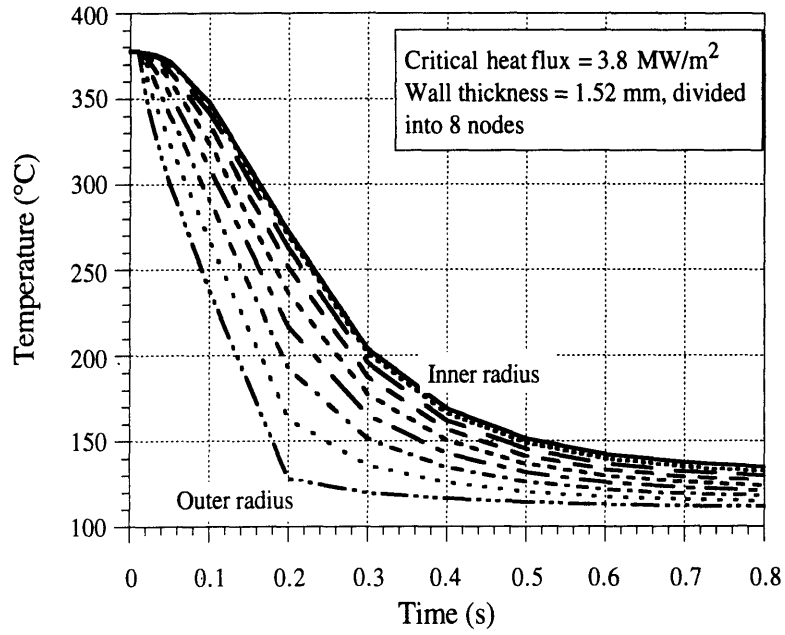


Figure 9-10 Calandria tube cooldown for inadvertent flooding process

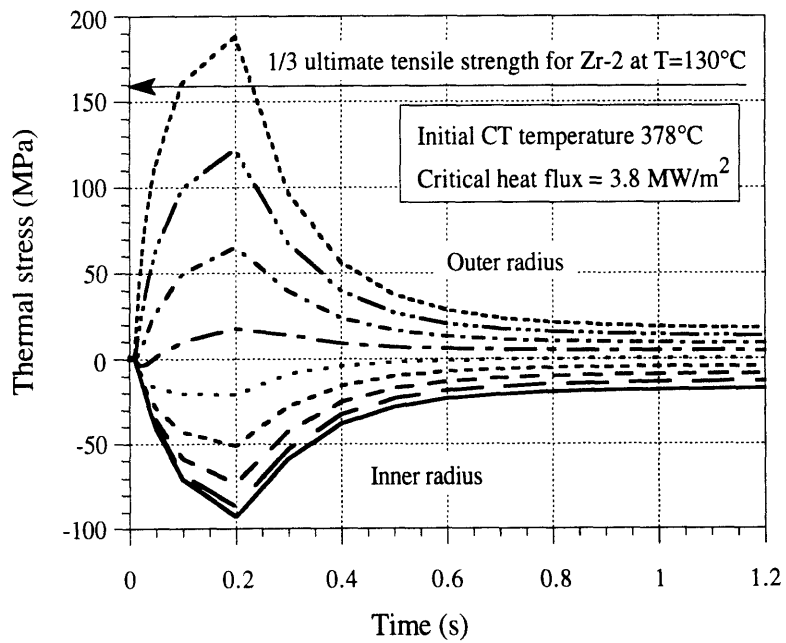


Figure 9-11 Time development of thermal stress in the calandria tube wall for inadvertent flooding process

peak stress at the outer surface exceeds the criterion of 1/3 ultimate tensile strength for Zr-2 by 30MPa for a very short period of time (about 0.1s). This is a quite satisfactory situation.

The LOCA scenario was also selected for investigation because it results in a higher initial temperature of the calandria tube at the time the tube is flooded with cold water. The results are shown in Figures 9-12 and 9-13. To show the quenching process in more detail, only a short time span of 1 second, following the time when the top row of calandria tubes is flooded, is plotted. An interesting observation to note is that the thermal stress in this process is even less than in the second case, even though the initial temperature of the calandria tube is higher. The reason for this behavior lies in the lower heat flux due to the higher ΔT_{sat} in the transition region in this LOCA case (note that in the temperature-controlled transition region, heat flux is inversely-proportional to ΔT_{sat}).

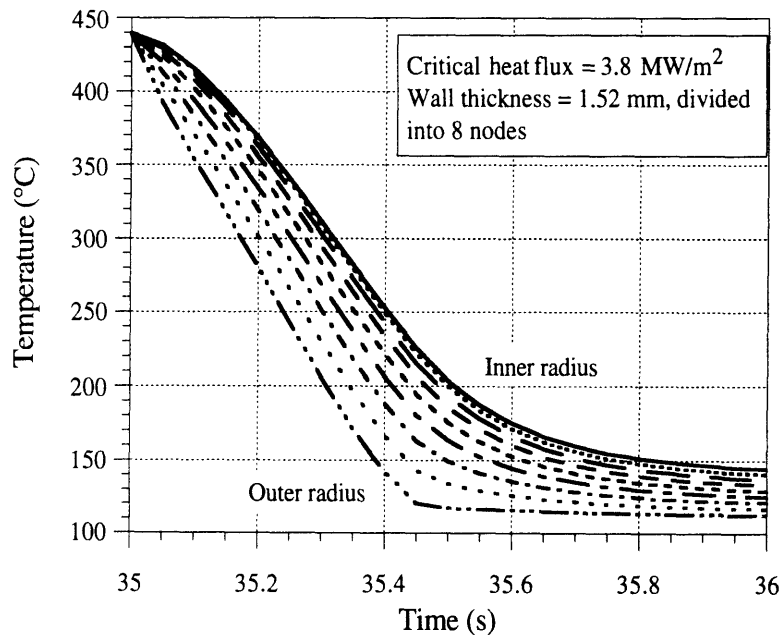


Figure 9-12 Calandria tube cooldown for LOCA without scram scenario

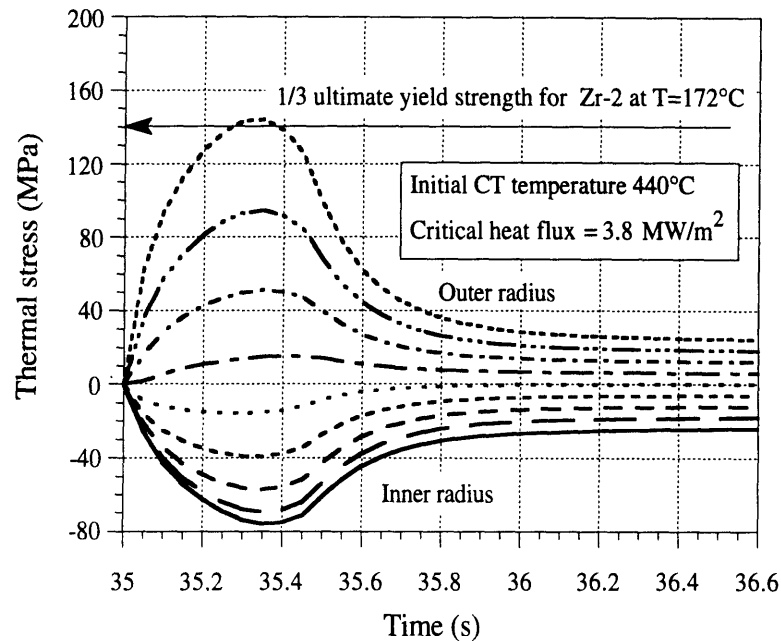


Figure 9-13 Time development of thermal stress in the calandria tube wall for LOCA without scram scenario

The above analysis of thermal stress in the calandria tube from cold-water flooding suggests that calandria tubes should be able to withstand the quenching process undamaged. Thermal stress depends strongly on the boiling regime and on the value of critical heat flux and minimum heat flux. Experiments would be needed to determine the boiling curve for calandria tubes more exactly. Relatively high peak thermal stresses may require the use of Zr2.5%Nb instead of Zr-2 as a material for calandria tubes.

9.6 SUMMARY

The PTLWR fuel channel is of similar design to that of CANDU units. However, it operates at higher primary system conditions and higher fast neutron flux. The issues associated with fuel channel operation under these performance-limiting conditions have been discussed. The key parameters affecting the fuel channel lifetime are higher fast neutron flux and elevated temperature. Over time fast flux increases axial elongation of the fuel channel, which could be accommodated by increased bearing travel allowance. Accelerated diametral expansion due to higher flux and

operating temperature may be a limiting factor for the life of PTLWR pressure tubes. It is expected that the pressure tubes would need to be designed for easy replacement, once in a plant lifetime. Problems with pressure tube cracking initiated by zirconium hydride blisters from enhanced hydrogen transport due to thermal gradients are eliminated in the PTLWR fuel channel since there are no cold spots.

Flooding of the calandria space with cold water poses a challenge to the fuel channels due to significant thermal stresses. Stress analysis of both the pressure tube and the calandria tube has been performed. It has been shown that the maximum stress in the hottest pressure tube does not exceed the 1/3 ultimate tensile strength criterion. Hence, pressure tube reusability should not be affected by the flooding process. Also, calandria tube can withstand the quenching without excessive thermal stresses. The analysis also confirmed the need to protect the pressure tube from direct contact with cold flooding water.

Finally it is noted that in the detailed design stage, experiments on critical heat flux and minimum heat flux would need to be carried out to eliminate the uncertainties in these two variables, which have a significant impact on thermal stress in the calandria tubes. Also, stress concentration areas would have to be analyzed, in particular, at the connection of the calandria tube to the calandria side wall. Regarding the high fast fluence, alternative fuel arrangements with a higher heavy metal loading should be considered in any future work.

Chapter 10

REFLECTOR AND CONTROL ROD COOLING CONSIDERATIONS

10.1 INTRODUCTION

The proposed PTLWR concept employs a graphite reflector surrounding the gas-filled calandria space. This feature differs from CANDU reactors which use a D₂O reflector. A D₂O reflector was not used in the PTLWR design because of concerns with reactivity excursions, should the separating wall between the calandria space and the reflector breach causing calandria flooding with D₂O. As discussed in Chapter 4, the graphite reflector is neutronically equivalent to a D₂O reflector. However, it is more difficult to cool than the liquid reflector. This Chapter will briefly discuss the issues of reflector cooling; Section 10.2 will evaluate energy deposited in the reflector and Section 10.3 will propose some cooling concepts and assess their thermal performance.

Another issue, discussed in Section 10.4, is the cooling of control rods. PTLWR control rods are inserted in silicon carbide guide tubes penetrating downward through the end reflector and are cooled primarily by radiation to the guide tubes, and then by conduction of the heat through the graphite reflector to the primary coolant in the fuel channels. This differs from CANDU units where the control rods are inserted in the guide tubes, which are immersed in a cold moderator.

10.2 REFLECTOR HEATING

The reflector is heated by gamma rays and neutrons escaping from the core. Neglecting neutron heating, since the neutron contribution is small compared to gamma heating, a simplified estimate of gamma heating can be obtained using a rule of thumb, stating that all photons within 1/4th of a

mean free path escape from the outer surface of the core. Therefore, the fraction of gamma radiation escaping into the reflector, f_λ , can be approximated as

$$f_\gamma = \frac{\dot{Q}_{\text{esc},\gamma}}{\dot{Q}_\gamma} = \frac{\lambda/4 \pi D L}{\pi D^2/4 L} = \frac{\lambda}{D} \quad (10-1)$$

where D is core diameter and λ is photon mean free path in the core. The photon mean free path can be calculated from the homogenized core density and a mass absorption coefficient. Homogenizing the core solid material and coolant with the voided space, the homogenized core density can be evaluated as

$$\rho_{\text{hom}} = \frac{\sum_{i=1}^N V_i \rho_i}{V_{\text{core}}} = \frac{3.4979 \times 10^5 \text{ g/cm}^3}{\pi 450^2 \text{ cm}^2} = 0.55 \text{ g/cm}^3 \quad (10-2)$$

Assuming a typical value for mass absorption coefficient-to-density ratio

$$\frac{\mu_a}{\rho} = 0.025 \text{ cm}^2/\text{g}, \quad (10-3)$$

which is almost the same for all materials, the mean free path for gamma rays can be estimated as

$$\lambda = \frac{1}{\mu_a} = \frac{1}{0.025 \rho_{\text{hom}}} = \frac{1}{0.025 (0.55)} = 72.7 \text{ cm} \quad (10-4)$$

Finally, the fraction of gamma rays escaping from the core to the cylindrical reflector can be evaluated by virtue of Eq. (10-1)

$$f_\gamma = \frac{\lambda}{D} = \frac{72.7}{900} = 0.08$$

The total gamma heating from fission, including delayed gammas is 11%, which yields for the rated power of 3899 MWt, total gamma heat generation $\dot{Q}_\gamma = 429$ MWt. From this heat rate, the fraction $f_\lambda = 0.08$ escapes, i.e.,

$$0.08 \times 429 = 34 \text{ MWt or } 0.88\% \text{ of rated power.}$$

A more exact calculation of reflector heating including both the neutron and gamma heating can be obtained using MCNP. The detailed MCNP full-core model #2, described in Chapter 4, has been used to accomplish this task. Edits of neutron and gamma heating in the reflector from prompt and capture gammas yielded the following values:

- neutron heating $q_n = 0.0188 \text{ W/g}$, and
- prompt and capture gamma heating $\gamma_{\text{prompt} + \text{capture}} = 0.0455 \text{ W/g}$.

To incorporate delayed gamma heating, gamma heating from prompt and capture gammas can be corrected by a coefficient obtained from a typical gamma heating apportionment in light water reactors

- prompt gamma $\gamma_{\text{prompt}} = 6.33 \text{ MeV}$,
- capture gamma $\gamma_{\text{capture}} = 6.72 \text{ MeV}$, and
- delayed gamma $\gamma_{\text{delay}} = 6.97 \text{ MeV}$.

The scaling coefficient is thus:

$$C_{\text{tot}} = \frac{\gamma_{\text{prompt}} + \gamma_{\text{capture}} + \gamma_{\text{delay}}}{\gamma_{\text{prompt}} + \gamma_{\text{capture}}} = \frac{6.33 + 6.72 + 6.97}{6.33 + 6.72} = 1.53 \quad (10-5)$$

which gives for the total gamma heating

$$\gamma_{\text{total}} = C_{\text{tot}} (\gamma_{\text{prompt}} + \gamma_{\text{capture}}) = 1.53 (0.0455) = 0.0696 \text{ W/g} \quad (10-6)$$

Using the total mass of the radial graphite reflector, $m_g = 6.9 \times 10^8 \text{ g}$, reflector heating from neutrons and all gamma rays can be calculated as

$$\dot{Q}_{\gamma+n} = m_g (\gamma_{\text{total}} + q_n) = 6.9 \times 10^8 (0.0696 + 0.0188) = 61 \times 10^6 \text{ W} = 61 \text{ MWt} \quad (10-7)$$

from which 48 MWt is by gamma heating and 13 MWt by neutrons. Comparing gamma heating of 48 MWt to the simple estimate of 34 MWt, it can be seen that the simple estimate yields about 30% lower values. This is not very surprising since homogenizing the core underestimates the escape of gamma emissions by streaming through the void space.

The MCNP result for total gamma and neutron energy deposition in the two end reflectors is 43 MWt. Hence, the total power generated in the radial

and axial reflector is 103 MWt, or 2.6% of rated power, which compares to 5.4% generated in CANDU D₂O moderator. However, the heat generated in the reflector has high availability (i.e., high temperature) and can be virtually all recovered, while in CANDU units, heat generated in the cold moderator does not contribute to power generation.

The power density profile in the radial reflector can also be obtained using MCNP full-core model #2 by editing gamma and neutron heating in various radial segments of the reflector. The results are presented in Figure 10-1. Since most of the reflector heating results from gamma rays, the curve should resemble the conventional exponential attenuation equation. The best fit to MCNP data in the form of the attenuation equation, with attenuation coefficient $\mu=0.04$, is also shown in Figure 10-1. Figure 10-1 shows that the heating curve deviates from the attenuation equation near the inner surface of the reflector where the power density tends to be higher. This is due to the increased neutron heating in the inner portion of the reflector and the smaller volume of the inner regions caused by the annular shape of the reflector (the reflector is not exactly a slab, for which the cited attenuation equation is valid)

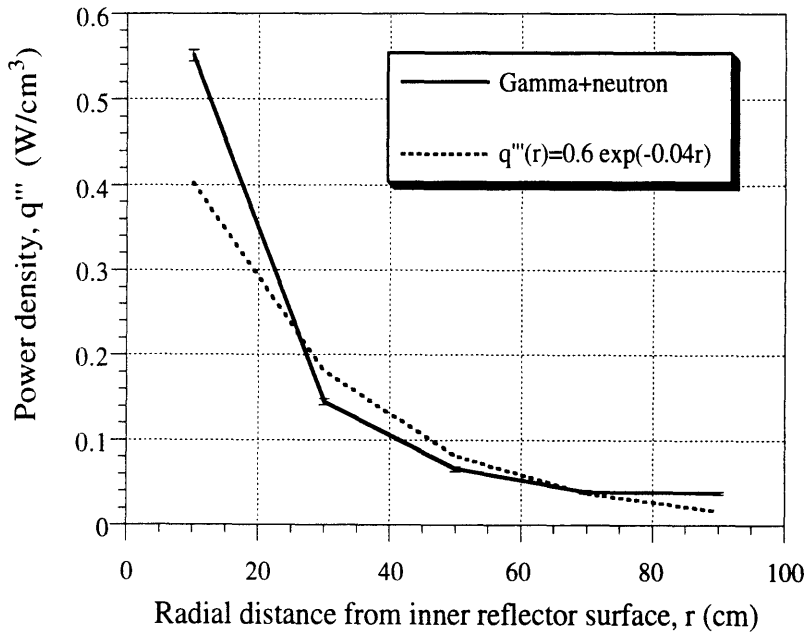


Figure 10-1 Power density distribution in the radial reflector

10.3 REFLECTOR COOLING CONCEPTS

10.3.1 Cooling of the Axial Reflector

The axial reflector is cooled by the primary coolant flowing inside the pressure tubes. The reflector operates at temperatures higher than the temperature of the fuel channels and the heat generated in the reflector is transferred to coolant across the calandria tube, the gap between the calandria tube and pressure tube and the pressure tube wall. Part of the fuel channel lattice, penetrating the reflector, is presented in Figure 10-2. Figure 10-2 also shows a 2-D computational cell used for the analysis of the cell temperature profile. The boundary conditions are zero heat flux at symmetry planes, bulk temperature of the coolant and heat transfer coefficient between the pressure tube and the coolant.

The analysis was performed using the finite element package ALGOR at the plane with maximum power density. The power density in the reflector, q''_{max} , was obtained from MCNP and coolant boundary conditions were calculated from the steady-state thermohydraulics model of a fuel channel, described in Chapter 6. The variable with the largest uncertainty is the contact conductance between the graphite reflector and the calandria tube. At this stage, a contact conductance of $300 \text{ W/m}^2\text{-K}$, corresponding to a 1mm helium-filled gap, has been utilized. Detailed design of the calandria tube-graphite reflector interface needs to consider dimensional changes of graphite due to irradiation as well as thermal expansion, and to provide for fuel channel replacement. One possible arrangement is shown in Figure 10-3. It is based on the experience acquired in the RBMK reactors, where the thermal bridge between the pressure tubes and graphite moderator blocks is provided by an array of inner and outer graphite rings.

Analysis results are plotted on a 3-D graph in Figure 10-4, where the x and y coordinates correspond to those shown in Figure 10-2. The largest temperature jump occurs across the graphite-calandria tube interface, which is the controlling heat transfer resistance. Better design of this interface could reduce this temperature jump, and hence reduce the

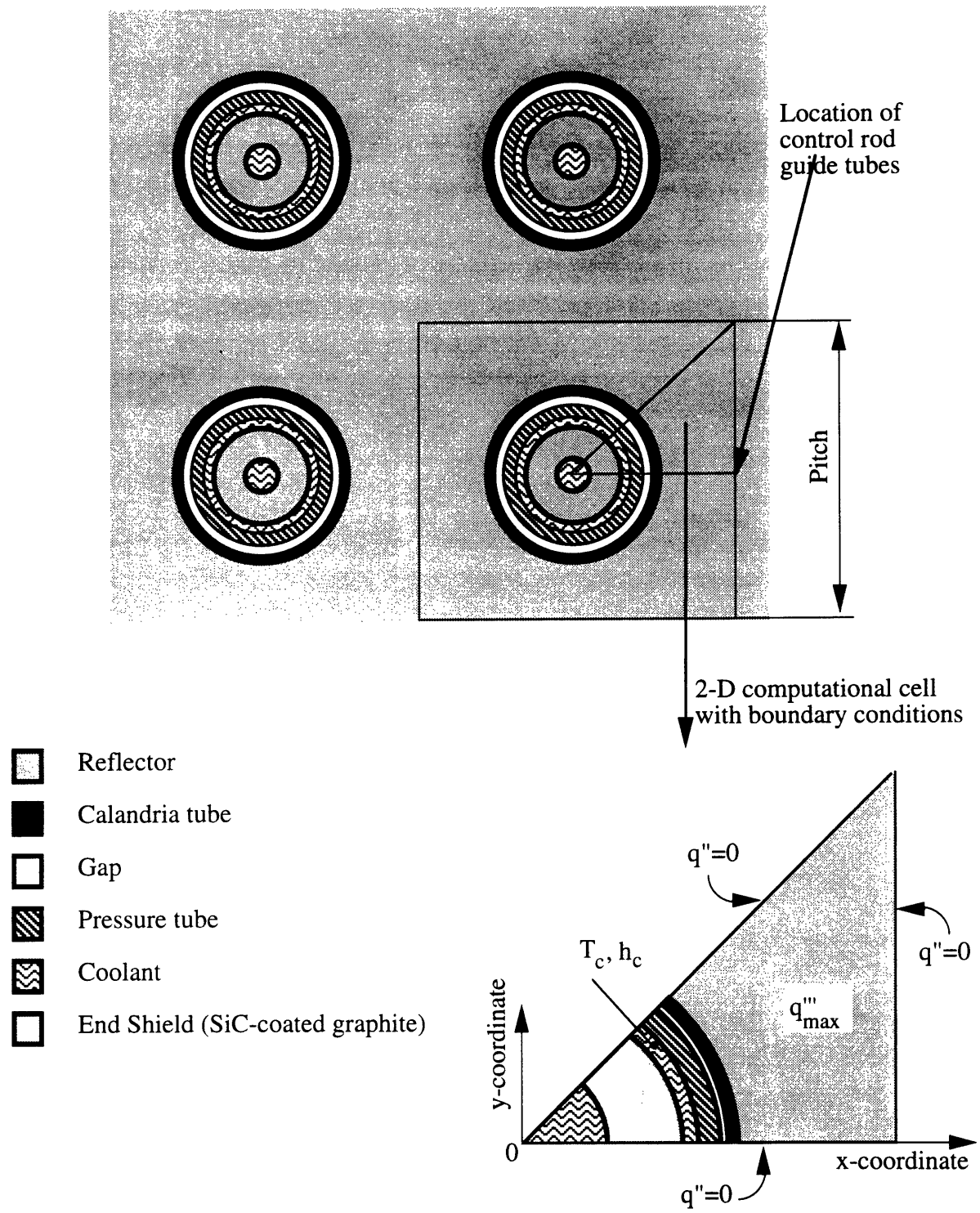


Figure 10-2 Fuel channels penetrating the reflector and a 2-D computational cell

maximum reflector temperature. Nevertheless, the maximum temperature of about 650°C is satisfactory for graphite if the reflector is maintained in an appropriate gas environment to prevent oxidation. The maximum temperature of 650°C is comparable to the operating temperature of the graphite moderator in the RBMK reactors (about 700°C), which have a mixture of helium and nitrogen between the graphite columns.

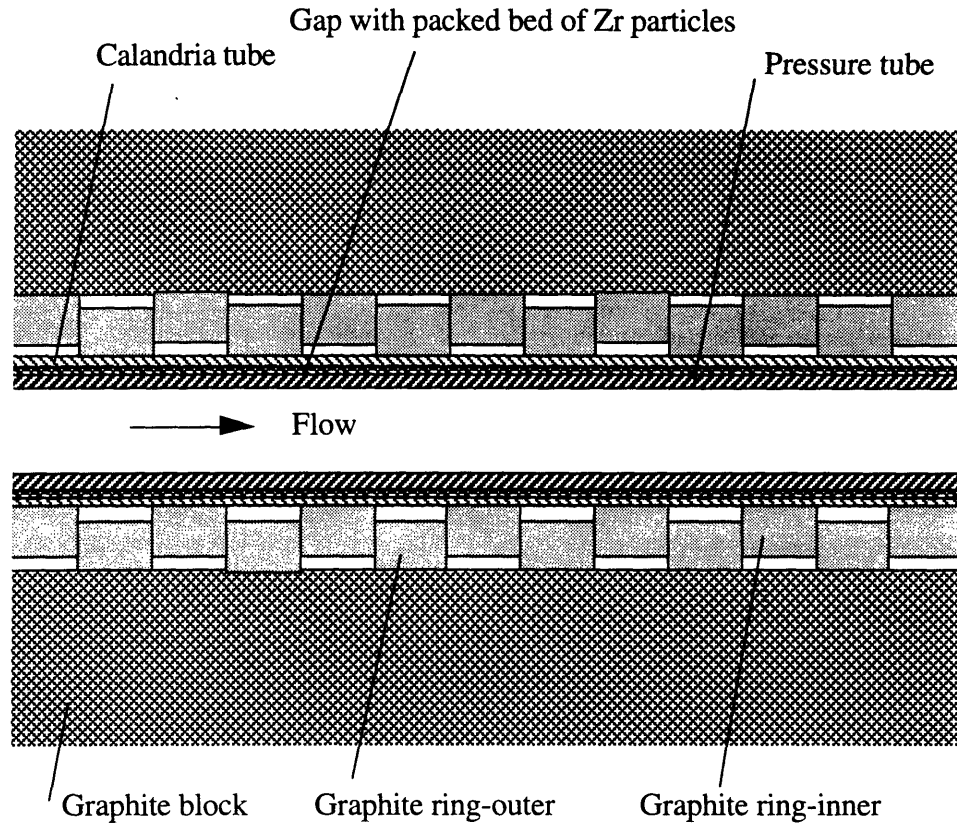


Figure 10-3 Possible arrangement of graphite reflector and fuel channel

10.3.2 Cooling of the Radial Reflector

One possibility to cool the radial reflector is from the outer side by transferring the heat to the shield tank. The maximum temperature of the inner reflector face can be estimated analytically by deriving a temperature profile from the attenuation equation,

$$q'''(x) = q'''(0) \exp(-\mu_a x). \quad (10-8)$$

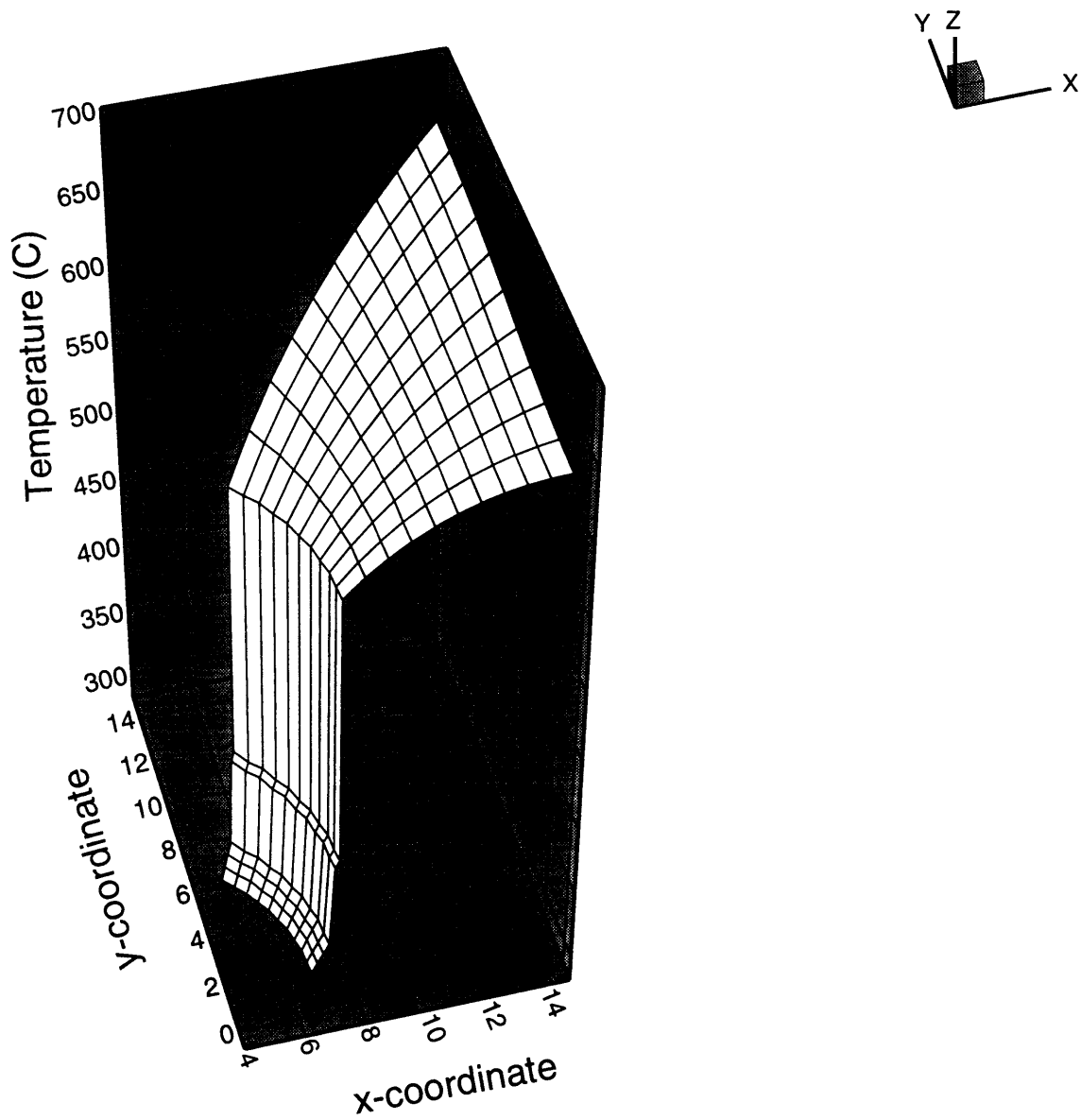


Figure 10-4 2-D Temperature profile in a the axial reflector around a fuel channel

Substitution of Eq. (10-8) into the 1-D steady state heat conduction equation for a slab yields

$$\frac{d^2T}{dx^2} = -\frac{q'''(x)}{k} = \frac{q'''(0) \exp(-\mu_a x)}{k} \quad (10-9)$$

Integrating for a zero heat flux boundary condition at $x=0$, gives the temperature gradient

$$\frac{dT}{dx} = \frac{q'''(0)}{k \mu_a} \exp(-\mu_a x) - \frac{q'''(0)}{k \mu_a} \quad (10-10)$$

and integrating again with boundary condition $T(x=t)=T_t$, yields the temperature profile

$$T(x) = \frac{q'''(0)}{k \mu_a} \left[\frac{\exp(-\mu_a t) - \exp(-\mu_a x)}{\mu_a} + t - x \right] \quad (10-11)$$

Substituting for constants $q'''(0) = 0.6 \text{ W/cm}^3$ and $\mu_a = 0.04 \text{ cm}^{-1}$ (from Figure 10-1), graphite thermal conductivity $k = 0.4 \text{ W/cm-K}$, reflector thickness $t = 100 \text{ cm}$, and the outer surface temperature $T_t = 100^\circ\text{C}$, results in a maximum temperature at the inner reflector surface $T_{\text{max}} = 3767^\circ\text{C}$. This clearly shows that it is not feasible to cool such a thick reflector from the outer surface only.

One possible reflector cooling scheme is shown in Figure 10-5. It employs pressure tubes running through the radial reflector. To minimize parasitic capture in the light water coolant and to make thermohydraulic conditions close to those in fueled channels, the pressure tubes contain twelve SiC-coated graphite plugs sliding on bearing pads and forming a cooling water annulus between the plug and the pressure tube. No calandria tubes are needed for these channels. The pressure tubes are located close to the inner reflector surface, where the heat generation is high. The scheme in Figure 10-5 proposes cooling of the outer portion of the reflector by transferring the heat to the shield tank. The other alternative would be to employ an additional ring of pressure tubes farther from the inner surface and recover all the heat with coolant.

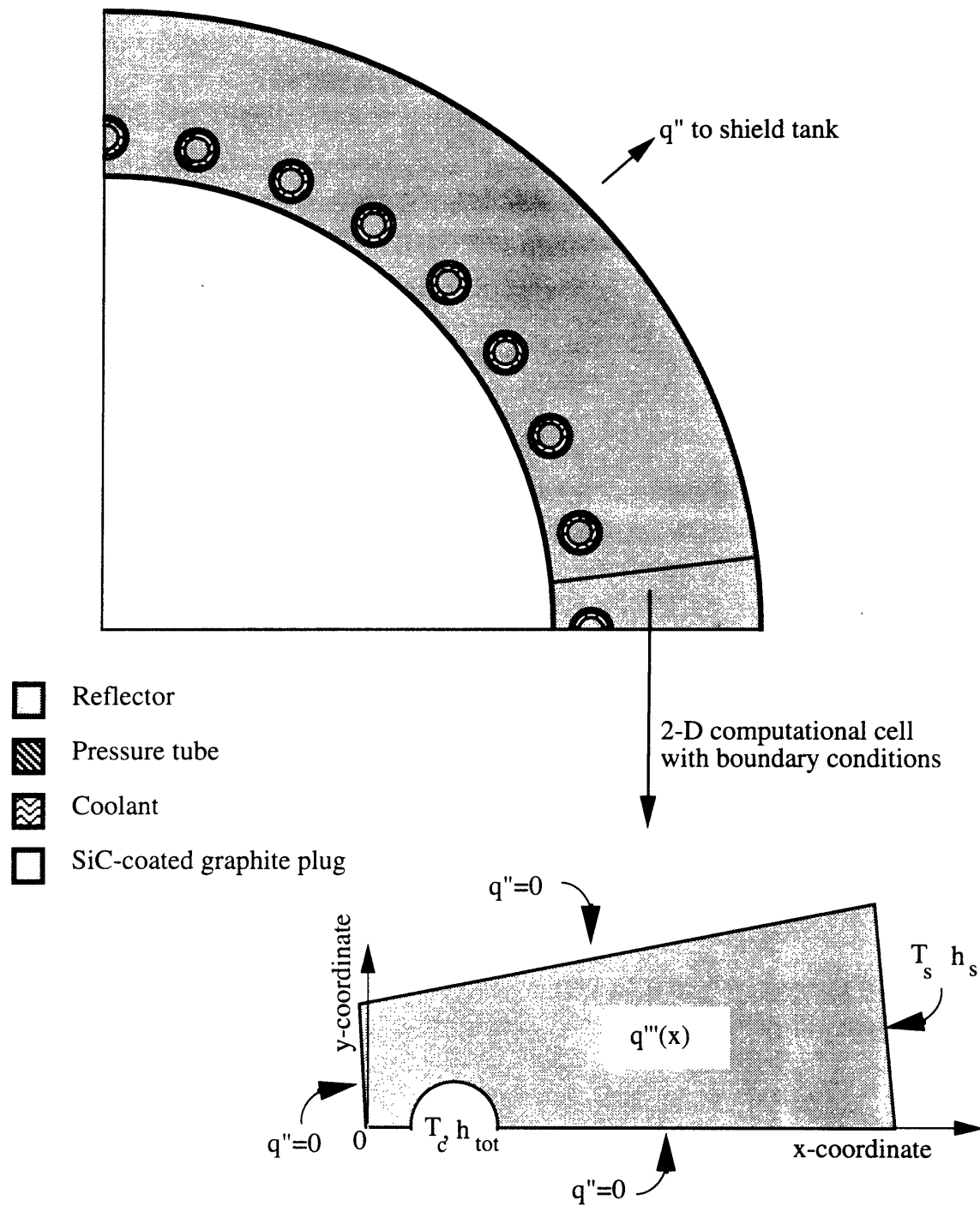


Figure 10-5 Concept of radial reflector cooling and a 2-D computational cell

A 2-D computational cell, shown in Figure 10-5, has been modeled using ALGOR. The power density profile as a function of the coordinate x is taken from Figure 10-1. The bulk temperature of the light water in the shield tank, T_s , was assumed to be 40 °C and the heat transfer coefficient between the reflector and the shield water, h_s , was taken to be 200 W/m²-K. The total heat transfer coefficient between the coolant in the pressure tube and graphite inner surface takes into account the contact resistance between graphite and the pressure tube, the heat transfer resistance of the pressure tube, and the heat transfer resistance between the bulk coolant and the inner wall temperature. It was evaluated from the relation

$$\frac{1}{h_{tot}} = \frac{1}{h_c} + \frac{\ln(R_{PTo}/R_{PTi})}{(k_{PT}/R_{PTi})} + \frac{R_{PTo}}{h_{contact} R_{PTi}} \quad (10-12)$$

where R_{PTo} and R_{PTi} are the outer and inner radii of the pressure tube*, respectively. The earlier discussion of contact resistance (see Section 10.3.1), $h_{contact}$, between the pressure tube and graphite, applies here as well. The results are plotted in Figure 10-6. It can be seen that the pressure tubes are very effective in decreasing reflector temperature (compare to 3767°C if the reflector is cooled from the outer surface only). However, the maximum graphite temperature of 1000°C, achieved in this cooling scheme is still too high. The reason for this high peak is the large spacing between the pressure tubes. To decrease this maximum temperature, more pressure tubes (the number of pressure tubes for the scheme shown in Figure 10-5 is 36) need to be employed. Doubling the number of pressure tubes in the ring would decrease this temperature sufficiently to about 600°C, while still having much larger pitch than the minimum pitch needed for plumbing of the feeder connectors.

* The dimensions of the pressure tubes are assumed the same as for fueled channels.

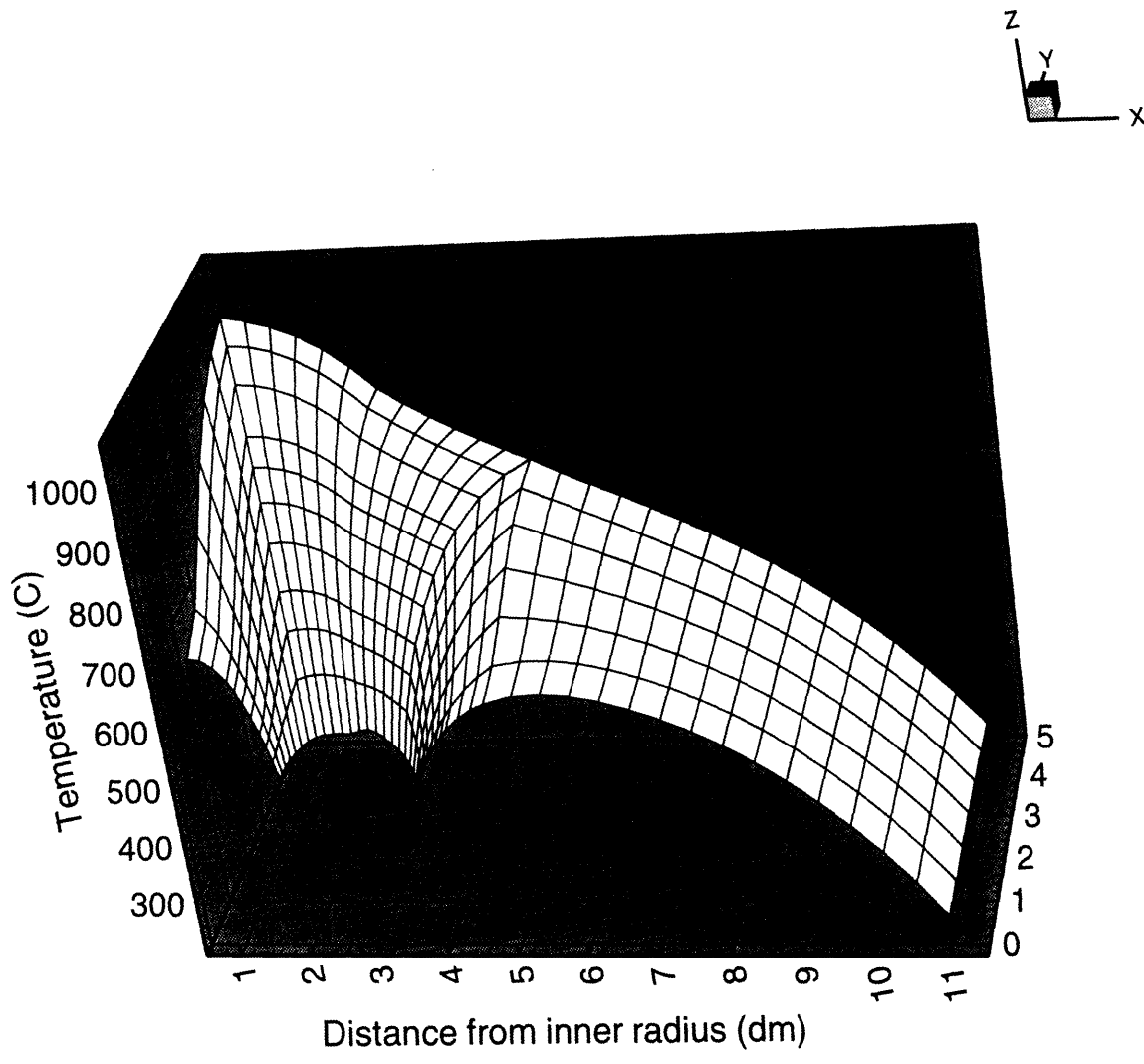


Figure 10-6 Temperature profile in the radial reflector adjacent to a cooling channel

10.4 CONTROL ROD COOLING

Control rods slide in vertical guide tubes between the fuel channels, penetrating the reflector, as shown in Chapter 4. Cooling of control rods is achieved primarily by radiative heat transfer to their channel wall and by conduction through the graphite reflector and pressure tubes to primary coolant. The location of control rod guide tubes with respect to the fuel channel in the computational cell is shown in Figure 10-2. Figure 10-4 shows that the temperature of the reflector at this location is about 600°C. The temperature of a control rod can be calculated from the radiation equation between two concentric cylinders

$$T_{\text{CRD}} = \sqrt[4]{\frac{\frac{1}{\epsilon_{\text{CRD}}} + \frac{R_{\text{GC}}}{R_{\text{CRD}}} \left(\frac{1}{\epsilon_{\text{GC}}} - 1 \right)}{2 \pi R_{\text{CRD}} \sigma} q' + T_{\text{GC}}^4} \quad (10-13)$$

where subscripts GC and CRD stand for the guide tube and control rod, respectively. The linear heat rate from gamma and neutron heating in control rods was obtained from the MCNP model, i.e.,

neutron heating	4.2 W/g,
gamma heating	0.22W/g, and
total heating	4.42 W/g,

which yields, for a boron carbide density of 1.75 g/cm³ and control rod radius $R_{\text{CRD}}=3.5\text{cm}$, a linear heat rate of $q'= 25,500\text{W/m}$. Using $R_{\text{GC}}=3.8\text{cm}$, typical values of emissivity for the stainless steel cladding of the boron carbide rods and silicon carbide guide tubes, and a temperature of 600°C for the guide tube, Eq. (10-13) gives a control rod temperature of 1113 °C. This temperature is below the melting temperature of stainless steel (1420°C). The tensile strength of stainless steel is severely reduced, however, at such high temperatures. Cobalt based alloys are suitable for applications up to 1100°C, but cobalt poses activation problems. Silicon carbide cladding can easily withstand these temperatures, but requires more research into its compatibility with boron carbide and its resistance to brittle fracture. A gap is needed between the SiC cladding and the control rod to allow for B₄C swelling due to helium release. A 1mm helium-filled gap leads to a

temperature rise of 200°C. Hence, the corresponding rod surface temperature is 1313°C. The temperature difference between the surface and the centerline is small (22°C) due to the high thermal conductivity of boron carbide (90W/m-K). The centerline temperature of 1335°C is well below the melting temperature of boron carbide (2470°C). Finally, it is noted that the conventional steel cladding of boron carbide control rods could also be used if the guide channels are actively cooled by flowing gas. A variety of other approaches is possible – for example cermets. Hence feasibility seems assured even though important details will be left for future work.

10.5 SUMMARY

The issues of reflector and control rod cooling have been briefly explored. Two methods of evaluating the gamma and neutron heating of the reflector have been described. The energy fraction deposited in the reflector is about one half of the energy fraction generated in the CANDU D₂O moderator. The high operating temperature of the graphite reflector enables one to recover virtually all this energy, and thus to reduce the heat loss during normal operation.

The axial reflector is cooled by the primary coolant flowing through the fuel channels. Cooling of the radial reflector is proposed by introduction of non-fueled pressure tubes containing dummy SiC-coated graphite elements to displace the flow of primary coolant to the pressure tube wall and to decrease parasitic neutron losses. The preliminary study suggests that sufficient cooling of both the axial and radial reflectors can be achieved.

PTLWR control rods move in vertical guide tubes penetrating the end reflector between fuel channels. The material proposed for guide tubes and for boron carbide absorber cladding is silicon carbide. Calculation confirmed that using these materials, control rods can be cooled by radiative heat transfer. The alternative option is to employ conventional stainless steel cladding of the control rods and add additional cooling of the guide channel cavity by forced convection gas flow. The detailed design of the control rods and their associated cooling system remains as part of future work.

Chapter 11

PASSIVE CONTAINMENT DESIGN AND ANALYSIS

11.1 INTRODUCTION

The reactor containment is a low-leakage boundary enclosing the calandria vessel, all reactor coolant system components, in-containment water storage pools and other supporting systems. Its primary purpose is to mitigate the consequences of accidents. It also provides the ultimate barrier to fission product release.

Containment is employed in all currently operating power reactors of western design. The proposed passive pressure tube LWR uses particle fuel which retains all fission products if the maximum fuel temperature remains below 1600°C. The analysis presented in Chapter 7 has demonstrated that even during large LOCA without ECCS and without scram the maximum fuel temperature is far below this limit. In the MHTGR, the silicon carbide coating of TRISO particle fuel is considered as a containment. The passive PTLWR has an additional barrier in the form of the silicon carbide coating of the fuel matrix, thus decreasing the probability of fission product release even further. Therefore, it would be theoretically possible to consider using confinement in lieu of the containment in the proposed concept; however the more conservative option to retain containment has been adopted.

There are two primary reasons for retaining the traditional defense in depth philosophy, with containment as an ultimate barrier. First, one cannot exclude catastrophic events, e.g., tornadoes or large earthquakes which could lead to loss of flooding water, and consequently to high fuel temperatures and fission product release. Second, in the current political environment, it would be almost impossible to build and license a nuclear power plant without containment. The importance of containment was also

amplified by the accidents at Three Mile Island and Chernobyl. The presence of containment at the Three Mile Island plant prevented the release of radioactivity while the absence of containment at Chernobyl led to significant release of fission products. The fear of accidental release of radioactivity to the environment is one of the main concerns of the general public, and one of the causes for the opposition to construction of new nuclear power plants. The goal to strive for is a nuclear plant which would rule out the need for evacuation and the possibility of significant land contamination even in severe accidents. Using the proposed PTLWR with a two-barrier fuel element enclosed in a passively cooled containment could accomplish this objective.

This Chapter describes the proposed conceptual design of a passively cooled containment for the PTLWR and the analyses performed to evaluate this design. Several options for simple passive cooling by air are studied and compared. The primary goal of this Chapter is to confirm that the maximum pressure reached in a passively air-cooled containment after LOCA remains within current practice for large dry containments. Correspondingly, the main body of the Chapter is devoted to Design Basis Accident (DBA) containment analysis with emphasis on long-term pressurization. Four cases of breaks in the containment are analysed using the computer code CONTAIN. To gain more insight into natural circulation patterns and thermal stratification effects inside a containment, the GOTHIC computer code is employed. The capabilities of the GOTHIC code are also used to evaluate the long-term behavior of the water level in the calandria as it is affected by returning condensate.

11.2 PRINCIPAL CONSIDERATIONS

In assessing the suitability of a containment configuration, the following principles were considered:

- Retention of structural integrity and acceptable leak tightness during normal operation, anticipated transients, design basis and severe accidents. To maintain structural integrity, the maximum temperatures and pressures which will be achieved during the most challenging event must remain at acceptable values. Additionally,

behavior under severe seismic events must be taken into consideration. Containment must also be designed such that its properties do not degrade with time e.g., by corrosion, and the crucial components should be made accessible.

- **Passive cooling.** To maintain consistency of passive decay heat removal throughout the overall plant design, it is highly desirable that the containment shell cooling in the accidents leading to containment pressurization can be achieved by natural phenomena only. This requirement limits the choice of primary containment shells to free standing steel containment. The thick prestressed-concrete containments can be readily excluded from further considerations because of the inherently low thermal conductivity of the concrete and their large wall thickness (around 1m). These lead to marginal heat transport rates through the wall. An important consideration associated with passive cooling is stratification of the containment atmosphere. The in-containment layout should provide pathways promoting natural circulation of the hot containment atmosphere to the air-cooled containment walls.
- **Simplicity, easy construction and low cost.** The containment design should take into consideration industrial experience regarding constructability and associated cost and schedule. The cost of the containment depends on its size, complexity and speed of construction. Containment size is related to power rating, size and configuration of the primary system, design pressure and passive cooling requirements. Higher power rating is associated with a larger Reactor Cooling System (RCS) and a higher coolant inventory which leads to higher containment pressures following blowdown in large LOCAs. The arrangement of the RCS components is typically optimized to minimize the containment space needed for enclosure. Too confined space around the RCS components makes operation and maintenance work more difficult, which leads to longer maintenance time and higher O&M cost. Hence, the current trend is to incorporate more free space into the design, following the example of German plants with large spherical containment as well as the ABB-CE new

containment for the System S80+ plant. This approach requires larger containments. The requirement of passive cooling also necessitates large containments to provide sufficient heat transfer area and a large free volume. Higher design pressure allows for containments with smaller free volumes to accommodate blowdown, but necessitates a thicker pressure boundary and higher cost. Finally, it is desirable that the containment configuration be simple, to reduce the cost and shorten the construction schedule.

11.3 CONTAINMENT CONFIGURATION

There are several basic PWR containment configurations which have been built so far. These include:

- cylindrical reinforced concrete containment with steel liner,
- cylindrical double wall reinforced concrete containment ,
- free standing cylindrical steel containment with concrete shield building, and
- free standing spherical steel containment with concrete shield building.

Adoption for this application of either of the first two configurations, with concrete primary shell, have to be eliminated since they do not provide a passive cooling option. The choice between configurations 3 and 4 was made in favor of configuration 3 due to its larger heat transfer surface and the easier design of passive cooling passages compared to option 4. It is a proven design except for the air annulus, which needs to be modified to allow for passive air cooling. The shield building, which typically has limited venting capabilities, must now accommodate enhanced continual venting and cooling of the primary steel shell. The proposed configuration of a free standing cylindrical steel containment with concrete shield building, in an arrangement adapted to the passive pressure tube LWR, is shown in Figure 11-1.

The in-containment arrangement of primary system components for the conceptual pressure tube LWR design is very similar to that of CANDU reactors, and is based on the optimization study for the CE-CANDU done by

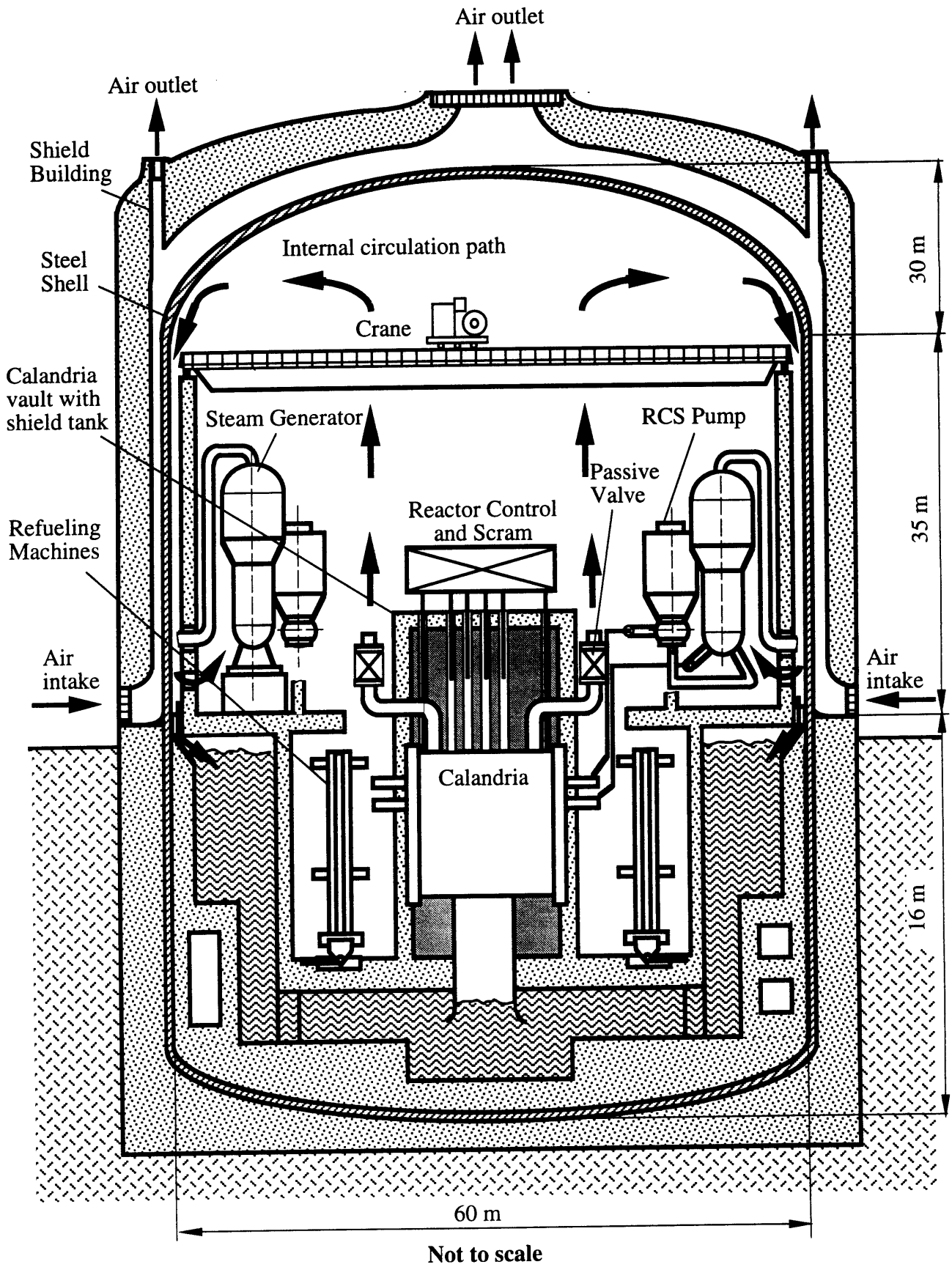


Figure 11-1 Schematic of containment arrangement for passive pressure tube LWR

Combustion Engineering, Inc.[Shapiro and Jesick, 1979]. Since the power of the CE-CANDU is uprated to 1260 MWe, as compared to the typical 600 MWe of conventional CANDUs, the size or the number of primary system components must be scaled up. The CE study considered two approaches of scaling up – six steam generators in a three-loop arrangement and two steam generators in a two-loop arrangement. The latter version is the same arrangement as in current CANDUs, except for the larger capacity. Therefore some development of larger-size steam generators and main coolant pumps, would be required. These are, however, still slightly smaller than those for current large LWR units, and within technology experience. Hence no problems are expected. The optimization study concluded that four steam generators in a two loop arrangement configuration is economically advantageous over the three-loop arrangement. In this arrangement, the containment diameter was found to be established by the length of the calandria and on-line refueling equipment space requirements; a containment shell inner diameter of 44.4m was found to be sufficient [Shapiro and Jesick, 1979]. For the presently proposed concept, two additional meters of diameter are needed to accommodate the side reflector. Moreover, some additional space is needed for flooding water located outside the calandria. The passive cooling requirement favors a large heat transfer surface, and hence large containment diameter. On the other hand, the large heat exchangers and pumps of CANDU moderator cooling systems are eliminated. Taking into consideration all these factors, and in particular, the desirability of a large heat transfer surface for passive cooling, a containment shell inner diameter of 60m was chosen. The minimum height of the containment is established by the space needed for the steam generators, and was taken to be the same as for CE-CANDU.

The resulting containment is a free standing cylindrical steel shell with a hemispherical dome surrounded by a vented annulus and reinforced concrete shield building. The steel shell has an inner diameter of 60 m, total height of 81 m, and thickness of 4 cm. It has an ellipsoidal shell at the base embedded in the reinforced concrete foundation mat. Part of the vertical cylindrical portion of the steel shell is also embedded in the reinforced concrete mat. This part has a height of about 16m. The upright

air-cooled cylindrical portion of the steel shell measures 35m. The hemispherical-shaped dome has a height of 30 m. The shield building is made of reinforced concrete of thickness of about 2m. Its main purpose is to protect the primary steel shell from external events, e.g. tornado or aircraft impact. It also provides radiation shielding if fission products are released into the containment. An annulus between the steel shell and the shield building is equipped with air intakes and air outlets to permit flow of ambient air. The air intakes are located above the ground level to avoid plugging by wind-entrained debris. Both the air intakes and the air exhaust are protected by grates to prevent the accidental entrance of large objects into the annulus. In addition to the large air outlet at the center of the containment dome, there are 20 small circular air outlets above the annulus gap. These outlets are dimensioned such that they accommodate about 40% of total air flow, thus decreasing air flow around the steel dome where flow area is limited. This design increases air velocity due to the smaller pressure drop at the exit. The chosen containment design is in many aspects similar to the concept studied by Ebasco for the New Production Reactor (NPR) [Williams et. al., 1993], or the concept studied by the Joint Siemens-Framatome venture - International Nuclear Power (NPI) [Erbacher and Neitzel, 1992]. Therefore, more development in this area is expected, the results of which would be readily applicable to the proposed pressure tube LWR concept.

An important characteristic of this containment design involves the location of primary system components relative to the air-cooled portion of the containment. Figure 11-1 shows the calandria and, especially, the entire pool with flood water located below ground level and not cooled by air. The purpose of this arrangement is twofold. First, it prevents rapid loss of flood water, should a severe seismic event disrupt the steel shell*. Second, all primary system components and piping are located in the lower region of the containment, which fixes the locations of potential breaks in the

* Note that in such case, even if the steel shell and concrete mat are disrupted, the leakage of flood water through the gaps in the concrete and into the soil would be small, thus giving the operators more time to replenish the water.

lower region. This assures good mixing of containment atmosphere following primary system blowdown. Full scale experiments have proven that in LOCAs with break locations in the upper containment region, the atmosphere in the containment does not get mixed and remains stratified [Wolf, 1993]. Such a situation is highly undesirable in a passively cooled containment because the effective heat transfer surface would be significantly decreased, since the substantial low-elevation portion of the containment wall which is not exposed to the hot steam would remain at low temperatures, and consequently yield very low heat transfer rates in this region. On the other hand, the HDR experiments showed that in LOCAs where the break is in the lower region, the containment atmosphere remains well mixed during the entire transient. Therefore placing primary system components subject to potential breaks in the lower region, as shown in Figure 11-1, significantly reduces the possibility of stratification. Nevertheless, a high-location break is possible in case of the rupture of steam lines from steam generators.

To prevent potential stratification, two features are designed into the containment. First, a crane wall supporting a polar crane creates a passage for promoting natural circulation in the passive cooling mode. As the arrows in Figure 11-1 show, the heated atmosphere rises inside the crane wall, is cooled along the containment shell and returns outside the crane wall. Condensate on the shell is returned back to the pool, while carry-under noncondensibles are recycled back through passages placed at low elevation. The crane wall also provides protection against missiles and fluid jets. A second important feature which would play a key role in eliminating eventual stratification is the low-elevation location of the steam exhaust lines from the calandria. Upon opening of a passive valve, which is followed by calandria flooding, all decay heat is removed in the form of steam released from the calandria. This steam will establish circulation patterns by entrainment of stagnant containment atmosphere in turbulent buoyant plumes rising from the valve exhaust piping to the top of the building. The importance of this fact will be emphasized by the analysis given in Section 11.5.3, which shows that the first pressure peak from the blowdown is of minor importance compared to the secondary pressure peak from decay heat. The secondary pressure peak sets the limit on passive

cooling performance, and at this critical time, the location of the steam exhaust responsible for this pressure peak is guaranteed always to be at a low elevation regardless of the break location. Both features would also facilitate hydrogen mixing, although it is noted that hydrogen release is very unlikely*.

Another important feature associated with the PTLWR containment is the flooding pool. As was shown in Chapter 8, its primary purpose is to flood the calandria and to provide a heat sink for the fuel. In the long term, it also absorbs significant energy as sensible heat and decreases heat load on the containment shell. The volume of the flooding pool is sized (4200 m³) to release its sensible heat gradually during the long-term pressurization period until the pressure peak is passed, thus decreasing both the rate of pressure rise and the magnitude of the peak. This approach has the advantage of allowing early steam release (after the flood water in the calandria, not the whole pool, reaches the saturation temperature) from the calandria in the form of a jet, thus promoting containment atmosphere mixing. An alternative approach is to employ a vapor suppression system similar to Turrichia's LIRA containment design [Turrichia, 1993], where the entire pool is brought to saturation first, thus significantly delaying the long-term pressurization phase. The same function can be accomplished in the proposed design by directing the exhaust pipes downstream of the passive valve back to the flooding pool, and by increasing the pool driving water head to maintain a sufficiently high calandria water level.

11.4 PASSIVE COOLING CONSIDERATIONS

Passive cooling of the containment is a challenge to the designer since relatively high heat transfer rates need to be removed by natural phenomena only, while the maximum design pressure, and hence the

* There is no hydrogen release from ceramic fuel. Hydrogen could be released from reaction of zircaloy calandria tubes with water if flooding comes later than about 15 minutes.

temperature difference between the containment wall and ambient, is limited. Consequently, the means to enhance the heat transfer rate is limited to only two variables - the heat transfer area and the heat transfer coefficient. Various passive cooling options have been reviewed in [Hejzlar et. al., 1993a] and analyzed in [Hejzlar et. al., 1991]. These options included:

- enhancement of the heat transfer coefficient
 - by replacing air cooling of part of the containment wall with an evaporating water pool,
 - by the use of a high chimney, and
 - by augmentation of the heat transfer surface (e.g. grooves, dimples or ribs);
- enhancement of the heat transfer surface area
 - by finning of the containment shell and
 - by increasing containment dimensions, i.e., diameter and height.

The above options are briefly summarized on Figure 11-2. A large containment shell with bare wall at a uniform temperature of 130°C having a diameter of 60m and an effective height of 65m was used as a reference case. The other alternatives considered use the same dimensions, but employ additional design changes to augment heat transfer, as shown on Figure 11-2. Decay power removable from each concept is also shown. The analysis tools used to evaluate these power levels are described in Appendix C.

The configuration with an evaporating water pool attains the highest removable power (50MWt). Another advantage of this configuration is that the power removed from the containment wall is the highest at the beginning of the transient, when the decay heat level is high, while at the later stage when the decay power is small the water has been evaporated, and heat energy is removed indefinitely by the air only. Problems associated with this design are threefold. First, to make efficient use of the high heat transfer potential of the pool, great care must be taken to maintain the containment atmosphere well mixed, so that the low portion of the containment shell facing the pool at the outside is exposed to a sufficiently

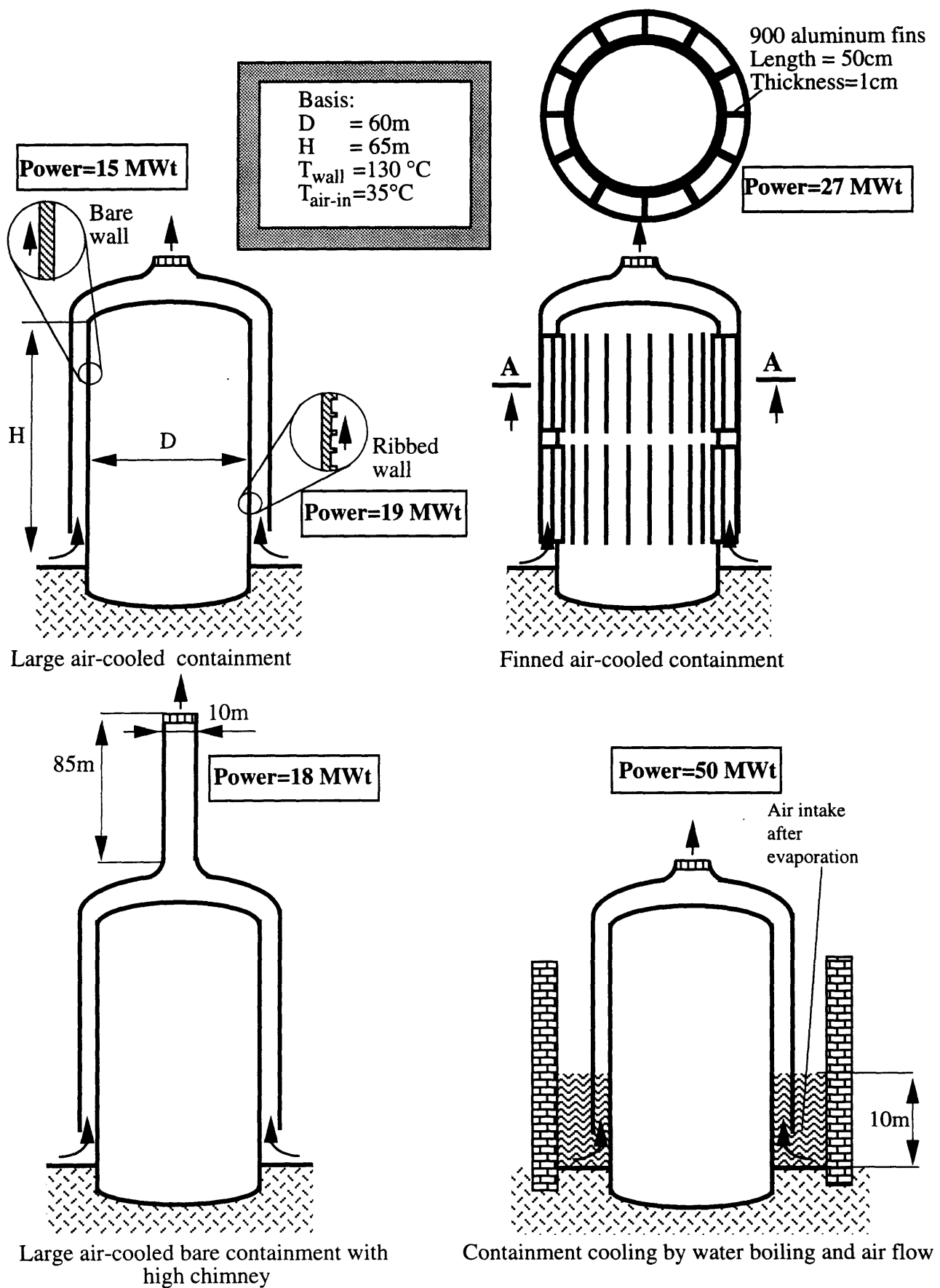


Figure 11-2 Considered alternatives for containment passive cooling

high driving temperature to initiate nucleate boiling. Second, the pool is vulnerable to large seismic events. Finally, the pool requires protection against freezing as well as maintenance and control of the steel shell to prevent its corrosion. Although these problems could be overcome, this option was rejected for the proposed concept. Moreover, the passive pressure tube LWR has a large quantity of water for flooding inside the containment, which provides a large heat sink and decreases the heat load on the containment shell. Hence the large heat transfer rates provided by the water pool at the outside are not needed. Note that the increase of heat transfer coefficient can be also accomplished by wetting the containment shell as in the Westinghouse design for AP600 [Slember, 1990]. Although this option provides an effective heat transfer enhancement and is not so sensitive to containment atmosphere stratification*, it requires a large amount of water located at high elevations, making it even more vulnerable to strong seismic events than the pool at the bottom. It also requires initiation of water flow at the right time—not an easy task to accomplish if completely passive actuation is required. In view of the above considerations, the choice of air cooling only was made.

Use of a high air chimney (attached for example to the cooling tower) was rejected for the following reasons. The attainable power (18 MWt) is less than some other alternatives, such as fins; moreover about the same power increase can be achieved by ribbing the containment wall – a much simpler technique. Additionally, such high structures would be prone to failure in large seismic events, and costly.

Fins can provide a significant enhancement of the heat transfer coefficient to the air. This was previously shown in scoping studies for LWR containments [Hejzlar et. al., 1991] as well as for the alternative cooling of a prestressed pressure vessel for the HTGR [Hejzlar et. al., 1993b]. However, they add complexity and increase the cost. Note that although the attainable

* This statement refers to the sensitivity to temperature stratification, i.e., from the heat transfer viewpoint, not to hydrogen stratification.

power (27MWt), shown on Figure 11-2, is large it is achieved by relatively long aluminum fins which would be difficult to weld to the steel shell.

A cheaper and easier to manufacture alternative is the use of ribs rolled into the outer surface of the steel plates from which the containment shell is assembled. Contrary to fins, which achieve heat transfer augmentation primarily by providing a larger heat transfer surface, repeated horizontal ribs on the hot containment wall disturb the laminar sublayer of turbulent flow and introduce more turbulence near the wall hence increasing the effective heat transfer coefficient. Thermal-hydraulic performance of ribs depends on Reynolds number, rib height to hydraulic diameter ratio, pitch to height ratio, rib shape and the flow attack angle. For a given Re number, the optimum performance was found to be for a pitch to height ratio of 10 and attack angle of 45° [Han, 1970]. Using Han's correlation [Han, 1970] and the optimum geometry parameters, rib height and annulus gap were optimized to maximize the removable power (see Appendix C for details). This maximum power (19MWt) is shown on Figure 11-2. The increase is about 80% compared to the bare-wall configuration.

The simplest alternative – an air-cooled large bare steel shell – was chosen as a containment for the passive pressure tube LWR. The analyses presented in Section 11.5 will show that adequate passive cooling of the proposed pressure tube LWR containment can be achieved at pressures which fall within the range of design pressures for large dry containments. Hence, the use of more complex alternatives is not warranted.

11.5 CONTAINMENT ANALYSIS

The purpose of this analysis is to show that the containment pressure in the limiting accident remains below the design limit using only passive cooling. Note that active systems such as containment sprays and fans are available, but no credit for the functioning of these systems is taken. First, a design basis accident for containment analysis will be defined.

11.5.1 Containment Design Basis and Beyond Design Basis Considerations

The U.S. code of federal regulations states that “the reactor containment structure, including access openings, penetrations, and the containment heat removal system shall be designed so that the containment structure and its internal compartments can accommodate, without exceeding the design leakage rate and with sufficient margin, the calculated pressure and temperature conditions resulting from any loss-of-coolant accident” [10 CFR 50, 1993, Appendix A, Criterion 50]. These margins should reflect the effects of potential energy sources which have not been included in the determination of the peak conditions (e.g. the energy in steam generators, energy from metal-water and other chemical reactions that may result from degradation but not total failure of the emergency cooling system), and limiting experimental data available for defining accident phenomena as well as the conservatism of the calculational model and input parameters.

Since the containment response must be satisfactory in any loss-of-coolant accident, the entire spectrum of postulated LOCAs, including size and location, needs to be evaluated and the limiting LOCA with respect to containment conditions identified. In LWRs, typically the most important postulated LOCAs include either loss-of-primary coolant, steam line break or feedwater line break. Multiple breaks (e.g. LOCA and steam line break) are beyond the design basis scope. Detailed analysis of the entire spectrum of potential accidents including various break sizes is beyond the scope of the present work, moreover it is not fully possible at this stage of conceptual design since data on all systems involved are not available. Typically, the design pressure in both PWRs and CANDUs is derived from the primary system LOCA, but the steam line break accident (SLB) may also result in high pressures. In SLB accidents, the discharged steam becomes superheated if the SG water level falls below the top of the tube bundles, and can cause higher containment wall temperatures. Hence, these two accident scenarios – primary system LOCA and steam line break, both with double ended breaks – will be considered.

The United States Nuclear Regulatory Commission’s (USNRC) acceptance criteria specify that “the loss-of-coolant accident analysis

should be based on the assumption of loss of offsite power and the most severe single active failure in the emergency power system (e.g. diesel generator failure), the containment heat removal systems (e.g., a fan, pump, or a valve failure) or the core cooling systems (e.g., a pump or valve failure)”[USNRC,1987]. In the dry calandria design, these criteria are more than satisfied, since the PTLWR employs no diesel generators, nor does it need an ECCS. Regarding the active containment cooling systems such as sprays and fans, no credit for their function will be taken in the analysis.

The design of the CE-CANDU primary system, also adopted in the PTLWR, employs an isolation valve, placed in the line connecting the two independent loops to the pressurizer, which isolates the unbroken loop on containment high pressure. Hence not all the primary system inventory would be blown down. Nevertheless, since the USNRC acceptance criteria for containment analysis of postulated secondary system pipe ruptures requires one to take into consideration the most severe active failure of secondary system isolation provisions (e.g. main steam line isolation failure)[USNRC,1987], complete failure of this isolation valve in the PTLWR primary system loop will also be assumed.

For the CE-CANDU reactor, the limiting design basis accident for containment analysis was identified to be a double-ended rupture of a hot header at the surge line connection [Shapiro and Jesick, 1979]. The schematic layout of the primary system with break location is shown in Figure 11-3. Since the primary system of the PTLWR, except for fuel channels, is identical to the CE-CANDU primary system, the same scenario of primary system break will be assumed for the PTLWR. In accordance with the the USNRC criteria, simultaneous failure of the isolation valve between the loops is also assumed.

Four cases will be analyzed:

- 1.Double-ended rupture of a hot header at the surge line connection, with isolation valve functioning.
- 2.Double-ended rupture of a hot header at the surge line connection combined with isolation valve failure.
- 3.Main steam line break with main steam isolation valve (MSIV) failure.

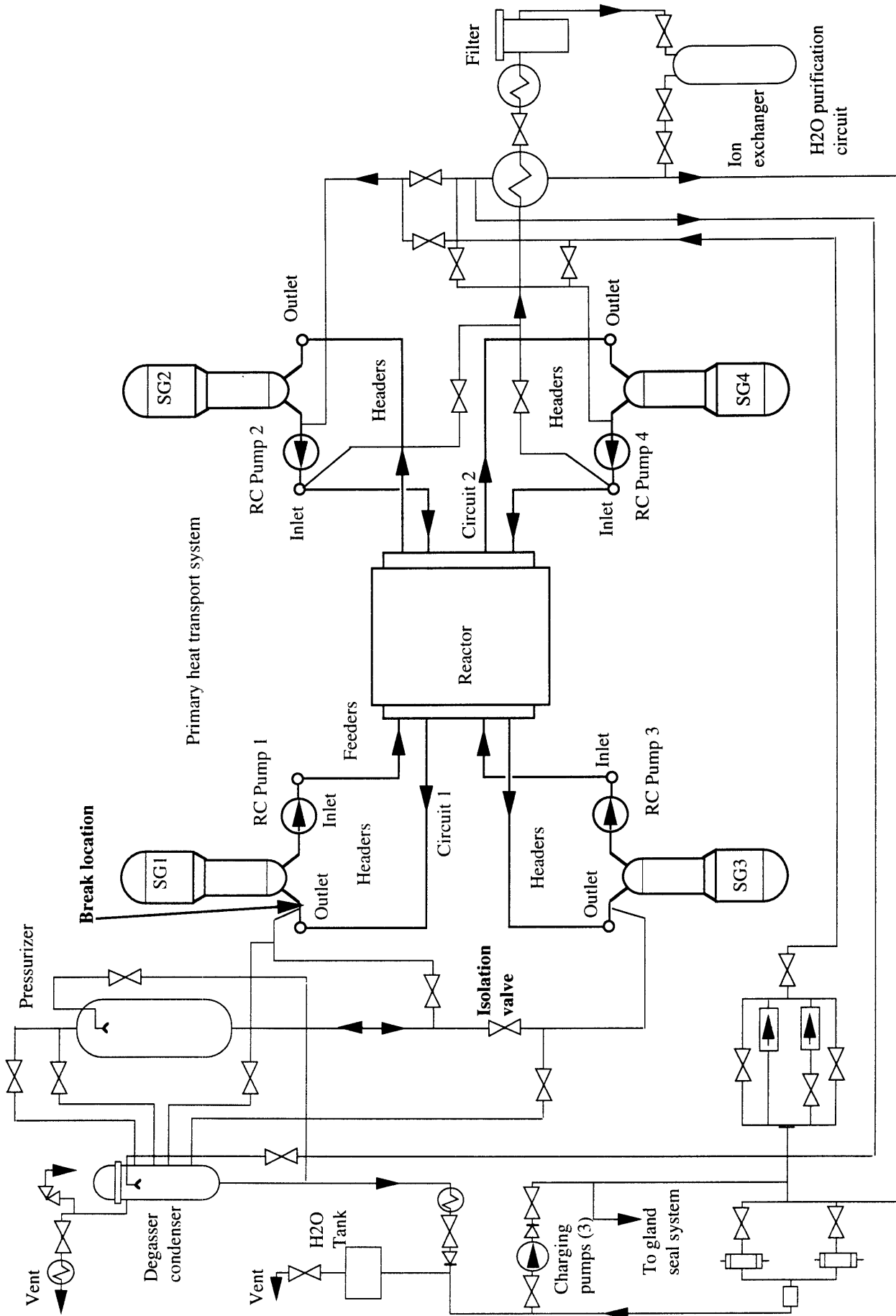


Figure 11-3 Schematic flow diagram of primary system with break location (from Shapiro and Jesick, 1979)

4. Combined double-ended rupture of a hot header at the surge line connection with isolation valve failure and main steam line break (cases 2 and 3 combined).

Case 1 is the most likely scenario if a primary system break occurs, and is included for comparative purposes. Case 2 assumes isolation valve failure to comply with USNRC acceptance criteria. Case 3 assumes a main steam line break with simultaneous MSIV failure. The higher pressure or temperature resulting from either case 2 or case 3 will establish the DBA conditions. Case 4 assumes coupled failure of both primary and secondary systems, which could hypothetically happen during a severe seismic event. The purpose of the last case is to evaluate containment response beyond the DBA scenario.

Finally, it should be noted that recently, strong attention has been paid to containment performance in severe accident sequences resulting in core melt. Although these scenarios are in the category of beyond DBA, it is desirable that the containment barrier retains its protection function even under the extreme conditions posed by these events. Again, the detailed severe accident analysis of the proposed containment concept is beyond the scope of this conceptual design, as the detailed layout and dimensions of all containment compartments and equipment would be needed. Moreover, it is expected that core melting in the proposed reactor would be possible only should the calandria flooding hypothetically fail. This is very unlikely because

- the system is passive, works at low pressure and does not depend on electric power,
- there are several redundant and diverse valves,
- there is a long time available for the operator to initiate flooding manually, if everything else fails.

Even if core melt was initiated, the corium would fall into the large cool water pool which is in direct communication with the calandria space, where it would be quenched, and the decay heat would be ultimately removed. This would be accomplished by boiling and steam evaporation and condensation on containment walls. The advantage of this design is that

the flooding water is already available to mitigate the consequences of a severe accident with corium melt.

Regarding hydrogen issues associated with severe accidents, the following comments will be made at this stage of the study. First, hydrogen generation from the fuel matrix will be very small and only at high temperatures, because the kinetics of the SiC and graphite reactions are much slower than for the Zircaloy-water reaction. Thus the total amount of both the heat and hydrogen gas per kg are significantly less than from a typical LWR fuel. However, there is a hypothetical possibility of H₂ generation from the Zircaloy pressure tubes and calandria tubes should these reach the temperature for significant Zircaloy-water reaction (about 1200°C), if flooding fails. To prevent hydrogen concentration buildup from reaching explosive limits, catalytic igniters and recombiners developed by Siemens [Heck et. al., 1991] can be deployed in the containment. These devices do not require any external power source and remain fully functional during the entire accident, which is in accord with the overall passive concept.

11.5.2 Analysis tools

There are two computer codes used for the analysis of the proposed PTLWR containment – CONTAIN and GOTHIC. The CONTAIN computer code [Murata et. al., 1990] was selected as the main analysis tool for long-term pressurization. The GOTHIC computer code [George et. al., 1991] was primarily used to study thermal stratification effects inside the containment. In addition, a separate computer code RISRAD was developed to calculate passive air cooling of a containment wall. The results from this code were coupled to the CONTAIN 1-cell model and to scale the heat transfer coefficient in GOTHIC from natural turbulent convection heat transfer correlation values to the values appropriate for an air annulus. The code RISRAD is described in Appendix C.

11.5.2.1 CONTAIN Computer Code

The CONTAIN code was developed at Sandia National Laboratories under sponsorship of the USNRC. In addition to the capabilities of calculating physical conditions in DBAs (analyzed in this work), it can predict chemical, and radiological conditions inside the containment building following the release of radioactive material from the primary system under severe accident conditions. The phenomena modeled include:

- steam/air thermodynamics,
- aerosol behavior,
- fission product behavior,
- intercell flow,
- condensation/evaporation on structures and aerosols,
- heat conduction in structures,
- radiative heat transfer,
- core/concrete interactions,
- radioactive heating, and
- thermal-hydraulic and fission product decontamination aspects of engineered safety features.

It is clear from the above review that the CONTAIN code is a rather robust tool for DBA analysis where severe accident phenomena do not come into play. The DBA analysis could be done by CONTEMPT [Hargroves, 1979] or GOTHIC. Nevertheless, the CONTAIN code was chosen as the main analysis tool because it can calculate a long-term pressurization transient in less CPU time than GOTHIC. Another advantage of CONTAIN is that it employs logic which enables switching between natural convection and forced convection for heat transfer between structures and atmosphere, where appropriate. The current version of GOTHIC employs only a natural convection correlation which leads to significant underestimation of the heat transfer coefficient from the containment shell to air in the present situation. The input data structure of CONTAIN enables the user to invoke only those models which are needed for the analysis. Hence, the models which are not pertinent to the analyzed case are easily eliminated from the computational flow.

CONTAIN treats a containment system as a network of interconnected cells which communicate with each other by means of gas flow, liquid flow and/or heat flow. Each cell is divided into two subcells – the upper cell, which consists of a gaseous atmosphere and the heat transfer structures, and the optional lower cell, which can include a coolant pool, layers of fuel debris, molten metal, molten concrete and a concrete floor. The upper atmosphere is assumed to be thoroughly mixed. The drawback of this lumped parameter approach is the difficulty in correctly predicting flow patterns within the volume, and handling stratification effects. Although the proposed PTLWR containment is designed to avoid potential thermal stratification, it is necessary to verify that the design is working correctly regarding this aspect and that the assumption of a well-mixed atmosphere holds. To handle stratification effects in CONTAIN, the containment volume must be subdivided into a large number of smaller cells. This would result in high CPU requirements and still would not necessarily guarantee correct results since the buoyant plume behavior requires solution of a finite difference nodalization of the momentum and energy equations, including turbulence. Thermal stratification phenomena will be assessed in a separate Section 11.5.5 using the GOTHIC code.

The CONTAIN code has been extensively verified and validated with experimental data. Some validation exercises are reviewed in [Murata et. al., 1989]. With respect to large LOCAs within the scope of the DBA investigated here, some of the most important validation data sets were obtained from German tests at HDR [Wind,1983]. The thermal-hydraulic conditions for a full scale steam blowdown LOCA simulated at HDR were calculated by CONTAIN in a blind prediction mode. Temperatures and pressures predicted for this design basis accident over a wide range of time scales were in excellent agreement with experimental data [Murata et. al., 1990]. This test, however, did not result in stratified conditions. As mentioned above, care must be taken if the containment atmosphere becomes thermally stratified. In such cases, the assumption of a thoroughly mixed atmosphere does not hold, so that incorrect containment wall temperature predictions would result.

Two models of the PTLWR containment were built – a 1-cell model and a 9-cell model. The 1-cell model describes the entire containment as one cell with boundary conditions at the containment walls. Boundary conditions are calculated by a separate code RISRAD. It is intended for fast parametric studies. The 9-cell model describes the containment by 5 cells and the passive cooling configuration with outside environment by 4 cells. It is used to confirm the results of the 1-cell model and to check the flow patterns inside the containment.

11.5.2.2 GOTHIC Computer Code

GOTHIC is a general purpose thermal-hydraulic code package for analyses of nuclear plant containment/confinement buildings. The code is based on the COBRA-NC [Wheeler et. al., 1986] package for containment analysis, but a significant amount of improvements of both the models and modeling capability has been done since [George et. al., 1991].

GOTHIC solves mass, momentum and energy balances for three separate phases – vapor, continuous liquid and droplets. The phases can be in thermal nonequilibrium, with each phase having its own temperature and velocity. Interface mass, momentum and energy transfer is calculated by mechanistic models. In addition, the vapor phase can consist of a mixture of steam and noncondensable gases, and a separate mass balance is maintained for each component of this multicomponent mixture. The code incorporates heat conduction in structures and specific models for engineered safety equipment, such as pumps, heat exchangers, fans, valves and vacuum breakers. The drawbacks of the current version are the absence of radiative heat transfer and limitation of the convective heat transfer correlation between a structure wall and the fluid to a natural convection-type, which is not appropriate for strong buoyancy-induced flows such as encountered in passive air cooling.

A major advantage of GOTHIC is the option for 3-D analysis of the thermalhydraulic behavior of containment atmosphere in selected volumes. Full treatment of momentum transport, including the option of a

one-parameter anisotropic turbulence model, enables the analyst to simulate buoyant plumes and to correctly predict the temperature distribution and natural circulation patterns inside a containment with a stratified atmosphere. Lumped parameter modeling or combination of lumped parameter models with 2-D or 3-D models of selected volumes is also possible. The code has been verified on a wide range of analytic tests and large-scale experimental tests, the latest being the tests performed on the HDR containment in Germany [Wolf, 1993]. GOTHIC results show relatively good agreement with experimental data [Wolf et. al., 1994] which includes stratified containment conditions.

11.5.3 A 1-Cell CONTAIN Model

The 1-cell model treats the entire free volume of the containment as one cell. The cell is enclosed by a cylindrical wall and a spherical dome-shape wall, both air-cooled at the outside, and contains internal concrete and steel heat sinks.

Passive cooling of the containment shell is calculated by a separate code RISRAD described in Appendix C. RISRAD calculates buoyancy-induced air flow through the annulus between the containment shell and the shield wall and heat transfer from the containment shell by convection and radiation. The advantage of RISRAD is that it can use very fine nodalization, and hence evaluate buoyancy driving force better than it would be possible with CONTAIN (fine nodalization of the air riser would require excessive computer run time). It also uses a heat transfer correlation obtained experimentally on a riser geometry under conditions very close to those experienced in the PTLWR annulus. Boundary conditions in RISRAD are either axial heat flux profile or hot wall temperature profile. The coupling between CONTAIN and RISRAD is established via hot wall temperature at the outer surface as follows. Using the axially constant containment shell wall temperature and optimum annulus gap thickness (see Appendix C for the discussion of optimum gap), RISRAD is run to obtain power removable from the shell. Then the effective heat transfer coefficient with respect to air inlet temperature, $T_{air,in}$, is calculated as a function of the wall temperature only, i.e.,

$$h_{\text{eff}}(T_{\text{wall}}) = \frac{\dot{Q}_{\text{tot}}(T_{\text{wall}})}{S_{\text{wall}}(T_{\text{wall}} - T_{\text{air,in}})} \quad (11-1)$$

where \dot{Q}_{tot} is the total power removed from the containment shell and S_{wall} is the heat transfer surface of the containment shell,

$$S_{\text{wall}} = \pi D_{\text{wall,o}} H_{\text{wall-air}} + \frac{1}{2} \left[4 \pi \left(\frac{D_{\text{wall,o}}}{2} \right)^2 \right] \quad (11-2)$$

$H_{\text{wall-air}}$ is the height of the air-cooled cylindrical portion of the containment shell. Note that the effective heat transfer coefficient includes both convection and radiation. Both the power and the effective heat transfer coefficient from Eq. (11-1) are shown as a function of containment wall temperature on Figure 11-4. Power deviates from linear dependence due to the increasing contribution of radiation, since radiative heat transfer varies with the fourth power, compared to convective heat transfer which is proportional to the first power.

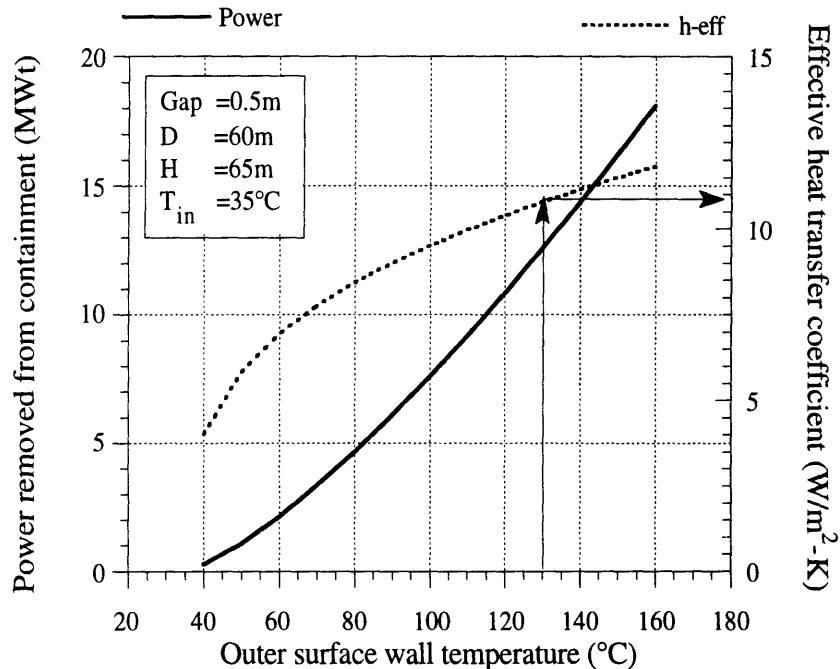
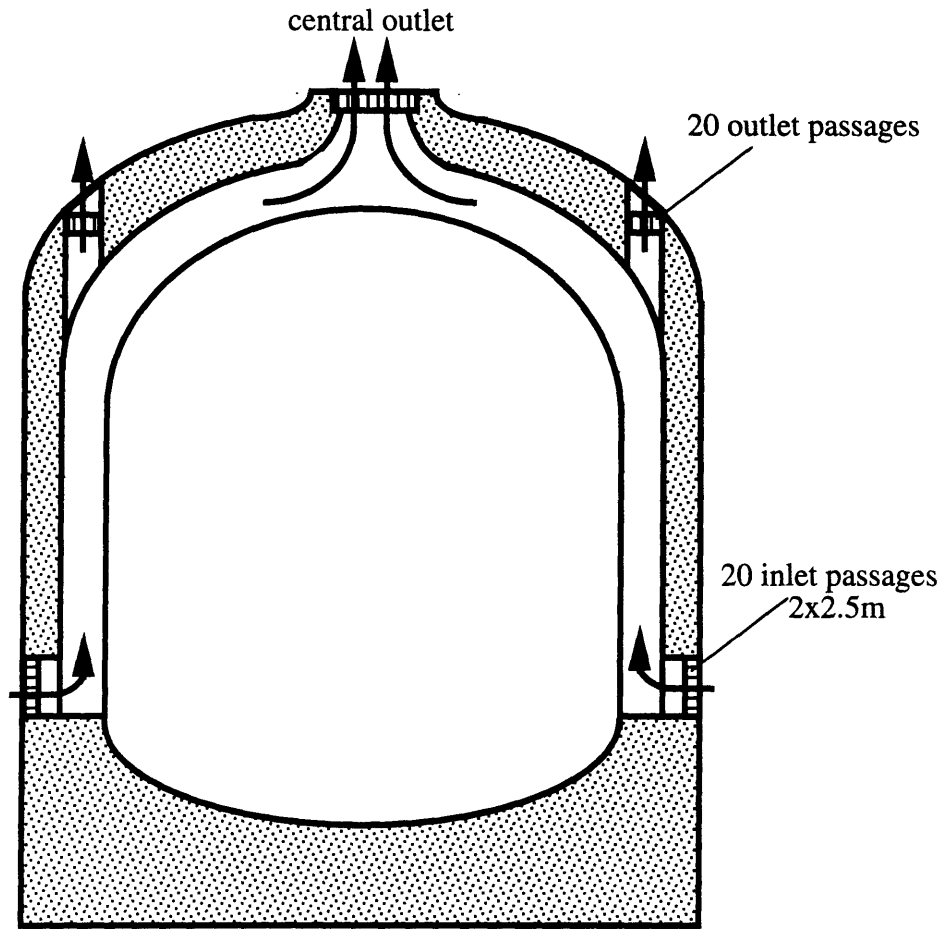


Figure 11-4 Effective heat transfer coefficient and power as a function of containment wall temperature

Key annulus parameters used as input data in RISRAD are also shown on Figure 11-4. The performance of air cooling is strongly dependent on the design of air inlet and outlet ducting. It is desirable that the flow area of both the inlet and outlet ducting is large and the form losses small, to minimize pressure losses across these ducts. The flow area is, however, limited to maintain good structural integrity of the concrete shell. Figure 11-5 shows the proposed design of air inlet and outlet ducting. There are 20 inlet passages evenly distributed around the circumference and provided with grates. Form losses of inlet and outlet air passages with grates were taken from [Idelchik,1986] as 2.4 and 3, respectively. Air outlet ducting consists of two different passages – the central hole and 20 much smaller passages above the annular gap, as shown in Figure 11-5. This arrangement decreases the pressure loss at the outlet without making the central passage too large, and still provides sufficient cooling of the dome. The dimensions of the central hole and small passages are chosen such that 60% of the flow proceeds through the central hole and 40% is via the passages. The results presented in Figure 11-4 are based on this arrangement of inlet and outlet passages.

The reference air inlet temperature in Eq. (11-1) was chosen because CONTAIN allows only one input variable to vary with time – either heat transfer coefficient or the air bulk temperature, but not both. The air inlet temperature, which remains constant during the entire transient, is used as a constant boundary condition in CONTAIN, and the effective heat transfer coefficient is the time-dependent boundary condition. Power removed from the containment thus exactly corresponds to the power calculated by RISRAD. However, iterations between RISRAD results and CONTAIN are necessary as the containment wall temperature, which depends on heat transfer coefficient to air, is not known a priori. This is accomplished using an estimated h_{eff} -time curve for the first containment run and updating the curve using Figure 11-4 and the T_{wall} -time curve obtained by CONTAIN. Since the time constant of the wall is large, only 1 iteration is necessary, i.e., two CONTAIN runs are sufficient to converge. To facilitate this process, an interface program was written, which processes CONTAIN output and RISRAD output to create the h_{eff} -time curve used as input data for the next CONTAIN run.



Top view

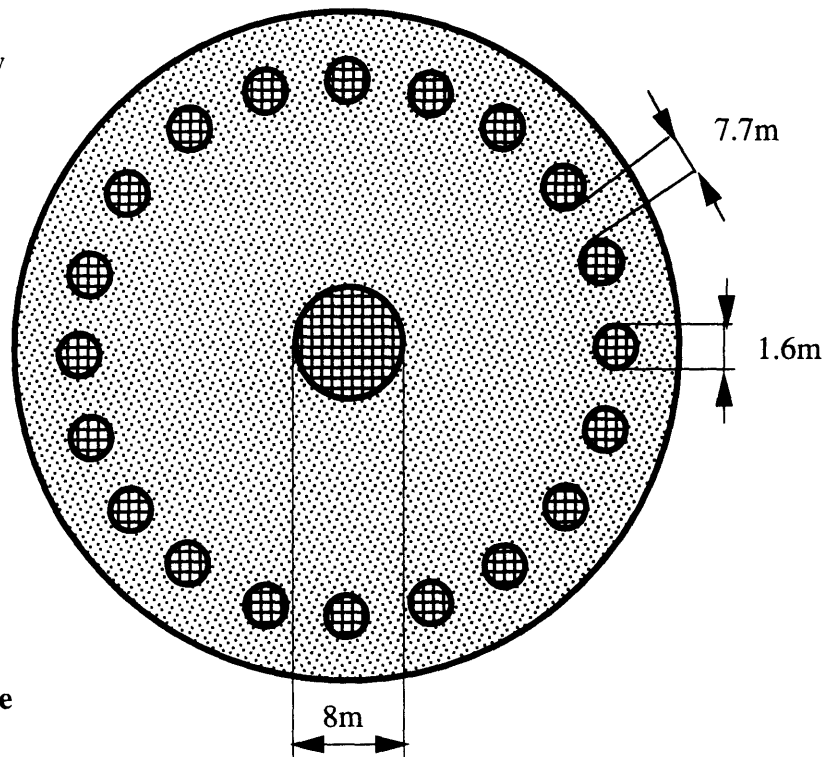


Figure 11-5 Arrangement and dimensions of air inlet and outlet passages

11.5.3.1 Case 1 Double-ended rupture of a hot header at the surge line connection with isolation valve functioning.

The first case to be analyzed represents a typical primary system LOCA for the CE-CANDU reactor. The accident sequence is given in Table 11-1.

Table 11-1 Accident sequence for containment analysis-Case 1

Time (seconds)	Event
0	Double ended rupture in a hot leg at the surge line connection, coupled with station blackout
5	Calandria flooding is initiated from low primary pressure
7	Unaffected loop and pressurizer are isolated by a valve which closes on containment high pressure (0.14MPa). The valve closure time was assumed to be 6 seconds, including 1 second actuation delay
10	Blowdown of the entire affected loop ends
30	Flooding of the entire calandria is accomplished.
550	Decay heat and released stored energy from reflector and fuel matrix starts the evaporation of steam from the calandria

CONTAIN Input data

To be able to evaluate containment response to a LOCA, an evaluation of the mass/energy releases from the ruptured primary system must be made. Mass and energy inventory in the primary and secondary systems were taken from CE-CANDU data [Shapiro and Jesick, 1979], and are summarized in Table 11-2. The primary system for the proposed dry calandria design is kept identical to CE-CANDU except for fuel channels. The fuel channels for the dry calandria design are longer by 2 meters because of the side reflector, but have less flow area. There are also additional unfueled pressure tubes for the cooling of the radial reflector.

Taking into account all these differences results in a slightly larger volume (by about 15%) of dry calandria channels compared to the CE-CANDU design. Since, the channels constitute only 5% of the total primary coolant inventory, this difference is negligible, i.e., 0.7%. More significant is the difference between light water and heavy water density. Light water is lighter by about 9% than heavy water at the same operating conditions, which makes the H₂O coolant inventory smaller compared to a D₂O inventory in the same volume. Nevertheless, the analysis in this study will use the CE-CANDU heavy water discharge data, i.e., conservatively slightly higher discharge mass rates. Other conservatisms employed in generating the CE-CANDU discharge data are:

Table 11-2 Mass and energy inventory for the proposed pressure tube LWR
(adapted from Shapiro and Jesick, 1979)

Component	Coolant Volume* (m ³)	Coolant Mass (kg)	Coolant Energy † (J)	Metal Energy † (J)
Affected Loop - Primary	214.8	146,817	2.1x10 ¹¹	1.5x10 ¹¹
Affected Loop - Core	--	--	--	1.6x10 ¹⁰
Unaffected Loop - Primary	214.8	146,817	2.1x10 ¹¹	1.5x10 ¹¹
Unaffected Loop - Core	--	--	--	1.6x10 ¹⁰
Pressurizer & Surge Line				2.6x10 ¹⁰
Liquid	38.7	22,964	3.7x10 ¹⁰	
Steam	27.6	2,809	7.4x10 ⁹	
Steam Generator (1 of 4)				4.0x10 ¹⁰
Liquid	67.1	48,801	6.3x10 ¹⁰	
Steam	114	4,653	1.1x10 ¹⁰	

*Volumes in the table include the increase to account for pressure and temperature expansion from operating conditions to room temperature.

† Relative to 0°C

- no credit for flow resistance from the affected primary loop to the break was taken,
- no credit for steam binding.

CANDU reactors, as well as the dry calandria design, have smaller primary coolant inventory than PWRs. As shown in Table 11-3, which

Table 11-3 Comparison of mass and energy primary system inventory for PWR, CANDU, CE-CANDU and PTLWR *.

	PWR	CANDU	CE-CANDU	PTLWR
Power (MWth)	3411	2180	4029	3899
Volume* of primary coolant (m ³)	3.4x10 ⁵	1.2x10 ⁵	2.9x10 ⁵	2.9x10 ⁵
Pressure (MPa)	15.5	10	15	15
Average coolant temperature (°C)	308.5	288.5	318	318
Average density (kg/m ³)	708.35	810	684	680
Coolant mass (kg)	2.4x10 ⁵	9.7x10 ⁴	2x10 ⁵	2x10 ⁵
Coolant mass per MWth (kg/MWth)	70.6	44.5	49.6	51.3
Energy (J)	3.3x10 ¹¹	1.2x10 ¹¹	2.9x10 ¹¹	2.9x10 ¹¹
Energy per MWth (J/MWth)	9.7x10 ⁷	5.7x10 ⁷	7.2x10 ⁷	7.4x10 ⁷

* Before expansion

** Parameters for CANDU and PWR taken from [Knief, 1992], parameters for CE-CANDU taken from [Shapiro and Jesick, 1979].

compares primary system coolant mass and energy inventories for the PWR, a typical CANDU, the CE-CANDU and the dry calandria design, the mass inventory of the dry calandria design is about 25% less than the PWR

inventory. Moreover, if the isolation valve closes, a substantial portion of primary coolant will not be released into the containment. Hence, the pressure peak from primary system blowdown is expected to be relatively low.

Mass/energy release data (obtained from CE-CANDU analysis [Shapiro and Jesick, 1979]) are given in Figures 11-6 through Figure 11-9. Figure 11-6 and Figure 11-7 represent the release from the unaffected loop. The unaffected loop and the pressurizer are assumed to be isolated from the containment at the 7th second. Isolation is based on 1 second delay time to reach the containment pressure setpoint of 1.35 ata, a 1 second instrumentation delay, and 5 seconds for valve closure. Figures 11-7 and 11-8 give the release data from the affected loop. The loop blows down completely during a 10 second period [Shapiro and Jesick, 1979]. No metal to water heat transfer was considered during the blowdown.

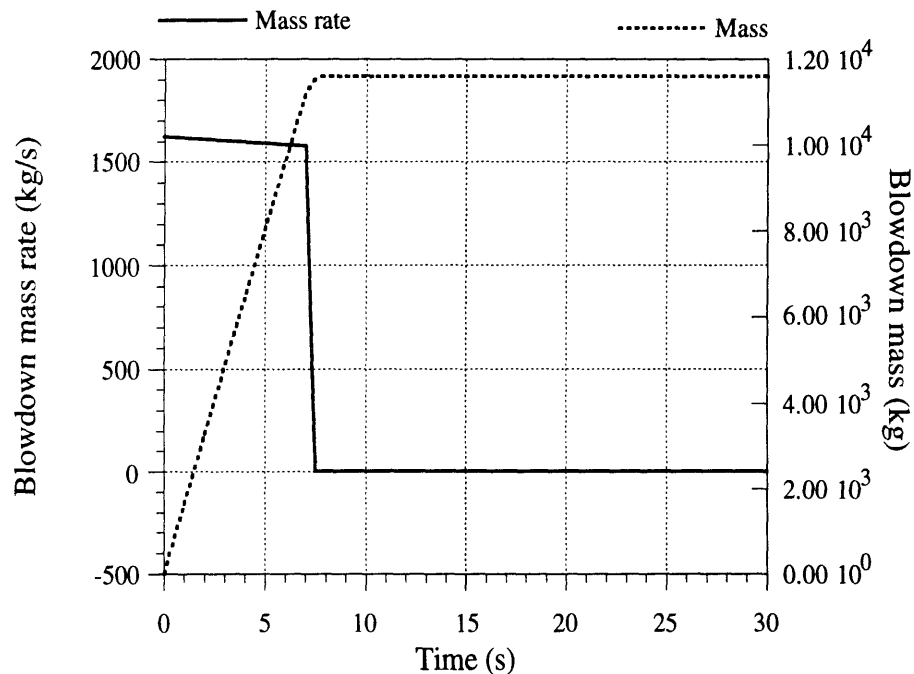


Figure 11-6 Case 1 - mass release from unaffected loop following the break of an outlet header

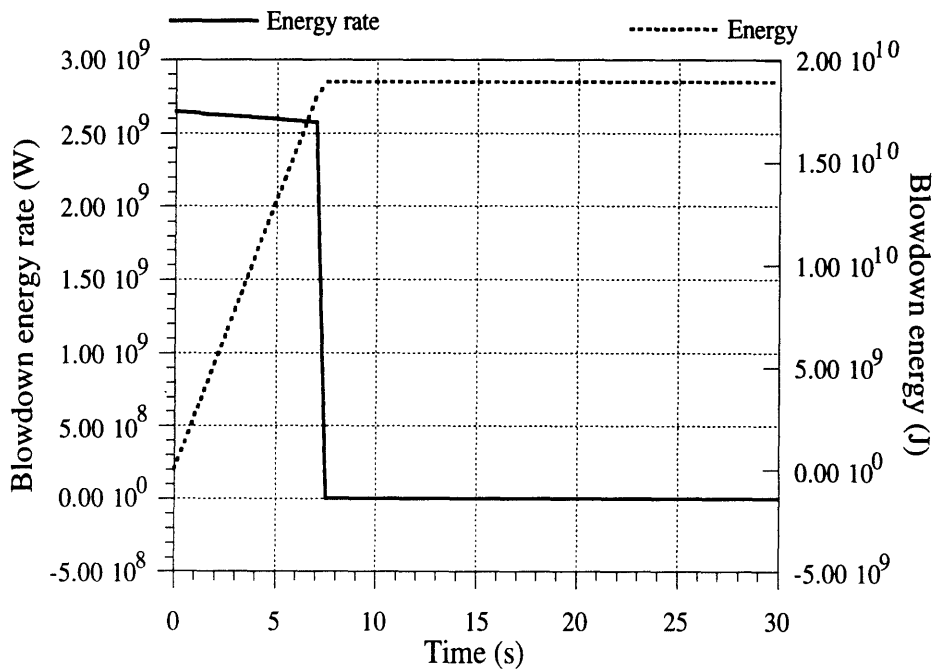


Figure 11-7 Case 1 - energy release from unaffected loop following the break of an outlet header

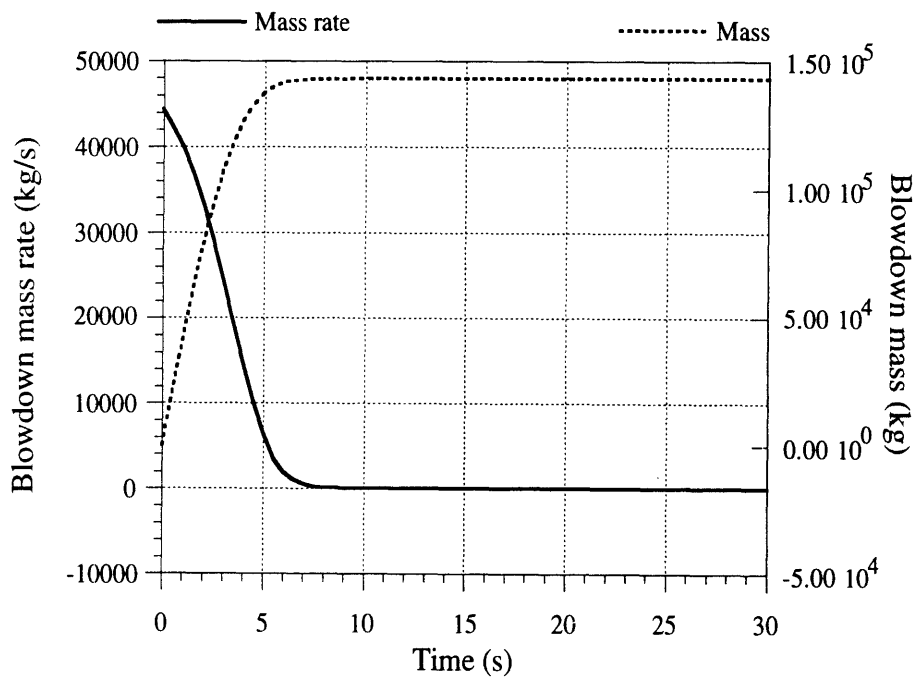


Figure 11-8 Case 1 - mass release from affected loop following the break of an outlet header

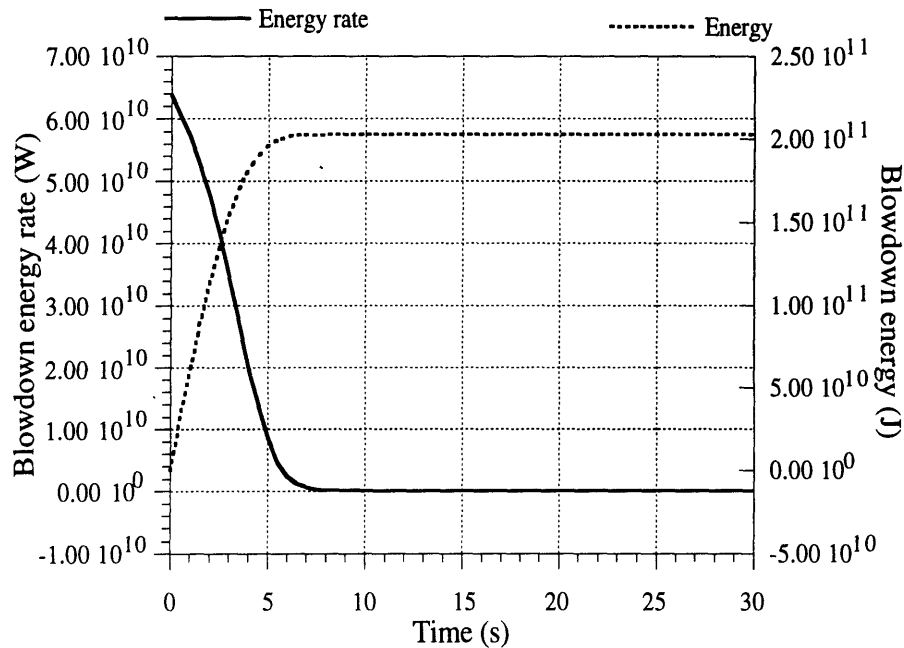


Figure 11-9 Case 1 - energy release from affected loop following the break of an outlet header

Besides the energy from the primary coolant, other energy sources need to be taken into account. USNRC acceptance criteria specify that the following sources of energy should be considered in analysis of loss-of-coolant accidents:

- reactor power,
- decay heat,
- stored energy in the core,
- stored energy in the reactor system metal, including the reactor vessel and reactor vessel internals,
- metal-water reaction energy, and
- stored energy in the secondary system including the SG tubing and secondary water.[USNRC, 1987]

Reactor power will be calculated in the LOCA without scram scenario, i.e., no credit for the functioning of shutdown systems is taken. Contrary to CE-CANDU, which begins the reflood phase at 10.1 seconds, there is no energy release from reflood in the dry calandria design, because no emergency cooling system is present. All decay heat, and stored energy in

the core and reactor vessel including stored (Wigner) energy released from graphite is deposited in flooding water in the calandria with subsequent boil-off. This time-dependent energy source, i.e., steam flow from the calandria, is obtained from the separate model described in the next section. Stored energy in the reactor system metal outside the vessel is typically removed during the ECCS reflooding phase in LWRs. Primary system piping remains dry after blowdown in the absence of ECCS cooling in the proposed dry calandria design. Hence its energy release to the containment atmosphere will be through direct heating and evaporation of water droplets from hot surfaces. This hot primary system metal will be modeled separately by slab heat sources of initial uniform temperature corresponding to the average temperature of out-of-core primary system metal, having two representative thicknesses, $t_1=0.5\text{cm}$ and $t_2=5\text{cm}$. The effective surfaces of the slabs were determined from the metal energies given in Table 11-2 and an initial uniform temperature, T_{init} ,

$$S_1 = \frac{E_1 [c_p (T_{\text{init}} - 0^\circ\text{C})]}{\rho t_1} ; S_2 = \frac{E_2 [c_p (T_{\text{init}} - 0^\circ\text{C})]}{\rho t_2} , \quad (11-3,4)$$

where E_1 is the stored energy in the metal with representative thickness t_1 , and E_2 is the stored energy in the metal with representative thickness t_2 . No metal water reaction in the proposed design was considered, since the maximum Zircaloy temperatures do not exceed 500°C .

Mass/energy release from calandria

The decay heat from the fuel and stored energy from the core metal and reflector are removed through the heatup and boil-off of flooding water. The sequence of mass/energy release from the calandria is assumed according to Table 11-4.

The following stored energy is assumed to be released immediately into the flooded calandria:

- energy stored in pressure tubes

$$E_{\text{PT}} = N_{\text{ch}} L_c \frac{\pi}{4} (D_{\text{PT0}}^2 - D_{\text{PTi}}^2) \rho_{\text{Zy}} c_{\text{Zy}} (\bar{T}_{\text{PT}}) (\bar{T}_{\text{PT}} - \bar{T}_{\text{PT0}}) , \quad (11-5)$$

Table 11-4 Events assumed to calculate mass/energy release data from calandria

Time period	Event
0- $\tau_{\text{flood-end}}$	<p>Flooding of calandria, all energy stored in the calandria tube, pressure tube and reflector liner are released into flood water (no steam is released from calandria)</p> <p>Energy from fission and Wigner energy release are stored in fuel matrix</p>
$\tau_{\text{flood-end}}$ - $\tau_{\text{saturation}}$	<p>Decay heat*, initial stored energy in fuel matrix, including Wigner energy release, and fission energy and heat transferred from the reflector, heat up the flood water in the calandria until saturation temperature is reached (no steam is released from the calandria)</p>
$\tau_{\text{saturation}}$ - τ_{infinity}	<p>Decay heat, initial stored energy in fuel matrix, including Wigner energy release and fission energy and heat transferred from the reflector, evaporate the steam escaping from the calandria into the containment</p>

*The decay heat curve is the ANS curve including decay heat from gammas directly heating the flood water (compare to decay heating of fuel matrix which is less by the portion of gamma heat deposited in the flood water).

- energy stored in calandria tubes

$$E_{CT} = N_{ch} L_c \frac{\pi}{4} (D_{CT0}^2 - D_{CTi}^2) \rho_{Zy} c_{Zy} (\bar{T}_{CT}) (\bar{T}_{CT} - \bar{T}_{CT0}), \text{ and} \quad (11-6)$$

- energy stored in reflector liner

$$E_{RL} = \left(L_c \pi D_c t_{RL} + 2 \frac{\pi}{4} D_c^2 t_{RL} \right) \rho_{Zy} c_{Zy} (\bar{T}_{RL}) (\bar{T}_{RL} - \bar{T}_{RL0}) \quad (11-7)$$

Energy release from the reflector is calculated using the following simplifying assumptions:

- reflector wall can be represented by a lumped parameter model with average integral temperature

$$\bar{T}_R = \frac{1}{t_R} \int_0^{t_R} T(x) dx \quad (11-8)$$

- thermal resistance of the reflector liner and thermal resistance of liner wall-flood water interface (subcooled boiling or saturated boiling) can be neglected compared to the resistance of the thick reflector wall,
- the effective conduction length can be taken as 1/3 of the reflector thickness, and
- the bulk temperature of the flood water in the calandria is kept constant, and equal to the saturation temperature, throughout the entire transient.

Figure 11-10 shows the calculational model of the reflector. The time dependent conduction equation with ΔT as the main dependent variable can be written

$$m_R c_{pR} \frac{d(\Delta T)}{dt} = k_R \frac{\Delta T}{t_R/3} S_R \quad (11-9)$$

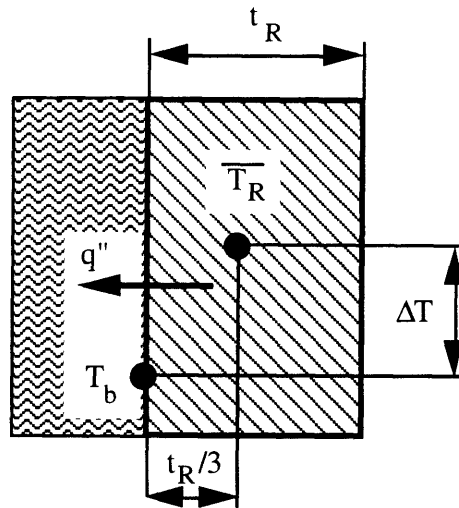


Figure 11-10 Simplified representation of reflector wall for calculation of energy release

where ΔT is the temperature difference between the reflector lumped-parameter temperature, \bar{T}_R , and bulk flood water temperature, T_{sat} . S_R is the heat transfer surface of the reflector in contact with flood water, and k_R is the thermal conductivity of the reflector, which is assumed constant. Equation (11-9) can be solved for ΔT

$$\Delta T(\tau) = \Delta T_0 \exp\left(\frac{-\tau}{TC}\right) \text{ with time constant } TC = \frac{m_R c_{pR} t_R/3}{k_R S_R} \quad (11-10)$$

where $\Delta T_0 = \Delta T(\tau=0)$ represents initial conditions. To account for the assumed Wigner energy release, the initial average reflector temperature is increased as

$$\bar{T}_{R,0} = \frac{1}{t_R} \int_0^{t_R} T_0(x) dx + \frac{E_{WG}}{m_R c_{p,R}} \quad (11-11)$$

to obtain the initial temperature difference $\Delta T_0 = \bar{T}_{R,0} - T_{\text{sat}}$. Note that this assumption is highly conservative, since a large temperature increase in the reflector would be needed to release the stored energy. The reflector cooling is partially lost upon LOCA (part of the reflector is cooled at the outside by shield-tank water). Loss of cooling would have the tendency to increase the temperature. However, the fission gamma and neutron heating of the reflector disappear following shutdown and most gammas from decay heat are absorbed in flood water once the calandria is flooded. Hence the temperature of the reflector will be decreasing, and the release of Wigner energy is very unlikely. Nevertheless, it is assumed that all the Wigner energy stored in the graphite is immediately released leading to the temperature increase of the reflector. The amount of Wigner energy decreases with increasing irradiation temperature, and increases with fluence; and saturates for high fluences. Various portions of the reflector operate at temperatures between 300°C and 800°C. The saturation value of Wigner energy (i.e., after very long exposure) for the lowest temperature of 300°C will be taken, [Nightingale, 1962]

$$e_{WG} = 50 \text{ cal/g}; E_{WG} = m_R e_{WG} (4.1855 \text{ J/cal}) \quad (J) \quad (11-12)$$

Again, this is a conservative value since most of the graphite in the reflector will operate much higher than 300°C where Wigner energy is considerably lower, and not all the stored energy is released in temperature excursions.

The heat rate from the reflector into flood water in the calandria can be written

$$\dot{Q}_R(\tau) = k_R S_R \frac{\Delta T(\tau)}{t_R/3} = \frac{k_R S_R}{t_R/3} \Delta T_0 \exp\left(\frac{-\tau}{TC}\right) \quad (11-13)$$

Initial stored energy in the fuel matrix, E_{mat} , was calculated using the temperature distribution obtained by the simplified 1-D model described in Chapter 7,

$$E_{mat} = N_{ch} \sum_{i=1}^N \Delta V_i (\bar{T}_i - 0) \rho_i c_{pi}(\bar{T}_i) \quad (11-14)$$

where ΔV_i are volumes per unit length and \bar{T}_i is core average temperature for the i -th node. Note that the properties ρ_i and c_{pi} refer to either graphite matrix or fuel compacts depending on the node number.

Fission energy, E_{fiss} , was integrated in time using the power history from the point kinetic equations for the LOCA without scram scenario described in Chapter 7.

$$E_f = P_{rated} \int_0^{\tau_1} P_f(\tau) d\tau = P_{rated} \sum_n \frac{P_f^{n-1} + P_f^n}{2} \Delta\tau \quad (11-15)$$

where τ_1 represents the time where relative fission power is zero and P_{rated} is rated reactor power.

Wigner energy released from the matrix during the temperature excursion is calculated as

$$E_{WGmat} = m_{mat} e_{WG} (4.1855 \text{ J/cal}) \quad (J), \quad (11-16)$$

where ew_G is, similarly as for the reflector, conservatively taken at an irradiation temperature of 300°C (the matrix operates in the range of 310-700°C).

Release of initial stored energy, Wigner energy released to the graphite matrix and integrated energy from fission into the flooding water is controlled by the large thermal resistance of the gap between the fuel matrix and the pressure tube (see Figure 7-13 in Chapter 7). Hence, the thermal resistance of the matrix, pressure tube and calandria tube walls can be neglected compared to the thermal resistance of the gap. Using a lumped parameter model with uniform matrix temperature, \bar{T}_{mat} , the heat conduction equation can be written

$$V_{mat} (\rho c_p)_{mat,eff} \frac{d(\Delta T_{mat})}{d\tau} = k_{gap-eff} \frac{\Delta T_{mat}}{t_{gap}} S_{mat} \quad (11-17)$$

where ΔT_{mat} represents the temperature difference between the matrix temperature, \bar{T}_{mat} , and the pool temperature. The effective thermal conductivity of the gap, $k_{gap-eff}$, due to conduction, convection and radiation was obtained from the model described in Section 7.4. The effective heat capacity of the matrix is calculated by volume averaging of the fuel compacts and graphite

$$(\rho c_p)_{mat,eff} = \frac{V_g (\rho c_p)_g + V_f (\rho c_p)_f}{V_g + V_f} \quad (11-18)$$

Equation (11-17) can be solved, similarly as for the reflector, for the temperature difference

$$\Delta T_{mat}(\tau) = \Delta T_{mat,0} \exp\left(\frac{-\tau}{TC_{mat}}\right) \text{ with } TC_{mat} = \frac{V_{mat} (\rho c_p)_{mat,eff} t_{gap}}{k_{gap-eff} S_{mat}} \quad (11-19)$$

where the initial temperature difference is calculated from the previously considered energies evaluated in Eqs. (11-14) through (11-16)

$$\Delta T_{mat,0} = \frac{E_{mat} + E_{WGmat} + E_f}{V_{mat} (\rho c_p)_{mat,eff}} \quad (11-20)$$

Finally, the total heat rate released from all energy sources into the flood water is calculated as

$$\dot{Q}_{\text{mat}}(\tau) = k_{\text{gap-eff}} S_{\text{mat}} \Delta T_{\text{mat}}(\tau) , \quad (11-21)$$

where $\Delta T_{\text{mat}}(\tau)$ is given by Eq. (11-19).

The decay heat curve can be expressed by fitting the decay heat source to a polynomial of eleven exponentials [McFagen et. al., 1984]

$$\dot{Q}_{\text{dec}}(\tau) = \dot{Q}_{\text{rated}} \sum_{j=1}^{11} E_j \exp(\lambda_{d,j} \tau) , \quad (11-22)$$

with the group decay constants and relative yields given in Table 7-3. Equation (11-22) has been compared with the ANS standard curve and the differences did not exceed 4% [McFagen et. al., 1984].

The time when the saturation temperature in the calandria is reached is obtained from an energy balance equation

$$m_{\text{FLW}} c_{\text{pFLW}} (T_{\text{sat}} - T_{\text{FLW0}}) = E_{\text{CT}} + E_{\text{PT}} + E_{\text{RL}} + \int_0^{\tau_{\text{sat}}} [\dot{Q}_{\text{Dec}}(\tau) + \dot{Q}_{\text{R}}(\tau) + \dot{Q}_{\text{mat}}(\tau)] d\tau , \quad (11-23)$$

where the mass of flood water in the calandria , m_{FLW} , is given as

$$m_{\text{FLW}} = \rho_{\text{FLW}} \frac{\pi}{4} (D_c^2 - N_{\text{CT}} D_{\text{CT0}}^2) L_c , \quad (11-24)$$

and T_{FLW0} is the initial flood water temperature. The integral in Eq. (11-23) can be readily evaluated using Eqs. (11-13), (11-21) and (11-22), i.e.,

$$\int_0^{\tau_{\text{sat}}} [\dot{Q}_{\text{Dec}}(\tau) + \dot{Q}_{\text{R}}(\tau) + \dot{Q}_{\text{mat}}(\tau)] d\tau = \dot{Q}_{\text{Rated}} \sum_{i=1}^{11} \frac{e_i}{\lambda_i} [1 - \exp(-\lambda_i \tau_{\text{sat}})] + \frac{k_{\text{R}} S_{\text{R}}}{t_{\text{R}/3}} \Delta T_0 \text{TC} \left[1 - \exp\left(-\frac{\tau_{\text{sat}}}{\text{TC}}\right) \right] + \frac{k_{\text{gap-eff}} S_{\text{mat}}}{t_{\text{gap}}} \Delta T_{\text{mat},0} \text{TC}_{\text{mat}} \left[1 - \exp\left(-\frac{\tau_{\text{sat}}}{\text{TC}_{\text{mat}}}\right) \right] . \quad (11-25)$$

Substituting Eq. (11-25) into Eq. (11-23) yields an equation which can be solved for the unknown τ_{sat} . Starting with time τ_{sat} , steam is released from the calandria into the containment according to the equation

$$\dot{m}_s(\tau) = \frac{\dot{Q}_{\text{Dec}}(\tau) + \dot{Q}_{\text{R}}(\tau) + \dot{Q}_{\text{mat}}(\tau)}{I_{\text{sub}} c_{\text{pFLW}} (T_{\text{sat}} - T_{\text{FLW0}}) + h_{\text{fg}}(p_{\text{steam}})} , \quad (11-26)$$

where I_{sub} is the subcooling flag, which is equal to 1.0 until the time when all the flood water from the containment passes through the calandria and equals 0.0 beyond this time (it is assumed that the condensate returning from the condensing surfaces in the containment is saturated. The steam evaporated from the calandria is assumed to be saturated carrying the enthalpy

$$h_s(\tau) = h_g(p_{steam}) \quad (11-27)$$

The partial steam pressure, p_{steam} , in Eqs.(11-26) and (11-27) is not known a priori, hence the steam mass flow rate and enthalpy are recalculated using the pressure from a previous CONTAIN run (note that 2 runs are necessary because of the iteration between RISRAD and CONTAIN). A short computer program was developed to solve the above equations in time. The output of the program writes mass/energy release data from the calandria in the format which can be used directly by the CONTAIN code. Decay heat rate as well as the heat rate from the reflector and from the fuel matrix and their integrated counterparts are shown in graphical form in Figure 11-11. It can be seen that, in the long term, the reflector and matrix contributions are small compared to the decay heat. Steam flow rate from the calandria is shown on Figure 11-12. Figure 11-13 summarizes all mass release sources for Case 1. Loop1 represents the unaffected loop, loop2 represents the affected loop. It is interesting to note that although the steam flow rate from the calandria is small in magnitude, the integrated mass released from calandria to containment is large at later times, and it is the main contributor to long-time pressurization of the containment.

Free Volume and Internal Heat Sinks

Free containment volume represents very important input data. Since the detailed layout of the containment design is not available, the free containment volume was obtained by scaling up the CE-CANDU data. The CE-CANDU containment has the same shape as the proposed containment for the PTLWR with a gross volume of 89,878m³ and free volume of 76,455m³. Using the dimensions given in Figure 11-1 one obtains for the gross volume

$$V_{\text{gross}} = \frac{\pi}{4} 60^2 (35+15) + \frac{1}{2} \left[\frac{4}{3} \pi \left(\frac{60}{2} \right)^3 \right] = 1.98 \times 10^5 \text{ m}^3 \quad (11-28)$$

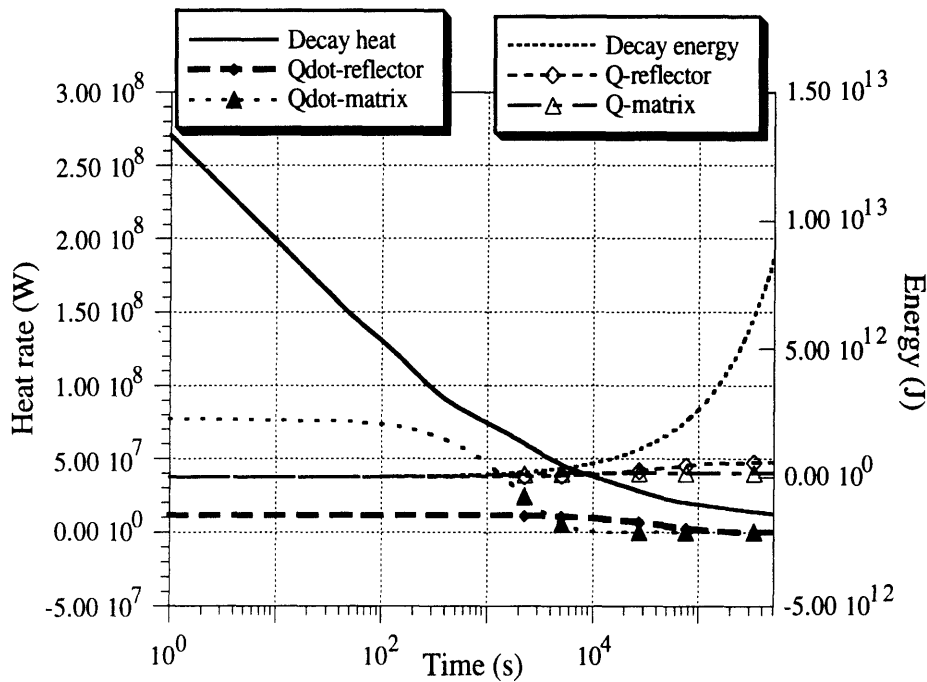


Figure 11-11 Decay heat and heat rates from stored energy in the reflector and fuel matrix released into calandria water

To obtain the free volume, the above number is scaled down by the ratio of free volume to gross volume for CE-CANDU, i.e.,

$$V_{\text{free}} = V_{\text{gross}} \frac{76,455}{89,878} = (1.98 \times 10^5) 0.85 = 1.7 \times 10^5 \text{ m}^3 \quad (11-29)$$

This is a fairly large free volume. The largest large dry PWR containments have typical free volumes of about $1 \times 10^5 \text{ m}^3$, hence the proposed containment has a 70% larger free volume than the large dry PWR containments. This trend is consistent with the large advanced passive containment design proposed for Nuclear Power International's (NPI) large next generation LWRs [Erbacher and Neitzel, 1992].

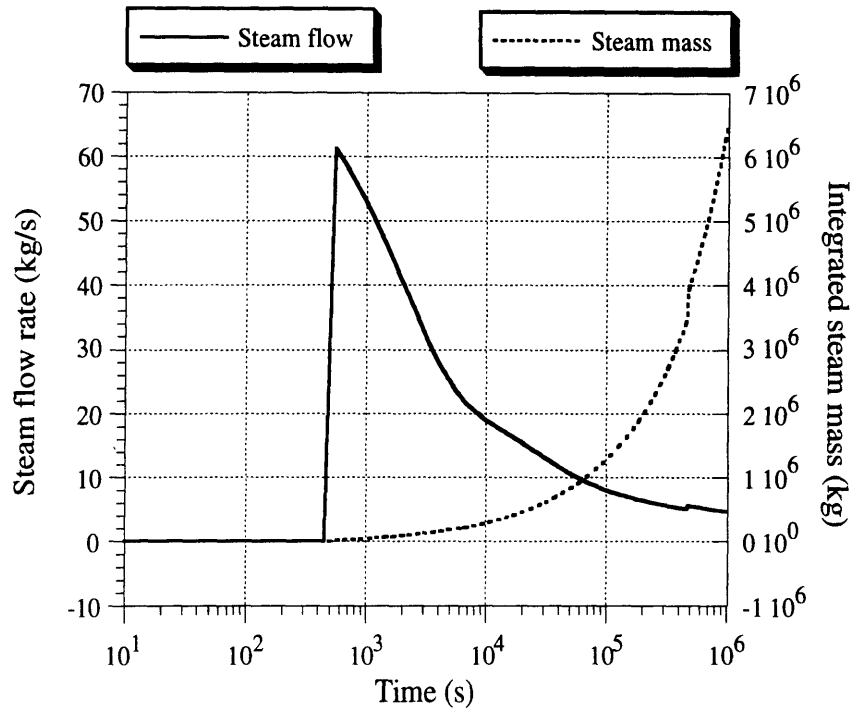


Figure 11-12 Steam mass flow rate and integrated steam mass released from calandria as a result of decay heat and core stored energy

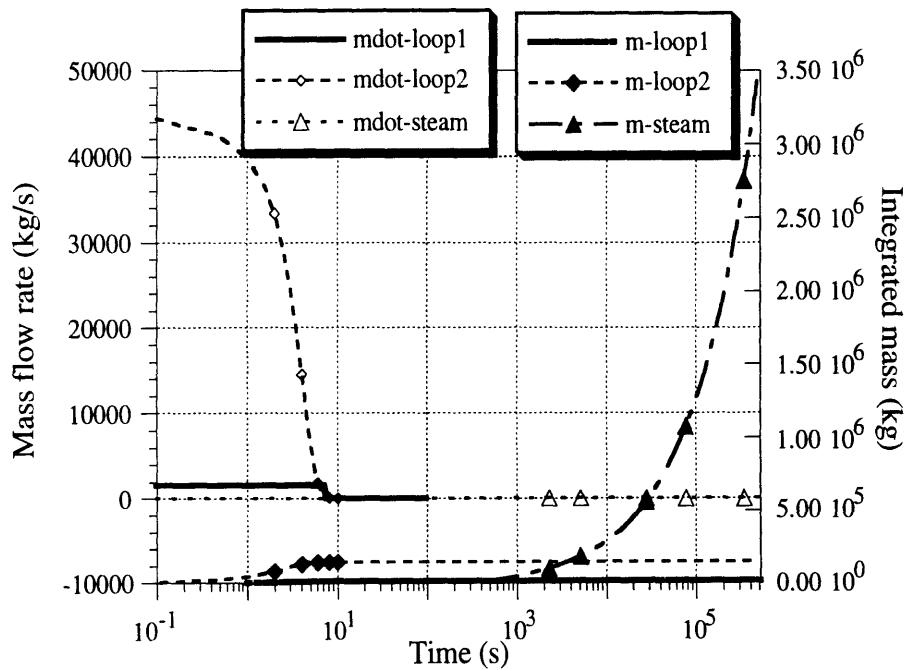


Figure 11-13 Case 1-summary of mass sources released to containment

In the long-term pressurization scenario, heat sinks inside the containment become an important factor in reducing containment peak pressure. Considerable effort would be required to determine the exact value of heat sink capacity that would properly represent the proposed conceptual design. Hence, the estimates summarized in Table 11-5 were made. Table 11-6, which compares the mass of the heat sinks used for the PTLWR containment with available data from other commercial plants, shows that both the concrete and steel heat sinks were chosen such that they fall within the range of commercial LWRs.

Discussion of the results

The calculated history of the containment pressure for the 1-cell model is given in Figure 11-14. Saturation temperature (corresponding to partial steam pressure), gas temperature, and containment wall temperature at the outer surface are shown in Figure 11-15. Containment pressure exhibits two peaks. The first peak results from primary system blowdown, the second peak represents long-time containment pressurization from steam carrying decay heat released from the calandria. The maximum peak of 3.37 bars is reached at about 2×10^5 seconds (55 hours). Heat rates to internal structures, containment walls, pool and decay power are shown in Figure 11-16. At the time of 55 hours, i.e., when the pressure peak is reached, decay heat is equal to 16 MWt, the heat removal rate from the containment wall is about 10.5 MWt, 3.8MWt is being transferred to concrete, and the remaining 1.7 MWt is being stored in the pool. Even at this long time, a significant heat rate is absorbed in the concrete, hence, the mass and total surface of internal concrete structures are very important to the accuracy of long-term pressurization computations. At 5×10^5 seconds, all latent heat available in the pool is exhausted. This results in the tertiary pressure peak. The trace of saturation temperature, "T-sat," on Figure 11-15 corresponds to the history of the partial pressure of steam. The real temperature of the gas/steam mixture, designated as "T-gas", exhibits an additional peak at time of 1000 seconds. This peak results from heating of the containment atmosphere by the hot primary metal. Note that the hot primary metal heats containment atmosphere directly; this differs from typical LWRs where most of the primary metal stored energy is released

during the reflood phase in the form of steam at saturation temperature, hence superheat is not present. Containment wall temperature follows saturation temperature with significant delay.

Table 11-5 Summary of internal heat sinks

Heat sink number	Shape/material	Area (m ²)	Thickness (m)
1	Slab/concrete(floor)	2500	1.2
2	Slab/concrete	8000	1.2
3	Slab/concrete	14000	0.3
4	Slab/concrete	9000	0.1
5	Slab/steel (cold)	2000	0.06
6	Slab/steel (cold)	30000	0.01
7	Slab/steel (hot)	41000	0.006
8	Slab/steel (hot)	3800	0.04

Table 11-6 Comparison of internal heat sink mass for various commercial LWR containments and PTLWR heat sinks used in the analysis

Material/Plant	Surry*	Zion*	Bellefonte*	PTLWR
Steel	2x10 ⁶ kg	3x10 ⁶ kg	9x10 ⁶ kg	3.3x10 ⁶ kg
Concrete	40x10 ⁶ kg	40x10 ⁶ kg	60x10 ⁶ kg	40x10 ⁶ kg

*Data taken from [Williams et. al., 1993].

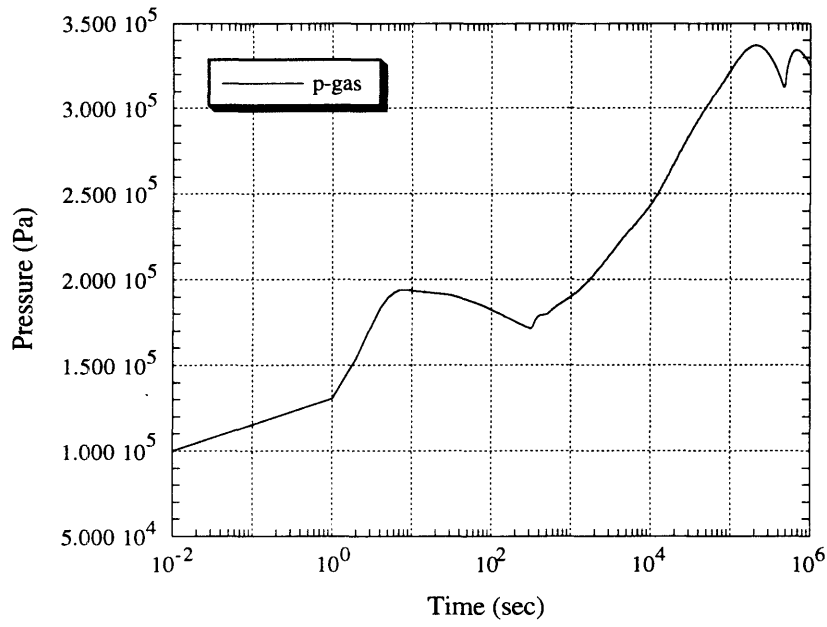


Figure 11-14 Case 1 - containment pressurization history

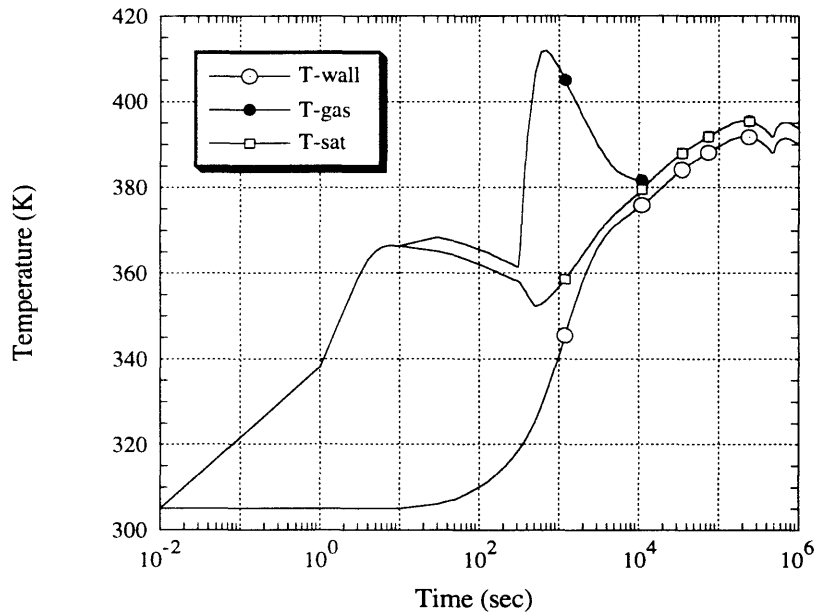


Figure 11-15 Case 1 - containment gas, saturation and wall outer surface temperature histories

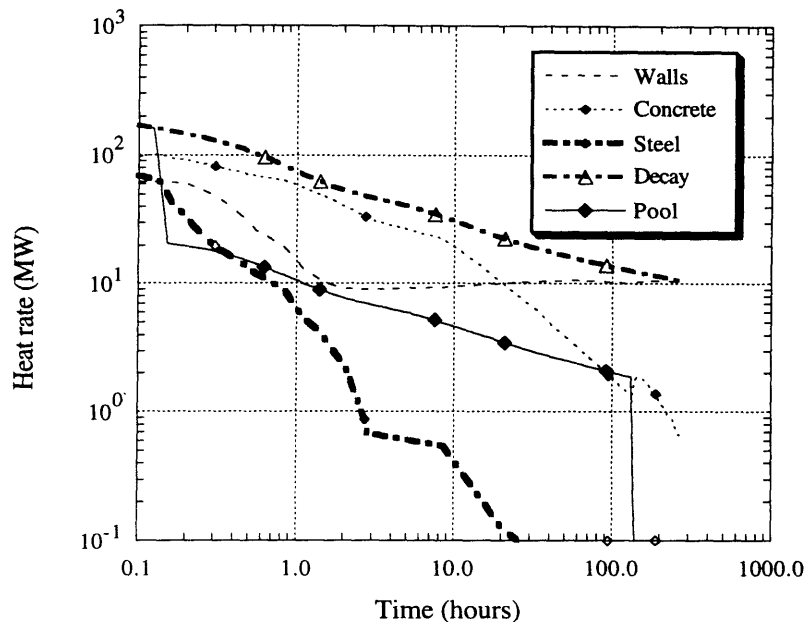


Figure 11-16 Case 1 - Decay power and heat rates to structures

Several important conclusions can be drawn from Figures 11-14 and 11-15. First, both pressure peaks are relatively low, hence a containment with a design pressure of 0.42MPa (60 psi) could handle this DBA accident. Secondly, the peak from the blowdown is small compared to the long term pressurization from decay heat. Moreover, passive containment wall cooling does not participate in blowdown-pressure peak reduction, as can be seen from the containment wall temperature trace. Therefore, even if the containment atmosphere becomes stratified as a result of the blowdown, any potential impairment of containment passive cooling from stratification would not have a visible effect on the magnitude of the first peak. Thirdly, the long-term pressurization peak is limiting for the design pressure and for the performance of the passive air cooling system. Since the steam released from the decay heat is always released at a low elevation, natural circulation will be established such that the hot steam escaping from the calandria will rise to the top of the containment and condense along the cooled walls, breaking up potential stratification (see [Wolf, 1993] and Section 11.5.5.3 for experimental and theoretical confirmations of this hypothesis, respectively). As a result, all of the air-

cooled containment wall will be exposed to high containment temperature and the heat transfer to air in the annulus should not be impaired.

11.5.3.2 Case 2 Double-ended Rupture of a Hot Header at the Surge Line Connection, with Isolation Valve Failure.

The Case 2-scenario is the same as described for Case 1 except for the mass release data from the unaffected loop. The unaffected loop is assumed to blow down completely. The blowdown rate, however, is significantly slower than the blowdown rate of the affected loop due to the longer path and the large flow resistance of the piping. The analysis performed for the CANDU-CE design [Shapiro and Jesick, 1979] showed that it would take about 300 seconds to release all mass and energy from the unaffected loop and pressurizer. Since the time dependent release data were not reported beyond the 7th second, the total mass and energy integral was released in the time interval between zero and 300 seconds as shown on Figures 11-17 and 11-18. The slopes and intersection time of the two lines were chosen such that the total integrated mass and energy match the known total integrals.

The containment pressure history is shown on Figure 11-19. Compared to case 1, the first pressure peak is increased by about 20% and shifted to longer time. This change is consistent with the different release data than for case 1. The increase of the second, limiting, peak is negligible-only 2%. Gas temperature, saturation temperature and containment wall temperature at the outer surface are shown in Figure 11-20. Conclusions given for case 1 apply also for case 2.

The importance of the mass and surface of concrete internal heat sinks can be seen from Figure 11-21. Figure 11-21 compares the pressure history of the base Case 2 with a Case 2 in which the mass and surface of concrete internal heat sinks are reduced by 50%. This 50% reduction in concrete mass leads to a significant increase of the pressure peak (by about 38%).

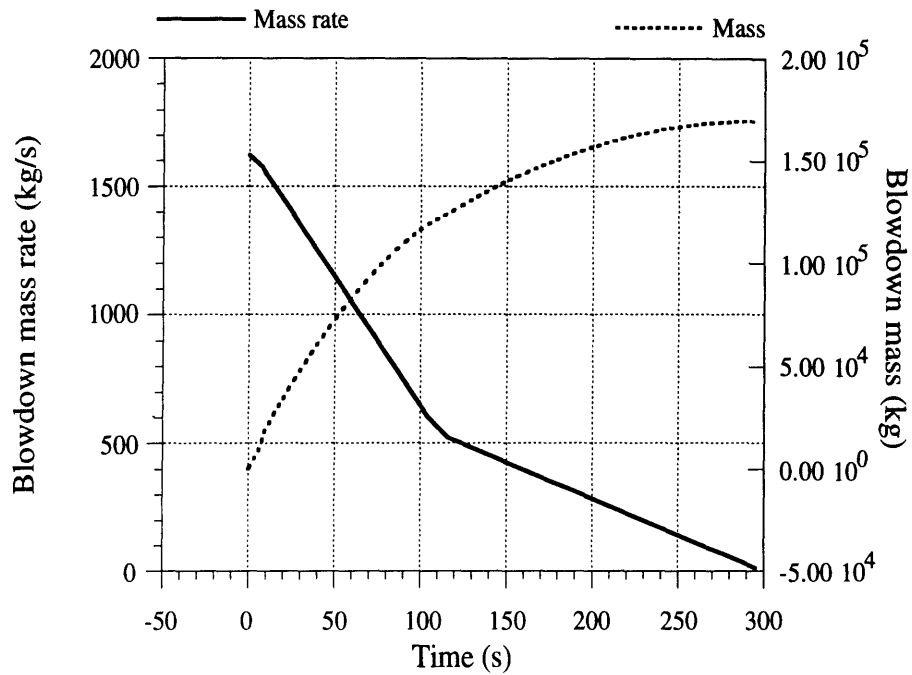


Figure 11-17 Case 2 - mass release from unaffected loop following the break of outlet header

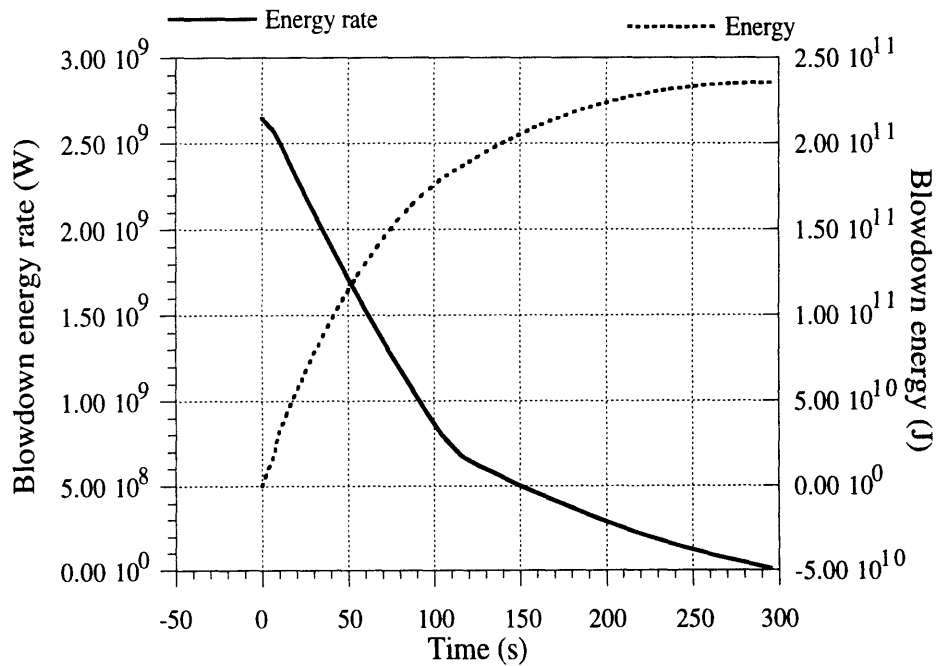


Figure 11-18 Case 2 - energy release from unaffected loop following the break of outlet header

Hence for long-term containment pressurization, the accurate determination of internal concrete heat sinks will be very important in more detailed analyses.

11.5.3.3 Case 3 Main Steam Line Break with Main Steam Isolation Valve Failure.

The Case 3-scenario differs from Case 1 in its mass/energy release data. Mass and energy release sources from affected and unaffected loops are replaced by mass/energy release data from a steam line break. The data were taken from the analysis for the CANDU-CE design [Shapiro and Jesick, 1979] and are shown on Figures 11-22 and 11-23.

Figures 11-24 and 11-25 show containment pressure and temperature histories. The pressure peak from blowdown is comparable to the pressure peak from blowdown of the entire primary system (Case 2); the pressure peak from decay heat is affected only marginally. The main difference from the previous cases is higher gas temperature, which also persists for a longer time. Superheated steam coming from steam generators with uncovered tubes is the primary contributor to this peak.

11.5.3.4 Case 4 Combined Double-ended Rupture of a Hot Header at the Surge Line Connection, with Isolation Valve Failure and Steam Line Break with Main Steam Isolation Valve Failure

Case 4 assumes all previously considered failures to occur simultaneously. Moreover, no credit for containment active cooling systems is taken. According to current standards, this is clearly beyond the design basis accident case. Containment pressure and temperatures histories are shown in Figures 11-26 and 11-27. Even in this case, blowdown pressure does not exceed the decay heat pressure peak, which reaches a maximum value of 0.356MPa (5.6% higher than for Case 1). Considering the severity of the accident, the increase in the second pressure peak is relatively small. A slight increase in the containment design pressure (by 5.6%) would be

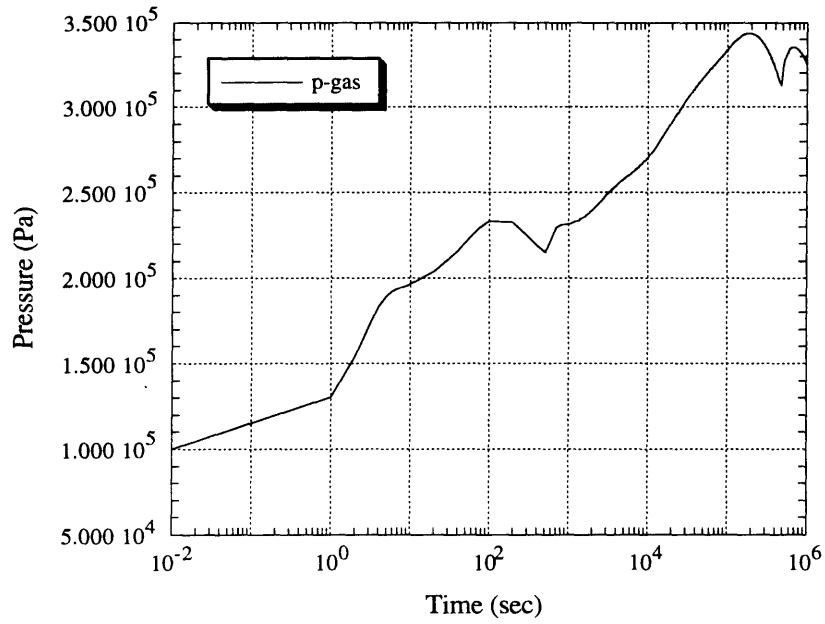


Figure 11-19 Case 2 - containment pressurization history

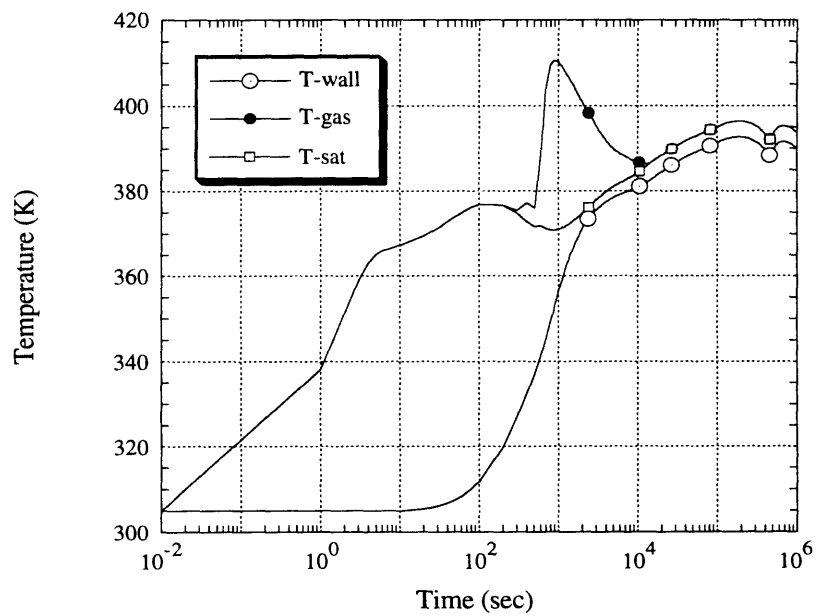


Figure 11-20 Case 2 - containment gas, saturation and wall outer surface temperature histories

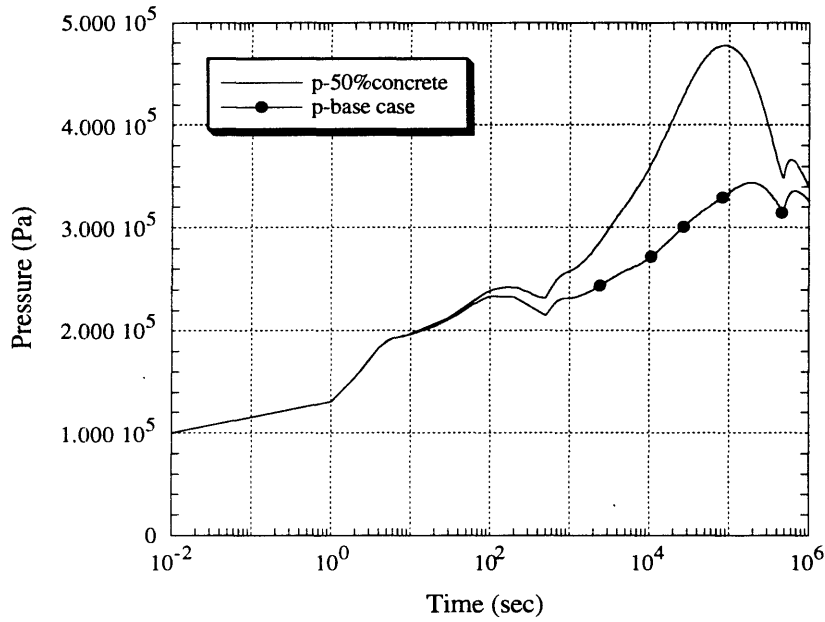


Figure 11-21 Case 2 - Comparison of pressure for the base case and a containment with reduced mass of internal concrete structures

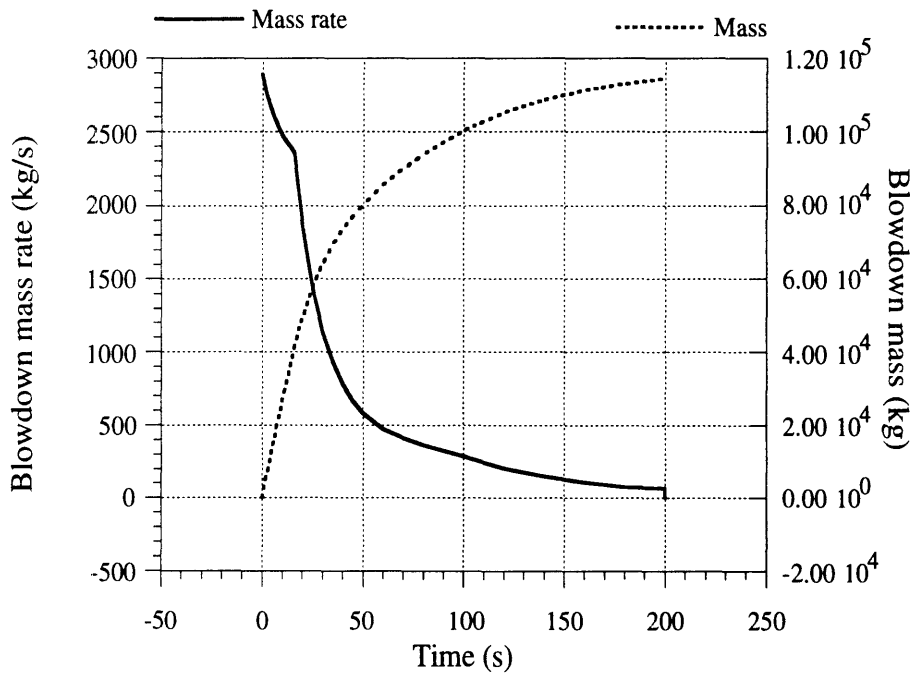


Figure 11-22 Case 3 - mass release in steam line break accident

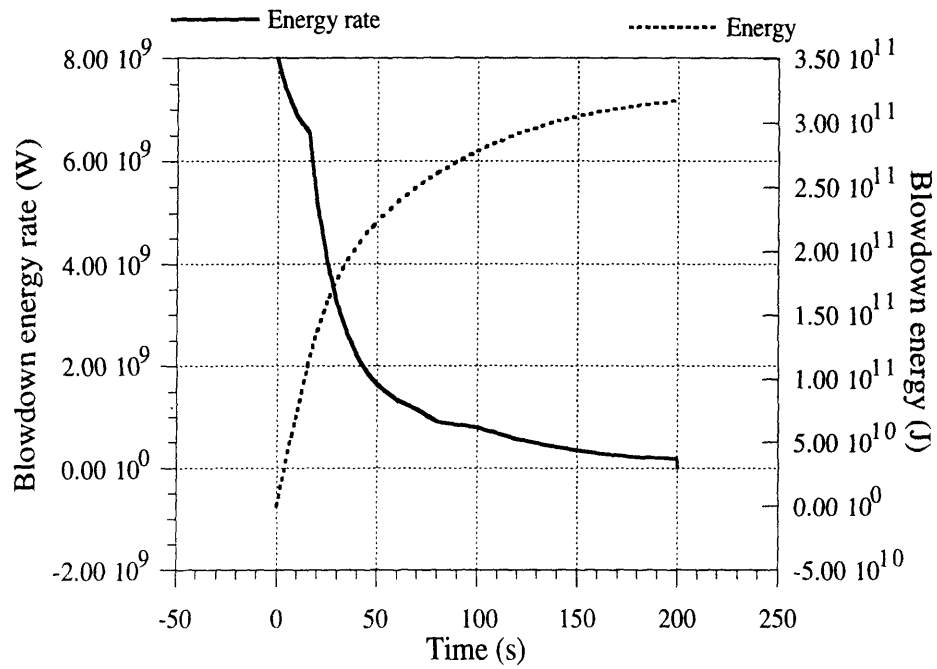


Figure 11-23 Case 3 - energy release in steam line break accident

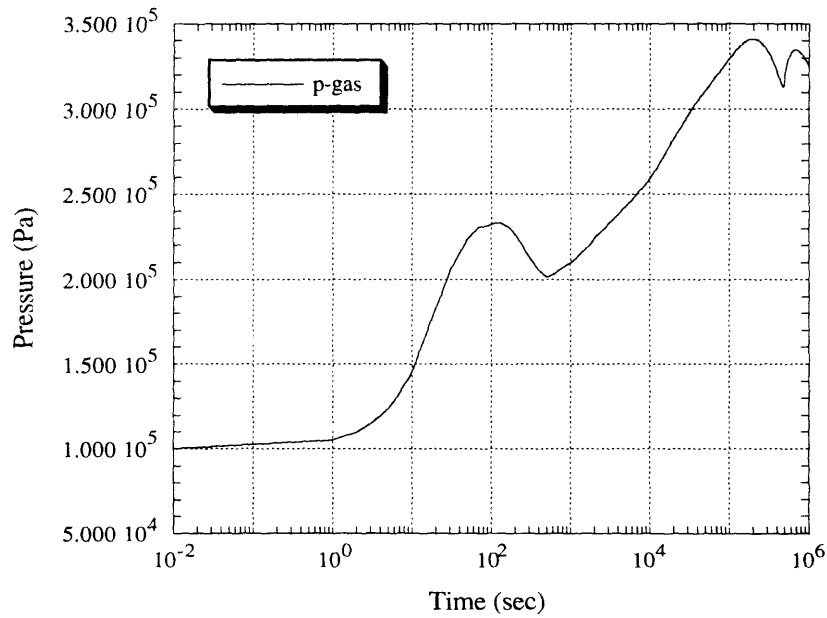


Figure 11-24 Case 3 - containment pressurization history

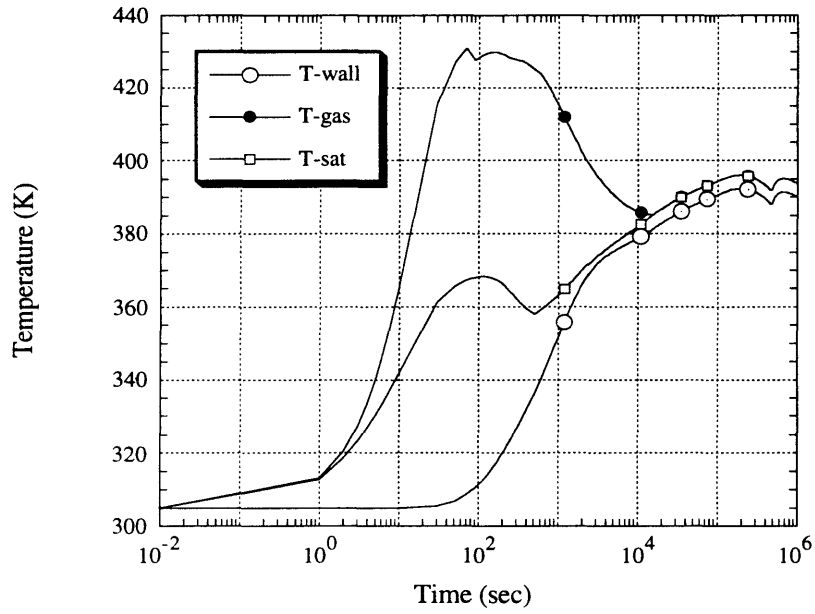


Figure 11-25 Case 3 - containment gas, saturation and wall outer surface temperature histories

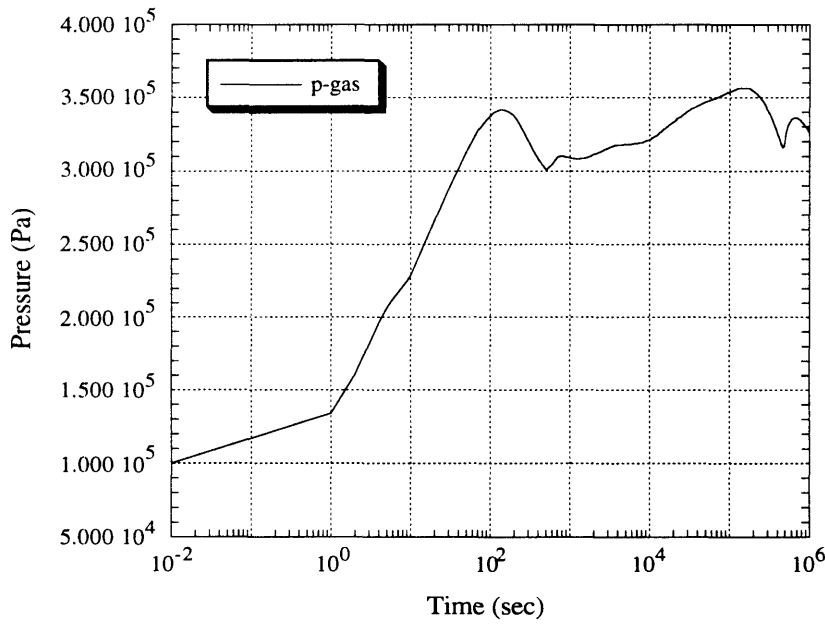


Figure 11-26 Case 4 - containment pressurization history

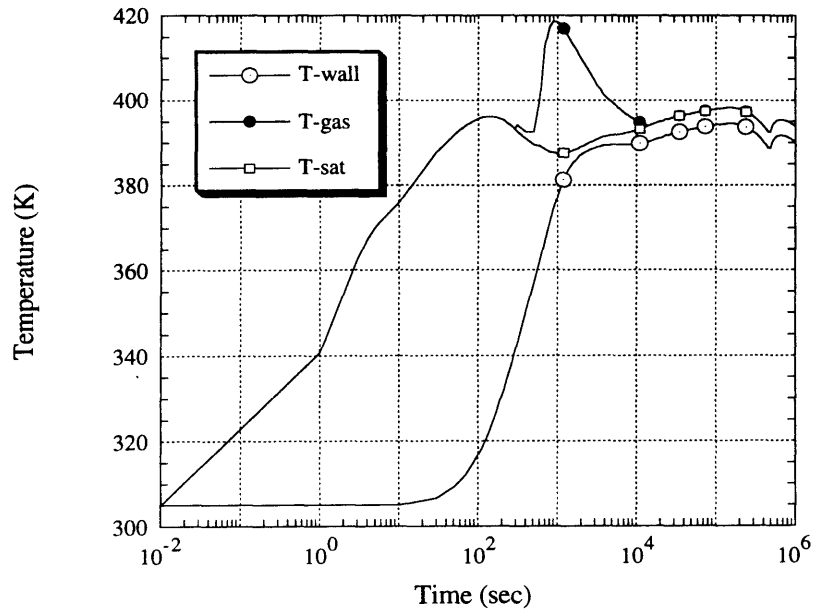


Figure 11-27 Case 4 - containment gas, saturation and wall outer surface temperature histories

required to handle this accident. Adding 10% margin to the calculated first peak would set the containment design pressure at 0.392 MPa (57psi), which falls within the range for the design pressure of 0.07–0.65MPa [Gavrilas et. al., 1994] in currently operating plants with large dry containments..

11.5.4 A 9-cell CONTAIN Model

11.5.4.1 Model Description

The 1-cell model allows coupling of a passively-cooled annulus (pre-calculated by a separate code) to a CONTAIN 1-cell model in a simple manner, while decreasing CPU and memory requirements for CONTAIN. The model assumes that a natural circulation pattern will be established such that the hot steam from decay heat will rise to the top of the containment and return, while condensing, through the gap between the

crane walls and the air-cooled shell, yielding a perfectly mixed atmosphere. To confirm that the expected natural circulation patterns will establish, and hence the adequacy of the 1-cell model, a 9-cell CONTAIN model shown schematically on Figure 11-28 was developed. The 9-cell CONTAIN model also allows for the independent comparison of the performance of the passive air cooling system with the RISRAD code.

The model consists of a calandria cavity cell (cell 1), containment mid-region cell (cell 2), containment dome cell (cell 3), 2 cells representing the space between the crane wall and an air-cooled shell (cell 4 and 5), 3 cells representing the passive air cooling system (cells 6,7 and 8) and the environment cell (cell 9). Cell volumes and heights are given in Table 11-7.

Table 11-7 Cell volumes and heights for the 9-cell CONTAIN model

Cell	Description	Volume (m ³)	Height (m)
1	Calandria vault	3.8x10 ⁴	14
2	Mid-portion	4x10 ⁴	30
3	Dome	7x10 ⁴	35
4	Upper downcomer	1.1x10 ⁴	15
5	Lower downcomer	1.1x10 ⁴	15
6	Lower air annulus	1427	15
7	Middle air annulus	1427	15
8	Upper air annulus	3370	35
9	Environment	1x10 ³⁰	20

Bold arrows in Figure 11-28 represent flow paths between the cells. Flow path data are summarized in Table 11-8. The model is set up such as to avoid any dead cells by having more than one flow path connecting every volume. To approximate natural circulation in the CONTAIN code, both center of mass and flow path elevations were defined for all cells [Murata

⑨ Environment

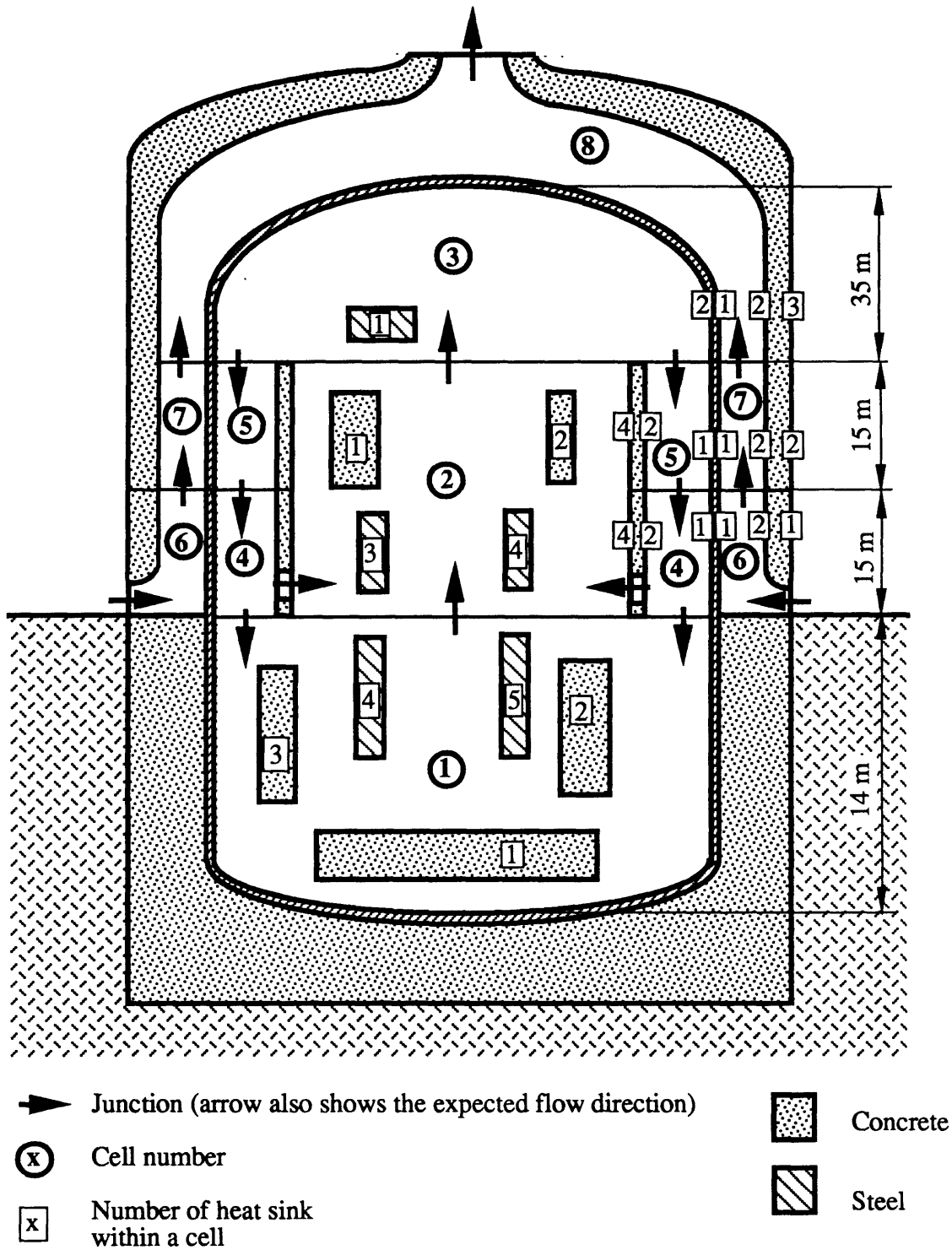


Figure 11-28 A 9-cell CONTAIN model of the containment for the passive pressure tube LWR

et. al.,1990]. Internal heat sinks from the 1-cell model were proportionally distributed among containment cells as shown in Figure 11-28. Structures that provide a common conduction boundary between two cells were divided approximately according to their half-thickness and half of the structure was placed in each cell. Structures in adjoining cells were thermally connected using the “structure connect” option in CONTAIN input. For example, in Figure 11-28, half of the steel wall between the containment dome and upper air annulus, i.e., structure #2 within cell 3 is thermally connected to another half of the steel wall, i.e., structure #1 within cell 8.

Table 11-8 Junction data for a 9-cell CONTAIN model

Junction	Junction area (m ²)	Inertial length(m)	Elevation (m)
(1,2)	800	40	14
(2,3)	1800	60	44
(3,5)	710	35.5	44
(5,4)	710	47	29
(4,2)	200	8	14.5
(4,1)	20	1.4	14
(6,7)	95	6.3	29
(7,8)	95	4.75	44
(8,9)	72	14.4	81
(9,6)	100	40	14

11.5.4.2 Analysis of Case 2 with the 9-cell Model .

Case 2 – double-ended rupture of a hot header at the surge line connection, with isolation valve failure – was analyzed using the 9-cell CONTAIN model. The input data for the 9-cell model are listed in [Hejzlar, 1994]. Figure 11-29 compares the pressure history calculated by the 9-cell model to the pressure history obtained by the 1-cell model. The 9-cell model yields lower pressures for the entire time span, hence the 1-cell model gives conservative results. The first peak is lower primarily for two reasons. First, the blowdown occurs into the calandria vault cell, which has a large concentration of internal heat sinks. Hence the condensation rate on the heat sinks is increased due to a larger temperature difference between cell atmosphere and heat sink walls, as compared to the 1-cell model. Secondly, circulation of the atmosphere inside the containment enhances heat transfer between the containment atmosphere and heat sinks, which also leads to lower containment pressures. The smaller, and earlier, second pressure peak is the consequence of the higher CONTAIN heat transfer coefficient between the containment shell and air compared to the heat transfer coefficient from the ANL heat transfer correlation applied in the 1-cell model through the use of the RISRAD code (see comparison of correlations in Appendix C). Histories of selected temperatures are shown in Figure 11-30. A significant difference between temperatures in cell 1 and cell 3 can be observed up to 10^4 seconds. However, at the time when the peak is reached, temperatures in all in-containment cells are close together, i.e. containment atmosphere is well mixed. The temperature in cell 1 exhibits an additional peak at about 1000 seconds due to energy release from hot primary metal located in the calandria vault. Temperature “Tair-out” designates air temperature at the outlet, “Twall-7” is the outer containment wall temperature in cell 7 and “Tconc-7” is the inner-surface temperature of the concrete shield building wall. Velocities through selected junctions are shown in Figure 11-31. Significant atmosphere circulation in the space between the crane wall and containment shell (junction J3-5) can be observed. Air velocity in the annulus (junction J7-8) compares very well to the velocity obtained using the RISRAD code.

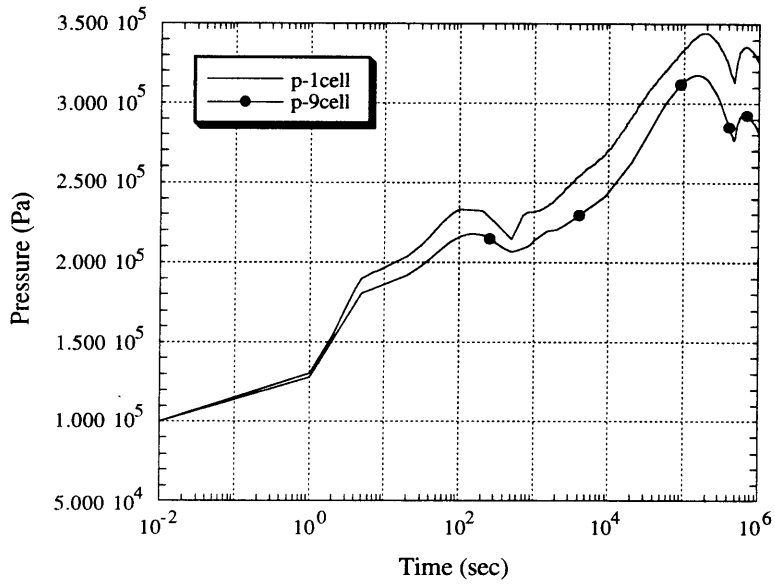


Figure 11-29 Comparison of pressure history for Case 2 using 1-cell and 9-cell models

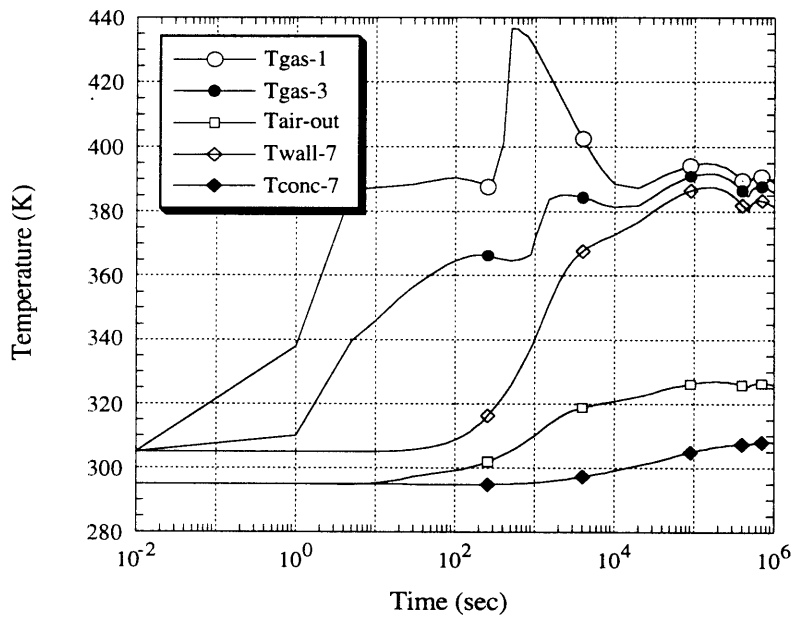


Figure 11-30 Histories of selected temperatures from the 9-cell model

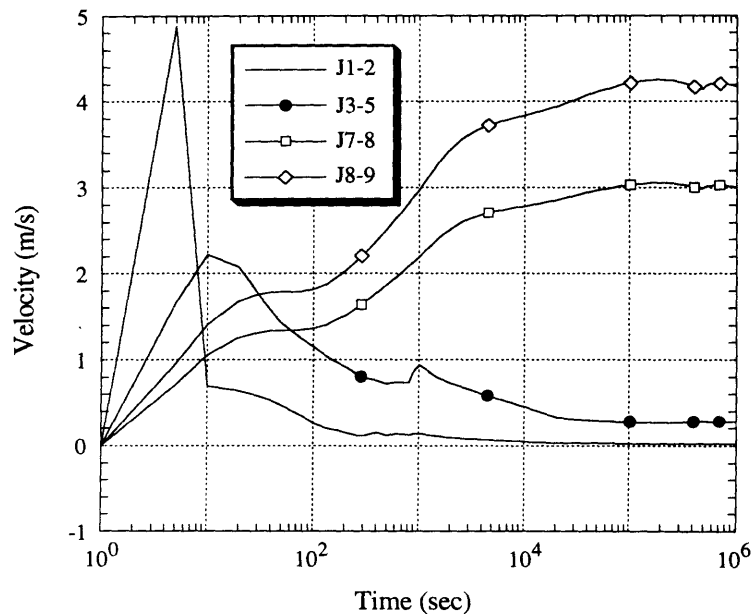


Figure 11-31 Velocities through selected junctions from the 9-cell model

11.5.5 Investigation of Effects of Thermal Stratification Inside Containment on Passive Containment Cooling Using GOTHIC

11.5.5.1 Introduction

The main goal of this section is to further verify the hypothesis of a well mixed containment atmosphere for the proposed design. Section 11.3 explained the rationale behind the containment arrangement to avoid potential thermal stratification problems which could lead to deterioration of heat transfer from the containment steel shell to air. It was suggested that significant thermal stratification should not occur in the proposed PTLWR containment arrangement. A CONTAIN 9-cell model discussed in Section 11.5.4 confirmed the expected circulation patterns inside containment. However the CONTAIN lumped parameter approach has its limitations with regard to the detailed prediction of thermal stratification.

Because CONTAIN cannot predict flow patterns within a volume, a large number of small subvolumes would be needed to increase the resolution. Such an approach would result in an extremely large CPU requirement while still not fully capturing directional momentum transport including turbulent effects – factors important in handling buoyant plumes. This can be accomplished by the GOTHIC computer code which incorporates full 3-D treatment of the field equations.

This Section is divided into two parts – the first part gives the comparison of the GOTHIC lumped parameter model with the CONTAIN model and long-term water level behavior in the calandria, and the second part deals with thermal stratification issues. To gain more understanding of thermal stratification phenomena in a containment, various factors influencing thermal stratification are identified and explored.

11.5.5.2 Lumped Parameter GOTHIC Model

Before proceeding to a multicell containment model for studying thermal stratification, it is of interest to build a lumped parameter GOTHIC model for comparison with CONTAIN results. Such a model is shown on Figure 11-32. Containment free volume is modeled as one cell (cell 2) with the same internal heat sinks as in a 1-cell CONTAIN model. The air annulus is represented by 7 subvolumes thermally connected to the containment atmosphere by 7 heat conductors (1 through 7) representing the containment shell. Junctions 1 and 2 connecting the annulus with ambient represent air intakes and outlets. Volumes 4 and 5 model the flooding pool and calandria space, respectively, interconnected by a gas lock (junction 6). Condensate from the heat sinks is collected at the bottom of the containment and returned to the flooding pool via junction 5. Junction 7 represents exhaust piping from the passive valve. Boundary conditions 3 and 4 modeling blowdown from affected and unaffected loops are identical to those in the CONTAIN model described in Section 11.5.3. Long-term time-dependent heat generation is modeled by a heat conductor 14, submerged in the pool inside the calandria. The time-dependent heat-generation curve corresponds to the sum of all the energy sources as given

Volumes: 1 - Environment
 2 - Upper containment
 3 - Air annulus
 4 - Flooding pool
 5 - Calandria

BC junctions: 3 - Blowdown from unaffected loop
 4 - Blowdown from affected loop

x - junction numbers

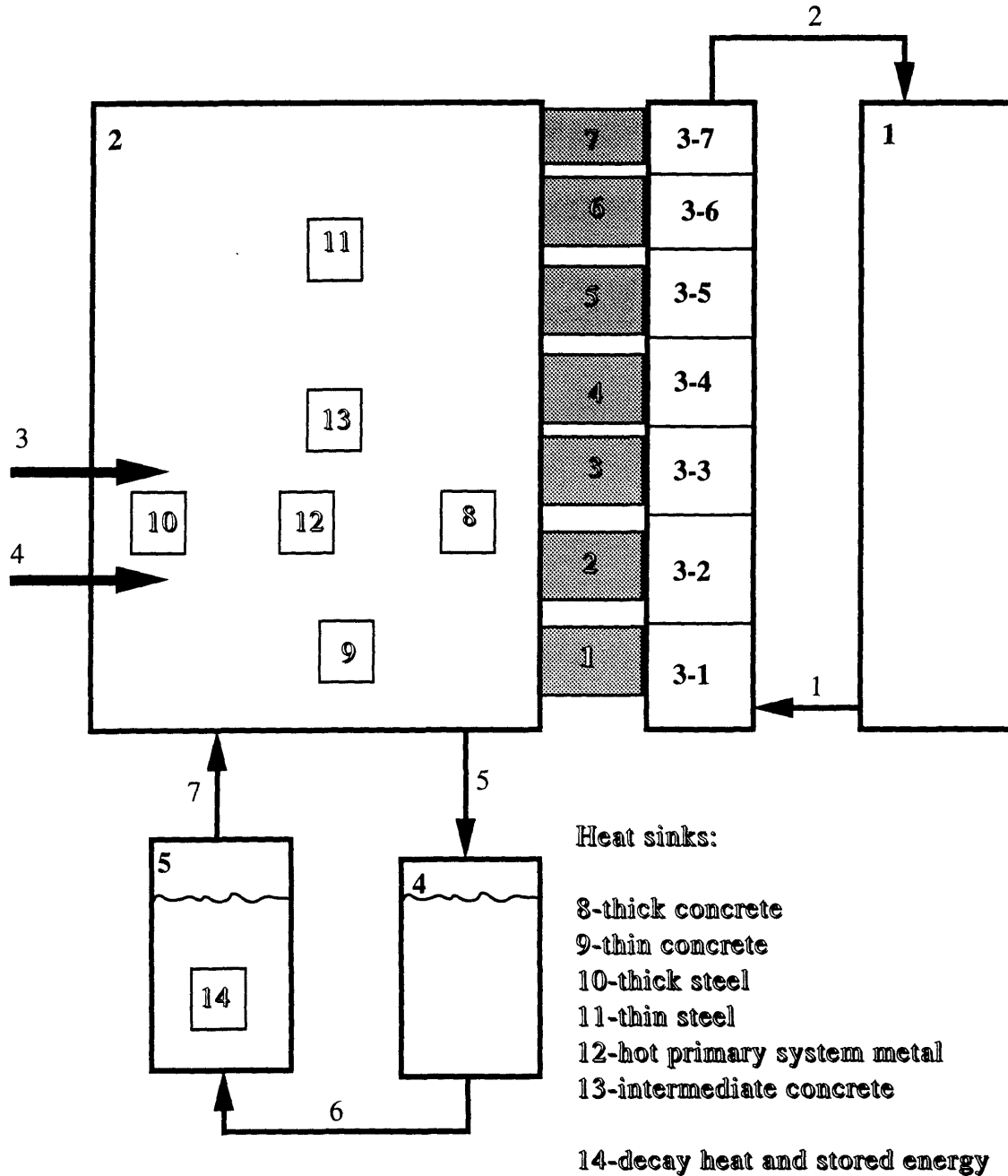


Figure 11-32 Schematic of lumped parameter GOTHIC model of PTLWR containment

by Eqs. (11-13), (11-21) and (11-22). Since these Eqs. already incorporate time constants of the reflector and the matrix, the properties of the heat conductor 14 are set such that the heat generated in the conductor, including the heat transfer coefficient between the conductor and the pool, is released immediately into the pool (i.e., very small conductor heat capacity and very large conductor thermal conductivity and heat transfer coefficient).

The current version of GOTHIC does not include a forced convection-type correlation needed for the heat transfer coefficient between the shell and air nor radiative heat transfer. These drawbacks were solved in a similar manner as for the 1-cell CONTAIN model. The RISRAD code was used to produce the curve of the effective heat transfer coefficient, including radiation, as a function of outer containment wall temperature. The effective heat transfer coefficient is defined similarly as in Eq. (11-1) except for the reference inlet temperature, $T_{air,in}$, which is replaced by air temperature at the midplane. Using this known function of effective heat transfer coefficient versus wall temperature, the heat transfer coefficient in GOTHIC was scaled up by the time-dependent multiplier (ratio of the effective heat transfer coefficient to the GOTHIC heat transfer coefficient) using a “forcing function” feature available in GOTHIC. Similarly as for the CONTAIN 1-cell model, two runs of GOTHIC are needed because the wall temperature versus time curve is not known a priori.

Comparison of GOTHIC and CONTAIN results

The pressure histories for the Case 2 scenario calculated by GOTHIC and the CONTAIN 1-cell model are compared in Figure 11-33. Three main differences can be observed – the difference in magnitude of the blowdown peak, the time difference in the initiation of long-term pressurization and the absence of the tertiary peak.

First, the blowdown peak (and consequently the maximum pressure peak) calculated by GOTHIC is about 15% less than the peak obtained by CONTAIN. The reason for this discrepancy lies in the different condensation heat transfer coefficients used. The CONTAIN condensation heat transfer is based on basic condensation processes given in [Collier,

1981). GOTHIC model employs Uchida's correlation [Uchida et. al., 1965], which has been experimentally verified on typical PWR blowdown scenarios. However, the PTLWR blowdown scenario for Case 2 differs from a typical LWR scenario in that it exhibits a fast blowdown phase of the affected loop (see first subpeak) and a prolonged blowdown phase at a slower rate from the unaffected loop. This second phase is responsible for the main blowdown peak, and it is here where the discrepancy occurs. Since the CONTAIN condensation heat transfer model incorporates the physics of the phenomena, while Uchida's correlation is based on experiments with a limited range of validity (not verified on a double-peak blowdown case) the CONTAIN results may be better suited for this scenario. CONTAIN also gives more conservative results.

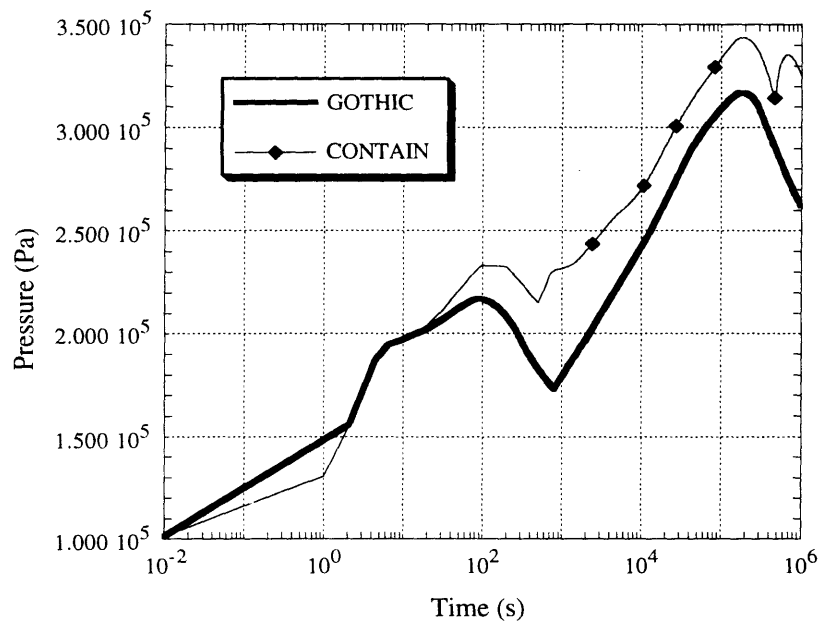


Figure 11-33 Comparison of pressure histories for Case 2 by CONTAIN and GOTHIC models

The GOTHIC model predicts a later time (800 versus 500 seconds) for the long-term pressurization initiation. This difference is the consequence of simplifying assumptions in the model for generation of the steam mass flow rate from the calandria, as presented in Section 11.5.3 which assumes

constant saturation temperature of the water in the calandria, i.e., the increase of saturation temperature due to a pressure increase is not included. Therefore, evaporation begins conservatively earlier in the CONTAIN model.

The CONTAIN tertiary peak at 4×10^5 seconds is not observed in the GOTHIC results. This is also the consequence of the simplifying assumption of constant saturation temperature of the pool water employed in the model. Also, the higher pressure in the pool (as compared to the pressure of the containment atmosphere) due to the water head was not included in CONTAIN calculations. Because of these assumptions introduced into CONTAIN input data, the pool reaches the saturation state earlier. The sensible heat of the pool above a temperature of 100°C , for pressure above atmospheric pressure, is therefore not taken into account, which results in a tertiary pressure peak from the increased steam generation. A more exact treatment of the integrated pool-calandria-containment system using GOTHIC shows that the pool will reach saturation at a later time. Thus the CONTAIN results are conservative. The temperature histories of the flooding water in the calandria and the pool are shown in Figure 11-34. Water in the calandria reaches the saturation temperature at about 1000 seconds (this corresponds also to the initiation of long term pressurization on Figure 11-33), afterwards the temperature is maintained at the saturation temperature corresponding to the partial steam pressure. The temperature of the pool remains below saturation temperature during the entire transient.

Long-term Tracking of Calandria Water Level

Maintenance of the water level in the calandria above the top row of fuel channels over the long term is an important consideration. The water level in the calandria depends on a sufficient supply of returning condensate to the flooding pool. The GOTHIC code offers the capability to model the water level in the main pool coupled to the flooded calandria including the condensate recirculation. The lumped parameter GOTHIC model shown on Figure 11-32 was used to verify that the amount of condensate mass returning to the pool is sufficient during the entire transient.

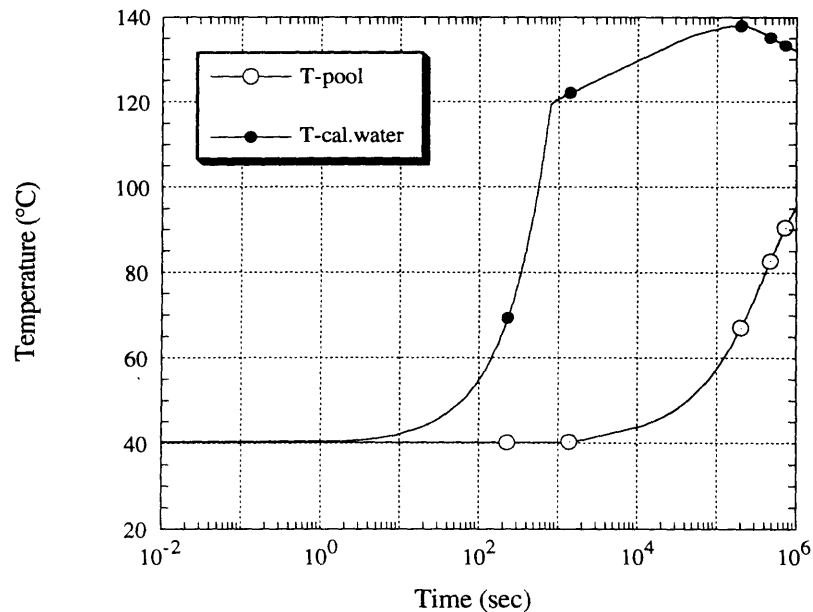


Figure 11-34 Histories of liquid temperature in the pool and calandria for Case 2 from GOTHIC

The pool is designed as a sump which collects all the condensate from containment walls and structures. The upper end of junction 5, which simulates the returning condensate is located 0.06 m above the floor level. This allows accounting for about 1.4×10^5 kg of condensate losses, which are assumed not to return to the pool. The calandria flooding system is designed such that at the end of the flooding process, the water level in the calandria is in equilibrium with the water level in the pool with a water column level about 5cm above the upper row of calandria tubes. This state was set as an initial condition, with water level of 9m, for both pools. The results are illustrated in Figures 11-35 and 11-36. Figure 11-35 shows the water level in the calandria and the pool. At first, a water level increase in the calandria is caused by the decrease of water density due to heat up. The later increase follows the water level of the pool, which also exhibits an increase as excess condensate returns to the pool. The important conclusion is that the calandria water level remains above the top row of fuel channels during the entire transient. Note that in the final design, the behavior of the water level can be optimized by changing the flow area of the

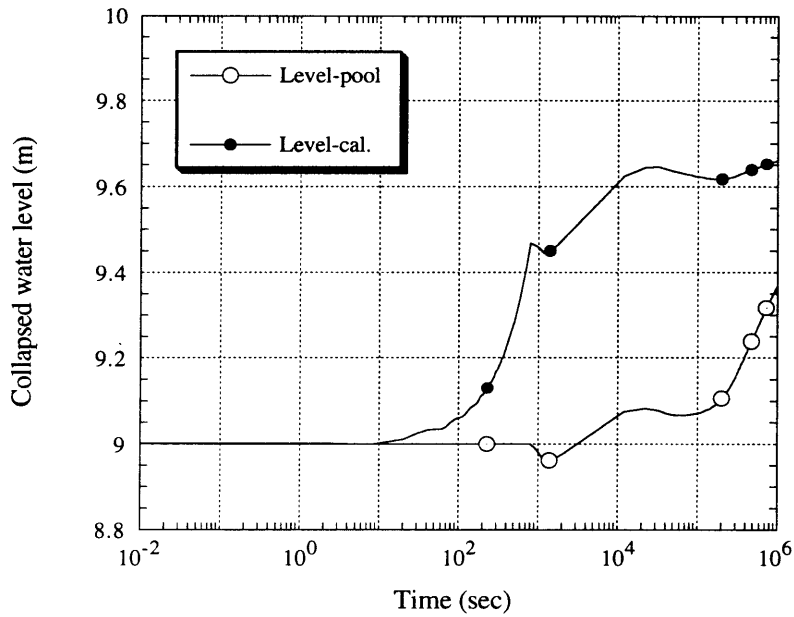


Figure 11-35 Histories of water levels in the pool and calandria

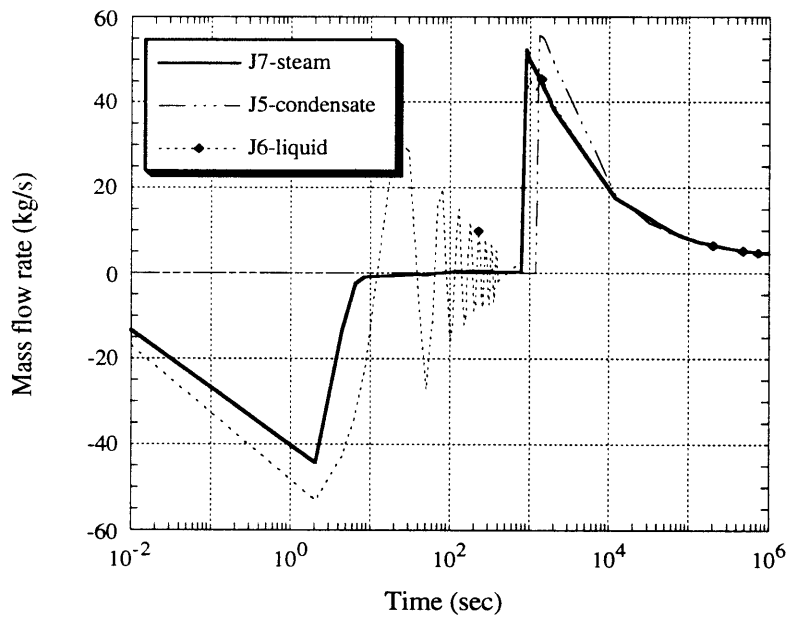


Figure 11-36 Steam evaporation, condensate return and flow through the gas lock

outer pool and changing the resistance to steam flow in the exhaust piping. Figure 11-36 shows the history of flow rates for vapor evaporated from the calandria (“J7-steam”), returning condensate (“J5-condensate”) and liquid flow through the gas lock (“J6-liquid”). Following the pressure wave from blowdown, the flow in junction 6 exhibits oscillations because of the different inertia of the pools, and the difference in pool surface areas exposed to the pressure wave; at later times the flow reaches a balance with steam flow evaporated from the calandria.

Alternative Design of Flooding Pool with Vapor Suppression System

Section 11.3 suggested another alternative for the calandria flooding system using the available flooding pool also as a suppression pool and redirecting steam from the calandria through the suppression pool, delaying in this manner long-term containment pressurization. Potential advantages of this alternative are shown on Figure 11-37. Figure 11-37 was generated using a GOTHIC model identical to the model shown on Figure 11-32, except for the pool volumes 4 and 5 which were lumped together into one pool with heat source representing release of the decay heat and stored energy from the core.

Figure 11-37 suggests that using the flooding pool for vapor suppression results in about a 10 hour delay in the initiation of the long-term pressurization and in a 17% decrease of the maximum pressure peak. The maximum pressure peak is reached at a much later time, i.e. 5.8 days, compared to 2 days for the reference case. Therefore, with respect to containment design, the vapor suppression system is preferable. The design of such a flooding system, however, would be more complex to ensure reliable functioning.

11.5.5.3 Key Factors Affecting Thermal Stratification

The containment analysis performed so far assumed a well-mixed containment atmosphere. Potential thermal stratification in a passively-cooled containment would have a negative impact on air cooling of the shell

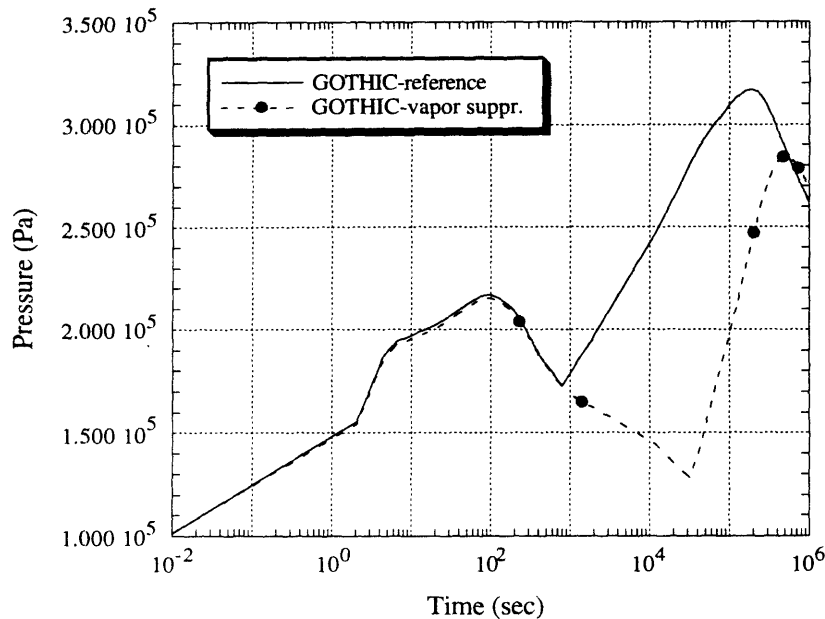


Figure 11-37 Potential improvements for the performance of calandria flooding using a vapor suppression system

and could significantly increase the maximum pressure peak. Section 11.3 described the design features employed to avoid, or at least to minimize, this problem. The main objective of this section is to confirm that these features work as expected, and that the assumption of a thoroughly mixed atmosphere in the containment holds. To gain more insight into this issue, key factors influencing thermal stratification are identified and explored.

GOTHIC Model with Full 3-D Nodalization of PTLWR Containment

The GOTHIC model used to analyze thermal stratification effects is shown schematically in Figure 11-38. Containment free volume is divided into a calandria space (volume 3) comprising the calandria vault, flooding pool, refueling system and associated equipment, and an upper containment (volume 4). The calandria space, which is represented by a lumped parameter model, is located below the main floor and is not in contact with the air-cooled wall, as shown on Figure 11-1. The upper

Volumes: 1 - Environment
 2 - Air annulus
 3 - Calandria space
 4 - Upper containment

BC junctions: 3 - Blowdown from unaffected loop
 4 - Blowdown from affected loop
 5 - Steam from decay heat and stored energy

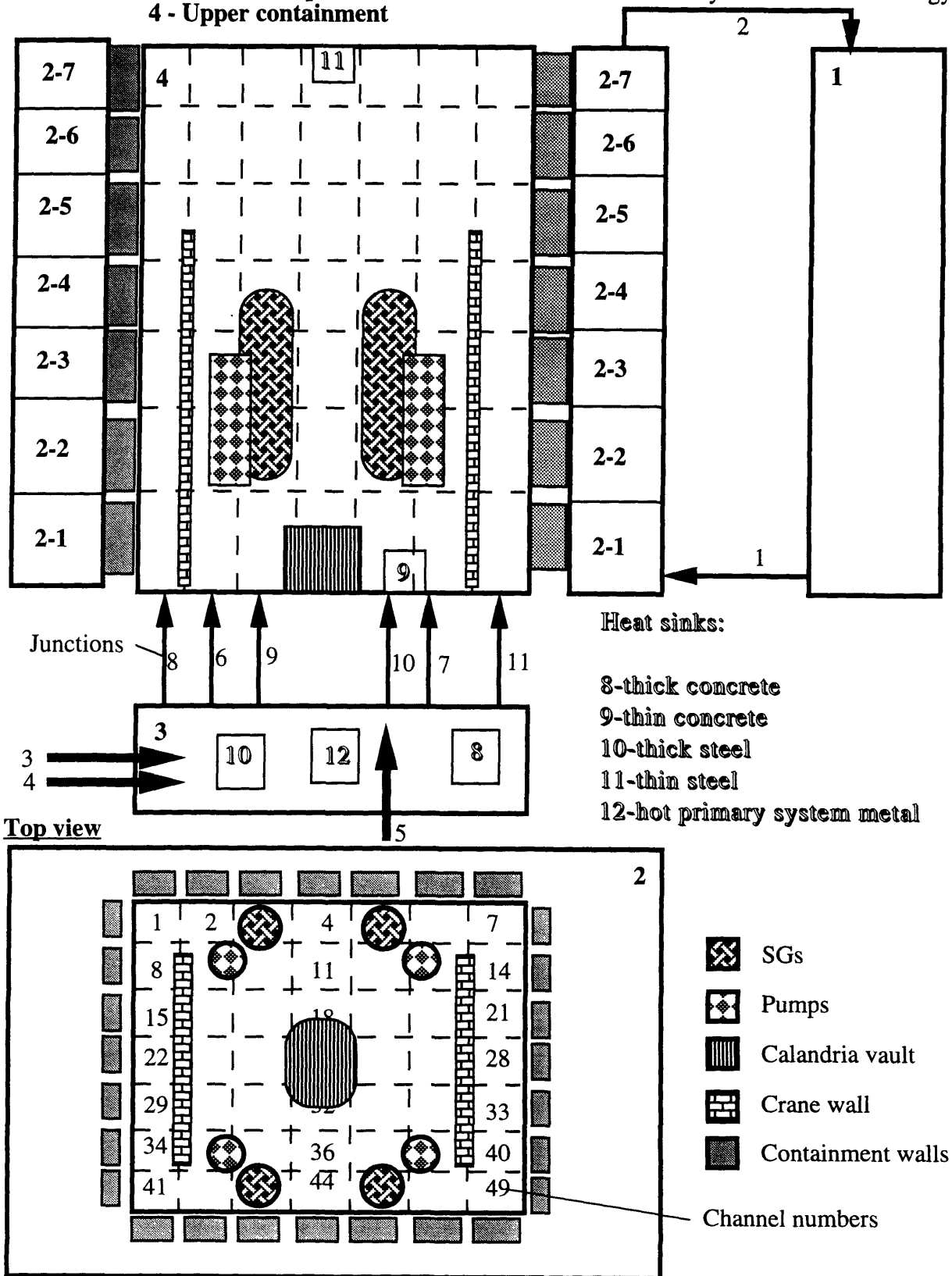


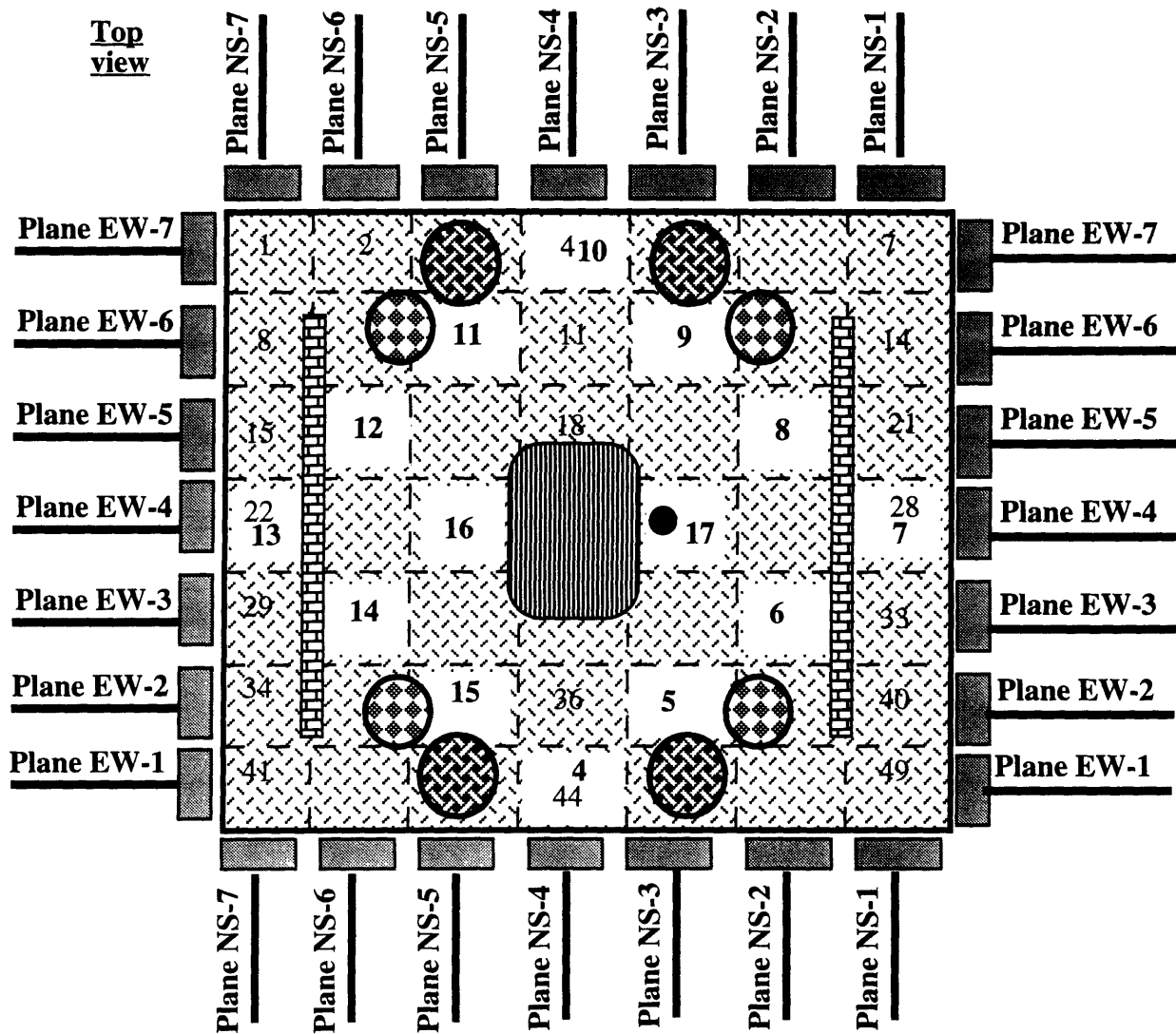
Figure 11-38 Schematic of a GOTHIC multidimensional model for the PTLWR containment

containment space is subdivided by a 7x7x7 mesh into 343 subvolumes. The mesh size is a compromise between the goal of obtaining sufficient information on natural circulation patterns while keeping the CPU requirements reasonable. Major equipment such as steam generators, RCS pumps, the upper part of the calandria vault and crane walls are modeled by blocking the appropriate flow areas using the GOTHIC “variable table” option. Internal heat sinks are the same as described in Section 11.5.3, and they have been split between the calandria space and upper containment as shown on Figure 11-38. The air-cooled annulus (volume 2) is modeled by 7 vertically stacked subvolumes. Vertical meshing of the air annulus corresponds exactly to the vertical meshing of the upper containment. The thermal connection between the air annulus and upper containment is provided by 196 external thermal conductors (each subvolume of upper containment facing the containment wall is equipped with a thermal conductor as shown schematically in the top view). The heat transfer coefficient on the air side is modified using the time-dependent multiplier from the RISRAD code in the same manner as in Section 11.5.5.2. The calandria space is thermohydraulically connected to the meshed upper containment by a set of junctions shown in the expanded top view in Figure 11-39. Figure 11-39 also shows the designation of cut planes used later to show velocity vectors in various containment regions. The arrangement of boundary conditions shown in Figure 11-38, i.e., blowdown from affected and unaffected loops, and steam generated from decay heat and discharging into the calandria space will be considered a reference case.

GOTHIC Runs to Study Factors Affecting Thermal Stratification

The following factors having influence on thermal stratification inside a passively cooled containment have been identified:

- elevation of the long-term steam release,
- break elevation,
- presence of crane walls or baffle, and
- form of long-term steam release (e.g., plume or jet).



xx - numbers for junctions connecting lower calandria space and subdivided containment space
 xx- numbers for channels in the subdivided containment space







- | | |
|---|--|
|  SGs |  Crane wall |
|  Pumps |  Steam jet from calandria |
|  Calandria vault |  Floor |

Figure 11-39 Top View of the multidimensional GOTHIC model for the PTLWR containment with location of junctions between calandria space and upper containment, and the designation of cut planes

To investigate the effects of these individual factors, five* GOTHIC runs listed in Table 11-9 and shown schematically in Figure 11-40 were performed.

Table 11-9 List of GOTHIC runs with the key factors influencing thermal stratification

Run #	Break elevation	Elevation of long-term steam release	Crane walls	Form of long-term steam release
1*	Low	Low	Yes [†]	Plume
2	High	Low	Yes [†]	Upward jet
3	High	High	Yes [†]	Upward jet
4	High	High	No	Upward jet
5	High	Middle	No	Upward jet

*Reference case.

[†] Crane walls on the east and west faces, no crane walls on the south and north.

Run #1

Run #1 is a reference case with the break in the primary system located at a low elevation (the Case 2 scenario described in Section 11.5.3.2 was considered), low-elevation long-term steam release in the form of a plume and with crane walls to promote natural circulation along the containment walls. Release of steam in the form of a plume is achieved by discharging the steam into the calandria space as shown in Figure 11-38 and turning-off the option of momentum transport for junctions connecting the calandria space and upper containment. Figure 11-41 shows the history of

* Two additional models were run for different configurations with adiabatic walls and with adiabatic walls at the top and cooled walls at the bottom. Since these runs do not pertain to this design, they will not be detailed further. It suffices to say that adiabatic walls sustain thermal stratification and that cooling at the bottom only does not break the stratification once established.

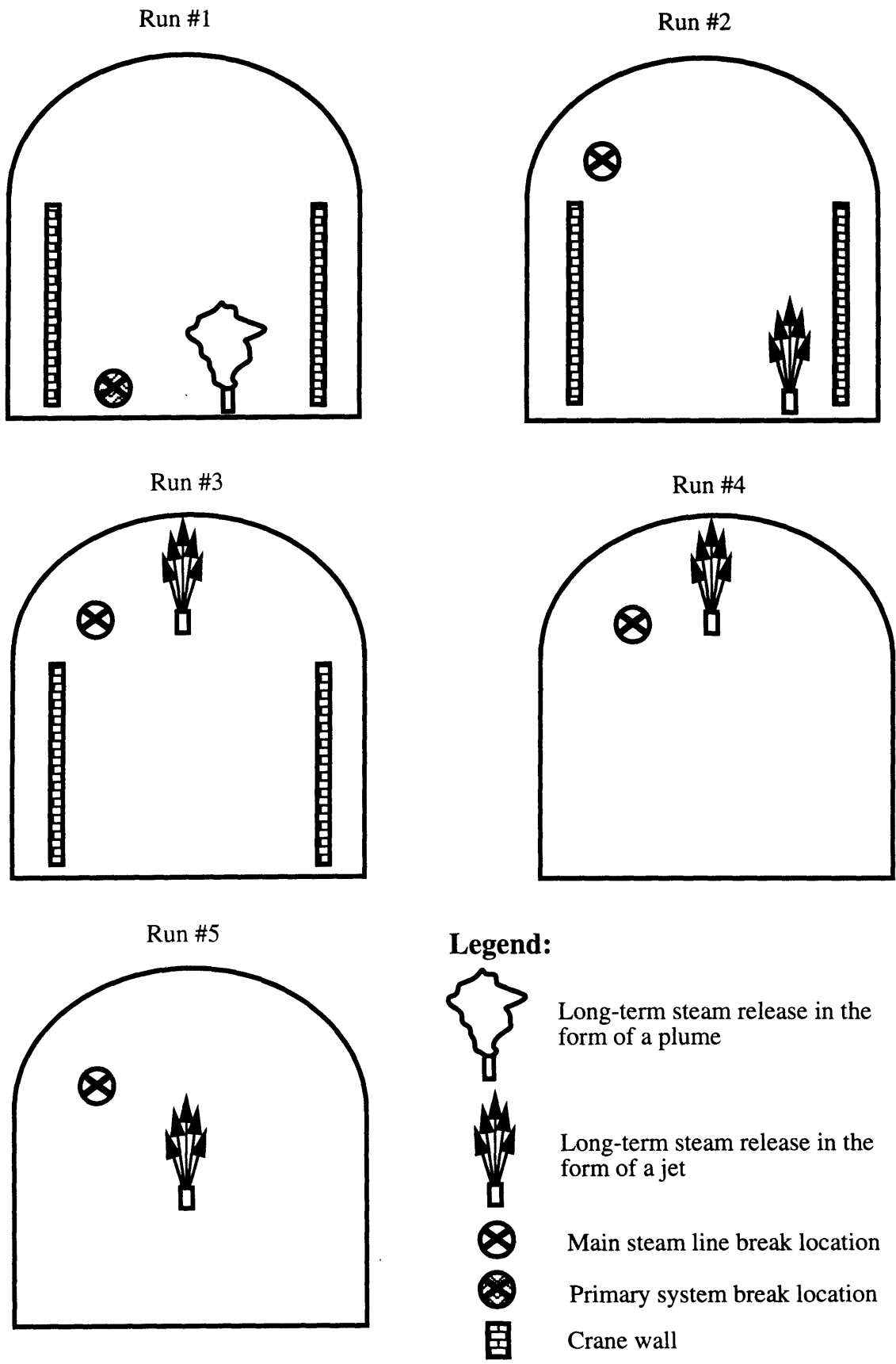


Figure 11-40 GOTHIC runs and factors affecting thermal stratification

atmosphere temperatures in the calandria space ,”T-cal.space”, and three axial levels, “T-level1”, “T-level4”, and T-level7”, where levels 1 and 7 designate the bottom and top level, respectively. It can be observed, that after blowdown, the atmosphere in the upper containment is well mixed. Figure 11-42 shows the axial inner-wall temperature profile along the containment height at 1.95×10^5 seconds (time of the maximum pressure peak). The temperature difference between the top and the bottom of the containment shell is small. The reason for such a uniform temperature profile can be observed on Figure 11-43, which shows velocity vectors of vapor projected onto four selected cut planes (see Figure 11-39 for designation of these cut planes). Hot steam from decay heat rises from the calandria space through the center of the upper containment to the top and returns down along the air-cooled containment walls, thus exposing, the entire steel shell to high temperature. Circulation behind the crane wall seems to be more pronounced than near the wall without the crane wall. This can be seen from velocity vectors at plane NS-1(with crane wall) and EW-1 (without crane wall).

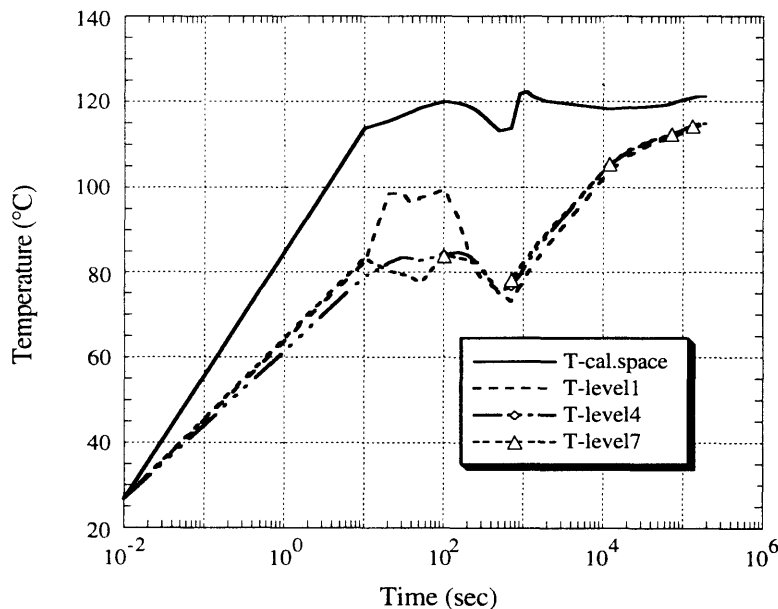


Figure 11-41 Histories of selected containment atmosphere temperatures for Run#1

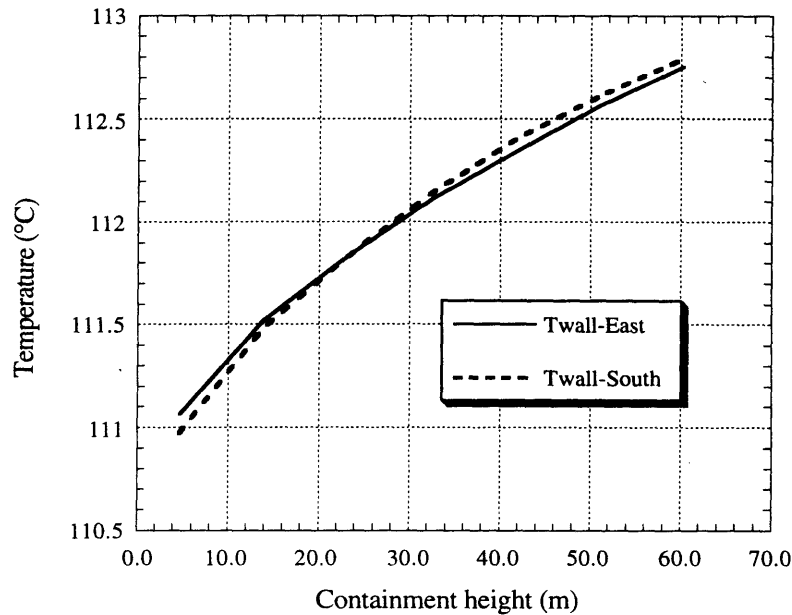


Figure 11-42 Temperature profile at inner surface of containment shell at 1.95×10^5 seconds for Run#1

Run #2

Run #2 explores the effect of the location of the break. It assumes that a steam line break (Case 3 scenario described in Section 11.5.3.2) is located 40m above the main deck. Long-term steam release is assumed at low-elevation in the form of a jet directed upward and located in channel 26 (see Figure 11-38 for channel numbers). The configuration of crane walls is the same as for Run #1. Following the blowdown at high elevation, thermal stratification was established to some extent*, but broken by the long-term hot steam arising from the jet. Figure 11-44 shows the velocity profiles at

* The extent of thermal stratification at the end of blowdown from the steam line break was very small since the violent discharge of the steam from the break promotes mixing of the entire containment atmosphere. Also note the different cut planes shown in Figure 11-44. This change in cut planes was made to avoid showing large velocities near the jet, which would make other velocities too small to see.

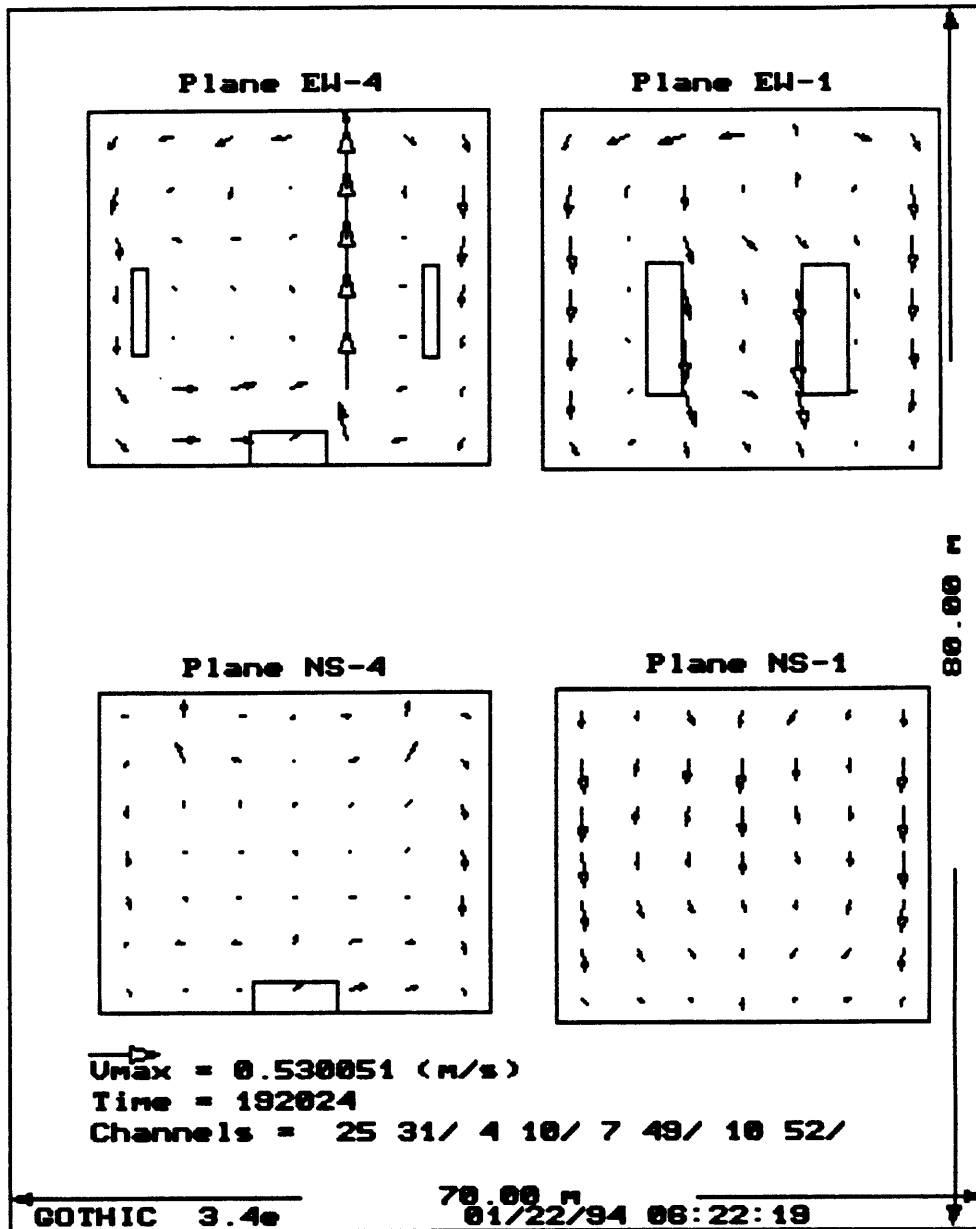


Figure 11-43 Velocity vectors at 1.95×10^5 seconds for Run#1

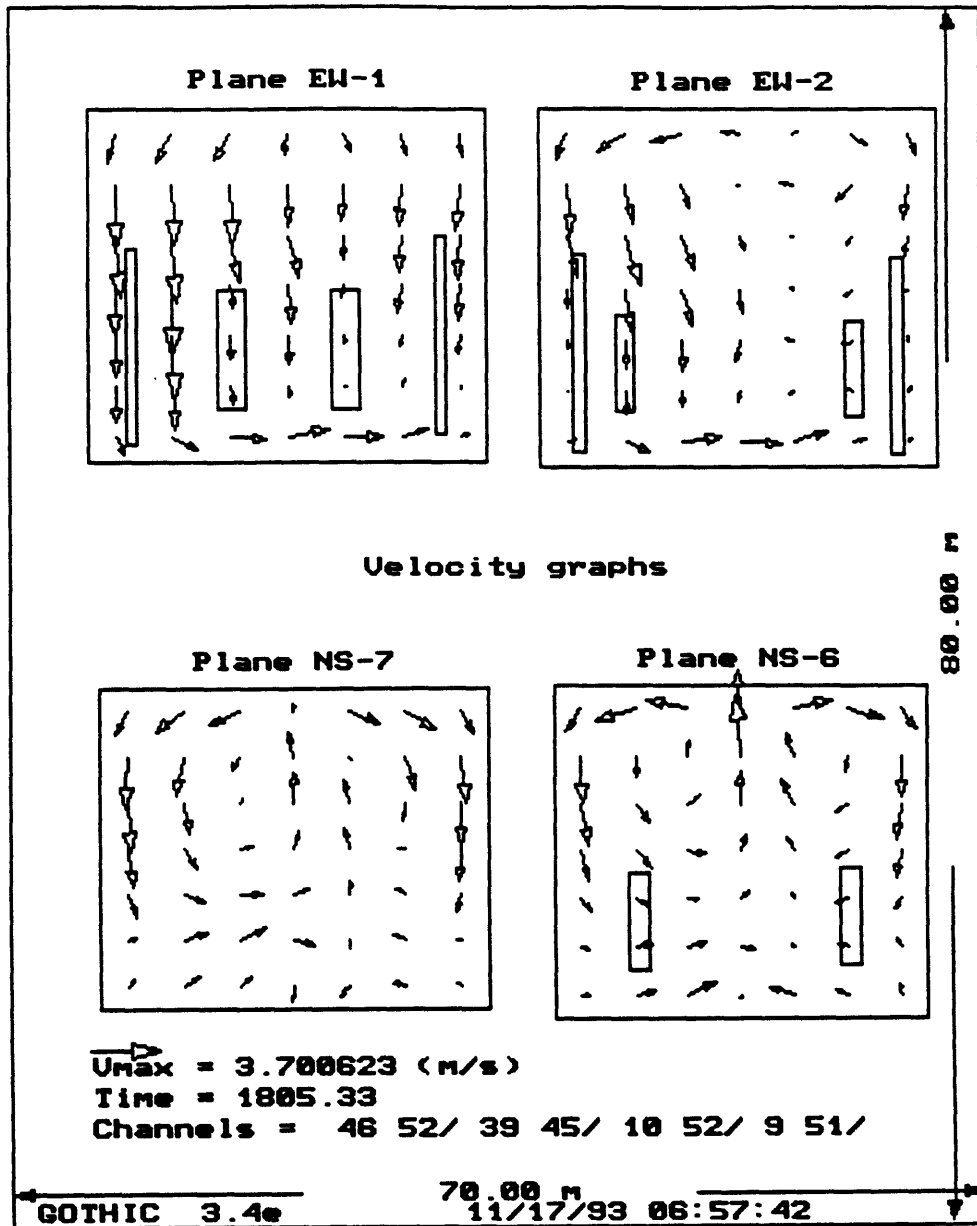


Figure 11-44 Velocity vectors at 1805 seconds for Run#2

1805 seconds. Significant natural circulation patterns can be observed with vapor entrained by a jet stream rising from the jet to the top and returning down along the wall. Once the natural circulation patterns are established, a state of well mixed containment atmosphere is retained beyond 1805 seconds, and the scenario was not calculated further to save computer time. The conclusions to be drawn from this run are twofold. First, thermal stratification resulting from the blowdown at high elevation is not significant due to very high steam velocities from the break, which promote atmosphere mixing in the whole containment. Second, the low-level location of the long-term decay heat release breaks thermal stratification which may eventually result from the high level break.

Run #3

Run #3 is a hypothetical case which assumes that the steam from decay heat is released at the top of the upper containment. The steam jet was directed upward and placed in the central volume of the highest layer of nodes (under the roof). The break location and the crane walls are the same as those described for Run #2. Figure 11-45 shows the time development of the inner-wall (west wall) temperature profile. Significant axial nonuniformities can be observed as the wall heats up. At 12,000 seconds, the upper half of the containment wall is hot, while the lower portion remains substantially cooler, with its first 10 meters 50 °C cooler than the upper half. The hot front moves very slowly downward as time progresses, but a large temperature difference between the top and the bottom remains. The reason for this situation is observed on Figure 11-46. The hot steam cannot reach low elevations since the atmosphere in the containment creates circulation cells in the upper portion of the containment. The location of long-term steam release is thus a very important factor in containment pressurization events.

Run #4

Velocity vectors on Figure 11-46 suggest that the crane wall may impair the development of circulation cells between the cooled containment wall

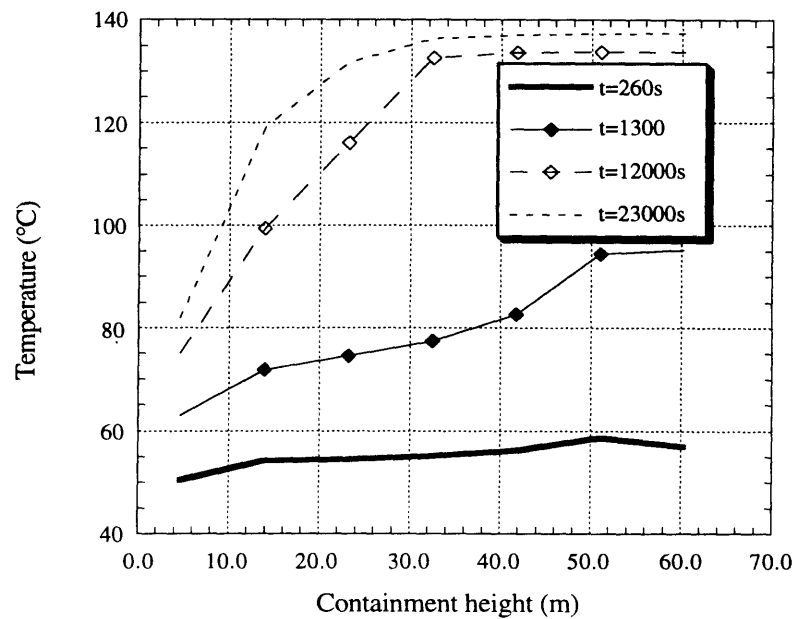


Figure 11-45 The development of inner-wall temperature profile for Run#2

and the center, and thus make the situation worse once thermal stratification has been established. To evaluate the effect of crane walls, Run #4, which uses the same configuration as Run #3 but without the crane walls was run. The results, presented in Figure 11-47 show that the crane wall used in the proposed concept does not have any significant impact on the scenario once thermal stratification has been established. Note, however, that this conclusion is not general, since a higher crane wall may have a more pronounced effect.

Run #5

Release of the steam from decay under the roof is a hypothetical situation. A more realistic location of a high-elevation long-term release point in an LWR containment would be somewhere in the midplane depending on the break location. Run #5 gives the assessment of such a scenario. The steam is released in the form of a jet directed upward and

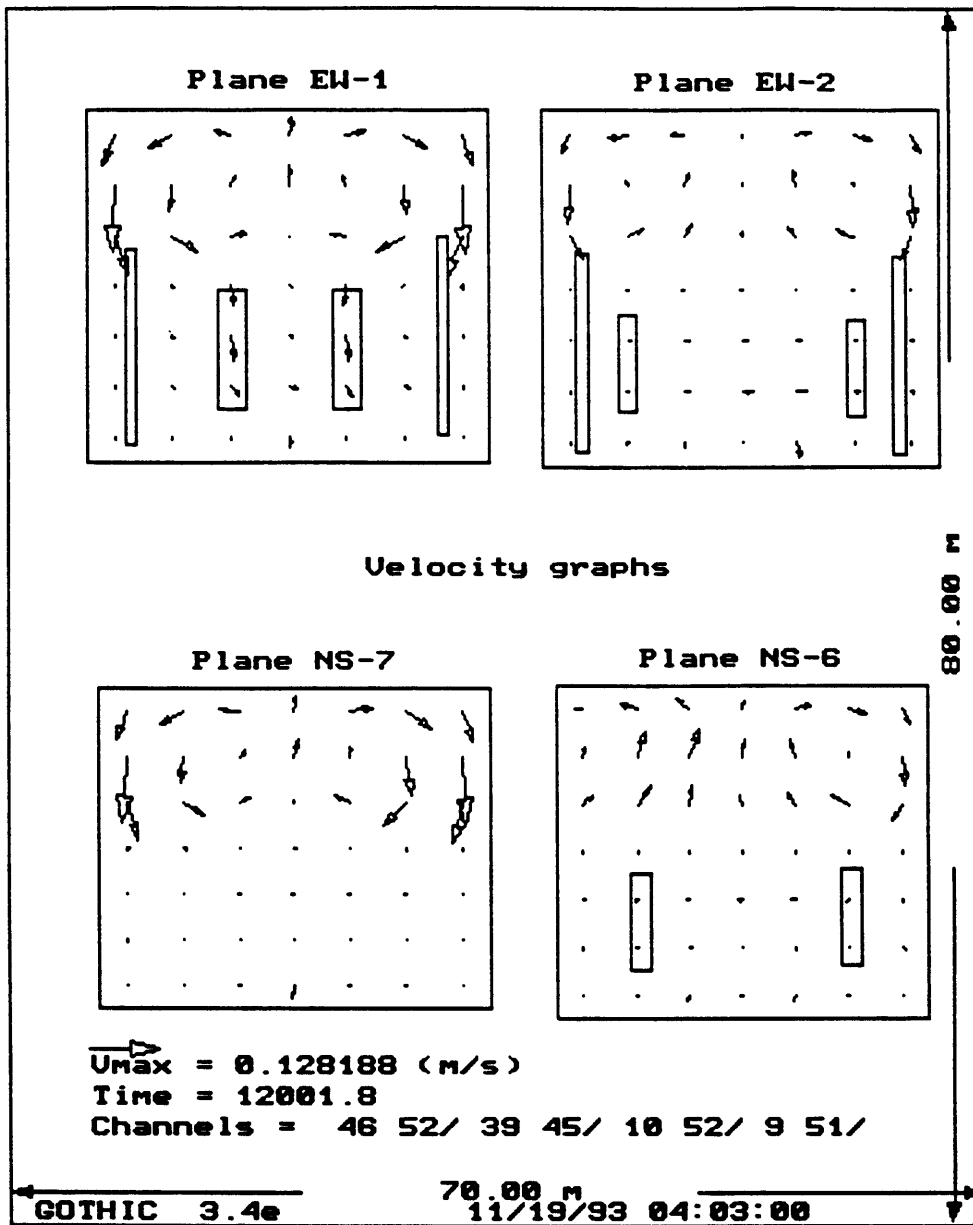


Figure 11-46 Velocity vectors at 12,000 seconds for Run#3

placed in the axial center of the subdivided upper containment. Velocity patterns in Figure 11-48 show significant natural circulation. No thermal stratification is evident for this case, however, caution should be exercised regarding the generalization of these results because different containment arrangements with obstructions preventing communication between the space below and above the jet may yield a quite different situation.

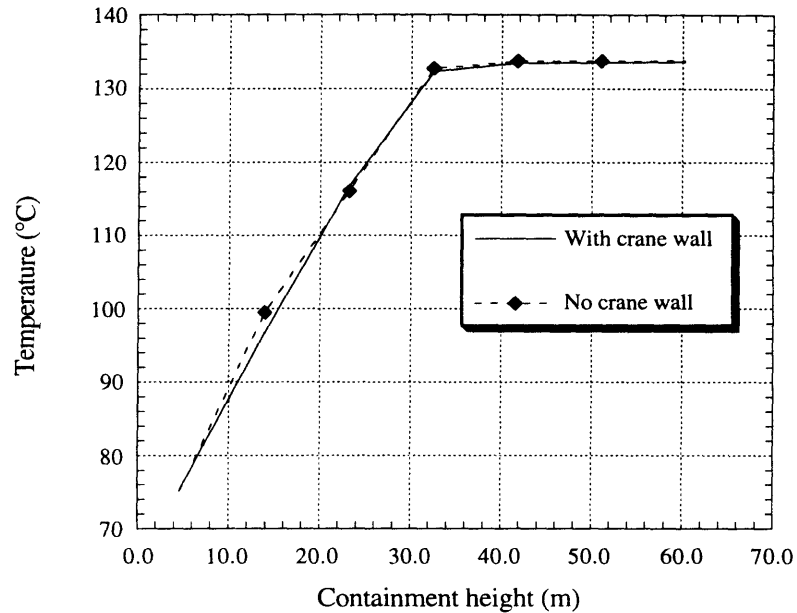


Figure 11-47 Comparison of inner-wall temperature profile at 12,000 seconds for arrangement with and without the crane wall

11.5.5.4 Conclusions

The results of reference Run #1 confirm that the assumption of a well mixed atmosphere in the proposed design holds even if the steam from decay heat is released in the form of a plume. This is an important conclusion with respect to the proposed design, which guarantees low-elevation long-term steam release. Moreover, the release of the steam from

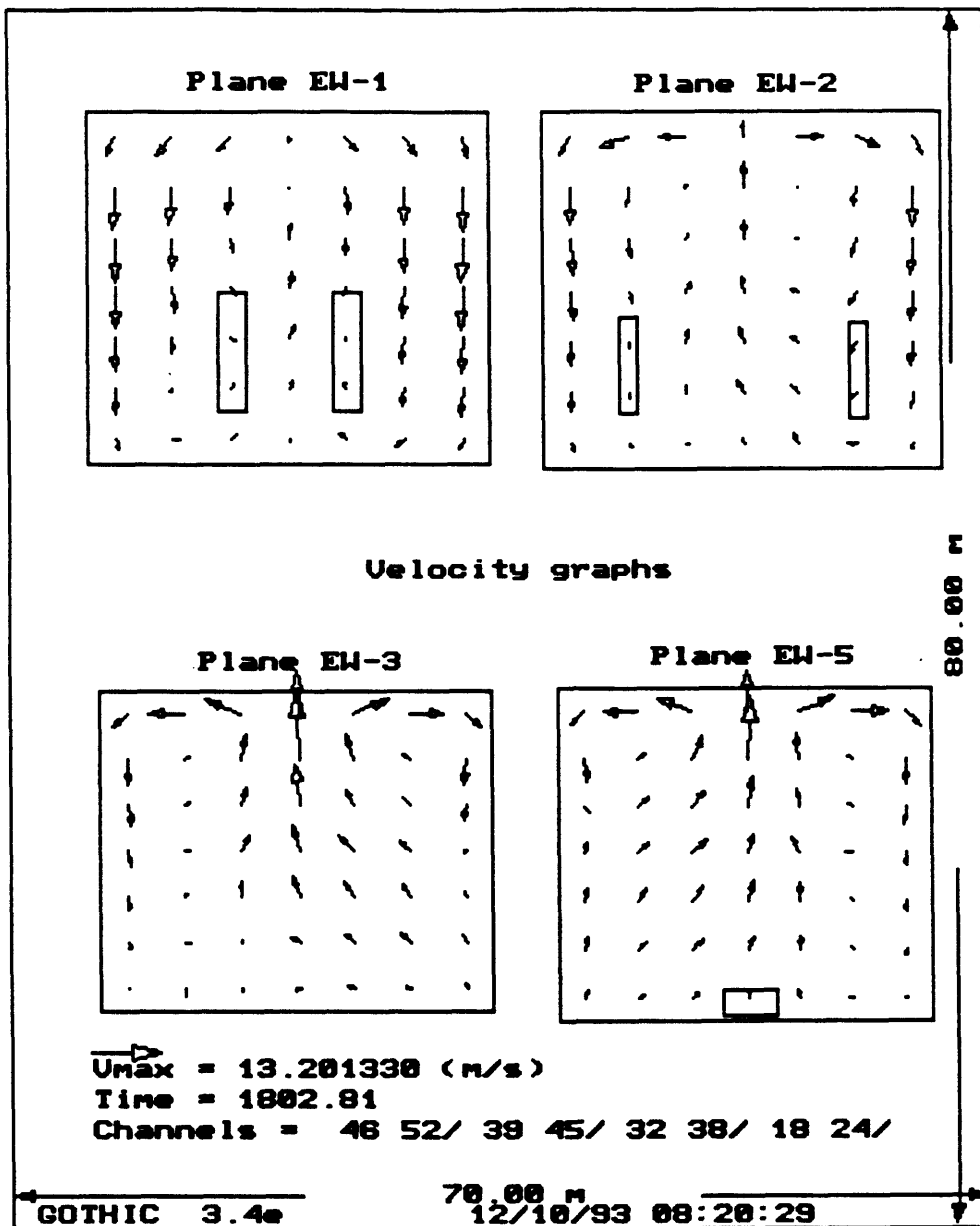


Figure 11-48 Velocity vectors at 1805 seconds for Run #5

the exhaust piping will be in the form of a jet directed upward. This will promote natural circulation and atmosphere mixing to a larger extent than that observed for a plume.

The lessons with respect to the key factors influencing thermal stratification, learned from the described runs, will be summarized next:

Elevation of the long-term steam release (from decay heat)

Elevation of the long term steam release is the dominant factor with respect to thermal stratification. A high-elevation release results in significant thermal stratification while a low-elevation release leads to stratification breakup and ensures a well-mixed containment atmosphere. In the dry calandria concept, long-term steam release at low elevation is guaranteed by the design. Consequently, the atmosphere should be well-mixed in the long-term.

Mid-elevation release leads also to good atmospheric mixing, but one needs to consider the details of in-containment arrangement. Note that containment arrangement in relation to the location of long-term steam release can also affect thermal stratification. If the steam release from decay heat occurs in the upper portion of the containment and the communication between the upper and lower part is restricted by internal structures, thermal stratification can result. This factor was not evaluated, since the detailed containment design which would be needed to quantify this factor is not available.

Elevation of the break.

Blowdown elevation is of minor importance for two reasons. First, the passive cooling of the containment shell does not play any significant role during the short blowdown period. Hence cooling cannot be impaired by thermal stratification. Secondly, the high velocity of the coolant escaping from the break leads to relatively good atmosphere mixing in the entire volume. However, this conclusion may not be true for all containment

configurations, as it also depends on the arrangement of rooms and structures inside the containment.

Crane walls or baffle.

The crane wall is used in the proposed design to promote natural circulation. Calculations showed that it can enhance circulation if the long-term heat source is located at low elevation. If the long-term steam release is at high elevation, a crane wall or other baffle-like constructions do not improve natural circulation. They can even have the reverse effect, because they can break up circulation cells between the center of the volume and the cold walls. In any case, crane walls or baffles can not be used as the only means to break up thermal stratification. In the dry calandria design, the use of crane wall is warranted as it enhances the already established natural circulation pattern in the desired direction.

Form of long-term steam release

Two forms of steam release have been investigated – a plume and a jet. An upward-directed jet of steam located in the lower portion of the containment significantly enhances natural circulation and mixing. The contribution of the jet located at high elevation to stratification breakup is negligible. Releasing the steam in the form of a plume at the bottom is sufficient to establish natural circulation and to attain a mixed atmosphere.

11.6 SUMMARY

Analyses presented in this chapter confirm that the maximum pressures reached in the proposed containment with passive air cooling remain within the range of design pressures for large dry containments of currently operating PWRs. The main reasons for the feasibility of air cooling only is the large free volume, the large heat capacity of the water pool and the large heat storage capability of internal heat structures, primarily concrete.

Future work should also optimize the design, taking into account economic considerations. A large containment shell with bare walls was chosen because of its simplicity and satisfactory performance. Simple solutions are generally less costly. Nevertheless this may not be true for the large containment, since increasing the containment size leads to a larger shield building, and hence an increase in cost and construction time for these structures. A detailed optimization study based on containment performance and the overall economics may show other passive cooling options to be preferable. In particular, an option with vertical fins would allow a significant decrease in containment volume, and cost, while retaining a high heat transfer rate. Preliminary studies performed by Babcock & Wilcox (B&W) confirmed such a trend [Menaker et. al., 1990]. The alternative of flooding coupled with a vapor suppression system also offers reduction of containment free volume, and hence cost reduction, as the preliminary results from Section 11.5.5.2 suggest. Based on similar studies by Turrichia [Turrichia,1993], a larger in-containment pool might also prove beneficial and cost effective.

The susceptibility of the air cooling system performance to various external events such as strong wind effects, tornadoes or blockages of air inlets and outlets should be also further investigated. However, based on ANL studies of the Reactor Vessel Auxiliary Cooling System (RVACS) for LMR applications [Tzanos and Hunsbedt, 1993], the effects of wind are expected to be small, and can be compensated for by air-intake design.

The CONTAIN run for a 50% reduction in the volume of internal concrete structures revealed significant sensitivity of the containment pressure to the amount of concrete present. More detailed design work needs to take into account more exact consideration of the amount of concrete and its distribution inside the containment to decrease the uncertainty associated with concrete heat sinks. Extensive sensitivity studies with respect to other system data should be also performed in order to estimate prediction uncertainties, to evaluate the effect of these data on containment pressure, and to identify the most important variables which have the best potential for improving containment performance.

Chapter 12

ASSESSMENT OF PTLWR SYSTEM RESPONSE TO ACCIDENTS

12.1 INTRODUCTION

The main thrust in the conceptual design of the passive pressure tube LWR was directed towards its performance in a loss of coolant accident without the replenishment of primary coolant. In practice, there is an entire spectrum of accidents and situations a reactor must withstand without core damage, and without releasing any radioactive substances into the environment. The purpose of this chapter is to assess the PTLWR's response to the various scenarios which could potentially threaten the core integrity or the environment, or the economic investment. A comprehensive evaluation with supporting calculations is a task which cannot be accomplished within the scope of this work. Therefore, the evaluation will be done in a comparative manner. The PTLWR concept is based extensively on CANDU design and has some features common to PWRs. Consequently, many PTLWR accidents or transients will be almost identical to those in CANDU or PWRs. Since the CANDU and PWR scenarios have been extensively analyzed, and are well understood, it will be assumed that the accidents which do not significantly differ (or are less challenging) from those of CANDU or PWR can be handled in a satisfactory manner by the PTLWR concept as well. Only the accidents which are substantially different from CANDU or PWR scenarios will be pointed out and studied in more detail.

The accidents will be classified according to EPRI specifications [Harrison et. al., 1986] into four event categories:

- condition I – normal operation,
- condition II– incidents of moderate frequency,

- condition III – infrequent events, and
- condition IV – limiting faults.

Normal operation envelopes all modes of planned plant operation including startup, power operation, refueling, and shutdown. Incidents of moderate frequency are defined as conditions beyond normal operation which are expected to occur during one calendar year of plant life. These incidents should be accommodated with, at most, a reactor shutdown, with the plant able to return to normal operation after corrective action is taken. Infrequent incidents are the scenarios that can affect one or more of the radioactive material barriers. Although these events are not expected to occur, their occurrence cannot be excluded during the plant lifetime. Partial fuel element damage may occur but loss of function of the reactor cooling system or containment barriers is not included in this group. Limiting fault events are not expected to occur in any nuclear power plant. These scenarios are postulated events for determining the design basis.

There are other accidents which are in the beyond design basis category for current LWRs, but may require special analysis. These accidents will be discussed separately as special events even though they may be handled within the design basis domain for the PTLWR. Incidents of moderate frequency, infrequent events, limiting faults, special events and important design criteria for each event are summarized in Table 12-1.

PTLWR primary system performance during normal operation has been analyzed throughout this work, and will not be further discussed. Incidents of moderate frequency will be covered in Section 12.2, infrequent events will be discussed in Section 12.3, limiting fault events will be the subject of Section 12.4, and special events will be covered in Section 12.5.

Table 12-1 Summary of accidents considered in the PTLWR
(adapted from Harrison et. al., 1986)

Event	Criteria
Incidents of moderate frequency	
Uncontrolled CRD withdrawal (loss of regulation in CANDUs)	DNBR, system pressure, FDL ^a
Inadvertent opening of SG relief or safety valve	DNBR, dose
Excessive increase in secondary steam flow	DNBR, FDL
Turbine trip, loss of external electrical load, inadvertent closure of MSIV	DNBR, system pressure, FDL
Partial loss of forced reactor coolant (RC) flow	DNBR
Loss of feedwater flow	System pressure
Chemical and volume control system malfunction	Time to pressurizer filling for operator action
Loss of auxiliary ac power	DNBR, system pressure, dose
Increase in feedwater flow or decrease in feedwater temperature	DNBR, FDL
Inadvertent opening of pressurizer safety or relief valve	DNBR, FDL
Instrument line break	Dose
Infrequent events	
Complete loss of forced reactor coolant flow	DNBR
Refueling incidents	DNBR, FDL, dose
Flow blockage of a coolant channel	DNBR, FDL
Small break loss of coolant accidents	DNBR, FDL

Table 12-1 (continued)

Limiting faults	
Steam line break	DNBR, containment pressure, dose
RC pump shaft seizure	DNBR, system pressure, dose
Feedwater system pipe break	System pressure, pressurizer water volume, dose
Large break loss of coolant accident	DNBR, FDL
Special Events	
Station blackout	Core cooling
Anticipated transients without scram	Pressurizer pressure, core cooling

^aFuel Design Limits

12.2 INCIDENTS OF MODERATE FREQUENCY

12.2.1 Uncontrolled CRD Withdrawal (Loss of Regulation)

Inadvertent reactivity insertion by control rods in current LWRs could be caused by control rod motion or by control rod ejection. Ejection of control rods is not possible in CANDUs and in the PTLWR since control rods do not penetrate the pressure boundary (in CANDU, control rods move in guide tubes submerged in low-pressure, low-temperature moderator; in the PTLWR control rods move in guide channels in the end reflector). Therefore the only unplanned reactivity insertion by control rods could be caused by uncontrolled withdrawal of control rods. Such a transient could be a result of a reactor control system malfunction. In CANDU units, this incident is termed "loss of regulation" event. Since the control system of the

PTLWR resembles that of CANDU reactors more than that of PWRs, a comparison with CANDU units will be performed.

In CANDUs, the maximum reactivity insertion rate which can be obtained from all control rod devices being driven simultaneously out of the core is 0.35 mk/s [Banerjee and Hancox, 1981]. Fast loss of regulation events are detected and counteracted by neutron power log rate trips, while the slow events are detected by high neutron power trips. Extensive analyses of these events show that even reactivity insertion rates of 2mk/s result in modest neutron power transients before being terminated by the shutdown systems.

Following CANDU practice, the PTLWR also employs neutron power log rate and high neutron power trips to terminate power excursions from uncontrolled withdrawal of control rod banks. The larger magnitude of the Doppler coefficient in the PTLWR compared to that of CANDU reactors combined with a large margin to fuel centerline temperature limit would significantly limit power excursions in the PTLWR concept. Since the PTLWR fuel is capable of operating in the post-CHF regime, DNBR can be exceeded without causing fuel damage. Hence, it is expected that events with uncontrolled withdrawal of control rod banks in the PTLWR concept should pose less of a challenge than in CANDUs or in PWRs.

12.2.2 Inadvertent Opening of SG Relief or Safety Valve

An inadvertent opening of the turbine bypass, relief, or safety valves with failure to close may cause the depressurization of the main steam system. This results in an increase in heat removal by the secondary side and consequent reduction in primary coolant temperature. Since the PTLWR concept has a negative coolant temperature coefficient, the cooldown of the primary system leads to reactivity insertion. This process is similar to that of PWRs, hence the comparison will be made with PWRs (note that in CANDUs, the process is reversed due to the positive void coefficient).

An inadvertent depressurization of the main steam system in PWRs typically leads to an automatic reactor trip on high power level, low DNBR,

or low SG water level. Pressure and temperature of the primary system decreases, which leads to a reactivity increase. Typically a secondary criticality is reached with all scram rods inserted. The safety injection system is initiated, generally on low steam line pressure, which injects borated coolant. An increased boron concentration in the coolant then renders the reactor subcritical.

In the PTLWR, cooldown of the primary system results in less reactivity insertion because the reactivity versus average coolant temperature curve (from the operating point towards lower temperatures) is flatter than that of PWR. For a typical temperature decrease of 60 °C for a PWR, the reactivity insertion is about 31 mk [Harrison et. al., 1986]. It can be deduced from reactivity versus coolant density curves, presented in Chapter 4, that for the same temperature decrease of 60°C in the PTLWR concept the reactivity insertion is about 8mk for the fresh core and 19mk for the equilibrium core. This much smaller reactivity insertion does not exceed shutdown margins, and no boron is necessary to make the reactor subcritical. Furthermore the large decrease in primary system pressure in this scenario will initiate calandria flooding, and render the reactor deeply subcritical.

12.2.3 Excessive Increase in Secondary Steam Flow

Excessive increase in secondary steam flow is a rapid increase in steam flow that causes power mismatch between the reactor power and the steam generator load demand. Typically, the reactor control system is designed to accommodate a limiting step load increase and ramp load increase (values depend on reactor vendor). An increase which exceeds the predefined values leads to reactor trip. In PWRs, excessive increase in secondary steam flow leads to an increase in reactor power due to negative coolant temperature feedback, similarly as in the previously discussed case, except that the transient is much milder. The DNBR is the key criterion to be satisfied.

In the PTLWR concept, this scenario will result in a smaller power increase at a lower rate than in a PWR due to the smaller reactivity insertion upon cold water ingress (see Section 12.2.2). Moreover, the DNBR

is not a crucial concern for the PTLWR fuel, since it can operate without damage in the post-CHF regime.

12.2.4 Turbine Trip, Loss of External Electrical Load, and Inadvertent Closure of Main Steam Isolation Valve

In the turbine trip event, the turbine stop valves close rapidly (typically 0.1 second) on loss of trip fluid pressure actuated by one of several possible turbine trip signals. The reactor is tripped directly (unless below 50% power) from a signal derived from the turbine stop valves. If a direct reactor trip signal is not transmitted, the reactor would typically trip on high primary system pressure. Closure of the turbine stop valves results in a loss of steam flow and an immediate rise in secondary system pressure and temperature. The automatic turbine bypass system is initiated to limit the pressure rise. In U.S. PWRs, it can typically accommodate up to 85% of rated steam flow. If the turbine trip is, however, actuated by a loss of condenser vacuum signal, steam dump to the condenser is precluded, and the turbine bypass system is not available. For such situations, the excess steam is released to the atmosphere, the main feedwater flow is lost and feedwater flow is supplied by the auxiliary feedwater system.

A similar scenario to the turbine trip event is a loss of external electrical load, which results in an automatic fast closure of the turbine control valves. Since the closure time of these valves is longer than the closure time of stop valves (approximately 0.3 seconds), this event leads to a less severe transient in primary system parameters than for the turbine trip scenario. Another scenario with similar consequences is the inadvertent closure of main steam line valves. Since the closure time of the turbine stop valves is shorter than that of the MSIVs, the turbine trip event is more limiting. The worst case – turbine trip actuated by loss of condenser vacuum – will be considered.

The PTLWR concept is similar to CANDU, hence its behavior in a turbine trip scenario will resemble the behavior of CANDU units, if the reactor trip is initiated directly from the turbine trip signal. If this trip is not initiated, the PTLWR reactor will trip from high primary system pressure, while CANDU reactors may experience a trip from high neutron

power due to their positive coolant temperature coefficient. A similar situation is present in Combustion Engineering (CE) or BabcoX&Wilcox (B&W) plants at BOL, since they have a positive coolant temperature coefficient at BOL. If feedwater is also not available, the PTLWR steam generators provide a heat sink in the SG secondary side water inventory for about 25 minutes to remove decay heat (similar to CANDUs), which provide the operator with sufficient time to establish an alternate heat sink, such as the shutdown cooling system. The shutdown cooling system has a heat removal capacity of 7% of operating power and is capable of removing the heat at full operating pressure.

The question to be resolved in the final design stage is whether to initiate calandria flooding in a turbine trip event. Since the frequency of this scenario is not negligible, it is preferable to avoid calandria flooding and to handle this event by reactor trip and the shutdown cooling system. Hence, the dead band of the means for flooding actuation should be selected to be above the pressure peaks expected in turbine trip.

12.2.5 Partial or Loss of Forced Reactor Coolant Flow

A partial loss of forced reactor coolant flow can be caused by mechanical or electrical failure in a reactor coolant pump, or from a fault in the power supply to the main coolant pump. Partial loss of reactor coolant flow in CANDU or PTLWR units, e.g., if one main coolant pump fails, does not significantly affect core cooling because the coolant flow in the affected circuit can be maintained at approximately 70% of the nominal value. This characteristic is due to the presence of two main coolant pumps in one loop; hence if one pump fails, the second pump can maintain the flow.

In a partial loss of forced flow, an increase in coolant temperature may occur due to the impaired heat removal rate from the fuel bundles. Hence the reactor power needs to be decreased to compensate for lower heat removal rates. This can be accomplished by power cutback to 70% power. Because of the temporary mismatch between the heat flux and the decreasing flow through the affected fuel channels, the DNBR margin is temporarily reduced. The management of this incident is similar to that in

a CANDU and should not pose any challenge to the PTLWR. The negative coolant temperature coefficient in the PTLWR will be beneficial since it will assist in the reduction in neutron power. Failure of both coolant pumps in a circuit constitutes a complete loss of cooling event, described in Section 12.3.1.

12.2.6 Loss of Normal Feedwater Flow

A loss of normal feedwater can be caused by feedwater pump failure, valve malfunctions or loss of offsite ac power supply. It results in a reduction in the heat removal capabilities of the secondary system. The reactor is tripped on low water level in the steam generator (SG) or on high pressurizer pressure. Steam generator pressure rises until it is relieved by atmospheric valves which are automatically opened to the atmosphere. The condenser for turbine bypass is assumed to be unavailable in this scenario. The secondary water inventory in steam generators begins to decrease and auxiliary feedwater pumps are started automatically, typically on low water level in the SG. If the auxiliary feedwater delivery fails, the CANDU and PTLWR SG secondary side water inventory provides a heat sink for about 25 minutes to remove decay heat*. This allows for sufficient time to establish an alternate heat sink through the shutdown cooling system. Calandria passive flooding is not necessary, but it is available as a backup if the shutdown cooling system fails. Handling of this event is similar to CANDU practice. The negative coolant temperature coefficient in the PTLWR is beneficial prior to shutdown.

12.2.7 Chemical and Volume Control System Malfunction

Operator error or a false electrical signal may result in an increase in reactor coolant inventory through chemical and volume control system charging pumps. In PWRs, an addition of unborated primary grade water to the primary system can also lead to boron dilution, and hence to an addition of positive reactivity. This type of accident is not possible in

* Note that the SG tubes are designed to withstand the full primary system pressure and can be boiled dry.

CANDU or PTLWR units because they do not have any chemical shim in the coolant. An inadvertent increase in reactor coolant inventory is characterized by increased pressurizer pressure and water level in the pressurizer. In the most limiting case – if the pressurizer level channel used for charging control fails in the low direction while charging is under automatic control – charging flow is at maximum level and the letdown flow is isolated. The worst postulated failure for this event is typically the failure of the pressurizer level channel, thus defeating the reactor trip on two-out-of-three high pressurizer level channels. To prevent filling the pressurizer solid, the operator must be relied upon to terminate the charging. In the PTLWR concept, this incident does not differ from that of CANDU, hence no additional provisions are needed.

12.2.8 Loss of Auxiliary AC Power

A complete loss of nonemergency ac power may result in the loss of power to the plant auxiliaries, such as the reactor coolant pumps, condensate pumps, etc. The loss of power may be caused by a complete loss of offsite grid and simultaneous turbine generator trip. This scenario is typically more severe than turbine trip since the decrease in heat removal is accompanied by a flow coastdown, which further reduces the capability of the primary system to remove heat from the core. The reactor trips and the plant vital instrumentation is supplied from emergency dc power sources. Bypass to condensers is assumed unavailable. The steam generator pressure rises as there is no steam removal until automatic relief valves or safety valves relieve the secondary steam to the atmosphere. The standby diesel generators begin to supply plant vital loads, including motor-driven auxiliary feedwater pumps. Decay heat removal from the core to steam generators is provided through natural circulation.

The loss of nonemergency ac power event in the PTLWR concept is similar to that in CANDU. The main difference is in the absence of diesel generators in the PTLWR concept. Hence the auxiliary feedwater pump needs to be turbine driven. Passive calandria flooding can serve as a backup for residual decay heat removal.

12.2.9 Increase in Feedwater Flow or Decrease in Feedwater Temperature

In PWRs, an increase in feedwater flow results in reduced reactor coolant temperature and consequently in an increase in reactor power due to their negative coolant temperature coefficient. This event may be caused by full opening of a feedwater control valve due to a feedwater control system malfunction or an operator error, an increase in feedwater pump speed, or startup of an auxiliary feedwater pump. Similar effects are experienced to those in events with decrease in feedwater temperature, which may be caused by a failure of feedwater heaters. The reactor is typically tripped on high neutron power.

The PTLWR response is comparable to that of a PWR. However, the power increase will be much less than in a PWR since the reactivity insertion in cold water ingress events is much smaller than that in PWRs (see Section 12.2.2 for more details). Moreover, the capability of the fuel matrix to operate in the post-CHF regime reduces the concern with decreased DNBR. It is expected that reactor trip will not be needed for these events.

12.2.10 Inadvertent Opening of Pressurizer Safety or Relief Valve or Instrument Line Break

The inadvertent opening of a pressurizer safety or relief valve can be caused by a mechanical failure of the valve, a spurious electrical signal, or an operator error. It leads to a decrease in reactor coolant system inventory and a decrease in reactor coolant system pressure. As the pressure drops, the water in the pressurizer flashes to steam, which is discharged into the pressurizer relief tank. Pressurizer water level begins to decrease. In PWRs, a reactor trip is typically initiated on low primary system pressure while in CANDUs the reactor would be tripped on high neutron power. With respect to its negative coolant void coefficient, the PTLWR behavior in this scenario would resemble that of a PWR. The reactor will be tripped on low reactor coolant pressure, however, the pressure decrease with time would correspond to CANDU behavior due to the similarity in primary system geometry. Since the pressure decrease is significant in such a scenario, calandria flooding would be initiated if the operator does not

identify the problem in time, and does not isolate the discharge by shutting off the block valves.

Another incident resulting in a similar response of the primary system is an instrument line break. If the failed instrument line penetrates the containment, an additional criterion is dose released outside the containment. Since the PTLWR fuel elements have two barriers to fission product release to the coolant – SiC coating of fuel particles and SiC coating of the matrix, the probability of coolant contamination from fission products should be less than for conventionally clad fuel. The higher neutron flux results in a higher N-16 activity per kg of coolant. Although the amount of coolant in the core is less than in the CANDU (by about 20%), the coolant activity is expected to be slightly higher in the PTLWR than in CANDU.

12.3 INFREQUENT EVENTS

12.3.1 Complete Loss of Forced Reactor Coolant Flow

A complete loss of forced reactor coolant flow may result from simultaneous loss of electrical supplies to all reactor coolant pumps. Since it poses a greater challenge to safety limits than the partial loss of forced reactor coolant flow, it is this event that is typically analyzed. In a complete loss of forced flow, a rapid increase in coolant temperature may occur due to the impaired heat removal rate from the fuel bundles. To mitigate this rapid reduction in coolant flow rate, the pumps are provided with high rotational inertia. In both CANDUs and PWRs, this increase is terminated by tripping the reactor to prevent departure from nucleate boiling. The negative coolant temperature coefficient in a PWR assists in the reduction in neutron power, early in the accident. However, because of the thermal capacity of the fuel, the heat flux is reduced more slowly than neutron power and also slower than the rapid decrease in coolant flow. Therefore, the DNBR margin is temporarily reduced.

The PTLWR concept retains the CANDU primary system layout, hence this scenario will be handled in a similar manner as in the CANDU. CANDU shutdown systems must be designed to respond promptly to prevent a neutron power increase from its positive coolant void coefficient.

The negative coolant temperature coefficient in the PTLWR may allow one to relax requirements on the scram system. A significant advantage of the PTLWR concept is the ability of its fuel to operate in the post-CHF regime. Therefore, even if the CHF margins are not satisfied, the fuel would not sustain any damage. It is expected that the reactor should be able to withstand even complete loss of flow without scram while safe fuel matrix limits are not exceeded. In this scenario, the reactor would be inherently shut down by the negative Doppler coefficient (enhanced upon voiding) and negative coolant void coefficient. This expectation needs to be confirmed, however, by detailed analysis.

12.3.2 Refueling Incidents

On-line refueling requires temporary connection of the fueling machines onto the primary system. Since during this procedure, the machines become part of the pressure boundary, failure of the refueling machines may constitute a breach of the primary system boundary. There are also failures associated with reclosing the fuel channel. Because these failures lead to breaks in the pressure boundary, they are considered as small LOCAs, and will be discussed under small break LOCAs.

Another possible scenario considered in CANDU safety analysis is the discharge of an entire fuel string of 12 bundles into the containment. The resulting temperatures of the discharged fuel elements and release of radioactive material into containment was found to be well within the containment capability [Banerjee and Hancox, 1981]. The high-heat capacity of the PTLWR fuel elements can accommodate significant heat generation without cooling before the limiting fuel temperature of 1600 °C is reached. The analysis of adiabatic fuel matrix heat up from decay heat generation, presented in Chapter 7, showed that the matrix can remain without any cooling for several minutes before the temperature at which increased fission product release is expected, is attained. This could give the operator time to flood the refueling floor and establish sufficient cooling of the discharged elements and thus prevent any fission product release. If no action is taken, the accident would be similar to that analyzed for CANDU units. However, the amount of fission products contained in the discharged fuel elements is higher than in CANDU fuel because PTLWR

equilibrium burnup is about 10 times more while the amount of heavy metal contained in the fuel elements is only 6 times less. At very high temperatures, the graphite matrix may catch fire and contribute to the rate of fission product release. Detailed analysis of this accident should be performed in future work.

12.3.3 Flow Blockage of a Coolant Channel

Since the CANDU and PTLWR concepts employ separate fuel channels, which do not communicate in a transverse direction, as do PWR fuel bundles, hypothetical blockage of the coolant channel during normal operation could lead to impairment of heat removal from the fuel, and consequent fuel damage. To prevent the blockage of coolant passages in CANDU fuel bundles, CANDU units employ inlet strainers with a mesh size less than the smallest passage in the fuel bundle. Hence, the total blockage of the fuel channel is highly unlikely. As in CANDUs, the PTLWR concept employs inlet strainers to prevent the blockage of the coolant channels. However, since the parallel coolant channels within a fuel channel do not communicate in the transverse direction as CANDU coolant passages do, a hypothetical blockage of one coolant channel is more challenging than for the CANDU fuel bundle.

To investigate the behavior of fuel elements with blockage of a coolant channel, a heat transfer model was developed using the finite element package ALGOR. The model assumes total blockage of one out of eighteen intermediate coolant channels, which have the smallest flow area and are thus the most likely to suffer flow blockage. Further it is assumed that the blockage of this channel is complete, i.e. there is no coolant inside the channel. This situation was modeled by setting the heat transfer coefficient in this channel to zero. Figure 12-1 shows the temperature distribution for an equilibrium core at the plane of maximum power density. The temperature of the matrix at the coolant channel circumference is raised from its nominal value of 341°C to 831°C and the maximum fuel centerline temperature in the fuel compacts in the proximity of the plugged channel is increased from 1215°C to 1295°C. Both the matrix and fuel centerline temperature remain below the design limits. Therefore, the PTLWR fuel element is tolerant to single coolant channel blockage. The plausible

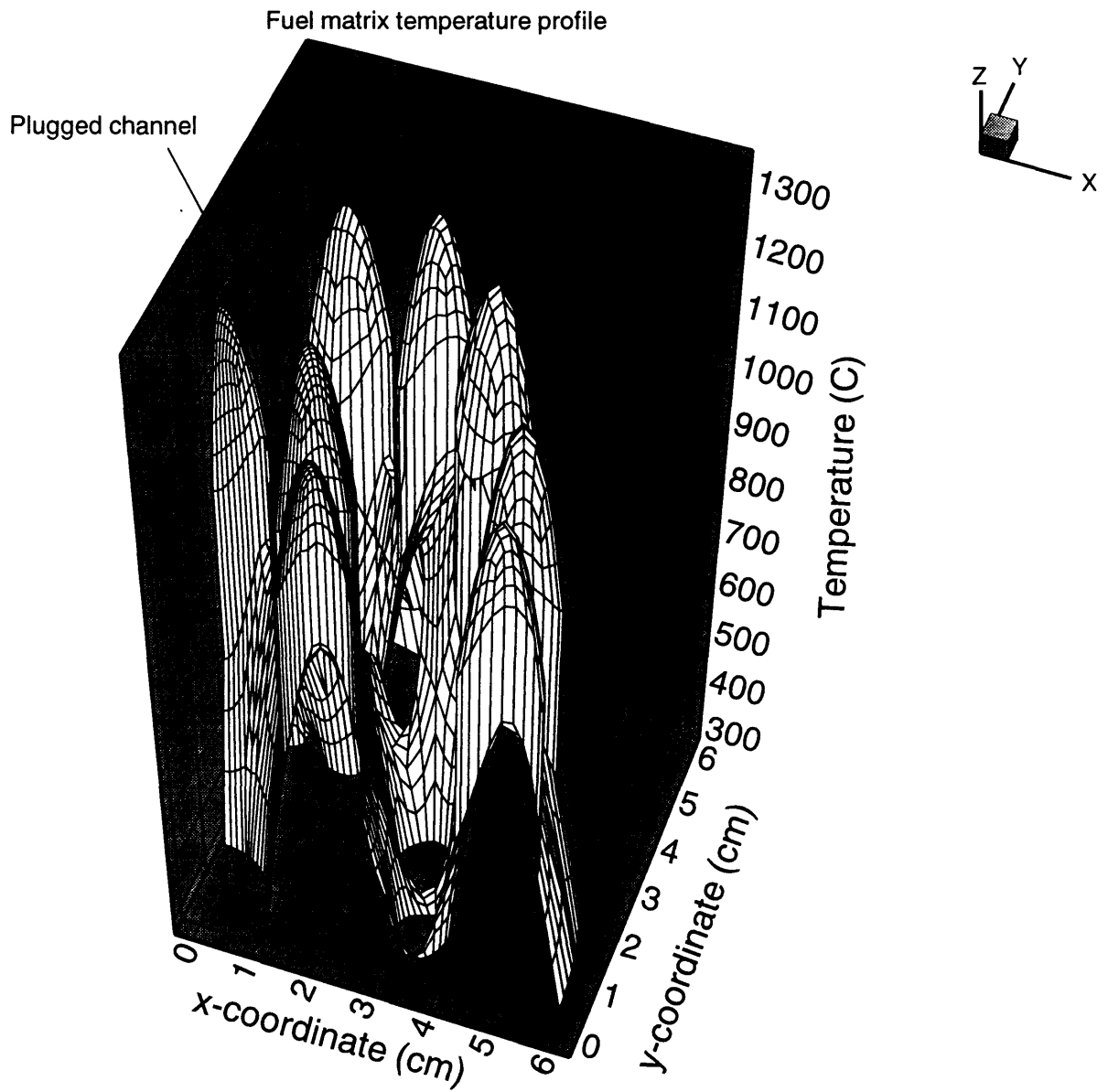


Figure 12-1 Temperature profile in the PTLWR fuel matrix with one-out-of-eighteen coolant channels plugged

performance of the PTLWR fuel in this scenario is the consequence of the high temperature limits of the matrix and effective heat redistribution to neighboring coolant channels*.

12.3.4 Small Loss of Coolant Accidents

Small loss of coolant accidents may be caused by various breaks. In the CANDU and in the PTLWR, small pipe ruptures are more likely to occur than in PWRs since the total length of small-diameter primary system piping is larger. Small LOCAs can occur by failure of a main reactor coolant pump seal, the failure of a steam generator tube, the failure of a fuel channel end fitting, and the failure of a feeder. Small LOCAs result in a loss of reactor coolant system inventory and a primary system pressure decrease. Since these incidents are similar to inadvertent opening of pressurizer safety or relief valves, described in Section 12.2.10, they will not be discussed here.

One particular incident which requires special attention is the simultaneous break of a pressure tube and its calandria tube, since the discharge of reactor coolant into the calandria space cover gas may affect the flooding process. It should be noted that the catastrophic failure of the pressure tube is highly unlikely since the critical crack length is less than the wall thickness of the pressure tube. Gas between the pressure tube and calandria tube serves for continual monitoring of any leak so that crack initiation can be identified early. The calandria tube may contain the pressure tube rupture. This has been confirmed by the Pickering accident where the pressure tube ruptured but the calandria tube remain intact. However, no credit for calandria tube integrity will be taken in the analysis. The analysis has been performed using the GOTHIC containment model, shown in Figure 12-2.

* Note that during normal operation, the azimuthal heat flux profile in the intermediate coolant channels shows a relatively low heat flux at the location facing the neighboring coolant channel. Hence, this portion of the heat transfer surface, which is not very effective during normal operation, becomes efficient if the neighboring channel is plugged.

Double-ended rupture of a pressure tube is assumed at time zero. The ruptured pressure tube was selected to be in the top row since this represents the worst case (note that ruptures at low elevations are submerged by flood water early, and the steam escaping from the break will condense, substantially decreasing the pressure rise. The pressure set points were selected at 0.28 MPa (0.04 MPa above operating calandria pressure) for both the flooding valves and safety valves. Since the primary system pressure is the same as in PWRs, a typical PWR value of the critical mass flux through the break ($G_{\text{break}} = 11,400\text{kg/m}^2\text{-s}$) and enthalpy at break discharge have been assumed. The value of mass flux was selected at the time of the break, i.e., when it is at its maximum, and kept constant throughout the transient. Similarly, the largest enthalpy value achieved in PWR blowdown has been chosen and kept constant throughout the entire transient. Both these assumptions are conservative. In particular, the mass flux decreases with time, and the pressure tubes have a relatively large length-to-diameter ratio, which will result in reduced critical flow rates.

The water level and the calandria pressure following the simultaneous rupture of the pressure tube and calandria tube are shown in Figure 12-3. The discharge from the break results in a pressure rise in the calandria. The higher calandria pressure pushes the water pool into the containment (not seen on the water level because the water flows through a horizontal pathway, located at zero elevation) until the pressure set point for both the flooding valves and safety valves is reached. After the valves are opened, the pressure falls and the calandria space is flooded. The flooding time is only slightly longer than for the normal flooding process without the in-core break. This is due to the significantly higher additional flow area of the safety valves. If the total flow area of the safety valves is decreased by 50%, flooding of the top rows could not be achieved because of the elevated calandria pressure needed to discharge break flow through the valves. On the other hand, it is noted that in case of a pressure tube break, the rate of discharge of primary system inventory is small, hence the rapid submergence of the top rows is not crucial, as in the case of a large LOCA.

- Volumes:** 1 - Environment
 2 - Upper containment
 3 - Air annulus
 4 - Flooding pool
 5 - Calandria

- 4 - Blowdown from ruptured pressure tube
 3 - Exhaust from safety valves
 7 - Exhaust from flooding valves

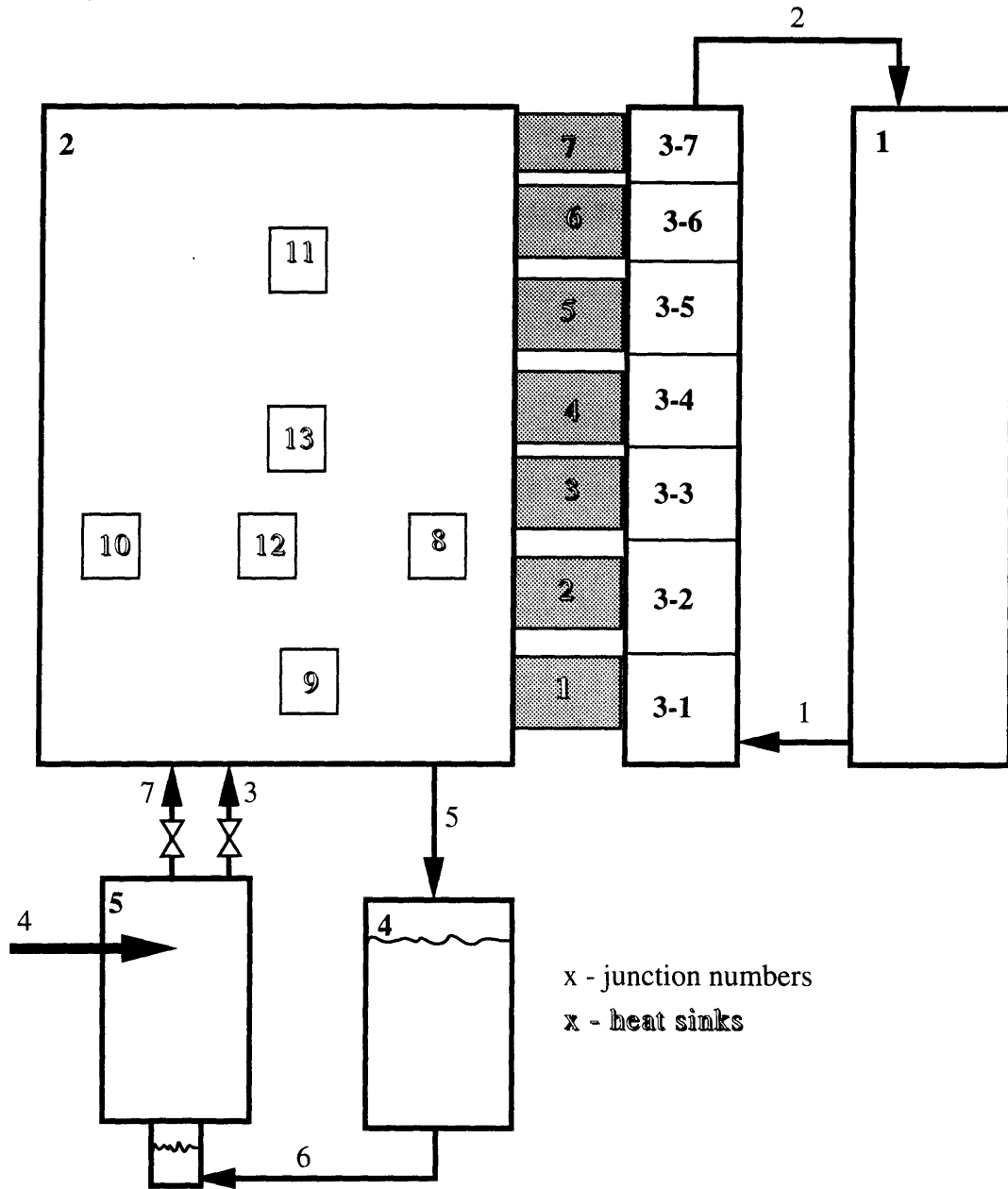


Figure 12-2 Schematic of GOTHIC model for calandria flooding following in-core pressure tube rupture

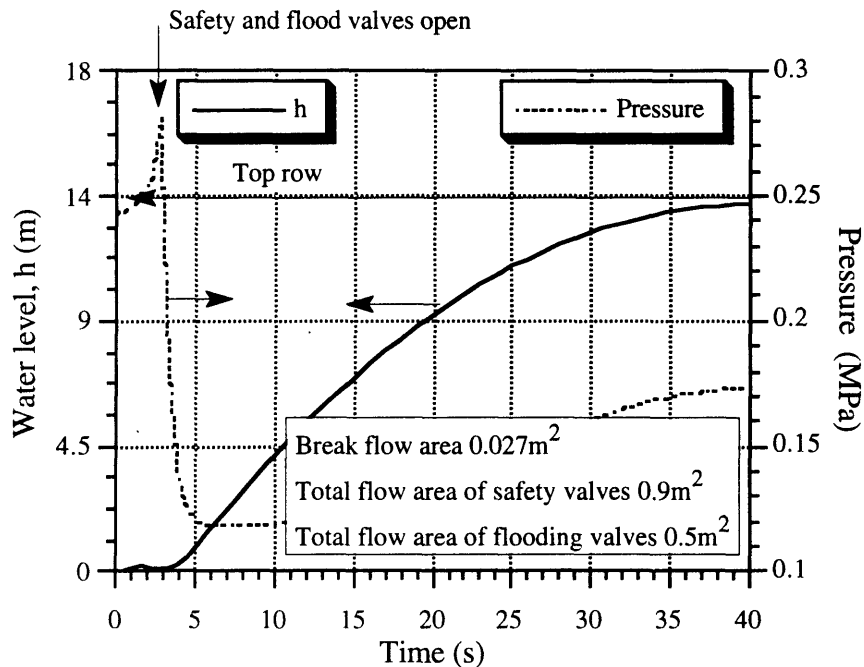


Figure 12-3 Water level in calandria and calandria pressure following pressure tube rupture

Rupture of the fuel channel may lead to damage of a neighboring fuel channel. It has been shown that a channel failure in CANDU units will not propagate to other pressure tubes [Muzumdar, 1987]. This conclusion would need to be, however, confirmed for the PTLWR design because the absence of the moderator outside calandria tubes may make this design more susceptible to such scenarios.

12.4 LIMITING FAULTS

12.4.1 Steam Line Break

Postulated hypothetical rupture of a secondary system steam line would result in a rapid depressurization of the main steam system, and consequently to a reduction in primary coolant temperature and primary system pressure. In CANDUs reduced coolant temperature leads to power reduction while in PWRs and in the PTLWR, it results in reactivity insertion due to their negative coolant temperature coefficient. The PWR analysis typically assumes that the most reactive control rod is stuck in its

fully withdrawn position. In this case, there is a possibility that after reactor trip, the reactor will become critical and return to power. Since the reactivity cannot be reduced by control rods, the only means for ultimate shutdown is an increase of boron concentration. The boric acid is delivered through the safety injection system. Once sufficient boron is present in the core to balance the excess positive reactivity from the decreased temperature of the coolant, the reactor power is reduced until the reactor is shutdown.

The PTLWR behavior will differ since there is no boron and because of the different magnitude of the coolant temperature coefficient. The reactivity insertion will be much less than in a PWR because the PTLWR is designed to operate closer to the peak on the reactivity versus fuel-to-moderator volume ratio curve. A typical temperature drop in this event is about 100°C for a PWR, which corresponds to a reactivity insertion of about 54 mk [Harrison et. al., 1986]. For the same temperature decrease of 100°C, the reactivity insertion for the PTLWR concept is about 8mk for the fresh core and 22mk for the equilibrium core. This compares to the 100mk shutdown margin provided by the scram system. This margin is available even if all control rods in the power cutback group are stuck. Hence, the reactor has ample margin to remain subcritical without the need for boron. Moreover, the large decrease in primary system pressure in this scenario (typically by 50%) will initiate passive calandria flooding, which will render the reactor deeply subcritical by 1300mk.

12.4.2 Reactor Coolant Pump Shaft Seizure

Reactor coolant pump seizure is a highly improbable event but it may be hypothesized that the pump impeller might severely rub on its stationary member and seize. Following the instantaneous seizure of a reactor coolant pump shaft, the flow through the affected loop is reduced very rapidly, leading to a heat transfer mismatch between the heat generation in the fuel and heat removal from the fuel to coolant, and a consequent drop in the DNBR. The reactor is tripped on low reactor coolant flow. In CANDUs, the event is accompanied by an initial power increase due to the positive void coefficient. CANDU analysis, which assumes one shutdown system unavailable, shows that transient dryout will occur (MDNBR=0.5) but the

shutdown system will prevent fuel centerline melt [Shapiro and Jesick, 1979].

In CANDUs, the flow rate in the affected loop is typically reduced to 60% of its nominal value. Chapter 6 showed that the PTLWR fuel elements can operate at full power with 50% flow rate, which is a more limiting case than that resulting from pump seizure. Therefore, the PTLWR fuel elements are not affected by this scenario due to their ability to operate in the post CHF regime.

12.4.3 Feedwater System Pipe Break

A major feedwater line rupture is defined as a break in a feedwater line which prevents the addition of feedwater to the steam generators to maintain their shell side fluid inventory. Fluid from the steam generator may also be discharged through the break. Typically, a break location is postulated such that it prevents subsequent addition of auxiliary feedwater. Depending on the size of the break and the plant operating conditions, the break can cause either an RCS cooldown by an excessive energy discharge through the break, or an RCS heatup. The latter scenario will be considered here since excessive RCS cooldowns have been discussed under the steam line break section.

The event is typically analyzed on the basis of a limiting scenario which assumes failure of the feedwater control system, the decrease of water levels in all steam generators until the low-low steam generator level reactor trip setpoint is reached, and a double-ended rupture of the largest feedwater line [Harrison et. al., 1986]. The residual heat is removed through boiloff of SG secondary side inventory supplied by auxiliary feedwater to intact steam generators. The main concern is that no substantial overpressurization of the primary system occurs. The PTLWR behavior will be similar to that of CANDU except for the inherent neutron power decrease due to its negative coolant void coefficient, prior to reactor trip. In addition to heat removal by boiloff of auxiliary feedwater in the intact steam generator in a loop, the shutdown cooling system can be aligned to remove the decay heat. Calandria flooding remains as a passive backup.

12.4.4. Large Break Loss of Coolant Accidents

Large loss of coolant accidents may be initiated in the CANDU or PTLWR by breaks in the reactor inlet header, reactor outlet header or a pump suction header. LOCA analysis is more complicated in CANDU systems than in PWRs because of the increased complexity of the primary system. Due to the specifics of CANDU primary system layout, limited breaks of large pipes may lead to more severe fuel conditions than a full double-ended break. For example, a 20% break of the inlet header is a critical stagnation break size which results in a sustained period of flow stagnation and the highest fuel temperatures, while a 100% break of the inlet header results in an immediate large flow reversal [Banerjee and Hancox, 1981]. The PTLWR primary system will experience similar phenomena since its layout is identical to that of CANDU. Since the PTLWR fuel channels can withstand LOCA regardless of the coolant conditions in the fuel channels, this situation is of no concern. Analysis in Chapter 7 showed that all critical temperatures in the fuel channel are well below their design limits even if there is no coolant inside the fuel channels.

The inlet header break is the largest primary system component which can fail. The capability to accommodate the break of the largest primary system component in a design basis accident spectrum is an advantage of the PTLWR over PWRs where the hypothetical catastrophic failure of the pressure vessel is beyond design basis. Note that failure of pressure tubes, which replace the pressure vessel in a sense, is also handled as a design basis accident. Catastrophic failure of the calandria vessel is highly unlikely since it is a low-pressure vessel (pressure 0.17MPa above atmospheric). But even if the calandria ruptures it would release the pressure of the cover gas and result in calandria flooding and reactor shutdown. The long-term cooling would not be affected, because the calandria is enclosed by a light water-filled calandria vault with concrete walls which serves as a shield tank and would prevent the leak of flood water and subsequent decrease in containment pool water level.

12.5 SPECIAL EVENTS

12.5.1 Station Blackout

For current LWRs, station blackout is a beyond design basis accident in a severe accident category which may lead to core damage and ultimately to containment failure. The accident is characterized by loss of off-site and on-site power and a failure to start diesel generators. The complete failure of ac power renders all ac-powered ECCS trains unavailable. The only power supply available is dc power from batteries until they are depleted (typically after 3-4 hours) Both turbine and reactor are tripped, but because the core decay heat cannot be removed, reactor coolant system pressure and temperature increase until the point where the primary system inventory will be released through the pressurizer relief valve. If the offsite power is not restored or the diesel generator is not recovered, there are no means to replace the lost inventory and the core will eventually uncover and sustain damage. If no mitigating measures are applied, the molten corium may melt through the vessel (or even through the containment wall) and pressurize the containment which may fail. In CANDU reactors, decay heat from the fuel channels can be removed to the moderator, which provides a heat sink for several hours, even if all coolant is lost while the fuel channel boundary remains intact. Fuel will be severely damaged in such an event but would not melt. However, if the cooling of the moderator cannot be maintained in the long term, the moderator would begin to boil and be eventually expelled from the calandria, which would lead to overheating of the fuel channels and their slumping onto the calandria bottom [Snell et. al., 1988].

The PTLWR design does not rely on any ac power source for ultimate decay heat removal. Therefore, it can cope with the station blackout sequence indefinitely without sustaining core damage. This scenario can be included in the design basis domain. It is noted, however, that a risk analysis of the core damage frequency needs to include a very improbable, but physically possible event – failure to initiate flooding. Failure to flood the calandria would lead to core damage and is beyond design basis.

12.5.2 Anticipated Transients without Scram

An anticipated transient without scram (ATWS) is an expected incident with a concurrent failure of the reactor protective system (RPS). The RPS, which automatically trips the reactor if variations and trends of important plant parameters indicate the existence of a situation potentially damaging to the reactor, is very unlikely to fail because it is actuated by numerous independent and diverse system parameters, it consists of several redundant channels, and is fabricated to the highest possible standard for power reactor equipment. ATWS events are not design basis events.

Since the ATWS scenarios encompass a wide spectrum of anticipated transients, they will not be described here. Instead, only common characteristics of two different groups of accidents – ATWS transients which result in RCS pressure increase and ATWS transients which lead to RCS pressure decrease will be discussed.

The ATWS events with increasing pressure are characterized by a mismatch between the reactor power and the heat removal from the reactor coolant system. In PWRs the events of greatest concern are typically the complete loss of feedwater flow or the complete loss of flow event. The heatup of the RCS depends on reactor power, which in turn depends on reactivity feedback dictated by the fuel and coolant temperature changes as well as coolant density changes. In CANDUs, the positive coolant void coefficient exacerbates the pressure peak. The increase in primary system pressure typically causes opening of pressurizer relief valves and primary safety valves. The increase in the primary system pressure is expected to be high. For example, a complete loss of feedwater ATWS in a CE PWR results in a pressure increase of about 80% in time period of about 90 seconds [Harrison,1986].

An ATWS with pressure-increase-type event in the PTLWR is expected to be much less severe than in a PWR or CANDU for the following reasons:

- the operator has an independent, diverse shutdown system by means of calandria flooding (note that in addition to passive flooding

initiation, the operator can always initiate flooding from the control room),

- automatic flooding is initiated by high reactor pressure (although later than could have been done by the operator) if the operator does not initiate passive flooding, and consequent reactor shutdown, and
- the PTLWR has a higher negative Doppler coefficient (about 60%) which is further increased on coolant density reduction, accompanied by primary system heatup.

On the other hand, the negative coolant temperature coefficient is about 40% less than in a PWR, thus leading to a smaller power reduction from coolant feedback. Overall, the combined feedback from the Doppler coefficient and coolant temperature coefficient is higher due to the higher Doppler coefficient. Therefore, the maximum pressure peak is expected to be less, even if the negative reactivity insertion from flooding is not considered. The key factor in reducing the primary pressure peak is, nevertheless, the flooding process which can shut down the reactor in several seconds (note that full reactor shutdown is achieved once the flood water covers two bottom rows of fuel channels, which happens in less than 2 seconds from the time of passive valve opening). Therefore, the coolant system pressure rise in the PTLWR is expected to be much less than that of a PWR or CANDU.

The decreasing pressure category of ATWS events is characterized by uncontrolled removal of energy from the primary system through a stuck open pressurizer relief valve or a small primary system pipe break. Reactor coolant system pressure and reactor density decreases. In PWRs, this results in a negative reactivity insertion. When saturation pressure is reached, increased void formation further reduces reactor power due to the negative void coefficient. On the other hand, in CANDUs this accident leads to positive reactivity insertion from the positive void coefficient, and CANDU designers must rely only on the Doppler coefficient to terminate the neutron power rise.

As in the case of ATWS with pressure increase events, the PTLWR concept is able to handle this accident without exceeding fuel channel

design limits. This has been confirmed in Chapter 7, where the more severe loss of cooling scenario without scram has been studied.

12.6 SUMMARY

This Chapter has discussed the behavior of the proposed PTLWR concept in various accident scenarios. The accidents were treated in three categories according to EPRI specifications – incidents of moderate frequency, infrequent events, limiting faults and a separate category of special events. The discussion has been conducted in a comparative manner with PWR and CANDU reactor types.

In the incidents with an increase in heat removal by the secondary system, the PTLWR behaves similarly to a PWR, but it will exhibit less of a neutron power increase prior to reactor trip due to smaller reactivity insertion for the same coolant temperature drop. For accidents with a decrease in heat transfer by the secondary system, the PTLWR retains the capability of CANDU units which employ a shutdown cooling system able to remove decay heat at full pressure, and large shell side SG inventory, which provides a heat sink for about 25 minutes before boiloff, thus allowing adequate time to align the shutdown cooling system. In addition, the PTLWR has an independent passive flooding system as a backup. The power peak prior to reactor trip will be less than that of CANDU due to the negative coolant temperature coefficient.

Accidents with decrease of reactor coolant flow rate do not pose any particular challenge to the PTLWR concept because its fuel elements can operate in post-CHF condition even at full power without exceeding fuel design limits. Therefore, even in the event of a hypothetical main coolant pump shaft seizure, no damage of the PTLWR fuel elements occurs while for a PWR and CANDU, partial fuel damage is predicted. The ability of the PTLWR fuel elements to operate in the post-CHF regime is a significant advantage, which makes the PTLWR fuel resistant to failure in most of the accidents where the DNBR criterion is challenged.

Potential reactivity accidents in PWR, CANDU and PTLWR units are summarized in Table 12-2. An advantage of the PTLWR over a PWR is that

no pressure assisted control rod ejections are possible. Also, all the reactivity incidents associated with the dilution or removal of coolant or moderator poison are eliminated.

The major contribution of the PTLWR is its capability to handle ATWS and station blackout – the major contributor to the core damage frequency in current PWRs and CANDUs – without sustaining core damage. This is primarily due to the redundant, diverse reactor shutdown provided by means of passive flooding, which concurrently provides a heat sink for long-term decay heat removal. Moreover, the path which links the heat sink to the core is entirely independent of the normal reactor core cooling system, hence it does not require any depressurization, and is not interfered with by the coolant escaping from the core through the break in the form of a two-phase mixture or steam flow. Also, the absence of a large pressure vessel eliminates the hypothetical catastrophic failure of a large pressure vessel and allows us to handle a break of the pressure boundary anywhere in the plant as a design basis event.

Table 12-3 gives a summary of behavior for various classes of accidents for the PTLWR and the key advantageous factors.

Table 12-2 Potential reactivity accidents in PWR, CANDU and PTLWR
(adapted from IAEA, 1993)

Class of accidents	PWR	CANDU	PTLWR
Control system failure	Control rod bank withdrawal	Control rod bank withdrawal or drain of liquid zones	Control rod bank withdrawal
Control rod (cluster) ejection	Pressure assisted control rod cluster ejection due to housing failure	N/A	N/A

Table 12-2 (continued)

Class of accidents	PWR	CANDU	PTLWR
Coolant/temperature and void effects	<ul style="list-style-type: none"> • Increase in heat removal by secondary side • Steam line break • Transients during operation with positive moderator temperature coefficient 	<ul style="list-style-type: none"> • Loss of primary coolant • Core coolant flow rate decrease 	<ul style="list-style-type: none"> • Increase in heat removal by secondary side • Steam line break
Dilution or removal of coolant/moderator poison	<ul style="list-style-type: none"> • Inadvertent poison removal • Injection of diluted accumulator or refueling water at shutdown • Injection of diluted water after LOCA • Ingress of secondary water • Restart of primary coolant pumps with cold dilute water in loop 	<ul style="list-style-type: none"> • Inadvertent poison removal • channel rupture when the moderator is poisoned 	N/A
Miscellaneous	Misloading fuel assemblies	<ul style="list-style-type: none"> • Accidents when control rods are grossly mispositioned 	None identified

Table 12-3 Summary of PTLWR behavior for various class of accidents with the key advantageous aspects.

Class of accidents	PTLWR behavior similar to:	Major advantageous aspects		
		Mechanism	New limits	Ultimate
Uncontrolled CRD withdrawal	CANDU except for positive void coefficient	No pressure ejection, large negative Doppler coefficient	Can operate in post-CHF regime	–
Decrease in heat removal by the secondary system	CANDU except for positive void coefficient	Negative void coefficient	Can operate in post-CHF regime	Flooding
Increase in heat removal by the secondary system	PWR	Small reactivity insertion on coolant temperature decrease	Can operate in post-CHF regime	Flooding
Decrease in reactor coolant system flow rate	CANDU except for positive void coefficient	Negative void coefficient	Can operate in post-CHF regime	–

Table 12-3 (continued)

Decrease in reactor coolant inventory	CANDU except for positive void coefficient	Negative void coefficient	Can operate in post-CHF regime	Flooding
Increase in reactor coolant inventory	CANDU	No boron	–	–
Channel plugging	CANDU	–	Can operate in post-CHF regime	–
Refueling accidents	CANDU	–	Can operate in post-CHF regime	–
LOCAs	CANDU except for positive void coefficient	Negative void coefficient	Fuel does not require presence of coolant	Flooding
Accidents with ATWS	CANDU except for positive void coefficient	Negative void coefficient	Can operate in post-CHF regime	Flooding, diverse shutdown
Station blackout	CANDU except for positive void coefficient	No ac power source needed	Fuel does not require presence of coolant	Flooding, decay heat dump to ambient indefinitely

Chapter 13

ECONOMIC CONSIDERATIONS

13.1 INTRODUCTION

Although the primary thrust in the development of the passive pressure tube LWR was increased safety, one needs to bear in mind that the reactor must first be economic and then be safe. Hence, an approximate economic evaluation is needed to establish a baseline for its economic performance and compare it with other operating reactors.

Power costs from nuclear power plants have three primary components:

- fuel cycle cost,
- capital cost, and
- operation and maintenance cost.

The purpose of this Chapter is to make an assessment of these components. The latter two items represent an extensive project, which cannot be addressed in detail within the framework of this work. Therefore, only qualitative estimates, based on comparison with currently operating CANDU reactors, will be given.

13.2 FUEL CYCLE COST ESTIMATE

Figure 13-1 shows the calculational schematic for a materials balance for the once-through fuel cycle and the nomenclature used in this Chapter. The assessment of fuel cycle cost assumes no fuel reprocessing, as is current practice in the U.S. The only cost from the back end materials balance is the cost of indefinite storage of the spent fuel, which is the de

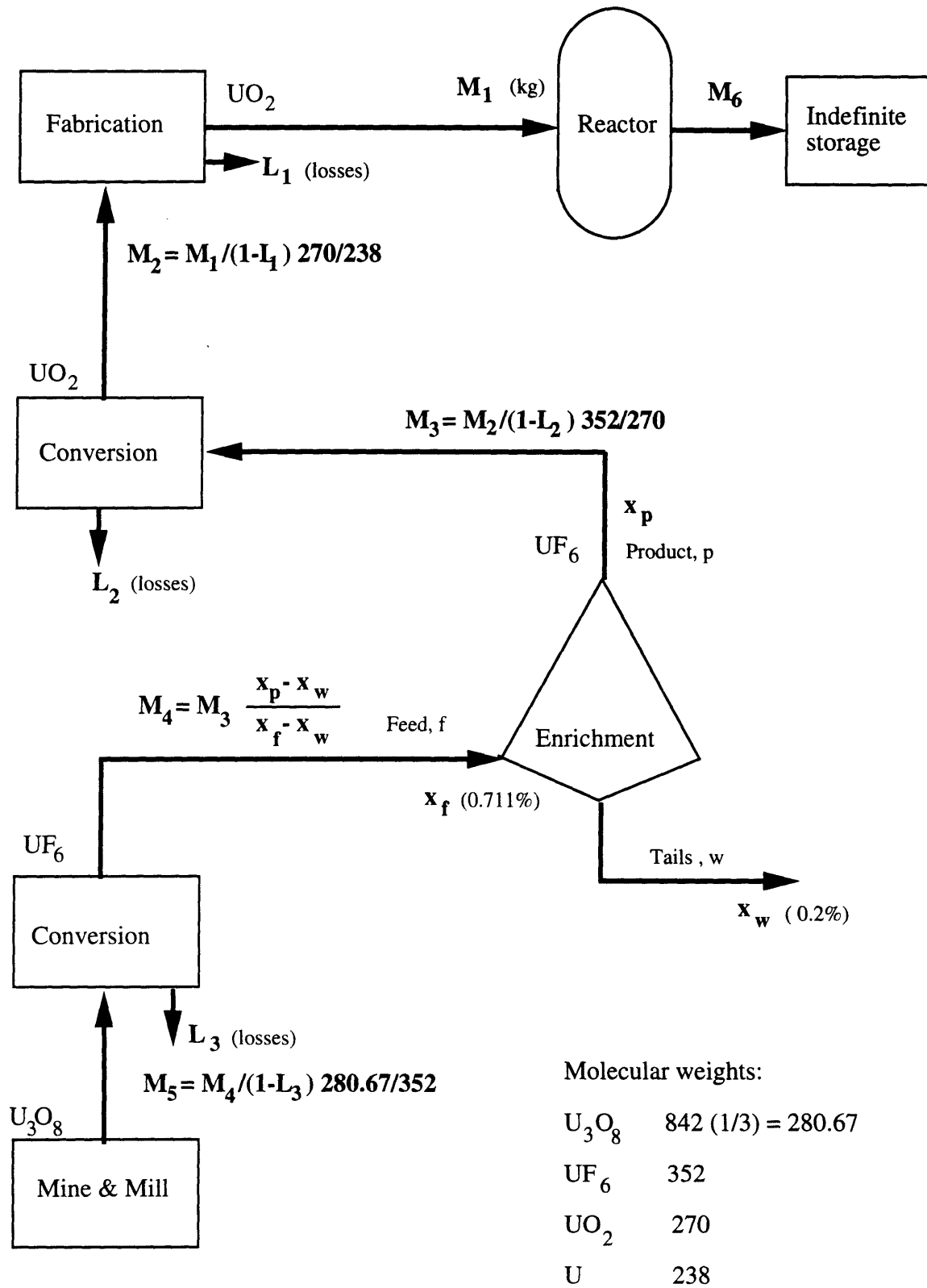


Figure 13-1 Material balance for once-through fuel cycle

facto status facing utilities in the U.S. Also, the 1mill/kWhr DOE waste disposal fee, which is the same for all reactors and fuel designs, has not been assessed. Reactors considered for comparison are a typical PWR, and a CANDU unit for both natural and slightly enriched uranium* fuel. General reactor performance specifications are summarized in Table 13-1.

Table 13-1 General reactor specifications for PWR, CANDU, CE-CANDU, and PTLWR design.

	PWR	CANDU	CE-CANDU	PTLWR
Electrical Power (MWe)	1100	2069	1260	1260
Thermal Power (MWt)	3300	600	4029	3899
Thermal efficiency (%)	33.3	29	31.3	32.4
Enrichment, w/o	4.15	0.711(nat)	1.2	7
Avg.discharge burnup (MWd/MT)	45000	7500	19750	77000
Capacity factor	0.8	0.9	0.9	0.9
In-core residence time (yr)	4.06	1.05	2.479	1.88
Core heavy metal loading(MT/GWe)	79	158.3	131.8	24.6
Fuel throughput (MT/GWe-yr)	19.5	151	53.2	13.1
U ₃ O ₈ requirements (MT/GWe-yr)	166.7	167.3	115.3	193

The discharge burnup for the dry calandria design was calculated by combining the MCNP and ORIGEN2 codes, as described in Chapter 4. The discharge burnup can be approximated by a linear equation

$$B_d = 25 + 17.33 (e-4) (MWd/kg) \quad (13-1)$$

* The CE-CANDU design was taken as a reference case for a CANDU with SEU fuel

where e is enrichment in %. The constants in Eq. (13-1) were calculated using the MCNP+ORIGEN2 discharge burnup results evaluated for three different enrichments: 4%, 6%, and 7%. Table 13-2 shows the discharge burnup as a function of enrichment.

Table 13-2 Discharge burnup versus enrichment for the dry calandria design

Enrichment (%)	4	6	7	8	9	10	12
B _d (MWd/kg)	25	56	77	94	112	129	164

In-core residence time in Table 13-1 was calculated from the relation

$$\tau = \frac{B_d \text{ (MWd/MT)} M_1 \text{ (MT)}}{P_{th} \text{ (MWth)} 365 F_c} \quad (13-2)$$

where M_1 is core heavy metal loading, P_{th} is thermal power and F_c is the capacity factor.

The last three items in Table 13-1 were normalized to 1000 MWe, i.e., 1GWe, for easy comparisons, i.e.,

- core loading

$$M'_1 = M_1 \text{ (MT)} \frac{1000 \text{ (MWe)}}{P_e \text{ (MWe)}}, \quad (13-3)$$

- fuel throughput

$$\dot{M}_1 = \frac{M'_1 \text{ (MT)}}{\tau}, \quad (13-4)$$

- and U₃O₈ requirements, following the calculations shown on the material balance in Figure 13-1

$$\dot{M}_5 = \frac{M_1 \text{ (MT)}}{(1-L_1)(1-L_2)(1-L_3)} \frac{x_p - x_w}{x_f - x_w} \frac{280.67}{238} \frac{1.102 \text{ ST}}{1\text{MT}} \frac{1000 \text{ (MWe)}}{P_e \text{ (MWe)}}. \quad (13-5)$$

Table 13-3 Economic parameters for once-through fuel cycle

	PWR	CANDU	CE-CANDU	PTLWR
Yellowcake price (\$/kg)	50	50	50	50
Separative work including conversion (\$/SWU)	110	-	110	110
Fabrication (\$/kg)	200	60 ^b	80 ^b	300 ^c
Indefinite storage (\$/kg) ^a	143	143	143	143
Carrying charge rate (%)	12	12	12	12
Tails assay (%)	0.2	0.2	0.2	0.2
Fabrication loss (%)	0	0	0	0
Conversion loss	0.05	0.05	0.05	0.05
Years prior to commercial use:				
• procure yellowcake	2	1	2	2
• complete enriching and conversion	1	-	1	1
• complete fabrication	0.5	0.5	0.5	0.5
• complete spent fuel storage (cask)	-2	-2	-2	-2

^a Taken from [Pilat, 1993].

^b Taken from [Boczar and Dastur, 1993].

^c Estimated 50% higher than the fabrication of PWR fuel. Note, however, that this estimate carries a large uncertainty. It is based on 1974 fabrication cost of HTGR fuel elements [Guentay, 1975]. Fifty percent difference between the fabrication cost of HTGR fuel elements and that of PWR fuel elements in the 1974 is assumed to remain the same in 1994 dollars. This uncertainty is very difficult to reduce at this stage, since no mass production of HTGR (let alone PTLWR) fuel elements is in place, and what information is available is proprietary.

The economic parameters used in the evaluation of fuel cycle cost are summarized in Table 13-3.

Fuel cycle cost was calculated using the materials balance shown in Figure 13-1 for the materials flow and unit costs given in Table 13-3. The amount of irradiated fuel, M_6 , is assumed to be the same as the amount of fuel loaded to the reactor, M_1 (the decrease in heavy metal weight due to burnup is small compared to the total heavy metal weight, and is therefore neglected, as is customary). The amount of SWU was calculated from the SWU balance shown in Figure 13-2 as

$$\text{SWU} = p V(x_p) + w V(x_w) - f V(x_f) \quad (13-6)$$

where

$$V(x) = (1-2x) \ln\left(\frac{1-x}{x}\right) \quad (13-7)$$

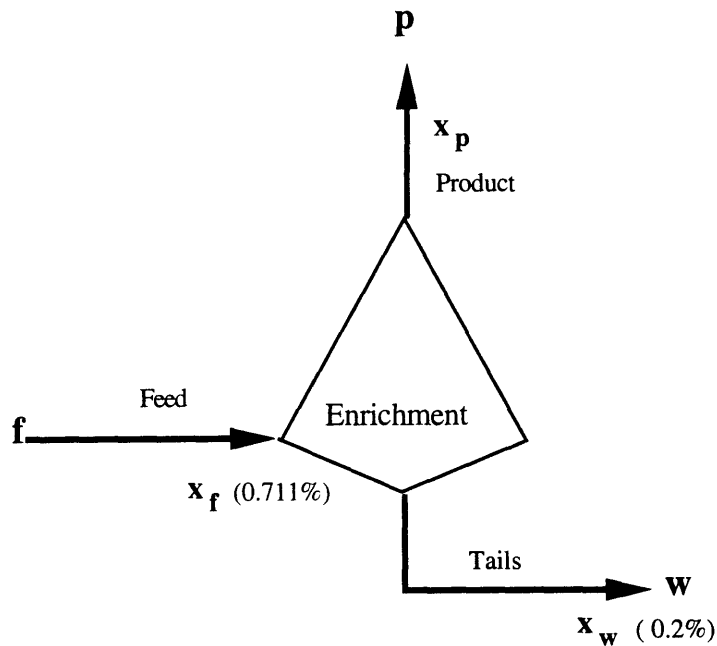


Figure 13-2 Parameters for SWU balance

Carrying charges are added (relative to the midpoint of irradiation) as follows

$$\text{Charge}_i = \text{Cost}_i \left(\Delta T_i r + \frac{\tau}{2} r \right) \quad (13-8)$$

where $Cost_i$ is the total cost of item i , r is the carrying charge rate, and ΔT_i is the time interval between the time item i is paid for and the time of fuel insertion into the core (in case of fuel disposal, ΔT_i is the time between fuel discharge and the time expenses for fuel disposal are paid for).

The fuel cycle cost formulae have been incorporated into a computer code. The results are summarized in Table 13-4. The fuel cycle cost of the PTLWR fuel is in the range of PWR fuel cycle costs, and higher than that of CANDUs. Since there is a significant uncertainty in the fabrication cost of the PTLWR fuel elements, the sensitivity of the total fuel cycle cost to this item is plotted in Figure 13-3. It can be seen that even if the fabrication cost is doubled, the PTLWR fuel would still remain competitive (a total fuel cycle cost of 5.9 mills/KWhr). The fuel cycle cost for the PTLWR fuel can be decreased by increasing the enrichment. This can be observed in Figure 13-4, which shows fuel cycle cost and U_3O_8 requirements as a function of enrichment. Since the particle fuel can withstand burnups to about 100 MWd/kg, the current burnup, 77 MWd/kg, can be increased, without exceeding fuel burnup limits. However, it has been shown in Chapter 4 that increasing the enrichment increases the local power ripple when the fresh fuel bundle is inserted into the core. This power ripple can be further reduced by using burnable poison in the fresh fuel bundles and by introducing more sophisticated refueling schemes. Thus the higher enrichment can be tolerated. In any event, the gain in fuel cycle cost is not very substantial because the cost versus burnup curve becomes flatter for enrichments beyond 7%. Consequently, the option of increasing enrichment was not pursued further, at this conceptual stage.

An interesting point to note is that the LEU CANDU fuel cycle cost does not show a big advantage over PWR fuel. Although the front end cycle cost is considerably less than that of a PWR, including the price for spent fuel storage increases the total fuel cycle cost of CANDUs substantially. This is because of the very high heavy metal throughput for CANDU reactors fueled by natural uranium. This high throughput is the consequence of very low achievable burnup, but it can be significantly decreased using slightly enriched uranium (SEU) fuel, as can be clearly observed from Table 13-4. In contrast, the PTLWR design has the lowest heavy metal throughput

Table 13-4 Comparison of fuel cycle cost for PTLWR with PWR and CANDUs

	PWR	CANDU (LEU)	CE-CANDU (SEU)	PTLWR
Cost of yellowcake (mills/kWhr)	1.60	1.14	0.84	1.50
Cost of enrichment and conversion (mills/kWhr)	2.87	0	0.60	3.10
Cost of fabrication (mills/kWhr)	0.72	1.30	0.65	0.58
Cost of post-irradiation storage (mills/kWhr)	0.20	1.90	0.59	0.15
Total cost (mills/kWhr)	5.39	4.34	2.68	5.33
Including D ₂ O inventory cost	-	6.82	5.16	-

Note: costs do not include the federally mandated 1mills/kWhr waste disposal fee

(an order of magnitude lower than CANDU). This may play an important role in the future, where the price of spent fuel disposal is likely to increase because of growing environmental concerns. On the other hand, the PTLWR fuel is the most radioactive (per kgHM) but the best-protected, by two barriers: the SiC coating of the particle fuel and the SiC coating of the graphite matrix. It should be also pointed out that the indefinite storage charge on a kg of heavy metal basis slightly favors the PTLWR fuel, which has small heavy metal loading. If this item is costed per unit volume, relative to LWR fuel the total fuel cycle cost would be higher than the tabulated value (5.90 mills/kWhr).

Table 13-4 shows two levels for total CANDU fuel cycle costs. The second cost includes the price of heavy water for CANDUs. Heavy water cost may be included in either the capital cost or in the fuel cycle cost. In this work, it will be included in the fuel cycle cost. The inventory of heavy water for a

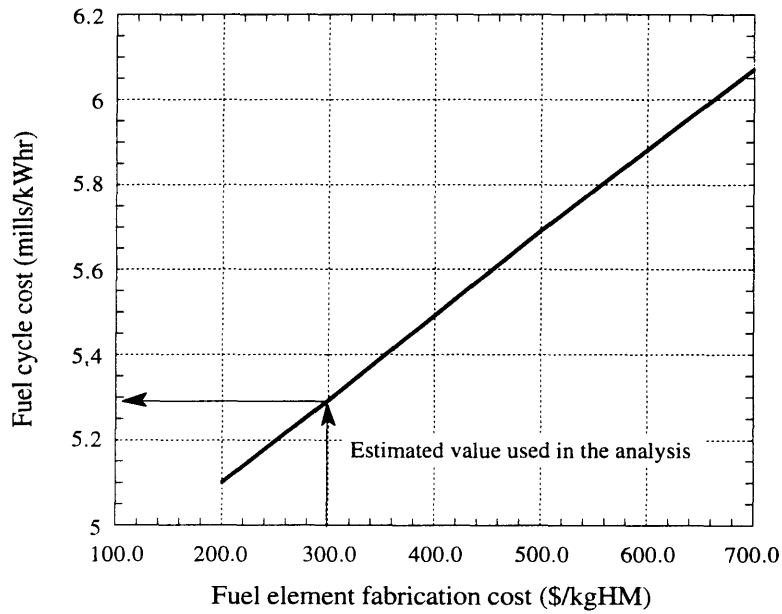


Figure 13-3 Sensitivity of the total fuel cycle cost to the fabrication cost of the PTLWR fuel elements

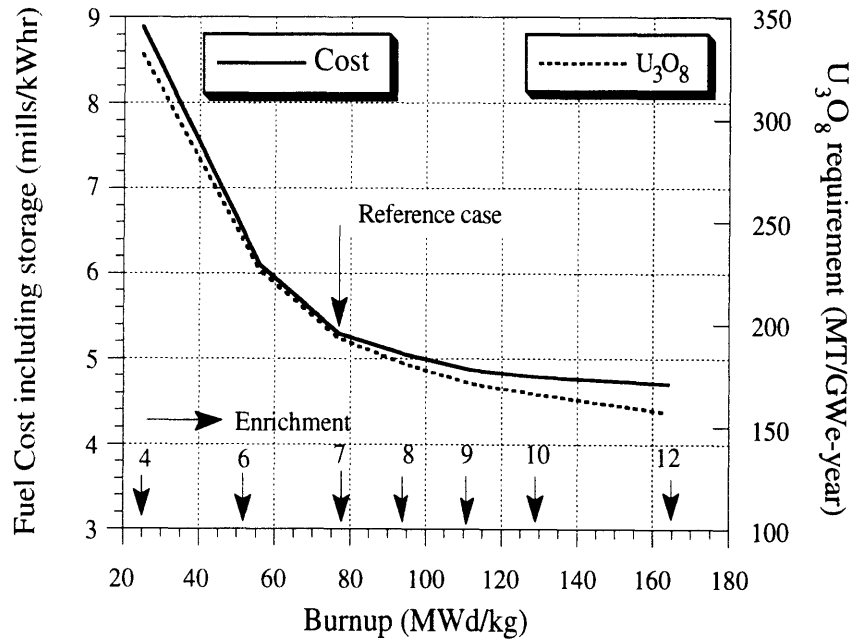


Figure 13-4 Fuel cycle cost and U_3O_8 requirements for the PTLWR concept

1260 MWe plant is 818,516.6 kg [Shapiro and Jesick, 1979], which gives 650 kg/MWe. Using a current price of heavy water of \$250/kg, a capacity factor of 0.9 and a carrying charge rate of 12%/year yields

$$\frac{650 \text{ kg/MWe} (250 \text{ \$/kg}) 1000 \text{ mills/\$} (0.12 \text{ yr}^{-1})}{1000 \text{ kWe/MWe} (8766 \text{ hr/yr}) 0.9} = 2.48 \text{ mills/kWhr} \quad (13-9)$$

which needs to be added to the fuel cycle cost of CANDU reactors. This gives a fuel cycle cost for CANDU of 6.82 mills/kWhr, and for CE-CANDU 5.16 mills/kWhr. Although CE-CANDU fueled with slightly enriched uranium exhibits the lowest fuel cycle cost among the four reactors investigated here, the advantage is not so significant if the cost of heavy water inventory is included. There are other costs associated with heavy water such as losses and cost of upgrading which are usually included in operational and maintenance costs. If instead allocated against the fuel they would add another penalty of about 0.20 mills/kWhr (see Section 13.4).

13.3 CAPITAL COST: QUALITATIVE ESTIMATE

Since the development of a detailed capital cost estimate is an extensive project and it is not the purpose of this work, only a qualitative evaluation will be made. Shapiro and Jesick [Shapiro and Jesick, 1979] performed an economic study of the capital cost of large HWR for U.S. siting. They report the overnight capital cost of a 1260 MWe HWR (excluding the heavy water inventory) to be \$587/kWe in 1978 dollars. This compared to \$543/kWe for a 1256 MWe PWR plant. The 8% higher capital cost of CANDU was attributed primarily to

- primary system piping,
- refueling machines,
- large moderator heat rejection system,
- D₂O upgrader, and
- lower net efficiency.

Among these, the moderator rejection system and D₂O upgrader are eliminated in the dry calandria design and the thermodynamic efficiency is increased to PWR levels by increasing the primary system pressure and

eliminating heat losses in the moderator. However, there is an additional cost for the large graphite reflector and additional cooling channels running through the radial reflector, plus the safety-grade passive flooding valves and cover gas control system. Hence, it is expected that the capital cost of the dry calandria design would remain slightly higher than for a PWR in 1978 dollars.

The elimination of diesel generators, emergency core cooling system trains and associated safety-grade equipment in the dry calandria design should lead to cost reduction. Also, the substantial present experience and advances realized from designing CANDU 3, where emphasis is put on plant simplification and cost reduction, could be applied to the dry calandria design. But since similar trends can be observed in current advanced PWR designs, it is not expected that this would lead to significant cost benefits over PWRs. The benefit of the proposed PTLWR is the large power rating achievable without the necessity of having an ECCS, since the reactor can survive LOCA without conventional emergency core cooling. This large power rating together with the absence of diesel generators and all redundant emergency cooling trains could result in a capital cost per kWe benefit compared to that for advanced passive LWRs, which also eliminate diesel generators and active ECCS, but have relatively small power output.

13. 4 OPERATING AND MAINTENANCE COSTS: QUALITATIVE ESTIMATE

Similarly as in the previous section, only a relative comparison of operating and maintenance (O&M) cost will be done. Shapiro and Jesick evaluated O&M cost in 1979 for both the PWR and CANDU. They give the numbers of 1.76 mills/KW_{hr} for PWR and 2.13 mills/KW_{hr} for CANDU. Thus the O&M cost for CANDUs was about 21% higher than that of PWRs in the 1970s. The difference is attributed to

- irrecoverable losses of D₂O,
- cost of upgrading recoverable losses, and
- the maintenance cost of refueling machines.

Typically, 1% of the D₂O inventory is lost per year, which gives

$$\frac{(0.01) 650 \text{ kg/MWe} (250 \text{ \$/kg}) 1000 \text{ mills/\$}}{1000\text{kWe/MWe} (8766 \text{ hr/yr}) 0.9} = 0.20 \text{ mills/kWhr} \quad (13-10)$$

The cost of upgrading constitutes approximately 0.1 mills/kWhr [Shapiro and Jesick, 1979]. Hence, the D₂O related maintenance is responsible for the major difference between PWR and CANDU O&M cost, i.e., for about 16% of the total O&M cost. The remaining difference is 5%. For the dry calandria design with H₂O, all heavy water related costs are eliminated. Therefore, the operational and maintenance cost of the dry calandria design is expected to be only slightly higher than for PWRs, mainly because of the refueling machines and more complicated primary system piping. The O&M cost has increased recently in both PWRs and CANDUs, but it is assumed here that the proportions have remained the same.

Note that the elimination of diesel generators and associated safety grade electrical systems in the dry calandria design should reduce O&M cost. Since it is difficult to quantify the exact amount, and since the same reduction is expected for the advanced passive LWRs, this reduction was not taken into account in this assessment.

13.5 SUMMARY

An estimate of fuel cycle cost and a qualitative assessment of the capital and operation and maintenance costs for the proposed PTLWR concept have been performed. An assessment of the fuel cycle cost suggests that the fuel cycle cost for the PTLWR fuel falls in the range of current PWRs. The fabrication cost of the PTLWR fuel elements is not available and better quantification is not possible at this stage because mass production of fuel elements of this type is not in place. Since only a rough cost estimate of this item has been made, the final fuel cycle cost will be subject to revision of the fabrication cost, and may be higher than the values given here. For example, doubling the fabrication cost could increase the PTLWR total fuel cycle cost from 5.33 to 5.91 mills/kWhr. This is still competitive, especially if the higher burnup capability of the fuel can be explored. The capital and

O&M costs are expected to be slightly higher than those for PWR plants, due to more complicated primary system piping and the large refueling machines.

Chapter 14

OVERALL SUMMARY DESCRIPTION OF THE INTEGRATED PTLWR DESIGN

14.1 INTRODUCTION

The passive Pressure Tube Light Water Reactor (PTLWR) is an innovative light water cooled and moderated reactor concept having a large power rating, developed with strong emphasis on passive safety. The main effort is directed towards the reactor's ability to reliably discharge decay heat to the ultimate heat sink without the need for replenishment of primary coolant in loss of coolant accidents while ensuring the integrity of the fuel and reusability of major reactor components. Additionally, it is required that the accidents leading to large temperature increases result in inherent reactor shutdown.

This chapter gives a technical summary of the integrated PTLWR design. Section 14.1 reviews the major goals and the strategy adopted in attaining the key objective of retaining fuel integrity in loss of coolant accidents (LOCAs) without delivering primary coolant to the fuel bundles. The overall reference design is described in Section 14.2, followed by a list of the main design parameters. The concept exhibits some unique physics characteristics, which are summarized in Section 14.3. Section 14.4 is focused on thermal hydraulic characteristics of a fuel channel during normal operation. Fuel channel behavior during LOCA is discussed in Section 14.6. The PTLWR employs a large light water pool in the containment, which passively enters the low-pressure calandria to provide redundant reactor shutdown and a heat sink. The flooding process will be discussed in Section 14.7. Section 14.8 is devoted to containment design and the performance of its passive cooling system. The behavior of the PTLWR

concept in various accident scenarios is briefly reviewed in Section 14.9. Comparison with other reactor designs will be presented in Section 14.10.

14.2 KEY OBJECTIVES AND RATIONALE

The key objective of this work was to design a passive, light water-cooled and moderated nuclear power reactor having a power rating of at least 1000 MWe that can ensure integrity of the fuel and reusability of the major reactor components without the requirement for replenishment of primary coolant inventory. In addition, the reactor physics characteristics should satisfy the fundamental requirement that power increase leads to inherent reactivity reduction and accidents leading to large temperature increases should lead to inherent reactor shutdown. Since, independent of the level of safety, any nuclear power plant contains radioactive material and involves a certain amount of risk, and because one cannot rule out what is physically possible, the objective of the design is also to reduce the risk of severe accidents and their consequences to extremely improbable values by retaining conventional defense in depth, i.e., to put as many barriers between the fuel and the environment as possible to prevent fission product release.

The achievable power rating of nuclear reactors is limited by their capability to remove generated power at the location of highest power density without exceeding safe temperature limits on the cladding and the fuel. The traditional approach is to establish a nominal power such that these safe limits are not exceeded, both during steady state operation and plant transients. To stay within safe limits in loss of coolant accident scenarios, the practice is to replenish primary coolant inventory rapidly with emergency coolant (either by active or by passive means). The approach presented here is based on the postulate that the fuel elements should safely survive the total loss of coolant, hence eliminating the necessity of primary coolant replenishment. As a result, an additional constraint on the achievable reactor power output arises. This constraint stems from the requirement that voided fuel elements must be capable of dissipating the decay heat by natural phenomena such as conduction,

radiation, and convection in steam/air mixtures, without exceeding safe temperature limits.

The rated core power which would satisfy this requirement can be increased by increasing the maximum temperature limit of fuel cladding, the effective thermal conductivity of voided fuel bundles, the heat capacity of fuel bundles, by decreasing the distance between the fuel bundle centerline and the heat sink, and by decreasing the power peaking factor. The first three desirable characteristics were achieved by introducing coated particle fuel in compacts placed in a solid matrix with separate coolant channels. A significant reduction of the heat conduction path between the voided fuel and the heat sink can be achieved by introducing small-radii fuel modules enclosed in a pressure boundary and located in a low pressure heat sink. A considerable decrease in peaking factor can be attained through enhanced neutron streaming by increasing core void fraction during normal operation. The application of all the above principles in a coherent way lead to the design of the pressure tube LWR, which will be described next.

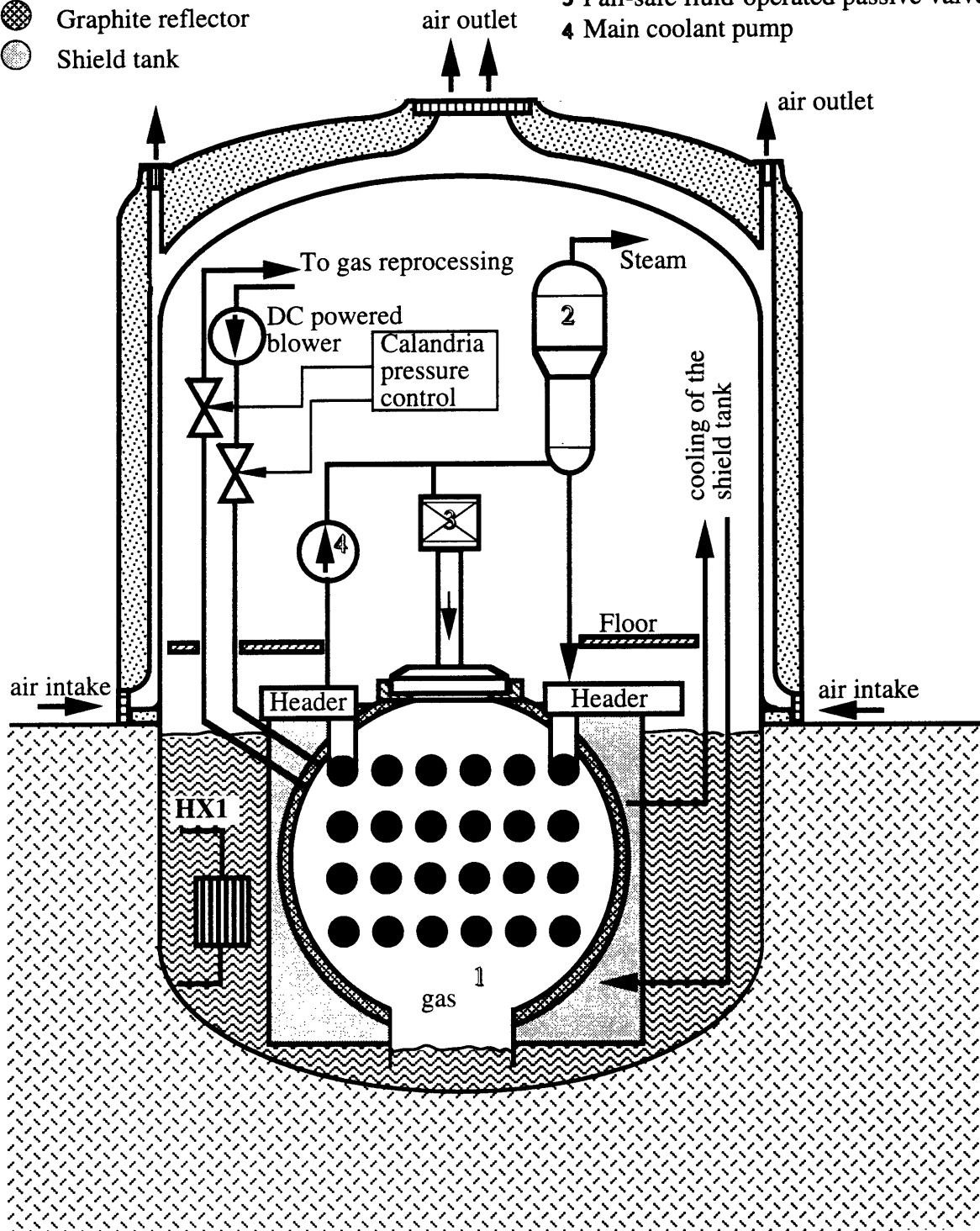
14.3 DESIGN DESCRIPTION AND MAIN DESIGN PARAMETERS

A schematic of the passive pressure tube LWR, also called the dry calandria design, is shown in Figure 14-1. Note that Figure 14-1 is highly schematic to show the principle of operation rather than the actual arrangement. To build on proven technology to the largest extent possible, the proposed design is based on CANDU reactors. It consists of fuel channels, calandria vessel, shield tank and an entire primary system very similar to those of CANDU units. There are, however, several major features which differ from current CANDU designs. These include

- dry calandria, with no moderator, surrounded by a solid reflector and connected by a gas lock to a large water pool,
- passive means to flood the calandria,
- passively air-cooled large containment, and
- fuel matrix in the pressure tube.

Under normal operation, the dry calandria space is filled with a gas under pressure slightly above atmospheric. The calandria bottom is

- Pressure tubes with fuel matrix
 - ⊙ Containment light water pool
 - ⊘ Graphite reflector
 - Shield tank
- 1 Dry calandria
 - 2 Steam generator
 - 3 Fail-safe fluid-operated passive valve
 - 4 Main coolant pump



Not to scale

HX1 heat exchanger to maintain containment water at ~40°C during operation

Figure 14-1 Schematic of the passive pressure tube LWR – overall concept

equipped with passages with extended vertical walls submerged in a large water pool in the containment (designated the containment water pool), the temperature of which is maintained at about 40°C. During normal operation, the containment water level is kept below the calandria bottom in the space within the extended vertical walls by maintaining the gas pressure in balance with the containment water column. The pressure level is maintained by a dc powered blower.

To minimize neutron losses, the calandria space is surrounded by a graphite reflector with an inner liner. The reflector is internally heated by neutrons and gamma rays during operation and must be continually cooled. The temperature of the graphite reflector is maintained sufficiently high (above 300°C) to eliminate stored energy buildup in the graphite. The axial reflector is cooled by the coolant in the pressure tubes penetrating the reflector. Cooling of the radial reflector is accomplished by non-fueled pressure tubes. Note that the high reflector temperature enables one to recover practically all the heat generated in the reflector, and hence improve plant efficiency. Finally, the calandria is submerged in a shield tank which attenuates neutrons escaping from the graphite reflector.

Figure 14-2 shows the reactor operation during LOCA. Upon a pre-defined disturbance of the primary system conditions the gas is released from the calandria, resulting in calandria flooding. Calandria flooding has four important purposes:

- it ensures the removal of decay heat from the calandria tubes by boiling, evaporation and subsequent condensation on containment walls during an accident,
- it shuts down the reactor (if still operating) and renders it deeply subcritical by excessive neutron absorption (even in the boiling mode)*,

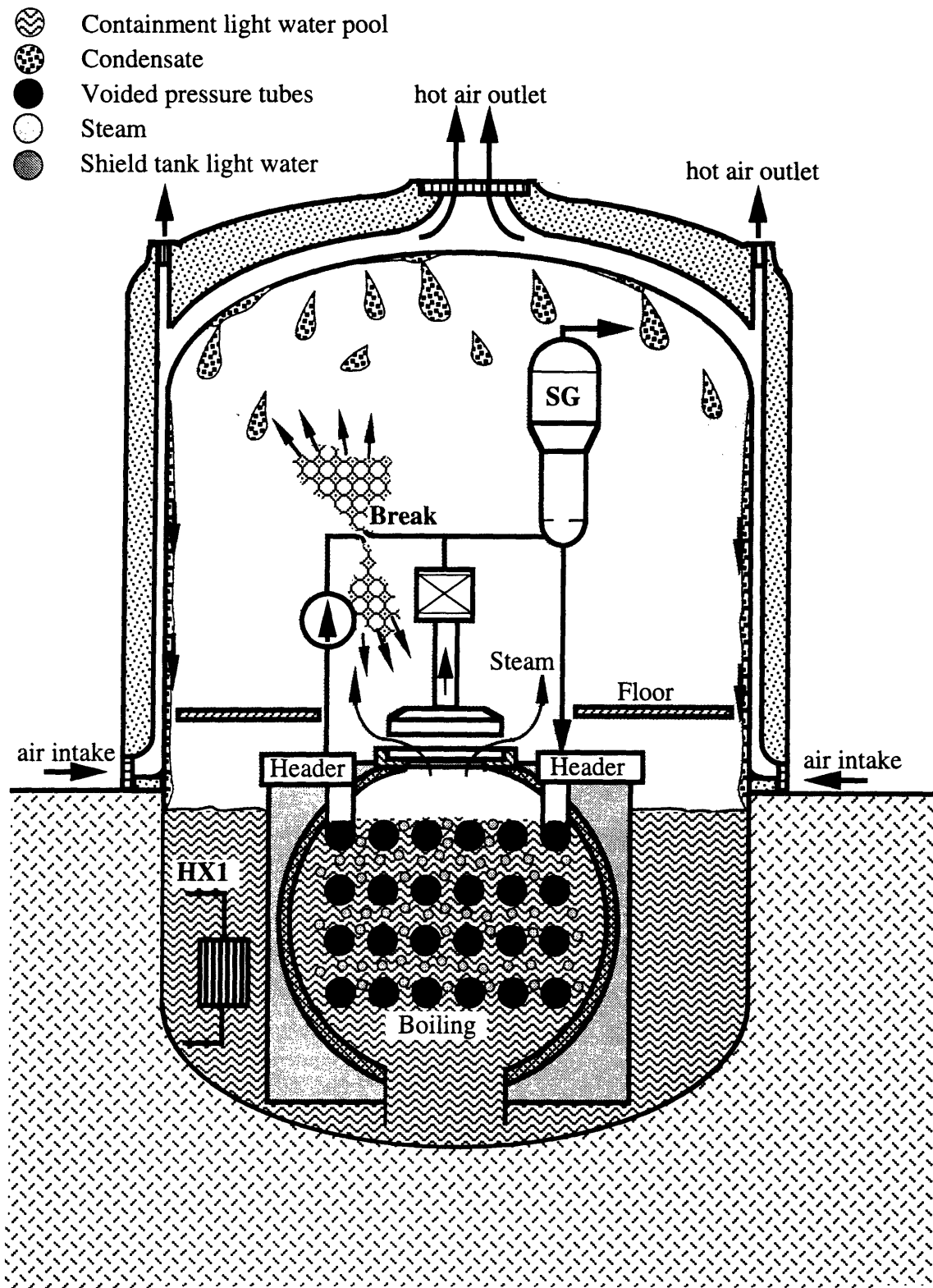
* Note that the flooding water is non-borated, and still provides a negative reactivity of about 250 β , once all pressure tubes are fully covered.

- it provides a large amount of water, which stores a considerable amount of decay energy, thus substantially reducing the heat rate transported through the containment walls early in the accident, and
- it considerably reduces the decay heat load on the fuel matrix (by about 40%) by absorbing a large portion of gamma heating which would have been otherwise deposited in the fuel matrix.

Once the temperature of the flooding water in the calandria gets close to saturation, steam which begins to escape from the calandria will condense on containment walls, and the condensate returns to the water pool, completing the heat transport circuit. The containment steel shell is cooled by an annular air chimney created by the space between the steel shell and the protective prestressed concrete shell. The containment decay heat removal system must handle both the full blowdown of the primary system and the decay heat generated in the core.

The actual arrangement of the calandria must provide for sufficient neutron shielding of upper decks, and space for refueling machines, as well as other equipment rooms. Furthermore, the water level below the calandria bottom should not be openly exposed to neutron flux in the calandria space to minimize parasitic losses. Calandria shielding can be achieved in the same manner as in existing CANDU reactors, by a light water shield in the concrete vault which supports the calandria. In the dry calandria design, the vault needs to be larger due to its additional graphite reflector. Figure 14-3 shows a cross section of the calandria, concrete vault and graphite reflector with the proposed arrangement of the passages for the intakes of flooding water and gas exhausts.

Several means to initiate flooding of the calandria are possible. A passive fluid-operated fail-safe valve, such as shown in Figure 14-4, could accomplish this purpose. The valve works on primary system pressure. Its dead bands are set such that they envelope pressure disturbances and transients which do not require reactor shut down. When the predefined envelope is exceeded, the valve opens the calandria closure seal and the water from the containment water pool floods the calandria. In case of a "low pressure" accident, e.g. loss of coolant accident, the primary system



Note: No emergency cooling systems in the primary system

Figure 14-2 Passive pressure tube LWR – operation during LOCA

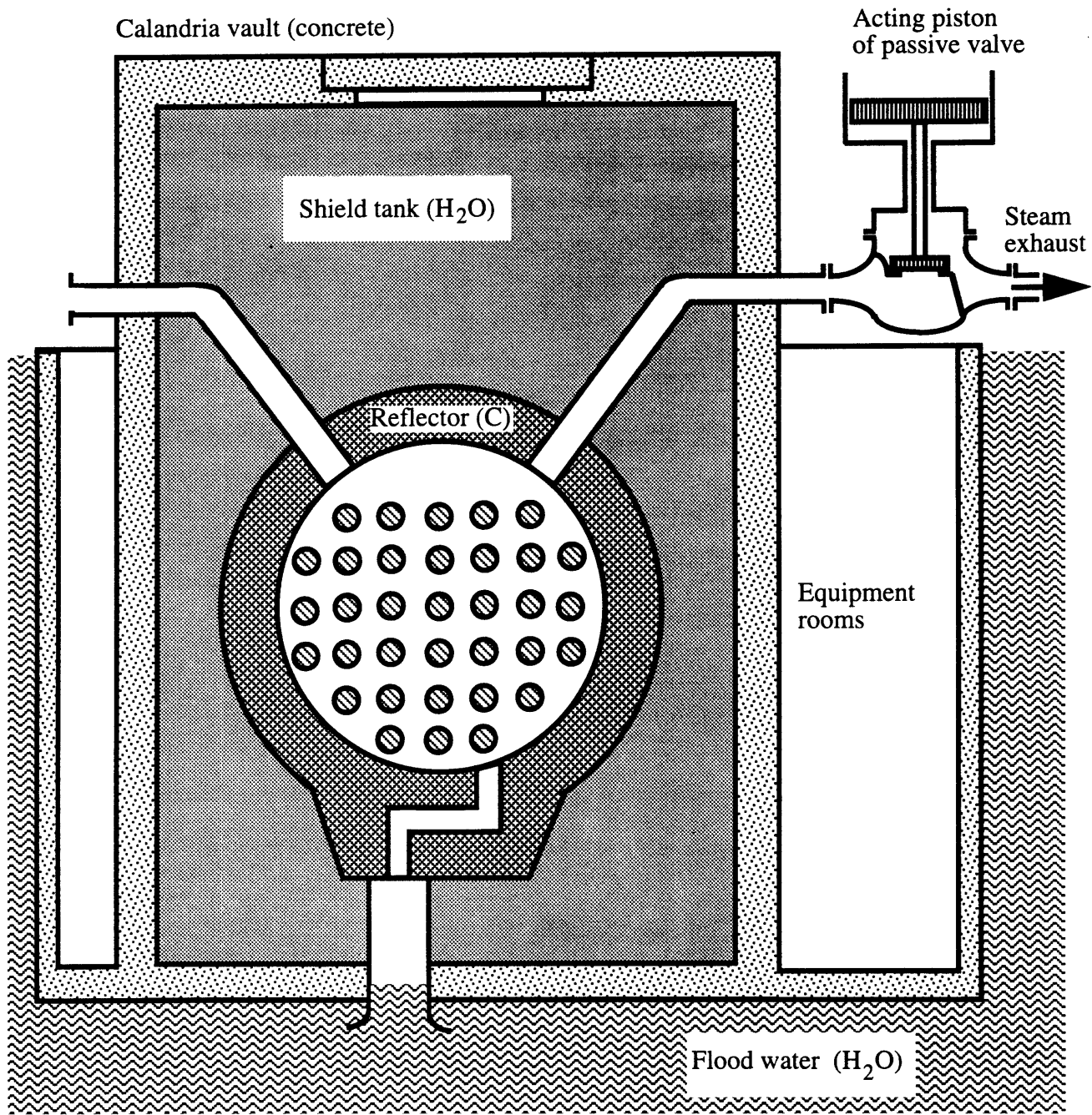


Figure 14-3 Cross section of calandria with passages for flood water intake and gas relief

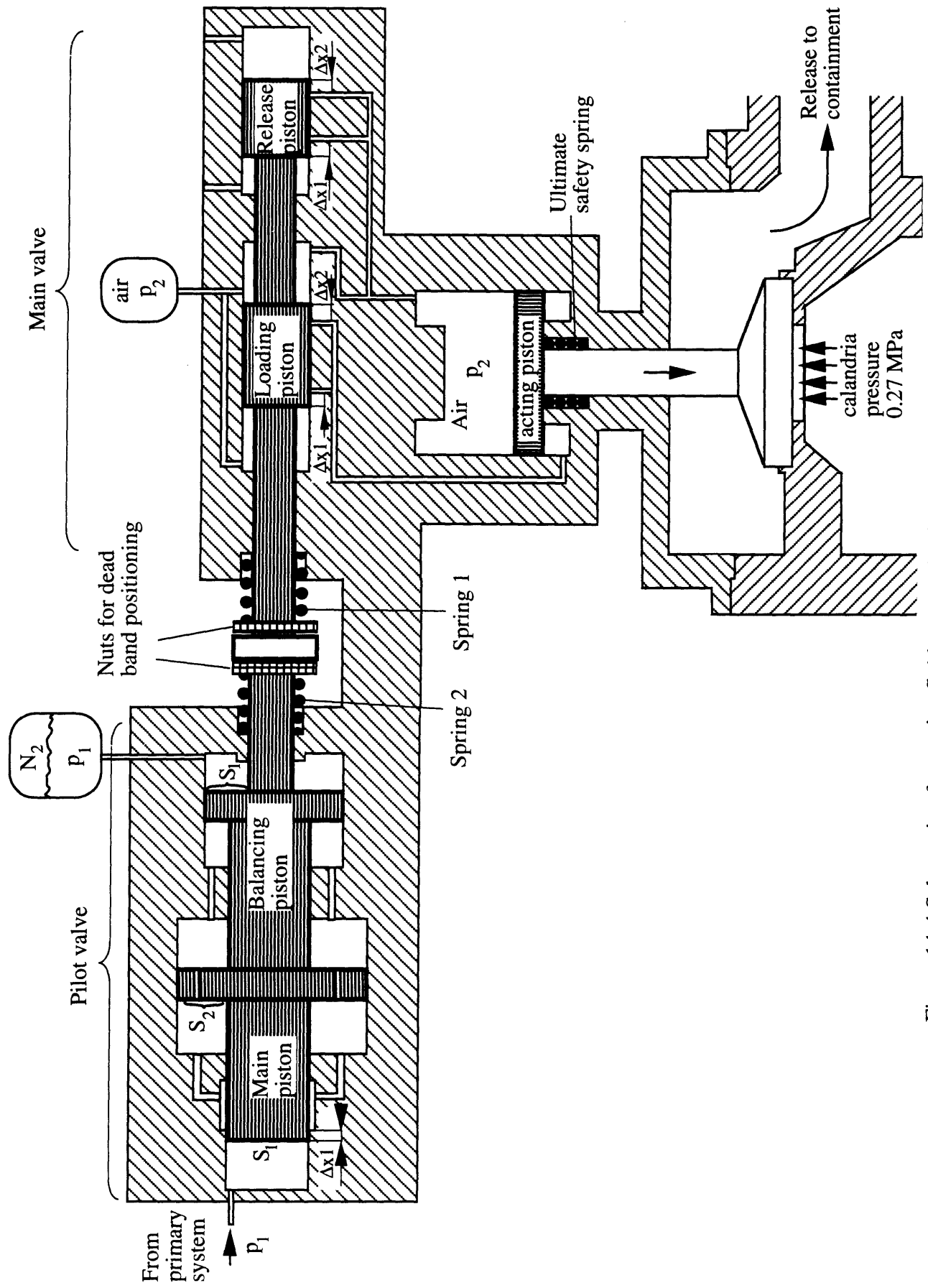


Figure 14-4 Schematic of a passive fluid-operated valve

pressure decrease leads to the movement of pistons to the left due to the difference between the force exerted by pressure in the balancing tank and the force from primary system pressure. This movement is opposed by spring 2, and continues without any action until the distance traveled by the pistons equals Δx_2 . At this point, the lower pressure limit is reached, the loading piston of the air-operated valve switches the air passages in such a way that the air pressure is released from the space above the acting piston and introduced below the acting piston, hence the acting piston moves upward and opens the calandria closure seal. Note that the valve must open both in case of "low pressure" accidents, e.g. loss of coolant accident, or in case of "a high pressure" accident, e.g. loss of heat sink. The valve is designed such that failures of various valve parts lead to valve opening. Hence the valve was designated as fail-safe in the sense that any failure results in the desirable action, i.e. valve opening. Other means (or the combination of various means) of calandria flooding can be also used. For example, the electrically powered blower maintaining the gas pressure while operating could be designed to lose power and hence depressurize the gas space upon predefined primary system disturbances.

Figure 14-5 shows the reference (one of several considered) fuel matrix arrangement in a fuel channel both in normal operation and in a LOCA situation, i.e., without a coolant. Several matrix materials have been considered. The most promising appears to be nuclear grade graphite fully coated by silicon carbide such that the graphite does not contact the coolant. Although graphite is compatible with light water coolant at the operating coolant temperature of 300°C, the silicon carbide coating is required to prevent excessive graphite oxidation at high temperatures in the absence of coolant. Fuel compacts contain TRISO particles and are arranged in two concentric rings. Cooling is accomplished by light water coolant flowing through 19 circular channels and one outer annular channel. The matrix elements are 50 cm long and slide in the channel on bearing pads. The pressure tube is surrounded by a protective tube, also termed the calandria tube. This tube has the primary function of preventing excessive pressure tube stresses which would have resulted had the cold water during flooding come into contact with a hot pressure tube still under pressure.

- ⊗ Pressure tube
- ⊕ Coolant
- Fuel matrix (silicon carbide coated graphite)
- ⊕ Fuel compacts with particle fuel
- ⊗ Containment water pool in calandria
- Steam/air mixture
- ⊗ Protective calandria tube

Normal Operation

Accident Operation

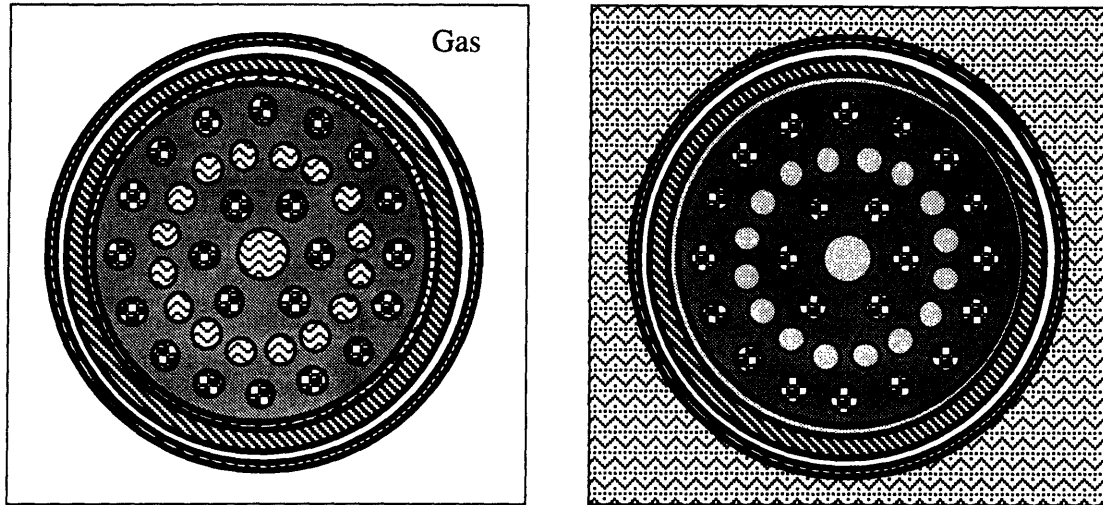


Figure 14-5 Fuel matrix in a fuel channel during normal and accident operation

The PTLWR primary system is essentially the same as that of a published CE-CANDU design except for the Emergency Core Cooling System (ECCS), which has been eliminated. The PTLWR retains CE-CANDU's shutdown cooling system which is used to reduce the temperature of the reactor coolant system (RCS) in post shutdown periods from normal operating temperature to plant maintenance temperature, and to maintain this temperature for a period of time.

The overall design parameters are summarized in Table 14-1.

14.4 REACTOR PHYSICS CHARACTERISTICS

The key reactor physics characteristics of the reference PTLWR design will be summarized. The goal is that they satisfy the objective of achieving an inherent shutdown in accidents leading to a large temperature increase.

Table 14-1 Summary of PTLWR design parameters

Parameters	Data
General	
core thermal power	3899 MWt
net electric power	1260 MWt
net efficiency	32.3%
power generated in fuel elements	3630 MWt
power generated in the reflector	104 MWt
power generated in pressure tubes	116 MWt
power generated in calandria tubes	35 MWt
average specific power (per kg of UO ₂)	130 kW/kg
average power density (per active core volume)	11 kW/l
average power density (per fuel channel)	70 kW/l
average power density (per fuel compact)	280 kW/l
total peaking factor (fresh core)	≤1.2
total peaking factor (equilibrium core)	≤1.35
core diameter	8.77 m
active core length	5.95 m
channel orientation	horizontal
Fuel matrix	
matrix material	SiC-coated graphite
fuel matrix outer diameter	120.8 mm
fuel matrix element length	500 mm
number of fuel compacts	26
diameter of fuel compacts in inner fuel ring	12.4 mm
diameter of fuel compacts in the outer fuel ring	12.7 mm
number of coolant channels	19
diameter of central coolant channel (roughened)	22.7 mm
diameter of coolant channels in intermediate ring	8.4 mm
minimum web thickness	4.5 mm
fuel material	coated UO ₂ kernels
alignment of coolant holes	key and dowel

Table 14-1 (continued)

Fuel channel	
number of fuel channels	740
lattice pitch	285.75 mm
material of pressure tubes (PTs)	Zr-2.5%Nb
material of calandria tubes	Zy-2
pressure tube inside diameter	128 mm
pressure tube thickness	5.79 mm
thickness of pressure tube-calandria tube gap	2 mm
thickness of calandria tube	1.52 mm
Reflector	
reflector material	graphite
reflector thickness	1 m
reflector operating temperature	~ 600 °C
reflector cooling medium	H ₂ O coolant in PTs
Calandria flooding system	
volume of flooding water	4200 m ³
flood water temperature	40°C
height of driving water column	14.5 m
number of bottom intakes for flood water	3
total flow area of bottom intakes	2.25 m ²
number of passive valves for flooding initiation	4
flow area for gas exhaust per valve	0.125 m ²
number of safety valves	4
flow area for gas per safety valve	0.22 m ²
operating gas pressure in the calandria space	0.24 MPa
Primary coolant system	
coolant	H ₂ O
core mass flow rate	14100 kg/s
core bypass flow rate (through unfueled channels)	224 kg/s
pressure (fuel inlet)	15.34 MPa
core pressure drop	0.7 MPa

Table 14-1 (continued)

temperature (fuel inlet)	298.9 °C
temperature (fuel outlet)	340.3 °C
average exit quality	0.5 %
maximum exit quality	0.6 %
minimum CHF power ratio (fresh core)	1.6
minimum CHF power ratio (equilibrium core)	1.7
Reactor physics	
fuel enrichment	7 %
discharge burnup	77,000 MWd/tonne
heavy metal loading	29 kg/MWt
on-line refueling scheme	bi-directional
void coefficient	negative
Doppler coefficient	$(-4 \text{ to } -1.1) \times 10^{-5} \Delta k/k$
prompt neutron lifetime	$1.5 \times 10^{-3} \text{ s}$
neutron migration length	110 cm
average thermal flux ($E \leq 0.6 \text{ eV}$) (fresh core)	$2.5 \times 10^{14} \text{ n/cm}^2\text{-s}$
average fast flux ($E > 0.6 \text{ eV}$) (fresh core)	$4.5 \times 10^{14} \text{ n/cm}^2\text{-s}$
Containment	
containment shell inner diameter	60 m
containment shell height	81 m
containment free volume	$1.7 \times 10^5 \text{ m}^3$
thickness of steel shell	4 cm
thickness of vented air gap	0.5 m
total flow area of air inlet passages	100 m^2
total flow area of air outlet passages	90 m^2

14.4.1 Method of Analysis

The PTLWR physics characteristics have been calculated using direct simulation of the neutron transport process. Use of a rigorous neutron transport method is needed in the highly-voided PTLWR core because the neutron mean free path is comparable to physical dimensions of the core

and because the neutrons exhibit a beam-like distribution; hence the main conditions for the validity of the conventional neutron diffusion equation are not satisfied. The Monte Carlo code MCNP was used to solve the neutron transport equation. Burnup calculations were performed by combining the MCNP code to obtain the system eigenvalue, and the fuel depletion code ORIGEN2 to obtain the change of fuel composition with burnup. Because of the unavailability of a PTLWR one-group effective cross section library required by ORIGEN2, a PWR library set of cross sections was used and the most important actinide cross sections were modified to match reaction rates obtained using MCNP.

14.4.2 Long Prompt Neutron Lifetime

The PTLWR reference design has a very long prompt neutron lifetime. Although light water is used in the dry calandria design, the prompt neutron lifetime is longer by an order of magnitude than for a typical LWR, and slightly longer than for a typical CANDU heavy water lattice (about 1.5 times). Most neutrons in the system are absorbed in the fuel. However, due to the large voids in the calandria, the neutrons have to travel a long distance, and hence it takes a long time, before they hit fuel nuclei. The reflector also contributes to an increase of the prompt lifetime since the neutrons undergo a large number of collisions in the reflector before they are returned back to the core. The low heavy metal loading also leads to a small volume-averaged absorption cross section.

14.4.3 Flat Thermal Flux Profile

The PTLWR reference design exhibits a flat thermal flux profile. The large void fraction in the calandria significantly increases the migration area, allowing for homogeneous dispersion of thermal neutrons over a large area of the core. Moreover, at the core periphery, where the population of thermal neutrons might otherwise tend to decrease, neutrons which have undergone moderation in the reflector are supplied. This provides for the exceedingly flat profile of the thermal neutron flux in both the axial and radial directions.

Since the contribution from fast fissions is small, the flat thermal flux profile translates into a flat power density profile in fuel compacts if the fuel composition is uniform, such as for the fresh core. In the equilibrium core, where the fuel composition is not uniform but varies along the channel, depending on the refueling scheme, the power density profile depends primarily on the initial enrichment and the distribution of fuel bundles with various burnups. Power density profiles for both the fresh core and the equilibrium core using bi-directional refueling with partial reshuffling are shown in Figure 14-6. It can be observed that for a short region near the reflector, power density is almost constant, with an axial peaking factor of only 1.13. The power density profile for the equilibrium core has a peaking factor of about 1.34. This peaking factor is still relatively low, considering the relatively large initial enrichment of 7%. Note that the shape of the power density profile for the equilibrium core corresponds closely to the shape of the critical heat flux (CHF) along the channel, hence the equilibrium core gives better CHF margins than the fresh core.

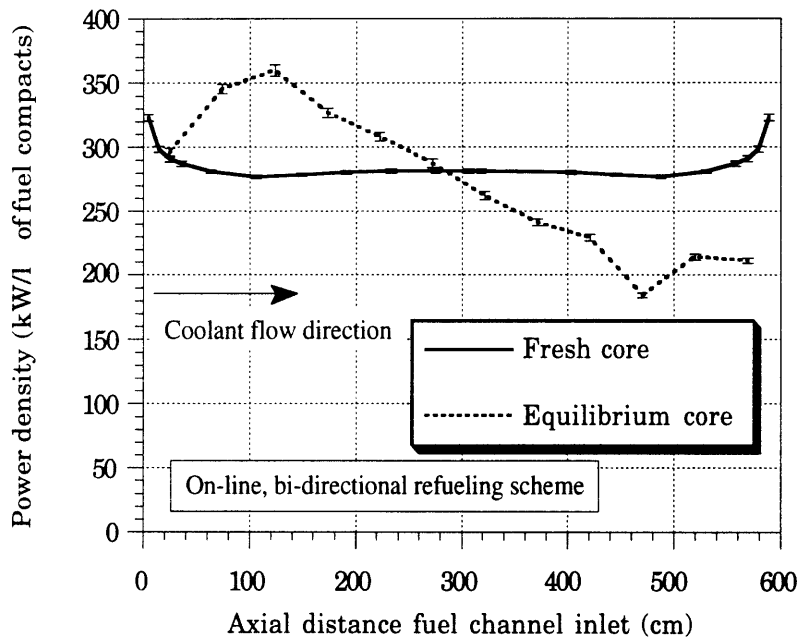


Figure 14-6 Power density profile in outer fuel ring

14.4.4 Tight Neutronic Coupling

The PTLWR core exhibits extremely tight neutronic coupling. The large void space, in combination with the relatively low density of heavy metal and the heterogeneous arrangement of the H₂O moderator results in a long neutron mean free path and a large neutron migration area. The neutron migration area for the PTLWR core is about 12,000 cm², which compares to about 50 cm² for conventional LWRs. As a result neutrons can see practically the entire core. Such a tight core coupling has three important consequences:

- no concerns with local criticality,
- the potential for reactor control from outside the core region, and
- inherent stability against Xenon spatial oscillations.

Physically, the entire core behaves as one nuclear unit and no local subregion can become critical. This differs from typical LWRs where several adjacent fuel assemblies can go locally critical. Furthermore, all reactor control can be achieved from outside the core, i.e., from the reflector, since the control rods are effective over a large core area. Hence, the local flux depressions from control rods inside the core are eliminated. PTLWR control rods move in vertical channels located in the axial reflector in the space between fueled pressure tubes, as shown in Figure 14-7. Finally, although the proposed PTLWR has very large physical dimensions, the reactor is inherently stable against xenon spatial oscillations, primarily due to its very large neutron migration area; consequently the conventional measures employed in LWRs and CANDUs to prevent this instability are not needed.

14.4.5 Well-Thermalized Neutron Spectrum

The PLTWR core is characterized by a well-thermalized neutron spectrum. This can be observed in Figure 14-8, which compares the PTLWR energy spectrum in the fuel with PWR and CANDU spectra, calculated for infinite lattices. With respect to the thermal to fast flux ratio, the pressure tube LWR is comparable to a CANDU heavy water lattice. Good neutron

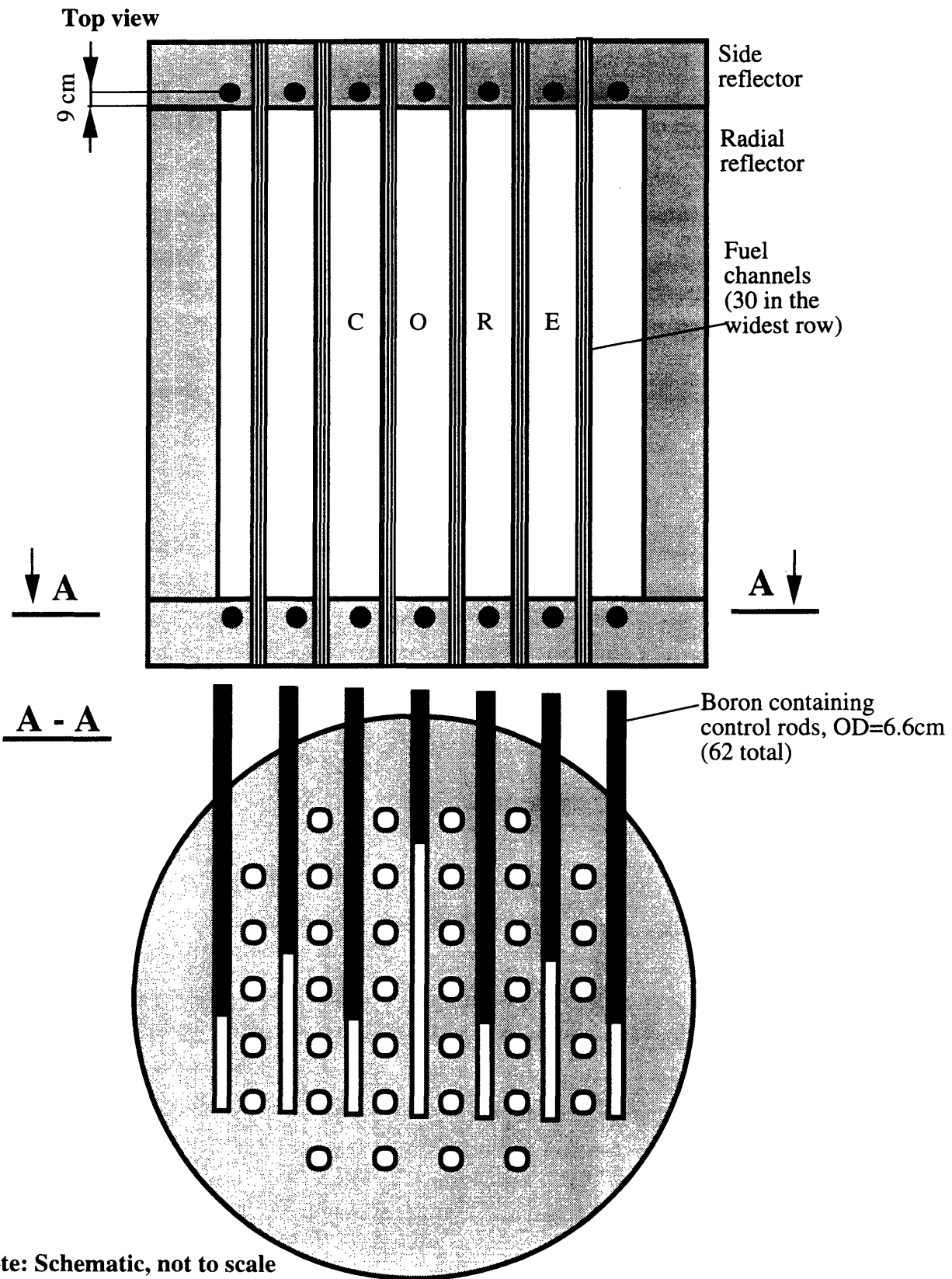


Figure 14-7 Schematic arrangement of control rods in the side reflectors of the PTLWR design

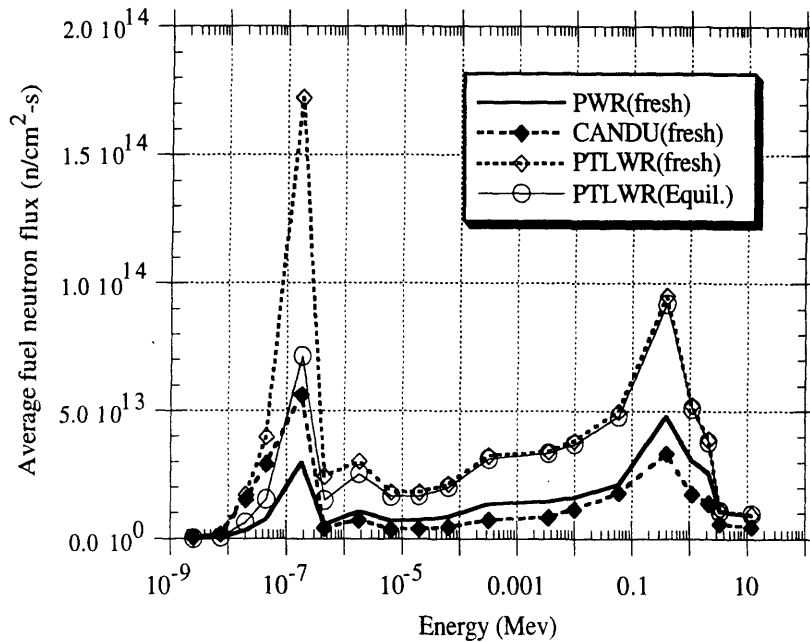


Figure 14-8 Comparison of energy spectra for the PTLWR with PWR and CANDU reactors

thermalization is achieved primarily due to the large moderator-to-fuel volume ratio and the large resonance escape probability. For the equilibrium core, the spectrum hardens due to the relatively large fraction of ^{239}Pu present in the PTLWR equilibrium core with high-burnup fuel.

14.4.6 High Thermal Flux and Fast Fluence

The drawbacks of the PTLWR concept are high absolute levels of thermal flux and fast fluence. This is a consequence of relatively low heavy metal loading, associated with the use of coated particle fuel. The average thermal flux for the fresh core is about 2 times higher than for a CANDU core; for the equilibrium core it is only 1.3 times higher. High thermal flux results in a higher xenon poisoning ratio at steady state, but, more importantly, after reactor shutdown or after a large power decrease. Provisions for full compensation of the large negative reactivity due to transient xenon buildup following reactor shutdown would be deleterious to fuel cycle economics. Hence only partial compensation is proposed. This is

similar practice to that for CANDU reactors, which employ adjuster rods to compensate for the buildup of ^{135}Xe in the first 30 minutes following reactor shutdown. More important, however, is the approximately 3 times higher average fast flux compared to that of the CANDU, because it has negative implications on the lifetime of the pressure tubes. Means to extend pressure tube lifetime under these high flux conditions would be required.

14.4.7 Large Negative Doppler Coefficient

As in all thermal reactors, the proposed concept exhibits a negative Doppler coefficient. Figure 14-9 shows that at nominal conditions (0.678g/cm^3), the Doppler coefficient is more negative than for a typical BWR. The Doppler effect is more strongly dependent on coolant voiding than for a BWR due to a higher coolant-to-fuel volume ratio. In accidents which would lead to fuel temperature increase, and consequently, to a decrease in coolant density (to 0.4g/cm^3), the negative magnitude of the Doppler effect can be more than doubled. Taking into account that the fuel operates at about 1100°C , but can safely withstand temperatures up to 1600°C , the large temperature margin on the fuel, combined with the large

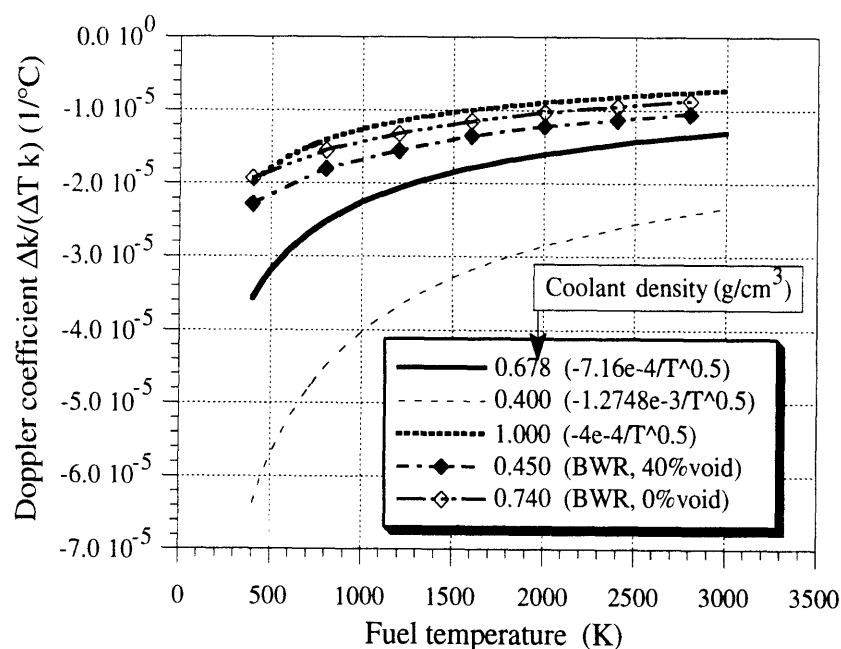


Figure 14-9 Doppler coefficient for the PTLWR as a function of fuel temperature and coolant density

Doppler coefficient (which is even substantially increased upon coolant voiding) leads to reactor inherent shutdown in large-temperature-increase scenarios in anticipated transients without scram (ATWS), by Doppler effect only.

14.4.8 Negative Coolant Void Coefficient

The PTLWR coolant void coefficient is negative under all reactor conditions. It is interesting to note that even though the H₂O moderator-to-fuel volume ratio is much higher in the dry calandria design than in a typical PWR (4.16 compared to 1.67 in a PWR) the system still exhibits a negative coolant void coefficient. The heterogeneity of the H₂O moderator plays an important role in this aspect, since the neutrons collide with the H₂O moderator less frequently than they would have done in a typical PWR geometry, where the moderator is evenly distributed around the fuel rods. Figure 14-10 shows the multiplication factor for the reference PTLWR

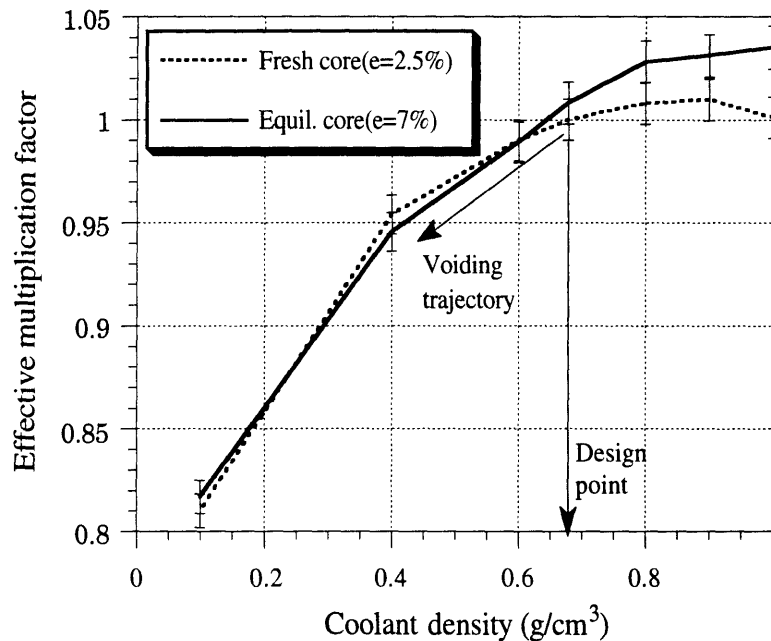


Figure 14-10 Effect of coolant voiding on reactivity

design as a function of coolant density and the trajectory of coolant voiding. The equilibrium core exhibits a more negative void coefficient. Maintenance of a negative void coefficient throughout the cycle is easier than in typical

PWRs because soluble boron was eliminated from the coolant. Therefore, the operating point can be designed closer to the optimum on the reactivity versus moderator-to-fuel-volume ratio curve (represented by coolant density in Figure 14-10 since fuel volume is kept constant). Consequently, positive reactivity insertions in accidents with cold water ingress result in a smaller neutron power increase than in PWRs.

14.4.9 Less Efficient Neutron Economy

The PTLWR has a less efficient neutron economy than a typical LWR. This is the consequence of higher parasitic losses compared to LWR cores. Thick pressure tubes to accommodate high operating pressure, higher leakage, and the low mass of fuel compared to the total mass of the core are the main factors contributing to relatively high parasitic losses. This drawback is, however, compensated by on-line refueling and the high burnup achievable with particle fuel. Parasitic losses can be improved by decreasing fuel channel pitch, and hence reducing neutron leakage or by increasing fuel loading within a channel, and hence increasing the fraction of neutrons absorbed in the fuel. Alternative fuel arrangements to accomplish this goal have been identified, but have not been analyzed in detail.

14.4.10 Slightly Positive Reflector Temperature Coefficient

The PTLWR concept has a slightly positive reflector temperature coefficient due to the shift in the thermal spectrum of the neutrons coming from the reflector to higher energies, which affects the averaged microscopic cross sections of nuclides in the fuel. The magnitude of the reflector temperature coefficient is, however, small (for the fresh core, an increase of reflector average temperature from the operating point of 800K to 1600K leads to an increase of reactivity by about 8mk only) and the temperature increase proceeds very slowly due to the long thermal time constant of the large graphite mass. If all the reflector cooling is lost and the reactor continues to operate at its nominal power rating, the rate of reflector temperature increase is about 0.1°C/s, i.e., it would take about 2.2 hours to increase the reactivity by these 8mk. Such small and extremely slow reactivity changes with reflector temperature should not pose any

significant safety problems. Moreover, loss of reflector cooling is possible only with simultaneous loss of core coolant, which results in reactor shutdown due to the negative void and Doppler coefficients which are much larger than the positive reflector temperature coefficient.

14.4.11 Diverse and Redundant Shutdown

The PTLWR reference concept achieves diverse and redundant shutdown by means of passive calandria flooding, which plays an important role in ATWS. Because of its core geometry, with large fuel channel spacing, nonborated light water entering the calandria behaves like a neutron trap and renders the reactor deeply subcritical even if the flooding water is in bulk boiling. There is no need for soluble boron and an associated chemical system. This differs from the Process Inherently Ultimate Safety (PIUS) concept which relies on soluble boron to achieve reactor shutdown. This diverse shutdown could be also compared to moderator dumping in CANDU systems, except for the difference that the dumping of the CANDU moderator results also in the undesirable loss of heat sink, while in the dry calandria design flooding provides both the heat sink and shutdown.

Figure 4-11 shows the behavior of the effective multiplication coefficient as a function of the number of flooded rows for the flooded core. Since the flood water makes the portions of control rods below the water level ineffective, the case of the cold core with all control rods fully inserted has been selected for the analysis. Exact thermohydraulic conditions in the upper portion of the calandria space (not yet flooded) are somewhat uncertain. Since the flooding water is subcooled by 60°C, escape of the steam from the water surface is expected to be small and steam content in this region should not exceed saturation conditions corresponding to calandria pressure. Reactivity behavior in Figure 4-11 was calculated for saturated steam in the upper space. Because the water content in the upper calandria space affects reactivity behavior, various possibilities need to be analyzed to assure that no large reactivity insertions are introduced during the calandria flooding process. The worst scenario would be if the violently boiling flooding water is entrained from the water pool into the upper calandria space and increases the water density beyond the saturation

level. Such a scenario is shown in Figure 14-12. Figure 14-12 models inadvertent reactor flooding during normal operation. It is assumed that after the first row is flooded the water level remains constant and the density of the steam/water mixture in the upper space is increased beyond saturation levels by liquid entrainment from the surface. Secondary criticality could be achieved at the optimum mixture density of about 0.15 g/cm³, but the peak reactivity does not exceed its prior critical value. Moreover, this is a hypothetical scenario, since the optimum density of 0.15 g/cm³ cannot be practically reached, as it is higher by an order of magnitude than the maximum possible mixture density, $\rho_{m,max}$, (also shown in Figure 14-12), given by a conservative estimate from thermohydraulic entrainment limits. After calculating various scenarios, it can be concluded that:

- for the most likely scenarios, with saturated vapor in the unflooded calandria space, the reactivity monotonically decreases with rising water level;
- for scenarios with entrainment of water droplets into the unflooded calandria space, reactivity first drops and later increases, but it does not exceed the prior critical value, even for the optimum mixture density;
- for scenarios of coolant spraying from a ruptured pressure and calandria tube without bottom flooding, reactivity can slightly exceed the prior critical value; but
- steam/water mixture densities yielding the maximum reactivity peak cannot be achieved either by spraying or by entrainment because they exceed thermohydraulic limits on spray density by an order of magnitude.

Hence, the reference PTLWR design does not exhibit reactivity excursions in scenarios involving the ingress of steam/water mixtures into the voided calandria space.

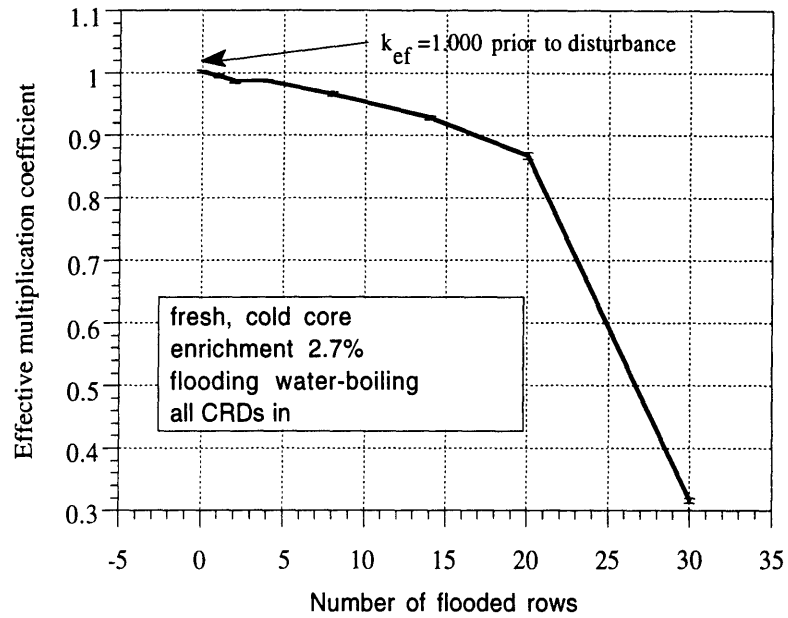


Figure 14-11 Reactivity behavior for calandria inadvertent flooding with saturated steam in unflooded region for cold core with all CRDs inserted

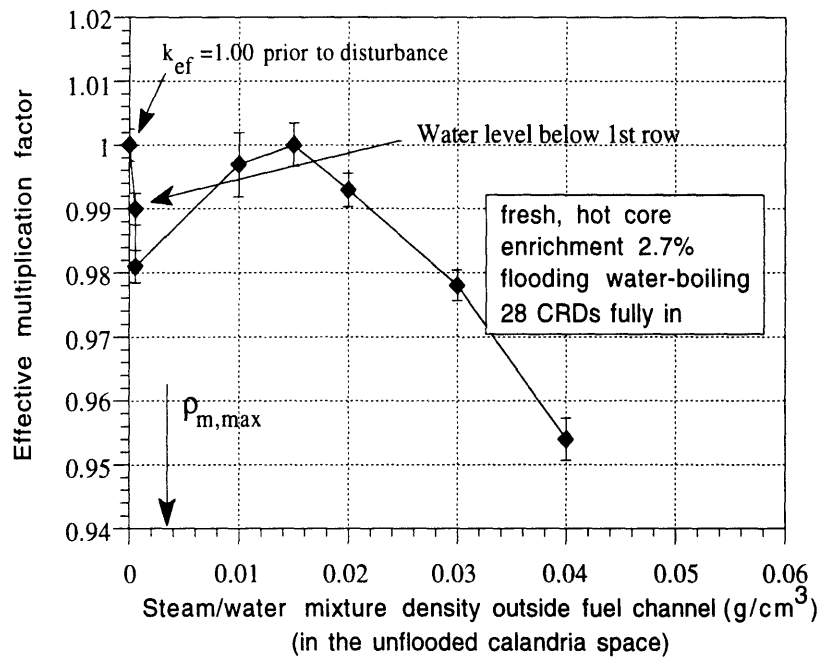


Figure 14-12 Reactivity behavior for calandria inadvertent flooding with hypothetical water entrainment for hot core

14.4.12 High Discharge Burnup

The PTLWR concept can achieve the relatively high discharge burnup realizable with particle fuel, but at the expense of higher enrichment than for a PWR. This is a consequence of the less efficient neutron economy in a high-leakage, low-loading PTLWR core. Figure 4-13 shows that the discharge burnup for the reference PTLWR is about 77,000 MWd/tonne (note that for on-line refueling the discharge burnup equals twice the equilibrium burnup) for an initial enrichment of 7%. Uranium utilization falls in between current and advanced PWRs. The burnup rate in the proposed PTLWR concept is faster than for current CANDUs, because of low heavy metal loading. However, fuel residence time is longer than for current CANDUs (the refueling rate is about one half that of a CANDU unit) due to the high achievable discharge burnup.

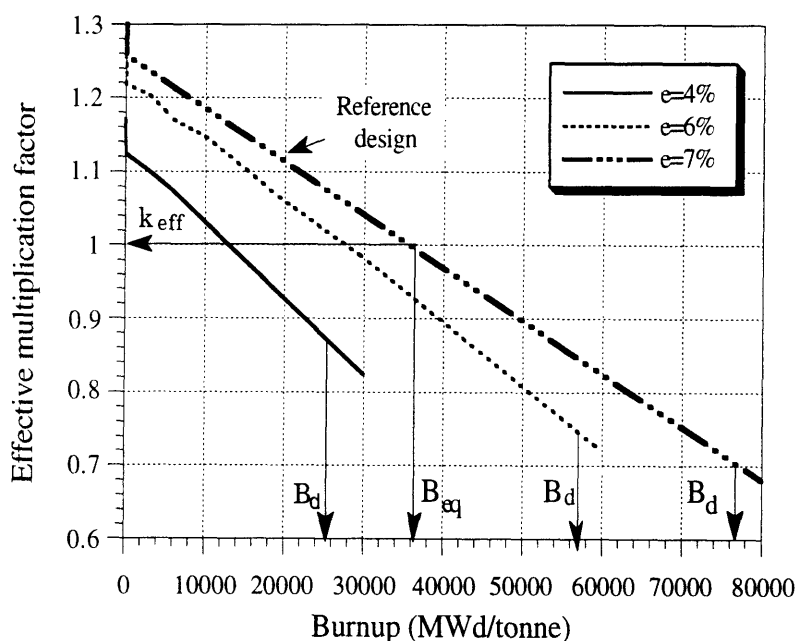


Figure 14-13 Effective multiplication factor as a function of burnup for various initial enrichments

14.5 FUEL CHANNEL THERMAL HYDRAULIC CHARACTERISTICS DURING NORMAL OPERATION

The key challenges to the fuel channel during normal operation are to satisfy the major thermal-hydraulic limits – the maximum fuel centerline temperature of 1300°C and the minimum critical heat flux ratio of 1.3. In addition, small fuel channel pressure drop is desirable, i.e., not more than the CANDU nominal pressure drop of 1 MPa. Identification of these parameters during normal operation requires a two-dimensional solution of heat conduction in the fuel matrix coupled to coolant flow in parallel, non-communicating coolant channels.

14.5.1 Method of Analysis

The analysis of heat transfer through the fuel matrix at the plane of maximum power density in the hottest fuel channel has been performed using the finite element code ALGOR. Solution of the heat conduction equation requires knowledge of boundary conditions in the fuel and in the coolant. The power density in fuel compacts has been obtained using the MCNP code. The boundary conditions at the coolant interface involve the heat transfer coefficient to the coolant, and the fluid bulk temperature. These parameters must be obtained by solving mass and energy balance equations for the coolant along the coolant channels. A separate code, PARCHANL (parallel channels), has been developed for this purpose. The PARCHANL code calculates the flow split in parallel noncommunicating channels and the bulk fluid properties, as well as the heat transfer coefficient and critical heat flux as a function of axial position. Besides the total mass flow rate, inlet pressure and inlet coolant temperature, PARCHANL needs the heat flux to individual coolant channels as a boundary condition. This heat flux is obtained, using the ALGOR code, at the plane of maximum power density, and by combining this result with the axial power density profile to get the heat flux profile as a function of axial position for every coolant channel. Since the heat transfer coefficient and coolant bulk temperature depend on the incident heat flux to coolant, and this heat flux in turn depends on both these variables, iterations on the heat transfer coefficient and coolant bulk temperature between ALGOR and

PARCHANL are necessary. Because the heat transfer coefficient to coolant is large, the convergence rate is very fast, requiring one to two iterations.

14.5.2 Performance for the Fresh Core

Figure 14-14 show the profile of bulk coolant temperature “T-fluid”, and the saturation temperature, “Tsat”, along each coolant channel. It can be observed that the central channel (#1-see Figure 14-5 for matrix with coolant channels) remains slightly subcooled at the exit, while the intermediate coolant channel (#2) and the outer annular channel (#3) reached the saturation state close to the channel outlet. The saturation temperature decreases slightly because of the decrease in local pressure. The exit quality is 0.5%, which is less than the average exit quality for CANDU of 2%. The highest exit quality for CANDU is 4.73%. Figure 14-15 shows the pressure decrease along each channel. The total channel pressure drop is about 0.7 MPa, which is less than the pressure drop of the reference CE-CANDU design by about 0.3 MPa. The smaller pressure drop is primarily due to significantly lower form losses in the PTLWR fuel channel.

Figure 14-16 plots the departure from nucleate boiling power ratio (DNBPR)* as a function of axial position using the AECL lookup tables. Since the heat flux in the PTLWR fresh core is essentially flat, except for a slightly higher heat flux at channel ends, burnout will always occur at the channel exit. From the point of view of CHF, the PTLWR design with a fresh core has a disadvantage, since it exhibits the highest coolant temperature at the location of the highest heat flux, while in CANDU, the highest coolant temperature is at the point of the lowest heat flux. In the PTLWR, this problem is compensated by a small peaking factor, resulting in a much smaller maximum heat flux (for the same core power) and by the higher mass flux of the coolant. Figure 14-16 also shows the operating

* DNBPR is defined as the ratio of the heat flux which, at a given location, yields departure from nucleate boiling condition over the operating heat flux. This ratio, incorporates a full heat balance and gives generally lower values than the conventional DNBR.

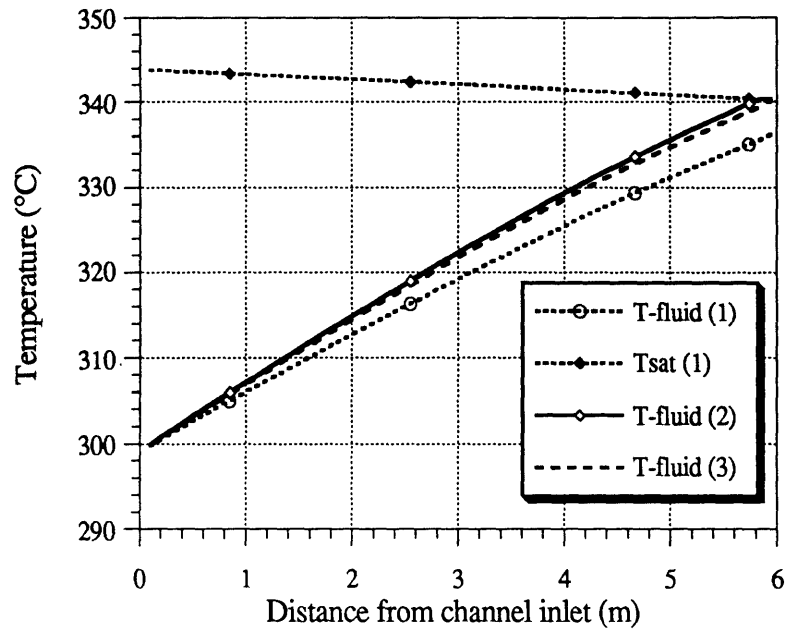


Figure 14-14 Bulk coolant temperature profile in PTLWR coolant channels

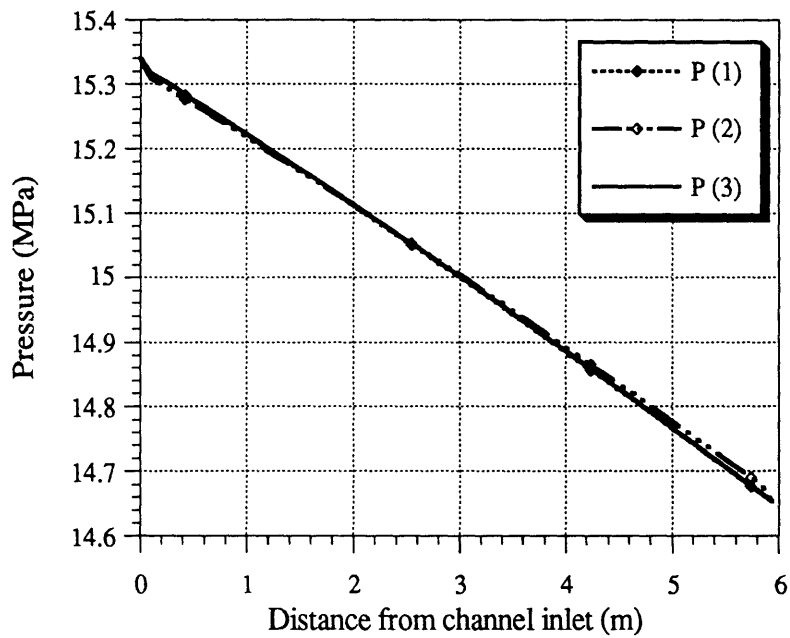


Figure 14-15 Pressure along PTLWR coolant channels

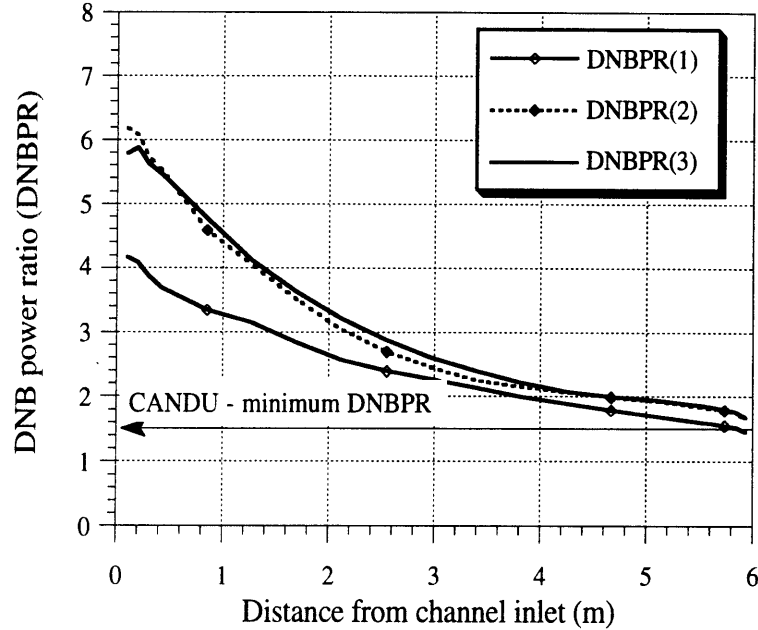


Figure 14-16 DNB power ratio along PTLWR coolant channels

point for CANDU reactors, which maintains the DNBPR at about 1.5 during normal operation. It can be seen that the lowest DNBPR point at the end of the channel corresponds to the CANDU operating point.

14.5.3 Matrix Performance in Post-CHF Regime

A considerable advantage of the PTLWR fuel matrix is its capability of operating in the post-CHF regime without exceeding fuel design limits. This feature was confirmed by decreasing the flow rate through the fuel channel by 50% while keeping the channel at full power. This leads to establishment of film boiling at the end of the channels. The temperature across the fuel matrix at the axial location of maximum power density, i.e., at the end of the channel where film boiling occurs, is presented in Figure 4-17. Comparing the curve for normal operation and for the post-CHF regime, it can be observed that the temperature increase for the post-CHF regime is only about 200 °C for the matrix surface temperature and about 100°C for fuel centerline temperature. Both temperatures remain below the design limit of 1300 °C. Hence, the traditional DNBR limit of 1.3 is of less

importance in the matrix fuel, and concerns of burnout-related problems during pump coastdown or pump seizure are practically eliminated.

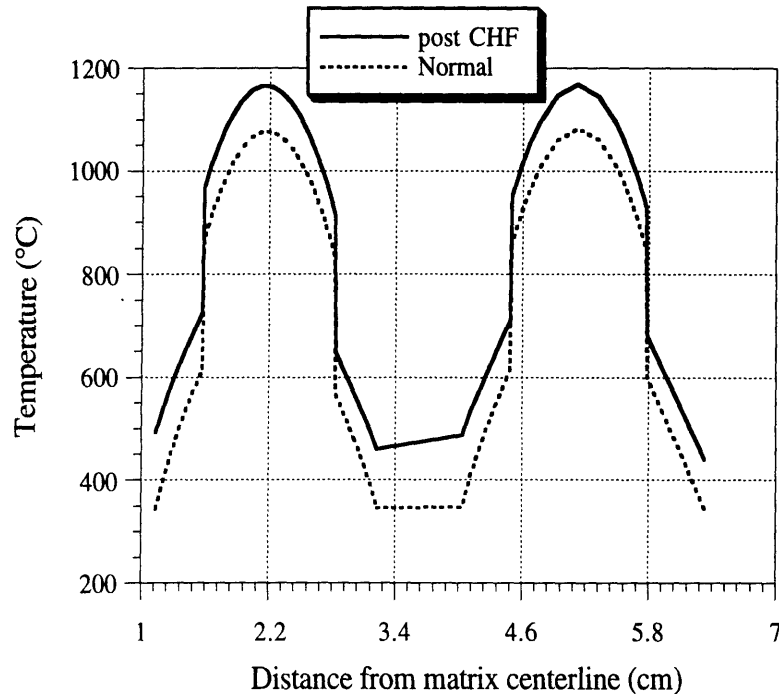


Figure 14-17 Fuel matrix performance during normal operation and in the post-CHF regime

14.5.4 Performance for the Equilibrium Core

The thermohydraulics of the equilibrium core differs from that of the fresh core due to its different power density profile, which depends, primarily, on the refueling scheme. The bi-directional refueling scheme with partial reshuffling, selected for the PTLWR design exhibits higher maximum power density close to the channel inlet and low power density near the channel outlet (see Section 14.4.3). The higher maximum power density results in increased maximum fuel centerline temperature, as can be seen in Figure 14-18 (by about 100°C to yield 1180°C, which is 120°C below the steady-state design limit). Figure 14-18 shows that there is a large temperature jump about 250°C across the fuel compact-matrix interface. This jump can be eliminated by using molded-block fuel element technology, developed by HOBEG [Hrovat, 1978], which eliminates the gap between the graphite matrix and fuel compact. On the other hand, the axial

Fuel matrix temperature profile

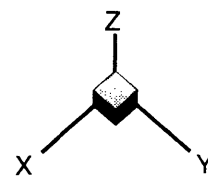
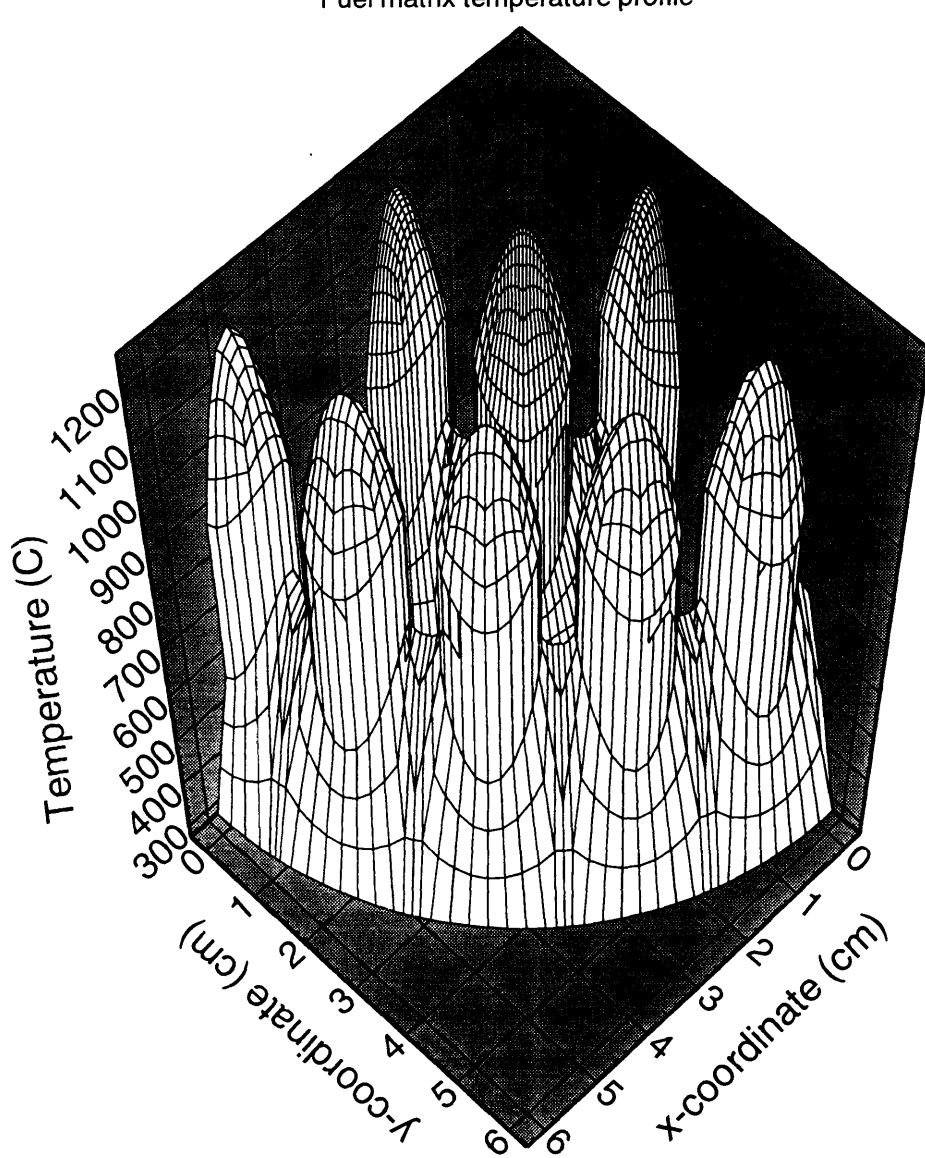


Figure 14-18 Maximum fuel matrix temperature profile for the equilibrium core

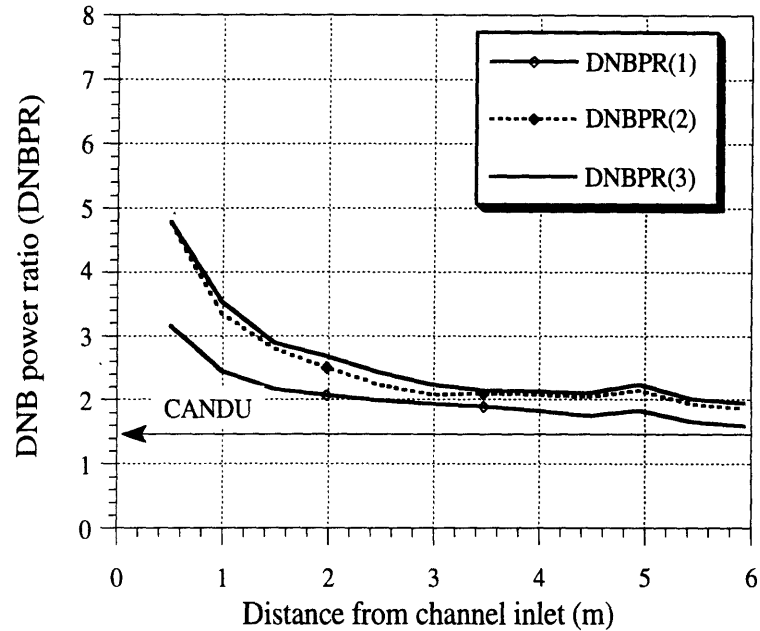


Figure 14-19 DNB power ratio along PTLWR coolant channels for equilibrium core

shape of the power density profile is very close to the shape of the critical heat flux curve, therefore the channel exhibits higher DNBR margin. This can be observed by comparing Figure 14-19 and Figure 14-16.

14.6 FUEL CHANNEL CHARACTERISTICS DURING LOCA

To achieve the key objective of surviving the loss of coolant accident without the requirement of replenishing the primary coolant, the fuel channel needs to be able to dissipate decay heat by conduction, radiation and convection in steam/air mixtures to the heat sink without exceeding safe temperature limits. These limits are 1600°C for TRISO particle fuel, 1300°C for the SiC coating to avoid excessive oxidation and 500°C for the pressure and calandria tubes to assure their reusability. The transient history of these critical temperatures in time has been calculated and compared to the design limits.

14.6.1 Method of Analysis

The transient analysis is based on the solution of the heat conduction equation coupled to the neutron point kinetics equation. A simplified 1-D heat transfer model has been developed. Circular fuel compacts, arranged in two rings, were transformed into fueled annuli such that the fuel volume was preserved. The graphite matrix body was also reshaped into a set of annuli which interlace the fuel annuli and annular coolant regions. To keep the temperature difference in the thin fueled annulus the same as in the cylindrical fuel compact, a geometry factor was introduced. The central coolant hole, coolant ring and coolant gap were treated for initial conditions as convective or boiling boundary nodes with boundary conditions of the heat transfer coefficient and the bulk coolant temperature (or saturation temperature in case of boiling). The intermediate ring of coolant holes has a graphite web between individual holes. During normal operation, there is practically no heat transfer radially across this web because all the heat is transferred to the coolant. However, following a loss of coolant accident, when no or negligible cooling is available via these cooling passages, the web becomes the primary contributor to heat dissipation out of the fuel matrix. To properly account for this phenomenon in LOCA situations, this region was treated as a massless conductor with effective thermal conductivity. The finite element package ALGOR was used to benchmark the results obtained from the 1-D model of the fuel matrix. Heat transfer across the gap between the matrix and the pressure tube was also transformed into a heat conduction problem using an effective conductivity which includes radiation, natural convection, and conduction through the gas in the gap. Power generation in the fuel compacts was calculated in a conventional manner as the sum of fission and decay power using point kinetic equations with 6 delayed groups and an 11-decay group model, respectively. Release of Wigner energy from the graphite matrix during heatup was also accounted for. To incorporate reactivity feedback from coolant voiding the change of core coolant density with time during LOCA was taken from CANDU analyses.

14.6.2 Fuel Channel Performance in LOCA without Scram

The accident simulated assumed a 100% break of the inlet header in both loops without scram. Moreover, all heat transfer coefficients in all coolant channels were set to zero at the same time as the break occurs, thus neglecting the energy carried away by the coolant during blowdown. The flooding process was assumed to be actuated 5 seconds after blowdown initiation, which is conservatively late. Consequently the top row becomes flooded at the time 35 seconds. Another conservatism in the analysis is introduced by setting the temperature of flood water to saturation, i.e., the subcooling was neglected.

The analysis result will be presented for the fresh core at the location of maximum power density. Figure 14-20 shows the temperature traces of the inner fuel ring, matrix surface at the central coolant channel, the pressure tube, and the calandria tube for the channel at the top row. Figure 14-21 plots the steady state temperature profile at 0 seconds and at 160 seconds, i.e., the time when maximum fuel matrix temperature is reached. At the time flooding water reaches the last row of fuel channels (35 seconds) the calandria tube surface temperature is slightly higher than the Leidenfrost point. Hence, the initial cooldown through the film boiling regime (after about 5 seconds) reduces the calandria wall temperature below the Leidenfrost point. Consequently, the calandria tube is rapidly quenched and its temperature drops close to the saturation temperature of flood water and is then maintained at this level until the end of the transient. The temperature of the pressure tube quickly follows that of the calandria tube, and the channel slowly cools down. All peak temperatures remain below their design limits.

Reactivity changes and relative power are plotted in Figure 14-22. As the primary coolant is lost, the rapid decrease in coolant density results in a large negative reactivity insertion and reactor shutdown. The contribution from the Doppler coefficient is positive because the fuel temperature drops, but is very small compared to void reactivity. Hence, the total reactivity is driven almost exclusively by coolant conditions in this scenario. Inherent reactor shutdown during LOCA without scram is a favorable characteristic different than for CANDU reactors, which exhibit a positive void coefficient,

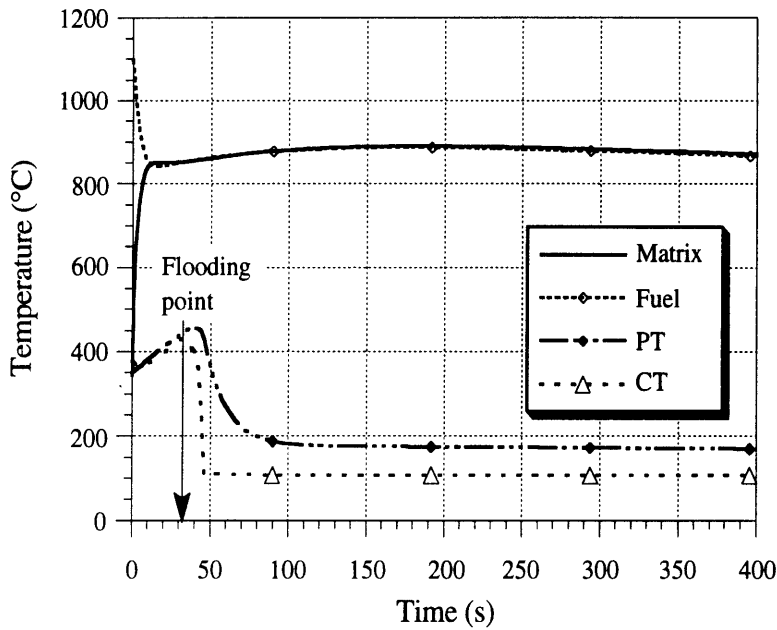


Figure 14-20 Time development of limiting temperatures following LOCA without scram

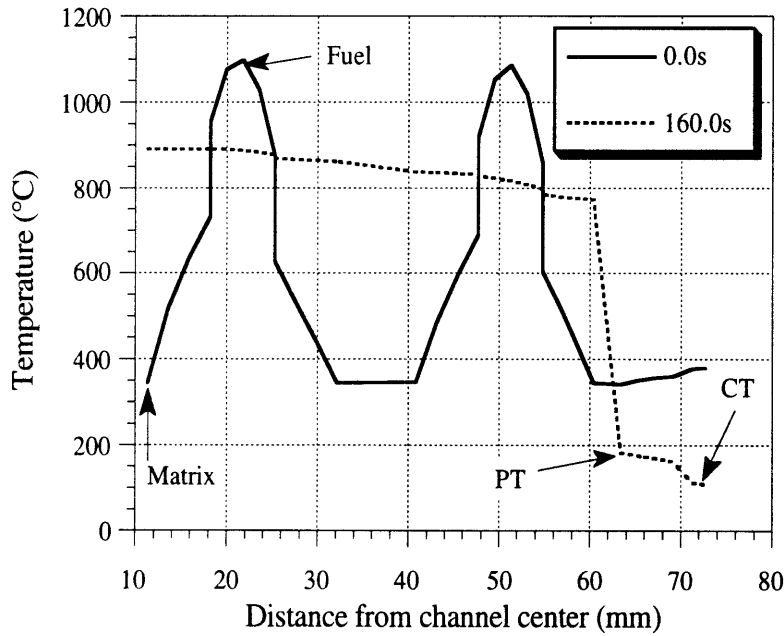


Figure 14-21 Radial temperature profile in the fuel channel following LOCA without scram

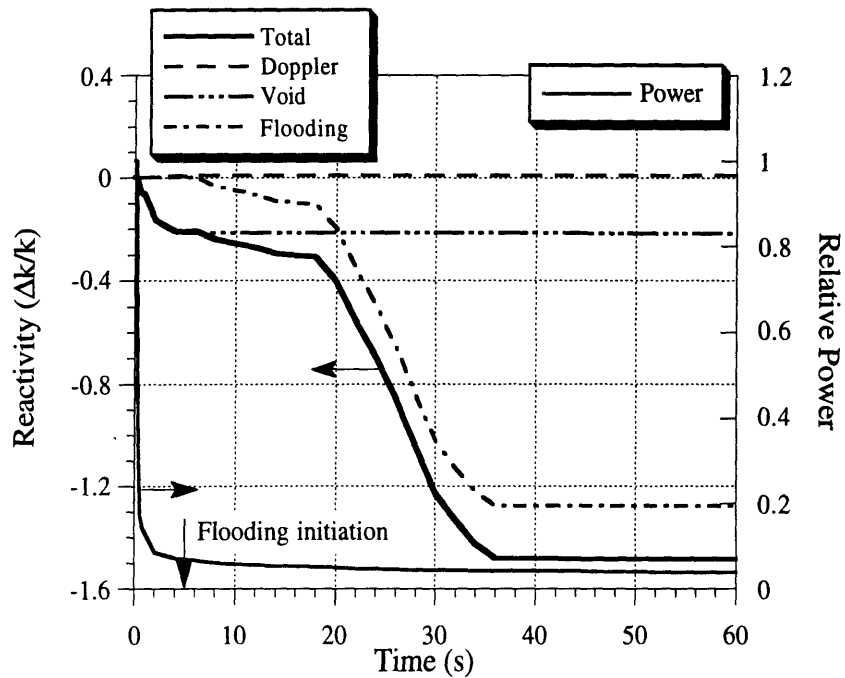


Figure 14-22 Reactivity changes during LOCA without scram

and must rely on reliable shutdown systems. Flooding brings additional negative reactivity into the system, which renders the reactor deeply subcritical (by about -200β).

Because of the uncertainties with the minimum film boiling heat flux, the worst possible scenario – one having sustained film boiling at the outer surface of the calandria tube, was studied. To achieve film boiling, the Leidenfrost temperature was artificially decreased and the flooding initiation was set at a later time so that the upper row is flooded at the 50th second. Figures 14-23 plots the time history of limiting temperatures. Both the fuel and maximum matrix surface temperatures reach higher maximum values than for the nucleate boiling case, but the difference is small (only about 20°C). The pressure tube temperature rises to about 500°C , until 50 s, when the flooding water reaches the last row. Since the calandria tube outer surface temperature is well above the Leidenfrost point, heat transfer to flooding water is by film boiling, and the pressure tube temperature remains at about 500°C . An important conclusion from this hypothetical scenario is that even if the calandria tube does not quench

below the Leidenfrost point, there is no problem in removing the heat load. In fact this scenario is preferable from the thermal stress point of view. Also note that there is no traditional CHF concern since the system can remove the heat under film boiling conditions.

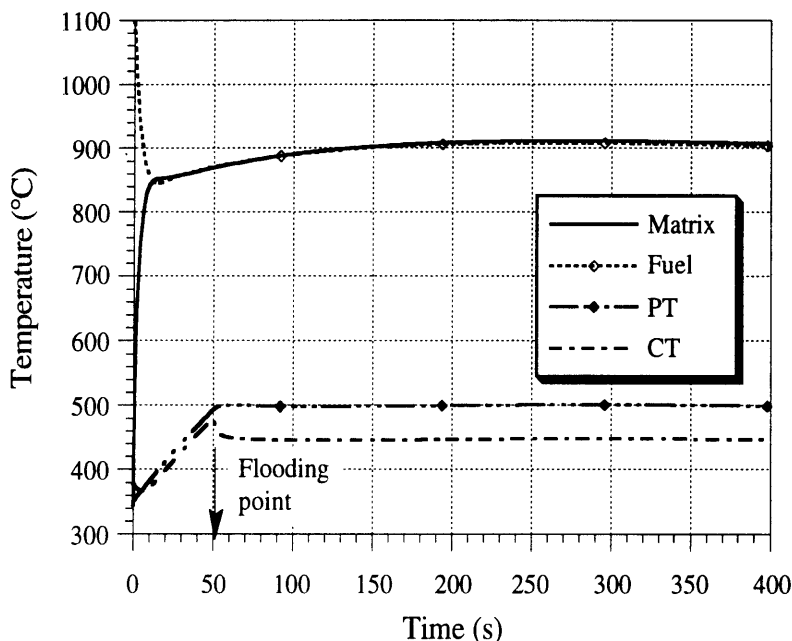


Figure 14-23 Time development of limiting temperatures for sustained film boiling at calandria tube surface

Finally, it is noted that the performance of the equilibrium core is identical except for slightly higher limiting temperatures (maximum fuel matrix temperature is increased by 30°C and pressure tube and calandria tube temperatures by 10°C).

It has been demonstrated that the decay heat in a LOCA without scram scenario can be removed without exceeding safe limits on the fuel, matrix and pressure tube, and without an emergency core cooling system. This capability of the proposed fuel-matrix-in-a-pressure tube design to passively dissipate the excessive power generated in the fuel to the heat sink without exceeding safe temperature limits, even if the fuel channel is voided, is the key advantage of the PTLWR. Furthermore, even one of the worst accidents which could hypothetically occur – LOCA without scram – does not result

in temperatures which would lead to fuel channel damage. These characteristics are primarily due to:

- the arrangement of the fuel in small modules distributed in a heat sink, having a very short conduction path between the fuel and the heat sink,
- the introduction of the fuel matrix which
 - retains high effective thermal conductivity in the absence of coolant,
 - reduces initial energy stored in the fuel, and
 - provides for high additional energy storage,
- a relatively flat power profile throughout the entire core, which decreases thermal limits imposed by the hot spot,
- a large flooding water-to-fuel matrix mass ratio, responsible for the deposition of a substantial portion of the gamma decay heat directly in the heat sink, hence reducing the decay heat load on the fuel matrix, and
- a large negative void coefficient, responsible for inherent reactor shutdown following LOCAs.

14.7 PASSIVE FLOODING CHARACTERISTICS

Flooding the calandria space with light water is a unique and very important feature of the PTLWR concept. It provides a heat sink independent of reactor primary coolant, and redundant reactor shutdown. The goal of this section is to confirm that the flooding of the top row of fuel channels can be accomplished fast enough so that in the total loss of coolant, none of the critical components of the fuel channel, i.e., the pressure tube, the calandria tube, the matrix and the fuel exceed their design limits.

The process of calandria flooding has been described using a mass conservation equation in the upper calandria space occupied by gas, or a steam/gas mixture, an energy equation for the lower calandria space occupied by liquid, and the momentum equation for flooding water between pool water level in the containment and water level inside the calandria. All equations are integrated simultaneously to obtain water level as a

function of time. Water level in the calandria, h , and water level in the containment, H are plotted in Figure 14-24. It can be observed that flooding of the top row of fuel channels is achieved in about 24 seconds. This time scale compares very favorably with the fuel heat-up time scale, where the fuel matrix can withstand an adiabatic heat up from decay heat for hundreds of seconds without exceeding allowed temperature limits. It is also three times less than the time when the maximum pressure tube temperature reaches the limit of 500°C , in an adiabatic heat-up scenario. The results in Figure 14-24 have been obtained under the assumption that all four passive flooding valves, having a total flow area of 0.5m^2 , open. A simulation of the failure of 2-out-of-4 valves to open resulted in extension of the flooding time by 10 seconds. This is a sufficiently rapid process taking into account that the adiabatic heat-up (from decay heat) of the fuel matrix to its limiting temperature (1300°C) takes hundreds of seconds, and heat-up of pressure tubes to their limiting temperature of 500°C takes about 70 seconds.

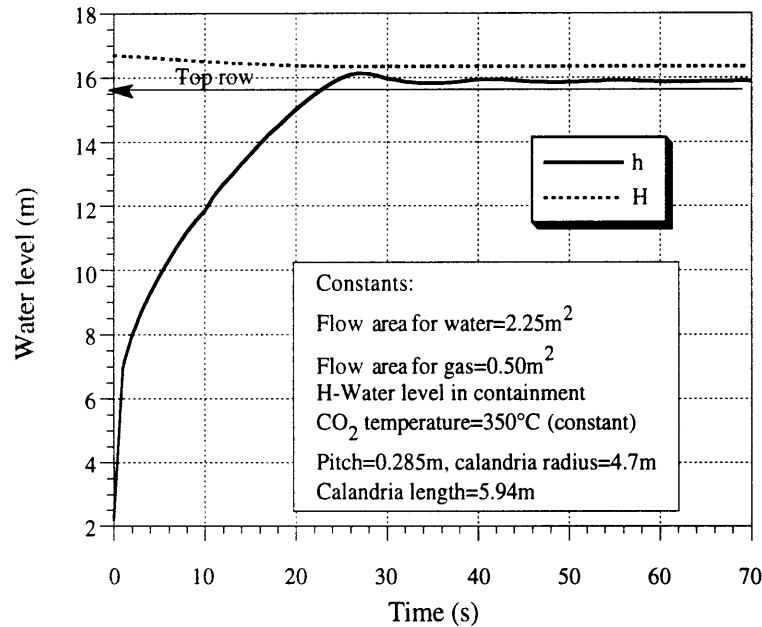


Figure 14-24 Water level in calandria flooding process

14.8 CONTAINMENT DESIGN CHARACTERISTICS

14.8.1 Containment Design Features

The containment proposed for the PTLWR concept is shown in Figure 14-15. It is a large, free standing cylindrical steel containment with a concrete shield building. Passive cooling of the steel shell is achieved by buoyancy-induced air flow. The purpose of the shield building is to protect the primary steel shell from external events, e.g. tornado or aircraft impact. An annulus between the steel shell and the shield building is equipped with air intakes and air outlets to permit flow of ambient air. The air intakes are located above ground level to avoid plugging by wind-entrained debris. Both the air intakes and the air exhaust are protected by grates to prevent the accidental entrance of large objects into the annulus. In addition to the large air outlet at the center of the containment dome, there are 20 small circular air outlets above the annulus gap. These outlets are sized such that they accommodate about 40% of total air flow, thus decreasing air flow around the steel dome where flow area is limited. This design increases air velocity due to the smaller pressure drop at the exit. The chosen containment design is in many aspects similar to the concept studied by Ebasco for the New Production Reactor (NPR), or the concept studied by the Joint Siemens-Framatome venture - International Nuclear Power (NPI).

To prevent potential stratification*, two features are designed into the containment. First, a crane wall supporting a polar crane creates a passage for promoting natural circulation in the passive cooling mode. As the arrows in Figure 14-25 show, the heated atmosphere rises inside the crane wall, is cooled along the containment shell and returns outside the

* Such a situation is highly undesirable in a passively cooled containment because the effective heat transfer surface would be significantly decreased since the substantial low-elevation portion of the containment wall which is not exposed to the hot steam would remain at low temperatures, and consequently yield very low heat transfer rates in this region.

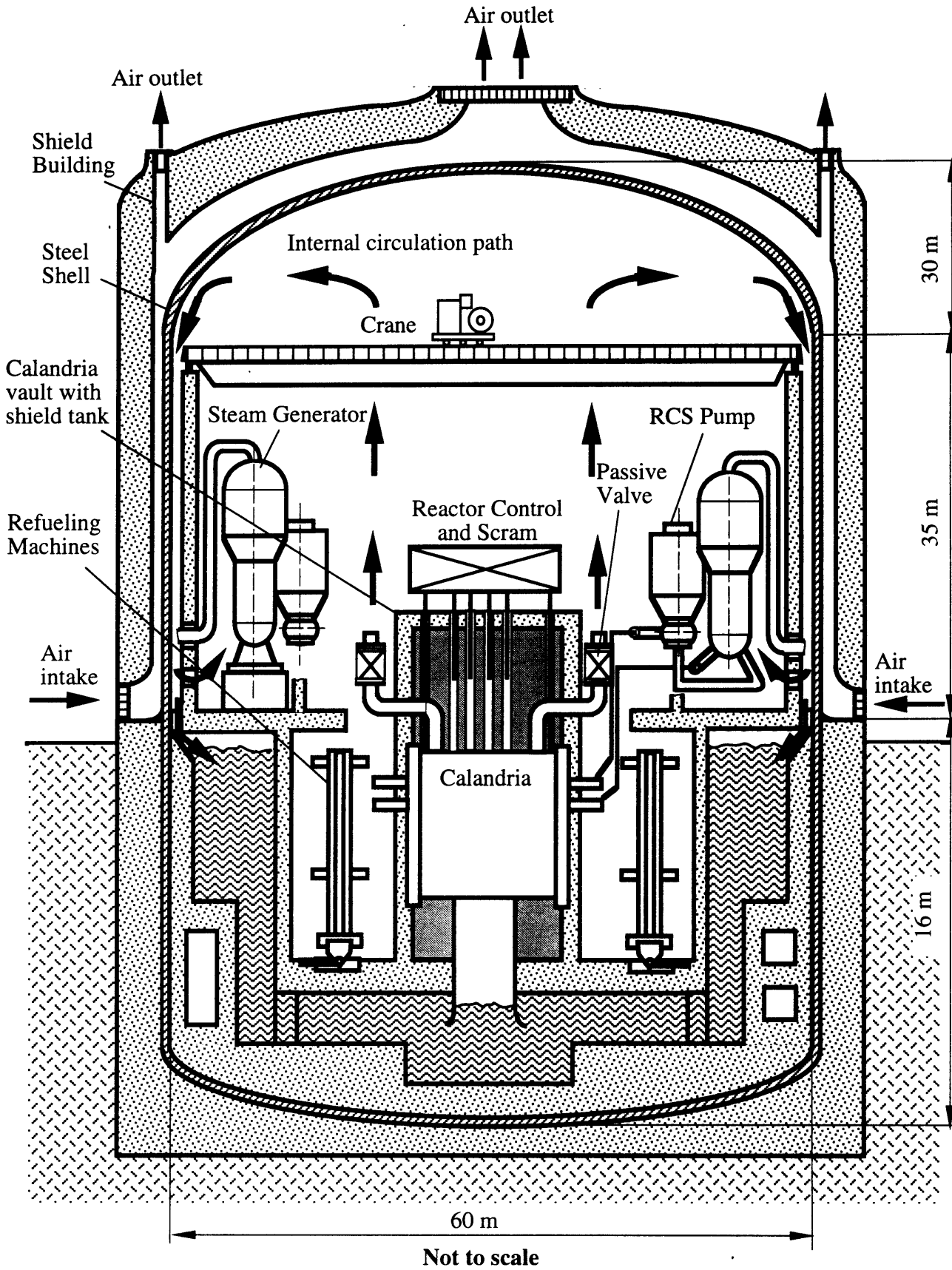


Figure 14-25 Schematic of containment arrangement for passive pressure tube LWR

crane wall. Condensate on the shell is returned back to the pool, while carry-under noncondensibles are recycled back through passages placed at low elevation. The crane wall also provides protection against missiles and fluid jets. A second important feature which would play a key role in eliminating eventual stratification is the low-elevation location of the steam exhaust lines from the calandria. Upon opening of a passive valve, which is followed by calandria flooding, all decay heat is removed in the form of steam released from the calandria. This steam will establish circulation patterns by entrainment of stagnant containment atmosphere in turbulent buoyant plumes rising from the valve exhaust piping to the top of the building. Since the pressure peak from long-term pressurization sets the limit on passive cooling performance, and because at this critical time, the location of the steam exhaust responsible for this pressure peak is guaranteed always to be at a low elevation regardless of the break location, the containment atmosphere is expected to be well mixed.

Another important feature associated with the PTLWR containment is the flooding pool. In the long term, the flooding pool absorbs significant energy as sensible heat and decreases the heat load on the containment shell. The volume of the flooding pool is sized (4200 m³) to release its sensible heat gradually during the long-term pressurization period until the pressure peak is passed, thus decreasing both the rate of pressure rise and the magnitude of the peak.

14.8.2 Analysis Results

The primary goal of this section is to confirm that the peak pressure in the proposed passively-cooled PTLWR containment, resulting from the limiting design basis accident for containment analysis, falls within the range of design pressures for typical large dry containments. Another goal is to confirm that the expected circulation patterns are established and that they will lead to a well-mixed containment atmosphere. The analyses were performed using computer codes CONTAIN and GOTHIC.

Since the PTLWR has two separate loops interconnected to a pressurizer through piping equipped with an isolation valve, a LOCA in one loop does not necessarily result in blowdown of the entire primary

system. For containment analysis, it is assumed that the isolation valve fails and the entire primary system inventory is discharged into the containment. Hence, double-ended rupture of a hot header at the surge line connection, with isolation valve failure was taken as a design basis accident scenario.

The CONTAIN-calculated history of the containment pressure for a 1-cell model is given in Figure 14-26. Saturation temperature (corresponding to partial steam pressure), gas temperature, and containment wall temperature at the outer surface are shown in Figure 14-27. The containment pressure exhibits two peaks. The first peak results from primary system blowdown, the second peak represents long-time containment pressurization from steam carrying decay heat released from the calandria. The maximum peak of 3.44 bars is reached at about 2×10^5 seconds (55 hours). Heat rates to internal structures, containment walls, the pool and decay power are shown in Figure 14-28. At the time of 55 hours, i.e., when the pressure peak is reached, decay heat is equal to 16 MWt, the heat removal rate from the containment wall is about 10.5 MWt, 3.8MWt is being transferred to concrete, and the remaining 1.7 MWt is being stored in the pool. Even at this long time, a significant heat rate is absorbed in the concrete, hence, the mass and total surface of internal concrete structures are very important to the accuracy of long-term pressurization computations. At 5×10^5 seconds, all latent heat available in the pool is exhausted. This results in the tertiary pressure peak.

The trace of saturation temperature, "T-sat," on Figure 14-27 corresponds to the history of the partial pressure of steam. The temperature of the gas/steam mixture, designated as "T-gas", exhibits an additional peak at 1000 seconds. This peak results from heating of the containment atmosphere by the hot primary metal. Note that the hot primary metal heats the containment atmosphere directly; this differs from typical LWRs where most of the primary metal stored energy is released during the reflood phase in the form of steam at saturation temperature, hence superheat is not present. Containment wall temperature follows the saturation temperature with significant delay.

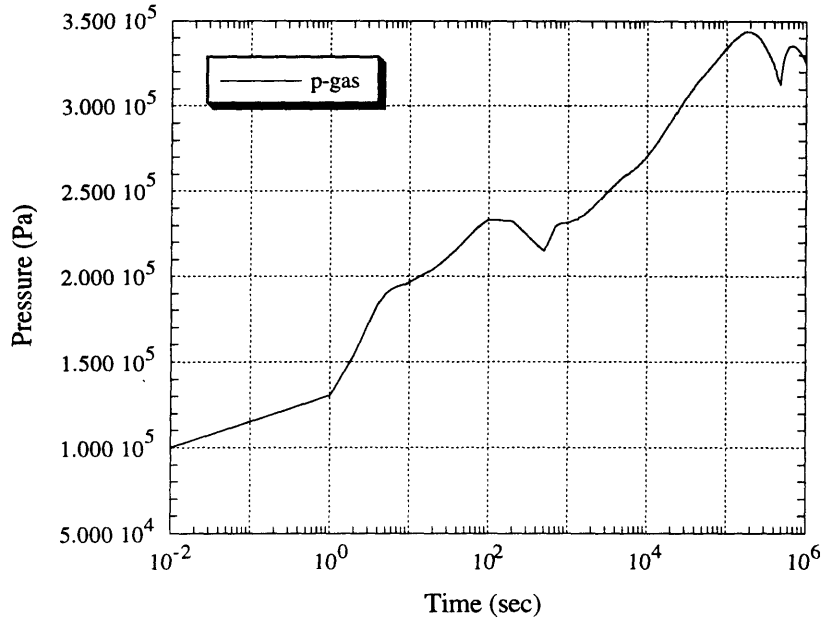


Figure 14-26 PTLWR containment pressurization history for double-ended rupture of a hot header with isolation valve failure

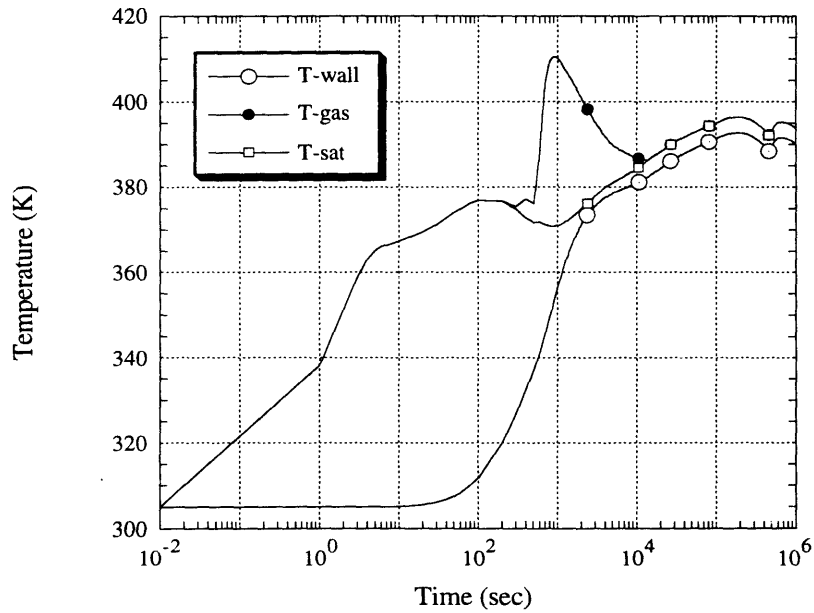


Figure 14-27 Containment gas, saturation and wall outer surface temperature histories for double-ended rupture of a hot header with isolation valve failure

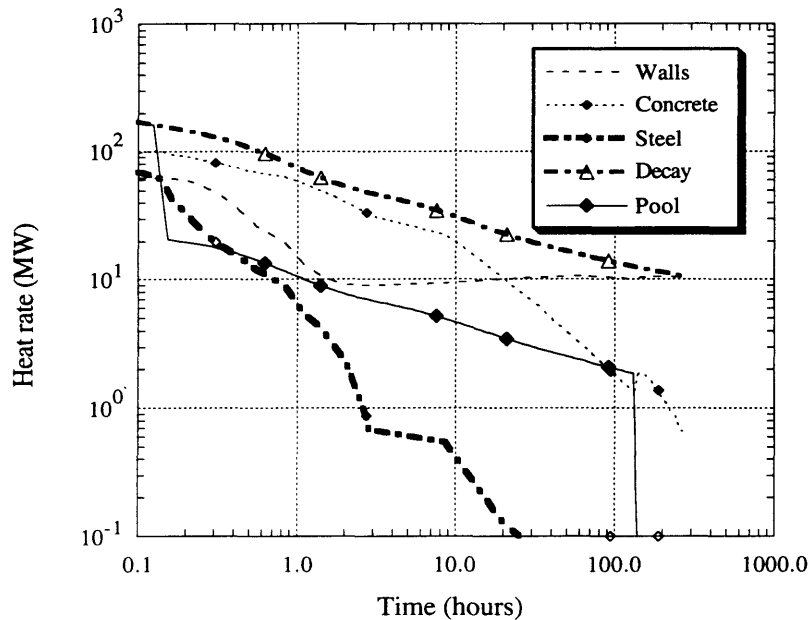


Figure 14-28 Decay power and heat rates to structures for double-ended rupture of a hot header with isolation valve failure

Several important conclusions can be drawn from Figures 14-26 and 14-27. First, all pressure peaks are relatively low, hence a containment with a design pressure of 0.42MPa (60 psi) could handle this DBA accident. Secondly, the peak from the blowdown is small compared to the long term pressurization from decay heat. Moreover, passive containment wall cooling does not participate in blowdown-pressure peak reduction, as can be seen from the containment wall temperature trace. Therefore, even if the containment atmosphere becomes stratified as a result of the blowdown, any potential impairment of containment passive cooling from stratification would not have a visible effect on the magnitude of the first peak. Thirdly, the long-term pressurization peak is limiting for the design pressure and for the performance of the passive air cooling system. Since the steam released from the decay heat is always released at a low elevation, natural circulation will be established such that the hot steam escaping from the calandria will rise to the top of the containment and condense along the cooled walls, breaking up potential stratification. As a result, all of the air-cooled containment wall will be exposed to high

containment temperature and the heat transfer to air in the annulus will not be impaired.

Since the containment design pressure is set by the secondary pressure peak and since the pressure peak from the blowdown is much smaller than the secondary peak, the proposed containment can handle even more severe scenarios within the design basis. One such scenario is a simultaneous double-ended rupture of a hot header at the surge line connection, with isolation valve failure and steam line break with main steam isolation valve failure. The pressure history, plotted in Figure 14-29, shows that even for this hypothetical event, the blowdown peak remains slightly below the secondary peak.

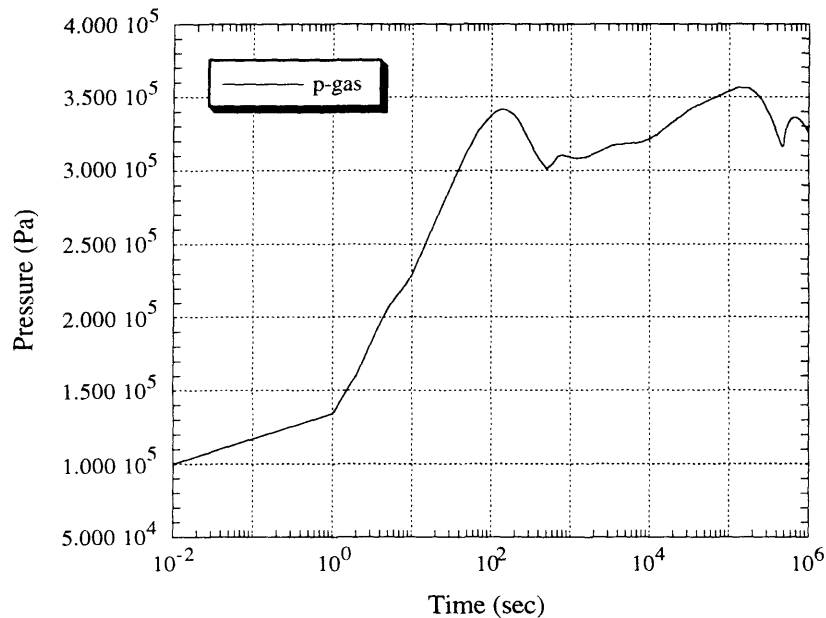


Figure 14-29 Containment pressurization history for simultaneous double-ended rupture of a hot header, with isolation valve failure and steam line break with main steam isolation valve failure

To confirm the circulation patterns inside the containment, a multidimensional GOTHIC model was developed. The results in the form of velocity vectors of vapor projected into four selected cut planes, shown in Figure 14-30, are presented in Figure 14-31. The situation in Figure 14-31

corresponds to the time when the maximum pressure peak is reached. Hot steam from decay heat rises from the calandria space through the center of the upper containment to the top and returns down along the air-cooled containment walls, thus exposing the entire steel shell to high temperature. As expected, hot steam release at low elevation promotes mixing of the containment atmosphere significantly. The temperature difference between the top and the bottom of the containment shell was found to be small, i.e., around 3°C. Circulation behind the crane wall seems to be more pronounced than near the wall without the crane wall. This can be seen from velocity vectors at plane NS-1(with crane wall) and EW-1 (without crane wall).

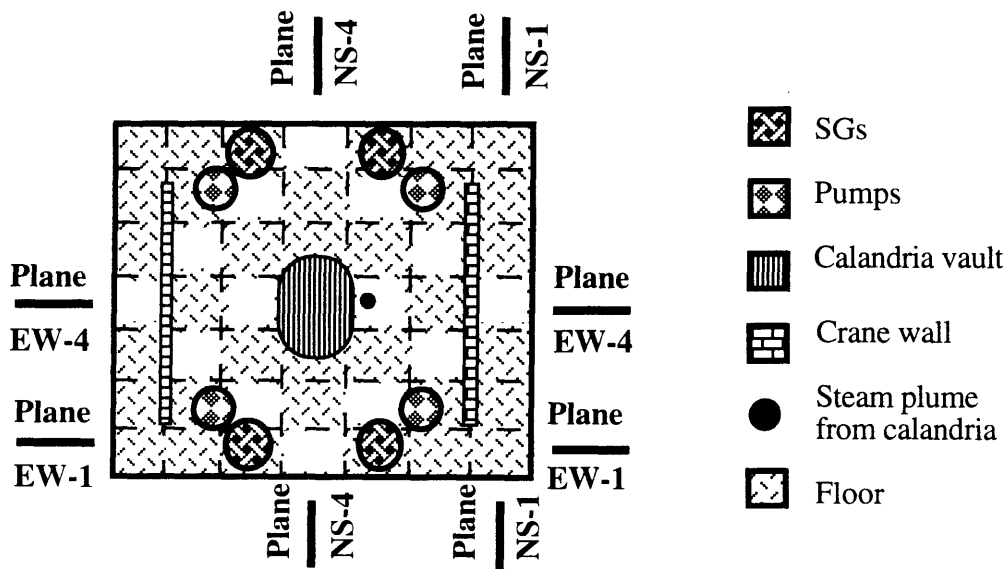


Figure 14-30 Top view of multidimensional GOTHIC model for the PTLWR containment with designation of cut planes

Analyses confirmed that the maximum pressures reached in the proposed containment with passive air cooling remain within the range of design pressures for large dry containments of currently operating PWRs. The main reasons for the feasibility of air cooling only is the large free volume, the large heat capacity of the water pool and the large heat storage capability of internal heat structures, primarily concrete.

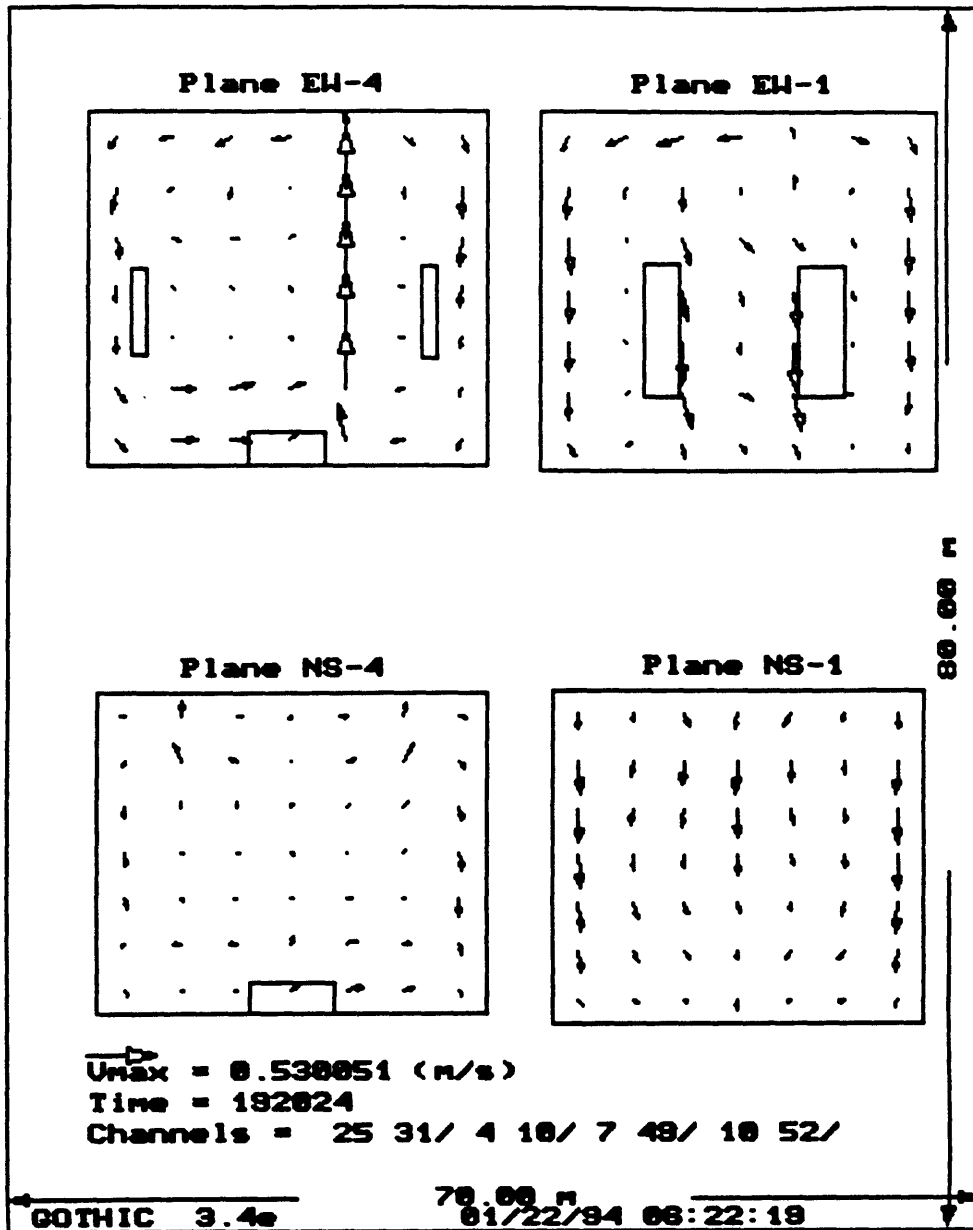


Figure 14-31 Velocity vectors at the time of maximum pressure peak

14.8 PTLWR PERFORMANCE IN VARIOUS ACCIDENTS

The PTLWR design employs a primary system similar to that of CANDU reactors and exhibits neutron physics characteristics of both CANDUs and PWRs. Hence, the PTLWR behavior resembles either that of CANDU or PWR under various accident scenarios. In the incidents with an increase in heat removal by the secondary system, the PTLWR behaves similarly to a PWR, but it will exhibit less of a neutron power increase prior to reactor trip due to smaller reactivity insertion for the same coolant temperature drop. For accidents with a decrease in heat transfer by the secondary system, the PTLWR retains the capability of CANDU units which employ a shutdown cooling system able to remove decay heat at full pressure, and large shell side SG inventory, which provides a heat sink for about 25 minutes before boiloff, thus allowing adequate time to align the shutdown cooling system. In addition, the PTLWR has an independent passive flooding system as a backup. The power peak prior to reactor trip will be less than that of CANDU due to the negative coolant temperature coefficient.

Accidents with decrease of reactor coolant flow rate do not pose any particular challenge to the PTLWR concept because its fuel elements can operate in a post-CHF condition even at full power without exceeding fuel design limits. Therefore, even in the event of a hypothetical main coolant pump shaft seizure, no damage of the PTLWR fuel elements occurs while for a PWR and CANDU, partial fuel damage is predicted. The ability of the PTLWR fuel elements to operate in the post-CHF regime is a significant advantage, which makes the PTLWR fuel resistant to failure in most of the accidents where the DNBR criterion is challenged.

Regarding potential reactivity accidents, the advantage of the PTLWR over a PWR is that no pressure-assisted control rod ejections are possible. Also, all the reactivity incidents associated with the dilution or removal of coolant or moderator poison are eliminated.

The key contribution of the PTLWR is its capability to handle ATWS and station blackout – the major contributor to the core damage frequency in

current PWRs and CANDUs – without sustaining core damage. This is primarily due to the redundant, diverse reactor shutdown provided by means of passive flooding, which concurrently provides a heat sink for long-term decay heat removal. Moreover, the path which links the heat sink to the core is entirely independent of the normal reactor core cooling system, hence it does not require any depressurization, and is not interfered with by the coolant escaping from the core through the break in the form of a two-phase mixture or steam flow. Also, the absence of a large pressure vessel eliminates the hypothetical catastrophic failure of a large pressure vessel and allows us to handle a break of the pressure boundary anywhere in the plant as a design basis event.

14.9 COMPARISON WITH OTHER REACTOR DESIGNS

Various PTLWR characteristics are compared with other reactor designs in Tables 14-2 through 14-4. The comparison is made with three reactor types – CANDU, PWR and RBMK since the PTLWR shares some common features with these reactor types. Namely, the PTLWR adopts the CANDU design of the heat transport system, it employs the light water moderator and coolant and primary system parameters close to those in PWRs, and it utilizes a graphite reflector as does the RBMK.

Table 14-2 Main characteristics of the PTLWR, CANDU, PWR and RBMK

	CANDU	PWR	RBMK	PTLWR
Moderator	D ₂ O	H ₂ O	Graphite/H ₂ O ^a	H ₂ O/Graphite ^a
Coolant	D ₂ O	H ₂ O	H ₂ O-boiling	H ₂ O
Fuel	UO ₂ pins	UO ₂ pins	UO ₂ pins	Particle fuel in compacts
Cladding	Zy	Zy	Zy	C/PyC/SiC/PyC coating
Reflector	D ₂ O	H ₂ O	Graphite	Graphite
Primary pressure-containing boundary	Horizontal pressure tubes	Pressure vessel	Vertical pressure tubes	Horizontal pressure tubes
Cycle	Indirect	Indirect	Direct	Indirect

^aPrimary moderator/secondary moderator

Table 14-3 Physics characteristics of the PTLWR, CANDU, PWR and RBMK

	CANDU	PWR	RBMK	PTLWR
Coolant void coefficient	Positive +16mk/100%void and decreases with irradiation to +11mk for equilibrium core	Negative under all conditions except at very high concentration of soluble boron	Positive ^a +20mk/100%void, +5mk/100%void at normal operation, becomes more positive with burnup	Negative under all conditions ^b
Moderator temperature coefficient	Negative	Negative/positive depending on core status	Strongly positive but slow due to long time constant of graphite	Negative
Reflector temperature coefficient	Negative	Negative	Positive	Positive but small and slow due to long time constant of graphite
Stability to Xe spatial oscillations	At full power unstable without control, hence spatial control provided	At full power unstable without control, hence spatial control provided	At full power very unstable without control, hence spatial control provided	Inherently stable at any power, spatial control not needed
Neutronic coupling of the core	Fair (adding 17 mk would make each half core critical)	Fair	Very weak (adding 6mk makes each half of the core critical)	Very strong
Doppler coefficient	Negative	Negative	Negative	Negative and strongly increases with voiding
Scram effect	Negative	Negative	Initially positive	Negative
Excess reactivity in the core	Small	Large at BOL	Relatively small	Small
Prompt neutron lifetime	Long	Short	Relatively short	Long

^aMost moderation is accomplished by graphite, but H₂O has relatively large absorption, hence on loss of coolant the absorption effect prevails. Also strongly dependent on reactor conditions, such as number of inserted control rods..

^bPrimary moderation is provided by H₂O, hence upon voiding, moderation is also lost, which hardens spectrum and significantly decreases fission rate in fissile species (note that the PTLWR design has a highly thermal spectrum)

Table 14-4 Safety-related intrinsic characteristics of the PTLWR, CANDU, PWR and RBMK

	CANDU	PWR	RBMK	PTLWR
Primary system fuel-containing boundary	Pressure tubes	Pressure vessel	Pressure tubes	Pressure tubes
<p>Implications:</p> <ol style="list-style-type: none"> 1. Pressure tubes are exposed to full neutron flux, hence tougher environment than for a reactor vessel (the PTLWR design is most challenging in this aspect). 2. Rupture of PT can be handled without serious consequences, in fact these failures have occurred in both CANDUs and RBMKs; while catastrophic PWR pressure vessel failure would lead to core melt. 3. Catastrophic failure is not possible with pressure tubes because the thickness of PT is less than the critical crack length (leak before break). 4. In-service inspectability is more difficult for pressure tubes than for the vessel, but a leak can be tested for very easily. 5. CANDU and PTLWR designs have an additional barrier around the fuel-containing pressure boundary (calandria tube) which can withstand full pressure in case of a break. 				
Fuel arrangement	Separate fuel channels	Fuel array	Separate fuel channels	Separate fuel channels
<p>Implications:</p> <ol style="list-style-type: none"> 1. For fuel in separate fuel channels, thermohydraulic conditions can be easily tested experimentally. 2. Faulty fuel in separate fuel channels is easily detected. 3. LOCA in the system with separate fuel channels is mitigated by the large hydraulic resistance of the piping (blowdown period is more protracted). 4. Separate fuel channels provide the possibility to place an alternative heat sink outside the fuel channels: <ul style="list-style-type: none"> CANDU-cold alternative heat sink (D₂O) always present in the LP vessel, PWR - no alternative heat sink present in the HP vessel, RBMK- heat source present in the LP vessel (hot graphite can become an alternative heat sink if fuel temperatures become too high), PTLWR-cold alternative heat sink present outside the LP vessel and passively introduced in accidents. 5. Separate fuel channels are more susceptible to flow blockage (i.e., no cross flow). 				

Table 14-4 Safety-related intrinsic characteristics of the PTLWR, CANDU, PWR and RBMK (continued)

	CANDU	PWR	RBMK	PTLWR
Primary coolant inventory	Relatively small	Large	Large	Relatively small
<p>Implications:</p> <ol style="list-style-type: none"> 1.Small coolant inventory results in small energy release in LOCA and hence lower containment pressure. 2.Large coolant inventory allows more time for corrective action due to longer time constants 				
Refueling	On-line	Batch	On-line	On-line
<p>Implications:</p> <ol style="list-style-type: none"> 1.In on-line refueling, faulty fuel can be easily replaced without necessitating reactor shutdown. 2.Fuel is more susceptible to jamming during on-line refueling. 3.Refueling machine becomes part of the extended primary system during on-line refueling and its malfunction could result in small LOCA. 4.Large seismic event during on-line refueling may result in the damage of inlet piping by sudden movement of large refueling machines. 5.In RBMK, the presence of heavy refueling machine above the core may damage the core if large malfunction occurs. 6.On-line refueling allows for low reactivity excess, and hence reduced potential for large reactivity excursions. 				
CRD location	In LP region	In HP region	In LP region	In LP region
<p>Implications:</p> <ol style="list-style-type: none"> 1.Location of control rods in LP region allows for simpler CRDM design and no pressure-assisted reactivity accident (like rod ejection in PWRs) is possible. 				

Table 14-4 Safety-related intrinsic characteristics of the PTLWR, CANDU, PWR and RBMK (continued)

Barriers to fission product release	3	3	2	4
<p>3 barriers are clad, primary system enclosure and containment (RBMK has no containment)</p> <p>4 barriers are SiC particle fuel coating, SiC matrix coating, primary system enclosure and containment</p> <p>Implication: More barriers reduces the probability of fission product release.</p>				
Tritium inventory	Large	Small	Small	Small
<p>Implications:</p> <p>1. Large tritium inventory requires special attention to protect plant personnel.</p> <p>2. Large tritium inventory leads to additional radioactivity release in an accident.</p>				

14.10 CONCLUSIONS AND FUTURE WORK RECOMMENDATIONS

An innovative design concept of a large, light water cooled and moderated reactor has been proposed and described. The design departs significantly from traditional LWR designs in terms of reactor physics, thermohydraulics during normal operation, and the decay heat removal process from the fuel during loss of coolant accidents. This conceptual study has confirmed that the proposed reference PTLWR design can achieve the key objectives of sufficient cooling of the fuel elements in the absence of primary coolant, large nominal power output, and inherent reactor shutdown in accidents leading to high temperatures. It can cope with station blackout and anticipated transients without scram without sustaining core damage. The fuel elements can operate in the post-CHF condition even at full power without exceeding fuel design limits, thus making the PTLWR resistant to fuel damage in accidents challenging the CHF limits.

Future work should focus on decreasing the fast fluence on pressure tubes by increasing the heavy metal loading using alternative fuel arrangements within the pressure tubes. The proposed concept of a pressure tube reactor with voided calandria space is by no means confined to the reference design studied in this work. Changing the fuel design in the fuel channel and introducing separate moderator, heterogeneously distributed in the calandria opens a plethora of new alternatives by offering an “additional degree of freedom” afforded by decoupling the moderator from the cooling function. A range of design alternatives can be demonstrated using for example the dry calandria versions for Pu burning and Pu production, or versions using alternative coolants that do not require high pressure.

Chapter 15

CONCLUSIONS AND FUTURE WORK DIRECTIONS

15.1 CONCLUSIONS

An innovative design concept of a large, light water cooled and moderated reactor has been proposed and described. The design departs significantly from traditional LWR designs in terms of reactor physics, thermohydraulics during normal operation, and the decay heat removal process from the fuel during loss of coolant accidents. This conceptual study has confirmed that the proposed reference PTLWR design can achieve the key objectives of sufficient cooling of the fuel elements in the absence of primary coolant, large nominal power output, and inherent reactor shutdown in accidents leading to high temperatures.

Although a comprehensive risk analysis in terms of core damage frequency remains to be done, the PTLWR concept offers some important safety enhancements in the LWR arena. These can be summarized as follows:

1. The PTLWR fuel elements are capable of operating in the post-CHF regime even at full power without exceeding the fuel design limits. Such a rugged fuel significantly increases reactor forgiveness in transients and accidents which would otherwise challenge conventional DNBR margins.
2. The risk of fission product release to the environment is reduced by increasing the number of barriers between the fission products and the environment from three to four. The barriers include the silicon carbide coating of particle fuel (which is considered as containment in the MHTGR), the silicon carbide coating of the fuel matrix, the primary system boundary and the containment shell.

3. The PTLWR is designed to survive loss of coolant accidents without the need of replenishing primary coolant, by dissipating the decay heat generated in the fuel matrix via conduction and radiation through the pressure tubes into the heat sink outside the fuel channels.
4. The PTLWR is capable of withstanding the ATWS and station blackout sequence – the major contributors to the core damage frequency in current LWRs – without sustaining core damage by having a redundant and diverse reactor shutdown means: passive flooding which concurrently provides a heat sink for decay heat removal. Moreover, the path which couples the heat sink to the core is entirely independent of the normal reactor core cooling system, hence it does not require any depressurization, and is not interfered with by the coolant as it escapes from the core through the break in the form of a two-phase mixture or steam flow.
5. The PTLWR can sustain without fuel damage a break in the primary system boundary, anywhere, as a design basis, including the failure of a core region boundary, by eliminating the massive pressure vessel.

Besides the above safety enhancements, the PTLWR is inherently stable against xenon spatial oscillations; it eliminates problems with local criticality, eliminates the need for chemical shim in the coolant and for associated equipment, it exhibits a relatively flat power density profile, and has very large prompt neutron lifetime, which makes the reactor more forgiving in prompt critical reactivity excursions.

The high fast fluence on pressure tubes and less efficient neutron economy are the main drawbacks. Overall, the proposed PTLWR concept offers a very promising alternative for advanced light water cooled and moderated reactors, worthy of further development in future work.

15.2 FUTURE WORK DIRECTIONS

Recommendations for future work can be divided into three major categories. The first category includes improvements in the analysis of the proposed PTLWR concept. The reader is reminded that the analyses which have been presented throughout this volume are at the level of a conceptual study, and are often simplified. Real reactor design requires the concentrated effort of many professionals rather than one-person involvement; therefore this study is by no means comprehensive. The areas which deserve special attention because of significant simplifications or omission will be pointed out in Section 15.2.1.

The second category involves various improvements or modifications within the proposed dry calandria concept. They primarily include ideas on how to improve the dry calandria concept, such as, for example, decreasing the fast neutron fluence. These will be summarized in Section 15.2.2.

Finally, the third category includes new ideas for a passive pressure tube reactor. The proposed pressure tube reactor with voided calandria space is an innovative design with some unique physics characteristics and is not limited to a light water primary coolant only. There are several combinations of coolants, moderator arrangement, and fuel arrangement, which could result in other passive pressure tube reactor designs. Additionally, the proposed reactor concept can be modified for plutonium burning or plutonium breeding. The areas of exploration for this type of reactor are large and largely unexplored. Several new ideas deserving further investigation will be suggested in Section 15.2.3.

15.2.1 Comprehensive Detailed Analysis of the Proposed Concept

The scope of this conceptual design study is limited and cannot cover all the aspects of reactor design. To confirm the key physics and thermohydraulic characteristics, simplified methods are often sufficient. Although these methods give satisfactory results for the purpose of the conceptual study, such as this work represents, they may not give sufficient accuracy for a real reactor design. This section will point out major

simplifications introduced in this analysis which need further refinement should this work be carried beyond the conceptual stage.

One of the key areas deserving further attention and development is the reactor physics for systems with very high neutron streaming. Although the Monte Carlo method used throughout this work is very accurate for these applications, it requires an extremely long CPU commitment. It is therefore desirable to calculate sets of effective diffusion coefficients, spanning the conditions of interest, which can be precomputed once and then used as input data in the standard LWR computer codes which are based on the neutron diffusion equation. Although several methods for obtaining effective diffusion coefficients in lattices with neutron streaming have been developed [Gelbard, 1983], these are mostly for lattices where voided space is small compared to space taken up by solid or liquid material. This differs significantly from the dry calandria design, where most of the space is occupied by voids (80%) and the neutron mean free path is comparable to core dimensions. Hence the validity of the methods developed for lattices where high density material is dominant needs to be confirmed or modified for void-dominant lattices.

Burnup calculations in this work were done using MCNP for eigenvalue calculations and ORIGEN2 for the change of fuel composition with burnup. Since an effective one-group ORIGEN2 cross section library is not available for the PTLWR design, the PTLWR fuel was burned up using a PWR library for the uranium-plutonium cycle, with the cross sections of the most important actinides modified to match the reaction rates obtained from MCNP. More accurate burnup calculations should be performed in the future. This could be done by developing a separate ORIGEN2 library for the PTLWR. The easier alternative would be to use the MCNP-ORIGEN2 Coupled Utility Programs (MOCUP) package, recently developed at Idaho National Engineering Laboratory (INEL), which provides the means to use MCNP for the neutronics solution and ORIGEN2 to perform depletion [Babcock et. al., 1993]. The third option is to utilize standard diffusion codes which incorporate burnup calculations, provided that the required sets of effective diffusion coefficients are developed.

The limited scope of this work allowed only for the qualitative discussion of various accidents rather than the comprehensive analysis usually called for. Future work should include more complex analysis of the entire accident spectrum using available sophisticated codes such as TRAC, RELAP5 or RETRAN.

Although the containment analysis has been fairly extensive, it could not incorporate all the details of in-containment layout at this preliminary stage. Since the containment pressure peak from long-term containment pressurization depends strongly on concrete heat sinks, detailed design work needs to take into account more exact consideration of the amount of concrete and its distribution inside the containment to decrease the uncertainty associated with these heat sinks. Extensive sensitivity studies with respect to other system characteristics should be also performed in order to estimate prediction uncertainties, to evaluate the effect of these characteristics on containment pressure, and to identify the variables which have the best potential for improving containment performance.

Another issue of high importance is a more detailed economics study than could be performed within the scope of this work. In particular, a good estimate of capital cost, operation and maintenance costs, and especially the fabrication cost of the PTLWR fuel elements, is necessary to judge PTLWR competitiveness with other advanced LWRs as well as with conventional power generation plants.

The PTLWR concept employs a fuel matrix containing particle fuel. Although both the matrix and the fuel are based on current technologies, their application in an LWR environment does not have the extensive experience now accumulated with conventional LWR fuel; this aspect needs more research and development. An extensive literature search suggests good compatibility of the proposed SiC-coated graphite matrix with the PTLWR environment, but there are not enough data on the behavior of a protective silicon carbide coating on a graphite matrix during thermal shock and during irradiation. A small-scale experimental program initiated at MIT will address the former issue, the latter must be investigated in a future irradiation program.

15.2.2 Improvements and Modifications of the Proposed Concept

The reference PTLWR design investigated in this study employs only one of many possible alternative fuel arrangements. Chapter 5 shows some alternative fuel arrangements which could be employed in the PTLWR concept. Desirable goals are to maximize heavy metal loading and consequently decrease fast fluence on pressure tubes, and to improve thermal hydraulic characteristics during normal operation while retaining good heat transfer capabilities from the fuel to the pressure tube wall if there is no coolant in the fuel channel. Detailed analysis of the proposed fuel arrangements with respect to these objectives should be performed in future work to identify the optimum design. Moreover, these fuel arrangements are by no means exhaustive and can serve as a starting point for the inventive designer to come up with new, innovative designs, which could have even better performance.

It has been shown in Chapter 4 that the power peaking in the proposed pressure tube LWR arises from variation in the bundle-to-bundle content of fissile material, rather than from thermal flux peaking, as is the case in currently operating reactors. A bi-directional refueling scheme with partial bundle reshuffling has been adopted. This scheme gives a relatively moderate power peaking factor in the channel of 1.35 at the relatively high initial enrichment of 7%. Other refueling schemes may provide flatter power density profiles. One alternative would be to refuel channels in the lower-flux regions with the fresh fuel to achieve partial burnup, and then move partially burned fuel bundles to fuel channels having higher thermal flux. Alternative refueling schemes, which minimize power peaking, should be explored in future work.

CANDU fuel channel pitch is optimized to provide the highest reactivity for natural uranium moderated by D₂O. Since there is no moderator outside the PTLWR fuel channels, the PTLWR design offers more freedom in the selection of the pitch. The minimum channel pitch is restricted by the space requirements associated with header plumbing and on-line refueling, but it is not restricted by reactor physics. In fact a smaller channel pitch is desirable since it decreases neutron leakage and allows placement of more fuel channels into a core of the same dimensions, and hence operation at

higher power. The reference PTLWR design adopted the same channel pitch as in CANDU units to stay within CANDU practice. If the currently used faceseal closure is used, the pitch can be decreased to 22.86 cm; employing a boroseal closure would allow a minimum pitch even lower, i.e., 20.4 cm [Hart, 1991]. This would allow increasing the number of fuel channels by about 160, thereby increasing net power to about 1550 MWe. Hence, further study of the PTLWR design for smaller fuel channel pitch is warranted. Another interesting option, which could double reactor power and further decrease the leakage would be a reactor design with another core set of fuel channels running in a transverse direction staggered between the original fuel channels.

The design of the gap between the pressure tube and the calandria tube has not been finalized and remains for future work. It was shown that even a small gap 2mm thick filled with a high-conductivity gas such as helium cannot achieve a sufficient heat transfer rate to dissipate decay heat from the fuel channel without exceeding the temperature limit on the pressure tube. Possible design solutions, which could attain the desired heat transfer rate of 60,000W/m², have been suggested. They include a packed bed of graphite pebbles, proposed by Tang [Tang, 1992], zirconia spheres as proposed by Dutton [Dutton, 1993], or a duplex tube, similar to those used in EBR-II sodium-water steam generators.

Preliminary analysis in Chapter 11 suggests that an alternative design of the flooding pool incorporating a vapor suppression system is beneficial since it delays containment pressurization by about 10 hours and decreases the pressure peak from long-term containment pressurization by 17%. A 10-hour delay in the initiation of steam release from the calandria is a significant advantage because it avoids steam release from the calandria (thus affecting the containment atmosphere) in many accidents which require calandria flooding or in case of inadvertent flooding. It also provides sufficient time for the operator to reestablish core cooling using the shutdown cooling system. Therefore, future work should include the design of a reliable flooding system with vapor suppression.

15.2.3 New Promising Alternatives for a Passive Pressure Tube Reactor

The proposed concept of a pressure tube reactor with voided calandria space opens a plethora of new reactor alternatives to be explored. Such an extensive scope of alternatives is facilitated by the additional degree of freedom afforded by decoupling the moderator from the cooling function, which relaxes the limits imposed by reactor physics and thermal hydraulics constraints. Currently operating thermal reactors, as well as advanced evolutionary and revolutionary reactors under development use fuel elements heterogeneously distributed in a homogeneous moderator. Many important reactor physics parameters, e.g., void coefficient, are a strong function of fuel/moderator ratio. However, the useful range of fuel/moderator ratios is limited because changes in this ratio to achieve desirable reactor physics characteristics are strongly coupled to thermohydraulics limits. For example, if one strives for a harder neutron spectrum by squeezing out as much light water as possible from the standard LWR lattice, cooling capabilities are affected, and impose a limit on the minimum practical pitch. This is not necessarily the case with the proposed concept, which allows changing the mass of heterogeneously distributed moderator in a voided calandria space (either in the dry or wet calandria version) without affecting the cooling capabilities of the channel. Hence, the designer has the additional variable –separate moderator – to work with. A range of design alternatives can be demonstrated using for example the dry calandria versions for Pu burning and Pu production. It was suggested in Chapter 4 that the dry calandria approach could be used to burn weapons grade plutonium. It will be shown later that this design can be modified into a high converting light water reactor using the same moderator, i.e., light water, to produce plutonium.

The following discussion presents possible variations of pressure tube reactors with voided calandria space which could be explored in the future. They include a Pu burner, a high conversion thermal reactor, other versions of passive pressure tube thermal reactors with alternative coolants, and a pressure tube fast reactor.

15.2.2.1 PTLWR for the Disposal of Weapons-Grade Plutonium.

Recent concerns with excess plutonium from dismantled nuclear warheads have intensified efforts to evaluate options for safe plutonium disposal [von Hippel and Feiveson, 1993], [Alberstein et. al., 1993], [Biswas et. al., 1993], [Brownson and Hanson, 1993], [Bowman and Venneri, 1993]. Section 4.4.9 reviewed key issues associated with weapons-grade plutonium burning in the proposed PTLWR concept. The discussion was based on limited calculations and it dealt only with the reference design, which is not optimized for Pu fuel. Hence, it is of interest to refine the calculations for a Pu fueled PTLWR and optimize the design for Pu burning. The PTLWR may well be a viable intermediate term reactor option for Pu burning.

15.2.2.2 PTLWR Thermal Breeder.

Although the immediate concern is to dispose of excessive weapons-grade plutonium, plutonium recycle may be of interest in the long term. Edlund first indicated in his papers [Edlund, 1975], [Edlund, 1976] that a high conversion ratio of about 0.9 can be achieved in LWRs based on the Pu-U fuel cycle by using a tight-pitch lattice. Edlund's idea was to harden the neutron spectrum by reducing the amount of moderator using a tight-pitch lattice. The hardened neutron spectrum increases the resonance absorption in ^{238}U , and hence the plutonium production. The use of heavy water coolant or a mixture of light water coolant with heavy water can accomplish the same result, since heavy water has inferior moderating properties compared to light water. Since Edlund, many studies have been performed on how to improve uranium utilization in LWRs. Earlier work is reviewed in [Correa et. al., 1979], more recently considerable investigation on this subject has been done in Europe and Japan [Berger et. al., 1992], [Chawla et. al., 1992], [Markl and Moldaschl, 1992], [Broeders, 1992], and [Mochida et. al., 1992].

The PTLWR concept employs on-line refueling, hence no neutrons are lost to poison control, and the conversion ratio is consequently higher.

Therefore, the PTLWR has a good potential to achieve a high conversion ratio if appropriately modified. To harden the neutron spectrum, the fuel loading must be increased and moderator mass decreased. One means to achieve this goal is to replace the matrix with particle fuel by tight-pitch UO_2 fuel elements with SiC cladding in a two-ring arrangement and no moderator in the voided calandria space. The center pin and inner ring of the bundle are removed and the space is filled with a SiC-cladded graphite cylinder. Such an arrangement will also decrease fast fluence and preserve passive dissipation of decay heat in the absence of coolant. Also, the void coefficient should remain negative (see Chapter 5 for preliminary assessment).

The good breeding potential of a pressure tube reactor with LWR coolant has been demonstrated, though in a different configuration [Ronen, 1990]. The pressure tube reactor concept proposed by Ronen uses 919 pressure tubes in a hexagonal arrangement in contact with one another. There is no moderator between the pressure tubes and no calandria tubes. The reactor uses light water coolant and ^{238}U - ^{235}U fuel with 6% enrichment of fissile plutonium (2.63% ^{235}U , 6% $^{239}\text{Pu} + ^{241}\text{Pu}$). The system was found to breed with respect to plutonium with an initial conversion ratio of about 1.10. Breeding was also demonstrated for heavy water as the coolant. AECL studies also indicate high attainable conversion ratios of CANDU pressure tube reactors for Pu/Nat U and thorium cycles [Veeder and Didsbury, 1985].

Although the leakage in the proposed thermal PTLWR breeder concept is higher than in the concept proposed by Ronen and will make it more difficult to achieve breeding, it is expected that the proposed passive pressure tube reactor with either light water or heavy water coolant could attain a high conversion ratio. Hence, further study of various configurations of a passive pressure tube reactor with high conversion ratio is of considerable interest.

15.2.2.3 Passive Pressure Tube Reactors with Alternative Coolants

One of the drawbacks of the proposed PTLWR is the need for thick-wall pressure tubes in the core, which are responsible for significant parasitic neutron absorption, and hence an increase in fuel enrichment. High-pressure-bearing tubes are needed because of the high operating pressure associated with the light water coolant. To decrease the mass of parasitic absorber in the core, it is warranted to explore the use of alternative coolants which can be used at low pressure. A review of various possible combinations of coolants, moderators and fuel arrangement in a passive pressure tube reactor is shown in Table 15-1 with the most promising paths marked by bold typeface. Advantages and disadvantages are listed in Table 15-2.

Table 15-1 Possible combinations in passive pressure tube reactors

Reactor spectrum	Coolant	Moderator	Fuel arrangement	Calandria arrangement
Thermal	H₂O	H₂O	Matrix 2-ring elements	Dry Wet
	CO₂	H₂O	Matrix 2-ring elements	Dry Wet
	He	H₂O	Matrix 2-ring elements	Dry Wet
	Organic	H₂O ZrH₂	Matrix 2-ring elements	Dry Wet
	Na NaK	or H ₂ O	Matrix 2-ring elements	Dry Wet
	Pb or Pb/Bi/Sn	ZrH₂ H₂O	Matrix 2-ring elements	Dry Wet
Fast	Na NaK	or -	Matrix 2-ring elements	Dry Wet
	Pb or Pb/Bi/Sn	-	Matrix 2-ring elements	Dry Wet

Table 15-2 Alternative Coolants for Passive Pressure Tube Reactors

Coolant	Advantages	Disadvantages
H ₂ O	<ul style="list-style-type: none"> •familiar technology •available in ambient •LWR experience base •low price 	<ul style="list-style-type: none"> •requires high pressure •high N-16 production rate with matrix fuel •corrosive
He	<ul style="list-style-type: none"> •HTGR experience base •inert •compatible with HTGR type fuel •high thermal efficiency 	<ul style="list-style-type: none"> •poor heat transfer •high pumping power •relatively high pressure
CO ₂	<ul style="list-style-type: none"> •AGR experience base •availability and low cost •compatible with graphite at moderate temperature 	<ul style="list-style-type: none"> •poor heat transfer •high pumping power •relatively high pressure
Organic	<ul style="list-style-type: none"> •low pressure •no N-16 •low reactivity •low corrosion •compatibility with UC •WR-1 experience base •no rapid LOCA 	<ul style="list-style-type: none"> •high radiation damage especially for matrix fuels •high melting temperature •flammability •fouling of heat transfer surfaces
Na or NaK	<ul style="list-style-type: none"> •low pressure •LMR experience base •could use IFR fuel •excellent heat transfer •potential high thermal efficiency 	<ul style="list-style-type: none"> •reactive with water and air •Na-24 activity •high melting point
Pb or Pb/Bi/Sn	<ul style="list-style-type: none"> •low pressure •Russian submarine experience •Israel MHD experience •could use IFR fuel •compatible with Zy •excellent heat transfer •potential high thermal efficiency 	<ul style="list-style-type: none"> •high melting point •Polonium activity from Bi •lead toxicity

Gas-Cooled Light -Water-Moderated Passive Pressure Tube Reactor.

Gas-cooled reactors require pressurized coolant to improve heat transfer characteristics, but pressure levels (on the order of 6MPa) are less than in a PWR (15.5 MPa). The main challenge in a gas-cooled light-water-moderated pressure tube reactor would be the attainment of adequate cooling during normal operation. Especially in a fuel matrix arrangement where the heat transfer surface is very limited, the concept may be difficult to design without significant degrading of channel power. A concept with 2-ring UO₂ fuel elements with silicon carbide cladding, may deserve some attention. The advantage of this concept is the possibility of operating at high temperatures, and thus achieving high thermal efficiency. However, use of Zircaloy pressure tubes would pose a problem at these temperatures. Problems with Zircaloy pressure tubes have been experienced at the heavy water moderated CO₂ cooled reactors LUCENS in Switzerland [Kraft, 1964] and A-1 in Czechoslovakia [Hulovec et. al., 1964]. It is therefore proposed that the Zircaloy pressure bearing tube be replaced by a SiC tube. Recent advances in ceramics technology allow the manufacture of long SiC tubes, though extensive research and development would be required to confirm satisfactory SiC tube behavior in a reactor core environment. This design employs only SiC, and no graphite in the channel. This allows the use of CO₂ coolant at higher temperatures. The surface of the SiC cladding can be roughened to enhance cooling during normal operation. An ancillary benefit of such treatment could be the improvement of decay heat dissipation during accidents. The dry calandria arrangement is not desirable because of the severe thermal shock on both the Zircaloy calandria tube and the SiC pressure tube during flooding (Note that the channel operating temperature is much higher than in the PTLWR concept). Reactor physics considerations will allow a desirable increase in the thickness of the moderator annulus surrounding the calandria tube as compared to a light water cooled wet calandria design [Tang, 1992], because there is no moderator inside the pressure tube. The challenge is the design of an effective thermal switch between the pressure tube and the calandria tube to decrease heat loss during normal operation. Recently, some progress in this area has been experimentally demonstrated [Novak et. al., 1994].

Organic-Cooled Light-Water-Moderated Passive Pressure Tube Reactor.

Organic coolants have been used in several heavy water moderated pressure tube reactors, the most widely known being the WR-1 reactor at Whiteshell in CANADA [Robertson and Hart, 1972]. This reactor operated successfully for a long period of time and established a good experience base for organic coolant. The key advantage of an organic cooled passive pressure tube reactor is the low coolant pressure at high coolant temperatures. This allows a decrease in pressure tube thickness and thus less parasitic absorption. Although a dry calandria version is theoretically possible, with a ZrH_2 matrix to provide for additional moderation, it is not viewed as a very promising alternative because of high radiation damage to the coolant from the high fast fluence associated with the low fuel loadings typical of matrix fuel. A wet calandria version appears to be promising, with a light water moderator annulus surrounding the calandria tube and a 2-ring fuel arrangement. Organic coolants are also compatible with uranium carbide whereas light water is not. Uranium carbide has 1.3 times higher density than UO_2 , which will allow increasing fuel loading and thus further decreasing fast fluence. The significantly higher thermal conductivity of UC (5.5 times) would allow operation at low fuel centerline temperatures and hence, low stored energy. A considerable advantage of this design is the elimination of rapid LOCA, due to the low pressure (about 2 MPa) of organic coolant. This fact should be explored in more detail, and it is expected that the analysis will show decreased requirements on decay heat removal rates during accidents. Consequently, conventional UO_2 fuel with Zircaloy cladding may be adequate.

Thermal Liquid Metal Cooled Passive Pressure Tube Reactor.

The idea of a thermal reactor cooled by liquid metal is not new. The new prototype graphite-moderated liquid metal cooled reactor HALLAM, USA [Starr and Dickinson, 1958] and the zirconium hydride-moderated sodium cooled reactor KNK-I, Germany [Harde and Stohr, 1964] are representative examples. A review of thermal spectrum LMRs emphasizing the economics of their fuel cycle is given in [Taylor and Driscoll, 1987].

Liquid metal coolants, such as sodium or lead, also provides the benefit of low pressure. In addition, they exhibit excellent cooling capabilities. However, the chemical reactivity of sodium with water and air introduces a potential for exothermic energy release during accidents, and leads to design complexity to prevent such reactions. Lead or the Pb/Bi/Sn coolants do not react with water or air which makes them preferable candidates. While lead coolant was used in some Russian submarines the available information on experience with this coolant is rather limited. Russian researchers are considering lead as a coolant for an electronuclear neutron multiplier [Barashenkov et. al., 1992]. Lead in the form $\text{Li}_{17}\text{Pb}_{83}$ has been adopted in the self-cooled blankets of the fusion reactors ITER and NET [Airola et. al., 1984], [Greenspan, 1986], [Klabukov et. al., 1992]. Recent experiments [Tulenکو, 1993] show that lead is compatible with Zircaloy. Hence, fuel arrangements of 2-ring conventional UO_2 fuel elements with Zircaloy cladding in a Zr 2.5%Nb pressure tube in a wet calandria arrangement would be worth exploring. In [Tulenکو, 1993] it is suggested that lead bonding be introduced between fuel pins and cladding to decrease stored energy in the fuel, and hence to improve LOCA fuel performance. Also, using lead as a low pressure (about 0.5MPa) coolant would prevent rapid coolant depletion following a hypothetical break in the primary system. Coolant remaining in the pressure tube would considerably improve heat transfer from the fuel to the pressure tube (cooled at the outside by the cold moderator annulus surrounding the calandria tube), thereby decreasing the maximum fuel temperature. In this case it is expected that Zircaloy cladding will be able to withstand accident temperatures. The high melting point of lead introduces some complexity into the design and into the on-line refueling system, but these problems should be technically solvable. Overall this seems to be a promising option.

Another possible option with lead coolant would be use of a ZrH_2 fuel matrix in a dry calandria arrangement; the hydrogen in zirconium hydride being the moderator. Zirconium hydride has been used in many TRIGA reactors in their UZrH fuel. Zirconium hydride has been also used successfully as moderator/reflector material in the sodium cooled thermal reactor in Karlsruhe (at coolant temperatures of 600°C), in the Russian nuclear thermionic reactor TOPAZ2, and is included in the GA thermionic

reactor design proposed for next generation space thermionic nuclear power [Simnad,1992]. Zirconium hydride is relatively stable in water, steam and air at temperatures up to 600 °C; the compatibility with lead would have to be confirmed. Experience with this material also showed that it could survive transients to 1000°C if the hydrogen content is limited to 1.7 a/o in order to control the hydrogen pressure to tolerable levels [Simnad, 1992]. Maximum temperatures during accidents are envisioned to remain quite below this value. A review of zirconium hydride as a fuel matrix material in the PTLWR did not revealed any major compatibility problems [Hejzlar et. al., 1993]. Reactivity changes due to coolant voiding are expected to be small, since the moderating contribution of the heavy metal coolant is very small compared to that of ZrH_2 .

Fast Liquid Metal Cooled Passive Pressure Tube Reactor.

The passive pressure tube concept cooled by lead and having a fast neutron spectrum, with a 2-ring fuel element configuration in a dry calandria arrangement is another interesting path to explore. Sodium as a coolant must be discarded because it would be very difficult to guarantee no contact with flooding water in case of pressure tube failure (or another compatible fluid would have to be used). Fuel of the matrix type can be used but a 2-ring fuel configuration is preferable due to higher achievable loadings and hence, less fluence. Fast reactors generally require more complex designs to achieve high safety levels and are difficult to design with negative coolant void coefficient. Since a passive pressure tube reactor exhibits large leakage, and the void coefficient tends to be negative for higher leakage, this concept may offer an attractive option to overcome the coolant void problem. Moreover, since the positive character of the sodium-void effect is introduced primarily by the moderating power of sodium, replacing traditional sodium coolant with lead should alleviate the problem even further. Lead or lead/bismuth have low neutron capture cross sections and high thresholds for inelastic scattering, making these coolants ideal in this respect. Calculations made for large reactors which exhibited a highly positive void coefficient for sodium coolant showed highly negative coolant void coefficients for a Pb/Bi eutectic. [Yiftah and Okrent, 1960]. Also, the cores of fast reactors are sensitive to dimensional changes such as bowing

or swelling, with reactivity increasing with compaction. This may not be the case in a pressure tube reactor with voided calandria, since the voided space in the calandria allows for a large swelling of fuel channels without displacing the coolant; the smaller effect of density changes on reactivity using lead instead of sodium is important in this aspect as well. However, this hypothesis needs to be confirmed. Another advantage of the dry calandria concept is the possibility of redundant shutdown by flooding with water, independent of other control systems. It may be beneficial to decrease the fuel-channel pitch to increase the mass of the fuel in the core relative to the total core mass. This will increase core fuel loading, and increase reactivity due to the reduced leakage, and thus lead to less parasitic losses in the reflector. The graphite reflector considered for the proposed PTLWR may need to be replaced by a different reflector with decreased slowing down power to avoid the power density peak from thermal flux near the reflector. A steel reflector, such as used in FFTF may be appropriate. The power density profile in this fast reactor is expected to exhibit a chopped cosine shape proportional to a typical fast neutron flux profile in a pressure tube reactor with voided calandria. This concept could also operate at higher coolant temperatures, and thus achieve higher plant efficiency. It is noted, however, that maximum coolant temperature would be limited by the Zr-2.5%Nb pressure tube material and Zircaloy cladding material if Zircaloy is used. Replacement by stainless steel as is the common practice in current fast reactors is possible. Since the system pressure is very low, the pressure tube-calandria tube system could be replaced by a steel duplex tube with thin walls keeping neutron parasitic losses at low level. Also, compatibility of lead with water may eliminate the need for an intermediate heat exchanger*, thus allowing the operation at lower primary coolant temperature at the same thermal efficiency as well as reducing equipment cost. Overall, the concept of a lead-cooled fast passive pressure tube reactor outlined above may deserve further investigation.

*Possibility of light water getting into lead primary coolant on steam generator tube rupture needs to be analyzed.

The above review of promising alternatives of passive pressure tube reactors is by no means complete. Other modifications and improvements are possible, and a broad avenue to explore novel configurations of coolant, moderator and fuel in heterogeneous arrangement remains open.

REFERENCES

- Airola**, J. et. al., "A Blanket Concept with Liquid $\text{Li}_{17}\text{Pb}_{83}$ for Tritium Breeding in INTOR-NET," Nuclear Eng. and Design/Fusion, Vol. 1, 1984, p.185.
- Alberstein**, D., A. M. Baxter, and C. J. Hamilton, "The MHTGR – Maximum Plutonium Destruction Without Recycle," ANS Trans., Vol. 69, November, 1993, pp. 94-95.
- ALGOR** Finite Element Analyses System, Set of Manuals from Algor Interactive System, Pittsburgh, Pennsylvania, 1990.
- Ambrosek**, D., CEGA, Personal Communication, April, 1993.
- Askew**, J. R., D. W. G. Harris, and L. J. Hutton, "The Calculation of Resonance Capture in Granular Fuels," DCPM 11/Winfrith 1, London, February 1971.
- Babcock**, R.S., D. E. Wessol, and C. A. Wemple, "MOCUP: MCNP-ORIGEN2 Coupling Utility Programs," ANS Trans., Vol. 69, Winter Meeting, San Francisco, November, 1993.
- Baker**, D. E., "Graphite as a Neutron Moderator and Reflector Material," Nuclear Engineering and Design, Vol. 14, 1970, pp. 413-444.
- Banerjee**, S., and W. Hancox, "An Overview of CANDU Reactor Safety and Thermohydraulics," ROE-ILO, Lectures presented at the Institute de Investigaciones Electricas, Guernavaca, Mexico, October, 1981.
- Barashenkov**, V. S., A. N. Sosnin and S. Y. Shmakov, "An Electronuclear Neutron Multiplier in an Apparatus with Lead Coolant," Soviet Atomic Energy, Vol. 72, No. 1, pp. 89-91.
- Barrett**, R. J., E. J. Gahan, G. Nugent, R. J. Reyer, and R. L. Schwartzberg, "Mini-Assessment of Advanced Technology Options for

NASAP:Homogeneous Molten Salt Sustainer Reactor, Graphite-Moderated Heterogeneous Gas Core Reactor,” ORNL/TM-7195, September 1980.

Barry, R. F., “LEOPARD-A Spectrum Dependent Non-Spatial Depletion Code for the IBM-7094,” Westinghouse Electric Corp., Report WCAP-3269-26, September, 1963.

Bell, I., “Calculation of the Critical Mass of UF_6 as a Gaseous Core, with Reflectors of D_2O , Be and C”, Los Alamos National Laboratory Rep. LA-1874, 1955.

Bell, M. J., “ORIGEN – The ORNL Isotope Generation and Depletion Code,” ORNL-4628, Oak Ridge National Laboratory, 1973.

Benedict, M., T. H. Pigford, and H. W. Levi, Nuclear Chemical Engineering, Second Edition, McGraw-Hill Book Comp., New York, 1981

Berger, H. D., H. Finnemann, M. Schatz, G. J. Schlosser, K.Thieme and M. Wagner, “Core Design Studies for a Tight Lattice Pressurized Water Reactor with Improved Fuel Utilization,” Kerntechnik, Vol. 57, 1992, pp. 31-36.

Bergles, A. E., and W. G. Thompson, “The Relationship of Quench Data to Steady-State Pool Boiling Data,” Int. J. Heat Mass Transfer, Vol. 13, 1970, pp.55-68

Biasi, L. et. al., “Studies on Burnout, Part 3,” Energia Nucleare Vol. 14, pp. 530-536, 1967 (Also quoted in Collier, 1981).

Biswas, D., R. W. Rathbun, and H. D. Garkisch, “Characteristics of a 100% MOX-Fueled PWR Design for Weapons Plutonium Disposition,” Trans. ANS, Vol.69, November 1993, pp.95-96.

Boczar, P. G., and A. R. Dastur, “CANDU/PWR Synergism,” paper presented at IAEA Technical Committee Meeting “Advances in Heavy Water Reactors”, Toronto, June, 1993.

Borkowski, J. A., G. E. Robinson, A. J. Baratta, and M. Kattic, "Time Domain Model Sensitivity in Boiling Water Reactor Stability Analysis Using TRAC/BF1," Nuclear Technology, Vol. 103, July 1993, pp. 34-47.

Bowman, C. D., and F. Venneri, "Accelerator-Driven Thermal Spectrum System for Weapons Plutonium Destruction," Trans. ANS, Vol.69, November 1993, pp.102-103.

Bowring, R. W., "Physical Model Based on Bubble Detachment and Calculation of Steam Voidage in the Subcooled Region of a Heated Channel," OECD Halden Reactor Project Report HPR-10, 1962 (Also cited in Collier, 1981).

Bowring, R. W., "A Simple But Accurate Round Tube, Uniform Heat Flux, Dryout Correlation over the Pressure Range 100-2000 psia," Report AEEW-R789, UKAEA, Winfrith, 1972 (Also cited in Collier,1981).

Bradfield, W. S., "On the Effect of Subcooling on Wall Superheat in Pool Boiling," J. of Heat Transfer, Vol. 89, August 1967, pp. 269-270.

Breitbach, G., and H. Barthels, "The Radiant Heat Transfer in the High Temperature Reactor Core after Failure of the Afterheat Removal Systems," Nuclear Technology, Vol.49, August 1980, pp.392-399.

Briesmeister, J. F., Ed., "MCNP - A General Monte Carlo Code for Neutron, Photon and Electron Transport, Version 3A/3B/4," Los Alamos National Laboratory Rep. LA-7396-M, 1986, Revised in 1988 and 1991.

Broeders, C. H. M., "Neutronic Investigations of an Equilibrium Core for a Tight-Lattice Light Water Reactor," Kerntechnik, Vol. 57, 1992, pp. 23-29.

Bromley, L. A., "Heat Transfer in Stable Film Boiling," Chem. Eng. Prog., Vol.46, No. 5, 1950, pp.221.

Brooks, G. L., and E. G. Price, "Fuel Channel Performance," AECL-9753, presented at the 28th Annual Conference of the Canadian Nuclear Association, June 12-15, 1988.

Brownson, D. A. and D. J. Hanson, "Evaluation of Weapons-Grade Plutonium Disposition Options," Trans. ANS, Vol.69, November 1993, pp.100-101.

Candelore, N. R., R. C. Gast, and L. A. Ondis, "RCP01 – A Monte Carlo Program for Solving Neutron and Photon Problems in Three-Dimensional Geometry with Detailed Energy Description," WATP-TM-1267, Westinhouse Electric Corporation, Bettis Atomic Laboratory, August, 1978.

Chalder, G. H. et. al., "U₃Si As a Nuclear Fuel," AECL-2874, May 29, 1967.

Chawla, R. et. al., "Analysis of PROTEUS Phase II Experiments in Support of Light Water High Conversion Reactor Design," Kerntechnik, Vol. 57, 1992, pp. 14-22.

Cheadle, B. A. "Operating Performance of CANDU Pressure Tubes," AECL-9939, April 1989.

Cheadle, B. A., C. E. Coleman, E. G. Price, V. K. Bajaj, and W. R. Clendening, "Advances in Fuel Channel Technology for CANDU Reactors," Paper presented at IAEA Technical Committee Meeting on Advances in Heavy Water Reactors, Toronto, June, 1993.

Chen, J. C., "A Correlation for Boiling Heat Transfer to Saturated Fluids in Convective Flow," ASME paper 63-HT-34, 1963.

Cerna, R., S. Ciperá, P. Hejzlar, B. Lidický, O. Ubra, and Z. Zuna, "Steam/Water Properties: Library of Computer Routines," Report Z-456A/1991, Czech Technical University, Department of Nuclear and Power Engineering, January 1991.

Cheung, F. B., and D. Y. Sohn, "Flow Development and Heat Transfer in a Reactor-Vessel Auxiliary Cooling System," Proceedings of the 9th International Heat Transfer Conference, Vol.4, 1990.

Cohen, K., HKF-109, Secret report by H. K. Fergusson Co., New York, 1950, cited in Miller, C. B., "Reflector Moderated Reactors", Nuclear Science and Engineering, Vol. 13, 1962, pp.301-305.

Collier, J. G., Convective Boiling and Condensation, McGraw Hill, 2nd edition, New York, 1981.

Croff, A. G., "A User's Manual for the ORIGEN2 Computer Code", Oak Ridge National Laboratory Rep., ORNL/TM-7175, 1980.

Croff, A. G., "Comparison of Experimentally Determined Spent Fuel Compositions with ORIGEN2 Calculations," ANS Trans., Vol. 39, 1981, pp. 215.

Croff, A. G., "ORIGEN2: A Versatile Computer Code for Calculating Nuclide Compositions and Characteristics of Nuclear Materials", Nuclear Technology, Vol. 62, No. 3, September 1983, pp.335-352.

Dahlberg, R. C., R. F. Turner, and W. V. Goeddel, "Fort Saint Vrain Nuclear Power Station – Core Design Characteristics," Nuclear Engineering International, Vol. 14, No. 163, December 1969, pp. 1073-1077.

Dastur A. R., and P. S. W. Chan, "The Role of Enriched Uranium in CANDU Power Plant Optimization," Paper presented at IAEA Technical Committee Meeting on Advances in Heavy Water Reactors, Toronto, June, 1993.

Dhir, V. K., and G. P. Purohit, "Subcooled Film-Boiling Heat Transfer from Spheres," Nuclear Eng. and Design, Vol. 47, No. 1, May 1978, pp. 49-66.

Diamond, D. J., "The Reactor Analysis Support Package (RASP), PWR Physics Analysis Guidelines," Vol. 5, Final Report, EPRI NP-4498, October 1986.

Dipprey, D. F., and R. H. Sabersky, "Heat and Momentum Transfer in Smooth and Rough Tubes at Various Prandtl Numbers," International Journal of Heat & Mass Transfer, Vol. 6, 1963, pp. 329-353.

Doroschuk, V. E., L. L. Levitan, and F. P. Lantzman, "Investigations into Burnout in Uniformly Heated Tubes," ASME Paper 75-WA/HT-22, 1976.

Driscoll, M. J., T. J. Downar, and E. E. Pilat, The Linear Reactivity Model for Nuclear Fuel Management, American Nuclear Society, La Grange Park, Illinois, 1990.

Dutton, R., “Advanced Fuel Channel Concepts,” Paper presented at IAEA Technical Committee Meeting on Advances in Heavy Water Reactors, Toronto, June, 1993.

Edlund, M. C., “High Conversion Ratio Plutonium Recycle in Pressurized Water Reactors”, Ann. Nucl. Energy, Vol.2, 1975, p. 80.

Edlund M. C., “Physics of Uranium-Plutonium Fuel Cycles in Pressurized Water Reactors”, Trans. Am. Nucl. Soc., Vol. 24, p. 508, 1976.

Elmaghrabi, M., and R. J. Klotz, “Low Density Moderation,” ANS Trans., Vol. 64, November 1991, pp. 355-356.

Emergency Core Cooling, Report of Advisory Task Force on Emergency Core Cooling, USAEC, 1967.

“ENDF-313, Benchmark Data Testing of ENDF/B data for Thermal Reactors,” BNL-NCS-29891, Brookhaven National Laboratory, July 1981.

Erbacher, F. J. and H. J. Neitzel, “Passive Containment Cooling by Natural Air Convection for Next Generation Light Water Reactors,” Proceedings of the Fifth International Topical Meeting on reactor Thermal Hydraulics, NURETH-5, Salt Lake City, 1992, Vol. 4, pp. 1235-1241.

Eto, M., and M. Shindo, “Development of Advanced Graphite Materials for Nuclear Facilities,” Int. Conf. on Design and Safety of Advanced Nuclear Power Plants, Tokyo, October, 1992, pp. P7.4-1 - P7.4-6.

Evans, W., P. A. Ross-Ross, J. E. LeSurf, and H. E. Thexton, “Metallurgical Properties of Zirconium-Alloy Pressure Tubes and Their Steel End-Fittings for CANDU reactors,” AECL-3982, September 1971, Also paper presented at the fourth U.N. International Conference on the Peaceful Uses of Atomic Energy, Geneva, September, 1971.

Federal Register, 10 CFR Part 50, Appendix A, Criterion 50-Containment Design Basis, January 1993.

Feinroth, H. "Feasibility Study on Use of Ceramic Cladding to Reduce the Severity of Reactor Accidents," Report for NRC, Gamma Eng. Corp. Rep. No. 8533-1, June 1990.

Forster, R. A., R. C. Little, J. F. Briesmeister, and J. S. Hendricks, "MCNP Capabilities for Nuclear Well Logging Calculations," IEEE Trans. Nucl. Sci., Vol. 37, No. 3, June 1990, pp. 1378.

Frisch, W., K. Liesch, and B. Riegel, "Identification of Improvements of Advanced Light Water Reactor Concepts," Commission of the European Communities, Final report, EUR 14296, 1993.

Fu, G., M. Gavrilas, P. Hejzlar, N. E. Todreas, and M.J.Driscoll, "Experimental and Analytical Evaluation of Gas-Cooled Reactor Cavity Cooling System Performance," Report MITNPI-TR-038, MIT, Department of Nuclear Engineering, December 1991, Revision 2, Also Journal of Heat Transfer, to be published in 1994.

Gardner, M. A., and R. J. Howerton, "ACTL: Evaluated Neutron Activation Cross-Section Library – Evaluation Techniques, and Reaction Index," Lawrence Livermore National Laboratory report UCRL-50400, Vol. 18, Part A, October 1978.

Gavrilas, M., P. Hejzlar, Y. Shatilla, and N.E.Todreas, Safety Features of Operating Light Water Reactors of Western Design, CRC Press, to be published 1994.

Gelbard, E. M., "Streaming in Lattices," in Advances in Nuclear Science and Technology, Eds. J. Lewis and M. Becker, Vol. 15, Plenum Press, New York, 1983, pp. 223-400.

Gendron, T. S. et. al., "Materials Irradiations in CANDU Fuel Bundles," AECL-10632, May 1992.

George, T. L., M. J. Thurgood, C. L. Wheeler, L. E. Wiles and S. W. Claybrook, "GOTHIC Containment Analysis Package," Technical Manual for EPRI, Version 3.4, July 1991, Numerical Applications, Inc.

Greenspan, E., "Fusion Reactors Blanket Nucleonics," Progress in Nuclear Energy, Vol. 17, 1986, pp. 53-139.

Griffith, P., Massachusetts Institute of Technology, Department of Mechanical Engineering, Personal Communication, January, 1993.

Groeneveld, D. C., "An Investigation of Heat Transfer in the Liquid Deficient Regime," AECL-3281 (Rev.), 1968, Rev. 1969.

Groeneveld, D. C., S. C. Cheng, and T. Doan, "1986 AECL-UO Critical Heat Flux Lookup Table," Heat Transfer Engineering, Vol. 7, no. 1-2, 1986.

Groeneveld, D. C., Chalk River Laboratory, Personal Communication, May, 1993.

Guentay, S., "Sensitivity Analysis of PWR and HTGR Fuel Cycle Cost," ANS Trans., Vol. 20, August 1975.

Gyftopoulos E. P., and G. P. Beretta, Thermodynamics Foundations and Applications, Macmillan Publishing Company, New York, 1991.

Haga, T., S. Hanazawa, and T. Kimura, "Critical Experiments on Light Water Lattices of UO₂ and Gd₂ O₃ Rods," Nucl. Sci. Eng., Vol. 69, No. 2, February 1979, pp. 231.

Haefele, W., "Prompt Überkritische Leistungsexkursionen in Schnellen Reaktoren," Nukleonik, Band 5, Heft 5, 1963.

Han, J. C., "Convective Heat Transfer Augmentation in Channels Using Repeated-Rib Roughness," Ph.D. Thesis, Massachusetts Institute of Technology, Department of Mechanical Engineering, February, 1970.

Han, J. C., M. J. Driscoll, and N. E. Todreas, "The Effective Thermal Conductivity of Prismatic Fuel," Massachusetts Institute of Technology,

Department of Nuclear Engineering, September 1989, (also in ANS Trans., Vol. 65, 1992, p. 280).

Hannerz, K., "The PIUS Principle and the SECURE Reactor Concepts," *Advances in Nuclear Science and Technology*, Vol. 19, 1987, pp. 41-108.

Harde R. and Stohr K. W., "A Sodium Cooled Power Reactor Experiment Employing Zirconium-Hydride Moderator," *Proceedings of the Third International Conference on Peaceful Uses of Atomic Energy*, Vol.6, Geneva, 31 August-September, 1964.

Hargroves, D. W. et. al., "CONTEMPT-LT/028 – A Computer Program for Predicting Containment Pressure-Temperature Response to a Loss-of-Coolant Accident." NUREG/CR-0255, TREE-1279, Idaho National Engineering Laboratory, Idaho Falls, ID, March, 1979.

Harrison, J. F., D. M. Butcheit, W. C. Beck, and H. D. Fulcher, "The Reactor Analysis Support Package (RASP), Volume 3:PWR Event Analysis Guidelines," NP-4498, Volume 3, Final report prepared for EPRI, May, 1986.

Hart, R. S., Atomic Energy of Canada Limited, Personal communication, December 1991.

Heck, R., W.Heinrich, V. Scholten, "Igniters and Recombiners for Hydrogen Reduction Following Severe Accidents," Siemens Service Report, September, 1991.

Heineman, J., M. Kraimer, P. Lottes, D. Pedersen, R. Stewart and J. Tessier, "Experimental and Analytical Studies of a Passive Shutdown Heat Removal System for Advanced LMRs," *Proceedings of International Topical Meeting on Safety of Next Generation Power Reactors*, Seattle, May, 1991.

Hejzlar, P., N. E. Todreas, M. J. Driscoll, "Passive Decay Heat Removal in Advanced Reactor Concepts," Massachusetts Institute of Technology, Department of Nuclear Engineering Report MIT-ANP-TR-003, May, 1991.

Hejzlar, P., N. E. Todreas, M. J. Driscoll, "Passive Decay Heat Removal in Advanced LWR Concepts," Nucl. Eng. Des. Vol. 139, No.1 January 1993a, pp. 59-81.

Hejzlar, P., "Passive Decay Heat Removal Options for the HTR Prestressed Cast Iron Vessel", in M. Geiss, W. Haefner, P. Hejzlar, A. Kneer, R. Schultz, and L. Wolf, "Experimentelle und Analytische Arbeiten zur Absicherung von Druckbehaltereinheit und Primaerzelle des HTR-Modul," Report BF-R 40056-03, April, 1993b

Hejzlar, P., N. E. Todreas, M. J. Driscoll, "Evaluation of Materials for the Fuel Matrix of a Passive Pressure Tube LWR Concept," Report MIT-ANP-TR-017, Massachusetts Institute of Technology, Department of Nuclear Engineering, December 1993c.

Hejzlar, P. , N. E. Todreas, and M. J. Driscoll, "Special Computer Codes and Supplementary Data for the Conceptual Design of a Large, Passive, Pressure-tube LWR," MIT-ANP-TR-021, Massachusetts Institute of Technology, Department of Nuclear Engineering, May 1994.

Henry, A. F., Nuclear-Reactor Analysis, The MIT Press, Cambridge, Massachusetts, 1986.

Hetsroni, G., Handbook of Multiphase Systems, Chapter 6, McGraw-Hill, New York, 1982.

Hirata, K., M. Negishi, C. Matsumoto, Y. Kinoshita, T. Nogaito, S. Shimoda, and C. L. Caso, "Advanced Pressurized water Reactor Plant," Nuclear Europe, Vol. 11, No. 12, 1989, pp. 22-23.

Hohorst, J. K., Ed., "SCDAP/RELAP5/MOD2 Code Manual, Volume 4: MATPRO – A Library of Materials Properties for Light-Water-Reactor Accident Analysis," NUREG/CR-5273, Vol. 4, February, 1990.

Howerton, R. J., D. E. Cullen, R. C. Height, M. H. MacGregor, S. T. Perkins, and E. F. Plechaty, "The LLL Evaluated Nuclear Data Library (ENDL): Evaluation Techniques, Reaction Index, and Descriptions of

Individual Reactions,” Lawrence Livermore National Laboratory Report UCRL-50400, Vol. 15, Part A, September 1975.

Hrovat, M., L. Rachor and H. Huschka, “Fabrication and Properties of Molded Block Fuel Elements for HTGR’s,” Nuclear Energy Maturity, Proceedings of the European Nuclear Conference, Paris, 1975, pp. 90-97.

Hrovat, M., “Development of High Power Block Fuel Elements for High Temperature Reactors,” Final report NUKEM-376, April 1978.

Hulovec, J. et. al., “Problems of Development and Construction of the First Czechoslovakia Nuclear Power Station,” Proceedings of the Third International Conference on Peaceful Uses of Atomic Energy, Vol.5, Geneva, 31 August-September, 1964 pp. 371-384.

Hwang, J. T. “Proof-of-Principle Studies of a Passive Water Cooled Containment Concept”, Ph.D. thesis, MIT, Department of Nuclear Engineering, to be published August, 1994.

“**HYDRO** seeks restart of Pickering 1 and 2,” Nuclear Engineering International, March 1984, pp. 5-6.

IAEA, “Reactivity Accidents,” Technical Reports Series, No. 354, International Atomic Energy Agency, Vienna, 1993.

Idel'chik, I. E., Handbook of Hydraulic Resistance, Hemisphere Pub., 2nd ed., 1986.

Inasaka, F., and H. Nariai, “Evaluation of Subcooled Critical Heat Flux Correlations for Tubes with and without Internal Twisted Tapes,” Proceedings of the Fifth International Topical Meeting on Reactor Thermal Hydraulics, NURETH-5, Salt Lake City, 1992, Vol. 3, pp. 919-928.

Irvin, T. F., Steam and Gas Tables with Computer Equations, Academic Press, New York, 1984.

Ishii, M., “Thermally Induced Flow Instabilities in Two-Phase Mixtures in Thermal Equilibrium,” PhD Thesis, School of Mechanical Engineering,

Georgia Institute of Technology, Atlanta, GA, June, 1971 (also cited in Saha et. al., 1976).

Ivey, H. J., and D. J. Morris, "On the Relevance of the Vapor-Liquid Exchange Mechanism for Subcooled Boiling Heat Transfer at High Pressure, AEEW-R137, 1962, (cited in Whalley, 1987, p.143).

Jackson, J. L., "The Effect of Oxidation, Thermal Cycling, and Irradiation on Silicon Carbide (SiC) Coated Graphite, USAEC Report BNWL-242, Pacific Northwest Laboratory, August, 1966. (Also cited in Baker, 1970).

Jens, W. H., and P. A. Lottes, "Analysis of Heat Transfer, Burnout, Pressure Drop and Density Data for High Pressure Water," ANL-4627, 1951 (also cited in Collier, 1981).

Kakac, S., R. K. Shah, and W. Aung, Handbook of Single-Phase Convective Heat Transfer, John Wiley&Sons, New York, 1987.

Kalinin, E.K., G. A. Dreytser, S. G. Zakirov, A. A. Vakhobov, K. Sh. Akzamov, Ye. S. Levin, "Improvement of Heat Transfer in Tubular Heat Exchangers by the Use of Grooved Tubes," Heat Transfer–Soviet Research, Vol. 13, No.4, July-August, 1981.

Kasten, P. R., Short Course on "Very High Temperature Gas-Cooled Reactors: Their Potential Applications and Markets," The University of Tennessee-Knoxville, Nuclear Engineering Department, August, 1990.

Kataoka, I., M. Ishii, and K. Michima, "Generation and Size Distribution of Droplets in Gas-Liquid Annular Two-Phase Flow," ANL/RAS/LWR 81-3, 1981.

Katto, Y., "Critical Heat Flux," in Advances in Heat Transfer, Eds. J. P. Harnett and T. F. Irvine, Jr., Vol. 17, Academic Press, New York, 1985.

Kennedy, P., and J. V. Shennan, "REFEL Silicon Carbide, The Development of a Ceramic for a Nuclear Engineering Application", TRG report 2627(S), Reactor Fuel Element Laboratories UKAEA, October 1974.

Kern, R., M. Bonaca, R. Rosztoczy, W. C. Copper-Smith, "Xenon Oscillation Studies for the Pickering Reactor," USAEC Report CEND-3932-2, Combustion Engineering, 1969.

Kinsey, R., Ed., "ENDF/B Summary Documentation ," BNL-NCS-17541 (ENDF-201), 3rd ed. (ENDF/B-V), Brookhaven National Laboratory, 1979, Revised 1980.

Knief, R. A., Nuclear Engineering, Theory and Technology of Commercial Nuclear Power, Hemisphere Publishing Corporation, Washington, 1992.

Koehler, W. K., "The Effect of Short Delay Times in Super-Prompt-Critical Excursions of Fast Reactors," ANS Trans., Vol.12, November, 1969.

Kraft, P., "The Lucens Experimental Nuclear Power Station," Proceedings of the Third International Conference on Peaceful Uses of Atomic Energy, Vol.5, Geneva, 31 August-September, 1964 pp. 431-439.

Kuehn, T. H., and R. J. Goldstein, "Correlating Equations for Natural Convection Heat Transfer Between Horizontal Circular Cylinders," International Journal of Heat & Mass Transfer, Vol. 19, No. 10, October 1976, pp. 1127-1134.

Kugeler, K., "Design Options for Future Advanced HTR," Int. Conf. on Design and Safety of Advanced Nuclear Power Plants, Tokyo, October, 1992, pp. 7.3-1 - 7.3-8.

Lee, M., and L. Y. Liao, "An Assessment of the Critical Heat Flux Approaches of Thermal-Hydraulic System Analysis Codes Using Bundle Data From the Heat Transfer Research Facility," Nuclear Technology, Vol. 105, February, 1994.

Lefevre, R. L. R. and M.S. T. Price, "Coated Nuclear Fuel Particles: The Coating Process and Its Model," Nuclear Technology, Vol. 35, No.2, September 1977, pp. 263-278.

Lellouche, G. S., "Reactor Size Sufficient for Stability Against Spatial Xe Oscillations", Nucl. Sci. Eng., Vol. 13, No. 1, May 1962, pp.60-61.

Lichtenstein, H., M. Cohen, H. Steinberg, E. Troubetzkoy, and M. Beer, "The SAM-CE Monte Carlo System for Radiation Transport and Criticality Calculations in Complex Configurations," EPRI-CCM-8, Electric Power Research Institute, June, 1979.

Little, R. C., and R. E. Seamon, "Comparing Fission Product Cross Sections," Los Alamos National Laboratory Internal Memorandum, X-6:RCL/RES-85-404 to M.G. Henderson, August, 1985.

Madhusudana, C. V., "Thermal Contact Conductance and Rectification at Low Joint Pressures," Int. Comm. Heat Mass Transfer, Vol., 20, No. 1, January-February 1993, pp. 123-132.

Mamourian, M., and P. Akhtar, "Analysis of Xenon-Induced Power Oscillations with λ -Modes," AECL-6185, April 1978.

Manaranche, J. C., D. Mangin, L. Maubert, G. Colomb, and G. Poullot, "Critical Experiments with Lattices of 4.75-wt%-²³⁵U-Enriched UO₂ Rods in Water," Nucl. Sci. Eng., Vol. 71, No. 2, August 1979, pp. 154.

Markl, H., and H. Moldaschl, "Development of a High Conversion Reactor in Swiss-German Cooperation," Kerntechnik, Vol. 57, 1992, pp. 7-13.

Marston, T. U., W. H. Layman, and G. Bockhold, Jr., "Utility Requirements for Safety in the Passive Advanced Light-Water Reactor," Nuclear Safety, Vol. 34, No.1, January-March 1993.

Matzie, R. A., J. Longo, R. B. Bradbury, K. R. Teare, and M. R. Hayns, "Design of the Safe Integral Reactor," Nuclear Engineering and Design, Vol. 136, 1992, pp. 73-83.

McCandless, R. J., and J. R. Redding, "Simplicity: The Key to Improved Safety, Performance and Economics," Nuclear Engineering International, Vol. 34, No. 424, November, 1989.

McCaughey, G. H., and G. H. Bidinger, "Film Effects of Fire Sprinklers on Low-Enriched-Uranium Storage Systems," ANS Trans., Vol. 56, June 1988, p.329.

McFaden, J. H. et. al., "RETRAN-02--A Program for Transient Thermal-Hydraulic Analysis of Complex Fluid Flow Systems," EPRI NP-1850-CCMA, Vol.1, Revision 2, 1984.

Melese, G. and R.Katz, Thermal and Flow Design of Helium-Cooled Reactors, American Nuclear Society, LaGrange Park, Illinois, 1984.

Menaker, B. J., R. E. Allen, and H. E. Painter, "Passive Containment Cooling for an Advanced Small Pressurized Water Reactor," Nuclear Technology, Vol. 91, No.1 , July 1990, pp. 75-80.

Meyer, P., "German Design Features and Safety Goals for the Next Generation of PWRs," IAEA Technical Committee Meeting to Review Safety Features of New Reactor Designs, Vienna, November 11-15, 1991.

Mendelson, M. R., "Monte Carlo Criticality Calculations for Thermal Reactors," Nucl. Sci. Eng., Vol. 32, No. 3, June 1968, pp. 319.

Mochida, T. et. al., "Effective Utilization of Uranium and MOX in Light Water Reactors," International Conference on Design and Safety of Advanced Nuclear power Plants, Tokyo, October, 1992, Vol. 3, pp. 19.2-1 - 19.2-9.

Murata, K. K., D. E. Carroll, K. E. Washington, F. Gelbard, G. D. Valdez, D. C. Williams, and K.D. Bergeron, "User's Manual for CONTAIN 1.1, A Computer Code for Severe Nuclear Reactor Accident Containment Analysis," NUREG/CR-5026, SAND87-2309, Revision 1.11, November 1989, Revised July 1990.

Muzumdar, A. P., and G. M. Frescura, "Consequences of Pressure/Calandria Tube Failure in a CANDU Reactor Core During Full-Power Operation," 8th CNS Conference, Saint John, New Brunswick, June 1987 (also cited in Snell et. al. , 1988, p.6).

Nightingale, R. E., Nuclear Graphite, Academic Press, New York, 1962.

Nikuradse, J., "Laws for flow in Rough Pipes", NACA TM 1292, 1952.

Novak, J., "Thermal Switch Concepts for Reactor Designs", Master Thesis, to be published in August, 1994, Massachusetts Institute of Technology, Department of Nuclear Engineering.

Nuclear News, "JAERI Has Developed High-burnup Plutonium Fuel for PWRs", Vol. 36, No. 12, September, 1993.

Nyer, W. E., "Mathematical Models of Fast Transients, " in Technology of Nuclear Reactors, MIT Press, 1964.

Oka, Y., et. al., "Conceptual Design and Development of Simplified LWRs in Japan," IAEA Technical Committee Meeting on Progress in Development and Design Aspects of Advanced Water-Cooled Reactors, Rome, Italy, September 1991.

Owens, C. G., "Passive Decay-Heat Removal Approaches for Light Water Reactors," S.M. Thesis, Massachusetts Institute of Technology, Department of Nuclear Engineering, February 1990.

Pasanen, A. A., "Fundamentals of CANDU Reactor Nuclear Design," A Lecture Series, TDAI-244, Trieste, January-March, 1980.

Pernica, R. and J. Cizek, "Critical Heat Flux Correlations for Rod Bundles," International Topical Meeting on Safety of Thermal Reactors, Portland, 1991.

Petrie, L. M., and N. F. Landers, "KENO V.a: An Improved Monte Carlo Criticality Program with Supergrouping," SCALE: A Modular Code System for Performing Standardized Computer Analyses for Licensing Evaluation," Vol. II, Sec. F11, NUREG/CR-0200, Rev. 4 , December, 1984.

Pilat, E. E., Lecture on Fuel Cycle Cost Estimate, presented at the Reactor Technology Program for Utility Executives, MIT, Cambridge, Massachusetts, June 1993

Price, E. G., "Highlights of the Metallurgical Behavior of CANDU Pressure Tubes," AECL-8338, October 1984.

Randall, D., and D. S. St. John, "Xenon Spatial Oscillations", *Nucleonics*, Vol. 16, No. 3, March 1958, p. 84.

Rastas, A., and C. Sundqvist, "Advanced Light Water Reactors: A Finnish-Swedish Proposal," Paper presented at European Nuclear Conference, Lyon, France, 1990.

Robertson, R. F. S., and Hart, R. G. "CANDU-OCR: Present Status and Future Potential," AECL-3924, 1972.

Rohsenow, W. M., "A Method of Correlating Heat Transfer Data for Surface Boiling Liquids," *Trans. ASME*, Vol. 74, 1952, pp. 969.

Rohsenow, Handbook of Heat Transfer, Mc Graw Hill, N.Y., 1973, pp. 13-28.

Ronen, Y., High Converting Water Reactors, CRC Press, Inc., Boca Raton, 1990.

Roshd, M. H. M, P. M. French, and R. T. Jones, "Nuclear Fuel Bundle Design with Reduced Void Effect," *ANS Trans.*, Vol. 26, 1977, pp. 603-604.

Rosner, D. E., Transport Processes in Chemically Reacting Flow Systems, Butterworths, Boston 1986.

Ross-Ross, P. A., "Fuel Channel Development for CANADA's Power Reactors," AECL-3126, May 1968.

Saha, P., M. Ishii and N. Zuber, "An Experimental Investigation of the Thermally Induced Flow Oscillations in Two-Phase Systems," *Journal of Heat Transfer*, November, 1976, pp. 616-622.

Schulten, R., "The HTR with SiC-technology," *Nuclear Engineering and Design*, Vol. 140, No. 2, May 1993, pp. 261-267.

Schleicher, R. W., and J. D. Wistrom, "Small Reactors Utilizing High Temperature Capability of Coated Particle Fuel," in Potential of Small Nuclear Reactors for Future Clean and Safe Energy Sources, Ed. H. Sekimoto, Elsevier Science Publishers, Amsterdam, 1992, p. 305.

Schmittroth, F., G. J. Neeley, and J. C. Krogness, "A Comparison of Measured and Calculated Decay Heat for Spent Fuel Near 2.5 Years Cooling Time," HEDL-7202, Hanford Engineering Development Laboratory, 1980.

Shah, M. M., "Improved General Correlation for Critical Heat Flux During Upflow in Uniformly Heated Vertical Tubes," Int. Journal of Heat and Fluid Flow, Vol.8, No. 4, December 1987.

Shapiro, N.L., and J. F. Jesick, "Conceptual Design of a Large Heavy Water Reactor for U.S. Siting," Combustion Engineering Rep., CEND-379, Vol. III, 1979.

Shewfelt, R. S. W., Failure Maps for Internally Pressurized Zr-2.5% Nb Pressure Tubes with Circumferential Temperature Variations," AECL-8399, January, 1986.

Shumway, R. "New Critical Heat Flux Method for RELAP5//MOD3: Completion Report," EGG-EAST-8443, EG&G, Idaho Falls, January 1989.

Simnad, M. T., University of California, San Diego, Center for Energy&Combustion Research, Personal Communication, April, 1992.

Sitamaran, S., Rahnema, F., "Criticality Analysis of Heterogeneous Light Water Reactor Configurations", Nuclear Science and Engineering, Vol. 113, No. 4, April 1993, pp. 239-250.

Slember, R. J., "From the Bottom up: Nuclear Technology Evolves for the Future, Part 1—the Advanced Passive Reactor," Trans. Am. Nucl. Soc., Vol. 61, 1990, p.253.

Smith, C. O., Nuclear Reactor Materials, Addison-Wesley Publishing Company, 1967.

Snell, V. G., S. Alikhan, G. M. Frescura, J. Q. Howieson, F. King, J. T. Rogers, and H. Tamm, "CANDU Safety under Severe Accidents," AECL 9606, 1988.

Sohn D.Y., and F. B. Cheung, "Turbulent Heat Transfer in the Developing and Fully Developed Regions of a Vertical Channel," National Heat Transfer Conference, No. 283, Vol. 87, Minneapolis, 1991, p. 336.

Spinks, N. J., Atomic Energy of Canada Limited, Personal Communication, December 1991.

Stacey, W. M. et. al., "U.S. Contribution to the International Tokamak Reactor Phase-2A Workshop," USA FED-INTOR/82-1, Vol. I, October 1982.

Stamatelatos, M. G., "Rational Approximations for Cross-Section Space-Shielding in Doubly Heterogeneous Systems," Nucl. Sci. Eng., Vol. 61, No. 4 December 1976, pp. 543-545.

Stamatelatos, M. G., and R. J. LaBauve, "Fine-Energy Cross-Section Space Shielding for Doubly Heterogeneous Reactor Cores," ANS Trans., Vol. 30, November 1978, pp. 716-717.

Starr, C., and R. W. Dickinson, Sodium Graphite Reactors, Addison Wesley, 1958.

Subbotin, V., "Safety Principles for Nuclear Power Installations Safety," Energy, Vol. 18, No. 10, pp. 1018-1019.

Taitel, Y., and A. E. Dukler, "A Model for Predicting Flow Regime Transitions in Horizontal and Near Horizontal Gas-Liquid Flow," AIChE J., Vol. 22, No. 1, 1976, pp. 47-55.

Tang, J. R., "A Light Water Cooled and Moderated Pressure Tube Reactor Concept with Passive Decay Heat Removal," Ph.D. Thesis, Department of Nuclear Engineering, Massachusetts Institute of Technology, May, 1992.

Tang, J. R., N. E. Todreas, and M. J. Driscoll, "Conceptual Design features for a Passive Light Water Cooled and Moderated Pressure Tube Reactor (PLPTR)", Int. Conf. on Design and Safety of Advanced Nuclear Power Plants, Tokyo, October, 1992, Vol. I, pp.4.2-1 – 4.2-8 (also to be published in Nuclear Technology, July 1994).

Taylor, E. L., and M. J. Driscoll, "A Comparative Analysis of IFR Fuel Cycle Economics," Report MITNPI-TR-009, Massachusetts Institute of Technology, Department of Nuclear Engineering, Cambridge, 1987.

Thom, J. R. S., et. al., "Boiling in Subcooled Water during Flow in Tubes and Annuli," Proc. Inst. Mech. Eng., Vol. 180, 1966, pp. 226.

Tipton, T. J., Ed., The Reactor Handbook, Vol. I, Hemisphere Publishers, New York, 1960.

To W. M., and J. A. C. Humphrey, " Numerical Simulation of Buoyant, Turbulent Flow – 1. Free Convection along a Heated Vertical Flat Plate," International Journal of Heat & Mass Transfer, Vol.29, No. 4, April 1986, pp. 573-592.

Todreas, N. E., and M. Kazimi, Nuclear Systems I, Hemisphere Publishing Corp. New York, 1990.

Tong, L. S., Heat Transfer and Two-Phase Flow, John Wiley and Sons, New York, 1965.

Tong, L. S. , "Prediction of Departure from Nucleate Boiling for an Axially Non-Uniform Heat Flux Distribution," Journal of Nuclear Energy, Vol. 21, No. 3, March 1967, pp. 241-248.

Tong, L. S., "Boiling Crisis and Critical Heat Flux," USAEC Critical Review Series, Report TID-25887, 1972 .

Tong, L. S. and J. Weisman, Thermal Analysis of Pressurized Water Reactors, American Nuclear Society, LaGrange Park, Illinois, 1979.

Tong, L. S., Gaithersburg, Maryland, Personal Communication, April 1993.

Touloukian, Y. S., "Thermophysical Properties of High Temperature Solid Materials, Volume 3, Ferrous Alloys," Purdue University, 1967.

Tower, S. N., T. L. Schultz, and R. P. Vijuk, "Passive and Simplified System Features for the Advanced Westinghouse 600 MWe PWR," Nuclear Engineering and Design, Vol. 109, 1988, pp.147-154.

Tulenko, J. S., "An Innovative Fuel Design Concept for Improved Light Water Reactor Performance and Safety", paper presented at the DOE Nuclear Engineering Education Research Grant Program, Annual Review Meeting, February, 1993.

Turk, R. S., and R. A. Matzie, "System 80+™: PWR Technology Takes a Major Step up the Evolutionary Ladder," Nuclear Engineering International, Vol. 37, No. 460, November 1992, pp. 15-22.

Turricchia, A., "LIRA: An Advanced Containment System to Minimize the Accidental Radioactivity Release," Nuclear Safety, Vol. 34, January-March, 1993

Tzanos, C. P., and A.Hunsbedt, "Predictions of Wind Effects on RVACS Performance," Trans. ANS, Vol., 69, November, 1993, pp. 265-267.

Uchida, H., A. Oyama, and Y.Togo, "Evaluation of Post Accident Cooling Systems of LWRs," Proceedings of the Third Int. Conference on Peaceful Uses of Atomic Energy, Vol. 13, P/436, United Nations, New York, 1965.

USNRC, U.S.Nuclear Regulatory Commission, "Standard Review Plan for the Review of Safety Analysis Reports for Nuclear Power Plants," LWR Edition, NUREG-0800, June 1987.

Veeder, J., and R. Didsbury, "A Catalogue of Advanced Fuel Cycles in CANDU-PHW Reactors", AECL-8641, June 1985.

Vignon, D., and D. Schneider, "NPI's New Reactor Takes a Further Step along the Evolutionary Road," Nuclear Engineering International, Vol. 37, No. 453, April 1992, pp. 16-20.

von Hippel, F., and H. Feiveson, "Disposition Options for Separated Plutonium," Trans. ANS, Vol.69, November 1993, p.89.

Voznessensky, V., I. Kuhtevitsh, and M. Rogov, "Advanced NPP VVER-500 with Passive Safety Systems," Int. Conf. on Design and Safety of Advanced Nuclear Power Plants, Tokyo, October, 1992, Vol. I, pp.4.4-1 – 4.4.7.

Walroth, C. F., F. McCord, R. J. Meyerm and J. J. Saurwein, "Post-irradiation Examination and Evaluation of Peach Bottom Molded Fuel Test Element FTE-18," GA-A13699, June 1976.

Wakabayashi, H., "ISER: An International Inherently Safe Reactor Concept," Nuclear Engineering International, June, 1988, pp. 45-46.

Walti, P., "Evaluation of Grain Shielding Factors for Coated Fuel Particles," Nucl. Sci. Eng., Vol. 45, No. 3, September 1971, pp.321-330.

Walti, P., and P. Koch, "MICROX, A Two-Region Flux Spectrum Code for the Efficient Calculation of Group Cross Sections," Gulf-GA-A10827, Gulf General Atomic, 1972.

Watanabe, Y., and E. T. Dugan, "Axial Reflector Correction for One-Dimensional Criticality Analysis of NVTR," Trans. ANS, Vol. 68, part A, June 1993, pp. 484-485.

Wemple, S. N., and S. N. Jashan, "Tracking the Energy Deposition Processes in a Reactor using MCNP," ANS Trans., Vol. 64, November 1991, pp. 574-575.

Whalen, D. J., D. E. Hollowell, and J. S. Hendricks, "MCNP: Photon Benchmark Problems," LA-12196, Los Alamos National Laboratory, September 1991.

Whalen, D.J., D. A. Cardon, J. L. Uhle, and J. S. Hendricks, "MCNP: Neutron Benchmark Problems," LA-12212, Los Alamos National Laboratory, November 1991.

Whalley, P. B., Boiling Condensation and Gas-Liquid Flow, Clarendon Press, Oxford, 1987.

Wilkins, D. R., R. C. Berglund, S. A. Hucik, and R. J. McCandless, "GE Advanced Boiling Water Reactors for the 1990's and Beyond," Int. Conf. on

Design and Safety of Advanced Nuclear Power Plants, Tokyo, October, 1992, Vol. I, pp.9.1-1 – 9.1.7.

Williams, D. C., J. J. Gregory, S. R. Tieszen and J. L. Tills, "Containment Loads Scoping Calculations for Severe Nuclear Reactor Accidents," SAND92-2774, February, 1993.

Williamson, M., and A. Majumdar, "Effect of Surface Deformations on Contact Conductance," Journal of Heat Transfer, Vol.114, November 1992, pp. 802-810.

Wind, F., "Versuchgruppe CONT-DAMPF Versuchs V44," PHDR Report No. 3.333, Kernforschungszentrum Karlsruhe, FRG, 1983

Wolf, L., "Experimental Tests of Safety Systems and Components HDR-Safety Program," presented at MIT Nuclear Power Safety Course, Cambridge, MA, July, 1993.

Wolf, L., H.Holzbauer, and M. Schall, "Comparison between Multi-dimensional and Lumped-parameter GOTHIC-Containment Analyses with Data," International Conference on New Trends in Reactor Thermohydraulics, Pisa, Italy, May, 1994.

Yiftah, S., and D. Okrent, "Some Physics Calculations on the Performance of Large Fast Breeder Power Reactors," USAEC Report ANL-6212, December, 1960.

Zuber, N., and M. Tribus, "Further Remarks on the Stability of Boiling Heat Transfer," Report 58-5, Univ. of California, Los Angeles, 1958 (also cited in Whalley, 1987).

Zukauskas, A. A., and J. J. Ziugzda, "Enhancement of Convective Heat Transfer," in O. G. Martynenko and A. A. Zukauskas, Eds., Heat Transfer - Soviet Reviews, Volume 1, Convective Heat Transfer, Hemisphere , New York, 1989.

Appendix A

REACTOR PHYSICS

A.1 BENCHMARK OF MCNP ON PWR AND CANDU LATTICES

The brief review of the MCNP code, in Section 4.3, showed that the code underwent an extensive validation and verification program, and that it can generate very accurate results. In order to gain experience with MCNP modeling and to verify the correctness of MCNP models on cells resembling those of interest, two benchmark models have been constructed. They include a fuel channel model of a typical CANDU reactor and a PWR fuel pin model, both in infinite lattice configuration. These benchmarks were developed together with J. Tang and are described in [Tang, 1992]. The comparison of the MCNP results with data showed very good agreement for both cases.

A.2 BENCHMARK OF MCNP+ORIGEN2 TANDEM AGAINST PWR BURNUP CURVE

Section 4.4.7 described the approach of combining MCNP and ORIGEN2 to evaluate the change of reactivity and fuel composition with burnup. It is necessary to test if this approach can yield sufficiently accurate results. Such a benchmark test is the purpose of this appendix section.

The benchmark test will be performed on the PWR cell with 1 fuel pin (from a 14x14 assembly of the Yankee nuclear power plant) which had been calculated using the LEOPARD depletion code. The cell is the same as that described in [Tang, 1992]. The ORIGEN2 code was used to burn PWR fuel with 3% initial enrichment using its effective one-group cross section library for PWRs with Pu-U fuel cycle. The concentration of major actinides and fission products versus burnup was produced. The actinides

included ^{234}U , ^{235}U , ^{236}U , ^{237}U , ^{238}U , ^{239}U , ^{237}Np , ^{238}Pu , ^{239}Pu , ^{240}Pu , ^{241}Pu , ^{242}Pu , ^{243}Pu , ^{241}Am , ^{242}Am , ^{243}Am , and ^{242}Cm .

Regarding the fission products, ^{135}Xe was treated separately; all other fission products were lumped into one group for use in MCNP. There are several fission product libraries available in MCNP. They include two sets for average fission product evaluated at the Lawrence Livermore National Laboratory (LLNL) and two sets evaluated at the Los Alamos National Laboratory (LANL) – average prompt fission product from ^{235}U fission and average prompt fission product from ^{239}Pu fission. The two LLNL evaluations yield close results, and the two LANL cases also yield close results. There are, however, significant differences between the LLNL and LANL sets, with the LANL sets having more neutrons in the system than with the LLNL sets [Little and Seamon, 1985]. Both LANL and LLNL average fission product libraries were run and the results compared to the LEOPARD benchmark. The LLNL-evaluated library ENDL-85 was found to give better agreement with LEOPARD results. Hence the Livermore new average fission product library, ENDL-85 was selected to model lumped fission products.

The results are presented in Figure A-1. The points denoted “MCNP+ORIGEN2” were calculated by the MCNP code using the fuel composition obtained by ORIGEN2 as MCNP input data. The agreement is surprisingly good. Therefore it is concluded that the suggested approach of combining MCNP and ORIGEN2 can produce a reasonably good burnup curve.

As has been earlier noted, there is now a combined package of these two codes, developed at Idaho National Engineering Laboratory, for this very purpose. It is recommended that this package be obtained for future use at MIT.

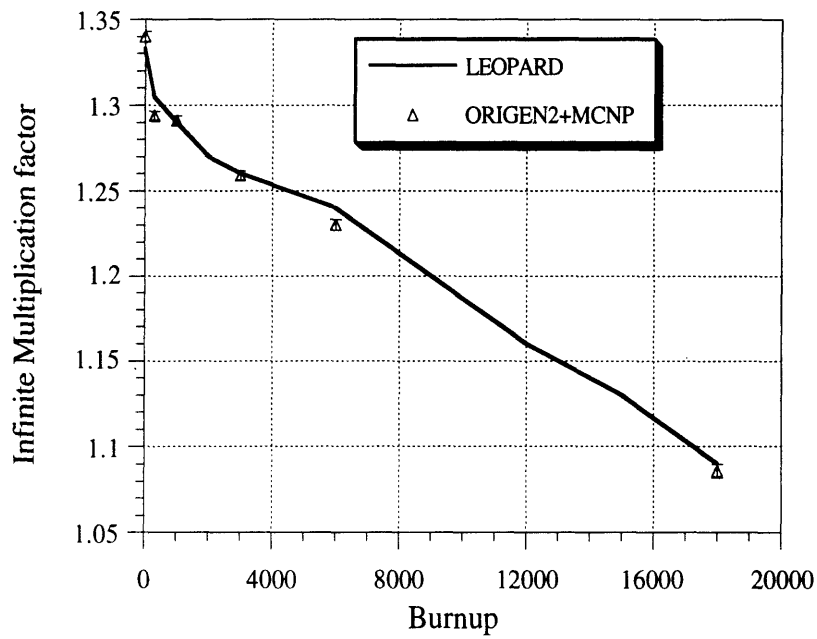


Figure A-1 Comparison of infinite multiplication factor calculated by MCNP+ORIGEN2 with LEOPARD results

Appendix B

CRITICAL HEAT FLUX CORRELATIONS

This Appendix complements Section 6.4.6 on critical heat flux analysis. Several CHF correlations for potential use in obtaining the CHF margins for the PTLWR coolant channels have been identified. These correlations are reviewed in Section B.1. Section B.2 discusses two alternative methods for calculating CHF margins in the low-quality region, and Section B.3 compares individual correlations in the range of parameters applicable to the PTLWR channels.

B.1 REVIEW OF CONSIDERED CHF CORRELATIONS

Six CHF correlations have been considered for calculating the critical heat flux in the PTLWR coolant channels. They comprise the W-3 correlation [Tong, 1972], the PI-1 correlation [Pernica and Cizek, 1991], the Bowring correlation [Bowring, 1972], the Shah correlation [Shah, 1987], the AECL look up tables [Groeneveld et. al., 1986], and the Katto correlation [Katto, 1985].

B.1.1 W-3 Correlation.

The W-3 correlation [Tong, 1972] is one of the most widely used CHF correlations. It can be applied to circular, rectangular, and rod-bundle geometries. The W-3 correlation was used in the form given in [Todreas and Kazimi, 1990],

$$q''_{CHF} = \{ (2.022 - 0.06238p) + (0.1722 - 0.001427p) \exp[(18.177 - 0.5987p) x] \} [(0.1484 - 1.596x + 0.1729 x |x|) 2.326 G + 3271] [1.157 - 0.869 x] [0.2664 + 0.8357 \exp(-124.1D_h) / (0.8258 + 0.0003413 (h_f - h_{in}))] \quad (B-1)$$

where q''_{CHF} is in kW/m², p is in MPa, G is in kg/m²-s, h is in kJ/kg, and D_h is in meters.

The CHF calculated from Eq. (B-1) was further corrected for partially heated channels (in channel #3, only part of the wetted perimeter is heated) by the relation

$$q''_{CHF,h} = q''_{CHF} \left\{ 1 - Ru \left[13.76 - 1.372 \exp(1.78x) - 4.732 (G/10^6)^{-0.0535} - 0.0619 (p/10^3)^{0.14} - 8.509 D_h^{0.107} \right] \right\} \quad (B-2)$$

where

$$Ru = 1 - D_e/D_h \quad (B-3)$$

Eq. (B-2) is in English units (p in psia., G in lb/hr-ft², D_h in inches).

To account for heat flux peaking, the CHF from equation (B-2) was corrected by an F factor, i.e.,

$$q''_{CHF,n} = q''_{CHF,h}/F \quad (B-4)$$

where

$$F = \frac{C \int_{z_0}^z q''(z') \exp[-C(z-z')] dz'}{q''(z) \{1 - \exp[-C(z-z_0)]\}} \quad , \text{and} \quad (B-5)$$

$$C = \frac{4.23 \times 10^6 [1 - x(z)]^{7.9}}{G^{1.72}} \text{ m}^{-1} \quad (B-6)$$

The coordinate z_0 represents the onset of nucleate boiling given by the Jens-Lottes correlation. The integration of the denominator in Eq. (B-5) can be performed using constant heat flux over the node yielding for node J (node representing the investigated location)

$$F = \frac{\exp(-C z_J) \sum_{j=j_s+1}^J q''(z_j) [\exp(C z_j) - \exp(C z_{j-1})]}{q''(z_J) \{1 - \exp[-C(z_j - z_{j_s})]\}} \quad (B-7)$$

where j_s is the number corresponding to coordinate z_0 , which denotes the node number where subcooled boiling according to Jens Lottes is initiated.

B.1.2 Pernica and Cizek Correlation (PI-1).

Recently, Pernica presented two new empirical CHF correlations having a wide range of validity [Pernica and Cizek, 1991], and compared them with 5300 sets of experimental data. The PI-1 correlation is given as

$$q''_{CHF} = 0.69 f(p_r, G) f(p_r) f(p_r, x_{in}) f(z/D_h) \left[\frac{1 + 2p_r - x}{2 + x} \right]^{k_2} T^{-0.8} \quad (B-8)$$

where

$$f(p_r, G) = (1 + 0.001 G p_r)^{0.8}, \quad (B-9)$$

$$f(p_r, x_{in}) = 1.4 - p_r - x_{in}, \quad (B-10)$$

$$f(z/D_h) = (1 + 0.005 z/D_h)^{-1}, \quad (B-11)$$

$$f(p_r) = \left(\frac{2.35 - p_r}{p_r + p_d} \right)^{0.7}, \quad (B-12)$$

$$p_d = 0; k_1 = 0 \quad \text{for } p_r \geq 0.3, \quad (B-13)$$

$$p_d = (2.2 + p_r)^{-1} - 0.4; k_1 = 0.6 - 2 p_r \quad \text{for } p_r < 0.3, \quad (B-14)$$

$$k_2 = 0.5 + 0.2 p_r^3 + k_1, \quad (B-15)$$

$$p_r = p/p_{crit}, \text{ and} \quad (B-16)$$

$$T = \frac{1}{q''(z) z} \int_0^z q''(z') dz' \quad (B-17)$$

The CHF is in MW/m², p is in MPa, G is in kg/m²-s, and D_h is in meters. Parameter T is the ratio of average heat flux from the channel inlet to the investigated coordinate z, over local channel heat flux. Eq. (B-17) was numerically approximated as

$$T = \frac{1}{q''_J \sum_{j=1}^J \Delta z_j} \sum_{j=1}^J q''_j \Delta z_j \quad (B-18)$$

where J is the node number at location z.

B.1.3 Bowring Correlation.

Bowring's correlation was obtained for water flow in heated vertical tubes with uniform heat flux. The correlation is given in the form [Bowring, 1972]:

$$q''_{CHF} = \frac{A + D_h G (h_f - h_{in})/4}{C + z} \quad (\text{B-19})$$

where

$$A = \frac{2.317 D_h G (h_g - h_f)}{4} \frac{F_1}{1 + 0.0143 F_2 \sqrt{D} G}, \quad (\text{B-20})$$

$$C = \frac{0.077 F_3 D_h G}{1 + 0.347 F_4 (G/1356)^n}, \quad (\text{B-21})$$

$$n = 2 - 0.00725 p, \quad (\text{B-22})$$

and coefficients F_1 , F_2 , F_3 , and F_4 are functions of pressure only. These functions are given in a tabular form. Linear interpolation was used to obtain in-between values. Alternatively, the coefficients are cited in a functional form by Hewitt in [Hetsroni, 1982].

B.1.4 Shah Correlation.

The improved Shah's correlation has the form [Shah,1987]

$$q''_{CHF} = Bo G h_{fg} \quad (\text{B-23})$$

where Bo is the boiling number, which is defined by an upstream condition correlation (UCC), or a local condition correlation (LCC), depending on Shah's correlating parameter

$$Y = \left(\frac{G D_h C_{pf}}{k_f} \right) \left(\frac{G^2}{\rho_f^2 g D_h} \right)^{0.4} \left(\frac{\mu_f}{\mu_g} \right)^{0.6} \quad (\text{B-24})$$

If $Y \leq 10^6$, the UCC is used. For $Y > 10^6$, the correlation that gives the lower value of Bo is used. The UCC correlation is defined as

$$Bo = 0.124 \left(\frac{D_h}{L_E} \right)^{0.89} \left(\frac{10^4}{Y} \right)^n (1 - x_{in,ef}) \quad (B-25)$$

where $n=0$ for $Y \leq 10^4$, and for $Y > 10^4$, n is defined by the following relations:

$$n = \left(\frac{D_h}{L_E} \right)^{0.54} \text{ for } Y \leq 10^6, \quad (B-26)$$

$$n = \frac{0.12}{(1 - x_{in,ef})^{0.5}} \text{ for } Y > 10^6. \quad (B-27)$$

The effective length, L_E , and effective inlet quality, $x_{in,ef}$, are given as

$$L_E = z \text{ and } X_{in,ef} = X_{in} \text{ for } X_{in} \leq 0, \quad (B-28)$$

$$L_E = z + \frac{D_h X_{in}}{4 Bo} \text{ and } X_{in,ef} = 0 \text{ for } X_{in} > 0. \quad (B-29)$$

The LCC correlation is expressed as

$$Bo = F_E F_x Bo_0, \quad (B-30)$$

where the entrance effect factor is

$$F_E = \max \left\{ \left(1.54 - 0.032 \frac{z}{D_h} \right), 0 \right\}, \quad (B-31)$$

and the boiling number at $x=0$ is defined as

$$Bo_0 = \max \left\{ 15Y^{-0.612}, 0.082Y^{-0.3} (1 + 1.45p_r^{4.03}), \right. \\ \left. 0.0024Y^{-0.105} (1 + 1.15p_r^{3.39}) \right\}. \quad (B-32)$$

The quality factor, F_x , is given for $x \geq 0$, by the following set of relations:

$$F_x = \left[1 + \frac{(F_3^{-0.29} - 1)(p_r - 0.6)^c}{0.35} \right] \quad (B-33)$$

where

$$F_3 = \left(\frac{1.25 \times 10^5}{Y} \right)^{0.833 x}, \quad (B-34)$$

$$c = 0 \text{ for } p_r \leq 0.6; \quad c = 1 \text{ for } p_r > 0.6 \quad (B-35)$$

For local quality $x < 0$, F_x is expressed as

$$F_x = \left[1 - \frac{(1 - F_2)(p_r - 0.6)}{0.35} \right]^c \quad (\text{B-36})$$

where factor F_2 , is defined via another factor F_1

$$F_1 = 1 + 0.0052 (-x^{0.88}) Y^{0.41} \quad \text{for } Y \leq 1.4 \times 10^7, \quad (\text{B-37})$$

$$F_1 = 1 + 0.0052 (-x^{0.88}) (1.4 \times 10^7)^{0.41} \quad \text{for } Y > 1.4 \times 10^7 \quad (\text{B-38})$$

such that

$$F_2 = F_1^{0.42} \quad \text{for } F_1 \leq 4, \text{ and} \quad (\text{B-39})$$

$$F_2 = 0.55 \quad \text{for } F_1 > 4. \quad (\text{B-40})$$

In the above equations, p_r is reduced pressure. Any consistent system of units can be used in Eq. (B-23) to obtain the CHF, since all correlating parameters are in dimensionless form. Note that the above equations are valid for all fluids except helium. The modified version of certain parameters for helium is given in the original paper [Shah,1987].

B.1.5 AECL Lookup Table.

A valuable source of CHF data for water was constructed by Groeneveld et. al. [Groeneveld et. al., 1986] at AECL. His lookup table is based on the Chalk River Nuclear Laboratories' CHF data bank, which contains more than 15000 CHF data points. It presents the CHF for 15 discrete values of pressures, 14 mass flux values and 21 local quality values, composed in a 3-D matrix. Linear interpolation is needed to obtain non-matrix values. To facilitate the use of the AECL table, the values were established on a separate disk file, which are read to a 3-D array in computer memory and interpolated per recommendations of Groeneveld [Groeneveld et. al., 1986], i.e., first interpolation with respect to pressure is performed, followed by interpolations with respect to mass flux and quality. Table data are based on vertical upflow in an 8mm-diameter tube, but correction factors are provided which enable application of the lookup table to other geometries. These factors are as follows:

subchannel or tube cross section factor which includes the diameter effect

$$K_1 = \left(\frac{0.008}{D_e}\right)^{1/3} \quad \text{for } 0.002\text{m} < D_h < 0.016\text{m}, \quad (\text{B-41})$$

$$K_1 = \left(\frac{0.008}{0.016}\right)^{1/3} \quad \text{for } D_h > 0.016\text{m}; \quad (\text{B-42})$$

bundle factor which predicts the correct trend in quality for rod bundles

$$K_2 = \min\{0.8, 0.8 \exp(-0.5 x^{1/3})\} ; \quad (\text{B-43})$$

grid spacer factor

$$K_3 = 1 + A \exp(-B L_{sp}/D_h), \quad A = 1.5 K_{form}^{0.5} (0.001G)^{0.2}, \quad B=0.1 ; \quad (\text{B-44})$$

heated length factor

$$K_4 = \exp\left(\frac{D_h}{z} e^{2\alpha}\right), \quad \text{for } \frac{z}{D_h} \geq 5, \quad (\text{B-45})$$

where α is the void fraction predicted by HEM;

axial flux distribution factor

$$K_5 = \frac{\bar{q}''_{js0}}{q''(z)} \quad \text{for } x \geq 0, \quad K_5 = 1.0 \quad \text{for } x < 0, \quad (\text{B-46})$$

where \bar{q}''_{js0} is the average heat flux from the axial location where $x=0$ to the location of interest, z ;

and flow factor for horizontal flow

$$\begin{aligned} K_6 &= 0 \quad \text{for stratified flow } (G < G_1) \\ K_6 &= 1 \quad \text{for nonstratified flow } (G > G_2) \\ K_6 &= \frac{G - G_1}{G_2 - G_1} \quad \text{for intermediate flow } (G_1 < G < G_2), \end{aligned} \quad (\text{B-47})$$

where the mass flux boundary between fully stratified and intermittent flow, G_1 , and the mass flux boundary between intermittent flow and annular flow, G_2 , are defined by Taitel and Dukler's [Taitel and Dukler,1976] flow regime map. A factor for vertical flow is also provided,

but it is not given here since the PTLWR design considers horizontal channels only.

The CHF value is finally calculated as

$$q''_{CHF} = K_1 K_2 K_3 K_4 K_5 K_6 q''_{CHF-table} \quad (B-48)$$

B.1.5 Katto Correlation

The Katto correlation [Katto, 1985] is a generalized correlation which covers a wide range of conditions and 14 kinds of coolants. Katto expressed the CHF data in terms of an inlet subcooling parameter, K and basic critical heat flux, q''_{co} , as

$$q''_{CHF} = q''_{co} (1 - K x_{in}) \quad (B-49)$$

The basic critical heat flux and the subcooling parameter are correlated in two regions, divided by the value of $\rho_v/\rho_l = 0.15$. In the first region for $\rho_v/\rho_l < 0.15$, three possible values of the basic critical heat flux are calculated first from the following set of equations:

$$\frac{q''_{co(1)}}{G h_{fg}} = C \left(\frac{\sigma \rho_l}{G^2 z} \right)^{0.043} \frac{D_e}{z} \quad (B-50)$$

$$\frac{q''_{co(2)}}{G h_{fg}} = 0.10 \left(\frac{\rho_v}{\rho_l} \right)^{0.133} \left(\frac{\sigma \rho_l}{G^2 z} \right)^{1/3} \left(1 + 0.0031 \frac{z}{D_e} \right)^{-1} \quad (B-51)$$

$$\frac{q''_{co(3)}}{G h_{fg}} = 0.098 \left(\frac{\rho_v}{\rho_l} \right)^{0.133} \left(\frac{\sigma \rho_l}{G^2 z} \right)^{0.433} \left(\frac{z}{D_e} \right)^{0.27} \left(1 + 0.0031 \frac{z}{D_e} \right)^{-1} \quad (B-52)$$

where

$$\begin{aligned} C &= 0.25 && \text{for } z/D_e < 50, \\ C &= 0.25 + 0.0009 (z/D_e - 50) && \text{for } 50 \leq z/D_e \leq 150, \text{ and} \\ C &= 0.34 && \text{for } z/D_e > 150. \end{aligned}$$

The final value of basic critical heat flux is determined as follows:

$$\begin{aligned} \text{If } q''_{co(1)} < q''_{co(2)} \text{ then } q''_{co} &= q''_{co(1)}. \\ \text{If } q''_{co(1)} > q''_{co(2)}, \text{ then } q''_{co} &= \min(q''_{co(2)}, q''_{co(3)}). \end{aligned}$$

The subcooling parameter is evaluated from the following equations:

$$K(1) = 1.043 \left[4C \left(\frac{\sigma \rho_1}{G^2 z} \right)^{0.043} \right]^{-1}, \quad (\text{B-53})$$

$$K(2) = \frac{5}{6} \left(0.0124 + \frac{z}{D_e} \right) \left[\left(\frac{\rho_v}{\rho_1} \right)^{0.133} \left(\frac{\sigma \rho_1}{G^2 z} \right)^{1/3} \right]^{-1}, \text{ and} \quad (\text{B-54})$$

if $K(1) > K(2)$ then $K = K(1)$,
if $K(1) < K(2)$ then $K = K(2)$.

For the region of $\rho_v/\rho_1 \geq 0.15$, two additional possible values of CHF are calculated:

$$\frac{q''_{co(4)}}{G h_{fg}} = 0.234 \left(\frac{\rho_v}{\rho_1} \right)^{0.513} \left(\frac{\sigma \rho_1}{G^2 z} \right)^{0.433} \left(\frac{z}{D_e} \right)^{0.27} \left(1 + 0.0031 \frac{z}{D_e} \right)^{-1}, \quad (\text{B-55})$$

$$\frac{q''_{co(5)}}{G h_{fg}} = 0.0384 \left(\frac{\rho_v}{\rho_1} \right)^{0.60} \left(\frac{\sigma \rho_1}{G^2 z} \right)^{0.173} \left(\frac{z}{D_e} \right)^{0.27} \left[1 + 0.280 \left(\frac{\sigma \rho_1}{G^2 z} \right)^{0.233} \frac{z}{D_e} \right]^{-1}, \quad (\text{B-56})$$

and the final value is determined from inequalities:

If $q''_{co(1)} < q''_{co(4)}$ then $q''_{co} = q''_{co(1)}$.
If $q''_{co(1)} > q''_{co(4)}$, then $q''_{co} = \max(q''_{co(4)}, q''_{co(5)})$.

The subcooling parameter is calculated from

$$K(3) = 1.12 \left[1.52 \left(\frac{\sigma \rho_1}{G^2 z} \right)^{0.233} + \left(\frac{z}{D_e} \right)^{0.27} \right] \left[\left(\frac{\rho_v}{\rho_1} \right)^{0.60} \left(\frac{\sigma \rho_1}{G^2 z} \right)^{0.173} \right]^{-1}, \text{ and} \quad (\text{B-57})$$

if $K(1) > K(2)$ then $K = K(1)$,
if $K(1) < K(2)$ then $K = \min(K(2), K(3))$.

Finally the CHF is obtained from Eq. (B-49) using the appropriate q''_{co} and subcooling parameter K .

B.2 TWO METHODS FOR CALCULATING THE CHF MARGINS IN SUBCOOLED OR LOW-QUALITY REGIONS

Two types of CHF correlations for the subcooled or low quality region have been proposed. The first type (type 1) has the form

$$q''_{CHF} = f(G, x, p, D_h) \quad (B-58)$$

or, if the effect of heated length, L , is taken into account

$$q''_{CHF} = f(G, x, p, D_h, L), \quad (B-59)$$

where G is the mass flux, p is pressure, x is local equilibrium quality and D_h is channel hydraulic diameter. Typical examples of these correlations (or CHF look-up tables) are the Biasi correlation [Biasi et. al., 1967] AECL look-up table [Groeneveld, 1986], and Russian CHF tables [Doroschuk, 1976].

If the local quality, x , is eliminated by incorporating the heat balance along the channel up to the point of interest, z , i.e.,

$$x = x_{in} + \frac{P_h}{G A h_{fg}} \int_0^z q''(z) dz, \quad (B-60)$$

where A and P_h are channel flow area and heated perimeter, respectively, the CHF correlation takes the form (type 2)

$$q''_{CHF} = f(G, x_{in} \text{ (or } h_{in}), p, D_h, z) \quad (B-61)$$

A typical example of the latter type is the Bowring correlation [Bowring, 1972]. There are some correlations which make an attempt to take into account upstream condition effects by introducing an inlet condition variable (x_{in} or h_{in}) but do not incorporate a full heat balance. These correlations have both the inlet condition and the local condition as parameters, i.e.,

$$q''_{CHF} = f(G, x_{in} \text{ (or } h_{in}), p, D_h, x). \quad (B-62)$$

Typical examples are Tong's correlation [Tong, 1967] and the PI-1 correlation [Pernica and Cizek, 1991]. This type of correlation will be further designated as a semi-local correlation.

Suppose that the objective is to find the margin to CHF along the channel, i.e., the DNBR(z). There are two approaches to perform this task. In the first approach, the local equilibrium quality at the axial position of interest, z, can be calculated using the heat balance and the operating heat flux, q''_{oper} ; this local quality is then directly substituted into the CHF correlation to obtain the $q''_{CHF-local}$. Then DNBR is calculated as the ratio of $q''_{CHF-local}$ to the operating heat flux, q''_{oper} .

$$DNBR = \frac{q''_{CHF-local}}{q''_{oper}} \quad (B-63)$$

This approach will be designated for further discussion as the local condition approach (designated L on the figures) since the CHF is calculated at local conditions. Another possible designation for this approach could be the "direct substitution method" since the local operating conditions are directly substituted into the CHF correlation.

The heat balance (HB) curve represents the heat balance equation from the inlet up to the fixed point of interest, z,

$$q''(z) = \frac{(x - x_{in})}{T P_h z} G A h_{fg} \quad (B-64)$$

where

$$T = \frac{1}{q''(z) z} \int_0^z q''(z') dz' \quad (B-65)$$

is the ratio of average heat flux from the channel inlet to the investigated coordinate z, over local channel heat flux. Figure B-1 shows two curves in quality-heat flux coordinates. If the heat flux is uniform, T equals unity so that the HB curve is linear with x, as shown on Figure B-1. For the operating heat flux, q''_{oper} , the local quality, x, at the fixed location z corresponding to this heat flux can be found on the HB curve (point OP).

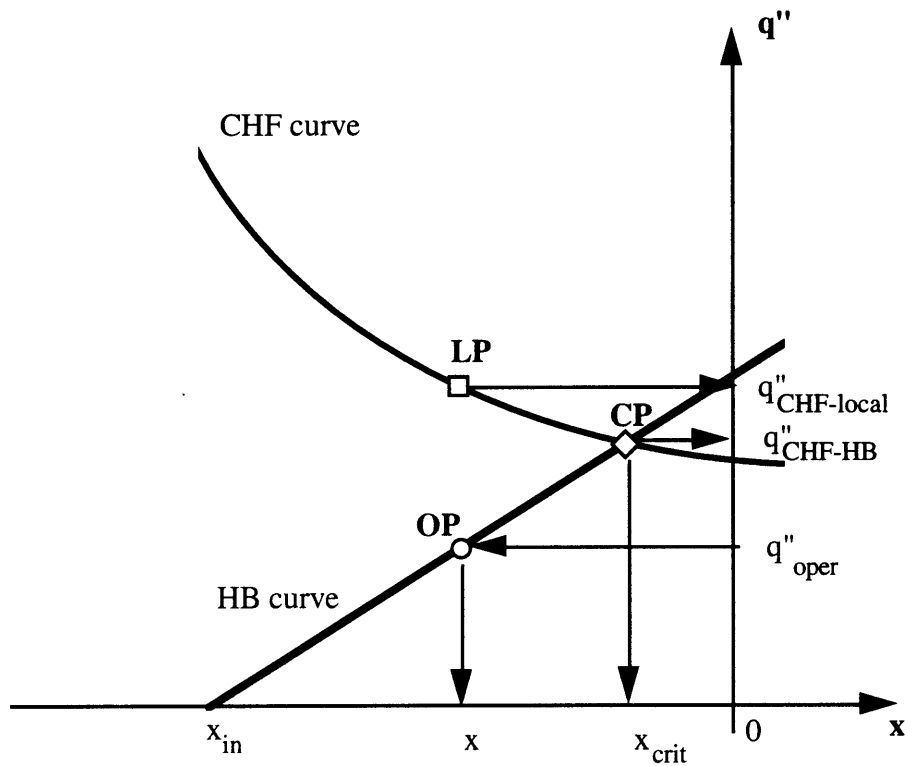


Figure B-1 Heat balance and CHF curves for uniform axial heat flux

The second curve is a typical CHF curve. The CHF correlation based on local conditions has a generally decreasing trend with x since CHF typically decreases as quality increases.

CHF by the local approach (LP point) can be found on the CHF curve from the local quality, x , i.e., using the local quality directly in the CHF correlation. In practice, the local condition approach has been used most often, since it is simple and does not require iterations. Many computer codes for reactor analysis such as COBRA, and RELAP, also use the local approach.

In the second approach, designated as the heat balance approach (HB), the $q''_{\text{CHF-HB}}$ at axial location, z , is calculated by varying the magnitude of the heat flux input into the channel, with the flux shape preserved, until the critical heat flux given by the CHF correlation at this given location is reached, i.e., a channel heat flux which achieves exactly critical conditions

at the point of interest, z , is found. In other words, one is looking for the intersection of the heat balance curve and the CHF curve, denoted in Figure B-1 as point CP (critical point). The CHF ratio is calculated as the ratio of $q''_{\text{CHF-HB}}$ over the operating heat flux, q''_{oper} ,

$$\text{DNBPR} = \frac{q''_{\text{CHF-HB}}}{q''_{\text{oper}}} \quad (\text{B-66})$$

The CHF ratio determined by the heat balance approach was designated the DNB power ratio (DNBPR) since it is closely related to critical power ratio. To find the intersection of the CHF curve and heat balance curve for type 1 correlations, an iterative process is necessary. One practical way to find the solution is to combine the heat balance equation (B-64) and the CHF correlation equation (B-58) as

$$\frac{(x - x_{\text{in}})}{T P_h z} G A h_{\text{fg}} - f(G, x, p, D_h) = 0 \quad (\text{B-67})$$

which can be solved for quality, x . The quality which satisfies Eq. (B-67) is the critical quality, x_{crit} , corresponding to the critical heat flux as defined by the heat balance method, $q''_{\text{CHF-HB}}$.

Note that the above iterative method is not necessary for the correlations of type 2, which effectively employ Eq. (B-67) as part of the correlation. The following discussion will deal with type 1 correlations (based on local conditions) or semi-local correlations.

The sketch in Figure B-1 indicates that the DNBR calculated by the local approach may be higher than that calculated by the heat balance approach. The magnitude of the difference depends on the correlation. If the slope of the CHF correlation is small, the difference is small, and vice versa.

Both approaches using the W-3 correlation, the AECL look-up table and the PI-1 correlation are compared on Figures B-2 through B-4. To make the case simpler, the geometry considered for this comparative study was a round tube with diameter of 8 mm and uniform heat flux of 1 MW/m². The other variables are mass flux $G=3000$ kg/s-m², pressure $p=10$ MPa, and inlet subcooling $x_{\text{in}}=-0.299$. All the parameters fall within the recommended range of the above correlations. Moreover, the tube diameter

of 8 mm corresponds exactly to the tube diameter for which the AECL look-up table experimental data were taken.

First, a type 1 correlation – the AECL look-up table – will be discussed. Figure B-2 shows that that for $DNBR \gg 1$, the local condition approach for the AECL look-up table gives much higher values than the heat balance approach. Groeneveld does not give any specific directions for table use in his 1986 paper, but he confirmed that the correct usage is the heat balance method [Groeneveld, 1993]. Note that this approach needs an iterative solution on a computer which, in essence, does not differ from other complicated correlations requiring computer implementation; hence the term “*lookup table*” is rather misleading, especially if one is looking into CHF margins. AECL lookup tables were also implemented into the RELAP5/MOD3 code. The report describing the implementation [Shumway,1989] does not suggest that the heat balance iterative approach was used, and it would not be surprising to find that the local approach was implemented. Because the CHF correlation in RELAP is mostly used for finding the correct heat transfer regime (rather than finding $DNBR > 1$), the local approach will give correct answers. However, the results with $DNBR \gg 1$ must be interpreted with caution since they will yield overestimated DNBR.

For the class of semi-local correlations, the PI-1 and W-3 correlations were evaluated. The PI-1 correlation is a semi-local correlation which includes recommendation of usage by the local approach. It gives very close results for both approaches, as can be seen from Figure B-3, even though it does not incorporate a full heat balance as part of the correlation. On the other hand, Figure B-4 shows that the W-3 correlation using the local approach gives a significantly higher prediction than the heat balance approach. Tong in his paper [Tong, 1967] defines the DNBR as a local ratio and recommends the local approach for his correlation.

He also confirms that this has been used as a design criterion and discussed thoroughly with licensing authorities in the past, and it is a well known fact that this approach gives higher values than does the power margin [Tong, 1993]. Also note that computer codes for reactor analyses

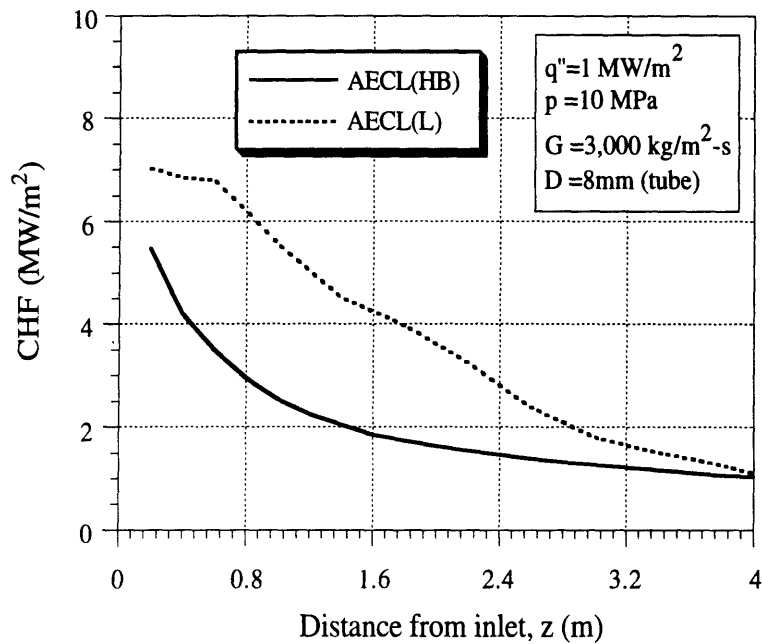


Figure B-2 Comparison of CHF from AECL lookup table evaluated from local and heat balance conditions

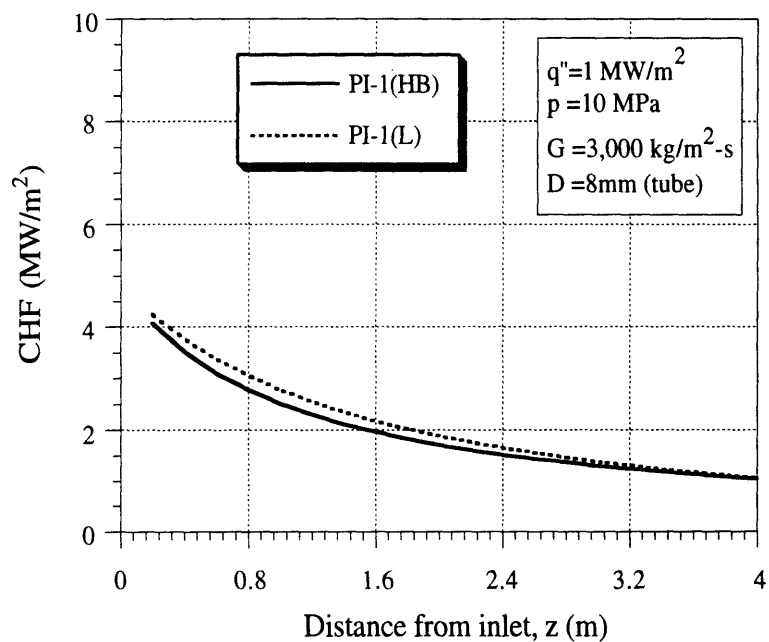


Figure B-3 Comparison of CHF from the PI-1 correlation evaluated from local and heat balance conditions

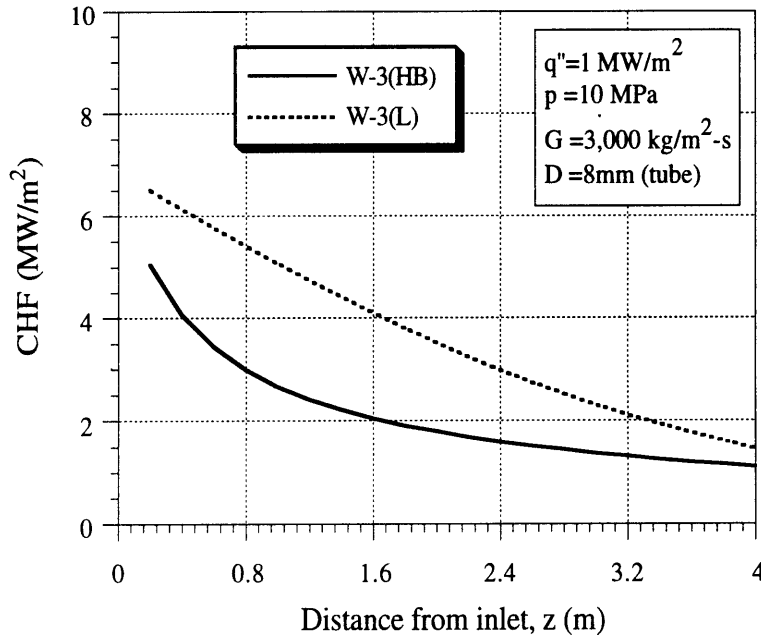


Figure B-4 Comparison of CHF from the W-3 correlation evaluated from local and heat balance conditions

such as COBRA, use the local approach in applying CHF correlations. But Figure B-4 suggests that this approach could overestimate DNBR if $DNBR > 1$, which is always the case in reactor analysis, where (in U.S. practice) the required $MDNBR \geq 1.3$ at 112% power. The question arises what is the $DNBR \gg 1$ predicted by the W-3 correlation using the traditional local approach. Two points can be made to show problems with this approach.

First, one would expect that comparing values of $DNBR > 1$ obtained from different correlations, if all parameters fall within the verified range for all correlations, would give reasonable agreement. And indeed, all three correlations converge to a good agreement using the heat balance approach, as shown in Figure B-5. Conversely, using the local condition approach, the discrepancies can be significant, as Figure B-6 suggests. Since only one CHF value can be correct at a given tube location, z , and since the CHF obtained from the AECL table by the heat balance method is correct (because the data were measured on an 8mm tube – the same as used in these calculations), it follows that the local approach for the W-3

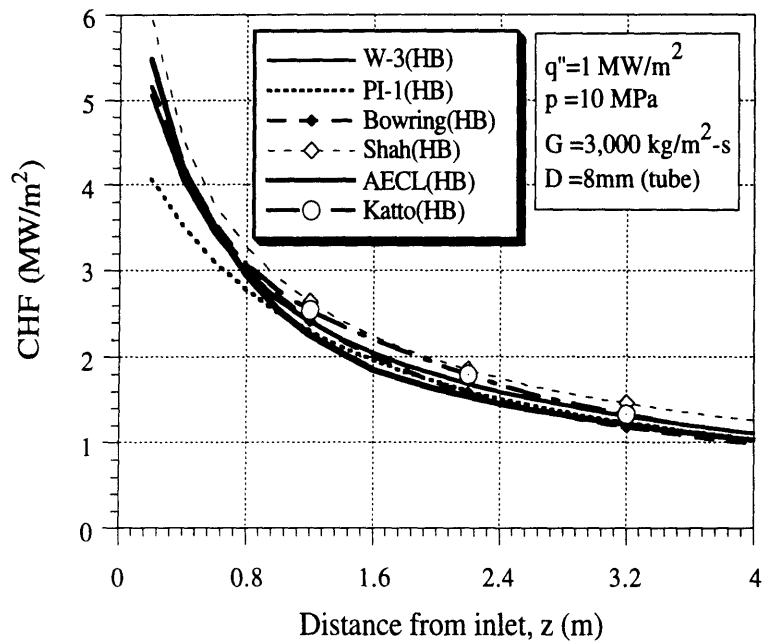


Figure B-5 Comparison of CHF correlations evaluated by heat balance method

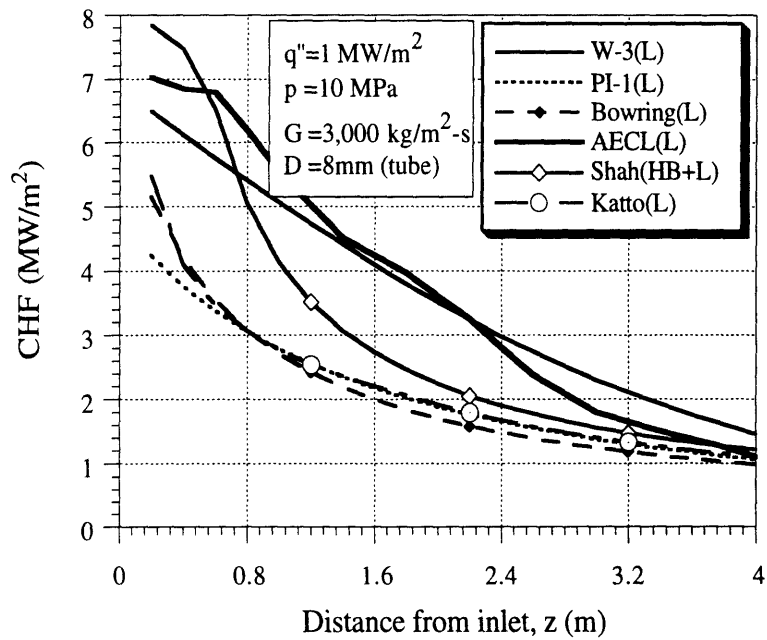


Figure B-6 Comparison of CHF correlations evaluated by local method

correlation will overestimate CHF for $DNBR \gg 1$. Secondly, the actual process in which the CHF at a given location in a channel would be achieved is by increasing the power (or decreasing the mass flux) to the channel until the CHF occurs. This process corresponds to the heat balance approach.

The above discussion shows that the heat balance method gives better results for the CHF margins than the local method. A similar conclusion was reached by Inasaka and Nariai [1992] who compared 10 CHF correlations, and in all 10 cases the HB method was found to give better results, sometimes by a large margin. Therefore the HB method will be used to evaluate the CHF margins in the PTLWR coolant channels.

B.3 COMPARISON OF THE SELECTED CORRELATIONS

All six selected correlations were evaluated by the heat balance method for the conditions experienced in the PTLWR coolant channels. The comparison for the central coolant channel and an intermediate coolant channel under normal operating PTLWR conditions is shown in Figure B-7 and Figure B-8. The heat flux profile was taken for the fresh core, i.e., almost uniform, with slight peaking near the ends of the channels.

The W-3 correlation prediction is shown only for the portion of the channel from about 3.5 m to the channel outlet at 6 m. At the locations below 3.5 m, the local quality is below -0.15, which is the lower limit of the validity range for the W-3 correlation. Since the W-3 results yield unreasonable CHF values outside the validity range for local quality, the data below this limiting quality were discarded. But even discarding these data, the W-3 results still significantly overpredict other correlations. This is probably the consequence of higher mass flux than the recommended W-3 range. Hence, the W-3 correlation was discarded from further consideration.

The Bowring correlation consistently underpredicts CHF, as compared to other correlations. This finding is surprising, since the only parameter

outside the recommended range is the channel length, which is not a key factor. However, closer review of Bowring's correlation by Hewitt, [Hetsroni,1982] shows that the actual measurements for the entire range of tube diameters cited in most literature were performed only in a limited pressure range (around 10 MPa). For the PTLWR operating pressure of 15 MPa, Bowring measured CHF only for small tube diameters of about 2mm. Hence, the hydraulic diameters of the PTLWR coolant channels significantly exceed (by 4 to 10 times) the verified range. Shah also reports that the Bowring correlation was found to have large deviations outside the verified validity range [Shah, 1987]. This fact is further confirmed by comparing Figure B-5 and Figure B-8. While for the pressure of 10 MPa (Figure B-5), the agreement with other correlations is very good, this is not the case for the pressure of 15 MPa (Figure B-8). Hence, Bowring's correlation was discarded.

Although the parameters are outside the range recommended for the use of the PI-1 correlation, the predictions of the PI-1 correlation show reasonable agreement with AECL table data. This correlation is valid for

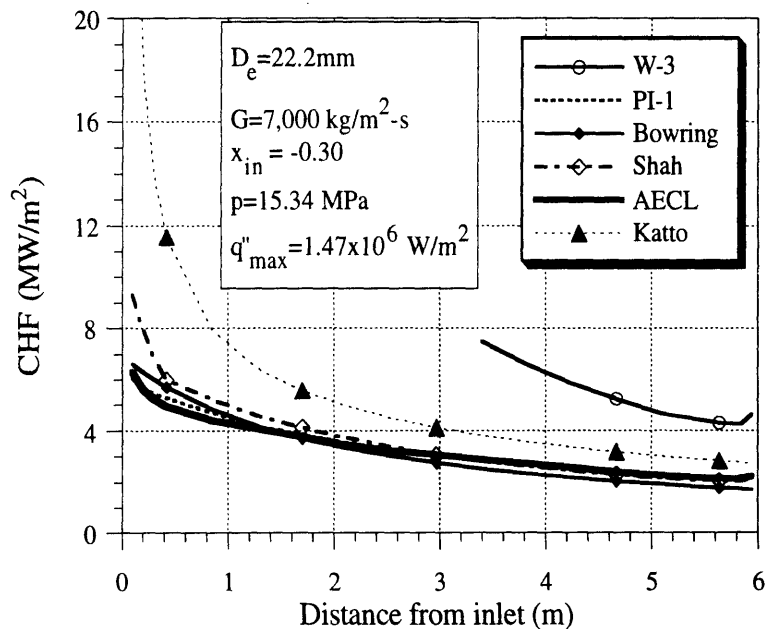


Figure B-7 Comparison of CHF correlations for the conditions of the central coolant channel

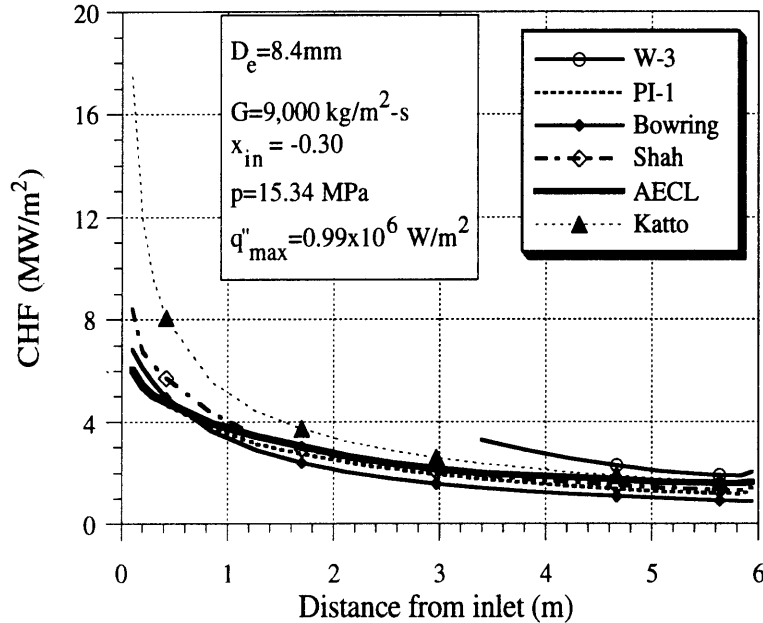


Figure B-8 Comparison of CHF correlations for the conditions of an intermediate coolant channel

bundle geometry, which can partially explain the discrepancy at low subcoolings. Since the PI-1 correlation is designed for bundles, it was discarded from further considerations.

The AECL lookup table, the Shah correlation and the Katto correlation are the only correlations under consideration that have a validity range large enough to envelope all the PTLWR operating conditions. The agreement among these three correlations is relatively good for both channels. The Katto correlation consistently predicts higher CHF values, especially at high subcoolings.

The AECL lookup table has been selected for the analysis of the PTLWR coolant channels because it is based on an extensive data base, and its CHF values for the PTLWR conditions fall in-between Shah's results and Katto's results. Also, the intermediate coolant channels have an inner diameter of 8.4 mm, which is very close to the test tube diameter of 8 mm for which the AECL data base has been obtained.

APPENDIX C

PASSIVE CONTAINMENT COOLING AND ANALYSIS

This appendix complements the containment analysis given in Chapter 11. It identifies air convection as a key resistance between the containment atmosphere and ambient air, and evaluates various alternatives to enhance the heat rate across this resistance. The main body of the appendix is devoted to the description of the methods used to analyze the alternatives considered. Two principal analysis codes have been developed – RISRAD and FINAIR. RISRAD is an improved version of the model of an annular riser described in [Hejzlar et. al., 1991]. It is intended for analyses of geometries with an annular gap for air flow, including radiative heat transfer and arbitrary inlet and outlet ducting. It was used for the alternatives of bare containment wall, bare containment wall with a tall chimney and ribbed containment wall. The program FINAIR is intended for the analyses of heated walls with fins, including arbitrary inlet and outlet ducting, and was used for the finned containment wall configuration. Code listings, sample input data and sample outputs are given in [Hejzlar, 1994].

C.1 CONTROLLING HEAT TRANSFER RESISTANCE BETWEEN CONTAINMENT ATMOSPHERE AND AMBIENT AIR

To achieve the objective of maximizing the heat transfer rate from containment atmosphere to the ultimate heat sink – ambient air, the major resistance to heat flow must be identified first. This can be easily done by considering a flat steel plate of the same thickness as the containment wall (e.g. 4cm) heated by condensation of hot steam on the inner side and cooled by convection to air on the outer side. Let us take as a reference typical values for the heat transfer coefficient for condensation in the presence of noncondensibles, $h_{con}=300 \text{ W/m}^2\text{-K}$, thermal conductivity of the steel wall $k=50\text{W/m-K}$, and the heat transfer coefficient to air under natural convection

$h_{\text{air}}=5 \text{ W/m}^2\text{-K}$. Figure C-1 shows the results for a constant temperature difference between containment atmosphere, T_{steam} , and ambient air, T_{air} . The curve “Steam side” was obtained by varying the heat transfer coefficient on the steam side while keeping the heat transfer coefficient to air and other variables constant, equal to their reference values. Conversely, the curve “Air side” was obtained by varying the heat transfer coefficient to air and keeping all other variables at their reference values. It is clearly seen that no noticeable increase in heat flux can be achieved even if the heat transfer coefficient on the steam side is increased by an order of magnitude. On the other hand, an increase in heat transfer coefficient on the air side yields a significant increase in the heat flux. The same conclusion can be drawn from Figure C-2 which shows the total resistance to heat transfer by increasing the heat transfer coefficients on both the steam side and the air side from their reference values up to 1000%. The removable power from the containment wall is controlled almost exclusively by heat transfer to air flow. Hence, all the effort will be focused on the enhancement of heat transfer to air flow.

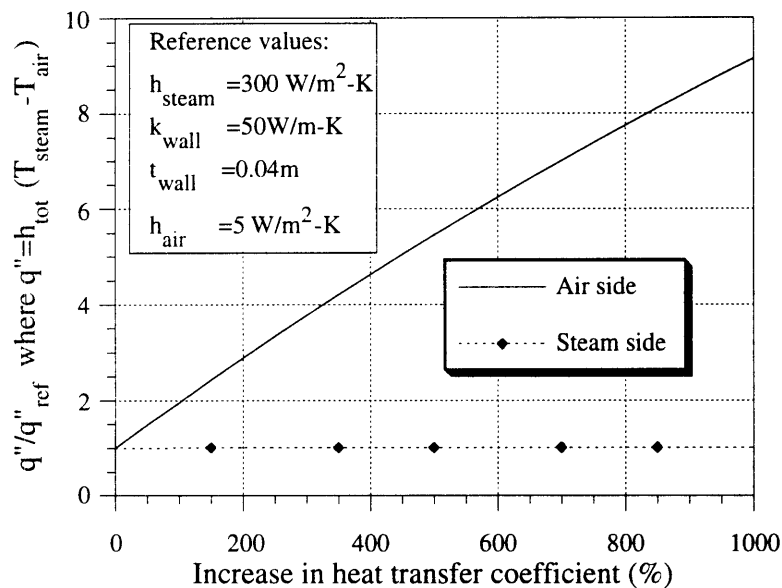


Figure C-1 Achievable enhancement of heat transfer through a containment wall by varying the heat transfer coefficient on the steam or air sides

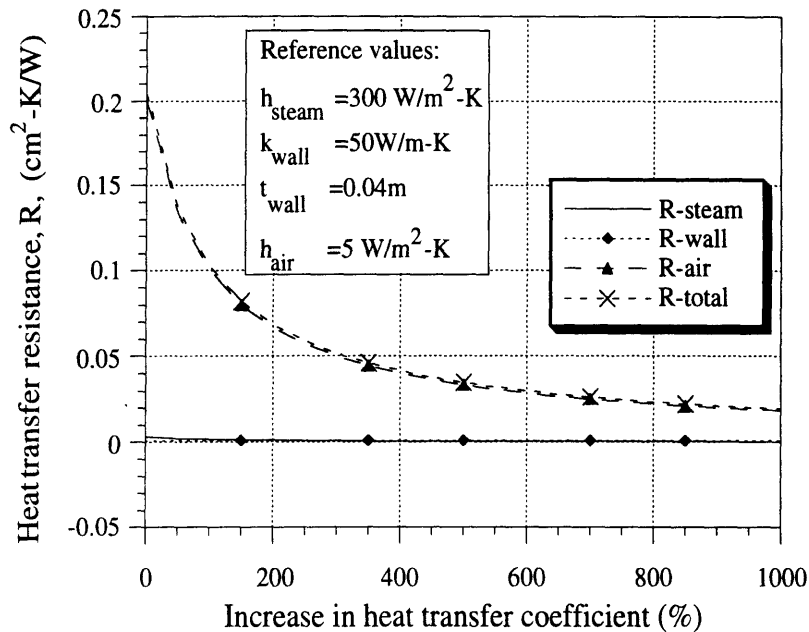


Figure C-2 Comparison of heat transfer resistances for the steam side, air side and steel wall

C.2 RISRAD - A COMPUTER PROGRAM FOR EVALUATION OF HEAT TRANSFER FROM A CYLINDRICAL BODY COOLED BY COUPLED CONVECTION TO BUOYANCY-INDUCED AIR FLOW AND RADIATION

C.2.1 Problem Formulation and the Assumptions Employed.

Several alternatives considered employ a containment steel shell surrounded by a shield wall; the difference is in the addition of a chimney or the treatment of the containment wall. These cases can be generalized to heat removal from a cylindrical body surrounded by a baffle such that an annular passage for air flow is provided. The model of a basic reference design shown in Figure C-3 will be described next. The body is surrounded by the duct wall around the entire circumference. The heat from the body is partially removed directly by convection to the air flowing through the annulus between the body and the duct wall, and partially by radiation to the cooler (outer) duct

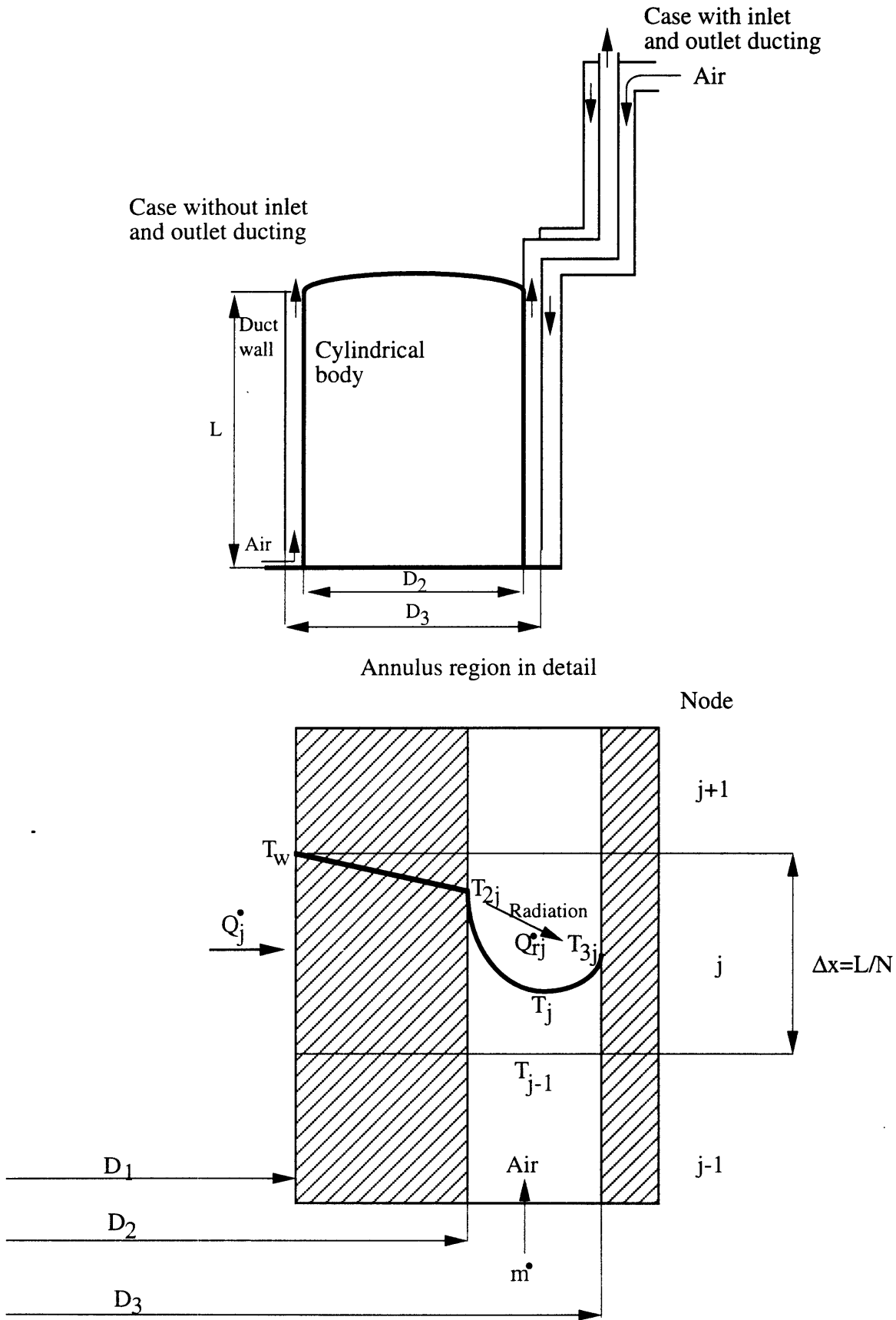


Figure C-3 Schematic of air cooling of a cylindrical body

wall and subsequent convection to the air flow. The arrangement can be such that the cold air intakes are located at the bottom and no stack above the cylindrical body is assumed or the air intake is located above the cylindrical body and cold air is brought to the body by downcomer ducting. To account for various potential arrangements, the model considers the general case. It is assumed that inlet ducting consists of N_1 nodes with different flow areas. Similarly, outlet ducting, including the exhaust stack, consists of N_2 nodes with different flow areas. Further, the outer wall of the cylindrical body is assumed to have either a constant heat flux or constant temperature boundary condition. The goal is to evaluate the heat rate removable from the cylindrical body in the configuration shown in Figure C-3.

The assumptions employed in the model are summarized as:

- steady state,
- the air flow is considered one dimensional, fully developed and turbulent,
- temperature on the inner cylindrical body wall is considered uniform along both axial and azimuthal coordinates (or the heat flux is assumed uniform),
- the surfaces participating in radiation are gray,
- the air inside the channel is a non-participating medium with respect to the radiation,
- acceleration pressure drop is neglected,
- the duct wall is perfectly insulated on the outside,
- the inlet ducting consists of N_1 nodes with different flow areas of arbitrary shape, and
- the outlet ducting consists of N_2 nodes with different flow areas of arbitrary shape.

C.2.2 Brief Description of the Model

C.2.2.1 Heat balance

As schematically shown in Figure C-3, the heated region (cylindrical body height) is divided into N equal nodes with the node length Δx . Define the heat transfer areas for the j -th node as

$$S_{2j} = \pi D_2 \Delta x \quad \text{and} \quad S_{3j} = \pi D_3 \Delta x$$

The total power conducted through the cylindrical body wall, \dot{Q}_j , is equal in the steady state to the power removed by the air, since the outside surface of the colder (duct) wall is assumed insulated, i.e.,

$$\dot{Q}_j = \dot{m} c_{pj} (T_j - T_{j-1}) = S_{2j} C_1 (T_w - T_{2j}) \quad (\text{C-1})$$

where

$$C_1 = \left[\frac{D_2}{2 k_{\text{wall}} \ln \frac{D_2}{D_1}} \right]^{-1}$$

The heat balance for the j -th node can also be written to reflect that the air is heated by convection from both bounding walls. The governing equation is

$$\begin{aligned} \dot{Q}_j &= \dot{m} c_{pj} (T_j - T_{j-1}) = \\ &= h_{2j} S_{2j} (T_{2j} - T_j) + h_{3j} S_{3j} (T_{3j} - T_j) \end{aligned} \quad (\text{C-2})$$

where the first term on the RHS of Eq.(C-2) denotes the power convected from the hotter (cylindrical body) wall and the second term denotes the power convected from the colder (duct) wall. Finally the power radiated from the hotter wall to the colder wall must be in equilibrium with the power convected to the air from this cold wall, since the outside surface of the cold wall is insulated.

$$\dot{Q}_{rj} = h_{3j} S_{3j} (T_{3j} - T_j) = C S_{2j} (T_{2j}^4 - T_{3j}^4) \quad (\text{C-3})$$

where

$$C = \sigma \left[\frac{1}{\epsilon_2} + \frac{D_2}{D_3} \left(\frac{1}{\epsilon_3} - 1 \right) \right]^{-1}$$

Eqs. (C-1), (C-2) and (C-3) are complemented by closure equations for heat transfer coefficients, h_{2j} and h_{3j} , and by an equation for air mass flow rate, \dot{m} . Convective heat transfer coefficients for the hot and cold wall, h_{2j} and h_{3j} , respectively are calculated from the correlations given in Section C.2.2.4.

C.2.2.2 Determination of Mass Flow Rate

The air flow rate is determined from the equation derived from the balance between buoyancy and pressure losses under the assumption of incompressible, one-dimensional fully developed turbulent flow.

$$\dot{m} = \sqrt{\frac{\Delta p_b}{c}} \quad (C-4)$$

The coefficient c represents the pressure drop due to the form and friction losses in the heated annular region, c_1 , and in the inlet and outlet ducting, c_2 .

$$c = c_1 + c_2, \quad (C-5)$$

$$c_1 = \sum_{j=1}^N (K_{c_j} + K_{f_j}) \frac{1}{2 \rho_j (A_j)^2}, \quad (C-6)$$

$$c_2 = \sum_{i=1}^{N_1+N_2} (K_{c_i} + K_{f_i}) \frac{1}{2 \rho_i (N_{R_i} A_i)^2} \quad (C-7)$$

where

N_1 = number of nodes with different flow areas from the air inlet up to the beginning of the heated region,

N_2 = number of nodes with different flow areas from the outlet of the heated region to the chimney outlet,

N_R = number of parallel flow paths in the ducting,

K_c = represents form losses, and

K_f = represents the friction factor, and is computed in the unheated region from [Idelchik, 1986]

$$K_{fi} = 0.11 \left(\frac{\zeta}{D_i} + \frac{68}{Re_i} \right)^{0.25} \frac{l_i}{D_i} \quad (C-8)$$

l_i and D_i are the length and hydraulic diameter for the i -th section of the unheated ducting, and ζ is the wall roughness. For heated nodalized regions, two cases are considered when evaluating the friction coefficient for the j -th node, $K_{fj} = f_{M,j} (\Delta x/D_e)$:

1. *Both the hot wall and the duct wall are smooth.* Then the Moody friction factor in the j -th node is given as [Idelchik, 1986]

$$f_{M,j} = 0.11 \left(\frac{\zeta}{D_e} + \frac{68}{Re_j} \right)^{0.25} \quad (C-9)$$

2. *Hot wall is fabricated with periodic ribs, duct wall is smooth.* Then the Fanning friction factor, f_j , on the hot wall is calculated first using Han's correlation [Han, 1977]

$$Re_j^+ (e_j^+) (\Phi/90^\circ)^{0.35} (\alpha/45^\circ)^{0.57} [10/(p/e)]^n = 4.9 (e_j^+/35)^m \quad (C-10)$$

where Re_j^+ and e_j^+ are defined as

$$Re_j^+ = \sqrt{2/f_j} + 2.5 \ln(2e/D_e) + 3.75, \text{ and} \quad (C-11)$$

$$e_j^+ = (e/D_e) Re_j \sqrt{f_j/2} \quad (C-12)$$

The repeated ribs placed on the hot vertical wall and the nomenclature used are shown schematically on Figure C-4. The exponents m and n are given as

$$\begin{aligned} m &= -0.4 \text{ for } e^+ < 35, & m &= 0 \text{ for } e^+ \geq 35; \text{ and} \\ n &= 0.53 (\alpha/90^\circ)^{0.71} \text{ for } p/e < 10. & n &= -0.13 \text{ for } p/e \geq 10. \end{aligned}$$

Note that Eqs. (C-10), (C-11) and (C-12) must be solved iteratively for the Fanning friction factor f_j . To account for the fact that the friction factor of the ribbed wall (surface $S_{2,j}$) is significantly higher than the friction factor of the smooth wall (surface $S_{3,j}$) the effective Moody friction factor of the channel is calculated as

$$f_{M,j} = \frac{4 f_j S_{2,j} + f_{M,3j} S_{3,j}}{S_{2,j} + S_{3,j}} \quad (C-13)$$

where $f_{M,3j}$ is the friction factor for smooth walls calculated from Eq. (C-9).

The Reynolds number in the j -th node of the heated region is defined as

$$Re_j = m \frac{D_e}{\mu_j A} \quad (C-14)$$

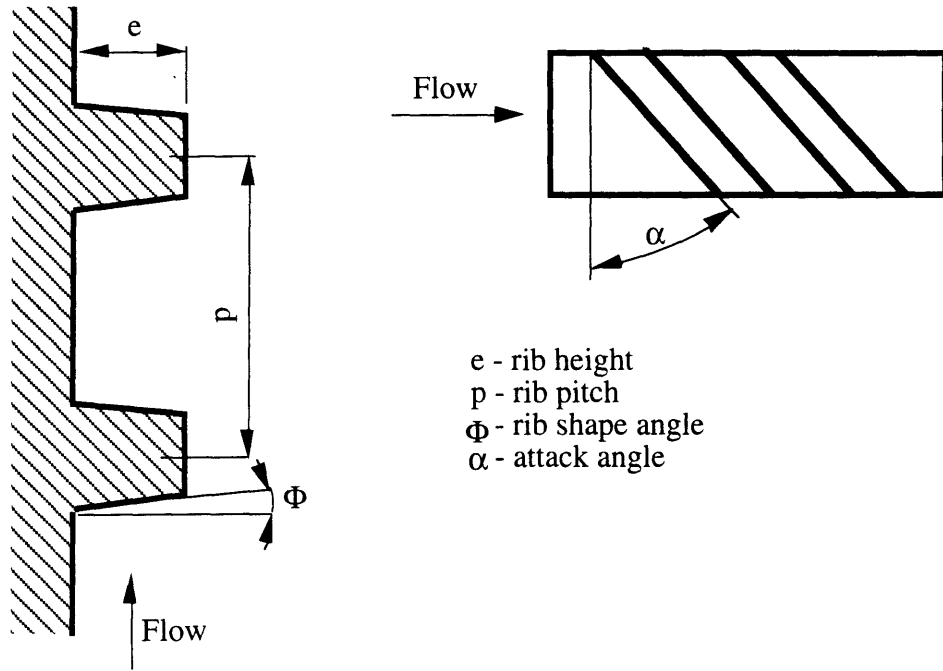


Figure C-4 Geometry and nomenclature for ribs on vertical wall

The dynamic viscosity, μ_j , thermal conductivity, k_j , and specific heat at constant pressure, c_{pj} , for the air are computed from polynomials as a function of the bulk average temperature in the node, e.g.

$$\mu_j = \sum_{i=0}^K A_i \bar{T}^i \quad (C-15)$$

where the polynomial degree, K , and the coefficients, A_j , are given in [Irvin,1984].

The thermal buoyancy is evaluated as

$$\Delta p_b = g \sum_{i=1}^{N1} \rho_i \Delta H_i - g \sum_{j=1}^N \rho_j \Delta x - g \sum_{i=1}^{N2} \rho_j \Delta H_j \quad (C-16)$$

where

ΔH is the elevation difference.

In equation (C-16), the first term denotes the buoyancy head in the section from the air inlet to the inlet of the heated region, the second term denotes the buoyancy head in the heated region and the last term denotes the buoyancy head in the exhaust ducting.

Air is treated as a perfect gas, and thus for the density the equation of state is used in the form

$$\rho_j = \frac{\bar{p}_j}{R \bar{T}_j} \quad \text{where } R = 287 \text{ J/kg-K} \quad (C-17)$$

Since the air flow rate, the heat transfer coefficients, h_{2j} and h_{3j} , and the Reynolds number are dependent on the unknown temperature, T_j , the solution is found through iteration.

C.2.2.3 Solution Procedure

The equations (C-1), (C-2) and (C-3) are solved for unknown temperatures T_{2j} , T_{3j} and T_j in the following manner:

First the temperature T_{2j} is found from Eq. (C-1)

$$T_{2j} = T_w - \frac{\dot{m} c_{pj}}{S_{2j} C_1} (T_j - T_{j-1}) \quad (C-18)$$

Temperature T_{3j} is found from Eq. (C-2)

$$T_{3j} = \frac{\dot{m} c_{pj} (T_j - T_{j-1}) - h_{2j} S_{2j} \left[T_w - \frac{\dot{m} c_{pj}}{S_{2j} C_1} (T_j - T_{j-1}) - T_j \right]}{h_{3j} S_{3j}} + T_j \quad (C-19)$$

Utilizing equations (C-18), (C-19) in Eq. (C-3) results in the following function $f(T_j)$

$$f(T_j) = T_j - K_1 - K_2 (T_{2j}^4 - T_{3j}^4) = 0 \quad (C-20)$$

where

$$K_1 = \frac{\dot{m} c_{pj} T_{j-1} + h_{2j} S_{2j} T_w + h_{2j}/C_1 \dot{m} c_{pj} T_{j-1}}{\dot{m} c_{pj} + h_{2j} S_{2j} + h_{2j}/C_1 \dot{m} c_{pj}}, \quad (C-21)$$

$$K_2 = \frac{C S_{2j}}{\dot{m} c_{pj} (1 + h_{2j}/C_1) + h_{2j} S_{2j}}, \quad (C-22)$$

and T_{2j} , T_{3j} are given by Eqs. (C-18), (C-19) respectively as a function of the unknown T_j . Equation (C-20) is then solved for T_j by the Newton iterative method. Once the temperature T_j is found, the temperatures T_{2j} and T_{3j} are computed from Eqs. (C-18), (C-19). There are three iteration loops performed — on mass flow rate, \dot{m} , the removed power $\dot{Q}_j = \dot{m} c_{pj} (T_j - T_{j-1})$ and outlet temperature T_N . Iterations proceed until the power conducted through the cylindrical body wall is equal to the power removed by the air circulation, the radiated power is in balance with power convected from the colder wall to the air, and the air flow pressure losses are in balance with the buoyant forces. A simplified flow diagram of the calculations is shown in Figure C-5.

For constant heat flux, the solution is simpler. Since the total heat flux, q'' , from the hotter wall is known, the bulk air temperature can be directly evaluated from an energy balance as

$$T_j = \frac{q'' S_i}{\dot{m} c_{pj}} + T_{j-1} \quad (C-23)$$

The temperature of the colder wall in the j -th node, T_{3j} , can be evaluated from equation (C-2) as

$$T_{3j} = \frac{\dot{m} c_{pj} (T_j - T_{j-1}) - h_{2j} S_{2j} [(T_{2j} - T_j)]}{h_{3j} S_{3j}} + T_j \quad (C-24)$$

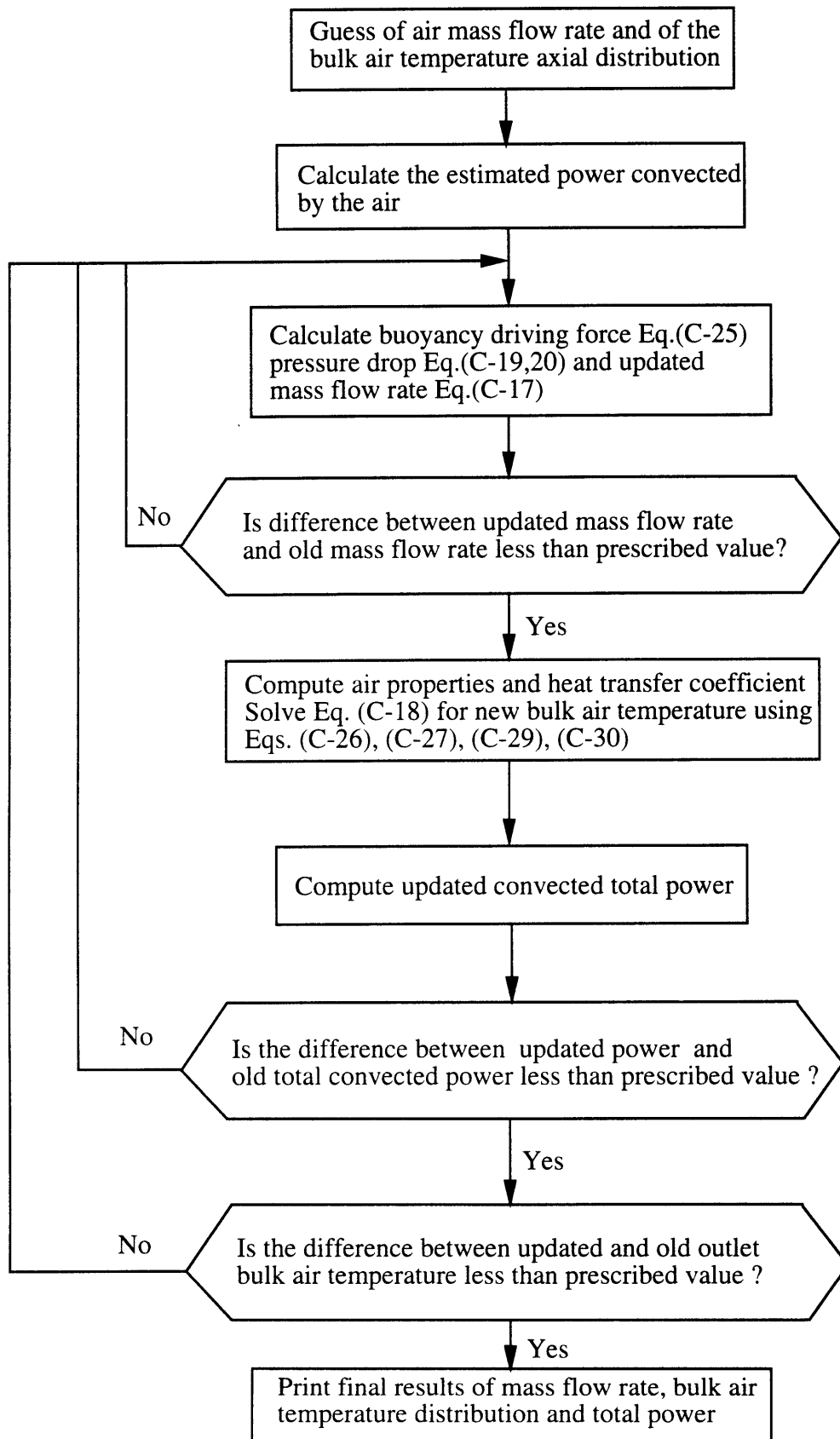


Figure C-5 A simplified flow diagram for the RISRAD code

The temperature of the hotter wall in contact with the air, T_{2j} , is obtained from equation (C-3), using for T_{3j} Eq. (C-24). The function for iterations on temperature T_{2j} is

$$f(T_{2j}) = S_{2j} C T_{2j}^4 - \left[\frac{\dot{m} c_{pj} (T_j - T_{j-1}) - h_{2j} S_{2j} [(T_{2j} - T_j)]}{h_{3j} S_{3j}} + T_j \right]^4 - S_{3j} h_{3j} \frac{\dot{m} c_{pj} (T_j - T_{j-1}) - h_{2j} S_{2j} [(T_{2j} - T_j)]}{h_{3j} S_{3j}} = 0 \quad (C-25)$$

Iteration loops for mass flow rate, removed power $\dot{Q}_j = \dot{m} c_{pj} (T_j - T_{j-1})$ and outlet temperature T_N are performed in the same manner as for the constant wall temperature problem. If the temperature on the inside surface of the body, T_{wj} , is of interest, it can be easily found from Eq. (C-1) as

$$T_{wj} = T_{2j} - \frac{\dot{m} c_{pj}}{S_{2j} C_1} (T_j - T_{j-1}) \quad (C-26)$$

A simple computer program written in FORTRAN 77 was developed on the basis of the equations given above, and used for evaluation of removable heat from the containment wall.

C.2.2.4 Correlation for the Heat Transfer Coefficient to Air Flow in an Annular Gap

Smooth wall

The correct value of the heat transfer coefficient between the ambient air and the riser walls is of primary importance. Unfortunately, experimental data for buoyancy-induced flows in annular geometry, and particularly for the large dimensions under considerations are extremely limited. This section will briefly review several correlations applicable to conditions of interest.

Attempts have been made to apply a natural convection correlation for turbulent flow along a vertical plate [Erbacher and Neitzel, 1992], in the form

$$Nu = 0.104 Ra^{1/3} \quad (C-27)$$

validated for a range of Rayleigh numbers from 9×10^9 to 1×10^{12} . Also, codes used for containment analysis such as GOTHIC [George et. al., 1991] apply this type of correlation. However, our calculations suggest that the buoyancy-induced flow in the narrow and tall annulus of typical containment dimensions falls into the forced convection regime, with Reynolds numbers up to 2×10^5 , rather than the free convection regime. Hence, the application of correlations appropriate for the natural convection regime, such as Eq. (C-27) using the Ra number, is inappropriate and may result in too conservative heat transfer rates. A forced convection correlation using the Re number is more appropriate.

This was confirmed by experimental measurements on an RVACS at Argonne National Laboratories (ANL) [Heineman et. al., 1988]. The correlation obtained from Argonne measurements is very close to the Dittus-Boelter forced convection correlation. Its form is

$$h_{2,j} = 0.0229 \text{ Re}_j^{0.8} \text{ Pr}_j^{0.4} \frac{k_{a,j}}{D_e} \left(\frac{T_w}{T_{a,j}} \right)^{-0.4} \left[1 + \left(\frac{z_j}{D_e} \right)^{-0.36} \right] \quad (\text{C-28})$$

where the ratio of the local wall temperature to the local air bulk temperature accounts for the large range of temperature differences between the wall and bulk air and the last term represents the development length. The ANL correlation was tested for a range of Reynolds numbers from 3×10^4 to 2.1×10^5 and z/D_e range from 0.56 to 13.35.

Another correlation for turbulent heat transfer in a vertical channel under conditions arising in decay heat removal from advanced reactors was developed by Sohn and Cheung [Sohn and Cheung, 1991]. Their correlation is based on numerical analysis using the two-equation k-D (with $D = \epsilon/\nu$) turbulent model of To and Humphrey [1986], which includes the effect of density fluctuations. Since there are several typographical errors in Sohn's paper, the correlation will be rewritten here. The Nusselt number in the developing region is given as

$$\text{Nu}_{2,j} = 0.0282 \text{ Re}^{0.676} \eta^{-0.0393} \left(\frac{2 \Omega_{H,j}}{1 + \gamma_{H,j}} \right)^{-0.0601} (x^+)^{-0.278}, \quad (\text{C-29})$$

$$\text{Nu}_{3,j} = 0.0282 \text{ Re}^{0.676} \eta^{-0.0393} \left(\frac{2 \gamma_{H,j} \Omega_{H,j}}{1+\gamma_{H,j}} \right)^{-0.0601} (x^+)^{-0.278} \quad (\text{C-30})$$

for the hot and cold walls, respectively. In the fully developed turbulent region, the Nusselt numbers for the hot and cold walls are correlated as

$$\text{Nu}_{2,j} = 0.105 \text{ Re}^{-0.0509} \eta^{0.298} \left(\frac{2 \Omega_{H,j}}{1+\gamma_{H,j}} \right)^{0.245}, \quad (\text{C-31})$$

$$\text{Nu}_{3,j} = 0.105 \text{ Re}^{-0.0509} \eta^{0.298} \left(\frac{2 \gamma_{H,j} \Omega_{H,j}}{1+\gamma_{H,j}} \right)^{0.245}, \quad (\text{C-32})$$

respectively. The location and the local Nusselt number at the transition point between the developing and fully developed regions is calculated as follows:

$$x_{2,\text{tr},j}^+ = 1.81 \text{ Re}^{1.24} \eta^{-0.824} \left(\frac{2 \Omega_{H,j}}{1+\gamma_{H,j}} \right)^{-0.812}, \quad (\text{C-33})$$

$$x_{3,\text{tr},j}^+ = 1.81 \text{ Re}^{1.24} \eta^{-0.824} \left(\frac{2 \gamma_{H,j} \Omega_{H,j}}{1+\gamma_{H,j}} \right)^{-0.812}, \quad (\text{C-34})$$

$$\text{Nu}_{2,\text{tr},j} = 0.0851 \text{ Re}^{-0.0108} \eta^{0.274} \left(\frac{2 \Omega_{H,j}}{1+\gamma_{H,j}} \right)^{0.270}, \quad (\text{C-35})$$

$$\text{Nu}_{3,\text{tr},j} = 0.0851 \text{ Re}^{-0.0108} \eta^{0.274} \left(\frac{2 \gamma_{H,j} \Omega_{H,j}}{1+\gamma_{H,j}} \right)^{0.270} \quad (\text{C-36})$$

for the hot and cold wall, respectively. The nondimensional coordinate x^+ is $1/G_z$ where G_z represents the Graetz number

$$G_z = \frac{\text{Re Pr}}{(z/D_e)}. \quad (\text{C-37})$$

If $x^+ < x_{\text{tr}}^+$ the flow is assumed to be in the developing region, if $x^+ \geq x_{\text{tr}}^+$, and the Nusselt number obtained from Eqs. (C-35) and (C-36) is less than the Nusselt number calculated by Eqs. (C-31) and (C-32), flow is assumed to be in the transition region, otherwise it is assumed to be in the fully developed region. The Reynolds number, Nusselt number, Prandlt number and Grashof

numbers for Eqs. (C-29) through C-36) are defined for air properties at the inlet; the other parameters are defined as follows (the properties are again defined at channel inlet):

gravity factor

$$\eta = \frac{\rho^2 g D_e^3}{\mu^2}, \quad (\text{C-38})$$

heat flux ratio (the ratio of convective heat flux from the cold wall, $q''_{3,j}$, and hot wall, $q''_{2,j}$)

$$\gamma_{H,j} = q''_{3,j}/q''_{2,j}, \quad (\text{C-39})$$

and the thermal loading factor.

$$\Omega_{H,j} = \beta \frac{(q''_{3,j} + q''_{2,j}) D_e}{k}. \quad (\text{C-40})$$

Note that for the developing and transition regions, the heat transfer coefficient is based on inlet temperature, T_{in} , while for the fully developed region it is based on bulk temperature, T_b . The Sohn and Cheung correlation was tested for the range of Re and Gr numbers $2,000 \leq Re \leq 2.5 \times 10^5$ and $1 \times 10^8 \leq Gr \leq 1 \times 10^{14}$, respectively.

Fu [Fu et. al., 1992] performed experiments on air in a long circular pipe for heated upflow at conditions close to those in MHTGR reactor cavity cooling system risers. Fu's correlation, which includes mixed convection effects, is given as [Fu et. al., 1991]

$$Nu_j = \frac{Nu_{MEj}}{1 + (5000/Re_j)^3} \quad (\text{C-41})$$

where the McEligot forced convection correlation is given by

$$Nu_{MEj} = 0.021 Re_j^{0.8} Pr_j^{0.4} \left(\frac{T_{w,j}}{T_{a,j}} \right)^{-0.5}. \quad (\text{C-42})$$

The Fu correlation is valid for $5 \times 10^3 \leq Re \leq 1 \times 10^6$ and a limited range of Grashof number, i.e., $1 \times 10^7 \leq Gr_q \leq 2.5 \times 10^8$.

The containment analysis code CONTAIN [Murata et. al., 1990] applies, for the forced convection heat transfer regime, a Dittus-Boelter type correlation, with higher multiplier (i.e., 0.037 instead of 0.023):

$$\text{Nu}_j = 0.037 \text{Re}_j^{0.8} \text{Pr}_j^{0.33} \quad (\text{C-43})$$

The Dittus-Boelter correlation is typically valid for a range of Re numbers from 10^4 to 10^6 . In CONTAIN, this forced convection correlation is applied if it produces higher Nusselt number than the turbulent natural convection correlation.

The Prandtl number in the j-th node of the heated region is based on node bulk temperature

$$\text{Pr}_j = \mu_j \frac{c_{p_j}}{k_j} \quad (\text{C-44})$$

Ribbed containment wall

The code incorporates the option of calculating heat transfer from a hot surface equipped with ribs to enhance heat transfer. The purpose of the ribs on the hot wall is to disturb the laminar sublayer of turbulent flow, which is the main thermal resistance in a wall-air interaction. This introduces more turbulence, and hence more effective heat transfer, near the wall. It was found experimentally that the friction factor and heat transfer coefficients depend on Re number, rib height to hydraulic diameter ratio, pitch to height ratio, rib shape and the flow attack angle. This dependence has been obtained from extensive experiments on air flow between two plates and correlated by [Han, 1970] in the following set of equations

$$\text{H}_{e_j}^+ (\alpha/45^\circ)^a = 10 (e_j^+/35)^b, \quad (\text{C-45})$$

$$\text{H}_{e_j}^+ = \frac{[f_j/(2\text{St}_j) - 1]}{\sqrt{f_j/2}} + \text{Re}_j^+, \quad (\text{C-46})$$

where Re_j^+ and e_j^+ are defined by Eqs. (C-11) and (C-12). The Stanton number, St_j , in the j-th node is based on total area, including rib area, defined by

$$St_j = \frac{h_{2s,j}}{c_{pj} \dot{m}/A} \quad (C-47)$$

Exponents a and b depend on attack angle and roughness Reynolds number, respectively

$$\begin{aligned} a &= -0.45 \text{ for } \alpha \geq 45^\circ, & b &= 0. \quad \text{for } e^+ < 35, \\ a &= 0.50 \text{ for } \alpha < 45^\circ, & b &= 0.28 \text{ for } e^+ \geq 35. \end{aligned}$$

Since heat transfer Eqs. (C-1) and (C-2) are based on projected area, the heat transfer coefficient obtained from Han's correlation is increased by

$$h_{2,j} = h_{2s,j} (p+2e)/p \quad (C-48)$$

to account for the additional surface of ribbed vertical walls. Because of the relatively small contribution of the duct wall to the overall heat transfer (i.e. $\leq 20\%$), no ribs are considered on the duct wall. The heat transfer coefficient between the duct wall and air is calculated from the smooth-wall correlation.

C.2.2.5 Comparison of Smooth Wall Correlations

All the correlations reviewed above were incorporated into the RISRAD code and compared for typical conditions of a large containment (annulus height of 65m, annulus width of 0.5m and constant heat flux of 1220 W/m²). The results are presented in Figure C-6. Note that the heat transfer coefficient shown in Figure C-6 was calculated from the buoyancy-induced air flow, which is also dependent on the heat transfer coefficient itself.

The natural convection correlation, Eq. (C-27), designated h-nat in Figure C-6 exhibits typical values for natural convection along a vertical plate and is about one half of the values obtained from forced convection correlations. The natural convection correlation does not show any improvement over a heated vertical plate, i.e., it does not reflect the increased air velocity through the annulus. Hence, a natural convection correlation like Eq. (C-27) is not adequate for the conditions arising in the annulus.

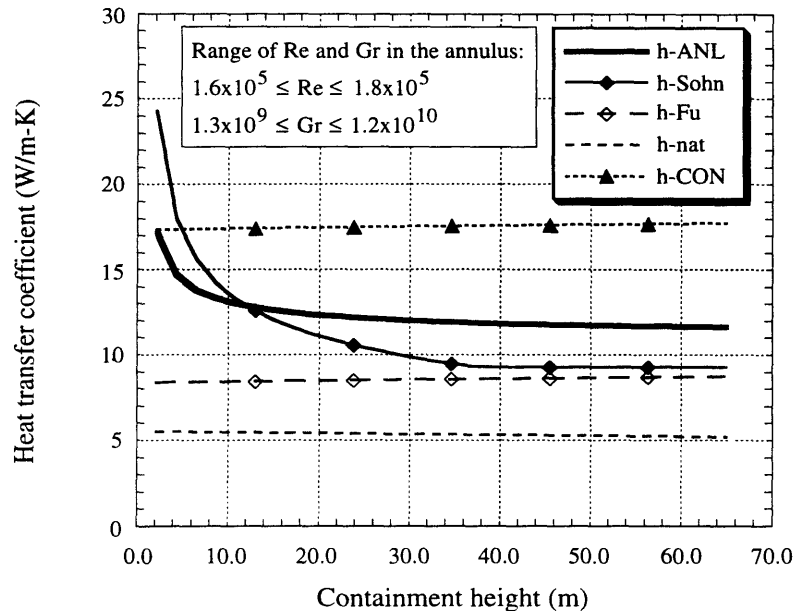


Figure C-6 Comparison of various correlations for heat transfer coefficient to air

Of the forced convection correlations considered, Fu's [Fu et. al., 1992] correlation gives the most conservative results. The advantage of Fu's correlation is that it incorporates mixed convection effects. It however, does not account for development length effects (although it is a local correlation) and the experiments were performed using a long circular pipe, which differs from annular geometry. Unless the flow falls into the mixed convection regime, which happens at a much lower Re numbers than those experienced in the gap, the Nu number can be approximated using forced convection correlations. Regarding the mixed convection effects, note that for Re numbers larger than 10^4 , results from Fu's correlation are identical to McEligot's forced convection correlation. Since the Re numbers in the annulus are on the order of 1.6×10^5 , the flow is clearly in the forced convection regime.

The forced convection correlation, Eq. (C-43), applied in the containment analysis code CONTAIN gives the highest values of the heat transfer

coefficient. This is because of the relatively large multiplier (0.037) in front of the Re number compared to the typical Dittus Boelter value of 0.023.

The Sohn and Cheung correlation is based on a physical turbulence model, hence it is applicable to the whole range of parameters for which the turbulence model is valid. Another advantage is that it gives separate correlations for the hot wall and the cold wall, taking into account the different velocities near both walls. The Sohn and Cheung correlation also suggests that the flow is thermally and hydrodynamically developing over a large portion of the channel. The heat transfer coefficient is significantly higher near the channel inlet than at the midplane, a fact not captured by the Fu or CONTAIN correlations. However, Sohn and Cheung's correlation is relatively complex, and more importantly, its validation against experimental data was very limited.

The ANL correlation (C-28) was verified in the range of Reynolds numbers between 0.3×10^5 and 2.1×10^5 . The Re number of 1.7×10^5 encountered in the annulus of the PTLWR containment falls within this tested range. Moreover, one of the wall temperatures (in constant wall temperature tests) was 122°C , which is also close to containment wall temperature for the proposed concept. It takes into account the developmental effects and falls in between the Fu correlation and the CONTAIN correlation. Compared to the Sohn and Cheung correlation, the ANL correlation lacks the capability to predict the difference between heat transfer coefficients at the hot and cold walls. This difference is, however, small and its effect on final results is negligible, so that the heat transfer coefficient between the duct wall and air, $h_{3,j}$, is evaluated also from Eq. (C-28). In reality, the velocity near the duct wall will be slightly lower than the air velocity near the hotter containment wall, as was confirmed by detailed numerical analysis [Cheung and Sohn,1990], and correspondingly, the heat transfer coefficient, $h_{3,j}$, will be lower than that predicted by Eq. (C-28). The error in total heat transfer rate will be small, since the heat flux from the duct wall is only about 20% of that from the heated wall. Also, applying the average velocity to determine the heat transfer coefficient for both the heated wall and the duct wall will lead to overall conservative values of heat transfer rate. This is because the real velocity in the hot-wall

boundary layer will be slightly higher than the average velocity calculated from the mass flow rate (giving higher real heat transfer coefficients $h_{2,j}$ than those calculated using the average velocity), and since the hot wall, which transfers much more energy by convection to air than the duct wall (about 80%), will contribute more to the total energy transfer, i.e., the effect of the underestimate of $h_{2,j}$ is by far more important with respect to the overall performance than the overestimate of $h_{3,j}$.

Based on the above discussion, the Argonne correlation was chosen for this analysis.

C.2.3 Verification of the RISRAD Code

Sufficient passive air cooling of the containment shell is a dominant factor in reducing containment pressure in the long term post-accident heat removal mode. Hence it is important that the uncertainty in the assessment of the heat transfer performance of the annulus is small. Since the analysis of the air passive cooling presented in this work relies heavily on the code RISRAD, it is desirable that RISRAD be validated against experimental data. A set of experimental data readily available from the MIT prefilled-water annulus experiment will be used for this purpose.

The prefilled water annulus experiment [Hwang, 1994] is being used to test passive containment shell cooling using an air-cooled annulus prefilled with water to enhance heat transfer rates in the initial stages of the accident. It can also be used for obtaining heat transfer data in a purely air-cooling mode. The detailed description of the apparatus is given in [Hwang, 1994]. The apparatus employs a 6m-high heated pipe surrounded by a baffle creating an annular space for air flow, with air intakes at the bottom. The baffle extends above the heated section to form a 15m-high insulated chimney, which provides an increased buoyancy driving force. The dimensions of the experiment are scaled such that the thermohydraulic conditions are close to those which would occur for a large power plant containment.

The above apparatus was modeled using the RISRAD code, and the results were compared to measured data. All input data needed for RISRAD

could be easily identified for the apparatus except for the emissivity of the heated stainless steel wall, which gives rise to some uncertainty. Therefore, the sensitivity of experiment performance with respect to this parameter was calculated. Figure C-7 shows the sensitivity of power removed by air and of the heat transfer coefficient to the emissivity of the heated stainless steel wall. It is evident that the contribution of radiation is not negligible. An increase in emissivity from 0.3 to 0.9 (i.e. 300% increase) increases the removable heat rate by about 40%. As a result the effective heat transfer coefficient defined here as

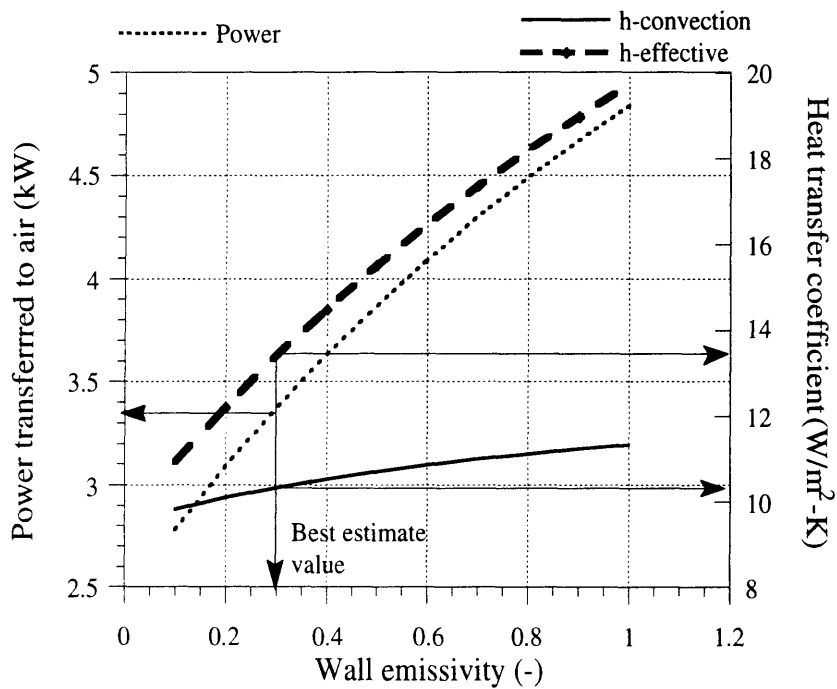


Figure C-7 MIT experiment - sensitivity to the emissivity of the hot wall

$$h\text{-eff} = \frac{\dot{Q}_{\text{tot}}}{S [T_w - (T_{a,\text{in}} - T_{a,\text{out}})/2]} \quad (\text{C-49})$$

is much higher than the real convection heat transfer coefficient defined as

$$h\text{-con} = \frac{\dot{Q}_{\text{tot}} - \dot{Q}_{\text{rad}}}{S [T_w - (T_{a,\text{in}} - T_{a,\text{out}})/2]} \quad (\text{C-50})$$

The best estimate value for the emissivity of annealed and polished stainless steel is around 0.3 [Touloukian, 1967]. The results for the best estimate value are also shown in Figure C-7 and compared with experimental data obtained in PRE_TEST02 [Hwang, 1994] in Table C-1. The agreement between code results and experimental data is excellent.

All key variables calculated by RISRAD agree very well with experimental data. The results confirm that the choice of the ANL heat transfer correlation is appropriate and that the code can model the performance of the air-cooled annulus adequately.

Table C-1 Comparison of RISRAD results with experimental data

Variable	RISRAD	Experiment PRE_TEST02	Error/Exper. uncertainty
Q_{tot} (kW)	3.37	3.36	0.3%/10.9%
h-eff (W/m ² -K)	13.39	13.42	0.2%/11%
\dot{m} (kg/s)	0.16	0.15	6%/2.8%
T_{out} (°C)	45.25	45.2	0.1%/1%
Re (-)	2.53E4	2.35E4	7.6%/9.6%

C.2.4 Heat Rate Removable from the Containment Wall

Four configurations have been analyzed:

- bare containment wall without chimney,
- bare containment wall with a tall chimney,
- ribbed containment wall without chimney, and
- grooved containment wall without chimney.

In all configurations, twenty screened inlet ducts with flow area of 5 m² each were chosen to bring the ambient air through the shield wall into the annulus. Similarly, a 72m² air outlet, also equipped with a screen, is adopted for all configurations. The other main parameters common to all configurations used in the analysis are:

- effective heated length of the containment shell 65m,
- containment shell outer diameter 60m,
- containment wall outer temperature 130°C,
- air inlet temperature 35°C.

C.2.4.1 Bare Containment Wall without Chimney

Power removable from the containment wall depends on the thickness of the annulus. This dependence is shown on Figure C-8. For a very narrow gap, the flow is too restricted, and large friction losses limit the flow rate, which leads to a large air temperature increase and a low temperature difference between the wall (kept constant) and bulk air temperatures. On the other hand, a large gap provides a large flow area and large air flow rates. This leads to low air heatup, small buoyancy driving force and low air velocity. Consequently, a decrease in heat transfer coefficient prevails over the increase in wall-bulk temperature difference, and the total power is decreased. The largest power of about 19 MWt is achieved for a gap thickness of 0.3 m. However, with respect to practical design considerations, a gap width larger than 0.3 m is desirable. Hence, a minimum gap thickness of 0.5m will be considered for more practical design purposes. A power of about 15 MWt is achieved using a gap thickness of 0.5m. This power level was introduced in Figure 11-2 in Chapter 11. Note that the optimum gap thickness also depends on the design of the air inlet and air outlet configuration. If the flow area of the ducting at the inlet and outlet is larger and the form losses smaller, the optimum shifts towards larger gap width. The heat transfer coefficient shown also on Figure C-8 is about 10W/m²-K for the gap width of 0.5m, which compares with about 5W/m²-K if the natural convection correlation of Eq. (C-27) is used. The contribution of radiation is

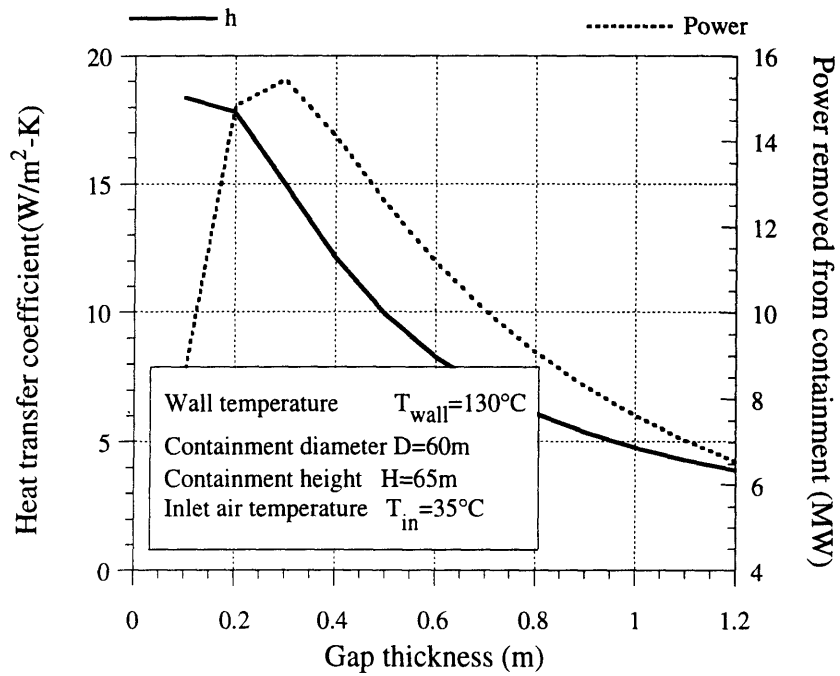


Figure C-8 Performance of the bare containment wall without chimney

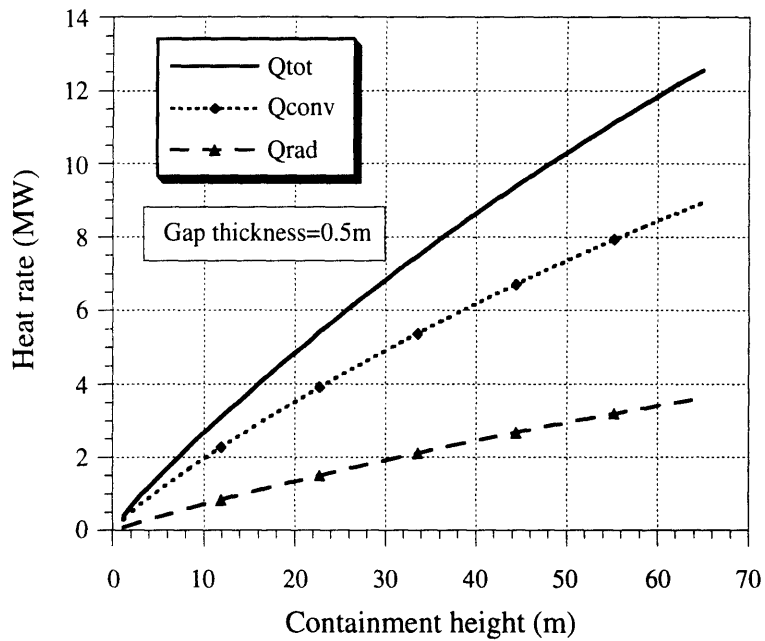


Figure C-9 Radiation, convection and total heat transfer rates from bare containment wall

not insignificant, as can be seen from Figure C-9, which was generated for a constant gap of 0.5m.

C.2.4.2 Bare Containment Wall with Chimney

The configuration with chimney has the same dimensions as the reference configuration of a bare containment wall. The chimney is assumed to have dimensions

- chimney height 85m,
- chimney inner diameter 10m.

Figure C-10 shows that the increase in power is about 53% compared to the case with bare wall containment. The disadvantage is a slight shift towards smaller optimum gap thickness than for the bare containment case (this is even more evident for larger flow areas of inlet and outlet ducting). Also, the cost of so tall a seismic-resistant structure would be high. The maximum achievable power of 18 MWt for a gap thickness of 0.5m was introduced in Figure 11-2 in Chapter 11.

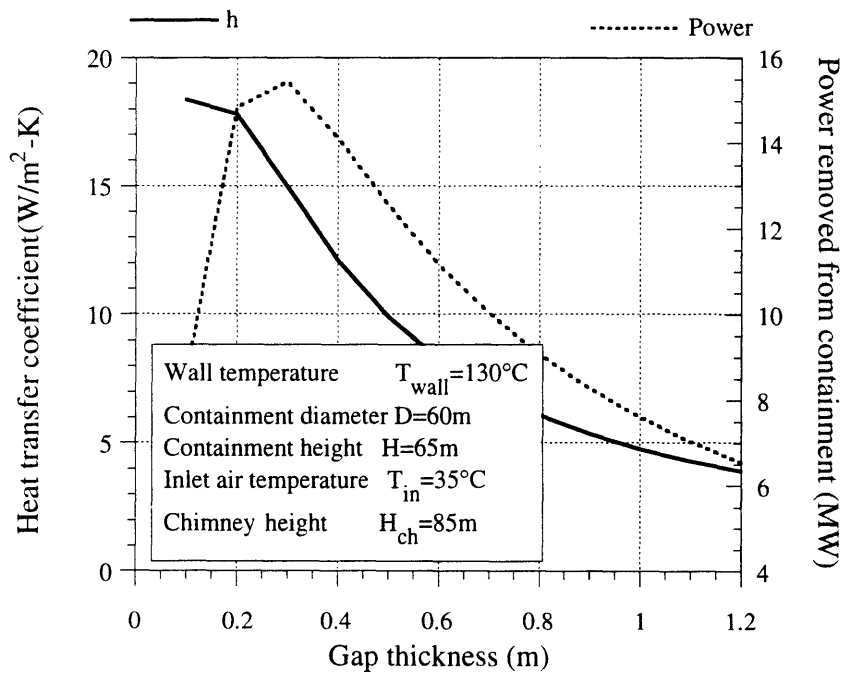


Figure C-10 Performance of the bare containment wall with chimney

C.2.4.3 Ribbed Containment Wall without Chimney

The configuration of this alternative is identical to the previous option except for periodically spaced ribs placed on the containment shell outer wall. For a given Reynolds number, the optimal thermal-hydraulic performance is given by a pitch to height ratio, $p/e=10$ [Han, 1970], [Zukauskas and Ziugzda, 1989] and for attack angle $\alpha=45^\circ$ [Han, 1970]. Using these optimum parameters and the shape angle $\Phi=55^\circ$ as fixed, optimum performance can be found by varying the gap thickness and the rib height. Figure C-11 shows achievable heat rate as a function of gap thickness for three rib heights. Note that the rib height to hydraulic diameter ratio varies for constant rib height, since the hydraulic diameter depends on gap thickness. Therefore, curves of fixed rib height are shown instead of more conventional e/D_e curves. Ribs with a height of 1cm spaced 10 cm apart give the best performance. A maximum achievable power of about 19 MWt for the optimum gap thickness was introduced in Figure 11-2, in Chapter 11. Figure C-11 shows that using ribs on the containment wall can increase removable power by about 25%, less

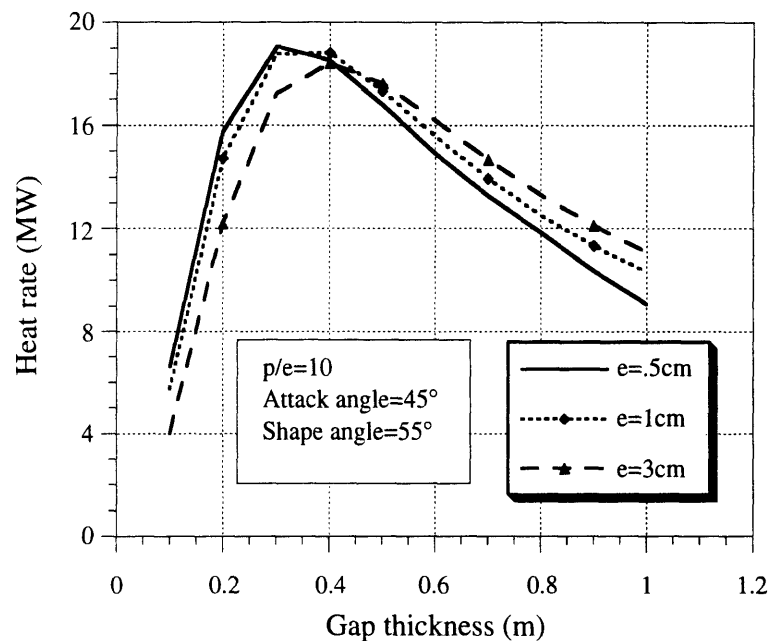


Figure C-11 Performance of the ribbed containment wall without chimney

gain than for the alternative with the high chimney. The advantage of this alternative is the shift of optimum annulus thickness to larger values than in the case of a bare wall, and a relatively low decrease in power beyond the optimum gap thickness. This would allow operation at higher power even for large gaps, which makes containment maintenance and inspection easier than small gaps.

C.3 FINAIR – A COMPUTER PROGRAM FOR EVALUATION OF HEAT TRANSFER FROM A FINNED CONTAINMENT WALL SURROUNDED BY A SUPPORTING SHELL

Finning the containment shell, and attachment of the fins to the outer annulus duct wall (surrounded by a concrete shield wall), as shown in Figure C-12, provides in addition to an increase in heat transfer, support for the steel shell, which can thereby withstand higher pressures. Note that the space between the fins, containment wall, and outer wall creates flow ducts for air: that is air risers. To analyze the heat transfer performance of such a system, a computer code was developed, which will be described next.

C.3.1 Description of the Model

Let us nodalize the axial height of the riser into N nodes and assume the temperature of the inner wall, T_w , constant over the entire axial length of the node. First, the derivation of effective heat transfer coefficient from the outer surface of the inner wall to the air will be given.

C.3.1.1 Derivation of Effective Heat Transfer Coefficient

Heat is conducted from the outer surface of the wall to the fin where part of the heat is convected to the air and the remaining part proceeds into the outer ring (duct wall). The heat flowing into the outer duct wall splits into two halves as shown schematically on Figure C-13. The heat flux from the outer ring to the reinforced concrete is assumed to be zero, hence all the heat

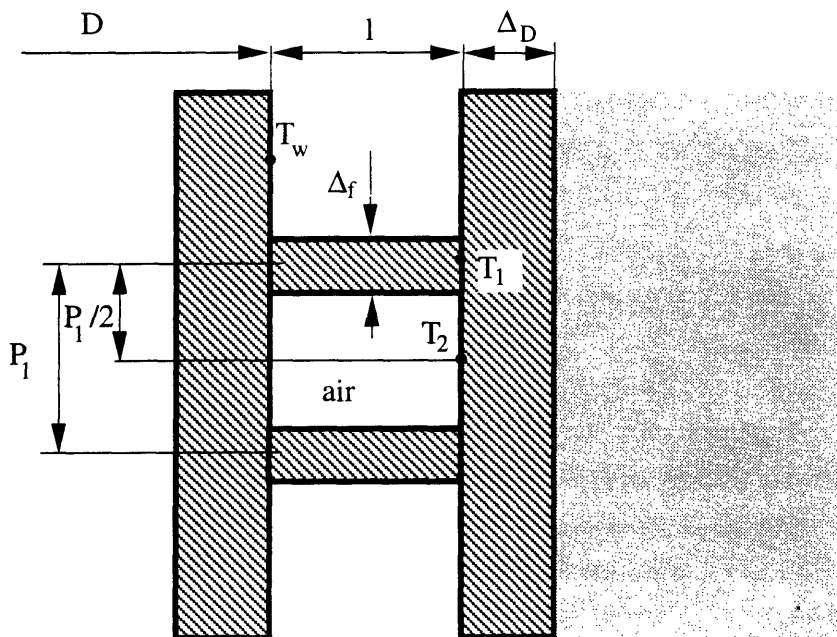
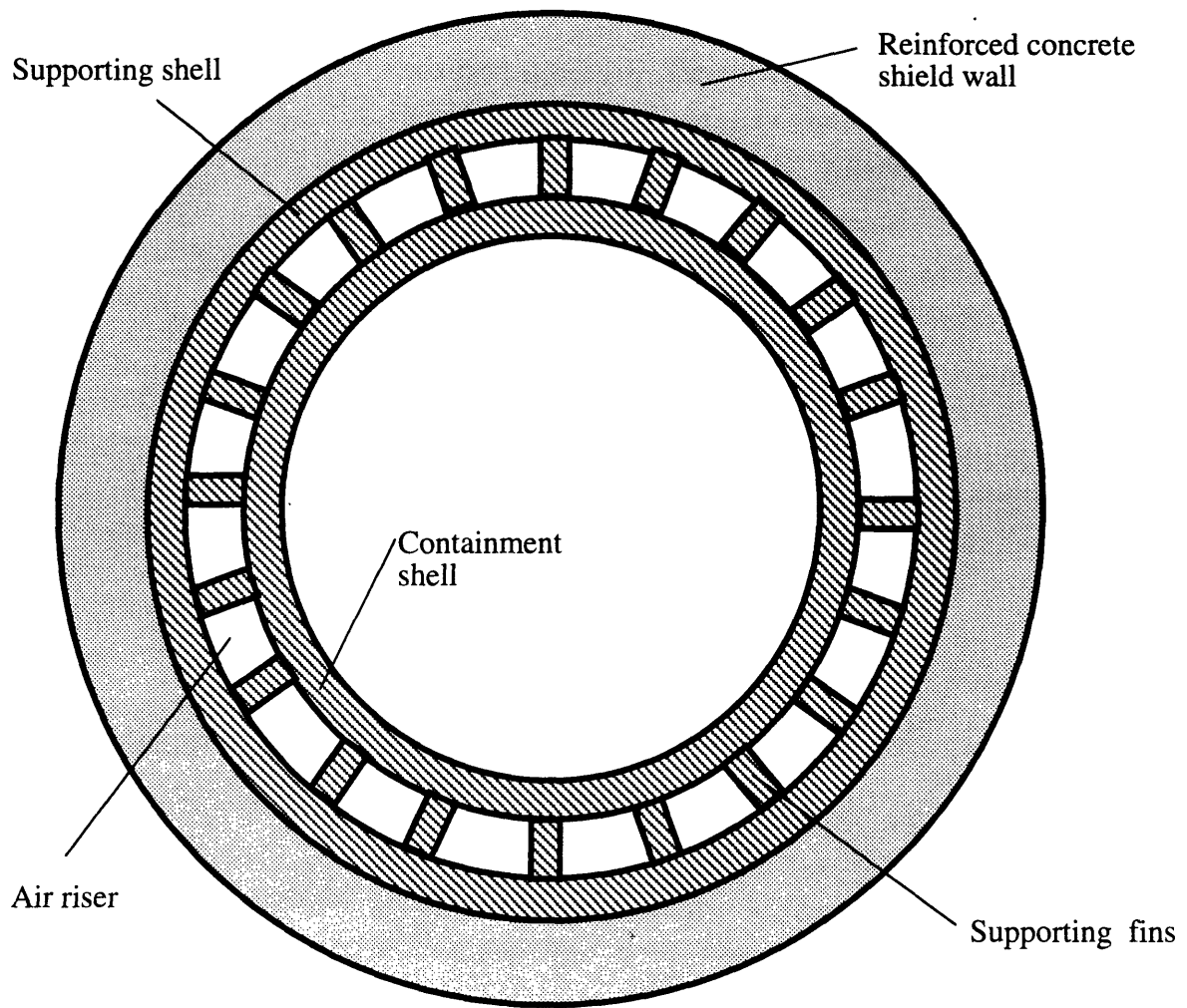


Figure C-12 Schematic of finned containment wall with supporting shell

from the outer ring is convected to the air. Because of symmetry, the heat flux at the distance $P_1/2$ from the fin midplane can be set to zero as shown in Figure C-13. Based on the above assumptions, the geometry from Figure C-13 is thermally equivalent to the geometry shown in Figure C-14, i.e., a two section fin. The duct wall part is substituted for by the second section, which has length equal to $P=P_1/2$, and is double the thickness of the duct wall. Note that radiation heat transfer between the hot wall of the inner ring and the colder walls of the outer ring and fins is neglected, hence the results will be conservative.

The conduction equation in the interval $0 < x_1 < l$ can be written as

$$\frac{d^2 (T - T_a)}{d x_1^2} = \frac{h_a \text{Per}_1}{k_1 S_1} (T - T_a), \quad (\text{C-51})$$

where the perimeter to conduction area ratio is defined as

$$\frac{\text{Per}_1}{S_1} = \frac{2 L_n}{\Delta_f L_n} = \frac{2}{\Delta_f}, \quad (\text{C-52})$$

and L_n is the axial length of the n-th node. Similarly, for the interval $0 < x_2 < P$, the conduction equation yields

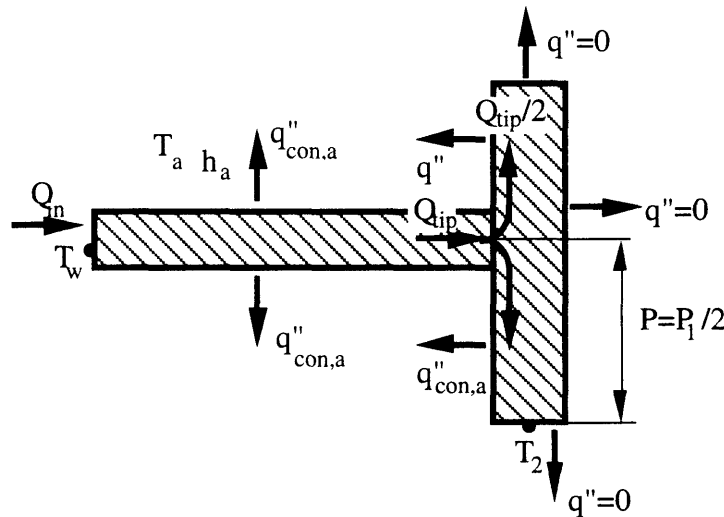


Figure C-13 Schematic of heat flow through the fin to the duct wall

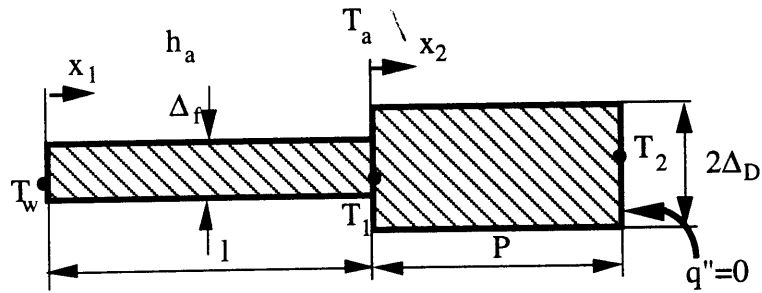


Figure C-14 Schematic of two section fin geometry

$$\frac{d^2 (T - T_a)}{d x_2^2} = \frac{h_a \text{Per}_2}{k_2 S_2} (T - T_a) \quad , \quad (\text{C-53})$$

with the perimeter to conduction area ratio

$$\frac{\text{Per}_2}{S_2} = \frac{2}{\Delta_D} \quad . \quad (\text{C-54})$$

Equations (C-51) and (C-53) and be normalized using the relative temperature

$$\theta = \frac{(T - T_a)}{(T_w - T_a)} \quad (\text{C-55})$$

and relative coordinates

$$\xi_1 = \frac{x_1}{l}; \quad \xi_2 = \frac{x_2}{P} \quad (\text{C-56,57})$$

as

$$\frac{d^2 \theta}{d \xi_1^2} = (m_1 l)^2 \theta \quad , \text{ and} \quad (\text{C-58})$$

$$\frac{d^2 \theta}{d \xi_2^2} = (m_2 P)^2 \theta \quad , \quad (\text{C-59})$$

where

$$m_1 = \sqrt{\frac{h_a}{k_1 (\Delta_f/2)}} ; m_2 = \sqrt{\frac{h_a}{k_2 (\Delta_D)}} \quad (C-60,61)$$

Boundary conditions imposed on Eqs. (C-58) and (C-59) are

$$\theta = 1 \text{ at } \xi_1 = 0, \quad (C-62)$$

$$\left[\frac{k_1 S_1}{l} \frac{d\theta}{d\xi_1} \right]_{\xi_1=1} = \left[\frac{k_2 S_2}{P} \frac{d\theta}{d\xi_2} \right]_{\xi_2=0}, \quad (C-63)$$

$$\theta_{\xi_1=1+} = \theta_{\xi_2=0-}, \text{ and} \quad (C-64)$$

$$\left[\frac{d\theta}{d\xi_2} \right]_{\xi_2=1} = 0 \quad (C-65)$$

Applying boundary conditions (C-62) through (C-65) to Eqs. (C-58) and (C-59), the solution for the temperature profile across the fin is obtained as

$$\theta = C_1 \exp(m_1 l \xi_1) + C_2 \exp(-m_1 l \xi_1); \quad \xi_1 \in (0,1) \quad (C-66)$$

$$\theta = C_3 \exp(m_2 P \xi_2) + C_4 \exp(-m_2 P \xi_2); \quad \xi_2 \in (0,1) \quad (C-67)$$

with the constants

$$C_1 = \frac{\exp(-m_1 l) (CC1+1)}{CC3 - CC2 (CC1)}, \quad (C-68)$$

$$CC1 = \frac{1-CC4}{1+CC4} \frac{k_2 \Delta_D m_2}{k_1 \Delta_f m_1}, \quad (C-69)$$

$$CC2 = \exp(m_1 l) - \exp(-m_1 l), \quad (C-70)$$

$$CC3 = \exp(m_1 l) + \exp(-m_1 l), \quad (C-71)$$

$$CC4 = \exp(m_2 P) / \exp(-m_2 P), \quad (C-72)$$

$$C_2 = 1 - C_1, \quad (C-73)$$

$$C_3 = \frac{C_1 CC2 + \exp(-m_1 l)}{1 + CC4}, \quad C_4 = C_3 CC4 \quad (C-74,75)$$

Fin efficiency is defined as the ratio of the heat dissipated over the total fin surface area, S_f , to that which would be rejected if the fin was isothermal at temperature, T_w , [Rohsenow,1973]

$$e = \frac{1}{S_f (T_w - T_a)} \int_{S_f} (T - T_a) dS_F = \frac{1}{T_w - T_a} \left\{ \left(\frac{T_w + T_1}{2} \frac{1}{1+P} \right) + \left(\frac{T_1 + T_2}{2} \frac{P}{1+P} \right) - T_a \right\} \quad \text{C-76}$$

To calculate the fin efficiency, temperatures T_1 and T_2 have to be evaluated first. This can be done using Eqs. (C-16) and (C-17) with $x_1=1$ and $x_2=P$, i.e.,

$$T_1 = T_a + (T_w - T_a) \{ C_1 \exp(m_1 1) + C_2 \exp(-m_1 1) \}, \quad \text{C-77}$$

$$T_2 = T_a + (T_w - T_a) \{ C_3 \exp(m_2 P) + C_4 \exp(-m_2 P) \}. \quad \text{C-78}$$

Note that temperature T_2 can be also calculated from Eq. (C-17) for $x_2=0$. This option can serve as a check on the correctness of the solution. Finally, the effective heat transfer coefficient between the base hot wall of temperature T_w and the air, in the n-th axial node, is computed as

$$h_n = \left(\frac{S_{w,n}}{(S_{w,n} + e S_{f,n}) h_{a,n}} \right)^{-1} \quad \text{C-79}$$

where

$$S_{w,n} = (\pi D - N_f \Delta_f) L_n, \quad \text{C-80}$$

$$S_{f,n} = N_f 2 (1 + P) L_n, \quad \text{C-81}$$

The heat transfer coefficient between the ambient air and the riser wall is evaluated from the ANL correlation [Heineman, 1991]

$$h_{a,n} = 0.023 \text{Re}_n^{0.8} \text{Pr}_n^{0.4} \frac{k_{a,n}}{D_e} \left(\frac{T_w}{T_a} \right)^{-0.4} \left[1 + \left(\frac{z_n}{D_e} \right)^{-0.36} \right] \quad \text{C-82}$$

where

$$\text{Pr}_n = \mu_{a,n} \frac{c_{p,a,n}}{k_{a,n}} ; \text{Re}_n = \dot{m}_a \frac{D_e}{\mu_{a,n} A_R N_R} \quad \text{C-83}$$

In Eqs. (C-82) and (C-83), N_R is the number of air risers, z_n is the axial coordinate of the n-th node, and D_e is the hydraulic diameter of the riser.

The heat rate transferred to the n-th axial node is written as

$$\dot{Q}_n = h_n \left(T_{w,n} - \frac{T_{a,n} + T_{a,n-1}}{2} \right) S_n = \dot{m}_a c_{p,n} (T_{a,n} - T_{a,n-1}) \quad (\text{C-84})$$

where the heat transfer area is defined by the relation

$$S_n = \pi D L_n. \quad (\text{C-85})$$

The dynamic viscosity, $\mu_{a,n}$, thermal conductivity, $k_{a,n}$, and specific heat at constant pressure, $c_{pa,n}$, for the air are computed from polynomials as a function of the bulk average temperature in the node, e.g.

$$\mu_j = \sum_{i=0}^K A_i \bar{T}^i \quad (\text{C-86})$$

where the polynomial degree, K , and the coefficients, A_j , are given in [Irvin,1984].

C.3.1.2 Determination of Mass Flow Rate

The heat transfer coefficient depends on air mass flow rate which, in addition on the riser geometry, depends on the arrangement of the inlet and outlet ducting and on the chimney height (if any of these features are employed). It is assumed that both inlet and outlet ducting are installed in several parallel paths to increase redundancy.

The air flow rate is determined from the equation derived from the balance between buoyancy and pressure losses under the assumption of incompressible, one-dimensional fully developed turbulent flow (neglecting the acceleration term)

$$\dot{m} = \sqrt{\frac{\Delta p_b}{c}}. \quad (\text{C-87})$$

The coefficient c represents the pressure drop due to the form and friction losses in the riser region, c_1 , and in the inlet and outlet ducting, c_2 .

$$c = c_1 + c_2, \quad (\text{C-78})$$

$$c_1 = \sum_{n=1}^N (K_{cn} + K_{fn}) \frac{1}{2 \rho_n (N_R A_n)^2}, \quad (C-79)$$

$$c_2 = \sum_{i=1}^{N_1+N_2} (K_{ci} + K_{fi}) \frac{1}{2 \rho_i (N_{Di} A_i)^2} \quad (C-90)$$

where

N_1 = number of nodes with different flow areas from the air inlet up to the beginning of the riser region,

N_2 = number of nodes with different flow areas from the outlet of the riser region to the chimney outlet,

N_D = number of parallel flow paths in the ducting,

N_R = number of risers,

K_c = form loss coefficient,

K_f = friction factor coefficient, which is computed in the heated region for the n-th node from [I.E.Idelchik, 1986]

$$K_{fn} = 0.11 \left(\frac{\zeta}{D_e} + \frac{68}{Re_n} \right)^{0.25} \frac{\Delta x_n}{D_e}; \quad (C-91)$$

for unheated regions

$$K_{fi} = 0.11 \left(\frac{\zeta}{D_i} + \frac{68}{Re_i} \right)^{0.25} \frac{l_i}{D_i}, \quad (C-92)$$

where l_i and D_i are the length and hydraulic diameter for the i-th section of the unheated ducting, and ζ is the roughness of the walls.

The thermal buoyancy is evaluated as

$$\Delta p_b = g \sum_{i=1}^{N_1} \rho_i \Delta H_i - g \sum_{n=1}^N \rho_n \Delta x_n - g \sum_{j=1}^{N_2} \rho_j \Delta H_j \quad (C-93)$$

where ΔH is the elevation difference.

In equation (C-93), the first term denotes the buoyancy head in the section of the ducting from the air inlet to the inlet of the heated section (risers), the

second term denotes the buoyancy head in the heated section and the last term denotes the buoyancy head in the exhaust ducting.

Air is treated as a perfect gas, and thus for the density the equation of state is used in the form

$$\rho_{a,n} = \frac{\overline{P_{a,n}}}{R \overline{T_n}} \text{ where } R = 287 \text{ J/kg-K.} \quad (\text{C-94})$$

Since the air flow rate, hot air temperature, $T_{a,n}$, the heat transfer coefficient and the Reynolds number are interdependent, the solution is found through an iterative process. There are three iteration loops performed: on mass flow rate, \dot{m}_a , hot air temperatures, $T_{a,n}$, and the removed heat $\dot{Q}_a = \sum \dot{m}_a c_{p,n} (T_{a,n} - T_{a,n-1})$. Iterations proceed until the conducted heat is equal to the heat removed by the air circulation, and the air flow rate is balanced with the buoyant forces. The computation procedure is very similar to the one presented on Figure C-5.

C.3.2 Achievable Heat Rates Removable from the Finned Containment Wall

Twenty inlet ducts were chosen to bring the ambient air through the shield wall into a lower plenum from where the air proceeds into the riser system. Heated air leaves the risers into an upper plenum and then it proceeds into the outlet (no chimney is used in this configuration). The dimensions of inlet and outlet ducts were taken the same as for the base case bare containment configuration. The main parameters of the fin cooling system used in input data are summarized below:

- effective heated length of the risers 65m,
- containment shell outer diameter 60m,
- fin length 0.5m,
- fin thickness 1cm,
- fin material Aluminum,
- containment wall outer temperature 130°C,
- air inlet temperature 35°C.

Since the removable heat rate depends on the flow area and hydraulic diameter of the riser, it is desirable to optimize riser dimensions. This optimization is performed for fixed length of the fin by varying fin number. The result is shown in Figure C-15. Figure C-15 shows that the optimum number of fins is about 1200. For a larger number of fins, the air flow passage is too tight, causing friction forces to dominate. A small number of fins results in a large flow area and in the small air velocity. Consequently, low heat transfer coefficient becomes a dominating factor responsible for a decrease of heat transfer rates. The next parameter to be optimized is the fin thickness, which affects fin effectiveness. Besides the fin thickness, fin effectiveness depends also on fin conductivity and the heat transfer coefficient. The dependence of the total effective heat transfer coefficient on fin thickness was explored, and it was found that the gain in the total effective heat transfer coefficient is small for fin thickness larger than about 1 cm. Hence the fin thickness of 1 cm was chosen.

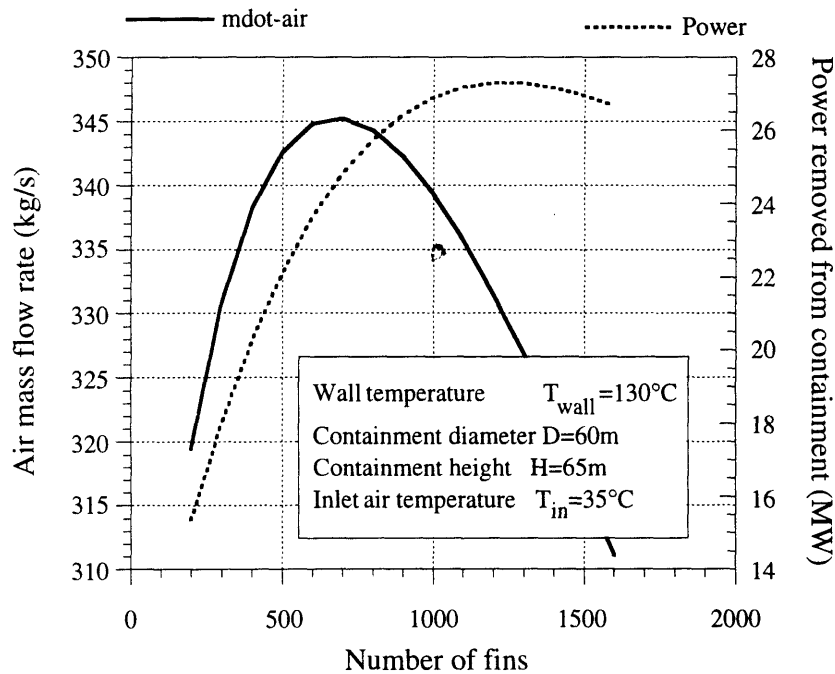


Figure C-15 Optimization of the number of fins

Figure C-15 shows that the achievable power which can be removed from the finned containment wall with 1200 aluminum fins is about 27 MWt. This heat rate was introduced in summary Figure 11-2 in Chapter 11.